

INTRAPLATE EARTHQUAKES AND THE STATE OF STRESS IN OCEANIC LITHOSPHERE

by

ERIC ALLEN BERGMAN

B.S., University of Arizona  
(1977)

SUBMITTED TO THE DEPARTMENT OF  
EARTH, ATMOSPHERIC, AND PLANETARY SCIENCES  
IN PARTIAL FULFILLMENT  
OF THE REQUIREMENTS  
FOR THE DEGREE OF

DOCTOR OF PHILOSOPHY

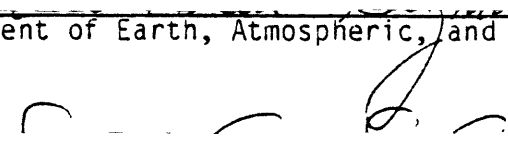
at the

MASSACHUSETTS INSTITUTE OF TECHNOLOGY


June 1984

© Massachusetts Institute of Technology 1984

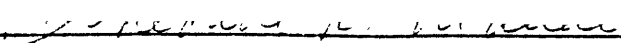
Signature of Author

  
Department of Earth, Atmospheric, and Planetary Sciences  
April, 1984

Certified by

  
Sean C. Solomon  
Thesis Supervisor

Accepted by

  
Theodore R. Madden  
Chairman, Department Committee

Eng.

MASSACHUSETTS INSTITUTE OF TECHNOLOGY  
**WITHDRAWN**  
**FROM** 1984  
**MIT LIBRARIES**

## INTRAPLATE EARTHQUAKES AND THE STATE OF STRESS IN OCEANIC LITHOSPHERE

by

ERIC ALLEN BERGMAN

Submitted to the Department of Earth, Atmospheric, and Planetary Sciences on April 27, 1984 in partial fulfillment of the requirements for the degree of Doctor of Philosophy in Geophysics

## ABSTRACT

Intraplate earthquakes are a primary source of information on the state of stress, internal deformation, and physical state of oceanic lithosphere. In order to better understand the relationship between oceanic intraplate seismicity and these important facets of lithospheric dynamics, we have conducted a systematic global survey of the distribution and source mechanisms of such earthquakes.

A catalog of oceanic intraplate earthquakes was constructed, based on a systematic search of the list of epicenters determined by the International Seismological Centre from January 1964 through December 1979. A notable feature of this catalog is that a special effort was made to represent accurately the seismicity in young oceanic lithosphere, which has been largely ignored in previous studies. Oceanic intraplate earthquakes prior to 1964 and since January 1980 have also been catalogued, but not in a systematic manner. The total number of oceanic intraplate earthquakes catalogued exceeds 1000.

By estimating the age of the lithosphere in which each event (for the years 1964 through 1979) occurred and assigning a seismic moment on the basis of moment - magnitude relations derived from the source studies conducted in this study, we investigated the pattern of seismic moment released per unit volume of seismogenic oceanic lithosphere as a function of lithospheric age. Oceanic lithosphere less than about 15 m.y. old accounts for a large fraction of the seismically-expressed deformation in oceanic lithosphere. After a sharp drop in activity at an age near 20 m.y., there appears to be a slow decline in moment release per unit volume, but the calculations in older lithosphere, in which few events have occurred in the last 20 years, may be strongly perturbed by occasional intense seismic episodes with repeat times much longer than the period of observation.

The source mechanisms of 58 of the largest events in the last 20 years have been determined by a formal inversion of long-period teleseismic P and SH waveforms, using a procedure developed by Nabelek [1984]. This technique yields reliable estimates of the centroid depth, double-couple mechanism, seismic moment, and source time function of the best-fitting point source, determined by a least-squares criterion applied to observed and synthetic waveforms. The inversion has significant advantages in efficiency and consistency over a forward modeling approach for the purpose of studying systematically a large number of earthquakes.

A broad region astride the Southeast Indian Ridge is found to have experienced, during the last two decades, a number of large earthquakes in lithosphere between 4 and 27 m.y. old. Nine of these events were studied with the body-waveform inversion method; all are characterized by normal faulting mechanisms with the T axis oblique or perpendicular to the local direction of spreading. Several of these events occurred at depths at which the temperature estimated from a simple plate-cooling model approaches 800°C. These earthquakes are therefore quite distinct from typical ridge axis earthquakes and also from intraplate earthquakes in older lithosphere, which are characterized by strike-slip or thrust-faulting mechanisms. A number of possible causes for these earthquakes are considered, but no single physical process appears to account for all the features of these events. Three events on the Antarctic plate are tentatively attributed to thermal and bending stresses associated with a positive depth anomaly between the Kerguelen Plateau and the Southeast Indian Ridge, the site of a proposed 'pipeline' in the upper mantle connecting the Kerguelen hotspot and Amsterdam and St. Paul Islands [Morgan, 1978]. The remaining events (in the Indian plate) are spaced along a significant portion of the Southeast Indian Ridge west of the longitude of the Ninetyeast Ridge, a feature which may act as an intraplate boundary between the two halves of the Indian-Australian plate. A speculative relationship between the near-ridge normal-faulting earthquakes and the response of the Indian plate to the continuing collision with Asia is suggested, but the mechanism is unknown. Another possibility, strengthened by a global survey of near-ridge earthquakes, is that relatively deep normal-faulting earthquakes occur with some regularity along all spreading ridge systems, and that this activity has been enhanced along the Southeast Indian Ridge. Small-scale convection beneath young oceanic lithosphere is an attractive source for such a perturbation, since there is independent evidence, in the form of high-resolution geoid height data, to support the existence of such a pattern of convection beneath young lithosphere of the Indian plate.

The northern Indian Ocean, in the vicinity of the Ninetyeast Ridge, is well known to be the most seismically active oceanic intraplate region on earth. We performed source studies of 11 earthquakes in this area, confirming the results of several previous studies and providing several new source mechanisms which help to delineate the character of the internal deformation of the northern Indian plate. These data support the view that the northern Ninetyeast Ridge is the site of partial decoupling between the Indian and Australian halves of the plate, stimulated by the abrupt change in boundary forces on the northern margin of the plate at this longitude. To the east, the plate subducts relatively smoothly at the Sunda Arc, while to the west, the northward motion of the plate is impeded by the continental collision between India and Asia. Consequently, there is little seismicity east of the Ninetyeast Ridge, but the ridge itself experiences frequent large earthquakes characterized by left-lateral strike-slip motion along the strike of the ridge. The lithosphere west of the ridge and in a region extending approximately from the equator to at least 11°N is dominated by north-south compression, which is expressed in a variety of deformational features in the sediments and acoustic basement. Earthquakes in this region occur throughout the

elastic core of the plate (to depths of 40 km below the seafloor) and are characterized by thrust faulting on planes striking east-west. Despite the strong variations in style of deformation and the presence of both major pre-existing zones of weakness and large bathymetric features, the principal stress orientations inferred from the focal mechanisms in this region define a consistent pattern: the direction of maximum horizontal compression appears to vary from nearly north-south in the Bay of Bengal to approximately northwest-southeast in the Wharton Basin east of the Ninetyeast Ridge.

Source studies were performed for 16 intraplate events in older lithosphere of the Pacific and Atlantic Oceans, accounting for virtually all recent large earthquakes in older oceanic lithosphere other than those in the northern Indian Ocean. The old oceanic lithosphere in the western Pacific is virtually aseismic. Most of these events appear to be associated with disturbed areas of the lithosphere, such as fracture zones or relict spreading centers. Many events in the Pacific are found in marginal or back-arc basins, where the source of stress relieved by them is difficult to identify. Several of the Atlantic earthquakes appear to represent a diffuse plate boundary zone between the North and South American plates, located east of the Lesser Antilles Arc. A zone of diffuse seismicity in the eastern Caroline Islands is associated with the reactivation of a plate boundary zone between the Caroline and Pacific plates, but no true plate boundary appears to exist at present and not all the earthquakes can be attributed to relative motion between the two plates. An unusually deep earthquake under Hawaii may be related to reactivation of the dormant volcano Mauna Kea.

An attempt was made to determine the source mechanisms of as many large earthquakes in young oceanic lithosphere as possible, in order to better understand the causes of the high level of seismicity found there. We were able to obtain source mechanisms for 31 such events, in all major oceanic regions. All types of focal mechanisms are observed, including thrust faulting in lithosphere as young as 3 m.y. and normal faulting in lithosphere as old as 35 m.y. Earthquakes with strike-slip mechanisms are frequently located on fracture zones, but the sense of offset is usually opposite that expected for a transform fault event. The P axes of thrust-faulting earthquakes frequently deviate from the orientation expected if 'ridge push' is a significant contributor to the stresses relieved by them. Normal faulting indicating extension in the direction of spreading apparently ceases very soon after plate creation. Normal-faulting events similar to those along the Southeast Indian Ridge are observed in other areas, but much less frequently. At any age up to 35 m.y., the deepest events are characterized by normal faulting, in all but one case with the T axis oriented oblique or parallel to the ridge axis. The one exception (T axis in the direction of spreading) occurred in young (4 m.y.) lithosphere along the Mid-Atlantic Ridge. This earthquake is similar to other near-ridge normal-faulting events in that the estimated temperature at the depth of the centroid (13.2 km) is approximately 800°C. This earthquake is therefore quite distinct from normal-faulting earthquakes occurring at the ridge axis, which are limited to very shallow depths. Thrust-faulting earthquakes are not observed below a depth of about 10 km,

but little activity of any sort occurs in the oceanic crust. Thermoelastic stresses related to the rapid early cooling of the lithosphere are an attractive explanation for several of these characteristics, including the observation of normal faulting at greatest depth, the sharp decline in seismicity at an age of about 15 m.y., the concentration of activity in the upper mantle immediately below the crust, and possibly the mechanisms and depths of some thrust faulting events. The higher levels of activity in some regions may be due to thermal perturbations from small-scale convection beneath the lithosphere.

Oceanic intraplate earthquakes appear to be reliable indicators of the state of stress in the source region, but several factors combine to reduce the likelihood that we will be able to exploit this conclusion to map out that portion of the intraplate stress field which is related to plate driving forces. One problem is that most oceanic intraplate seismicity occurs in young oceanic lithosphere and may be dominated by stresses related to the early tectonic evolution of oceanic plates. In old oceanic lithosphere there are few earthquakes, except in areas experiencing significant intraplate deformation. Vast expanses of old oceanic lithosphere remain unsampled and are unlikely to experience significant seismic activity over a reasonable period of time, because the old, stable plate interior is able to support elastically the relatively low ambient stress field due to such forces as 'ridge push'. Therefore, there may be a relatively narrow 'window' of oceanic lithosphere which can be effectively used to study the regional tectonic stress field. A tendency for thrust-faulting events to occur at shallower depths than strike-slip events may provide a means of estimating the magnitude of the principal stresses of the ambient lithospheric stress field, but further research is required to verify the generality of such an observation and to exploit it fully.

Thesis Supervisor: Dr. Sean C. Solomon, Professor of Geophysics

## ACKNOWLEDGEMENTS

My desire to be a scientist was largely stimulated by the example set by my grandfather, Dr. James A. Beal. My parents gave me confidence in my ability to accomplish anything I was willing to work for and showed remarkable patience with me during the years when nothing seemed worth the effort. My wife, Susan Saarinen, made innumerable sacrifices to give me the freedom to finish this thesis. She deserves most of the credit for making my career as a graduate student the most enjoyable and fulfilling time of my life (so far). The highest price for this accomplishment was paid by Katie, who is too young to understand why she saw so little of me in the last year. In return for frequent absences, she gave me unqualified love and appreciation; there can be no more effective remedy for the thesis blues than a few hours spent with such a child. Science is a quite self-indulgent pursuit, at least for me, and it is only fair to dedicate this thesis to the members of my family who encouraged and humored me for so long.

Speaking of indulgent, Sean Solomon deserves special thanks for allowing me the time and freedom to find my own way as a scientist at a time in my life when science was not always my highest priority. His instincts and ideas permeate my thesis work; my greatest hope as a scientist is that my future work may meet the standards I have learned from him.

Marc Sbar first steered me toward graduate school. Once I discovered I could be paid to be a student, I was hooked. It has certainly been an improvement over harvesting creosote bushes in the Arizona desert. Randy Richardson taught me how to do a first motion study and cautioned me against taking too seriously anything occurring within the confines of the Green Building. In addition, Marc's and Randy's theses provided the foundation for most of my research over the last six years. Wai-Ying Chung introduced me to synthetic bodywave techniques, which turned out to be vital to this research. John Nabelek was very generous with his time and knowledge when I was delving into his inversion programs (but he got a few things in return). My early years as a grad student were enriched in many ways by Dale Sawyer. Jim Muller engaged me in many instructive debates concerning bodywave modeling and auto mechanics and also played music at my wedding. Guerardo Suarez, Rob Comer, and Linda Meinke provided programs and data which facilitated much of the work in this thesis. Mary Baker collected numerous seismograms for me with nary a complaint. Jan Nattier-Barbaro provided frequent assistance with the processing of the numerous words in this thesis. Susan Saarinen did much of the drafting. Roy Wilkens offered much-needed relief from the thesis grind, in the form of a more-or-less open invitation to join him in various unproductive activities. He also encouraged me to finish my thesis by painting a glorious picture of life as a post-doc. He'd better be right. For everyone else who has read this far in the hope of finding their own name: don't worry, I haven't forgotten you.

This research was supported by the National Aeronautics and Space Administration under grant NAG5-44 and contract NAS 5-27339 and the National Science Foundation under grant EAR-8115908.

## TABLE OF CONTENTS

	Page
Abstract	II
Acknowledgements	VI
Chapter 1. INTRODUCTION	1
A Brief History of Oceanic Intraplate Earthquake Studies	3
Objectives of This Study	7
Thesis Outline	8
Chapter 2. A CATALOG OF OCEANIC INTRAPLATE EARTHQUAKES	
Introduction	12
An Expanded and Updated Catalog of Oceanic Intraplate Earthquakes	14
The Global Distribution of Oceanic Intraplate Seismicity	24
Magnitude - Frequency Relations	25
Seismic Moment Release as a Function of Lithosphere Age	28
Tables	34
Figure Captions	39
Figures	41
Chapter 3. SOURCE STUDIES BY BODY-WAVEFORM INVERSION	
Introduction	51
Body-Waveform Inversion Procedure	54
Pitfalls	59
Depth Resolution	65
Comparison - The 1966 El Golfo Earthquake	68
Comparison - The 1976 Friuli Earthquake	72
Tables	76
Figure Captions	78
Figures	80

Chapter 4. AN EXTENSIVE REGION OF NEAR-RIDGE NORMAL-FAULTING  
EARTHQUAKES IN THE SOUTHERN INDIAN OCEAN

Introduction	88
Southern Indian Ocean Tectonic Setting	89
Seismicity	91
Source Mechanisms	92
Stress Drop	99
Global Features of Near-Ridge Seismicity	100
Possible Causative Mechanisms for Normal Faulting	102
Tables	119
Figure Captions	122
Figures	126

Chapter 5. SOURCE STUDIES OF OCEANIC INTRAPLATE EARTHQUAKES IN  
THE NORTHERN INDIAN OCEAN

Introduction	140
Tectonic History of the Indian Plate	141
Source Mechanisms	145
Internal Deformation of the Indian Plate	156
Tables	167
Figure Captions	170
Figures	174

Chapter 6. INTRAPLATE EARTHQUAKES IN THE ATLANTIC OCEAN

Introduction	189
Source Mechanisms	189
Discussion	199
Tables	206
Figure Captions	208
Figures	211



## Chapter 7. INTRAPLATE EARTHQUAKES IN THE PACIFIC OCEAN

Introduction	225
Source Mechanisms	226
Discussion	238
Tables	244
Figure Captions	246
Figures	250

## Chapter 8. NEAR-RIDGE EARTHQUAKES AND THE TECTONIC EVOLUTION OF YOUNG OCEANIC LITHOSPHERE

Introduction	264
A Catalog of Near-Ridge Earthquakes	266
Source Mechanisms from Body-Waveform Inversion	268
Other Source Mechanism Data for Near-Ridge Earthquakes	282
Source Parameter - Age Relations	283
Near-Ridge Seismicity of the Indian Ocean	286
Deep Normal Faulting in Young Oceanic Lithosphere	289
Thermoelastic Stress and Near-Ridge Earthquakes	293
Secondary Convection beneath Young Oceanic Lithosphere?	296
Tectonic Evolution of Young Oceanic Lithosphere	297
Tables	302
Figure Captions	309
Figures	316

## Chapter 9. INTRAPLATE EARTHQUAKES AND THE STATE OF STRESS IN OCEANIC LITHOSPHERE: SUMMARY OF RESULTS

Introduction	356
Intraplate Earthquakes as Indicators of the State of Stress	357
Centroid Depth - Age Relations	360

Geographic Distribution of Seismicity and Lithospheric Stress	366
Summary	370
Figure Captions	375
Figures	376
References	378
Appendix A. Oceanic intraplate earthquakes 1906-1963	404
Appendix B. Oceanic intraplate earthquakes 1964-1983	410
Appendix C. Hawaiian seismicity 1964-1979	424
Appendix D. Gilbert Islands seismicity 1981-1983	428
Appendix E. Seismograph station codes and locations	433

## CHAPTER 1. INTRODUCTION

The theory of plate tectonics emerged in the late 1960's as a synthesis of two earlier concepts, continental drift and sea-floor spreading [Le Pichon, 1968]. Briefly, the plate tectonic hypothesis treats the lithosphere as being segmented into a small number of relatively rigid spherical caps or "plates", with horizontal dimensions much greater than their thicknesses. Steady relative motions between plates are the surface manifestation of the pattern of thermal convection in the mantle [Wilson, 1965; McKenzie and Parker, 1967; Morgan, 1968]. Magnetic lineations in the ocean basins provide a record of past plate motions and an estimate of present plate velocities [Vine and Matthews, 1963; Maxwell et al., 1970]. Most seismicity occurs at plate boundaries and the sense of relative plate motion is reflected in the style of faulting [e.g., Plafker, 1965; Sykes, 1967; Isacks et al., 1968]. Moreover, the timing and nature of major orogenies can be correlated with past plate boundary interactions, at least during the Cenozoic era [e.g., Atwater, 1970; Dewey and Bird, 1970].

A very small percentage of teleseismically-detected earthquakes are located away from the boundaries of the major plates [e.g., Barazangi and Dorman, 1969]. These "intraplate" earthquakes are largely ignored in first-order plate tectonics, which is simply a kinematic description of perfectly rigid lithospheric plates. However, as the focus of research has shifted to the dynamics of plate motions and the non-rigid behavior of the lithosphere, intraplate earthquakes have attained an importance far out of proportion to their numbers. This is because such earthquakes are a primary indicator of the extent and character of intraplate deformation and serve to delineate the

intraplate stress field, which is thought to reflect the distribution of plate boundary forces, i.e., the driving mechanism of plate tectonics. Many previous studies of intraplate earthquakes have focused on individual events [e.g., Mendiguren, 1971; Forsyth, 1973] or a small population with special relevance to a local tectonic problem [e.g., Stein and Okal, 1978]. There have been relatively few attempts [e.g., Sykes and Sbar, 1973; Sykes, 1978; Bergman and Solomon, 1980; and Wiens and Stein, 1983] to study intraplate earthquakes as a distinct class of seismicity, relevant to general questions concerning plate driving forces or the state of stress and mechanical properties of the lithosphere. With the goal of providing such a synthesis, this thesis is a comprehensive study of the distribution and source characteristics of intraplate earthquakes in oceanic lithosphere.

We have restricted consideration to oceanic regions for three main reasons: (1) Because of compositional differences, oceanic lithosphere conforms more closely than continental lithosphere to the model of thin rigid plates postulated by the plate tectonic theory. Also, oceanic lithosphere as a rule has a much shorter and better understood tectonic history than continental lithosphere. In combination, these two factors mean that many tectonic problems are more clearly and simply formulated for oceanic lithosphere. (2) In oceanic areas, intraplate seismicity provides one of the few means of studying the state of stress and internal deformation of the lithosphere, so it warrants particularly careful scrutiny. (3) The number of oceanic intraplate earthquakes recorded teleseismically in the last two decades (since the establishment of the World Wide Standard Seismograph Network, which will be our major source of data) is a large but manageable data set

for the systematic study to be conducted; inclusion of continental intraplate seismicity would too greatly enlarge the scope of such a study.

#### A BRIEF HISTORY OF OCEANIC INTRAPLATE EARTHQUAKE STUDIES

Banghar and Sykes [1969] reported focal mechanisms for four oceanic intraplate earthquakes in the Indian Ocean, but three of them (September 12, 1965, December 19, 1965, and February 17, 1966) are too near the ridge axis to have been recognized as such with the data then available. The fourth event (May 25, 1964) occurred on the Ninetyeast Ridge and is clearly an intraplate earthquake. The observation of a diffuse zone of seismicity in the northern Indian Ocean prompted Sykes [1970a] to suggest that a new island arc, stretching from India to Australia, might be developing there. Fitch [1972] obtained several more focal mechanisms of large intraplate earthquakes in the northern Indian Ocean; Fitch et al. [1973] first proposed that the P axes of intraplate earthquakes from India to Australia collectively delineate the geometry of a long-wavelength feature in the stress field of the Indian plate.

The November 25, 1965 earthquake in the Nazca plate was the first oceanic intraplate event to be deliberately studied with the object of inferring the orientation of greatest horizontal compression in the lithosphere and relating it to plate driving forces [Mendiguren, 1971]. Forsyth [1973] presented a less exhaustive study of an event (May 9, 1971) located in a corner of the Antarctic plate between two spreading ridge systems: the Pacific-Antarctic Ridge and the West Chile Rise. In both cases, the focal mechanism indicated thrust faulting with the P

axis oriented approximately perpendicular to the axis of the nearby ridge system (both ridge systems in the case of the 1971 event).

Sykes and Sbar [1973; 1974] were the first to present a global compilation of focal mechanisms of intraplate earthquakes (both oceanic and continental) and other indicators of lithospheric stress. Their study led to several important conclusions: (1) The state of deviatoric stress in the interior of many lithospheric plates is dominated by horizontal compression. (2) Over large regions, the orientation of the greatest horizontal principal stress seems to be coherent and may often be reflected in the focal mechanisms of intraplate earthquakes, although to infer the principal stress orientations from a single focal mechanism may lead to considerable error. (3) The first two observations are most easily attributed to the importance of the forces applied to plate boundaries, i.e., the driving mechanism of plate tectonics. (4) The transition between horizontal extension in the direction of spreading at the ridge axis and horizontal compression in the interior of oceanic plates occurs at a lithosphere age between 10 and 20 m.y. (This final conclusion is not confirmed by further investigation, as discussed in Chapter 8.) The pioneering work of Sykes and Sbar has served to motivate much of the subsequent research concerning intraplate earthquakes, including this thesis study.

Many recent studies concerning oceanic intraplate earthquakes have consisted of source studies of large or distinctive individual events, with little attempt to place the results in a global context. Stein [1978] investigated a swarm of normal-faulting earthquakes on the Chagos-Laccadive Ridge (including one of the events mistaken as a plate

boundary earthquake by Banghar and Sykes [1969]), but he was unable to account for their occurrence. An earthquake on the Emperor Trough, in the northern Pacific, however, appears to be a prime example of intraplate seismicity localized on a pre-existing zone of weakness [Stein, 1979]. A deep, complex event beneath Hawaii has been the subject of several studies [Unger and Ward, 1979; Butler, 1982], as has the large Bermuda earthquake on March 24, 1978 [Stewart and Helmberger, 1981; Nishenko and Kafka, 1982; Nishenko et al., 1982]. Other recent source studies of isolated earthquakes include Wang et al. [1979] and Okal [1980]. Fitch et al. [1980] and Kafka and Weidner [1979] both reported source studies of oceanic intraplate earthquakes, but more as examples of new methods of earthquake analysis than for insight into intraplate tectonics.

Studies utilizing a small population of oceanic intraplate earthquakes have been made for a variety of purposes. Richardson et al. [1979] compiled focal mechanisms of oceanic intraplate earthquakes as part of an effort to delineate the geometry of the global intraplate stress field, thereby placing constraints on the relative importance of various plate driving forces. Duschenes and Solomon [1977] used travel time residuals of long-period teleseismic shear waves from a number of oceanic intraplate earthquakes to investigate the evolution of the shear velocity structure of oceanic lithosphere. Hart and Butler [1978] carried out a similar study with one oceanic intraplate event (the Hawaiian earthquake of April 26, 1973) and one continental earthquake to investigate the difference in upper mantle shear velocity structures in the two source areas. Both Richardson and Solomon [1977] and Liu and Kanamori [1980] investigated stress drops of oceanic

intraplate earthquakes, stimulated by the assertion that intraplate earthquakes are characterized by higher stress drops than interplate events [Kanamori and Anderson, 1975].

Stein and Okal [1978] investigated the history of large earthquakes in the vicinity of the Ninetyeast Ridge and identified the ridge as the site of major internal deformation of the Indian plate. The presence of a local seismic network in French Polynesia has provided the opportunity to study the intraplate seismicity of an oceanic area to a much lower magnitude level than is possible with the World-Wide Standardized Seismograph Network (WWSSN) [Talandier and Kuster, 1976; Okal et al., 1980]. Okal [1981] investigated the oceanic intraplate seismicity of the Antarctic plate and concluded that it experiences a typical level of such activity, contrary to previous assertions [e.g., Sykes, 1978]. Okal also noted an association between sites of intraplate seismicity and the track of the Antarctic-Pacific-Nazca triple junction.

Several recent studies have made use of the variation of the maximum depth of faulting of intraplate earthquakes with lithospheric age to place constraints on the thermal and mechanical properties of the lithosphere: Chen and Molnar [1983] compiled a catalog of both oceanic and continental intraplate earthquakes with known source depths, whereas Wiens and Stein [1983] considered only oceanic events, but determined several new depths and thus had the benefit of a larger data set.

Only one study to date has dealt with the entire population of oceanic intraplate earthquakes: Bergman and Solomon [1980] presented a catalog of such earthquakes and considered the degree to which their



epicenters can be associated with prominent zones of (supposed) weakness in the oceanic lithosphere, such as fracture zones, and with large bathymetric features which might be sources of significant local stress. Oceanic intraplate earthquakes have also been the subject of a recent review article [Okal, 1983].

#### OBJECTIVES OF THIS STUDY

Since the pioneering study by Sykes and Sbar [1973], a major theme in research on oceanic intraplate earthquakes has been the use of source mechanisms to infer the state of stress in oceanic lithosphere and its relation to the forces driving plate motions. A primary objective of this thesis is to evaluate critically two fundamental aspects of the relationship between intraplate earthquakes and the state of stress in oceanic lithosphere: (1) What are the most important sources of stress relieved in oceanic intraplate earthquakes? In particular, are the forces which drive plate motions an important contributor? (2) How reliable an indicator of the state of stress in the hypocentral region is the focal mechanism of an oceanic intraplate earthquake?

An intraplate earthquake also represents non-recoverable internal deformation of the lithosphere, and a better understanding of the circumstances and modes in which oceanic lithosphere deforms is also sought in this thesis study. Such an understanding provides insight into the evolution of plate geometries, and in turn the pattern of mantle convection. We will be particularly interested in the extent to which the internal deformation of oceanic lithosphere is localized, perhaps along a zone of pre-existing weakness. A concentration of intraplate seismicity may also be attributed to intensified stresses in

the source region, however. If the source of stress released in the earthquakes can be determined, we may be able to distinguish between the two possibilities. The pattern and style of internal deformation are also influenced by the evolving mechanical properties of oceanic lithosphere, and we will consider what may be inferred from oceanic intraplate earthquake characteristics about the strength of the oceanic lithosphere as a function of age.

#### THESIS OUTLINE

The first contribution of this thesis is the compilation of a comprehensive catalog of oceanic intraplate earthquakes. Such a catalog may itself be studied to determine general properties of this type of seismicity, and it provides the background necessary for selecting and interpreting individual earthquakes. The catalog presented in Chapter 2 represents a significant expansion of that presented by Bergman and Solomon [1980]; a more systematic means of identifying intraplate seismicity, particularly near mid-ocean ridges, has been employed.

When the objective is to distinguish characteristics of oceanic intraplate earthquakes as a class and use these characteristics to make generalizations about the thermal and mechanical properties or state of stress and internal deformation of oceanic lithosphere, a single method of study, consistently applied to as many events as possible, is highly desirable. In this thesis, 58 of the largest earthquakes from the catalog are studied with a formal inversion of long-period teleseismic P and SH waveforms using the method developed by Nabelek [1984] and described in Chapter 3. This approach has several advantages over the trial and error approach of matching synthetic and observed waveforms.

The inversion converges much more rapidly than any forward modeling approach, allowing many more events to be studied. The criteria for matching synthetic and observed waveforms are more stable from event to event, and uncertainties in the results can be quantified. All of these advantages facilitate the detection and interpretation of systematic features of oceanic intraplate seismicity. In addition, formulation as an inverse problem allows us to use shear waves as well as P waves to estimate source parameters by matching observed waveforms. SH waves will be seen to be extremely useful in constraining focal mechanisms, but they are very difficult to utilize efficiently in a forward modeling approach.

In Chapters 4-8, the body-waveform inversion technique described in Chapter 3 is applied to source studies of the largest oceanic intraplate earthquakes in the Indian (Chapters 4 and 5), Atlantic (Chapter 6), and Pacific Oceans (Chapter 7). In Chapter 8, we examine the source characteristics of earthquakes in young (less than about 30 m.y. old) oceanic lithosphere in all three oceans. The emphasis in these chapters will be on combining the results of the source studies with the distribution of epicenters of other intraplate earthquakes to investigate several regional tectonic problems.

Chapter 4 focuses on a broad region in the southern Indian Ocean, along the Southeast Indian Ridge. Large near-ridge earthquakes, in lithosphere between the ages of 4 and 27 m.y., have occurred with unusual frequency in this region over the past two decades. Source studies for nine of these earthquakes are presented; they are all found to be characterized by normal faulting, with the T axis oriented oblique or perpendicular to the spreading direction. Moreover, several

of these events occur at depths at which standard plate cooling models predict temperatures in the neighborhood of 800°C. A number of possible explanations for these observations are considered. This work is also reported in Bergman et al. [1984].

In Chapter 5, we present source studies of a number of earthquakes in the northern Indian Ocean, the most seismically active oceanic intraplate region on earth. These earthquakes appear to be closely related to internal deformation of the Indian plate, stimulated by the continental collision between India and Asia. The large number of events in this region also provides an opportunity to observe the coherence of the regional stress field as reflected in the directions of the principal stress axes inferred from the focal mechanisms of oceanic intraplate earthquakes.

In Chapter 6, source studies of large intraplate earthquakes in the Atlantic Ocean are presented. The North Atlantic is one of the most thoroughly studied of the major ocean basins, offering the best opportunity for correlating the intraplate seismicity with other tectonic features. The North Atlantic contrasts with the Indian Ocean in that the spreading rate is lower, the tectonic history much simpler, and the boundaries of the oceanic plates are passive margins, rather than subduction zones or continental collision zones.

The source parameters of major intraplate earthquakes in the Pacific Ocean are presented in Chapter 7. The small number of such events, the poor station coverage, and the vastness and tectonic diversity of the Pacific Basin make it difficult to reach general conclusions about the overall state of stress or internal deformation of the lithosphere in this area. In several instances, however, the

intraplate earthquakes appear to be relevant to local tectonic problems.

Chapters 8 and 9 take a global perspective on the distribution and source mechanisms of oceanic intraplate earthquakes. The results of the regional studies presented in Chapters 4 through 7 suggest that intraplate earthquakes in young oceanic lithosphere have characteristics which distinguish them from both plate boundary events and earthquakes in the deep interior of oceanic plates. Source studies of near-ridge earthquakes from all three oceans are presented in Chapter 8 and combined with the results of Chapter 4 in order to investigate the early tectonic evolution of oceanic lithosphere. Important issues to be addressed include the nature of the transition from horizontal extension perpendicular to the ridge axis to horizontal compression in the deep intraplate stress regime, the dependence of focal depth and mechanism type on lithosphere age, and the source of the stress released in near-ridge earthquakes. This work is also reported in Bergman and Solomon [1984].

A global synthesis of the source mechanisms of oceanic intraplate earthquakes well-removed from mid-ocean ridges is presented in Chapter 9. A question of particular interest is the confidence with which such earthquakes may be used to infer the long-wavelength structure of the intraplate stress field, an application which was largely responsible for the initial interest in oceanic intraplate earthquakes. In this chapter, we also examine the issue of focal depth versus lithosphere age, considering the entire data set of source depths obtained in Chapters 4 through 8. Chapter 9 concludes with a summary of the major results of this thesis study.

## CHAPTER 2. A CATALOG OF OCEANIC INTRAPLATE EARTHQUAKES

### INTRODUCTION

The literature on oceanic intraplate earthquakes, as noted in the previous chapter, is dominated by source studies of those earthquakes large enough to be readily studied with traditional body wave and surface wave methods. In most cases, these events occurred deep in the interior of an oceanic plate, where they are readily noticed during even a casual perusal of the various earthquake bulletins. One of the obstacles to a broader perspective on the characteristics and significance of oceanic intraplate seismicity as a whole has been the lack of a systematic and comprehensive catalog of oceanic intraplate earthquakes which can provide a context within which such "single event" studies can be most profitably evaluated.

The catalog of oceanic intraplate seismicity assembled by Bergman and Solomon [1980] was global in scope, but the procedure used to identify oceanic intraplate earthquakes was rather unsystematic. In essence, it consisted of scanning the Bulletins of the International Seismological Centre (ISC) for "suspicious" events and then consulting tectonic or seismicity maps to confirm the classification of an epicenter as intraplate. The "geographic region" [Flinn and Engdahl, 1965] to which an earthquake is assigned by the ISC provides a relatively easy means of identifying many oceanic intraplate earthquakes, since some such regions are wholly or predominantly intraplate in nature. The majority of the 159 events listed in the 1980 catalog were identified because they occurred in one of these oceanic intraplate geographic regions. A significant amount of oceanic lithosphere, however, is contained within geographic regions primarily

associated with an oceanic plate boundary or continental margin. Except for a few particularly distinctive earthquakes, most oceanic intraplate earthquakes in these areas escaped notice. Despite its flaws, the 1980 catalog drew attention to the fact that oceanic intraplate earthquakes constitute a distinct class of seismicity which can be exploited to investigate a number of interesting tectonic problems. Subsequent studies which have made use of the 1980 catalog include those of Lilwall [1982], Weins and Stein [1983], and Okal [1983].

The 159 oceanic intraplate earthquakes identified by Bergman and Solomon [1980] are contained within 83 distinct sites of seismicity. For these representative epicentral regions, the seafloor bathymetry and tectonic history were examined and a judgement made as to whether the site should be considered associated with (1) a preexisting zone of weakness (such as a fracture zone) which might decouple the principal axes of the focal mechanism (assuming it is known) from the true orientation of the regional stress field [McKenzie, 1969], and (2) large bathymetric relief, which might be a source of significant local stress. Bergman and Solomon [1980] concluded that oceanic intraplate earthquakes are indeed commonly found in association with areas of the oceanic lithosphere which have been disturbed in some manner, though they show little association with large bathymetric features.

One might conclude from this result that most oceanic intraplate earthquakes are unreliable indicators of the regional stress field. Fitch [1972], however, noted that the P axes of a number of focal mechanisms of oceanic intraplate earthquakes in the northern Indian Ocean define a regionally-consistent NW-SE trending horizontal

compressive stress field which can be related to plate boundary interactions of the Indian plate [Richardson et al., 1979]. Bergman and Solomon [1980] observed that, in the presence of the Ninetyeast Ridge, a site of major intraplate deformation and large bathymetric relief, the regional consistency of the P axes of these widely-varying mechanisms suggests that the association of an earthquake with a zone of "preexisting weakness" is not necessarily a major impediment to the use of its focal mechanism to infer long-wavelength features of the intraplate stress field. A possible explanation of this result is that, at the scale appropriate for these earthquakes, such zones of prior deformation can be treated as consisting of a large number of preexisting faults with various orientations, so that seismic failure tends to occur on faults with large resolved shear stresses from the regional stress field. If this is the case, the principal axes of the focal mechanism will tend to have consistent alignments with the regional stress field, despite heterogeneities in oceanic lithosphere.

#### AN EXPANDED AND UPDATED CATALOG OF OCEANIC INTRAPLATE SEISMICITY

In this chapter, the catalog of Bergman and Solomon [1980] is updated to include more recent oceanic intraplate seismicity, and more importantly, expanded to include the results of a much more systematic survey of earthquakes near plate boundaries, particularly near mid-ocean ridges. The selection criteria have also been revised so that many more small events are retained. After a discussion of some of the more prominent features of the distribution of oceanic intraplate seismicity, the remainder of the chapter will be devoted to an investigation of the variation in seismic moment released in oceanic lithosphere as a function of age.



The catalog of oceanic intraplate seismicity prepared for this thesis study is divided into 4 sections (Appendices A-D): (1) A list of 174 earthquakes which occurred prior to 1964, the year in which the ISC began publishing earthquake locations and the World-Wide Standard Seismograph Network (WWSSN) reached full operational status. (2) The main catalog, containing 547 earthquakes located by the ISC (January 1964 to August 1981) and the NEIS (September 1981 to December 1983), except for those in the following two categories. (3) A list of 149 earthquakes located by the ISC in the vicinity of Hawaii during the period 1964-1979. (4) A list of 190 earthquakes involved in the most intense known episode of oceanic intraplate seismicity: the Gilbert Islands earthquakes of 1981-1983. In the following sections, brief descriptions are given of the manner in which the earthquakes in these sub-catalogs were selected.

#### Oceanic Intraplate Earthquakes from 1906 to 1963

Because oceanic intraplate earthquakes are relatively scarce and are distributed across a huge expanse of oceanic territory, and because there is essentially no historical record (i.e., felt reports) of such earthquakes, it is more difficult than usual to gain a reliable perspective on the long-term average seismicity in oceanic lithosphere. Consequently, there are several fundamental questions for which we have as yet no answers: (1) Are large areas of oceanic lithosphere essentially aseismic for their entire existence or will most of the brittle portion of the lithosphere experience seismic failure if we simply observe for a long enough period of time? (2) What is the repeat time for teleseismically detectable earthquakes in those oceanic intraplate regions which have been seismically active in the last two decades?

To begin to answer these questions, we searched several catalogs for oceanic intraplate earthquakes which occurred prior to 1964. These events are listed in Appendix A and their global distribution is shown in Figure 2.1. The major sources of data are Gutenberg and Richter [1954], Rothe [1969], Sykes [1970a], Lilwall [1982], and Okal [1984]. The epicentral coordinates listed by Sykes (for the Indian Ocean), Lilwall (for the Atlantic), and Okal (for the southern part of the Pacific plate) are considerably more accurate than those of the two earlier lists, since these earthquakes have been relocated by computer using modern travel time tables. The earliest epicenters reported by Gutenberg and Richter [1954], in particular, may move 1° or more when relocated in this manner. For this reason, we have generally resisted designating these older events as intraplate when they are within several degrees of a plate boundary. Okal [1984] notes that two apparently intraplate events in the Pacific (January 12, 1942 and December 23, 1942) are the result of mis-prints in several commonly-referenced catalogs. Reference to the ISS Bulletin reveals the error, but this type of error is likely to infect many catalogs of older earthquakes (including Appendix A).

Obviously, Appendix A is far from a complete picture of oceanic intraplate seismicity since the turn of the century, but when combined with the more complete catalog of events for the last two decades, it contributes significantly to an understanding of the long-term patterns of seismicity which are needed to answer the questions posed above.

#### Oceanic Intraplate Earthquakes Since 1964

The core of the catalog (Appendix B) is based on the ISC Bulletin for the years 1964-1979 inclusive, for which we obtained a magnetic

tape containing epicentral information for all reported events. For consistency, only earthquakes located by the ISC were included in Appendix B. We thus exclude earthquakes which were located only by other agencies; such earthquakes are invariably quite small and would contribute negligibly to the catalog. The tape contains epicentral data for over 180,000 earthquakes, each of which is coded with both the seismic and geographic region numbers of the regionalization scheme proposed by Flinn and Engdahl [1965] and further described by Flinn et al. [1974]. The seismic region numbers (53 in all) were used to break up the master ISC catalog into more manageable subsets.

Simply plotting all the shallow seismicity in an area will reveal many intraplate events, but this method can be misleading in the vicinity of plate boundaries with few recorded earthquakes, such as fast-spreading mid-ocean ridges. A better approach is to generate seismicity maps which can be overlaid on high-quality bathymetric and tectonic maps, where the plate boundaries are generally better defined. Even this approach presents problems if a systematic global search is contemplated, since many maps are published in projections which are difficult or impossible to reproduce without detailed information from the cartographer. Another problem concerns the compatibility and reliability of maps which were drafted at different times and for different purposes, and the fact that, for many oceanic areas, there has been a severe lack of suitable maps. The recent publication of a global series of high-quality bathymetric maps on a Mercator projection and at a single scale [General Bathymetric Charts of the Oceans, or GEBCO] has solved both problems.

The search procedure, then, consists of plotting all seismicity from the ISC catalog for every major oceanic area with a Mercator projection at the scale of the GEBCO series and visually identifying epicenters which are not associated with plate boundaries, as defined by the bulk of the seismicity and the bathymetry, or where necessary, by supplementary tectonic maps. Our criteria for deciding when an epicenter is too near a plate boundary to be classified as intraplate are necessarily subjective. The decision is based on the scatter in the plate boundary seismicity, the size of the standard errors in the epicentral coordinates, and the degree of confidence in specifying the actual location and extent of the plate boundary. Identifying the specific earthquake corresponding to a symbol on the plot requires searching the earthquake data file for all events in a small area around the epicenter.

Some of the earthquakes found in this manner have large standard errors in their locations. We excluded from the catalog any earthquake for which the standard error of either epicentral coordinate exceeds  $0.5^\circ$  or for which there were fewer than 10 observations. The number of arrival times actually used to locate an event may be smaller than the total number of observations. A histogram of the standard errors of the epicentral coordinates of the earthquakes in Appendix B is shown in Figure 2.2. The majority of such errors are under  $0.1^\circ$ , or approximately 10 km, but the true uncertainty of most teleseismic locations is greater, for several reasons.

The location procedure used by the ISC does not account for the biasing effect of uneven station distribution, a commonly encountered situation for small earthquakes in remote oceanic areas. We can

estimate the importance of this factor by considering a study of the accuracy of the locations of several small clusters of oceanic intraplate earthquakes in the South Pacific [Jordan and Sverdrup, 1981]. One part of the study involved the estimation of single-event locations, taking into account data "importances" in order to minimize bias in the epicenter due to an unbalanced station distribution. Table 2.1 lists the ISC coordinates, the single-event coordinates of Jordan and Sverdrup, and the difference between them for each of the events studied. Although in most cases the difference is less than  $0.1^\circ$ , it appears that the bias due to uneven station distribution can at least occasionally be as large as  $0.5^\circ$ .

It is well known that the focal depth estimated by inverting teleseismic travel times is very poorly resolved, having a strong trade-off with the origin time. Thus in many cases the focal depth is fixed at a "reasonable" value, typically 33 km (or more recently, 10 km) for shallow oceanic earthquakes. When the station distribution is unbalanced, error in the assumed or calculated focal depth produces bias in the epicenter. Wiens and Stein [1984] report such a case for an earthquake on October 29, 1975 near the East Pacific Rise. The ISC reported a depth of 100 km for this event, but body-waveform modeling and the surface wave radiation pattern constrain the depth to about 10 km. When this event was relocated, holding the depth at 10 km, the epicenter moved 25 km. We should note that the depth error in this case was much larger than is usually encountered.

When the biasing effects of poor station distribution and erroneous depth estimates are combined with the likely errors due to departure of the earth from the radially symmetric model employed in

the travel-time inversion, a conservative estimate of the potential location error for most of the events in Appendix B would be perhaps 30 km. Of course, the likelihood of significant location error increases dramatically with decreasing number of stations; this is one of the reasons (another is described below) for excluding from Appendix B events detected by fewer than 10 stations, regardless of the reported standard error of location.

The procedure used by the ISC to assign reported arrival times to specific earthquakes occasionally creates false events from chance associations of arrival times; such "earthquakes" are highly likely to be located in intraplate areas. Lilwall [1982] discusses this problem with regard to earthquakes in the Atlantic Ocean. Out of 182 events, Lilwall identified 3 (located with 5, 6, and 8 stations) as probably resulting from a chance association of arrivals. We made no attempt to detect such "earthquakes" in the course of assembling the catalog of oceanic intraplate events, but ignoring events with fewer than 10 observations should effectively filter most of them from our catalog.

The 1980 catalog contained only events with  $m_b \geq 4.7$ , because it was judged that there was little likelihood of obtaining information about the source mechanisms of smaller events. While this judgement is still held to be valid, we have included all identified oceanic intraplate events in Appendix B, subject to the criteria on location errors and number of reporting stations mentioned above, regardless of (or even in the absence of) assigned magnitude, in the interest of obtaining a more complete picture of oceanic intraplate seismicity. Many oceanic intraplate earthquakes in the magnitude range 4.7 to 5.0 ( $m_b$ ) are not assigned magnitudes because they were detected at only 10

or 20 stations, none of which reported amplitude information. This occurs especially frequently for earthquakes in the southern oceans. Although we may never know their mechanisms because of the minimal number of observing stations, knowledge of oceanic intraplate seismicity at low magnitudes helps define spatial and temporal patterns which aid in understanding the tectonic significance of the source mechanisms of larger events.

Appendix B also lists oceanic intraplate earthquakes which occurred since January 1, 1980, but this part of the catalog is not complete, particularly for young oceanic lithosphere, since the computerized search procedure outlined above could not be used. For earthquakes more recent than the latest issue of the ISC Bulletin (August 1981), the epicentral data given in Appendix B are from the monthly summaries of the Preliminary Determination of Epicenters (PDE) of the National Earthquake Information Service (NEIS). For earthquakes since October 1982, the epicentral data are from the preliminary data sheets of the PDE. There are a small number of local seismic networks operating in oceanic intraplate areas, such as on Hawaii [e.g., Koyanagi et al., 1976] and in French Polynesia [Talandier and Kuster, 1976]. The events reported by these networks are not included in the catalog unless they were also located by the ISC and meet the established criteria. All 547 epicenters of Appendix B are shown in Figure 2.3; with larger symbols denoting those earthquakes with  $m_b \geq 5.4$ .

Until now, we have been concerned primarily with the seismological criteria used in the selection of events for the catalog of oceanic intraplate seismicity, but since the distinguishing characteristic of

this catalog is tectonic rather than seismological in nature, a discussion of the tectonic criteria applied in the selection process is warranted. As in the 1980 catalog, we have excluded earthquakes which are likely to represent the release of bending stresses in the lithosphere seaward of subduction zones [e.g., Forsyth, 1982] and earthquakes located near continental rises.

There are two major concentrations of oceanic intraplate seismicity which are associated with hotspots: the Hawaiian Islands and the Galapagos Islands. Much of the seismicity in these areas accompanies volcanic activity is therefore of secondary interest to this thesis. The Hawaiian seismicity has been cataloged separately (Appendix C), as discussed in the next section, but we have excluded earthquakes in the vicinity of the Galapagos Islands from the catalog because they are intermingled on the north with seismicity associated with the Cocos-Nazca spreading plate boundary. The catalog of Hawaiian seismicity can be taken as an example of oceanic intraplate seismicity associated with a hotspot, but one with no interference from nearby plate boundary seismicity.

Earthquakes in the Drake Passage, between South America and Antarctica, appear to define a diffuse plate boundary zone [Forsyth, 1975], and are not included in Appendix B. (Earthquakes in the eastern Caroline Islands may also represent a diffuse plate boundary [e.g., Weissel and Anderson, 1978], but they have been included in our list). Where seafloor spreading has only recently begun, as in the Gulf of California or the Red Sea, too little oceanic lithosphere has been created to identify confidently any event as an oceanic intraplate earthquake. For the most part, we have made no effort to investigate



the seismicity of the numerous small marginal seas in the western Pacific. No earthquakes from the Gulf of Mexico or Mediterranean Sea have been included in the catalog. The region between Madagascar and Africa, which is certainly seismically active [e.g. Sykes, 1970a] and apparently of oceanic origin [e.g., Sclater et al., 1981a], has not been investigated.

#### Hawaiian Seismicity

Appendix C lists all ISC-located earthquakes in the vicinity of Hawaii (Lat. 15-25°N, Long. 150-160°W) for the years 1964-1979, selected under the same criteria used for Appendix B. Hawaiian earthquakes from the catalogs of Gutenberg and Richter [1954] and Rothe [1969] are listed in Appendix A. Because of the presence of a local seismic network, the hypocenters of recent earthquakes near Hawaii are known with greater accuracy than is the case for most oceanic intraplate seismicity. Figure 2.4 shows the locations of all the epicenters in Appendix C.

#### The Gilbert Islands Earthquakes

During the period 1964-1979, most of the western Pacific experienced very low levels of intraplate seismicity (Figure 2.3); even consideration of the historical seismicity in Appendix A does little to alter the conclusion that this huge area is nearly aseismic. Beginning in December 1981, however, and continuing almost continuously until March 1983, a very small region at the southeastern tip of the Gilbert Islands (Figure 2.5) experienced numerous earthquakes, up to  $m_b$  5.9, demonstrating that it may take a very long time to gain an accurate picture of the long-term intraplate seismicity of many areas. Appendix D contains epicentral data for 190 of these earthquakes, all recorded

by at least 10 stations. Because the ISC locations of these events are not yet available, the epicentral data given in Appendix D are from the monthly listings of the PDE.

#### THE GLOBAL DISTRIBUTION OF OCEANIC INTRAPLATE SEISMICITY

Reference to Figures 2.1 and 2.3 shows that most major ocean basins have experienced intraplate seismicity during the last 80 years, but the distribution of epicenters and magnitudes is not uniform. The patterns which appear in Figure 2.1 (1906-1963) are not always perpetuated in the seismicity since 1964 (Figure 2.3), emphasizing (as we will do at regular intervals in this thesis study) that great caution should be exercised in interpreting apparent patterns in oceanic intraplate seismicity.

There are several oceanic regions which have displayed very low levels of activity during this century. No intraplate events have been identified in the Arctic Basin, not even near-ridge events. In the South Atlantic there has been very little activity, even in young lithosphere, except in the far south. The Arabian Basin has also been notably quiescent, especially considering that portions of the Indian plate both to the south and the east have been intensely active. The northern and western Pacific Basin constitute a huge expanse of oceanic lithosphere which has experienced very low levels of intraplate seismicity in this century.

The eastern Pacific is seen to have been generally quite active, as have the North and the far South Atlantic, and the central and northern Indian Oceans basins. A distinctive cluster of seismic activity in the Caroline Islands (centered at about 5°N and 148°E) may denote a diffuse or incipient plate boundary, as will be discussed in

Chapter 7. In the North Atlantic, the seismicity since 1964 (and to a lesser extent prior to 1964) appears to define a linear, diffuse zone trending NW-SE from the northeastern corner of the Caribbean plate to the Mid-Atlantic Ridge. A similar but larger pattern roughly following the 90°E meridian is seen in the seismicity of the Indian Ocean for the last 20 years, but note that the earlier activity defines a quite different trend. These issues are investigated at greater length in the individual chapters devoted to the source mechanisms and regional tectonics of the Atlantic (Chapter 6), Pacific (Chapter 7), and Indian (Chapters 4 and 5) Oceans. There are a number of examples of repeated activity, sometimes at long intervals, at oceanic intraplate sites. This can be interpreted either as localization of activity on pre-existing weak zones in a homogeneous lithospheric stress field or as the result of locally produced stresses in a relatively homogeneous lithosphere. (The two positions are not mutually exclusive, however). This important question is considered in Chapter 9.

A significant portion of oceanic intraplate seismicity can be seen to occur in young oceanic lithosphere, less than about 30 m.y. old. We address this question more quantitatively in a later section of this chapter and Chapter 8.

#### MAGNITUDE - FREQUENCY RELATIONS

Temporally or spatially distinct groups of earthquakes are frequently compared by means of their magnitude - frequency distribution, expressed by the coefficients of the equation for a straight line

$$\log N(M) = a - bM \quad (2.1)$$

where  $M$  is a measure of magnitude and  $N$  is the number of events with magnitude  $\geq M$  [Gutenberg and Richter, 1954]. The coefficients  $a$  and  $b$  are usually estimated from a least squares fit to the data, but other treatments have been suggested [e.g., Aki, 1965; Shi and Bolt, 1982]. The intercept value  $a$  merely reflects the size of the catalog being used and has no tectonic significance. An extensive literature exists, however, on the interpretation of the slope  $b$ , particularly temporal variations of  $b$  for restricted populations of earthquakes, detection of which may facilitate the prediction of some earthquakes [e.g., Smith, 1981]. A rigorous treatment of the standard error of  $b$ , however, leads Shi and Bolt [1982] to conclude that many reported variations in  $b$  values may not be statistically significant.

Employing standard least squares analysis [Fischer, 1969], we calculated  $b$  values for the main catalog (Appendix B), the list of Hawaiian earthquakes in Appendix C, and the Gilbert Islands earthquake series (Appendix D). We used  $m_b$  as the measure of magnitude because it is much more commonly reported than  $M_s$ . Histograms of the  $m_b$  distribution of the three data sets are shown in Figures 2.6 and 2.7. Figure 2.8 shows the frequency - magnitude distribution for each data set and the corresponding regression line, the coefficients of which are listed in Table 2.2.

We had no trouble determining  $b$  values for the main catalog and the Hawaiian earthquakes ( $1.05 \pm 0.02$  and  $1.16 \pm 0.05$  respectively); the data are well fit by straight lines in the  $m_b$  range 4.4-5.3 for Hawaii and 4.9-5.9 for the main catalog. Because of the local seismic network on Hawaii, the threshold magnitude (magnitude below which the cumulative number of earthquakes falls away from the linear trend) is

lower than for the main catalog, which helps make up for the small sample of moderate sized events in the Hawaiian catalog. Magnitudes above 5.9 (main catalog) and 5.3 (Hawaii) were not used in the linear regression analysis; the small number of such events means that the occurrence of a single large event during the chosen time period can have an inordinate effect on the slope estimate. This sensitivity to the scatter of small samples of large earthquakes can also be reduced by estimating the b value with the maximum likelihood method [Aki, 1965].

The b-values obtained for the main catalog of oceanic intraplate earthquakes and the Hawaiian earthquakes are quite consistent with those reported for a variety of earthquake populations. Mid-ocean ridge seismicity is a notable exception, being generally characterized by higher b-values [e.g., Francis, 1968], an observation attributed to the high incidence of earthquake swarms [Sykes, 1970b]. The b-value estimated for the Hawaiian seismicity is not significantly higher at the  $2\sigma$  (95% confidence) level than that of the main catalog, even though much of the Hawaiian seismicity accompanies volcanic activity. Furumoto et al. [1973] report a b-value of 1.05, based on  $m_b$ , for long-term seismic activity at Hawaii.

The Gilbert Islands seismicity resists characterization by a single b value: the frequency - magnitude distribution between  $m_b$  4.8 and 5.7 is piecewise linear, with the break at  $m_b = 5.2$  (Figure 2.8). The estimated b-values for these two segments,  $1.13 \pm 0.01$  for  $4.8 \leq m_b \leq 5.2$  and  $1.87 \pm 0.04$  for  $5.2 \leq m_b \leq 5.7$  differ by much more than their standard errors (Table 2.2), however the true uncertainty may be significantly larger than the standard errors calculated using

the method of least squares [Shi and Bolt, 1982]. Lay and Okal [1984] estimated a b-value of 1.35 over the magnitude range 4.8-5.9, using the maximum likelihood method [Aki, 1965]. Francis [1974] reported a similarly complex frequency-magnitude pattern for earthquakes at the 1968 Fernandina caldera collapse, with  $b = 1.24$  for  $m_b < 4.9$  and  $b = 2.53$  for larger magnitudes. In a later chapter, we consider the source mechanisms of some of the larger events in the Gilbert Islands series and further discuss the tectonic significance of this unusual seismic activity.

#### SEISMIC MOMENT RELEASE AS A FUNCTION OF LITHOSPHERE AGE

The spatial pattern of the release of seismic moment in oceanic lithosphere provides insight into a variety of tectonic problems related to the state of stress and modes of internal deformation of the lithosphere. One useful way to parameterize this pattern is to consider the variation of seismic moment released in oceanic lithosphere as a function of age, since variations in the mechanical properties [e.g., Chen and Molnar, 1983; Wiens and Stein, 1983] and also in the state of stress [e.g., Dahlen, 1981] are thought to be related in fundamental ways to the age of the lithosphere.

Using the catalog of Bergman and Solomon [1980] as the primary source of data, Wiens and Stein [1983, 1984] found a marked decrease in the rate of seismic moment release with increasing age, but the number of earthquakes in the 1980 catalog is insufficient to reveal more than the overall trend. Performing a similar analysis on the updated catalog should provide much better resolution of the details of this pattern, particularly in young oceanic lithosphere, which was poorly represented in the 1980 catalog.

The primary data set for our study will be a subset of Appendix B, the ISC-located earthquakes from 1964 through 1979, because for this time period the catalog is essentially complete, both to small magnitudes and to very young lithospheric ages. We will also use the catalog of Hawaiian seismicity for the same years (Appendix C), but it will be kept distinct from the main catalog because, as we shall see, it dominates the seismic moment release in its age category, and much of the seismic moment released is related to volcanic rather than tectonic processes. The contribution of the Gilbert Islands earthquakes (Appendix D) to the seismic moment released in oceanic lithosphere will also be calculated. Although these earthquakes occurred outside the time window being considered, they provide insight into the degree to which we can regard 16 years of intraplate seismicity to be representative of the long-term rate of internal deformation of oceanic lithosphere.

Rather than attempt to specify a precise age for each earthquake in our catalog, we adopt the lithospheric age categories of Sclater et al. [1980] and assign each earthquake to one of the 13 "bins" by superimposing maps of oceanic intraplate seismicity and maps of the isochrons defining the age categories. Each event in Appendices B, C, and D is coded with the age category to which it was assigned. When an epicenter lies very near one of the isochrons, it has been assigned to the older age category. This was done to avoid biasing the results toward higher moment release in young lithosphere, which we already knew to be the dominant pattern.

A seismic moment was assigned to each earthquake, using magnitude-moment relations derived from the results of source studies.

of oceanic intraplate earthquakes described in later chapters. The body-waveform inversion technique used to perform these source studies is described in Chapter 3. The linear regression analysis assumes equal error in the dependent and independent variables [York, 1966].

Table 2.3 lists the data used to derive the  $m_b$ - $M_0$  and  $M_s$ - $M_0$  relations:

$$\log M_0 = 2.35 (\pm 0.20) \times m_b + 11.71 (\pm 1.13) \quad (2.2)$$

$$\log M_0 = 1.12 (\pm 0.07) \times M_s + 18.67 (\pm 0.41) \quad (2.3)$$

with  $M_0$  in units of dyne-cm. The range given in parentheses for the regression coefficients is one standard deviation. Figure 2.9 shows plots of the data and regression lines for the two relations. Not surprisingly,  $M_s$  correlates better with  $M_0$  (correlation coefficient  $r = 0.91$ ) than  $m_b$  does ( $r = 0.79$ ). In the absence of a seismic moment estimate from the body-waveform inversion, a moment was assigned to each earthquake based on the reported magnitude and (2.2) or (2.3), using  $M_s$  if both magnitudes were given. If no magnitude was reported,  $m_b$  4.5 was assumed.

The resultant seismic moment totals for oceanic intraplate earthquakes calculated using (2.2) and (2.3) are probably underestimates, for two reasons. First, there is no contribution from events below the threshold of teleseismic detection and location. Also, as we discuss in the next chapter, the seismic moment estimated from the body-waveform inversion tends to be a lower bound; the moment estimate generally increases with improved match to the observed waveforms. Moreover, the seismic moment estimated from long-period surface waves is often larger than that estimated from body waves. To the extent that this results from a breakdown of the point source



approximation, we may expect a bias toward low values for the seismic moments of the larger events in our catalog.

The maximum depth to which the oceanic lithosphere is capable of accumulating strain sufficient to result in an earthquake appears to be well-approximated by the depth to an isotherm in the range of 600°C to 800°C [Chen and Molnar, 1983; Wiens and Stein, 1983, 1984; Chapter 8 of this thesis], and thus varies strongly with age. Therefore, to gain a meaningful picture of the variation with age of the intensity of internal deformation of oceanic lithosphere, the seismic moment released in each age category must be normalized by the corresponding volume of seismogenic lithosphere in that age range. The depth used to calculate this volume is the average depth to the 800°C isotherm, calculated with the plate cooling model of Parsons and Sclater [1977]; the area is given by Sclater et al. [1980]. All data pertaining to this calculation are listed in Table 2.4 and the results are shown in Figure 2.10.

As expected, Figure 2.10 shows a strong decrease with age of the seismic moment release per unit volume of seismogenic lithosphere. The decrease is not smooth however; a particularly large drop occurs between the 9-20 m.y. and 20-35 m.y. bins. A detailed study of the source mechanisms of larger earthquakes in young oceanic lithosphere (Chapter 8) suggests that this drop occurs at about 15 m.y. From 20 to 80 m.y., the decline in seismic moment release appears to be quite gradual. The number of earthquakes contributing to the sum of seismic moment released in oceanic lithosphere older than 80 m.y. (excluding the Hawaiian and Gilbert Islands earthquakes) is small and the calculated values of moment release per unit volume therefore have more

scatter, but the general tendency for a steady decrease with age is evident.

A decrease with age of seismic moment release per unit volume of seismogenic lithosphere for ages greater than 20 m.y. is not so obvious, however, if the Hawaiian and Gilbert Islands earthquakes are included in the calculation (Figure 2.10). The Gilbert Islands earthquakes are sufficient to raise the moment release per unit volume of lithosphere aged 110-125 m.y. to a higher value than that of lithosphere 20-35 m.y. old. The Gilbert Islands swarm (or the Hawaiian seismicity) is not tectonically equivalent, however, to an equal number of events (with the same cumulative moment) scattered in space and time, but located in the same age bin. Thus, it would be misleading to reach a conclusion about the general pattern of seismic moment release in oceanic lithosphere without distinguishing the special nature of the Gilbert Islands swarm. Nevertheless, this example illustrates that a large fraction of intraplate deformation may occur as intensive bursts of activity at very long intervals; the widely scattered small events which characterize many oceanic regions may simply be background noise in between such bursts.

Although many more events contribute to the estimated seismic moment release in younger lithosphere and these values are more stable than those for older lithosphere, a single large event may still cause large fluctuations. For example, the difference between the seismic moment of the August 26, 1977 ( $M_S = 7.1$ ) estimated from a preliminary  $M_S$ - $M_0$  relation and that found in the body-waveform inversion was sufficient to change the calculated moment release per unit volume in the age range 9-20 m.y. by 50%. On November 30, 1983 the largest

oceanic intraplate event in recent decades ( $M_S = 7.5$ ) occurred near the Chagos Bank in the Indian Ocean, in lithosphere about 35 m.y. old.

This earthquake, with a probable seismic moment exceeding  $10^{27}$  dyne-cm, would completely dominate the calculation of seismic moment release per unit volume in any age range to which it might be assigned.

In summary, the data indicate a rapid decline in the intensity of seismically-expressed internal deformation of oceanic lithosphere over the first 20 m.y. and a slow decline in older lithosphere. This result can be used to set a lower limit of about 20 m.y. to the age at which oceanic lithosphere may be regarded as in an "intraplate" tectonic environment, in the sense intended by the studies of Sykes and Sbar [1974], Richardson et al. [1979], and Bergman and Solomon [1980]. At younger lithospheric ages, much of the seismicity apparently represents the release of stresses accumulated in the rapid tectonic evolution of young oceanic lithosphere, rather than stresses associated with the force system driving plate motions. This subject is discussed at greater length in Chapter 8.

TABLE 2.1 Comparison of Epicenters from the ISC and Jordan and Sverdrup  
[1981] for Earthquakes in the South Pacific Ocean

<u>Mo/Da/Yr</u>	ISC Lat. (s.d.) °N Long. (s.d.) °E	J and S [1981] Lat. (s.d.) °N Long. (s.d.) °E	<u>J&amp;S - ISC</u>
07/29/68	-7.52 (0.038) -148.32 (0.077)	-7.47 (0.048) -148.16 (0.058)	0.05 0.16
08/06/69	-7.61 (0.027) -148.14 (0.063)	-7.40 (0.047) -148.19 (0.048)	0.21 -0.05
01/19/73	-7.59 (0.022) -148.18 (0.050)	-7.36 (0.041) -148.24 (0.044)	0.23 -0.06
01/19/73	-7.63 (0.024) -148.08 (0.082)	-7.31 (0.055) -148.27 (0.062)	0.32 -0.19
03/06/65	-18.42 (0.036) -132.82 (0.038)	-18.40 (0.032) -132.85 (0.039)	0.02 -0.03
09/18/66	-18.38 (0.032) -132.87 (0.054)	-18.40 (0.031) -132.86 (0.060)	0.02 0.01
05/25/75	-18.39 (0.030) -132.99 (0.026)	-18.40 (0.037) -132.92 (0.055)	-0.01 0.07
10/31/77	-20.71 (0.038) -126.76 (0.031)	-20.72 (0.040) -126.95 (0.053)	-0.01 -0.19
01/05/78	-20.79 (0.023) -126.39 (0.035)	-20.80 (0.023) -126.94 (0.026)	-0.01 -0.55
02/19/78	-20.78 (0.044) -126.6 (0.12)	-20.83 (0.062) -126.7 (0.17)	-0.05 -0.1
03/11/78	-20.88 (0.043) -126.86 (0.052)	-20.89 (0.049) -126.96 (0.061)	-0.01 -0.10
07/13/78	-20.73 (0.042) -127.05 (0.054)	-20.78 (0.070) -127.09 (0.071)	-0.05 -0.04
07/25/78	-20.75 (0.029) -126.95 (0.043)	-20.76 (0.041) -126.97 (0.057)	-0.01 -0.02
02/26/79	-20.99 (0.072) -126.99 (0.057)	-20.94 (0.104) -126.7 (0.13)	0.05 0.29

Table 2.2 Magnitude - Frequency Distribution\* of  
Oceanic Intraplate Earthquakes

<u>Data</u>	<u>m<sub>b</sub> Range</u>	<u>a (s.d.)</u>	<u>b (s.d.)</u>
Full catalog (1964-1983)	4.9 - 5.9	7.62 ± 0.12	1.05 ± 0.02
Hawaii (1964-1979)	4.4 - 5.3	6.83 ± 0.22	1.16 ± 0.05
Gilbert Is. (1981-1983)	4.8 - 5.2	7.56 ± 0.05	1.13 ± 0.01
	5.2 - 5.7	11.43 ± 0.20	1.87 ± 0.04
	4.8 - 5.7	9.78 ± 0.35	1.57 ± 0.07

\* Least squares fit to:

$$\log_{10} N(M) = a - bM$$

where N is the number of events with magnitude equal to or greater than M. M is measured by m<sub>b</sub>.

Table 2.3 Magnitude - Moment Data Used to Derive Regression Relations<sup>a</sup>

<u>Mo/Da/Yr</u>	<u>m<sub>b</sub></u>	<u>M<sub>s</sub></u>	<u>M<sub>0</sub> (dyne-cm)</u>
05/25/64	5.7	6.0	1.2 x 10 <sup>25</sup>
10/23/64	6.2	6.3	4.9 x 10 <sup>25</sup>
09/09/65	5.8	6.2	2.4 x 10 <sup>25</sup>
09/12/65	6.1	6.0	3.7 x 10 <sup>25</sup>
10/07/65	5.8	5.6	5.3 x 10 <sup>24</sup>
10/31/65	5.3	5.4	5.3 x 10 <sup>24</sup>
12/19/65	5.5		1.3 x 10 <sup>25</sup>
02/17/66	6.0		7.5 x 10 <sup>25</sup>
01/07/67	5.5		1.2 x 10 <sup>25</sup>
11/10/67	5.2		2.8 x 10 <sup>24</sup>
11/11/67	5.3	5.2	3.5 x 10 <sup>24</sup>
03/02/68	5.5	5.4	8.4 x 10 <sup>24</sup>
08/20/68	5.6	5.0	4.5 x 10 <sup>24</sup>
09/03/68	5.6	5.9	5.9 x 10 <sup>24</sup>
09/14/68	5.4		1.1 x 10 <sup>24</sup>
10/08/68	5.8	5.8	2.0 x 10 <sup>25</sup>
08/08/69	5.7	6.0	1.8 x 10 <sup>25</sup>
01/21/70	6.1	6.6	1.4 x 10 <sup>26</sup>
03/31/70	5.5	5.7	7.6 x 10 <sup>24</sup>
04/25/70	5.1	5.1	1.7 x 10 <sup>24</sup>
10/10/70	5.8	6.3	5.2 x 10 <sup>25</sup>
05/09/71	6.0	6.0	5.5 x 10 <sup>25</sup>
06/26/71	5.9	6.4	4.9 x 10 <sup>25</sup>
09/30/71	6.0	5.5	9.2 x 10 <sup>24</sup>
05/02/72	5.9	5.5	1.8 x 10 <sup>25</sup>
05/21/72	5.6	4.9	4.1 x 10 <sup>24</sup>
10/20/72	5.7	5.8	2.5 x 10 <sup>25</sup>
11/24/72	5.2	5.2	3.0 x 10 <sup>24</sup>
04/07/73	5.8	6.6	9.6 x 10 <sup>25</sup>
04/26/73	5.9	5.9	3.7 x 10 <sup>25</sup>
05/03/73	5.5	5.5	8.7 x 10 <sup>24</sup>
06/29/73	5.4	4.9	2.8 x 10 <sup>24</sup>
08/30/73	5.8	5.2	4.7 x 10 <sup>24</sup>
11/17/73	5.4	5.5	4.8 x 10 <sup>24</sup>
04/12/74	5.5	4.9	1.6 x 10 <sup>24</sup>
06/25/74	6.1	6.6	1.4 x 10 <sup>26</sup>
07/01/74	5.5	5.6	3.2 x 10 <sup>24</sup>
11/20/74	5.8	5.6	6.6 x 10 <sup>24</sup>
09/11/75	6.3	5.8	1.2 x 10 <sup>25</sup>
09/19/75	5.9	6.1	3.9 x 10 <sup>25</sup>
03/29/76	5.8	6.5	9.0 x 10 <sup>25</sup>
08/30/76	5.8	5.9	1.8 x 10 <sup>25</sup>
11/02/76	5.8	6.5	7.6 x 10 <sup>25</sup>
11/02/76	5.6		6.1 x 10 <sup>24</sup>
02/05/77	6.1	6.2	3.6 x 10 <sup>25</sup>
08/26/77	6.3	7.1	5.4 x 10 <sup>26</sup>

(continued)

Table 2.3 (continued)

<u>Mo/Da/Yr</u>	<u>m<sub>b</sub></u>	<u>M<sub>s</sub></u>	<u>M<sub>0</sub> (dyne-cm)</u>
10/17/77	6.2	6.7	1.7 x 10 <sup>26</sup>
12/13/77	5.7	6.4	2.8 x 10 <sup>25</sup>
12/14/77	5.5	4.7	3.0 x 10 <sup>24</sup>
03/24/78	6.0	6.0	2.0 x 10 <sup>25</sup>
08/03/78	5.5	5.5	5.8 x 10 <sup>24</sup>
05/22/79	5.5	5.1	4.2 x 10 <sup>24</sup>
12/13/79	5.4	5.5	7.2 x 10 <sup>24</sup>
09/24/81	5.4	5.5	4.4 x 10 <sup>24</sup>
12/02/81	5.7	5.5	5.6 x 10 <sup>24</sup>
12/12/81	5.5	5.1	2.2 x 10 <sup>24</sup>

a) M<sub>s</sub> from ISC, NEIS, or published source study. m<sub>b</sub> from ISC.

Seismic moment from body waveform inversion.

Table 2.4 Seismic moment released per unit volume as a function of lithospheric age

Age Range <sup>a</sup> m.y.	Area <sup>a</sup> x10 <sup>6</sup> km <sup>2</sup>	Thick- ness <sup>b</sup>	Volume x10 <sup>8</sup> km <sup>3</sup>	# of Events	$\sum M_0^c$	$M_0/\text{Volume}$ (dyne/cm <sup>2</sup> )
0 - 4	14.2	7.6	1.08	23	177.	1639.
4 - 9	19.7	14.4	2.84	66	339.	1194.
9 - 20	31.8	21.6	6.87	98	788.	1147.
20 - 35	42.6	29.8	12.7	104	306.	241.
35 - 52	37.0	37.5	13.9	35	363.	261.
52 - 65	29.7	43.6	12.9	43	172.	133.
65 - 80	37.3	48.4	18.1	41	155.	85.6
80 - 95 <sup>d</sup>	27.9	53.0	14.8	18 (156)	44.4 (143.)	30.0 (96.6)
95 - 110	24.8	57.0	14.1	6	8.92	6.33
110 - 125 <sup>e</sup>	15.2	60.3	9.17	8 (198)	3.43 (147.)	3.74 (160.)
125 - 140	16.7	63.1	10.5	16	20.5	19.5
140 - 160	8.3	65.6	5.44	1	0.098	0.180
> 160	3.4	67.8	2.31	2	1.25	5.41

- a) Age ranges and corresponding areas from Sclater et al. [1981].
- b) Thickness (km) calculated as the average depth to the 800°C isotherm in the age range of interest, using the cooling model of Parsons and Sclater [1977].
- c) Sum of seismic moments (x10<sup>24</sup> dyne-cm) of all earthquakes in Appendix B in the age range of interest for the period 1964-1979. Method of assigning moments is discussed in the text.
- d) Values in parenthesis include Hawaiian seismicity (Appendix C).
- e) Values in parenthesis include the Gilbert Islands seismicity of 1981-1983 (Appendix D).



## FIGURE CAPTIONS

Figure 2.1 Global distribution of epicenters of oceanic intraplate earthquakes occurring prior to 1964 (Appendix A). Earthquakes with  $M$  or  $M_S$  magnitude  $\geq 6.5$  are indicated by larger symbols. Mollweide projection, centered at  $0^\circ$  longitude. Major oceanic spreading centers are approximately indicated by solid lines.

Figure 2.2 Histogram of the standard errors (in degrees) reported by the ISC for the epicentral coordinates of oceanic intraplate earthquakes for the years 1964-1979 (Appendix B). No events with errors of more than  $0.5^\circ$  have been included in the catalog.

Figure 2.3 Global distribution of epicenters of oceanic intraplate earthquakes occurring since January 1, 1964 (Appendix B). The epicenters around Hawaii for the years 1964-1979 (Appendix C) and the Gilbert Islands earthquakes of 1981-1983 (Appendix D) are indicated also, and shown in more detail in later figures. Earthquakes with  $m_b$   $\geq 5.4$  are indicated by larger symbols. Mollweide projection, centered at  $0^\circ$  longitude. Major oceanic spreading centers are approximately indicated by solid lines.

Figure 2.4 Distribution of seismicity near Hawaii (Appendix C). Bathymetry at 1000 m intervals from Mammerickx and Smith [1982].

Figure 2.5 Distribution of the epicenters of the Gilbert Islands earthquake series of 1981-1983 (Appendix D). Bathymetry at 1000 m intervals from Monahan et al. [1982].

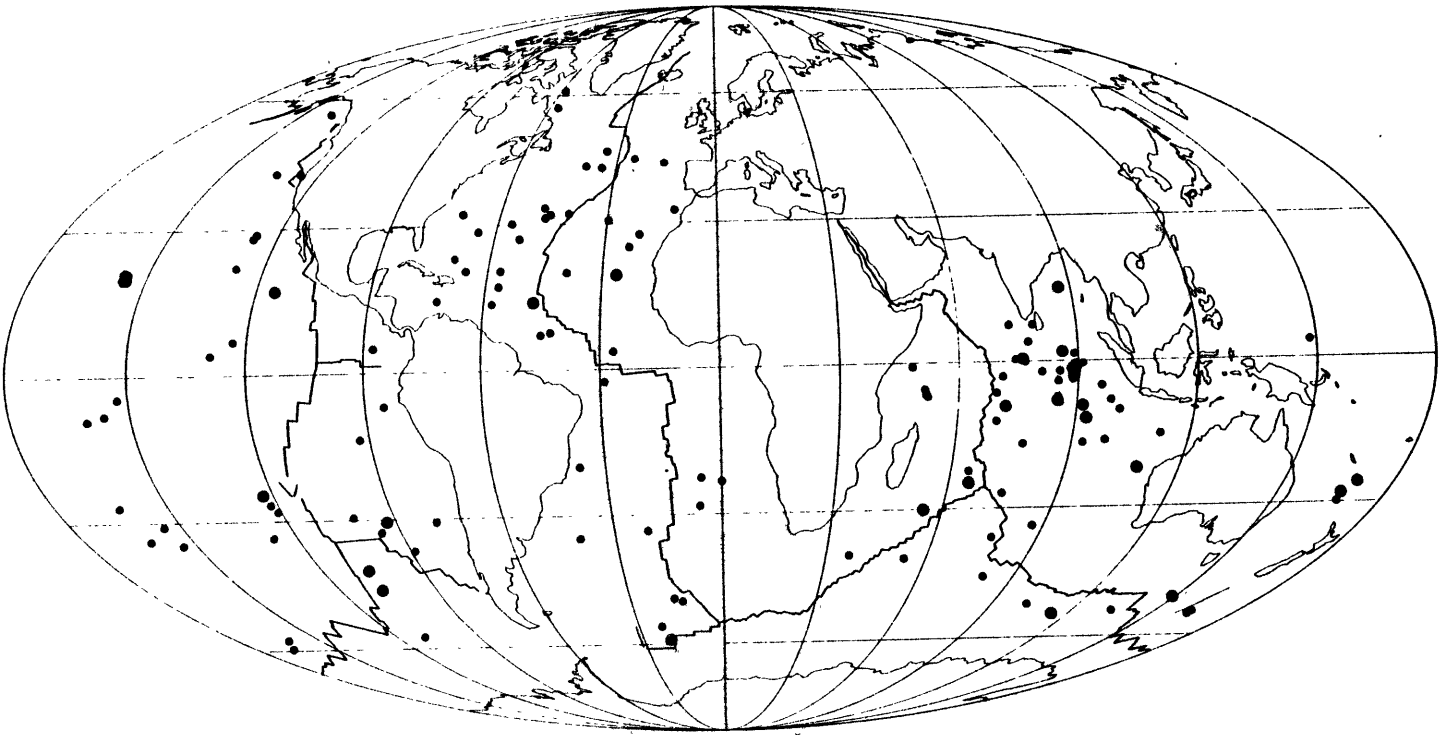
Figure 2.6 Histogram of the distribution of magnitudes ( $m_b$ ) for the main catalog of oceanic intraplate earthquakes (Appendix B).

Figure 2.7 Histograms of the distribution of magnitudes ( $m_b$ ) for Hawaiian seismicity for the years 1964-1979 (Appendix C) and the Gilbert Islands earthquakes series of 1981-1983 (Appendix D).

Figure 2.8 Frequency - magnitude distribution of the data shown in Figures 2.6 and 2.7, with the least squares fit to the data, as described in the text and Table 2.2.

Figure 2.9 Plots of  $m_b$  and  $M_s$  versus  $\log_{10} M_0$  for the data listed in Table 2.3, and the best fitting (in a least squares sense) lines through the data.

Figure 2.10 Seismic moment per unit volume of lithosphere released by oceanic intraplate earthquakes as a function of age for the years 1964-1979. For the calculation of the volume of seismogenic lithosphere within each age interval, the thickness is taken equal to the average depth of the 800°C isotherm. The effect of including Hawaiian seismicity and the Gilbert Islands earthquake series of 1981-1983 are indicated. Data are listed in Table 2.4.



**OCEANIC INTRAPLATE EARTHQUAKES 1906-1963**

**Figure 2.1**

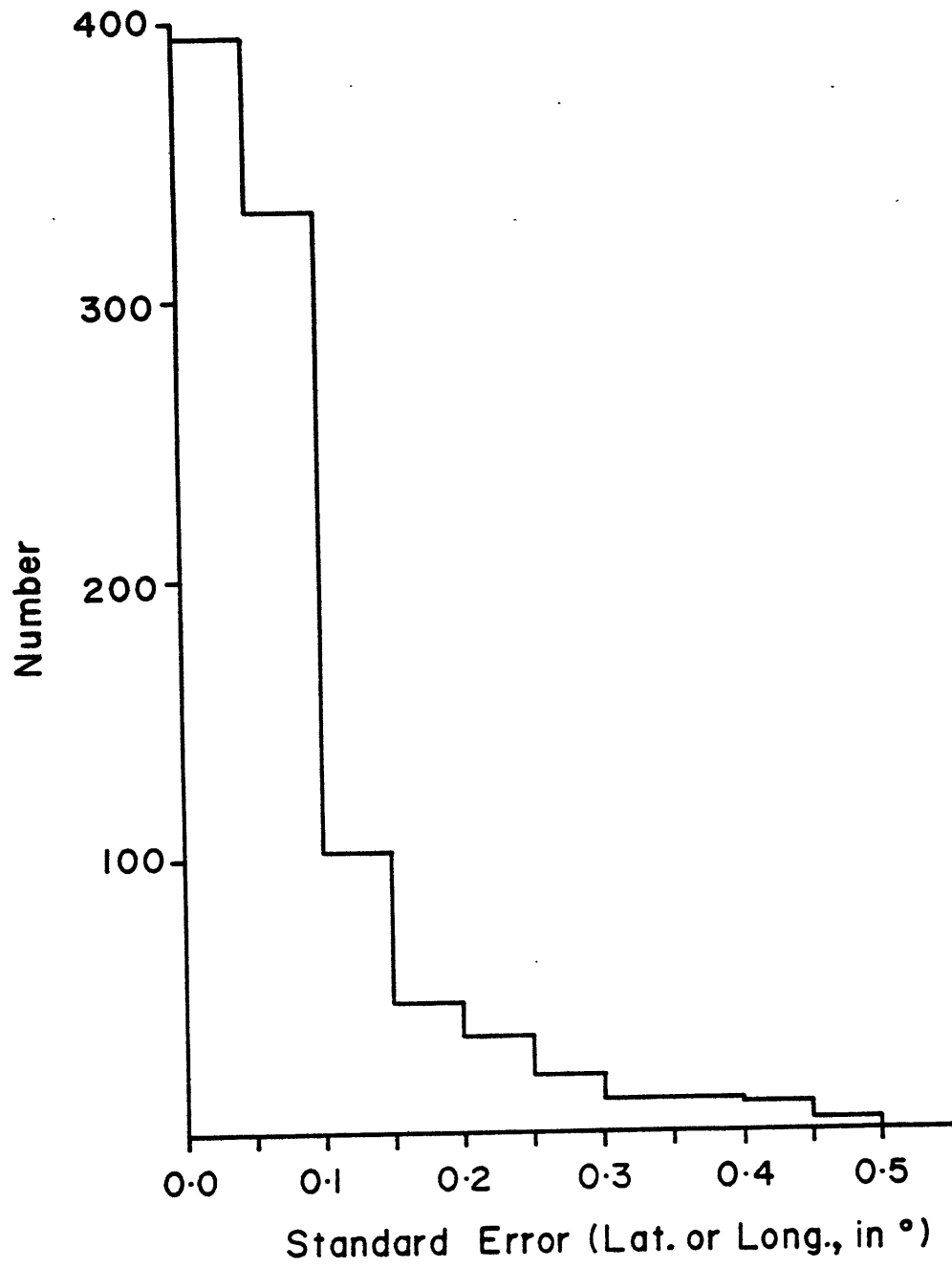
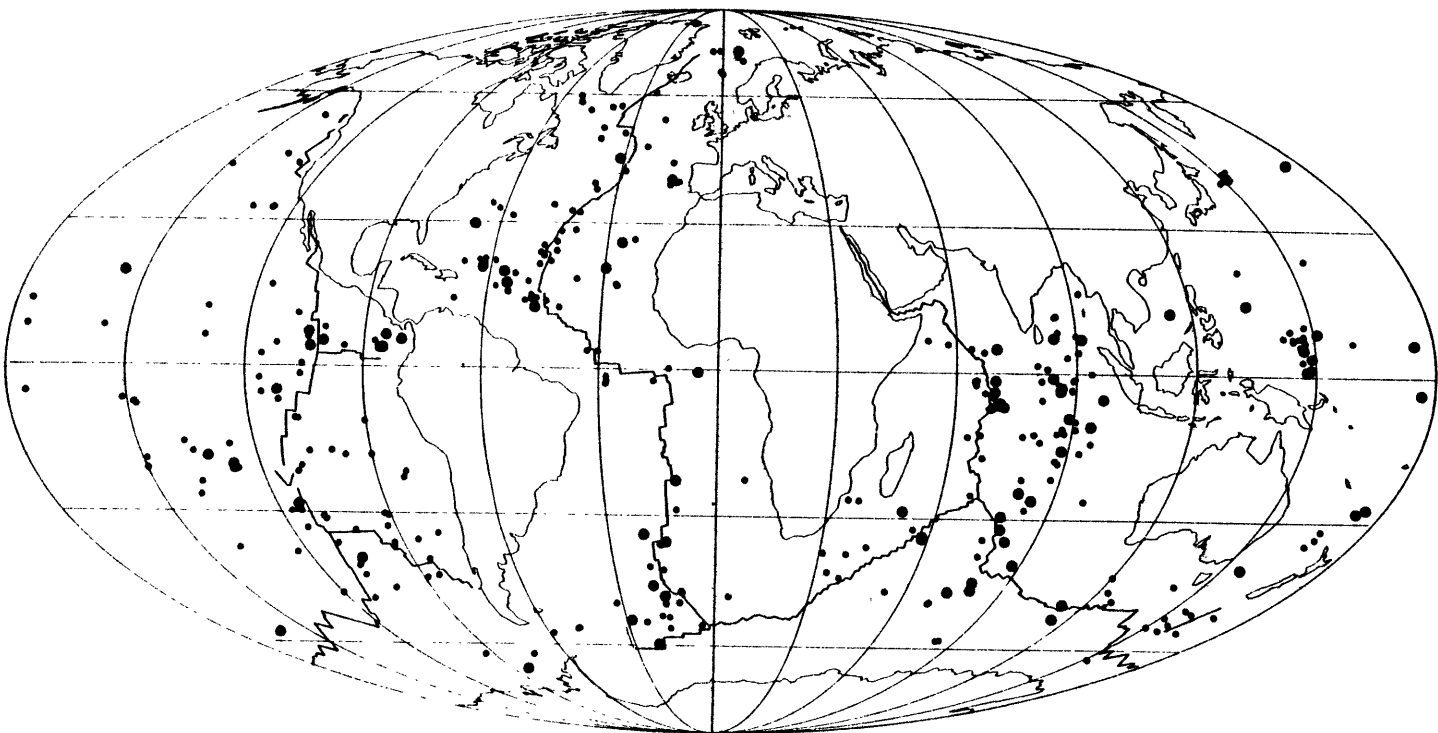


Figure 2.2



OCEANIC INTRAPLATE EARTHQUAKES 1964-1983

Figure 2.3

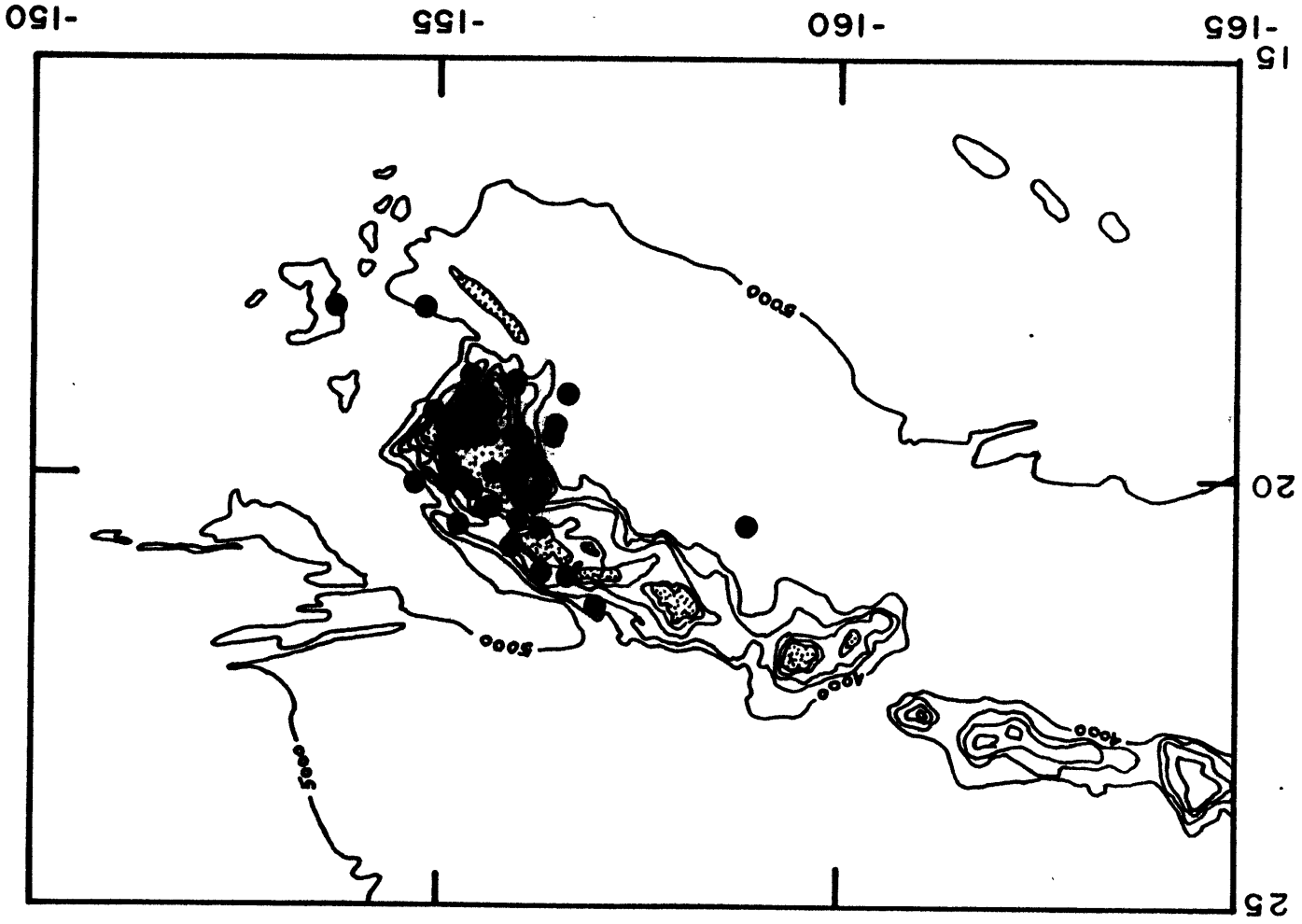


Figure 2.4

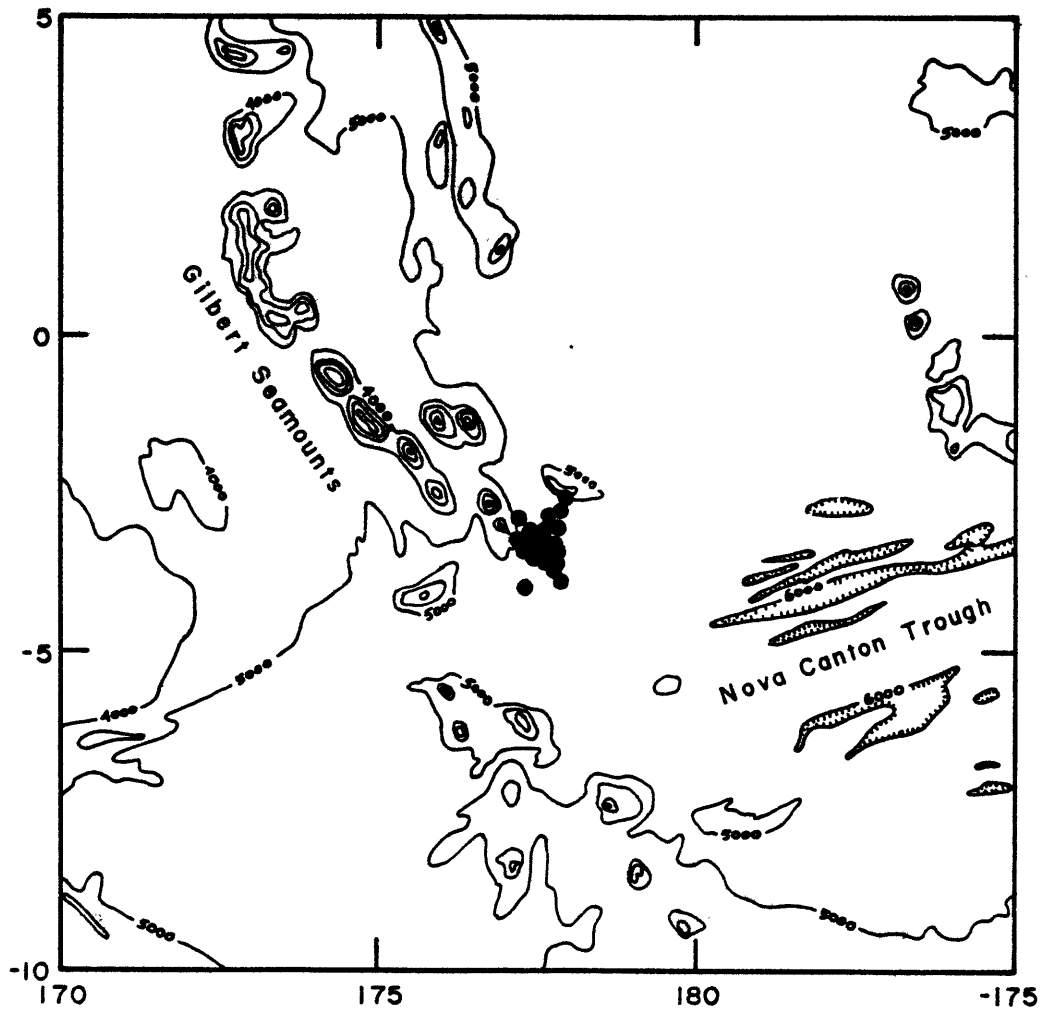


Figure 2.5

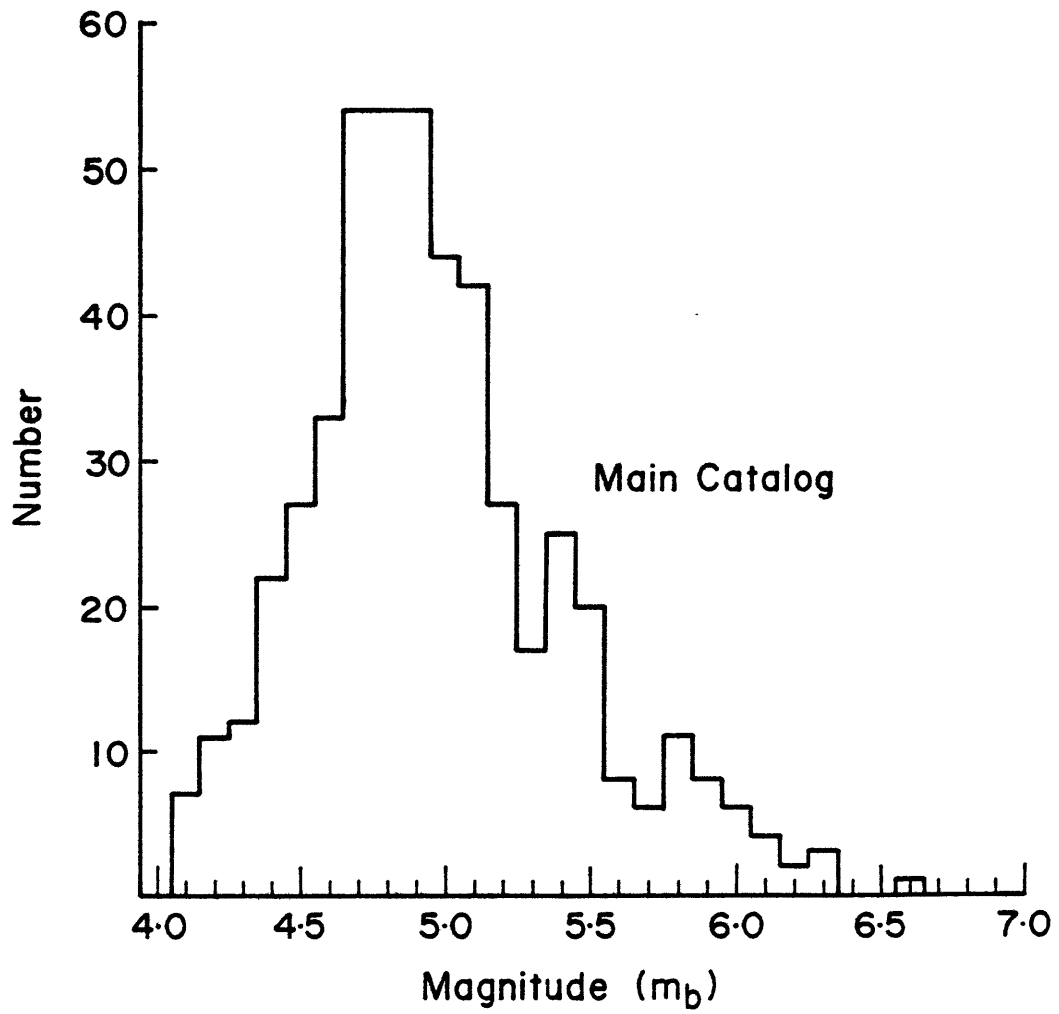


Figure 2.6



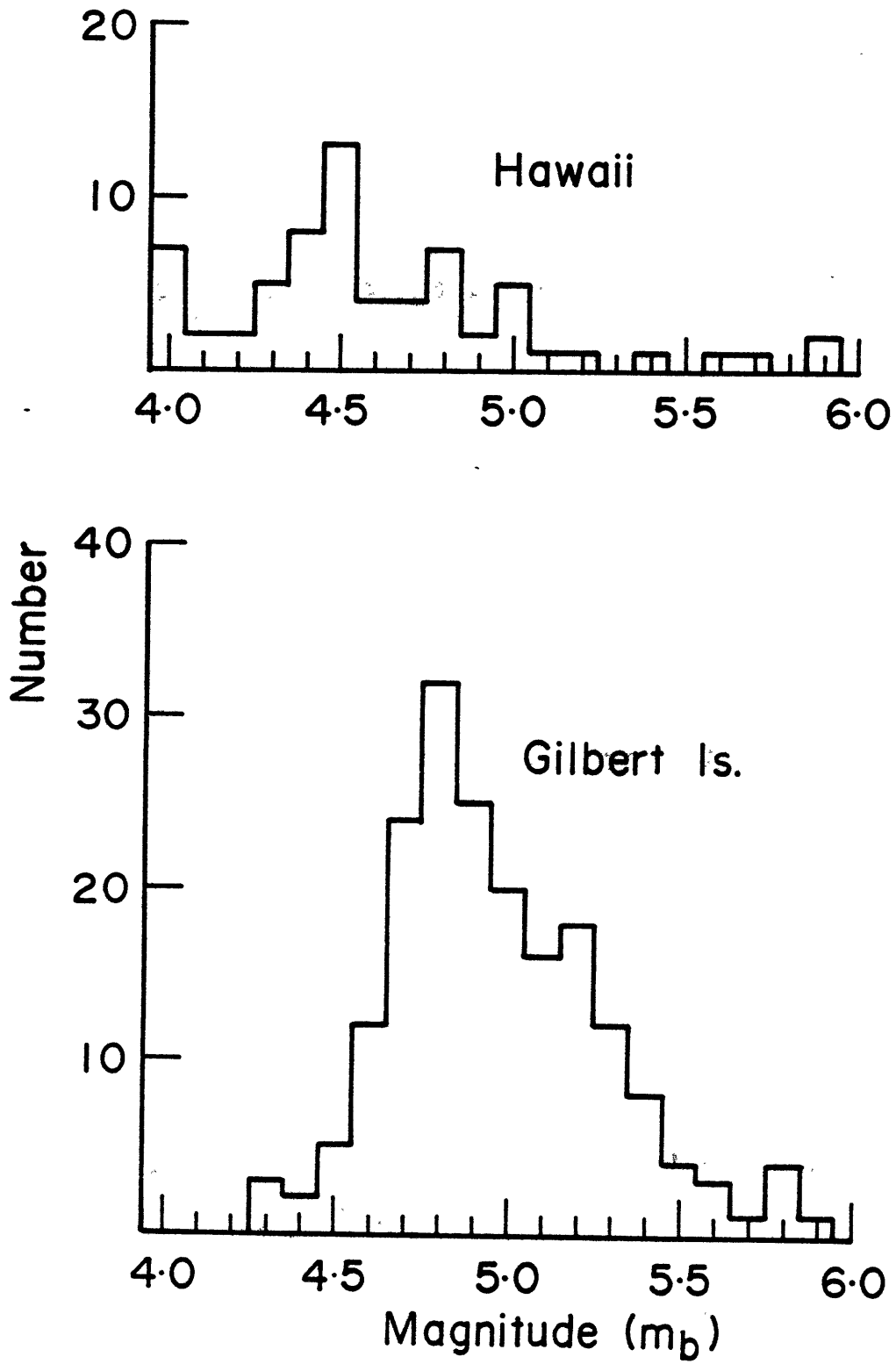
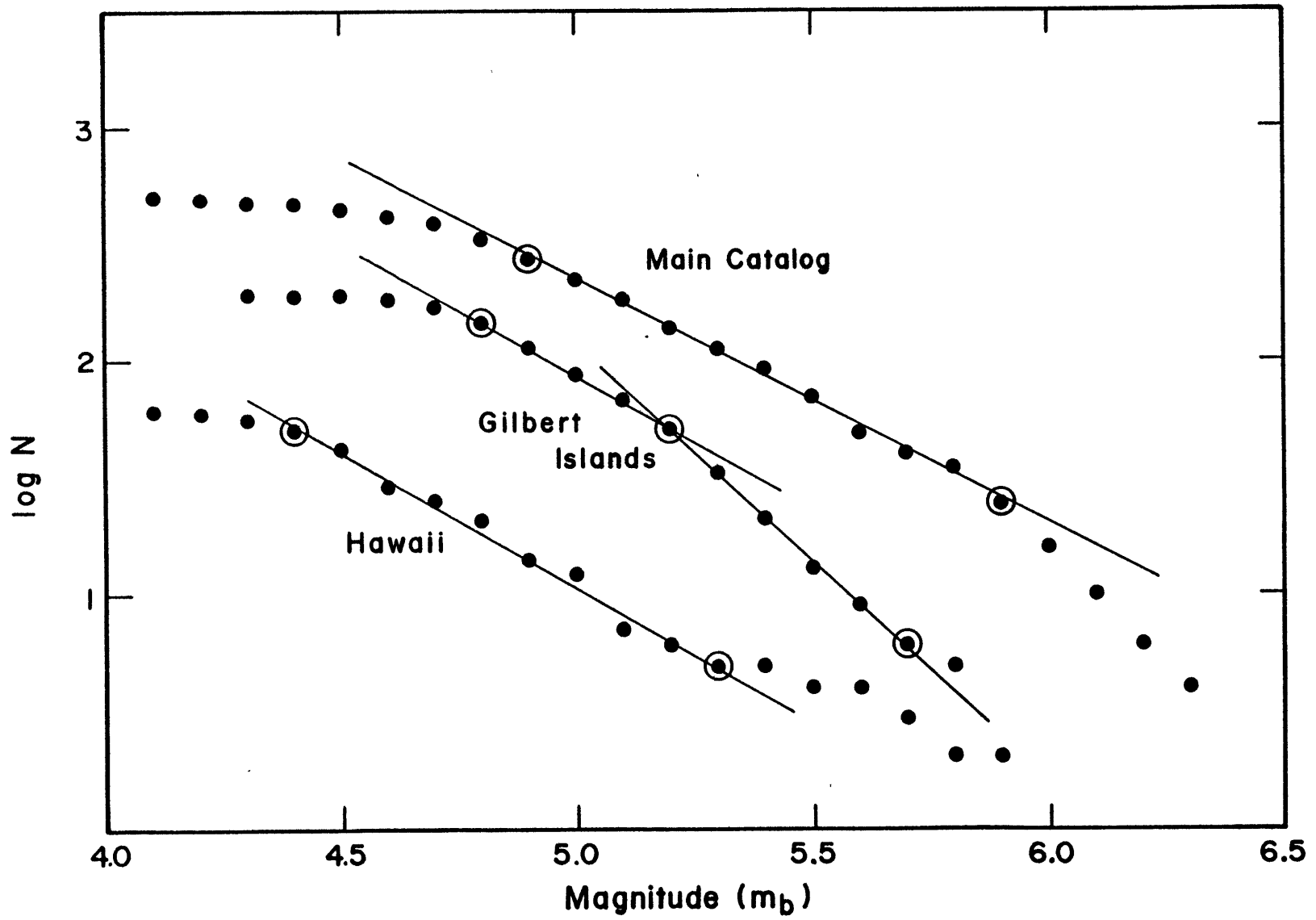


Figure 2.7

Figure 2.8



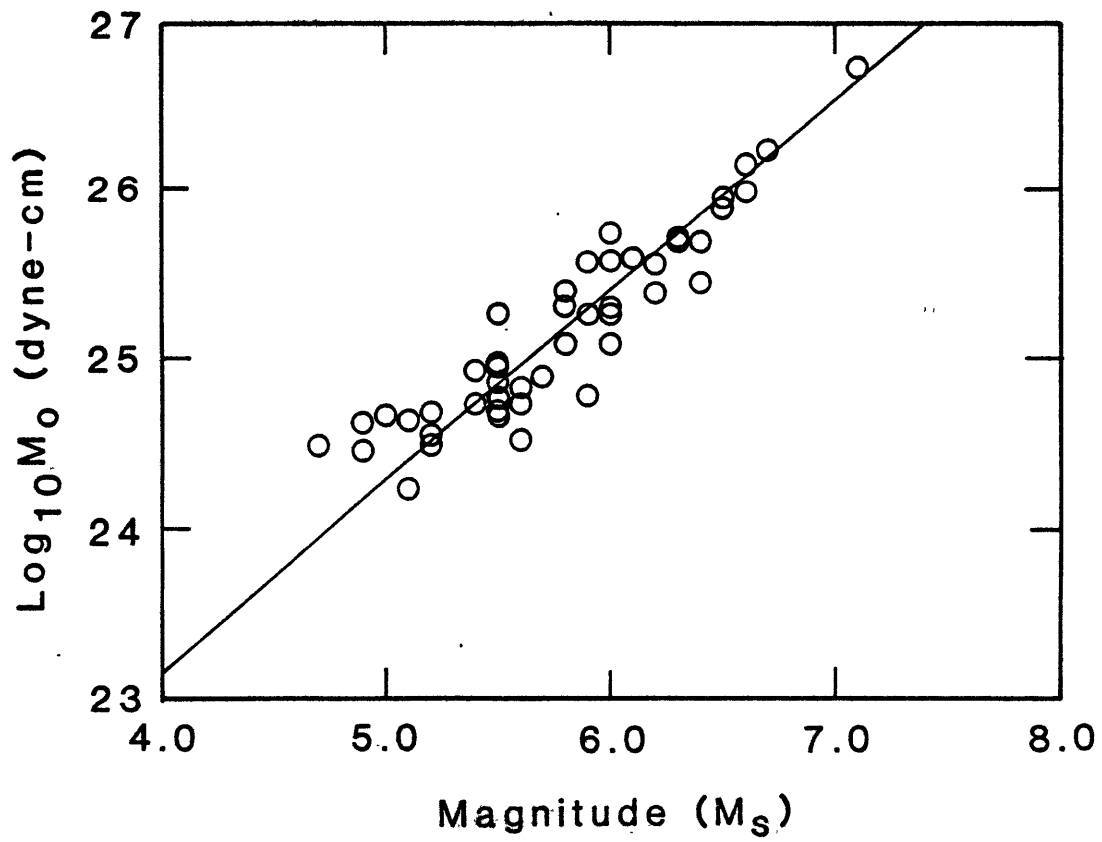
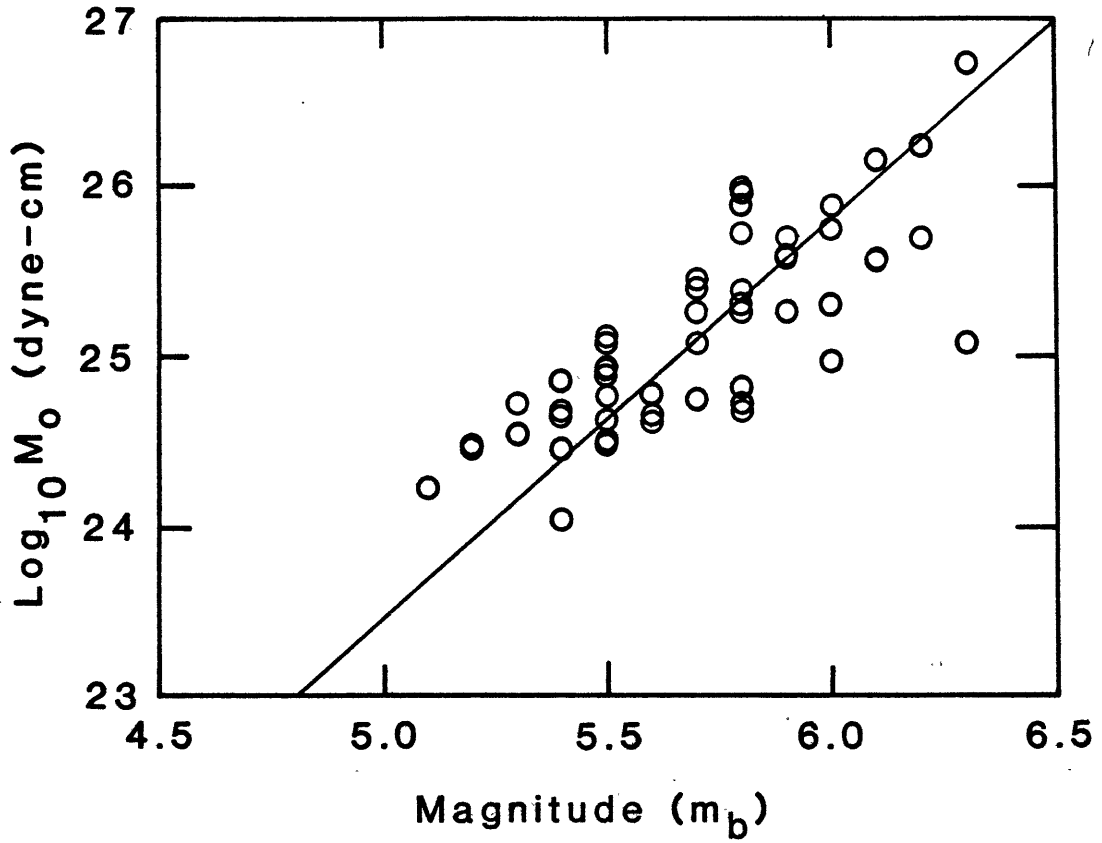
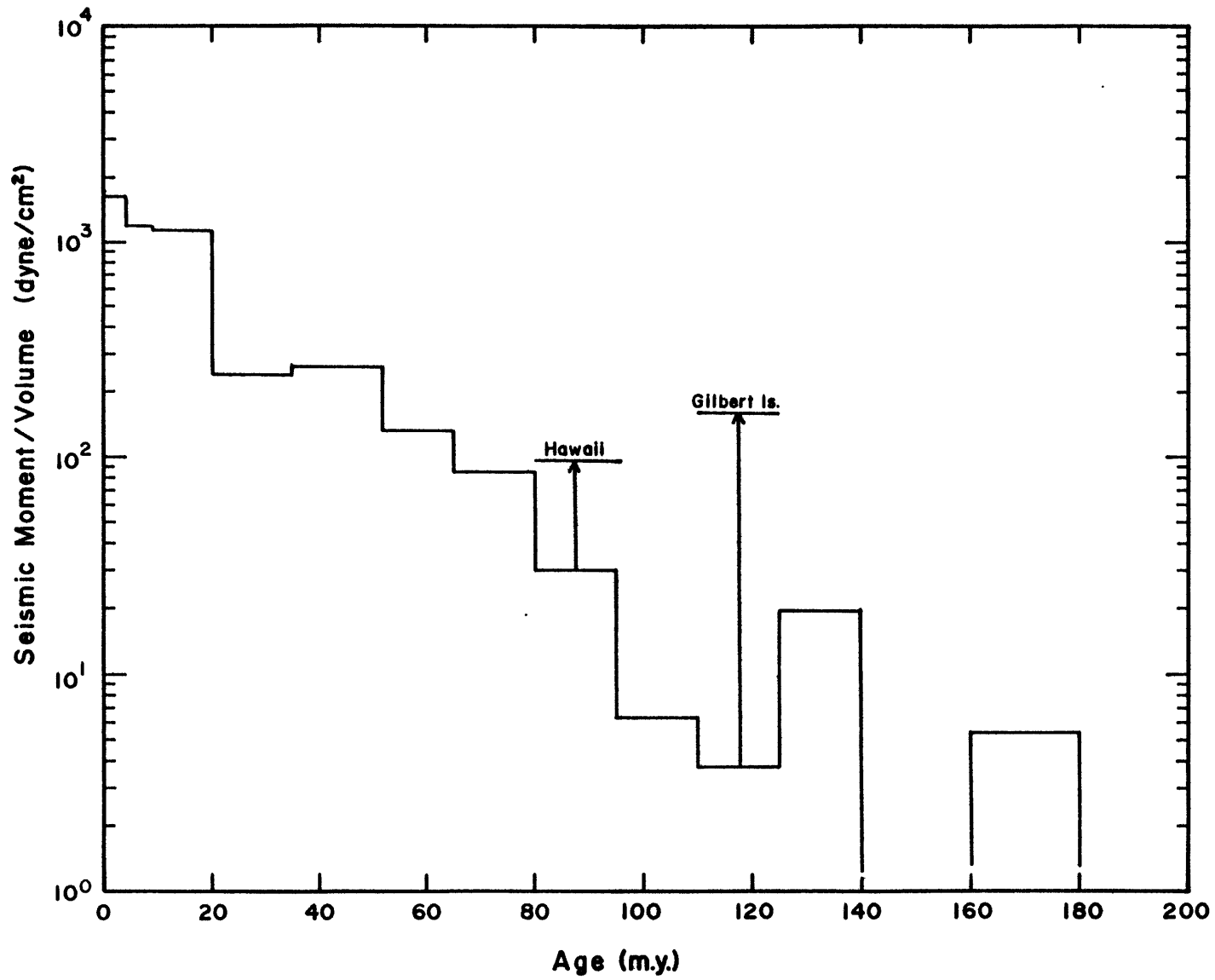


Figure 2.9

Figure 2.10



## CHAPTER 3. SOURCE STUDIES BY BODY WAVE INVERSION

## INTRODUCTION

The classical method of inferring teleseismic earthquake source mechanisms from P-wave first motions [e.g., Brumbaugh, 1979] works well when several conditions are met: (1) The earthquake must be large enough (minimum  $m_b$  of about 5.8 to 6.0) to produce clear first motions on WSSN long-period instruments, and (2) the station distribution must be adequate to constrain the nodal planes. Short-period first motion studies can be successful, but great care is required, and a large number of redundant readings is highly desirable. Oceanic intraplate earthquakes frequently violate both requirements, only rarely approaching an  $m_b$  of 6.0 and often occurring in remote areas where the station coverage only becomes adequate at larger epicentral distances, so that the first motion data samples only a small part of the focal sphere [Bergman and Solomon, 1980]. In particular, the fault strike of the ubiquitous intraplate thrust fault event is often completely undetermined by the first motion data, since at teleseismic distances every station records a compressional arrival [e.g., Sykes and Sbar, 1974].

Even when long-period P waves are observable, the true first motion from shallow events is easily missed, since surface-reflected phases can completely obscure the direct arrival [Trehu et al., 1981], or a station may be near-nodal and the emergent first arrival can be below the noise level. In such cases, a large number of stations and careful consideration of the waveforms is necessary to avoid mis-characterizing an earthquake. Simple fault plane solutions, of course, provide no information on focal depth.

Surface wave techniques have frequently been used as a supplement or alternative to first-motion studies [e.g., Forsyth, 1973; Stein, 1978; Okal, 1980]; their primary advantage is that the surface waves from shallow events are much larger than the body waves, so that source studies may be conducted on quite small events under certain conditions [e.g., Mendiguren, 1971; Kafka and Weidner, 1979]. Thus, the set of earthquakes available for a given study is enlarged. Furthermore, the data used in a surface wave study are generally of a longer period than those of a body wave study and the point source approximation is therefore more valid.

There are several important disadvantages, however, to a systematic study of oceanic intraplate earthquakes with surface-wave methods: (1) Surface wave studies are extremely laborious, requiring much digitizing and processing, thus limiting the number of events which can be studied in a reasonable amount of time. (2) It is highly desirable to use both amplitude and phase information [e.g., Patton and Aki, 1979; Romanowicz, 1981], but reliable information on phase velocities is lacking for many oceanic areas. (3) Lateral variations in earth structure cause multipathing and other effects which are very difficult to remove [e.g., McGarr, 1969; Bungum and Capon, 1974]. (4) The depth signature in surface waves is generally most prominent in the shorter periods which are those most highly contaminated by unmodelled propagation path effects [e.g., Weidner and Aki, 1973; Weidner, 1975].

In principal, given a sufficiently large and well-distributed set of source-receiver pairs, the lateral heterogeneities in shallow earth structure which most complicate the propagation of surface waves can be determined and their effect removed from earthquake source studies,

but this effort is now only in a preliminary stage. In cases where two or more earthquakes have very different focal mechanisms and are sufficiently close to one another, path effects can be removed from surface wave data to allow an unbiased study of the earthquake sources [e.g., Weidner and Aki, 1973]. Few oceanic intraplate earthquakes are suitable for such an analysis, however.

The development of computer codes to efficiently generate synthetic teleseismic body waves, for comparison with observed seismograms, has sparked a renaissance in teleseismic source studies [HelMBERger and Burdick, 1979]. Body wave synthesis techniques avoid or greatly reduce most of the problems associated with first-motion and surface-wave studies. Since much more of the waveform is used (equivalently, much more of the focal sphere is sampled, since the surface reflected phases are included) than in first-motion techniques, fewer stations and poorer station distributions can be accommodated. The amount of digitizing and processing required is small, relative to that required for surface wave studies. The only significant propagation effects in the distance range  $30^{\circ}$ - $90^{\circ}$  are geometric spreading and attenuation, which are easily modeled.

Source studies utilizing synthetic body waves have often been conducted in a trial-and-error manner, adjusting various parameters until a satisfactory fit to the available observed seismograms is achieved. Examples from the literature on oceanic intraplate earthquakes include Wang et al. [1979], Liu and Kanamori [1980], Stewart and HelMBERger [1981], Butler [1982], and Wiens and Stein [1983]. While this approach can yield good results, it suffers several drawbacks: (1) It can be extremely time-consuming, since it is very

difficult to know when no further improvement is possible. (2) The uncertainty of the results is qualitative at best. (3) If many events are being studied, it may be difficult to retain consistent criteria for the "best fit". (4) It is virtually impossible to make use of SH waves, since the radiation pattern is radically different from that of the P waves. As we shall see, SH waves provide valuable constraints on the focal mechanism in many cases.

→ A formal inversion of observed body waves, based on a quantitative measure of the difference between synthetic and observed seismograms, reduces or eliminates all these problems. Body-wave inversion studies of individual earthquakes are becoming common in the seismological literature [e.g., Burdick and Mellman, 1976; Ward, 1980; Langston, 1981; Barker and Langston, 1981]. The rest of this chapter describes a procedure, developed by Nabelek [1984], for estimating basic source parameters (focal mechanism, centroidal depth, seismic moment, and source time function) of earthquakes by a formal inversion of long-period teleseismic P and SH waves. This analysis technique will then be used for all the source studies of oceanic intraplate earthquakes presented in Chapters 4 through 7. This study marks one of the few applications of a body-wave inversion technique to the systematic study of a selected population of earthquakes for tectonic interpretation [e.g., Ward, 1983].

#### BODY-WAVEFORM INVERSION PROCEDURE

In the waveform inversion procedure of Nabelek [1984], synthetic seismograms for P and SH waves are generated using propagator matrices, as in Bouchon [1976]. They represent the complete body-wave response at teleseismic distances for a simple source (point or line) within a



layered velocity structure. The synthetic and observed seismograms are matched in a least squares sense, using standard linearized iterative techniques [Wiggins, 1972; Jackson, 1972, 1979; Tarantola and Valette, 1982]. The inversion is similar to the method of Langston [1981] and Ward [1980], except that the source depth is obtained directly as a product of the inversion. \*

The data are long-period body waves recorded by the World-Wide Standardized Seismograph Network (WWSSN) and Seismic Research Observatories (SRO) of the Global Digital Seismic Network (GDSN), digitized at intervals of 0.5 sec. The SH waves are obtained by projecting the observed horizontal component seismograms onto a line perpendicular to the azimuth from the station to the epicenter. The advantage of using SH waves is that, for somewhat different reasons, they provide much better resolution than P waves alone of the focal mechanism for both dip-slip and strike-slip mechanisms [Nabelek, 1984]. In selecting stations for inversion, we seek the best possible azimuthal coverage. When there are several stations with similar waveforms near one another, we select the one with the best signal-to-noise ratio, to keep the number of stations to a manageable level. For most events, we used between 10 and 15 records. \*

An important question then is: How small a data set can we use for a source study while preserving an acceptable degree of confidence in the results? Obviously, the definition of "acceptable" depends on the purpose for which any particular study is undertaken. We are most concerned here to determine efficiently the basic point source parameters of a large population of moderate-size earthquakes, not with the resolution of details of the fault geometry and rupture process

which is emphasized in many single-event source studies. Experience has shown that, given these priorities, there is little to be gained by using more than about 15 stations (total of P and SH) in the inversion. With typical station distribution, in which there are nearly always some significant gaps, 15 stations will adequately sample all of the focal sphere possible with body waves in the distance range  $30^{\circ}$ - $90^{\circ}$ . If station distribution is poor, as in the case of the El Golfo earthquake discussed below, using more than about 15 stations results in oversampling of some parts of the radiation pattern and simply increases the time and expense of the analysis, with only a small increase in confidence in the result.

In forward-modeling studies, a major motivation for working with a large, redundant set of waveforms is that it helps the modeler avoid being biased by the prominent high frequency portions of any individual waveform, which may not be present in the waveforms of nearby stations, and which presumably reflect peculiarities of the ray path and receiver characteristics more than fundamental source properties of the earthquake. The inversion technique, based on a least-squares criterion, naturally avoids this problem by being more sensitive to the long period portion of the waveforms. Thus, it is possible to use fewer waveforms in the inversion, with less concern about the biasing effects of the particular choice of stations.

In the inversion procedure, the source time function is parameterized as a series of elements whose number and width are specified. The relative amplitude of each element is found in the inversion. The elements may be either box functions or overlapping triangles. The triangular elements are generally superior for longer

time functions [Nabelek, 1984], but for many of the small events presented here, with time functions less than 3 s long, the box function elements are quite adequate. By using enough time function elements so that the relative amplitudes of later elements converge to values near zero, we are able to estimate the duration of faulting, which can in turn be interpreted in terms of rupture dimensions. No special significance is attached to small negative amplitudes late in the source time function, but large negative amplitudes generally indicate an instability, due either to a particularly poor starting model or a time function element width which is too short for the frequency content of the data. { —

In addition to the relative amplitudes of the source time function elements, we invert for the scalar seismic moment, centroidal depth, and double-couple orientation. The centroidal depth is the depth of the best-fitting point source, and roughly corresponds to the depth of the center of the rupture area [Dziewonski et al., 1981]. We note the distinction between centroidal depth and focal depth, determined during the standard location procedure from short period arrival times, which corresponds to the depth at which the rupture initiated. All centroidal depths reported in this thesis are relative to the top of the oceanic crust.

We assume that shallow intraplate earthquakes are caused by the shear failure of rock, and are thus well represented as a pure double couple. Resolution of the complete moment tensor for shallow events is difficult, and non-double-couple components can often be attributed to noise [e.g., Strelitz, 1978]. If significant non-double-couple components actually exist, some bias in our results would be expected.

Our convention for describing the double couple of the best-fitting point source follows Aki and Richards [1980]. The strike is specified so that the down-dip direction equals the strike direction plus  $90^\circ$ . Slip angle is measured counterclockwise from the direction of strike on the footwall and gives the relative direction of motion of the hanging wall. For example, a slip angle of  $270^\circ$  corresponds to normal faulting and a slip angle of  $180^\circ$  indicates right-lateral strike-slip motion. The three angles are given in the order: strike/dip/slip.

The inversion is carried out only on points in the time series which lie within a specified window, starting at the onset of the direct P or SH phase. The window varies in length between about 5 and 50 s, depending on the size and depth of the event, instrument type, and phase being modeled; window lengths of 10 to 20 s are typical. Each station is weighted inversely to the background noise level, which is estimated from the portion of the seismogram prior to the start of the window. Additional weighting may be specified to correct for some perceived bias in the data, such as poor station distribution or a systematic difference in amplitude due to different instrument type or wave type. Once such fundamental biases have been corrected, the inversion is insensitive to small variations in the station weights.

The assumed source structure consists of a water layer and single crustal layer over a mantle halfspace (Table 3.1). Water depth is estimated from bathymetric maps and sometimes adjusted slightly if a better fit to the observed sea-surface reflected phases can be obtained. The inversion windows are usually chosen to place little weight on the water reverberations, and we have not generally attempted to find a best-fitting water depth. In cases where a significant

thickness of sediment exists in the epicentral region (more than, say, a kilometer), a sediment layer is included in the source crustal structure. All other parameters of the source structure remain constant for all events. The receiver crustal structure is simply a halfspace, with properties appropriate to continental crust ( $V_p = 6.0$  km/sec,  $V_s = 3.46$  km/sec, density =  $2.5 \text{ g/cm}^3$ ), and it remains constant for all events.

### PITFALLS

There are many ways in which error and bias may be introduced into the body-wave inversion procedure. They can be grouped into a small number of categories, however: (1) Programming errors, (2) Data processing errors, (3) Biases related to model assumptions, and (4) Biases introduced during the inversion, which is highly interactive.

Programming errors are best eliminated from large interactive numerical analysis codes by reviewing the code for internal consistency and making comparisons with other programs to verify external consistency. In the case of the programs comprising the body-wave inversion package, both activities have been conducted more or less continuously, since the code is still being refined. The essential core of the analysis has remained unchanged during the period in which we performed all the source studies reported in this thesis. Numerous tests of the program, against both analytical results and other numerical codes, are described in Nabelek [1984].

The source mechanisms of oceanic intraplate earthquakes presented in the following chapters provide numerous opportunities for comparison with source parameters reported by other researchers. Aside from focal mechanisms, comparison with the seismic moment obtained from surface

wave studies and with the depth estimated by matching synthetic and observed P waves (forward modeling) are most common. Later in this chapter we present a relatively detailed comparison between our body-wave inversion results and the reported source mechanisms for two earthquakes, one characterized by strike-slip faulting and one by thrust faulting, which have been studied in detail using both body- and surface-wave techniques [Ebel et al., 1978; Cipar, 1980]. While differences certainly exist in particular cases, there is no evidence in these comparisons to suggest any systematic bias in our results with respect to other techniques.

By data processing errors, we mean errors in the data set used for the inversion, introduced either through mis-characterization of the raw seismograms (incorrect reported magnification or reversed polarity) or through mistakes in digitizing (skewness, wrong time base) and processing (entering an incorrect station parameter, for example).

We have encountered many cases in which the overall amplitude of the waveform at a station is inconsistent with the amplitude of the remaining waveforms, after correcting for different instrument gains. An obvious explanation for such an observation is that the reported gain is incorrect. The amplitude of the calibration pulse, measured on the original seismogram, and the reported calibration current can be used to check the reported gain, but there is no guarantee that the correct calibration current was reported. An alternative explanation, which deserves more study, is that some stations exhibit significant amplitude anomalies, presumably rooted in the shallow structure beneath the station. The inversion has been found to be insensitive to such amplitude variations, as long as they constitute a small subset of the

stations used for the inversion. In many cases, a nearby station with a more consistent amplitude is available and we simply ignore an anomalous station. Although it is often unnecessary, a waveform with anomalous amplitude may be kept from dominating the inversion by assigning it a lower weight.

Reversed polarity (unreported on the seismogram header) is seldom observed on the vertical component seismograms from which we obtain P waves; it is much more commonly observed on the horizontal components, from which SH waves are extracted. For example, the horizontal components at station PRE (Pretoria, South Africa) were found to have reversed polarity in every case checked over a period of about five years (1965-1970). The polarity is most easily checked if the P wave of the earthquake being investigated is clearly recorded on both horizontal components. Otherwise, one or more earthquakes large enough and in the proper direction to have produced well-recorded P waves on all three components, and as close as possible in time to the earthquake of interest, are used to check the polarity. All cases in which we have reversed the polarity of a waveform are noted in the discussion of the individual earthquakes.

Judging from a number of cases in which records were redigitized, digitizing errors do not contribute significantly to the uncertainty in the inversion results. Body-wave analysis in the time domain is much less sensitive to such errors than surface wave techniques, which usually entail transforming the digitized seismogram into the frequency domain.

The model used to generate the synthetic waveforms used in the inversion makes a number of assumptions and simplifications which may

introduce bias into the results. The first approximation we make is that we can treat the earthquake as a point source (we occasionally make use of a multiple-point source model or a horizontal line source for larger events). Point-source inversions performed on synthetic waveforms generated for finite faults and complex sources produce mechanisms which are good average representations of the true rupture history, even though the fit to the observed waveforms is sometimes poor [Nabelek, 1984]. For the purpose of investigating the regional deformation represented by oceanic intraplate earthquakes, the average mechanism found in the point source inversion is usually quite adequate.

Synthetic waveforms are generated with source and receiver structures parameterized as a small number (or none in the case of the receiver) of flat-lying layers over a halfspace. There are very likely to be spurious reflections associated with the assumed layered structure. Conversely, important reflectors may not be included, or may be placed at the wrong depth. The relative timing between direct and reflected phases is controlled by the thickness and seismic velocities assigned to each layer above the source depth. The centroidal depth is the parameter most affected by this type of bias. Bias in the focal mechanism may also be caused by the assumed velocity structure, since the calculated take-off angles to different stations are a function of the velocity at the source, and these angles directly affect the synthetic waveforms through the radiation pattern of the double couple mechanism. The difference between takeoff angles calculated with crustal and mantle velocities can exceed  $5^\circ$ . This type of bias is particularly important when there are large gaps in azimuthal coverage, a regrettably frequent occurrence.



Geometric spreading in the earth causes amplitude variations between stations at different epicentral distances. This variation must be removed from the observed records to avoid biasing the inversion toward stations at smaller epicentral distances, but the geometric spreading factor for a given epicentral distance cannot be determined with great precision. We interpolate values of the geometric spreading factor from a smooth curve which approximates the discrete values calculated numerically from travel time tables [Carpenter, 1967]. The geometric spreading factor changes most rapidly (increases) and is most uncertain at smaller epicentral distances.

The attenuation model used to generate synthetic body waves [Futterman, 1962] is probably not a significant source of bias in the results, because attenuation plays only a minor role in shaping waveforms in the WSSN long-period band. We have found no case in which it has appeared necessary to vary the attenuation constants  $t_p^*$  and  $t_s^*$  from typical values of 1.0 and 4.0 s, respectively.

Clearly, we wish to eliminate or minimize error or bias due to the various factors discussed above. The actual process of determining the source mechanism however, consists in large part of guiding (or biasing) the inversion so that it converges to a solution which not only minimizes the variance, but satisfies certain other criteria, which accumulate with experience, particularly the experience of performing source studies by forward modeling. The basic parameters used to 'steer' the inversion are the starting point and length of the inversion window for each station and the individual station weights.

The choice of starting point for the inversion window at each station is one of the most important interactive tasks in the

inversion. Even when the first break of the P wave at each station is clear, some adjustment may be necessary because the time function of the best-fitting point source will differ from the apparent time function at each station in proportion to the finiteness of the source. Other commonly encountered situations requiring adjustment of starting points are emergent waveforms and cases in which background noise obscures the first motion. The optimum starting points of SH waves are often more difficult to determine than those for P waves, because the noise level is usually higher and SH waves have a more emergent character. The normal strategy is to perform initial inversions with only the most clearly expressed P and SH waves, obtaining a solution which predicts reasonably good waveforms at stations with no weight. The remaining stations are then incorporated and the final refinements can be made.

Modifications to the length of the inversion window at each station are undertaken to restrict the inversion to the part of each waveform which contains information about the source. For example, we do not wish to use inversion windows so long that the inversion of P waves is dominated by the large water reverberations frequently observed after the primary P phases, since water reverberations contain little information other than the water depth. The water reverberations observed at different stations are often out of phase as well, and cannot all be simultaneously fit with the simple source model used in the inversion.

The main use of the station weights during the inversion is to remove a station temporarily, in order to work with a subset of stations with which it may be easier to establish a good starting model

for the final, full inversion. As discussed earlier, there are occasionally circumstances in which a bias in station distribution or fundamental difference in amplitude between different instrument or wave types can be reduced using station weights.

#### DEPTH RESOLUTION

The ability to determine easily the source depth of an earthquake to within several kilometers constitutes one of the great advantages of source studies utilizing body waveforms. The depth resolution routinely available with body wave methods is comparable to that of the most painstaking surface wave studies, i.e., those which utilize phase information at relatively short periods and remove propagation effects from the data in some manner. The standard method of determining source depth from surface wave data involves calculating one or more error functions of the observed and synthetic spectra for many source depths and selecting the depth which produces a minimum [e.g., Weidner and Aki, 1973; Aki and Patton, 1978; Romanowicz, 1981, 1982]. Using this method, the depth of an earthquake often can be determined to within several kilometers.

For comparison, we performed an analogous study with the body waves from two events: (1) The June 2, 1965 Mid-Atlantic Ridge earthquake studied by Weidner and Aki [1973], and (2) the 1976 Friuli, Italy earthquake discussed later in this chapter. The 1965 earthquake has a very distinctive depth signature; the depth resolution for this event approaches the limit possible with body waves recorded on long-period WWSSN instruments. The Friuli earthquake has a dip-slip mechanism with a very shallow dipping fault plane, i.e., a moment tensor with large  $M_{xz}$  and  $M_{yz}$  components. These components of the

moment tensor are relatively difficult to resolve for shallow sources and we expect the depth resolution for this event to be unusually poor. For these two earthquakes we determined the best-fitting point source parameters (including centroid depth) in the usual manner, then calculated the residual error with this solution at other depths (Figure 3.1). No iterations were allowed at other depths.

For the June 1965 earthquake, Weidner and Aki [1973] found a depth of  $3 \pm 2$  km below the seafloor, in excellent agreement with the centroid depth determined in the body-waveform inversion: 2.3 km. The standard deviation of the depth in the inversion is 50 m, however, and is clearly an underestimate. The residual vs. depth curve for this event (Figure 3.1a) suggests that the true uncertainty in centroid depth is perhaps 0.5 to 1 km. Attempts to obtain satisfactory fits to the observed waveforms of this event with the centroid fixed at different depths were successful only for depths within approximately 0.5 km of the optimum depth. A similar discrepancy is observed for the May 1976 Friuli earthquake: the standard deviation of the centroid depth (100 m) is much less than the resolution indicated either by the residual vs. depth curve (Figure 3.1b) or by the range of acceptable depths found during the course of performing the body-waveform inversion study. In practice, we found reasonably good solutions for this earthquake at depths ranging from about 6.5 to 10 km, with the lowest residual found for a depth of 9.5 km. Cipar [1980] estimated the depth of this event to be 8 to 10 km.

There are several possible contributing factors to the discrepancy between the standard deviation of the centroid depth and the empirical uncertainty. The parameter variances calculated in the least-squares

inversion are unbiased if the parameter is linear. The seismic moment is the only linear parameter; all others are at best weakly nonlinear and the depth is the most nonlinear. We therefore expect the estimated variance of the centroid depth to have the largest potential bias. In essence, the necessary conditions for defining a true variance of the centroid depth do not exist. This is clearly a subject which deserves further investigation, since body-waveform inversion studies are becoming routine in seismic source studies.

In choosing a starting point for the inversion window for each waveform, an artificial constraint on the depth is imposed. Because of the effect of source finiteness, the first motion of the observed long-period waveform (even if it is clearly observed) is not necessarily the correct starting time for the point source inversion. Using the cross-correlation to realign the synthetic and observed waveforms periodically during the inversion reduces this problem. The optimum procedure would be to use the short-period arrival time at each station to establish the starting point for the inversion window and also invert for the relative location of the centroid with respect to the point of initiation [Nabelek, 1984]. The residual vs. depth curves in Figure 3.1 are constructed without changing the starting points of the inversion windows so this factor cannot account for the discrepancy between formal and empirical resolution.

In a series of inversions of synthetic data contaminated by various types of noise, Nabelek [1984] estimated that the true uncertainty of the non-linear parameters determined in the body-waveform inversion is approximately 10 standard deviations. Our experience in conducting the source studies presented in the following

chapters supports this conclusion, particularly with regard to centroid depth. With the type of data used here, the best obtainable resolution for the centroid depth is estimated to be about 0.5 km, for shallow dip-slip events (on planes dipping about  $45^\circ$ ) such as the June 2, 1965 earthquake mentioned above. The depth of shallow strike-slip and vertical dip-slip events (such as the May 6, 1976 event) can be much more difficult to resolve and the uncertainty may be as high as 2 km. For most of the source studies presented here, the uncertainty in depth is estimated to be about 1 to 1.5 km. A variety of factors can degrade the depth resolution achievable for individual events.

#### COMPARISON - THE 1966 EL GOLFO EARTHQUAKE

On August 7, 1966, a large earthquake ( $m_b = 6.3$ ,  $M_s = 6.3$ ) occurred at the northern end of the Gulf of California ( $31.74^\circ$  N,  $114.51^\circ$  W) on the NW-trending San Jacinto fault, the southernmost element of the transform plate boundary in California. The source mechanism of this event was studied in some detail by Ebel et al. [1978], who matched synthetic P, SH, and surface waves to observed seismograms. The main reason for selecting this event for comparison is that the synthetic body waves presented by Ebel et al. [1978] are generated with the same technique used by the inversion program, but with an entirely distinct program. This provides an opportunity to make a detailed test of the synthetic waveforms generated by the inversion program. Given identical model parameters, the waveforms generated by the two programs should be indistinguishable.

We selected stations for inversion in the normal manner, seeking the best possible azimuthal coverage with a reasonable number of stations. In the case of the El Golfo earthquake, nearly all available

stations lie between azimuths of about  $330^\circ$  and  $140^\circ$  and unfortunately occupy only two quadrants of the radiation pattern. The only station in the Pacific in the permissible distance range is KIP, on Hawaii; it provides much-needed constraint on the dip of the fault plane in the study by Ebel et al., but our film record of this waveform was too faint to use. As we will see, the total absence of P-wave data in one hemisphere can lead to significant bias in the focal mechanism. Of the 9 P-wave stations selected, 6 were also used by Ebel et al. We obtained 6 SH waves for the inversion as well, but were unable to use WES, the only one of 4 SH waves for which Ebel et al. show the waveform. Both studies use the same layered source structure and attenuation constants (1.3 and 5.2 s for P and SH, respectively).

The best-fitting source parameters for the El Golfo earthquake were found by Ebel et al. [1978] to be a right-lateral strike-slip focal mechanism (140/85/183) at a depth of 10 km, with a triangular source time function 4 s in duration, and a seismic moment of  $5.0 \times 10^{25}$  dyne-cm (Figure 3.2). The surface waves are consistent with this mechanism, but indicate a somewhat larger moment,  $6.5 \times 10^{25}$  dyne-cm. A comparison between the synthetic waveforms for this mechanism shown by Ebel et al. [1978] (Figure 3.3) and the synthetic waveforms in Figure 3.2, which were generated with the inversion program, shows excellent agreement at the 6 P wave stations common to both. Although the time and amplitude scales are slightly different, it is quite apparent that even very minor features in the synthetic P waves of Ebel et al. are reproduced in our synthetics, as they should be. Because the geometric spreading factors in the two cases have not been equalized, some small differences in amplitude are expected.

We next conducted the body-wave inversion in the normal manner, retaining a 4 s triangular time function and the same station weights and inversion windows, to determine how much further the residual error could be reduced simply by varying the focal mechanism, depth, and seismic moment, the most readily manipulated parameters in a forward modeling study. A slight increase in depth (11.1 km) and decrease in seismic moment ( $4.0 \times 10^{25}$  dyne-cm) reduces the residual error by 14%. Iteration resulted in no significant change from the focal mechanism preferred by Ebel et al. (from 140/85/183 to 141/84/184). The observed and synthetic waveforms for this solution, along with the mechanism, are shown in Figure 3.4.

The source parameters determined in this inversion, along with the standard deviations, are listed in Table 3.2. As we discussed in the previous section, the a posteriori parameter variances calculated in the inversion are strictly meaningful only for a linear problem. In particular, the standard deviation of the centroid depth (the most nonlinear parameter) is consistently found to be perhaps an order of magnitude smaller than the uncertainty estimated from repeated trial inversions at different depths. Throughout this thesis study, we list the standard deviations of all inversion parameters as in Table 3.2 with the explicit understanding that they underestimate the true uncertainty of the solution. The standard deviations are sometimes useful, however, as indicators of the relative resolution for the source parameters of different earthquakes.

The next refinement to our source model was in the source time function: we replaced the 4 s triangular time function used above with 5 overlapping triangular elements, each 2.4 s in duration. With more



parameters in the source time function, the inversion converged to a solution only slightly better than the previous one, with a 5% further reduction of the residual error (Table 3.2). The centroid is slightly deeper than before, at 11.6 km, and the seismic moment rises to  $4.4 \times 10^{25}$  dyne-cm. The source time function has a small pulse at the end, but the main part of the rupture is very similar to the 4 s triangle used by Ebel et al., having a width of 4.8 s. The focal mechanism (140/81/185) differs from the previous solutions only in the dip of the fault plane. Tests indicate that the dip may be decreased to at least  $70^\circ$  while maintaining a low total residual error: the increased misfit at most P wave stations is offset by smaller errors for some SH wave stations. A dip of less than about  $80^\circ$  is not consistent with the observed P wave at KIP (shown by Ebel et al. [1978] but not available for our inversion). The observed and synthetic waveforms for this solution are shown in Figure 3.5.

Our final inversion for this event was performed as before, with a multi-element time function (4 triangular elements 3.0 s wide), but with the dip of the focal mechanism constrained to  $85^\circ$ . The residual error increases by 2% for this solution, but except for the dip, it varies little from the last solution (140/85/184,  $h = 11.9$  km,  $M_0 = 4.2 \times 10^{25}$  dyne-cm). The source time duration for this solution is about 6 s (Figure 3.6, Table 3.2).

Several conclusions may be reached from this comparison between the inversion technique and the source study of Ebel et al. [1978]: (1) The synthetic seismograms generated in the body-waveform inversion program agree in great detail with those generated by a program using the same algorithm but completely different coding, giving us

confidence that there are no programming errors in this portion of the program significant enough to bias the results of the inversion. (2) A carefully conducted forward-modeling study can achieve a fit to the observed waveforms which is as good as the inversion technique, and more to the point, produce as good an estimate of the basic source parameters. The tradeoff between depth and source time function is difficult to explore by trial-and-error, however. (3) Estimates of the seismic moment made from forward-modeling studies will tend to be higher than the moment obtained in the inversion, because most modelers naturally make the amplitude comparison between observed and synthetic waveforms at the prominent peaks, which are relatively short period features in the waveforms, whereas the inversion's least-squares criterion accentuates the longer period part of the waveform. (4) Poor station distribution can lead to significant bias in the focal mechanism, but has less effect on estimates of the depth, moment, or source time function.

#### COMPARISON - THE 1976 FRIULI EARTHQUAKE

On May 6, 1976 a large earthquake ( $m_b = 6.0$ ,  $M_s = 6.5$ ) occurred in the northeast corner of Italy ( $46.35^\circ\text{N}$ ,  $13.26^\circ\text{E}$ ), where the Friuli Plain underthrusts the Southern Alps. This region marks the boundary between the Eurasian plate and lithosphere of the Adriatic Sea, which along with neighboring coastal areas has been variously interpreted as a tongue of the African plate [McKenzie, 1972] or a microplate, the Apulian plate [Lort, 1971]. The main shock and some of the aftershocks were studied in detail with surface waves and long period body waves [Cipar, 1980] and also with short period body waves [Cipar, 1981]. In this section we compare the point source inversion results with the

source parameters determined in the long period body wave (P, SH, and SV) study of Cipar [1980]. This comparison provides a good example of an issue discussed above: the question of how many waveforms should be used in the inversion, at least in those cases in which we have the luxury of being selective.

Cipar modeled the waveforms of 14 P waves, 9 SH waves, and 8 SV waves in the long-period body wave portion of his study of the Friuli earthquake, while the inversion was conducted with 8 P waves and 5 SH waves. While it is clearly desirable to use as many waveforms as possible when one seeks the highest level of confidence about the inferred source parameters, the time required to process and analyze many waveforms places definite limits on the number of earthquakes which may be studied in a reasonable amount of time. As we shall see, the inversion solution, utilizing a significantly smaller data set, is quite compatible with the results of an unusually thorough forward-modeling study. No significant improvement in our knowledge of the average point source mechanism of this earthquake would result from the use of more waveform data in the inversion.

The synthetic body waves shown in Cipar [1980] are generated with a propagator matrix method which, given the same source parameters, should produce waveforms identical with those of the inversion, but an exact comparison between the waveforms of the two studies is not possible in this case because the crustal structure used by Cipar contains more layers than the inversion routine can accommodate. The inversions are performed with Cipar's layered structure except that 3 thin layers in the lower crust (layers 2, 3, and 4 of Table 4 in Cipar [1980]) have been combined into one layer of equivalent thickness, with

the seismic velocities of layer 3. This difference causes only minor differences between the waveforms, however, because the perturbation to Cipar's layered structure is quite small and because the earthquake source depth places it above these layers, in layer 1.

Cipar constrained the strike ( $N76^{\circ}E$ ) and dip ( $75^{\circ}S$ ) of one nodal plane for this event with the first motion data, and he matched synthetic P waves to observed records at several stations, judged to be insensitive to the exact orientation of the second nodal plane, to constrain the depth to about 8 or 10 km, with a trapezoidal source time function 4.5 s in duration. He then modeled SH and SV waves at different slip angles to determine a best-fitting slip angle between  $80^{\circ}$  and  $90^{\circ}$ . In the format used in this thesis, Cipar's focal mechanism is 76/75/85. The seismic moment of this event is estimated by Cipar to be  $2.9 \times 10^{25}$  dyne-cm from the body waves, but the 100 s Rayleigh waves he examined suggested a higher moment,  $5.0 \times 10^{25}$  dyne-cm. The observed and synthetic waveforms generated for the source mechanism of Cipar [1980] are shown in Figure 3.7.

For the inversion study of the Friuli earthquake, we started with Cipar's solution, which provides a reasonably good fit to all the waveforms we used, and refined the source parameters until little further improvement seemed likely. The inversion solution ( $78/76/77$ ,  $h = 9.5$  km,  $M_0 = 2.9 \times 10^{25}$  dyne-cm) listed in Table 3.2 differs negligibly from that of Cipar [1980]. The decrease in the residual error of the inversion solution relative to Cipar's solution is largely due to the source time function, which is about the same overall length as the trapezoid used by Cipar, but shaped more like an asymmetric triangle (Figure 3.8).

In summary, synthetic seismograms generated by the body-waveform inversion program used in this thesis study are indistinguishable from those generated by other programs when identical input parameters are supplied. Also, the source parameters of the August 7, 1966 El Golfo and May 6, 1976 Friuli earthquakes determined with the inversion technique are found to be in excellent agreement with those determined in detailed forward-modeling studies by Ebel et al. [1978] and Cipar [1980], respectively. Although an unbiased estimate of the average point source mechanism is reliably obtained in the inversion, the uncertainty of the source parameters, particularly centroid depth, is substantially underestimated. The true uncertainty is likely to be on the order of 10 standard deviations, typically about 5 to 10° in the angles describing the best double couple mechanism and 1 or 2 km in the centroid depth.

Table 3.1. Source structure assumed for calculation of synthetic seismograms

<u>Layer</u>	<u>V<sub>p</sub>, km/sec</u>	<u>V<sub>s</sub>, km/sec</u>	<u>Density, g/cm<sup>3</sup></u>	<u>Thickness, km</u>
Water	1.52	0.00	1.03	Variable
Sediment	2.00	0.80	2.00	Variable
Crust	6.40	3.70	2.90	6.0
Mantle	8.10	4.60	3.40	-

Table 3.2 Source mechanisms obtained from body-wave inversion<sup>a</sup>

Date	Moment <sup>b</sup>	$t_s^c$	Depth <sup>d</sup>	Strike	Dip	Slip
August 7, 1966 <sup>e</sup> (1)	40. $\pm$ 1.	4.0	11.1 $\pm$ 0.1	140.6° $\pm$ 0.7	84.4° $\pm$ 0.4	183.6° $\pm$ 0.4
(2)	44. $\pm$ 1.	4.8 $\pm$ 1.2	11.6 $\pm$ 0.2	139.7 $\pm$ 0.7	80.8 $\pm$ 0.9	184.6 $\pm$ 0.5
(3)	42. $\pm$ 1.	6.0 $\pm$ 1.5	11.9 $\pm$ 0.1	139.7 $\pm$ 0.7	85.0	183.6 $\pm$ 0.4
May 6, 1976	29. $\pm$ 2.	6.0 $\pm$ 1.5	9.5 $\pm$ 0.1	77.5 $\pm$ 0.7	75.7 $\pm$ 0.4	76.8 $\pm$ 1.7

a) Range indicated for each parameter is one standard deviation (formal error). The range of  $t_s$  is one half the width of the triangular source time function element used.

b)  $\times 10^{24}$  dyne-cm ( $10^{17}$  N-m)

c) Total duration of faulting, sec.

d) Relative to top of crust, km

e) Notes on special features of individual inversions:

- 1 4 s triangular source time function
- 2 full inversion (best solution)
- 3 constrained dip (85°)

## FIGURE CAPTIONS

Figure 3.1 Residual error vs. centroid depth for (a) the Mid-Atlantic Ridge earthquake on June 2, 1965 and (b) the Friuli, Italy earthquake on May 6, 1976. The best point source solution is found for each event and the residual error of this mechanism at a number of other depths is calculated. No iterations are performed at other depths.

Figure 3.2 Comparison of observed (solid lines) long-period P and SH waves for the August 7, 1966 El Golfo earthquake with synthetic waveforms (dashed lines) generated with the body-waveform inversion program but using the source mechanism reported by Ebel et al. [1978] (no iterations). P and SH radiation patterns are shown on the lower focal hemisphere (equal area projection). All amplitudes are normalized to an instrument magnification of 3000; the amplitude scales correspond to the waveforms that would be observed on an original seismogram from such an instrument. Symbols for both types of waves are: open circle - dilatation, closed circle - compression, cross - emergent arrival. For SH waves, compression corresponds to positive motion as defined by Aki and Richards [1980].

Figure 3.3 Comparison of the synthetic P waveforms generated by Ebel et al. [1978] with observed waveforms. Six stations (COL, CMC, GEO, SJG, BOG, and QUI) used by Ebel et al. were also used in the inversion study. A direct comparison may be made between the synthetics at these stations with those shown in Figure 3.2.

Figure 3.4 Comparison of observed P and SH waves for the August 7, 1966 El Golfo earthquake with synthetic waveforms calculated from the focal mechanism obtained in the inversion. The source time function was constrained to be a 4 s triangle, as used in Ebel et al. [1978].



The two vertical lines delimit the portion of each waveform used in the inversion. For further explanation, see Figure 3.2.

Figure 3.5 Comparison of observed P and SH waves for the August 7, 1966 El Golfo earthquake with synthetic waveforms calculated from the focal mechanism obtained in the inversion when the source time function is parameterized by 5 overlapping triangular elements, each 2.4 s in duration. See Figures 3.2 and 3.4 for further explanation.

Figure 3.6 Comparison of observed P and SH waves for the August 7, 1966 El Golfo earthquake with synthetic waveforms calculated from the focal mechanism obtained in the inversion when the source time function is parameterized by 4 overlapping triangular elements, each 3.0 s in duration. The dip angle of the fault plane is constrained to equal  $85^\circ$ . See Figures 3.2 and 3.4 for further explanation.

Figure 3.7 Comparison of observed P and SH waves for the May 6, 1976 Friuli earthquake with synthetic waveforms generated for the source mechanism reported by Cipar [1980]. See Figure 3.2 for further explanation.

Figure 3.8 Comparison of observed P and SH waves for the May 6, 1976 Friuli earthquake with synthetic waveforms calculated from the focal mechanism obtained in the inversion. See Figures 3.2 and 3.4 for further explanation.

Fig. 3.1

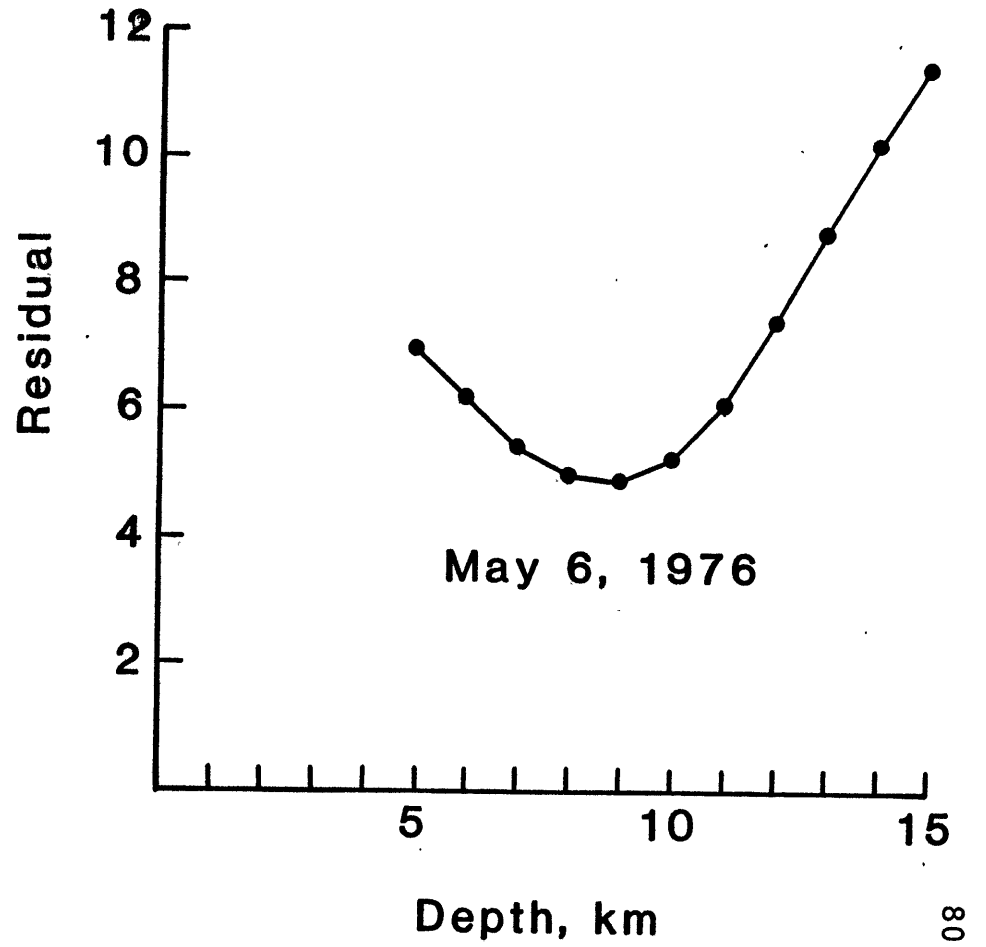
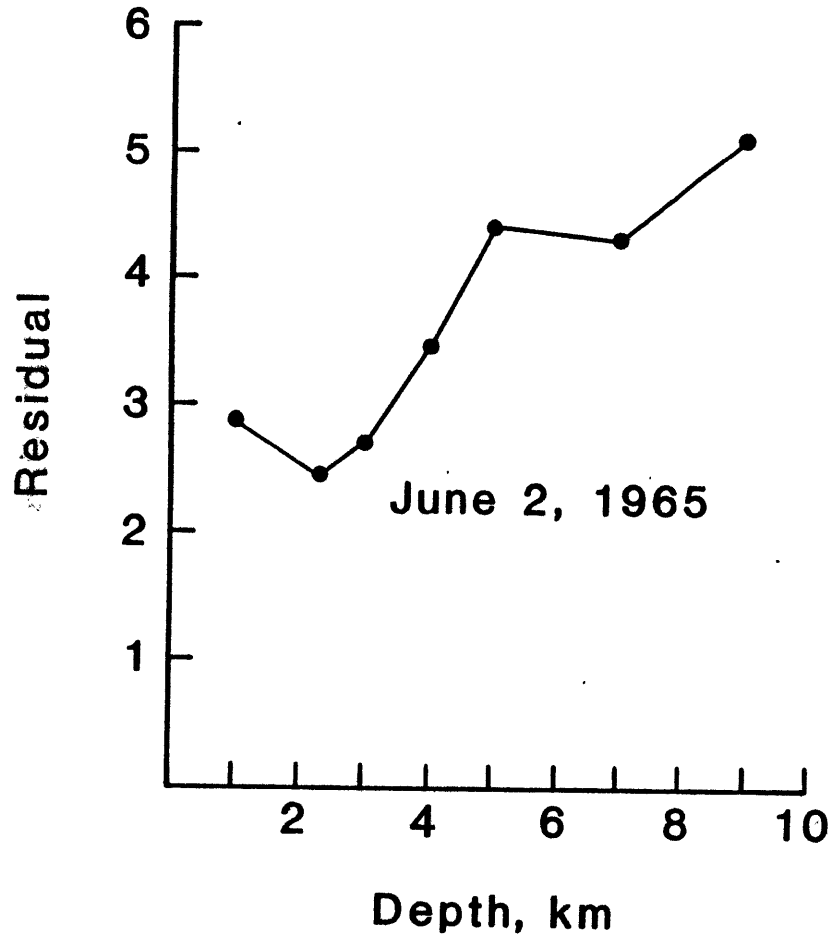
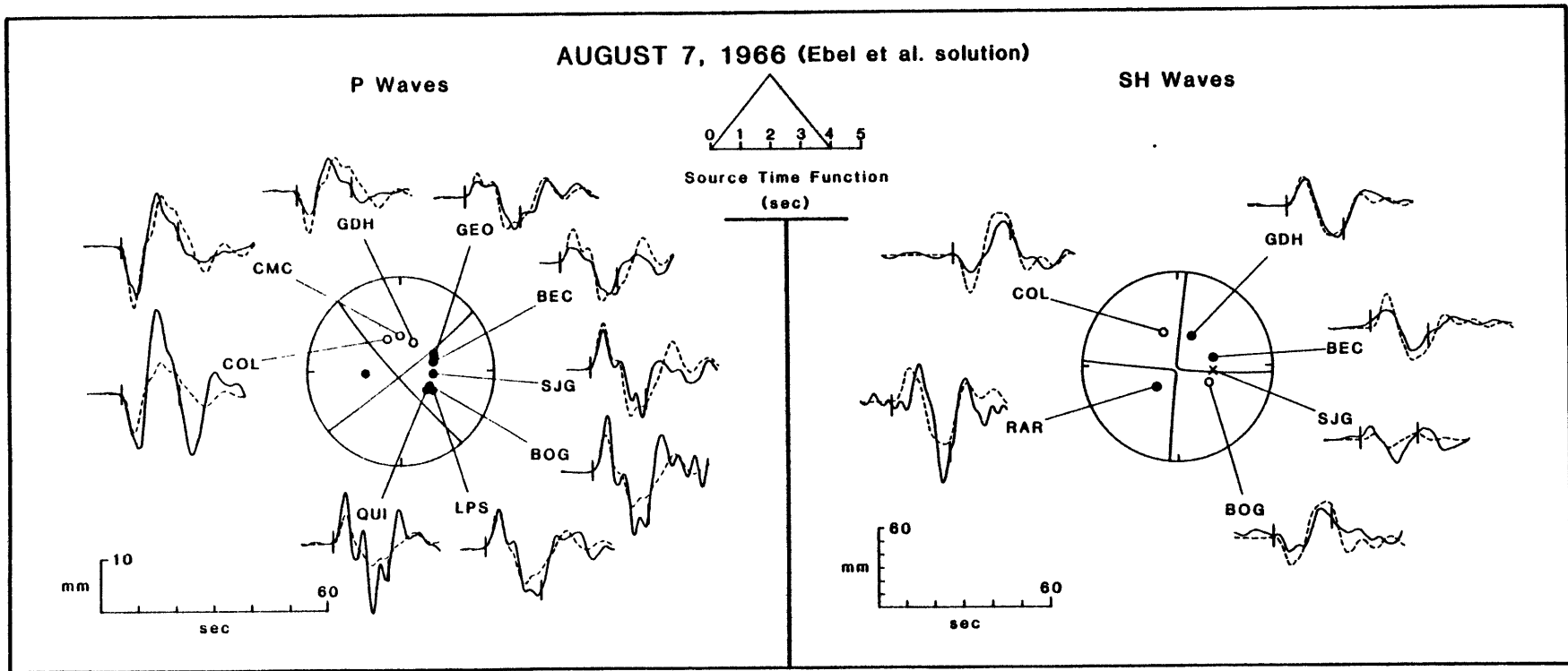


Figure 3.2



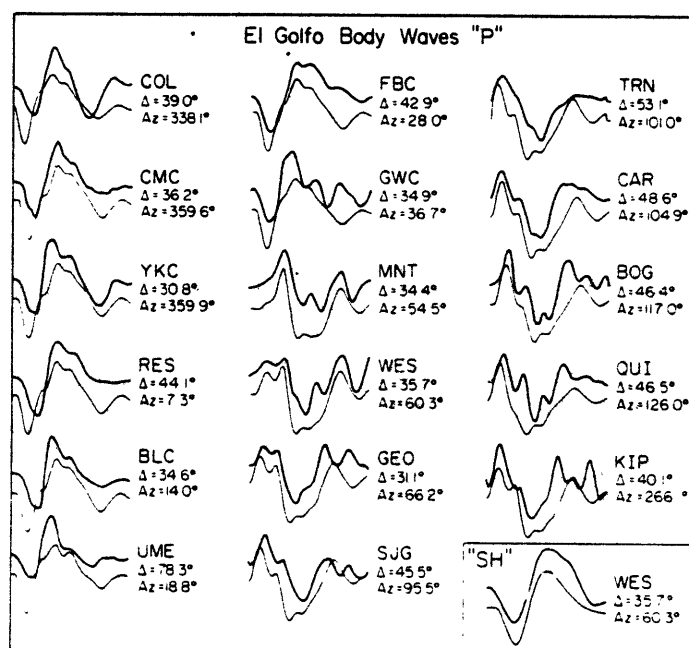
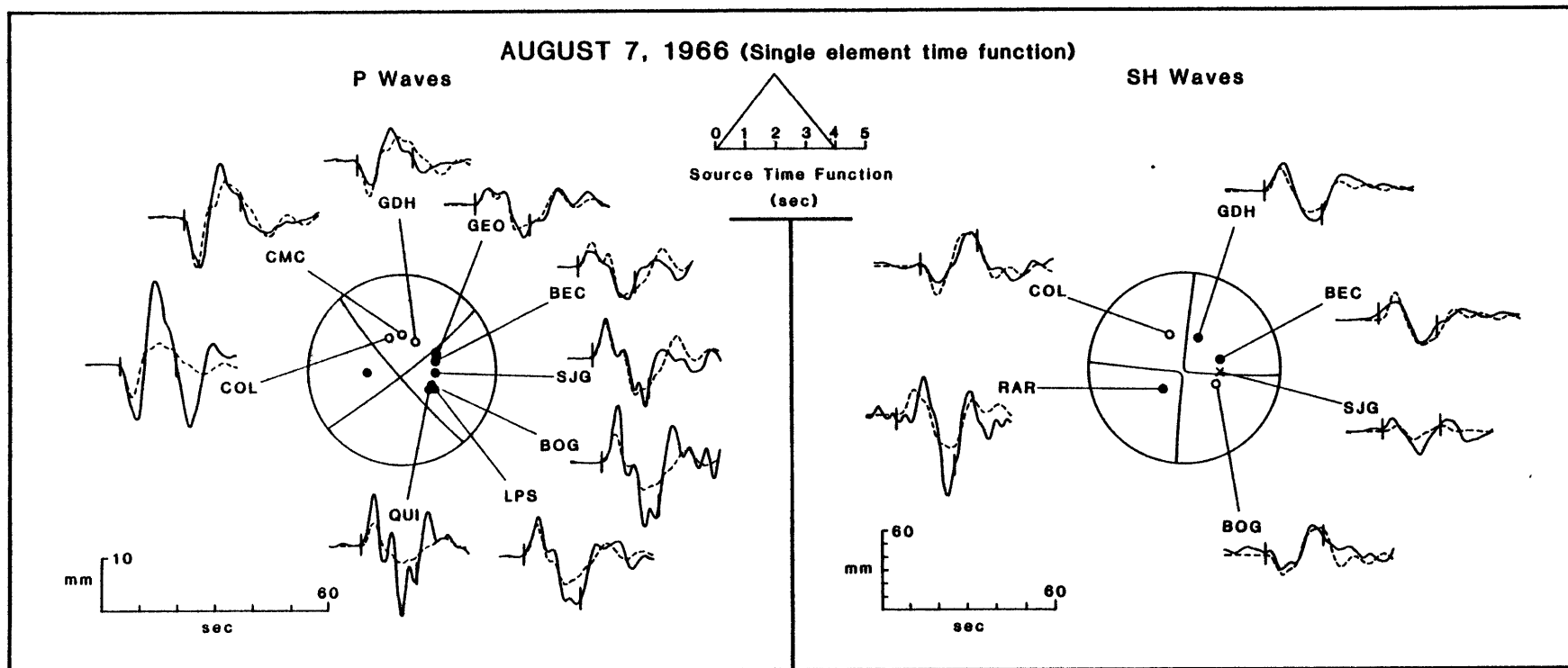


Figure 3.3



AUGUST 7, 1966 (Inversion solution)

P Waves

SH Waves

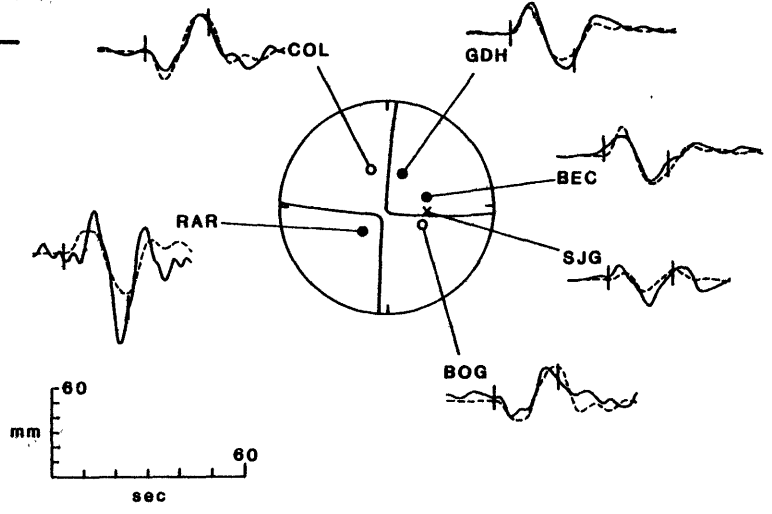
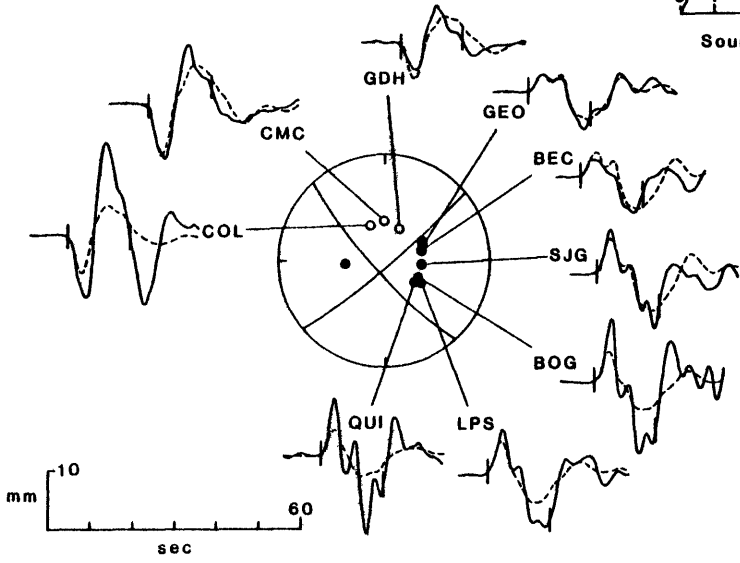
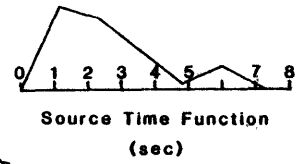
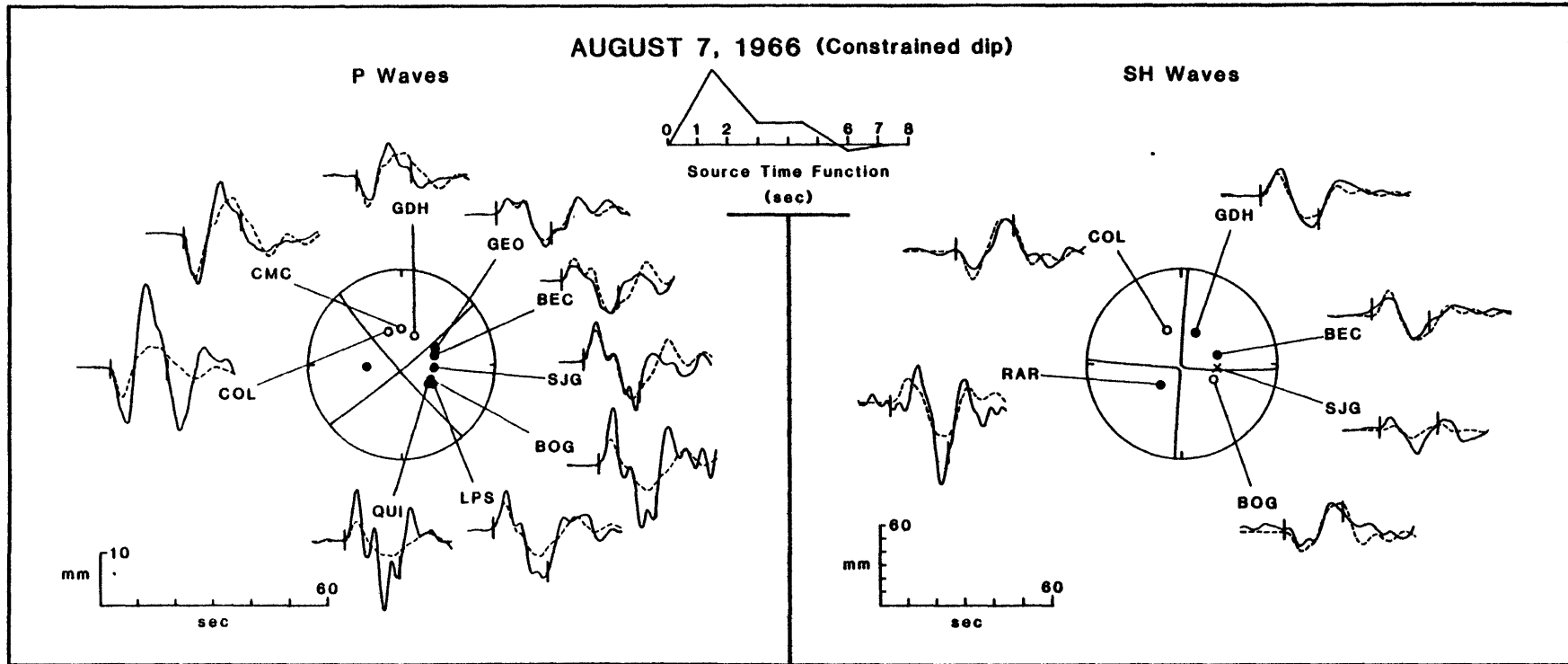


Figure 3.5



MAY 6, 1976 (Clpar solution)

P Waves

SH Waves

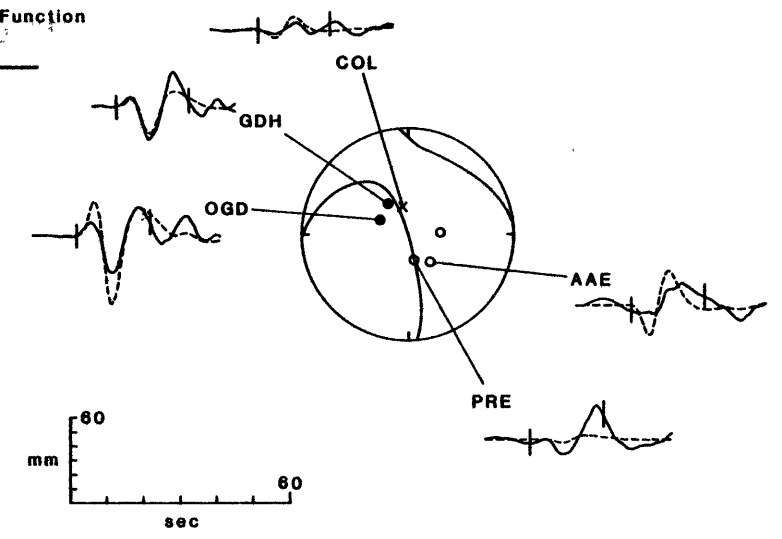
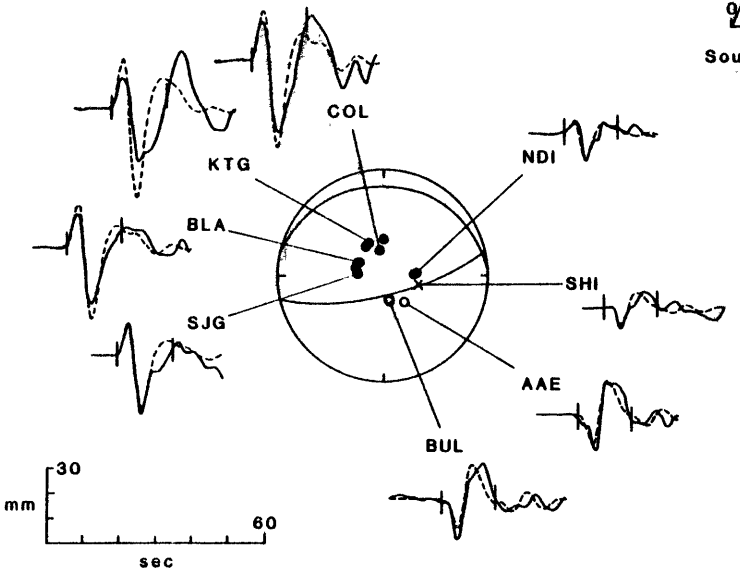
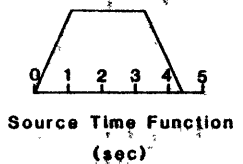


Figure 3.6



MAY 6, 1976 (Inversion solution)

P Waves

SH Waves

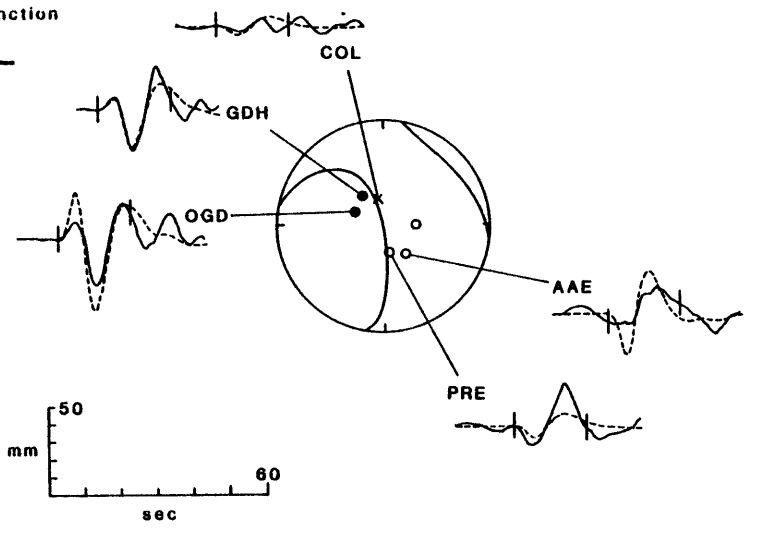
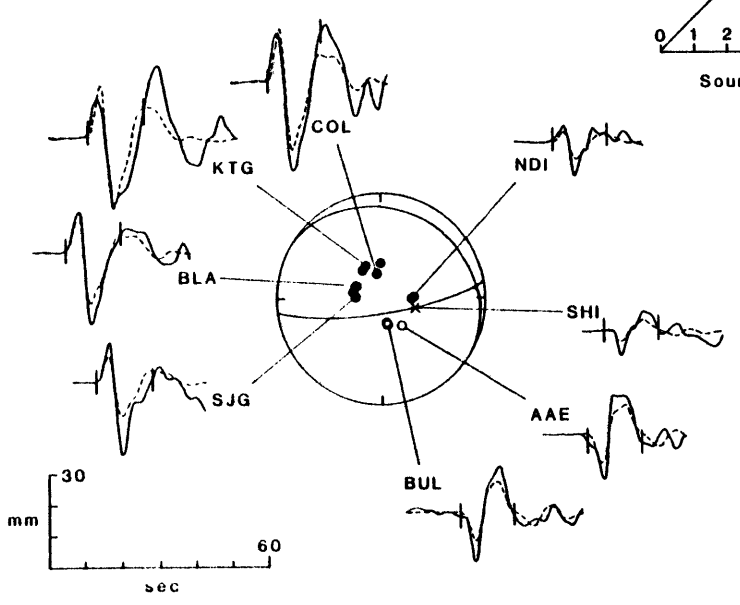
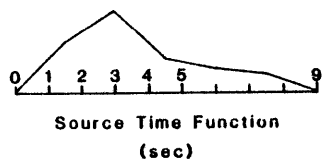


Figure 3.7

## CHAPTER 4. AN EXTENSIVE REGION OF NEAR-RIDGE NORMAL-FAULTING EARTHQUAKES IN THE SOUTHERN INDIAN OCEAN

### INTRODUCTION

It is widely known that intraplate earthquakes are generally characterized by thrust or strike-slip focal mechanisms, implying that the intraplate stress field is dominated by horizontal compression [Sykes and Sbar, 1974; Richardson et al., 1979; Bergman and Solomon, 1980]. In later chapters, we will present source mechanisms for many such "typical" oceanic intraplate earthquakes, including large thrust-faulting earthquakes in lithosphere as young as 3 m.y.

In this chapter, however, we consider a broad region of young oceanic lithosphere (4-27 m.y. old) along the Southeast Indian Ridge in which a number of large normal-faulting intraplate earthquakes have occurred over the last 20 years. We will refer to these earthquakes as "near-ridge" rather than "intraplate" to emphasize the fact that they may not be entirely free from the influence of tectonic processes related to plate creation. Our reference to these events, which range in body-wave magnitude  $m_b$  from 5.4 to 6.0, as "large" is relative to the typical magnitude range for intraplate and ridge-axis earthquakes, which rarely exceed  $m_b$  6.0 (Chapter 2). In global terms, the earthquakes in the region of this study are of only moderate size.

The source mechanisms of nine of these near-ridge earthquakes have been studied using the body-waveform inversion technique described in Chapter 3. For all nine events, the focal mechanisms are such that the T-axis tends to be subparallel to the ridge axis, implying that near-ridge deviatoric stresses in this region are characterized by tension parallel to the ridge and vertical compression. Although such

mechanisms for near-ridge earthquakes are not unique to this area, the high level of near-ridge seismicity and consistency of the focal mechanisms for this broad region is highly unusual (Chapter 8).

The comparatively frequent occurrence of large off-ridge earthquakes along a relatively short length of the world mid-ocean ridge system in the southern Indian Ocean is an important constraint on possible causative mechanisms. Using the source parameters from the body-waveform inversion as additional criteria, we evaluate several tectonic processes which could perturb the ambient state of stress in young oceanic lithosphere in a manner consistent with the observed location and style of faulting.

#### SOUTHERN INDIAN OCEAN TECTONIC SETTING

The area of study (Figure 4.1) includes the Southeast Indian Ridge from its western terminus at the Rodriguez Triple Junction (near latitude 25°S and longitude 70°E), eastward through the Amsterdam-St. Paul Islands region, to longitude 100°E. Other major structures in this part of the Indian Ocean are the Broken and Ninetyeast Ridges and the Kerguelen Plateau.

Magnetic anomalies identified in the Central Indian Ocean Basin have been correlated with the more complete data in the Crozet Basin to yield a consistent picture of the spreading history of the western half of the study area [Schlich, 1982]. East of the Kerguelen-Amsterdam Island axis, however, there are far fewer ship tracks and correspondingly less detail to the known spreading history. During the last 45 m.y., the geometry and spreading direction (northeast-southwest) have been essentially constant [Schlich and Patriat, 1967, 1971; Le Pichon and Heirtzler, 1968]. From 40 to 10 m.y. B.P.,

spreading was symmetric with a half-rate of about 25 mm/yr, but for the last 10 m.y., the Antarctic side (34 mm/yr) has been spreading somewhat faster than the Indian side (30 mm/yr) [Schlich and Patriat, 1971; Sclater et al., 1976].

Amsterdam and St. Paul Islands are tholeiitic volcanic constructs lying on the southwestern flank of the ridge, very near the ridge axis; both are historically active [Upton, 1982]. The volcanism which built the islands has been variously attributed to the presence of a hotspot at the ridge axis [e.g., Luyendyk and Rennick, 1977] and to a horizontal "pipe" in the asthenosphere from the Kerguelen hotspot [Morgan, 1978].

The Kerguelen Plateau extends over 2000 km from northwest to southeast toward the Antarctic continental shelf. The major portion of the plateau in the north shoals to about 1 km depth and is capped by two volcanic islands, Kerguelen and Heard. Ages of Kerguelen Island volcanic rocks range from 1 to 30 m.y. [Nougier, 1972]. There is geological evidence for recent volcanic activity on both islands [Upton, 1982], and earthquakes have been located both teleseismically (Figure 1) and by a local network [Oka, 1981] in the vicinity of Kerguelen Island. The northern part of the plateau is apparently of oceanic origin, formed by massive outpourings of magma onto pre-existing oceanic crust, but the southern part of the plateau may be partially of continental origin [Schlich, 1982; Upton, 1982].

Broken Ridge is considered to be a structure complementary to the Kerguelen Plateau, in the sense that both are thought to have been derived from an original construct formed by hotspot magmatism [Luyendyk and Rennick, 1977]. By this view, spreading on the Southeast

Indian Ridge bisected the parent construct beginning about 55 m.y. B.P. The hotspot remained beneath the Antarctic plate, in the vicinity of the Kerguelen Plateau, and the associated volcanism has continued to add material to its northern end.

#### SEISMICITY

All earthquakes which have been located in the study area are shown in Figure 4.1. Epicentral data are from Sykes [1970a] for events prior to 1964, from the International Seismological Centre (ISC) for events from 1964 through 1979, and from the National Earthquake Information Service (NEIS) for events from 1980 through 1982. We have plotted only events with  $m_b \geq 5.0$  from the NEIS catalog; otherwise all located events are shown. The epicenters of the nine earthquakes for which we conducted source studies are indicated in Figure 4.1, and epicentral information for these events is given in Table 4.1. None of the other near-ridge events which occurred in this area since the establishment of the World-Wide Standard Seismograph Network (WWSSN) is large enough to study with long-period body waves.

The tight clustering of most ridge events, including those relocated by Sykes [1970a] using pre-WWSSN data, and the coincidence of the seismicity with the ridge axis and transform faults as defined by bathymetric and magnetic anomalies, are strong pieces of evidence that the near-ridge seismicity is not an artifact of mislocation. The near-ridge earthquakes listed in Table 4.1 are among the largest in the entire study area and consequently are located with more precision than most of the ridge events, many of which were detected at fewer than 20 stations.

## SOURCE MECHANISMS

In this section we present the source mechanisms obtained from the inversion of P and SH waveforms, using the procedure developed by Nabelek [1984] and described in Chapter 3. The focal mechanisms and the observed and synthetic seismograms are given in a series of figures, with P waves and SH waves shown on separate focal spheres (with the appropriate radiation pattern) for clarity. The synthetics shown were generated with the single best-fit solution, and have not been individually rescaled for improved fit. The station code and geographic location of all stations used in the inversions are listed in Appendix E. The best-fitting source parameters for all earthquakes, together with formal errors, are given in Table 4.2.

### December 19, 1965 and February 17, 1966

The December 1965 earthquake (event 1,  $m_b = 5.5$ ) was the first in a sequence of at least 9 events (lasting into 1974) with virtually identical epicenters near  $32^\circ\text{S}$  and  $79^\circ\text{E}$ . The February 1966 earthquake (event 2,  $m_b = 6.0$ ) is the largest of the series, which included several other events with  $m_b > 5.5$ . Banghar and Sykes [1969] published first motion solutions for both earthquakes and found nearly identical normal-fault mechanisms (1965: 284/66/270; 1966: 275/64/270), although in neither case is the slip angle well constrained. The results of the inversion agree very well with these mechanisms, except that our solutions (Figures 4.2 and 4.3) have a modest component of strike-slip motion (1965: 302/67/301; 1966: 276/58/294). For both earthquakes, one nodal plane is well constrained by stations near one another with opposite P-wave polarities, and the slip angle is constrained by the SH waves. The dip angle, while constrained by the P

waves, is known no better than the take-off angles, which depend on the assumed velocity at the epicenter and may easily be in error by several degrees. The SH waves also constrain the dip, but with less dependence on take-off angles. This last fact accounts for the result that in some inversions the best-fitting solution violates the first-motion polarity of one or more P waves near a nodal plane. The fit to the observed SH waves for the December 1965 event is exceptionally good. The focal depth of the large 1966 earthquake is about 12 km, while the 1965 event is somewhat shallower at about 8 km. The seismic moment of the 1965 earthquake is  $1.3 \times 10^{25}$  dyne-cm, while the 1966 event has a moment of  $7.5 \times 10^{25}$  dyne-cm ( $1.3$  and  $7.5 \times 10^{18}$  N-m, respectively).

Tsai [1969] estimated the seismic moment of both earthquakes from observations of the Rayleigh wave amplitude spectra at two stations. He found an average moment of  $1.5 \times 10^{25}$  dyne-cm for the December 1965 earthquake and  $8.8 \times 10^{25}$  dyne-cm for the February 1966 event, both values being slightly higher than the moments found in the body-wave inversion, but well within the error of either method. Tsai's moments would have been smaller had he used shallow focal depths, instead of depths of 45 and 60 km, respectively.

Fitting the details of the P waves for the 1965 event with a single point source proved to be very difficult. By introducing a small precursory event located slightly southeast of the main rupture, we obtained better fits at some stations, but the focal mechanism of the precursor was very unstable with respect to the precise weights given to different stations, and it tended to have a mechanism very different from the later part of the rupture (predominantly strike-slip motion). Because of this instability and the small seismic moment

associated with the precursor, our final solution uses only a single point source, which we feel adequately represents the average rupture.

The observed waveforms for the large 1966 earthquake have a distinct azimuthal asymmetry in the apparent source time function which is diagnostic of a significant unilateral horizontal component to the rupture. The rupture for this earthquake was approximated as a horizontal line source (horizontally propagating point source) with unilateral rupture propagation. This source model is easily incorporated in the inversion by making the width of the individual source time function elements at each station a function of the angle between the rupture vector and the direction of the departing ray at the source. The line source is oriented parallel to the strike of the nodal plane and may rupture in either direction; trial inversions are performed with the four combinations of nodal plane and rupture propagation direction to find the preferred source model. The fit between the synthetic and observed waveforms for this event is best if rupture propagated from east to west along the fault plane oriented  $N84^{\circ}W$ . A value of 3.2 km/sec (70% of the mantle shear wave velocity) was used for the solution shown in Figure 4.3, but the rupture velocity is not well constrained by the waveforms.

A large fracture zone lies a short distance to the east of these epicenters (Figure 4.1). Some of the complexity (and tendency toward strike-slip motion) of the December 1965 event might result from its having occurred near the fracture zone, perhaps in response to stresses localized there. The 1966 earthquake may have also initiated near the fracture zone and then propagated away to the west under the influence



of a different stress system. A relative event-relocation analysis indicates that the epicenters of the 1965 and 1966 earthquakes are not resolvably different (M.H. Murray, personal communication, 1983).

October 8, 1968

Using first-motion polarities, Sykes and Sbar [1974] found a normal-faulting mechanism (34/60/270) for the October 1968 earthquake (event 3), but the slip angle is essentially unconstrained. Our mechanism is slightly different (7/53/267; Figure 4.4), but equally compatible with the first motions. The dip of one nodal plane is well constrained by the emergent character of the P wave at RIV, and the good distribution and signal-to-noise ratio of the P waves help compensate for rather poor SH waves. The seismic moment is  $2.0 \times 10^{25}$  dyne-cm and the focal depth is about 10 km.

May 3, 1973

The May 1973 earthquake (event 4) has been the subject of several previous studies. Bergman and Solomon [1980] found a normal-faulting mechanism (based on first-motion polarities and shear-wave polarizations) with one nodal plane apparently well constrained (170/70/270  $\pm$  30). Using surface wave amplitude spectra, Okal [1981] improved the mechanism (206/36/269) and inferred a focal depth of 45 km and a moment of  $1.4 \times 10^{25}$  dyne-cm. Wiens and Stein [1983a] modelled the long-period P waves, using Okal's focal mechanism, and demonstrated that the focus is shallower, about 15 km. In comparison, the inversion solution (Figure 4.5) indicates a focal depth of 14 km and a moment of  $8.7 \times 10^{24}$  dyne-cm. The emergent character of the P wave at WIN constrains the dip of the westward-dipping nodal plane. The distribution of the SH waves brackets a nodal plane and stabilizes the

strike of the double couple. The difference in seismic moment between our solution and that of Okal [1981] would be reduced had Okal calculated the best-fitting moment for a shallower depth. The focal mechanism found in the inversion (183/51/254) has a larger component of strike-slip motion than Okal's pure normal-faulting solution.

#### September 19, 1975

The epicenter of the September 1975 earthquake (event 5) is located near the tip of the Amsterdam Ridge, which appears to have been formed by magmatism along the Amsterdam Fracture Zone (Figure 4.1). The focal mechanism (241/63/280) is quite well controlled by the observed waveforms (Figure 4.6): the strike and dip of the NW-dipping nodal plane are tightly constrained by observed dilatations at AAE and SNG and the compressional arrival at P00, while the slip angle is constrained by the SH waves. Because of the many stations with nodal P-waves and possibly a systematic error in take-off angles, as discussed above, it was difficult for the inversion to converge to a solution which did not noticeably violate the first motion at some station: our solution places AAE slightly to the wrong side of the nodal plane (Figure 4.6). The P waves constrain the focal depth to about 22 km, deeper than any other event in this area, but the observed waveforms are not very well fit by the synthetics. Numerous attempts to find a more satisfactory solution at a shallow depth failed. The unfortunate station distribution, in which all the available P waves are near-nodal, is certainly responsible for some of the difficulty in obtaining a satisfactory fit. An unusually complex crustal structure in the source region is quite plausible and may account for some of the discrepancy. Alternatively, the poor fit may be due to complexities in the rupture process. The seismic moment is  $3.9 \times 10^{25}$  dyne-cm.

November 2, 1976

Several hours after the large ( $m_b = 5.8$ ) earthquake on November 2, 1976 (event 6), an aftershock (event 7,  $m_b = 5.6$ ) occurred which produced clear long-period waveforms at many stations. We studied both events and found similar focal mechanisms (main shock: 231/38/282 at 11 km depth; aftershock: 242/38/291 at 12 km depth), shown in Figures 4.7 and 4.8. Emergent P waves at MUN (main shock) and PMG (aftershock) constrain the dip angle of the southeast-dipping nodal plane.

The first earthquake has a seismic moment of  $7.7 \times 10^{25}$  dyne-cm and a source time function (7.5 sec) long enough to be able to resolve an azimuthal variation in apparent source duration. Using the same horizontally propagating point source model as for the February 1966 earthquake, an improved fit to the observed waveforms was obtained for unilateral rupture propagation from SW to NE, away from the ridge axis. Although the reported magnitude of the aftershock is nearly as large as the main shock, its seismic moment is smaller by more than an order of magnitude ( $6.1 \times 10^{24}$  dyne-cm). The earthquake was nonetheless very well recorded, and the fit of the synthetics to the observed waveforms is exceptionally good.

May 22, 1979

The May 1979 earthquake (event 8) has the smallest moment of the 9 events in this study ( $4.2 \times 10^{24}$  dyne-cm). Because a large, deep earthquake in Peru preceded it by several hours, many stations were still highly disturbed, and the GDSN was essentially unusable. We were able to find 5 good P-wave records from high-gain WWSSN stations; these waveforms constrain the source depth, but their poor azimuthal distribution would lead to a poorly constrained strike if the inversion

were conducted with only these records. We also obtained 3 good SH-wave records, which stabilize the solution. The focal mechanism (Figure 4.9) indicates nearly pure normal faulting (193/49/280) at a depth of 16 km.

#### September 24, 1981

The September 1981 earthquake (event 9) was only slightly larger than the May 1979 event ( $4.4 \times 10^{24}$  dyne-cm) and all the usable P-wave records lie in one hemisphere. The five well-distributed SH-wave records enabled the inversion to converge to a well constrained solution (145/37/250; Figure 4.10) at a depth of about 11 km.

Dziewonski and Woodhouse [1983] inverted GDSN data to obtain the moment tensor of this event, with the depth fixed at 10 km. Their best-fitting double-couple mechanism (141/48/238) is very similar to ours except that it has a slightly larger component of strike-slip motion and the dip angles of the nodal planes differ somewhat. They found a slightly smaller seismic moment,  $3.0 \times 10^{24}$  dyne-cm. In their semi-automated inversion, Dziewonski and Woodhouse [1983] use a normal mode summation technique which is insensitive to the precise timing of the arriving phases, allowing them to utilize a much longer portion of the seismogram, but only at periods longer than 45 sec and at the expense of poorer resolution of the  $M_{xz}$  and  $M_{yz}$  moment tensor components. Loss of resolution because of noise contamination is particularly likely for small shallow events [Trehu et al., 1981]. By also using WWSSN records, with information at shorter periods, resolution of the source depth, source time function, and mechanism of smaller events is improved, at the cost of a more time-consuming analysis.

## STRESS DROP

Using the seismic moment and the duration of the source time function obtained in the inversion, we have estimated the stress drop of each earthquake. The expression for stress drop is:

$$\Delta\sigma = C \frac{M_0}{\ell w^2} \quad (4.1)$$

where  $M_0$  is the seismic moment,  $\ell$  is the length (horizontal extent) and  $w$  the width (down dip) of an assumed rectangular fault.  $C$  is a non-dimensional constant depending on fault geometry and elastic moduli [Kanamori and Anderson, 1975]. For typical material constants  $C$  is near unity, and it has been set equal to 1 for these calculations.

Although the body-wave inversion procedure yields accurate estimates of the seismic moment and total duration of faulting  $t_s$  (Table 4.2), the interpretation of  $t_s$  in terms of fault dimensions  $\ell$  and  $w$  requires additional assumptions which can have a large effect on the calculated stress drop. The maximum dimension of the fault is assumed to correspond to the fault length  $\ell$  and to lie between  $v_r t_s$  (unilateral faulting) and  $2v_r t_s$  (bilateral faulting), where  $v_r$  is the rupture velocity. We have assumed an average rupture velocity of 3.2 km/sec, which corresponds to 70% of the mantle shear velocity in our assumed source structure. The fault width  $w$  is limited by two assumptions: that the vertical extent of faulting is no greater than the horizontal extent, and that  $w$  is less than twice the focal depth  $h$  multiplied by a geometric factor which accounts for typical fault dip:

$$w \leq \ell \quad (4.2)$$

$$w \leq 2.8h \quad (4.3)$$

We have calculated both a 'minimum' (bilateral faulting) and 'maximum' (unilateral faulting) stress drop. For each case,  $w$  is taken

as the smaller of the two limiting quantities in (2) and (3). This procedure should result in a reasonably good estimate of the minimum stress drop, since for such an estimate we are seeking to maximize the fault area, and the smaller of (2) and (3) is a reasonable upper bound to  $w$ . In the case of the maximum stress drop, however, where we seek to minimize fault area, neither criteria (2) nor (3) yields a reliable lower bound to  $w$ . Higher stress drops can result from choosing higher aspect ratios ( $l/w$ ). Our interpretation of  $t_s$  in terms of fault dimension assumes that the rise time (duration of the dislocation at a point) is zero. A finite rise time would reduce the inferred fault dimensions, increasing the calculated stress drops accordingly. Rise times for moderate earthquakes are very difficult to infer accurately from teleseismic records. The estimated stress drops are listed in Table 4.3. They range from 1 to about 30 bars (0.1 to 3 MPa). These values are consistent with other estimates of stress drop for earthquakes over a wide range of magnitudes and tectonic regimes; in particular, they are no higher than stress drops commonly found for plate boundary events, in contrast to the suggestion of Kanamori and Anderson [1975]. As discussed above, the waveforms of the February 1966 earthquake (event 2) and the large earthquake on November 2, 1976 (event 6) suggest unilateral rupture (maximum estimated stress drop), leading to estimated stress drops of 2 and 6 bars, respectively.

#### GLOBAL FEATURES OF NEAR-RIDGE SEISMICITY

In order to understand the tectonic significance of the earthquakes in this study, it is important to compare the activity in the southern Indian Ocean with the typical level of near-ridge seismicity and the characteristic style of deformation in other areas

of young oceanic lithosphere. A global survey of the distribution and source mechanisms of earthquakes in young oceanic lithosphere is presented in Chapter 8. In this section, some of the results of this global survey are extracted in order to establish a context for the discussion of the causative mechanisms of the Southeast Indian Ridge events which follows.

In addition to the region of present interest along the SEIR, several other areas of relatively intense near-ridge seismicity are noted in Chapter 8. One notable concentration of seismicity is in the vicinity of the Chagos Bank, near the intersection of the Carlsberg and Central Indian Ridges. Stein [1978] studied several of the events comprising a swarm (similar to the swarm that included events 1 and 2 of this study) and found them all to be characterized by normal faulting with the T-axes oblique to the local direction of spreading. In Chapter 8, we present source studies of several other events in the region, finding three cases of right-lateral strike-slip faulting on planes striking NE. The T-axes of these events are parallel to those of the normal faulting events.

Other than the Southeast Indian Ridge and Chagos Bank events, we have identified about 35 large near-ridge events, of which about 30 have known focal mechanisms, determined either in other investigations [e.g., Wiens and Stein, 1984] or by us using body-wave inversion. For these events, thrust or strike-slip faulting is observed as often as normal-faulting. Approximately 10 other near-ridge normal-faulting earthquakes are known for the entire remainder of the mid-ocean ridge system. In view of these observations, we favor the view that the Chagos bank events represent a northerly extension of the distinctive

pattern of near-ridge seismicity observed along the Southeast Indian Ridge, although the observation of both strike-slip and normal faulting suggests some local differences in the pattern of deformation. By this view, unless the historical seismic record is too short to be representative, the earthquakes of this study probably should not be considered entirely representative of the seismicity or the state of stress in young oceanic lithosphere. This issue is discussed at greater length in Chapter 8.

#### POSSIBLE CAUSATIVE MECHANISMS FOR NORMAL FAULTING

We have shown that there is a broad region, including both sides of the Southeast Indian Ridge, in which all known mechanisms of near-ridge earthquakes involve normal faulting with the inferred T-axis roughly perpendicular to the local direction of spreading (Figure 4.11). In this section, we consider a variety of tectonic processes which might plausibly produce normal-faulting earthquakes in young oceanic lithosphere, and we evaluate the relevance of each process to the earthquakes of this study. There is, of course, no necessity for all these earthquakes to have a single cause, but the unusual pattern of faulting leads us to give greater weight to tectonic processes which can account for a large subset of events. In fact, no single process appears to be adequate to account for all the observed faulting, and we will propose that the near-ridge normal-faulting earthquakes on opposite sides of the Southeast Indian Ridge arise from different causes.

We first consider several processes which can produce extensional stress in young oceanic lithosphere and which would be expected to contribute to the state of stress in many, if not all, oceanic plates:



(1) a latitudinal component of absolute plate motion, (2) thermal stresses due to plate cooling, (3) differential subsidence at fracture zones, and (4) off-ridge volcanism. These relatively typical processes may be contrasted with more 'anomalous' processes, which arise from some circumstance not characteristic of most oceanic regions: (1) bending stress due to lithospheric loading, (2) small-scale convection beneath the plate, (3) ridge migration, (4) stresses at ridge-transform intersections in the presence of an oblique regional stress field (5) a local thermal anomaly, or (6) a plate-wide 'perturbation' to the regional stress field.

This distinction between typical and anomalous processes is not a rigid one, but it does help in evaluating the likelihood that a given process is the primary cause of the observed faulting. To the extent that a proposed causative process is considered to be typical in the sense used above, similar seismicity should be observed along other mid-ocean ridges. We noted previously that the earthquakes in this study appear to be unusual. With the possible exception of the Chagos Bank seismicity (which we are inclined to view as part of the same tectonic pattern as the events along the Southeast Indian Ridge); no other region of this extent is known to be characterized by the high level and consistent style of off-ridge faulting observed along the Southeast Indian Ridge. Unless the last two decades of global seismicity are unrepresentative of the tectonics near mid-ocean ridges, all of the 'typical' processes must be discounted in favor of an explanation which can account for the particular distribution of near-ridge normal-faulting earthquakes observed in this study.

Another observation which is relevant in evaluating some of the proposed causative processes is that the pattern of seismicity seems to be asymmetric with respect to the ridge. The events on the Antarctic plate are clustered together opposite a short length of the Southeast Indian Ridge, whereas the Indian plate events are spaced along a much greater length of ridge at intervals of several hundred kilometers (Figure 4.11). If the Chagos Bank earthquakes are included in the pattern of Indian plate off-ridge seismicity, the contrast is even greater. The three Antarctic plate events are among the smallest in the study, and the total seismic moment released by them is 16 times less than that of the Indian plate earthquakes in this study, not including the other members of the earthquake series which includes events 1 and 2.

#### Latitudinal Plate Motions

Turcotte and Oxburgh [1973] and Turcotte [1974b] noted that for lithospheric plates with a northerly or southerly component to their absolute motion, the changing radius of curvature between the poles and equator leads to membrane stresses which may be large enough to cause faulting. For northerly motions of a plate created in the southern hemisphere, as in the case of the Indian plate, this mechanism predicts tensional stresses in the interior of the plate and compressional stresses at the periphery, a pattern opposite to the stresses indicated by the earthquake mechanisms in Figure 4.11. Latitudinal plate motions therefore play no role in producing the stresses relieved in the off-ridge earthquakes in this area.

### Cooling-Plate Thermal Stresses

As newly-created lithosphere spreads away from the ridge axis, it cools and contracts, producing tensional membrane stresses oriented oblique to the spreading direction [Turcotte and Oxburgh, 1973; Turcotte, 1974a]. The focal mechanisms of the off-ridge normal-faulting earthquakes in this study are consistent with the predicted deviatoric stresses. As noted above, however, cooling-plate thermal stresses should be equally important at all mid-ocean ridges and should be symmetric with respect to the ridge. Neither condition seems to hold for near-ridge normal-faulting earthquakes. We therefore conclude that, while thermal stresses associated with plate cooling may contribute to the stresses released in these earthquakes, other sources of stress are needed to account for the high level of such seismicity in the Indian Ocean and the apparent asymmetry of its distribution with respect to the Southeast Indian Ridge.

### Differential Subsidence

Differential subsidence results when adjacent parts of the lithosphere have different thermal histories and temperature-dependent density variations arise which require relative vertical motions to achieve isostatic equilibrium. One place where this may occur is at fracture zones, where lithospheric plates of different ages come into contact [DeLong et al., 1977]. Each segment of lithosphere at a distance from the fracture zone, by this argument, will tend to follow the empirical age-depth curve [Parsons and Sclater, 1977], in which subsidence is most rapid for young lithosphere. At a fracture zone, therefore, the younger side should subside relative to the older side; to the extent that the two halves of the plate are locked together, a

vertical shear traction will develop at the fracture zone. We would expect that an earthquake produced by this mechanism would have a very characteristic mechanism: near-vertical dip-slip faulting on a plane parallel to the fracture zone with the younger side down-thrown.

The Antarctic plate events have nodal planes which dip no more than about  $50^\circ$  and, with the possible exception of the May 1973 earthquake (event 4), which strike in a direction about  $30^\circ$  from the local trend of fracture zones (Figure 4.11). Two of the Indian plate earthquakes (events 3 and 5) are located on or near large-offset fracture zones, and the strikes of their nodal planes are close to those of the adjacent fracture zones (Figure 4.11). The steepest nodal plane of event 3 (October 1968) dips at only  $53^\circ$ , however, and event 5 (September 1975) has a nodal plane dipping at  $63^\circ$ . The sense of slip on these planes is correct, but the relatively shallow dip of the nodal planes makes it unlikely that differential subsidence is the primary cause of these two earthquakes. Events 1 and 2 (December 1965 and February 1966) are located near a fracture zone with significant offset (Figure 4.11), but the nodal planes which are most closely aligned with the fracture zone dip at only about  $30^\circ$ . As discussed above, this earthquake series may have initiated near the fracture zone. Events 6 and 7 (November 1976) are located opposite a section of the ridge with very small offsets where no significant stresses should develop from differential subsidence.

From a study of bathymetric profiles across major North Pacific fracture zones, Sandwell and Schubert [1982] concluded that very little, if any, vertical slip had occurred after the two plates moved beyond the ridge-transform intersection. Differential subsidence

results not in faulting by this view, but in lithospheric flexure. The resulting bending stresses can apparently be maintained for periods on the order of  $10^7$  years, but could conceivably lead to faulting. For the case of events 3 and 5 (both apparently on the younger side), the predicted horizontal stresses above the neutral surface are compressive, not extensional [Sandwell and Schubert, 1982]. At a depth of nearly 22 km, event 5 (September 1975) is likely to have occurred below the neutral surface. With this possible exception, we conclude that stresses localized on fracture zones do not play a significant role in producing the observed off-ridge seismicity.

#### Off-Ridge Volcanism

Much of the normal-faulting seismicity on the mid-ocean ridge system occurs as swarms and is attributed to volcanism in a broad sense [Sykes, 1970b]. In a remote oceanic region experiencing off-ridge volcanism, the smaller members of an earthquake sequence might not be recorded, leaving isolated events such as those observed in this study. Non-hotspot intraplate volcanism is apparently a normal consequence of the evolution of oceanic lithosphere [Batiza, 1982], but in the South Pacific, where a local seismic network provides good coverage of swarms related to intraplate volcanism, the earthquake mechanisms are characterized by reverse faulting and may be a response to a component of the regional compressive stress field [Oka et al., 1980]. There is no bathymetric evidence for volcanoes in the epicentral region of most of the events in this study (Figure 4.1). Event 4 (May 1973) is located near the northern end of the Kerguelen Plateau, which has been constructed by hot-spot volcanism, and event 5 (September 1975) is located near the tip of the Amsterdam Ridge, which may have been formed by volcanism along the Amsterdam Fracture Zone.

### Bending Stresses

Many authors have studied the response of the lithosphere to an applied normal load (such as a seamount) or bending moment (seaward of subduction zones) [e.g., Forsyth, 1979]. The details of the resulting stress field in the plate are highly dependent on the assumed rheology [Lambeck and Nakiboglu, 1981], but for large oceanic island loads, extensional stresses reaching at least 1 kbar may be induced in portions of the plate, particularly in the immediate vicinity of the load. There are no significant sources of bending stress near any of the Indian plate events, but the Kerguelen Plateau is potentially such a load on the lithosphere of the Antarctic plate. Houtz et al. [1977] found a small free-air gravity anomaly over the central portion of the plateau and concluded that the plateau is nearly compensated, probably by a thickened crust, and would therefore not be as significant a load on the lithosphere as would appear from its bathymetric relief. The large positive geoid anomaly over the plateau [Cazenave et al., 1980] appears to contradict this conclusion, but it is a longer-wavelength feature than the gravity profile and is possibly related to processes deeper in the mantle.

Of the three Antarctic plate events, the May 1973 earthquake (event 4) is located nearest to the edge of the Kerguelen Plateau, where bending stresses might tend to be largest. Using an analytical model for the flexural stresses in an elastic plate overlying a fluid halfspace [Brotchie, 1971], we calculated the deviatoric stresses which might exist in the epicentral region of the May 1973 earthquake due to the load, assumed to have cylindrical symmetry, of the northern part of the plateau. The radial and tangential stresses at the upper and lower

surfaces of an elastic plate 20 km thick, for a cylindrical load of 200 km radius, are shown in Figure 4.12. The actual magnitudes of the stresses are dependent on a variety of model parameters about which we have little information, but only the relative magnitude and sign of the radial and tangential components are needed to evaluate the importance of bending stresses in this case.

The sign of bending stresses changes at the neutral surface, and the magnitude of the stresses increases linearly with distance above or below it. In order to establish the position of the earthquake focus with respect to the neutral surface, we calculated strength envelopes for oceanic lithosphere between 10 and 30 m.y. in age. We followed the procedure of Goetze and Evans [1979], in which a brittle failure law (a function of the lithostat) limits the strength in the shallow portions of the plate, and a ductile flow law (dependent on temperature and strain rate) limits the strength at depth (Figure 4.13). The left-hand side of the envelope, for which the vertical stress is the greatest principal stress, is the appropriate curve for normal faulting. We assume that the depth range over which the lithosphere can support large deviatoric stresses corresponds to the thickness of the effective elastic plate. The May 1973 event occurred in lithosphere about 27 m.y. old, for which the depth range of significant strength is approximately 10 to 30 km, and the neutral plane is therefore assumed to be somewhat deeper than 20 km, since the strength of the lower part of the plate is greater than that of the upper part. At a depth of 19 km below sea level, the earthquake appears to lie above or very near the neutral surface (Figure 4.13). Unless the effective thickness of the plate has been severely reduced by a thermal anomaly, it is

unlikely that the earthquake could lie very far below the neutral surface. The mere fact that the focus is quite near the neutral surface makes it unlikely that bending stresses are significant for this event.

To account for this earthquake by perturbing an initially hydrostatic state of stress with bending stresses from the load of the plateau, both horizontal components of bending stress must be extensional and the tangential (or azimuthal) component of stress in the upper half of the plate must be more extensional than the radial component. Nowhere in the plate beyond the edge of the load (the relative location of the May 1973 event) are the radial and tangential stresses both extensional, with the tangential component most extensional (Figure 4.12). Only by assuming a vertical component of stress raised significantly above lithostatic (so that the radial component can be compressional but still less than the vertical) can the state of stress inferred from the focal mechanism be attributed to bending stresses, and then only if the earthquake lies below the neutral surface. We conclude that bending stresses are not the dominant cause of the May 1973 earthquake or the other Antarctic plate events, which are even less influenced by the load of the plateau.

#### Small-Scale Convection

As the lithosphere cools, instabilities at the asthenosphere-lithosphere boundary can evolve into convection cells at a scale smaller than plate dimensions [Richter, 1973]. At high relative velocities between the plate and underlying mantle, the preferred pattern of small-scale convection may be characterized by long rolls oriented in the direction of motion [Richter, 1973; Richter and



Parsons, 1975]. Such a pattern would induce horizontal extensional stress in the portions of the plate overlying lines of upwelling between two such rolls, and could also induce thermoelastic stresses in the lithosphere. The Antarctic plate moves little with respect to the mantle, but the absolute velocity vector of the Indian plate is nearly parallel to the spreading direction and the absolute velocity in the study area is about 72 mm/yr, according to model AM1-2 of Minster and Jordan [1978] (see Figure 1 of Pollack et al. [1981]).

Stark and Forsyth [1983] reported evidence, from S-wave travel time delays, for small-scale convective rolls in the northern Indian Ocean, with an apparent roll width of about 320 km. In this case, the sites at which the greatest extensional stress could be induced should be separated by about 640 km. This value is greater than the observed separation of most of the sites of off-ridge normal-faulting seismicity on the Indian plate. Haxby and Weissel [1983], however, have recently presented high-resolution geoid height data which they interpret to support the existence of small-scale convection beneath young lithosphere of the Pacific plate, with a wavelength of about 100-200 km, and similar features appear to be present in regions of young lithosphere on the Indian plate (J.K. Weissel, personal communication, 1984). In particular, there are linear geoid anomalies interpreted as signifying convective rolls oriented parallel to the direction of plate spreading in the same area as the near-ridge earthquakes on the Indian plate side of the SEIR. Similar geoid patterns are not observed on the Antarctic side of the SEIR.

The theory of Richter [1973] and Richter and Parsons [1975] predicts that that secondary convection rolls should not develop

beneath very young lithosphere, but recent numerical models of convection in a variable-viscosity asthenosphere permit the onset of boundary layer instabilities at a much younger lithosphere age than previously thought likely [Buck, 1984]. Although the evidence is far from overwhelming, the possible role of secondary convection in modifying the state of stress in young oceanic lithosphere is consistent with the available data and certainly deserves further investigation.

#### Ridge Migration

Stein et al. [1977] studied the effect of relative motion between a spreading ridge axis and the underlying mantle, and concluded that such a situation could lead to asymmetric spreading, with the trailing edge of the migrating ridge having the higher spreading half-rate. The physical process involves minimization of the viscous dissipation associated with the shear stresses between the asthenosphere and the plate on either side of the ridge. The correlation between the absolute velocity vector of the ridge and asymmetric spreading is quite good globally, and in particular, seems to hold for the Southeast Indian Ridge, which is spreading asymmetrically in the study area [Schlich, 1982]. Variations in the basal shear stress on the two diverging plates could conceivably produce extensional stresses in young oceanic lithosphere (possibly asymmetric with respect to the ridge), but the axis of greatest extension should be oriented parallel to the spreading direction, not perpendicular to it, as would be needed to account for the observed style of faulting. Moreover, asymmetric spreading occurs more obviously in other places, with few if any off-ridge normal-faulting earthquakes being observed.

### Stresses Near Ridge-Transform Intersections

Fujita and Sleep [1978] have modelled stresses near spreading ridge - transform intersections in the presence of a regional stress field which may not be aligned with the direction of spreading. If the axis of least principal stress for the regional field is oblique to the spreading direction, intensified extensional stresses parallel to the ridge can occur, but the largest such stresses are induced in the inside corner of the ridge-transform intersection. None of the events in this study are in the appropriate location.

### Local Thermal Stress

When excess heat is applied at the lithosphere-asthenosphere boundary, uplift and lithospheric thinning can occur [e.g., Mareschal, 1981]. Such uplift is the result of thermal expansion and phase changes, including partial melting. For models in which hot asthenospheric material actually intrudes the lithosphere, thinning and uplift may occur much more rapidly than if heat transfer is by conduction only [Withjack, 1979]. Faulting could result from stresses associated with thermal expansion alone, but buoyancy forces in the lower lithosphere give rise to additional stresses in a manner analogous to bending stresses caused by seamount loading. Bending will cause the central region of uplift to experience extensional stress in the upper half of the effective elastic core of the plate; any lithospheric thinning will tend to concentrate such stresses.

This mechanism seems unlikely for most of the Indian plate events. The September 1975 earthquake (event 5) could well be associated with a thermal anomaly, as discussed above, but its focal depth places it near the bottom of the depth range of significant strength, where such

bending stresses would resist normal faulting (see Figure 4.13, for lithosphere 13 m.y. old and a source depth of about 25 km below sea level). A separate thermal anomaly would have to be ascribed to each epicentral region.

Uplift and thermal stress provide an attractive explanation, however, for the three normal-faulting earthquakes on the Antarctic plate. The bathymetry in the region of these earthquakes (Figure 4.11) shows a broad area of seafloor somewhat shallower than normal between the plateau and the ridge; the residual depth anomaly is about 500 m (B. Parsons, personal communication, 1983). Houtz et al. [1977] attributed the depth anomaly to "a rather large thermally induced tectonic perturbation (which) has either prevented the flank of the Southeast Indian Ridge from subsiding in the normal fashion or has subsequently uplifted the seafloor." For a near-stationary plate such as the Antarctic, a relatively small increase in heat flux at the base of the lithosphere can cause significant uplift and thinning [Withjack, 1979; Pollack et al., 1981]. A possible source for the depth anomaly has been suggested by Morgan [1978], who proposed the existence of horizontal channels or "pipelines" in the asthenosphere through which primitive mantle material flows from intraplate hotspots to nearby ridge axes, producing a distinct type of hotspot island. One such "pipeline" is thought to extend from the Kerguelen hotspot to the Southeast Indian Ridge, terminating near Amsterdam and St. Paul Islands.

We attribute the residual depth anomaly to thermally-induced uplift; the required thermal anomaly may correspond to Morgan's [1978] asthenospheric channel. We propose that the normal-faulting

earthquakes between the Kerguelen Plateau and the Southeast Indian Ridge represent the release of thermal stresses and bending stresses associated with this uplift. While Morgan's proposed asthenospheric channel need not be straight, locally it should have an axis of symmetry which could account for the consistent orientation of the focal mechanisms (Figure 4.11). Alternatively, extensional stresses in the vicinity of a local thermal anomaly may be superimposed on a regional compressive stress field with greatest compression oriented perpendicular to the ridge axis (the "ridge-push force"). Then the B-axis (or null axis) of the focal mechanisms would be expected to align with the spreading direction. The B-axes of the three Antarctic earthquakes, however, appear to be aligned in a direction rotated about  $30^\circ$  from the spreading direction (Figure 4.11).

#### Plate-wide Stress Field Perturbation

If the Antarctic plate events are postulated to result from a local thermal anomaly, as discussed above, we are left with the need to account for a distinctive pattern of off-ridge seismicity involving a significant fraction of the young lithosphere of the western half of the Indian plate. We consider the events in the vicinity of the Chagos Bank [Stein, 1978] as part of this pattern (Figure 4.14). Such a pattern implies that the causative mechanism has plate-wide dimensions, yet is confined to the western half of the Indian plate, roughly west of the Ninetyeast Ridge. We therefore consider the possible nature and cause of a large-scale perturbation of the stress field which could account for the observed off-ridge seismicity on the Indian side of the ridge.

The state of stress and internal stability of the Indian plate have been the subject of much attention, stimulated by the observation of unusually high levels of intraplate seismicity in the northern Indian Ocean [e.g., Sykes, 1970a] and the proximity of the continental collision between India and Asia [Eittreim and Ewing, 1972]. This subject is treated at length in Chapter 5. The available data are consistent with a model in which the northern part of the Ninetyeast Ridge is the site of partial decoupling between the Australian half of the plate, which is subducting normally along the Sunda Arc, and the Indian half, which is deforming internally in response to increased compressive stresses associated with the continental collision to the north.

The intraplate seismicity in the northern Indian Ocean dies out rapidly south of latitude  $10^{\circ}\text{S}$ , but some activity continues into the southern Indian Ocean (Chapter 5). Internal deformation of the uppermost igneous crust observed in the northern Indian Ocean [Weissel et al., 1980] apparently has been proceeding since the Miocene, and it is unlikely that the younger portion of the plate could have escaped the influence of the processes producing this deformation. It is therefore tempting to ascribe the off-ridge normal-faulting earthquakes on the Indian side of the Southeast Indian Ridge to another aspect of the plate-wide response to the continental collision, but the exact process which leads to the observed style of faulting is difficult to specify.

Knowledge of the normal or ambient state of stress in young oceanic lithosphere is necessary in order to discuss perturbations which might account for the off-ridge seismicity. The deviatoric

stresses necessary to support lateral topographic and density variations accompanying plate cooling and subsidence are characterized by vertical relative tension and horizontal compression perpendicular to the ridge, increasing in magnitude from zero at the ridge to several hundred bars in old oceanic lithosphere [e.g., Lister, 1975; Dahlen, 1981]. This model is probably inadequate in the immediate vicinity of the ridge axis, since it is based on the assumption of zero strength there, and stresses from other plate-scale processes, such as basal shear, also contribute somewhat to the intraplate stress field. Many lines of evidence, however, suggest that the distributed ridge push force is the dominant source of stress in oceanic intraplate regions [e.g., Richardson et al., 1979; Richardson, 1983]. We assume that the state of stress in young oceanic lithosphere is at least qualitatively similar to the model of Dahlen [1981].

The perturbation to this state of stress needed to account for the observed style of faulting is a change of the vertical stress deviator from a small tensional value to a compression greater than the horizontal stress deviator perpendicular to the ridge. The axis of least principal stress would then be parallel to the ridge, as are the T-axes of the earthquake focal mechanisms. Thermal stresses from lithospheric cooling [e.g., Turcotte, 1974a] would then contribute to the observed style of faulting, but in the absence of enhanced vertical stress would lead to strike-slip faulting, since the greatest principal stress would be horizontal and perpendicular to the ridge. In young lithosphere, the ambient deviatoric stresses may be quite small, on the order of a few tens of bars [Dahlen, 1981], and the magnitude of deviatoric stress necessary to initiate normal faulting is less than that needed for thrust faulting (Figure 4.13).

The source of such a stress perturbation is unclear, however. A significant plate-wide horizontal compressive stress from the continental collision acts in the wrong direction to facilitate normal faulting. An intriguing possibility (but one difficult to test) is that increased vertical stress in young oceanic lithosphere is related to some feedback mechanism in the large-scale pattern of convection under the western half of the Indian plate, stimulated by the continental collision. A possible source of raised vertical stress at some sites in young oceanic lithosphere is small-scale convection, with which vertical normal stresses of several tens of bars may be associated [W.R. Buck, personal communication, 1984]. Further research is necessary to substantiate both the existence of small-scale convection beneath young oceanic lithosphere and to establish the relationship, if any, between the planform of such convection and near-ridge seismicity.



Table 4.1. Epicentral data\* for earthquakes studied

No.	Date	Origin time h m s	Lat. °S	Long. °E	$m_b$	$M_s$	Age** (m.y.)
1	December 19, 1965	22 06 33.0	32.24	78.87	5.5		4
2	February 17, 1966	11 47 57.3	32.20	78.93	6.0		4
3	October 8, 1968	07 43 22.8	39.85	87.74	5.8	5.8	5
4	May 3, 1973	23 11 04	46.14	73.22	5.5	5.5	27
5	September 19, 1975	03 37 11	34.74	81.88	5.9	6.1	13
6	November 2, 1976	07 13 17	29.36	77.65	5.8	6.5	10
7	November 2, 1976	11 19 15	29.24	77.79	5.6		10
8	May 22, 1979	01 55 55.8	43.81	79.00	5.5	5.1	9
9	September 24, 1981	21 09 42.6	45.65	79.86	5.4	5.5	14

\* Sources of data: ISC (1964-1979) and NEIS (1981)

\*\* Age of lithosphere estimated from magnetic anomaly identifications summarized in Schlich [1982] and magnetic chronology of LaBrecque et al. [1977].

Table 4.2 Source mechanisms obtained from body-wave inversion<sup>a</sup>

No.	Date	Moment <sup>b</sup>	$t_s$ <sup>c</sup>	Depth <sup>d</sup>	Strike	Dip	Slip
1	December 19, 1965	13. $\pm$ 1.	3.0 $\pm$ 1.5	8.3 $\pm$ 0.1	301.8° $\pm$ 1.1	67.1° $\pm$ 0.7	300.5° $\pm$ 1.6
2	February 17, 1966	75. $\pm$ 3.	10.5 $\pm$ 0.8	12.1 $\pm$ 0.2	275.9 $\pm$ 1.1	58.4 $\pm$ 0.5	293.9 $\pm$ 1.1
3	October 8, 1968	20. $\pm$ 1.	3.0 $\pm$ 0.5	10.2 $\pm$ 0.1	6.6 $\pm$ 1.3	53.1 $\pm$ 0.5	266.6 $\pm$ 1.0
4	May 3, 1973	8.7 $\pm$ 0.5	2.0 $\pm$ 0.5	13.7 $\pm$ 0.1	183.1 $\pm$ 1.2	50.7 $\pm$ 0.5	253.9 $\pm$ 1.0
5	September 19, 1975	39. $\pm$ 2.	6.0 $\pm$ 1.5	22.2 $\pm$ 0.1	241.0 $\pm$ 1.6	63.4 $\pm$ 0.4	279.9 $\pm$ 1.7
6	November 2, 1976	77. $\pm$ 3.	7.5 $\pm$ 0.8	11.1 $\pm$ 0.1	231.4 $\pm$ 1.5	37.8 $\pm$ 0.4	281.5 $\pm$ 1.0
7	November 2, 1976	6.1 $\pm$ 0.4	3.0 $\pm$ 0.5	12.4 $\pm$ 0.1	241.9 $\pm$ 1.8	38.0 $\pm$ 0.5	291.4 $\pm$ 1.0
8	May 22, 1979	4.2 $\pm$ 0.2	2.0 $\pm$ 0.5	16.3 $\pm$ 0.2	193.1 $\pm$ 0.8	48.7 $\pm$ 0.2	279.5 $\pm$ 0.7
9	September 24, 1981	4.4 $\pm$ 0.4	3.0 $\pm$ 0.5	11.2 $\pm$ 0.1	144.9 $\pm$ 1.7	36.6 $\pm$ 0.4	250.1 $\pm$ 1.4

a) Range indicated for each parameter is one standard deviation (formal error). The range of  $t_s$  is one half the width of the box function used, except for events 1 and 5, for which it is the full box function width.

b)  $\times 10^{24}$  dyne-cm ( $10^{17}$  N-m)

c) Total duration of faulting, sec. For events 2 and 6,  $t_s$  is the time function appropriate to a direction normal to the rupture vector for the horizontal line source used to model these events.

d) Relative to top of crust, km

Table 4.3 Minimum and maximum estimates of stress drop  
for earthquakes in this study

No.	Date	Stress drop, bars	
		Minimum	Maximum
1 <sup>t</sup>	December 19, 1965	2	15
2	February 17, 1966	1	2
3	October 8, 1968	3	23
4	May 3, 1973	4	33
5	September 19, 1975	1	6
6	November 2, 1976	2	6
7	November 2, 1976	1	7
8	May 22, 1979	2	16
9	September 24, 1981	1	5

---

Note: 1 bar = 0.1 MPa

## FIGURE CAPTIONS

Figure 4.1. Bathymetric and tectonic map of the study area (Mercator projection). Bathymetry, in m (corrected for the variation of speed of sound in sea water), is from Hayes and Vogel [1981] and Fisher et al. [1982]. Tectonic elements are from Schlich [1982]; ridge axis segments are shown as heavy dashed lines and fracture zones (defined by offsets in identified magnetic anomalies) as lighter dashed lines. Earthquake epicenters, shown as dots, are from Sykes [1970a] (1950-1964), ISC (1964-1979), and NEIS (1980-1982). Larger symbols indicate earthquakes with  $m_b \geq 5.5$ . Numbered epicenters indicate earthquakes studied by body-wave inversion (Table 4.1).

Figure 4.2. Comparison of observed (solid line) and synthetic (dashed line) long-period P and SH waves for the December 19, 1965 earthquake. The focal mechanism solution obtained from the inversion is plotted on the lower focal hemisphere (equal area projection). All amplitudes are normalized to an instrument magnification of 3000; the amplitude scales correspond to the waveforms that would be observed on an original seismogram from such an instrument. The two vertical lines delimit the portion of each time series used in the inversion. Symbols for both types of waves are: open circle - dilatation, closed circle - compression, cross - emergent arrival. For SH waves, compression corresponds to positive motion as defined by Aki and Richards [1980]. The relative amplitudes of the box function elements comprising the source time function are also shown. First motions read from long-period seismograms but not used in the inversion are also plotted.

Figure 4.3. Comparison of observed and synthetic P and SH waves for the February 17, 1966 event. See Figure 4.2 for explanation of symbols. The source model is a propagating point source with unilateral horizontal rupture propagation in the direction of strike ( $N84^{\circ}W$ ) at a rupture velocity of 3.2 km/sec. The source time function shown is the time function which would be observed in a direction normal to the rupture vector. At each station, the apparent source time function is identical in shape but compressed or expanded in length, depending on station azimuth and ray parameter.

Figure 4.4. Comparison of observed and synthetic P and SH waves for the October 8, 1968 event. See Figure 4.2 for explanation of symbols.

Figure 4.5. Comparison of observed and synthetic P and SH waves for the May 3, 1973 earthquake. See Figure 4.2 for explanation of symbols.

Figure 4.6. Comparison of observed and synthetic P and SH waves for the September 19, 1975 event. See Figure 4.2 for explanation of symbols.

Figure 4.7. Comparison of observed and synthetic P and SH waves for the main shock on November 2, 1976. See Figure 4.2 for explanation of symbols. This event was modeled as a propagating point source with unilateral horizontal rupture in the direction  $N51^{\circ}E$ . See the caption for Figure 4.3 for further explanation.

Figure 4.8. Comparison of observed and synthetic P waves for the aftershock on November 2, 1976. See Figure 4.2 for explanation of symbols.

Figure 4.9. Comparison of observed and synthetic P and SH waves for the May 22, 1979 earthquake. See Figure 4.2 for explanation of symbols. The amplitude-time scale in the lower right corner of the plot of SH waves is used for station NWA0; the other stations use the scale on the left.

Figure 4.10. Comparison of observed and synthetic P and SH waves for the September 24, 1981 event. See Figure 4.2 for explanation of symbols. The time-amplitude scales in the lower right corner of the plot of P and SH waves are used for SRO stations (NWA0, SH10, and SNZ0); the remaining stations (WSSN) use the left-hand scale.

Figure 4.11. Summary of focal mechanisms of the earthquakes studied by body-wave inversion, with other epicenters and tectonic elements as in Figure 4.1. The tic marks on each focal mechanism indicate the orientation of the horizontal projection of the T-axis. Several pre-WSSN epicenters relocated by Sykes [1970a] are indicated by the dates of the events. Bathymetric contours between the Kerguelen Plateau and the Southeast Indian Ridge indicate the region of the positive residual depth anomaly discussed in the text.

Figure 4.12. Axisymmetric bending stresses (radial and tangential) at the top and bottom surfaces of an elastic plate overlying a fluid halfspace and subject to a disk load of magnitude  $40 \text{ kg/m}^2$  and with a radius of 200 km. See Brotchie [1971] for details of the solution. Compressive stress is positive; 1 kbar = 100 MPa. The plate has an effective elastic thickness of 20 km and flexural rigidity of  $7.1 \times 10^{22} \text{ N-m}$ . The model roughly approximates the load of the northern Kerguelen Plateau; the May 3, 1973 earthquake would be located just beyond the edge of the load, at a radius of approximately 300 km, for this simplified geometry.

Figure 4.13. Strength envelope for 10, 20, and 30 m.y. old oceanic lithosphere, following Goetze and Evans [1979]. Compressive stress is positive; 1 kbar = 100 MPa. The left side of the envelope ( $\sigma_V > \sigma_H$ ) is appropriate for normal faulting, where  $\sigma_V$  and  $\sigma_H$  are the vertical principal stress and largest magnitude horizontal stress. Depths are relative to sea level. The focal depth of the May 1973 event is indicated by the horizontal dashed line. The thermal structure of the plate at each age is calculated from the model and parameters of Parsons and Sclater [1977]. The upper part of the strength envelope is controlled by the relation for frictional strength versus effective stress [Byerlee, 1978], assuming zero pore pressure. The limiting differential stress at depth is controlled by ductile flow of olivine, with a strain rate of  $10^{-15} \text{ sec}^{-1}$  and either a Dorn law ( $\Delta\sigma > 2.0 \text{ kbar}$ ) or power law ( $\Delta\sigma < 2.0 \text{ kbar}$ ) and constants as in Goetze and Evans [1979].

Figure 4.14. Schematic map of lithospheric deviatoric stress orientations inferred from focal mechanisms in the central and southern Indian Ocean. Outward-pointing arrows indicate extension (normal faulting), inward-pointing arrows indicate compression (thrust faulting). The sense of strike-slip faulting on the northern Ninetyeast Ridge is indicated. Base map from Heezen et al. [1977].

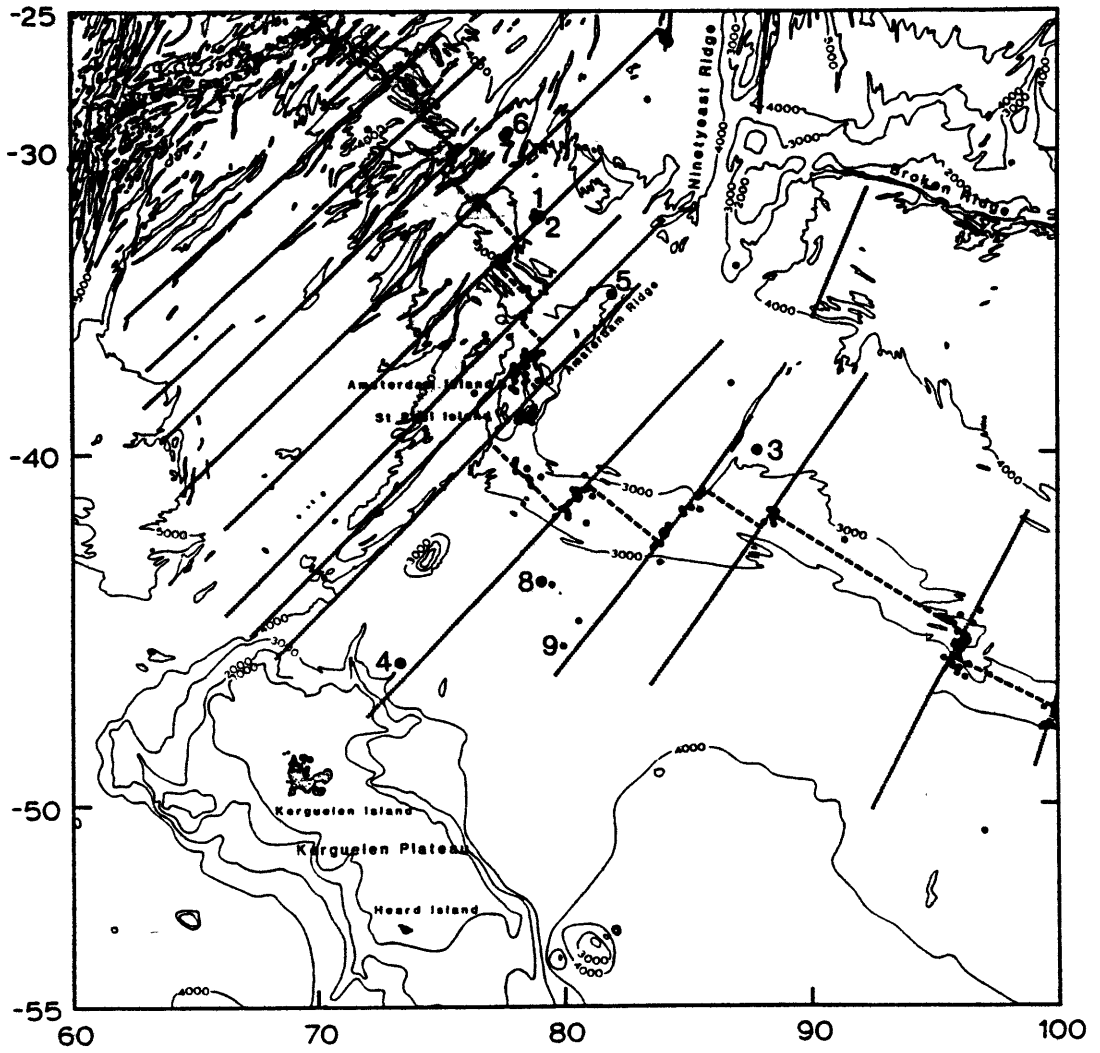


Figure 4.1



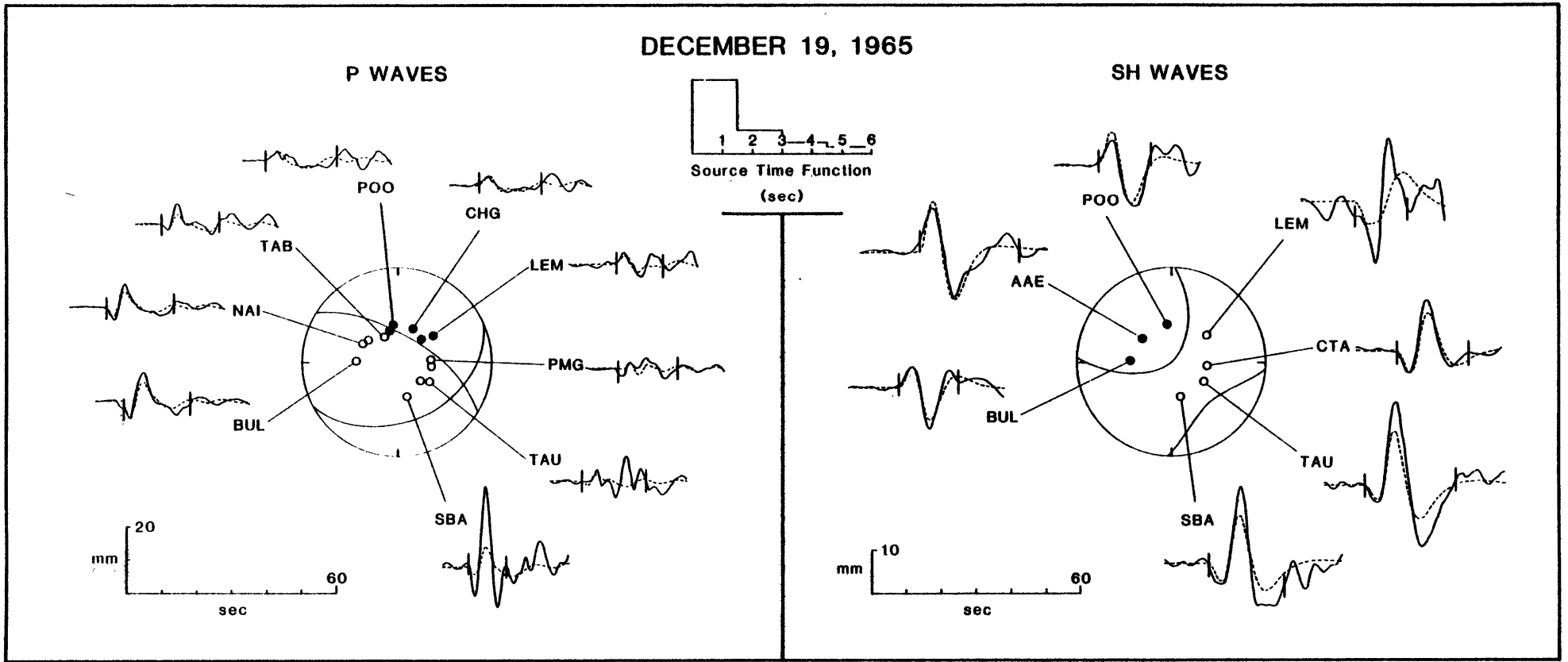


Figure 4.2

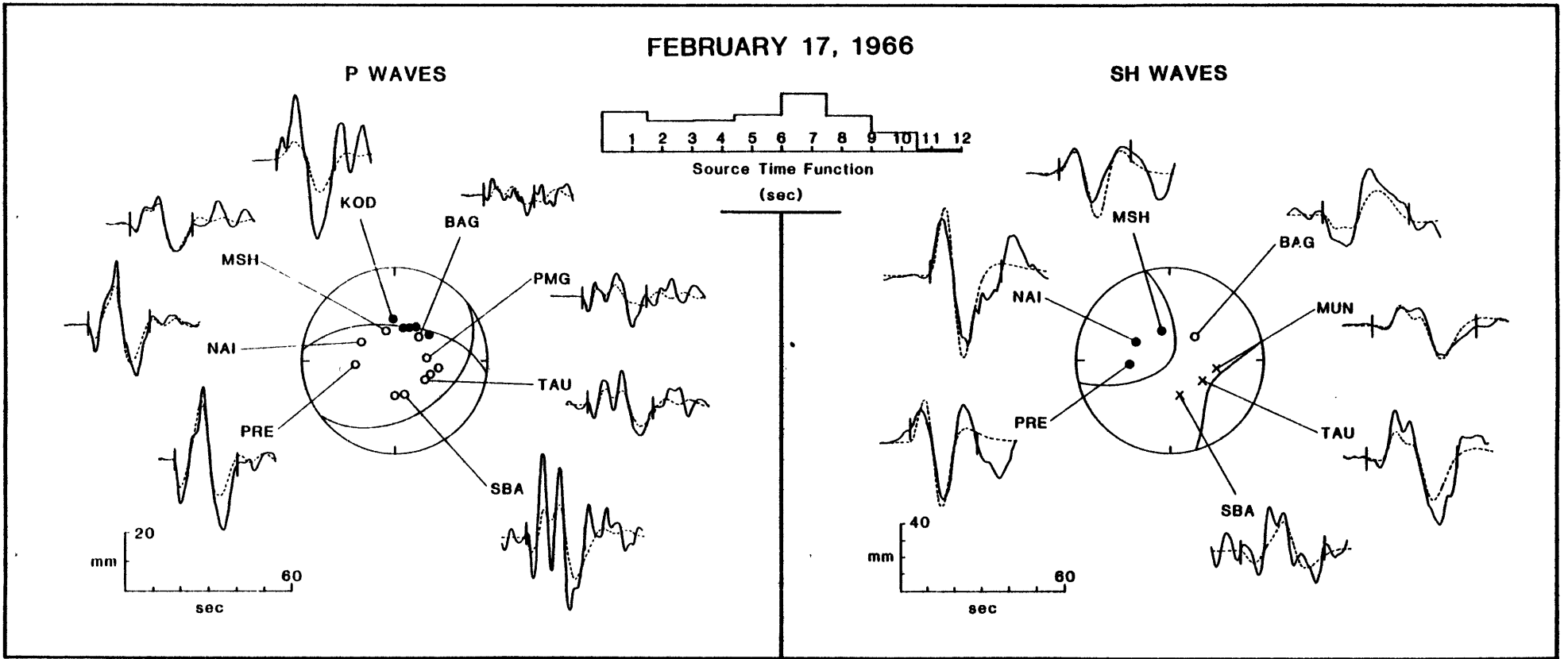


Figure 4.3

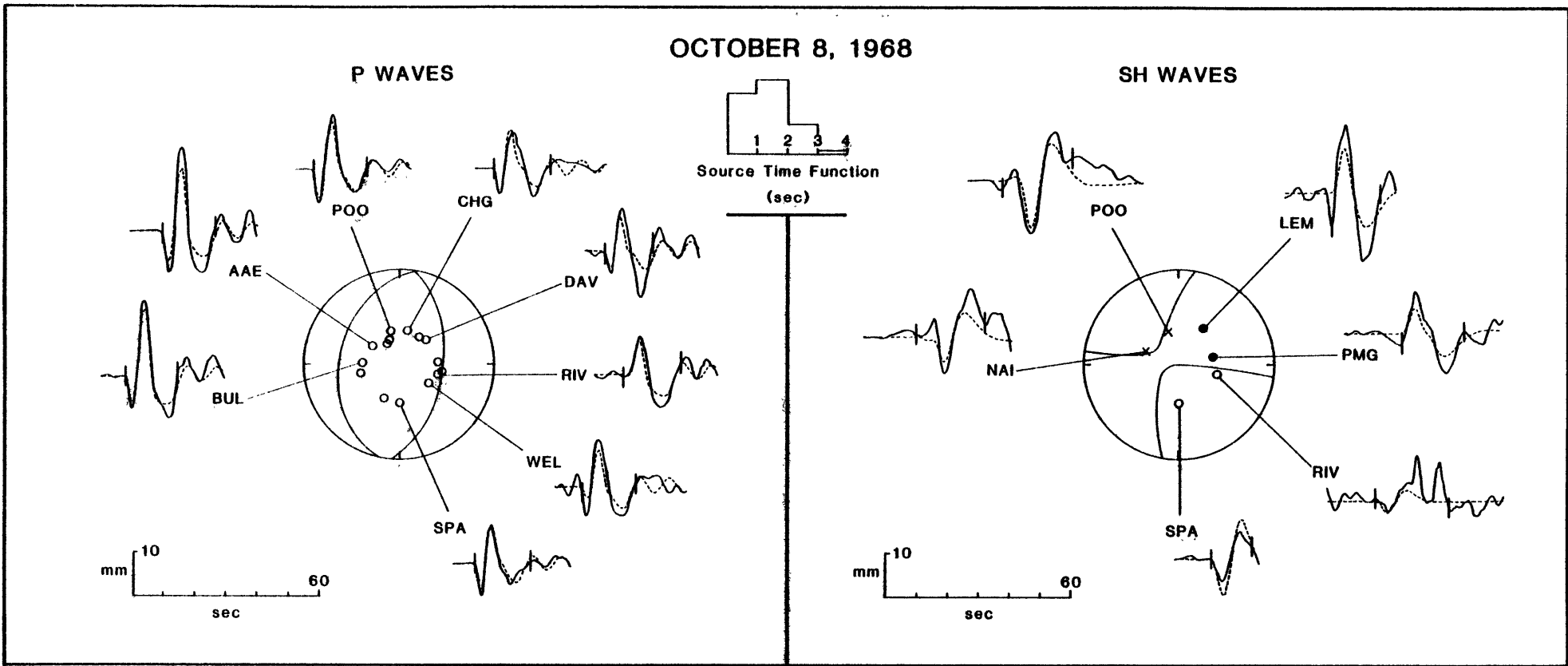


Figure 4.4

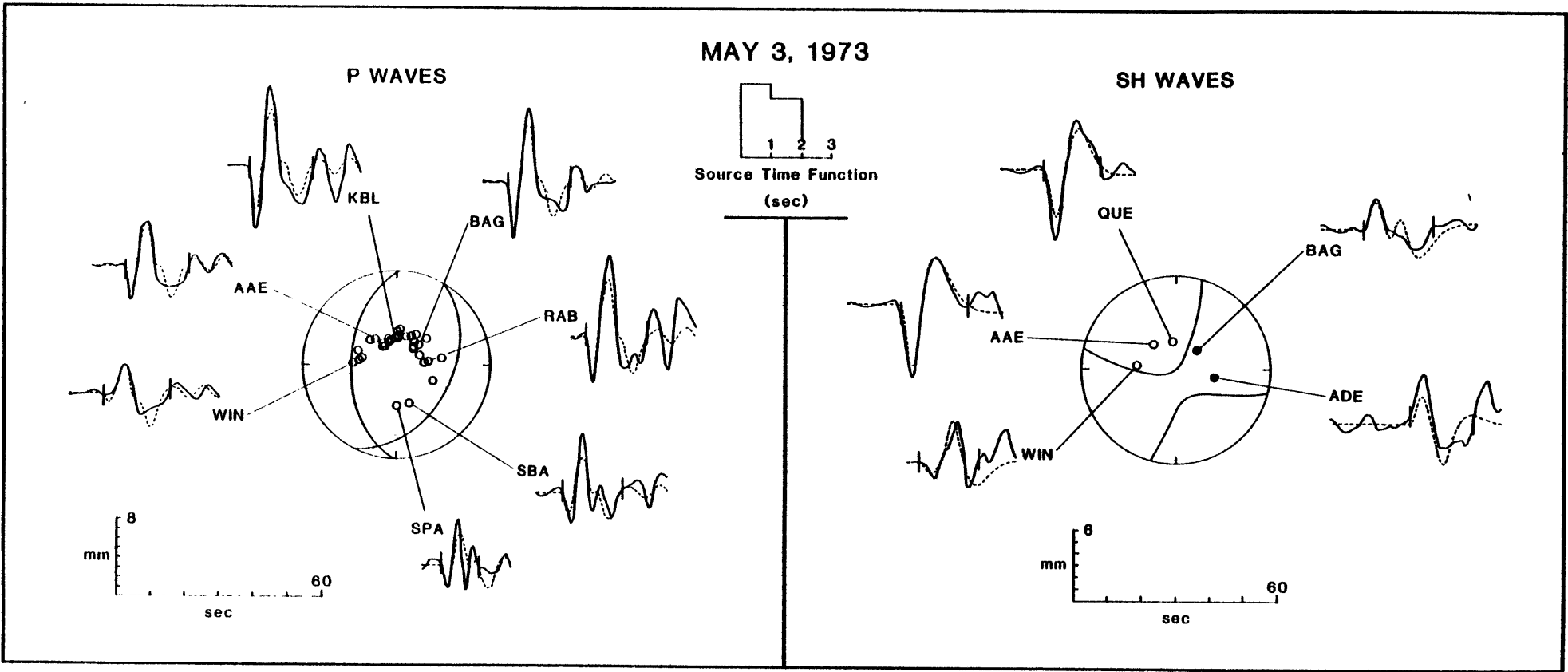


Figure 4.5

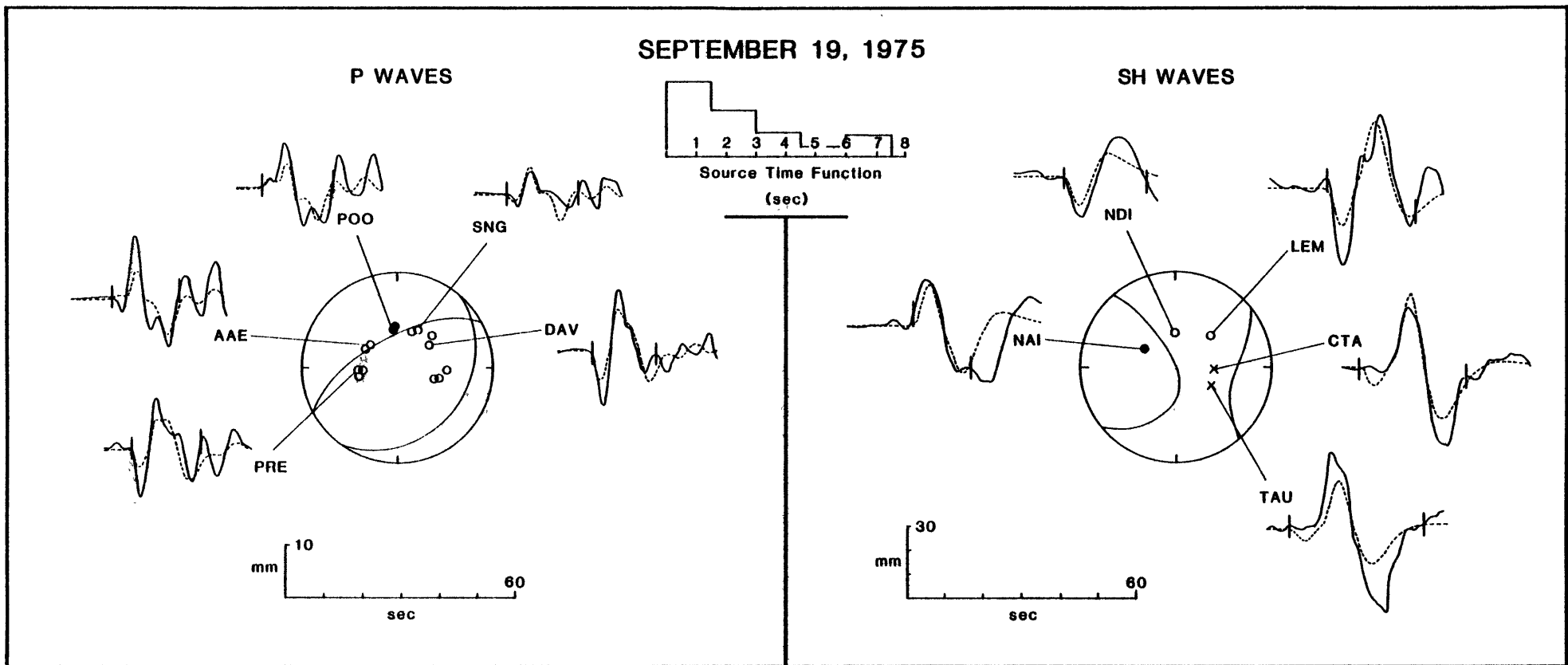


Figure 4.6

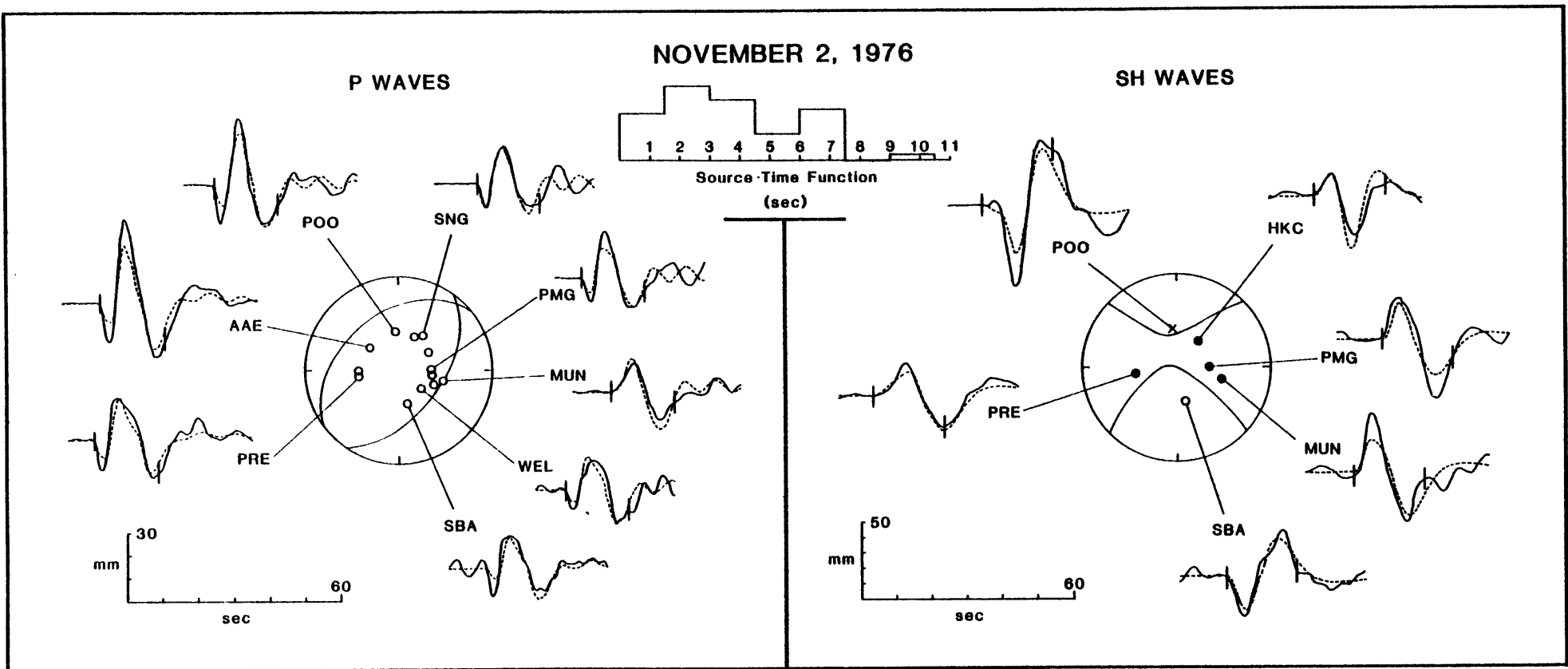


Figure 4.7

NOVEMBER 2, 1976

P WAVES

SH WAVES

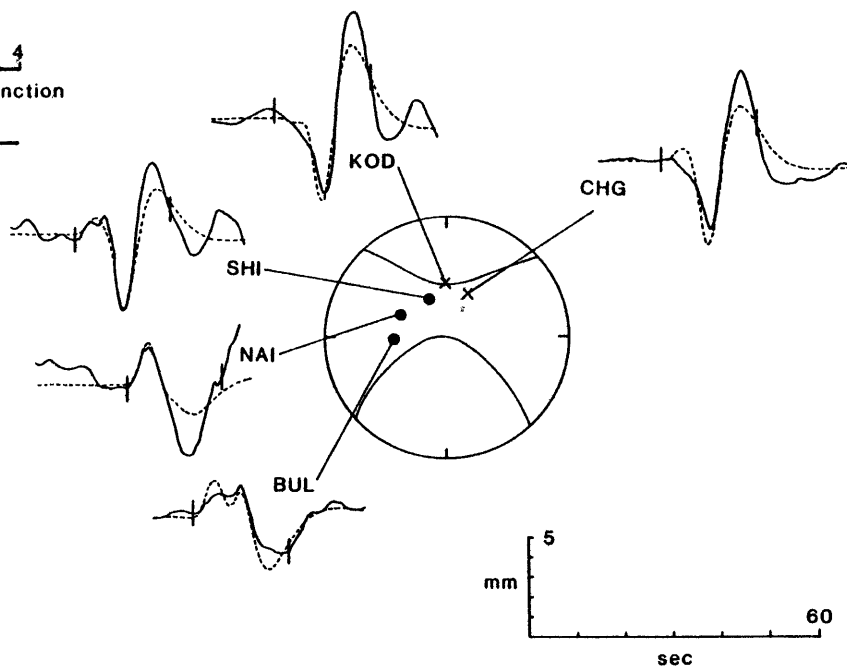
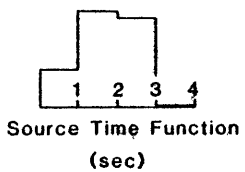
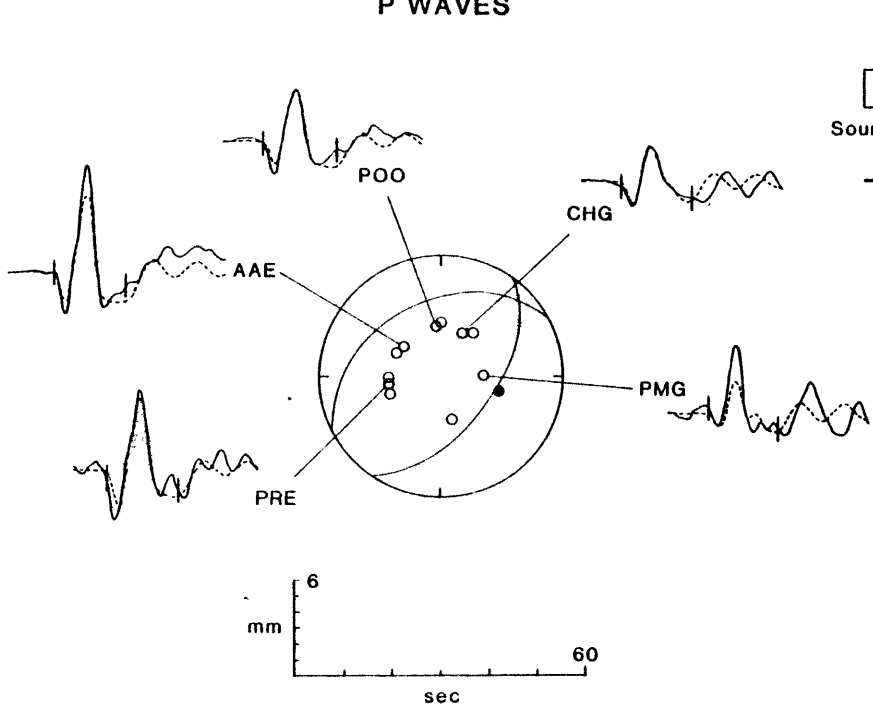


Figure 4.8

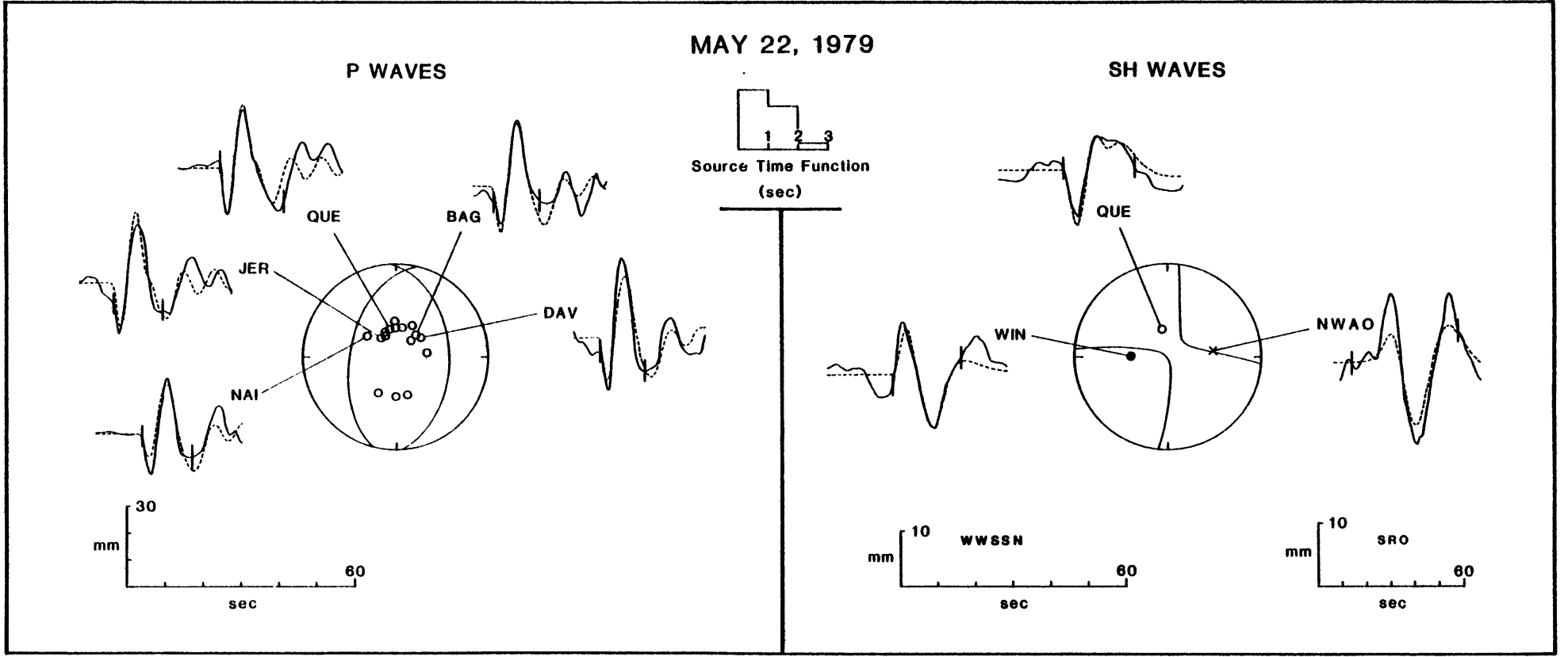


Figure 4.9



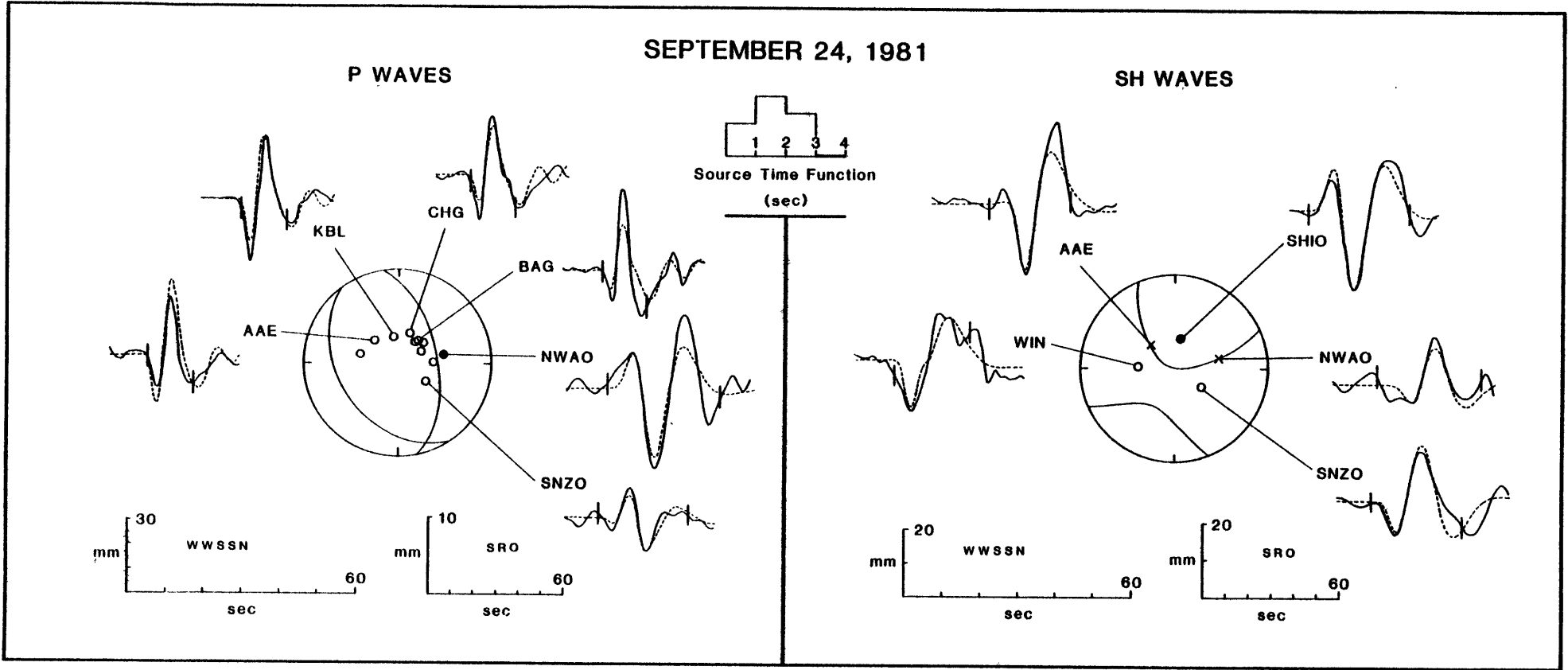


Figure 4.10

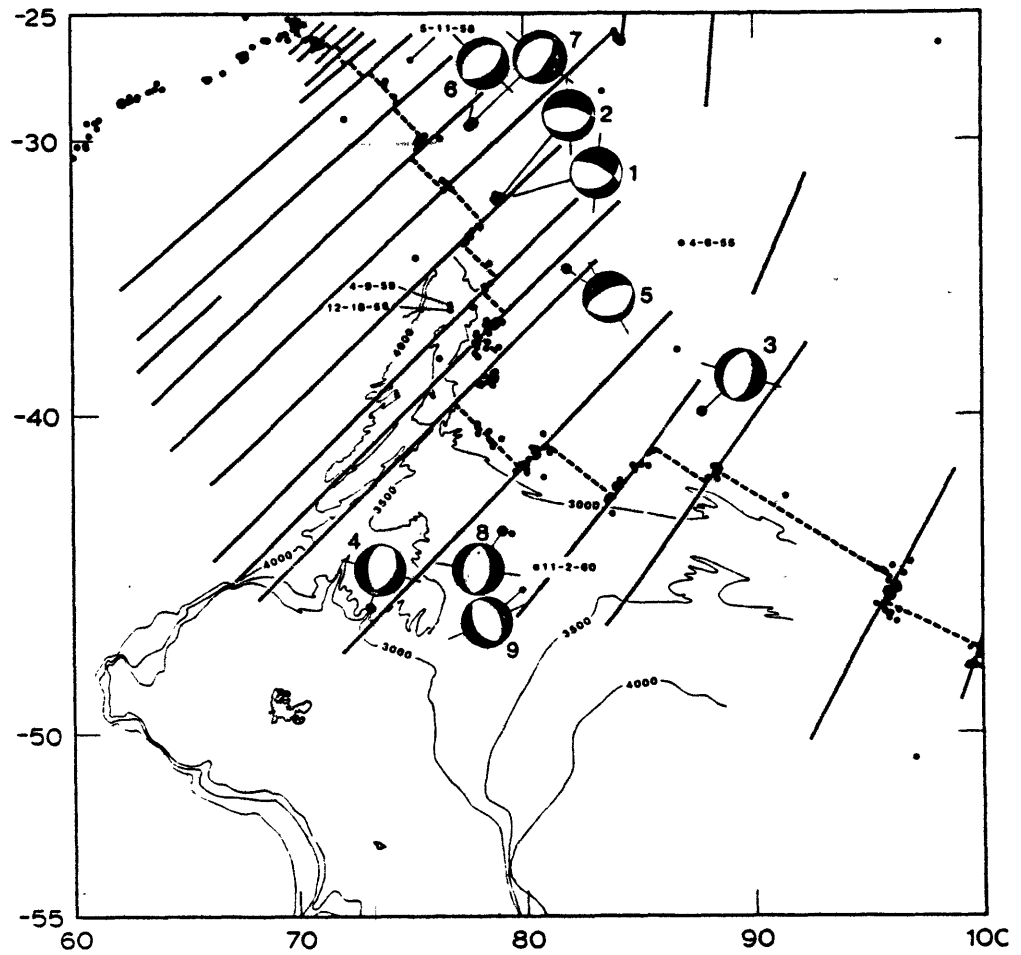


Figure 4.11

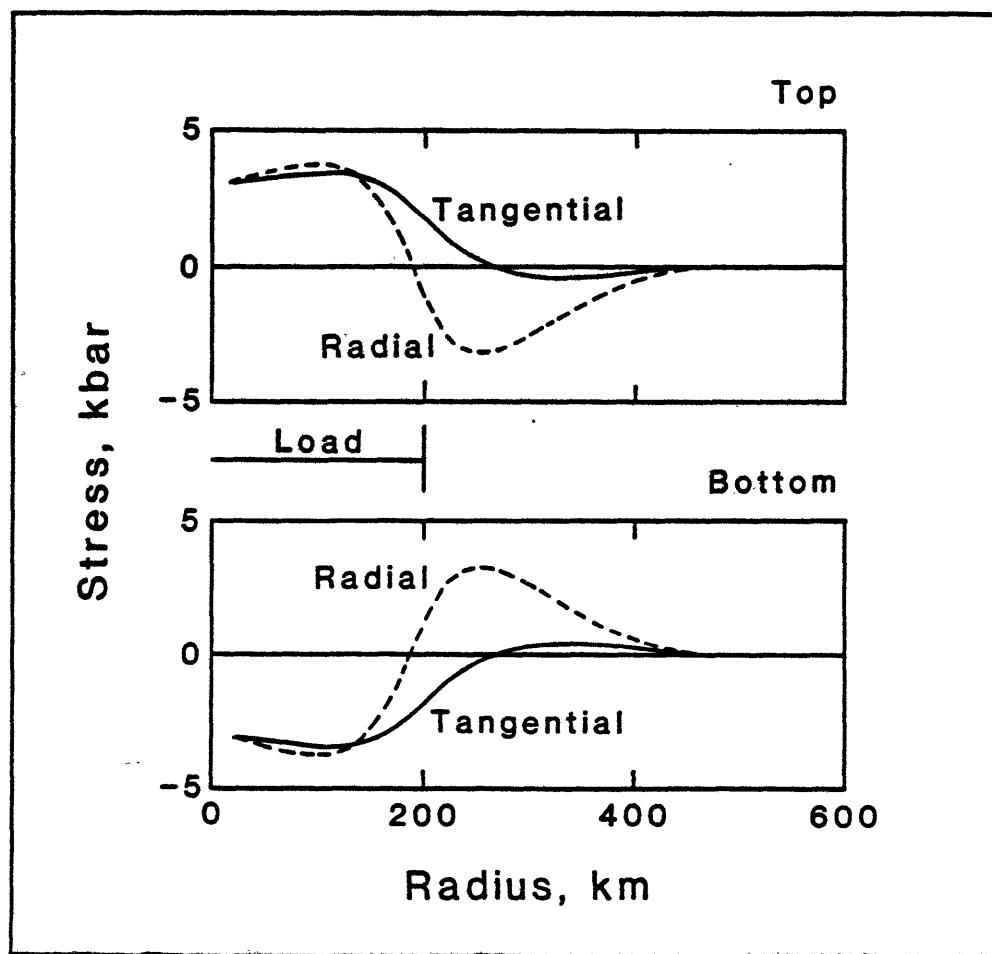


Figure 4.12

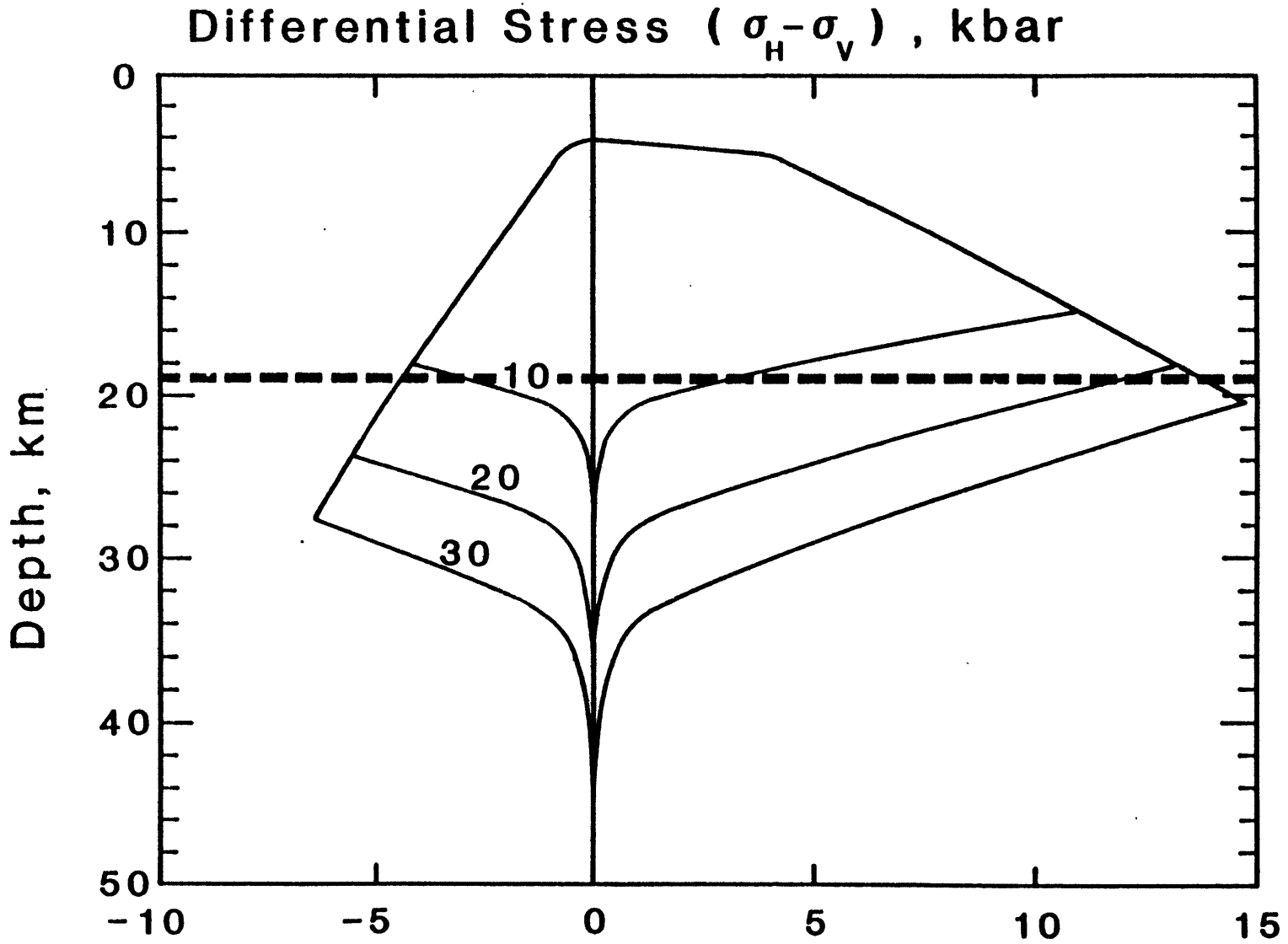


Figure 4.13

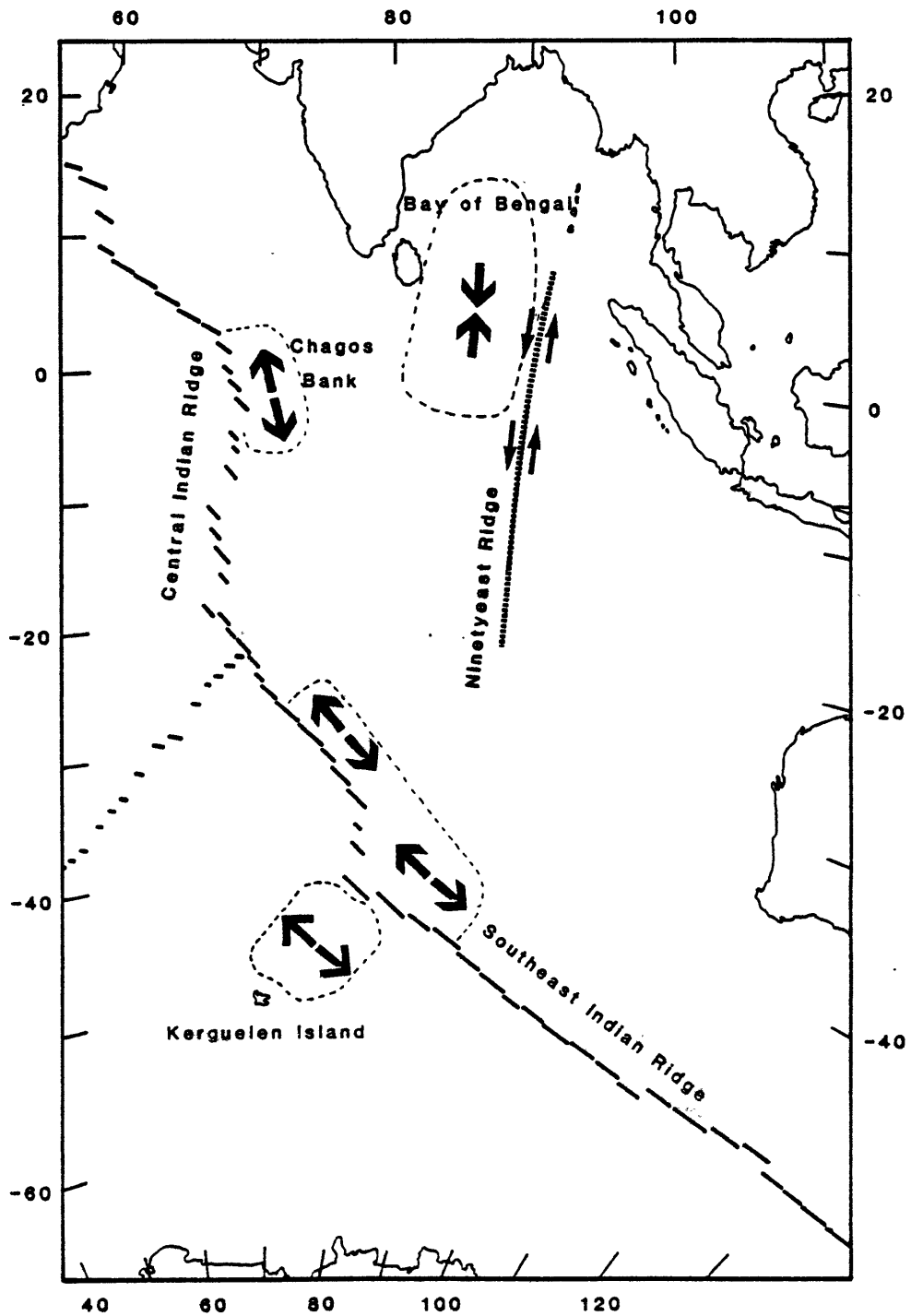


Figure 4.14

CHAPTER 5. SOURCE STUDIES OF OCEANIC INTRAPLATE EARTHQUAKES  
IN THE NORTHERN INDIAN OCEAN

INTRODUCTION

Gutenberg and Richter [1954, pp. 77-79] first commented on the frequent occurrence in the northern Indian Ocean of earthquakes with little apparent connection to other prominent seismic belts, although they proposed a minor seismic belt extending southwest from Sri Lanka to the Carlsberg Ridge. The association of many oceanic intraplate earthquakes with the Ninetyeast Ridge, a subject explored further by Stein and Okal [1978], was also noted by Gutenberg and Richter. With a larger and more accurate set of earthquake locations, Sykes [1970a] noted a pattern in the seismicity of the northern Indian Ocean which he interpreted as an incipient island arc complex between Sri Lanka and Australia. This pattern is clearly evident in Figure 2.1, showing oceanic intraplate epicenters for the years 1906-1963, but the trend of epicenters in the northern Indian Ocean since 1964 (Figure 2.3) is quite different, oriented N-S rather than NW-SE. No evidence has since emerged to support the nascent island arc hypothesis. A major objective of this chapter is to supplement seismicity patterns with source mechanisms of intraplate earthquakes in order to place constraints on the mode of internal deformation of the Indian plate.

Clearly, care must be exercised in the interpretation of short-term (i.e., decades) patterns in oceanic intraplate seismicity, but these and other studies [e.g., Stover, 1966; Rothe, 1969] emphasize the fact that the northern Indian Ocean has been the most seismically active oceanic intraplate region in this century. Stein and Okal [1978] make the point that the Ninetyeast Ridge is approximately as

seismically active as Southern California. The young lithosphere of the Indian plate also experiences unusually high levels of intraplate (or near-ridge) seismicity (Chapters 4 and 8).

In this chapter we present source mechanisms (obtained by inversion of long-period P and SH waveforms, as described in Chapter 3) of 11 earthquakes in the northern Indian Ocean, in the general vicinity of the Ninetyeast Ridge. These source mechanisms are used to place constraints on the nature of large-scale internal deformation in oceanic lithosphere of the Indian plate. The frequent occurrence of large earthquakes in this area also allows us to examine the coherency of the long-wavelength intraplate stress field as inferred from earthquake focal mechanisms.

#### TECTONIC HISTORY OF THE INDIAN PLATE

An understanding of the significance of the intraplate seismicity of the Indian plate requires an appreciation of at least the broad outline of the tectonic history of the region. The evolution of oceanic lithosphere in the Indian Ocean has been the subject of numerous studies and not a few disagreements, but data obtained by the Deep-Sea Drilling Program have led to general agreement on the major elements of a quantitative model [Veevers, 1977]. The account presented below essentially follows the syntheses of Johnson et al. [1976] and Curry et al. [1982]. Figure 5.1, a reproduction of Figure 18 of Curry et al. [1982], illustrates the main stages in the tectonic history of the oceanic portions of the Indian, Antarctic, and Australian plates.

The initial breakup of Gondwanaland occurred about 125 m.y.B.P., when the Indian plate separated from Antarctica-Australia along an axis

parallel to the present southeast coast of India (Figure 5.1A). Creation of oceanic lithosphere at this spreading axis (Figure 5.1B) continued until about 90 m.y.B.P. At some time between 110 and 80 m.y.B.P., a spreading ridge system developed between India and Antarctica, which had previously been separated by a transform boundary. Slow spreading between Antarctica and Australia may have begun at this time also [Mutter and Cande, 1983]. The resulting motion of the Indian plate was approximately N-S, parallel to a long oceanic transform fault which lay on the east side of the northern section of the Ninetyeast Ridge (Figure 5.1C). The en echelon pattern in the bathymetry of the northern part of the Ninetyeast Ridge (from about 5°S to at least 10°N) developed at this time when the SW-NE trending ridge axis was reorganized into a series of short E-W trending ridge segments, offset in a left-lateral sense by N-S trending fracture zones.

The Indian plate moved rapidly north at about 100 mm/y until about 53 m.y.B.P., when the Indian continent made initial contact with Asia (Figure 5.1D). At about 46 m.y.B.P., spreading ceased in the northwestern Wharton Basin, east of the Ninetyeast Ridge [Liu et al., 1983]. The onset of spreading on the present Southeast Indian Ridge inaugurated the current stage in the tectonic evolution of the Indian Ocean, in which the former Indian and Australian plates have had a single pole of rotation (Figure 5.1E). The Ninetyeast Ridge marks a dramatic transition in the tectonic style of the northern boundary of this plate. To the east, the Australian half of the plate is subducted at the Sunda Arc. West of the Ninetyeast Ridge, the continental collision between India and Asia has continued, perhaps in several



stages, as the Indian continent first collided with an island arc and finally the Asian continent. The present configuration of plates is shown in Figure 5.1F.

Because of its prominence in the tectonic framework of the northern Indian Ocean, the Ninetyeast Ridge merits a summary of current views on its formation and history. The ridge extends over 5000 km, from about 31°S to at least 17°N, but north of 10°N it is buried beneath sediments of the Bengal Deep-Sea Fan [Curray et al., 1982]. The ridge ranges in width between 150 and 250 km. The northern part of the ridge (north of about 6°S) has a blocky en echelon structure, interpreted by Curray et al. [1982] as the deformed remnant of the spreading center which first split India away from Gondwanaland. The southern part of the ridge is relatively straight and flat-topped, but becomes wider at about 15°S, the latitude of a prominent bathymetric feature on the west flank of the ridge named the Osborn Knoll by Sclater and Fisher [1974]. Gravity data indicate the ridge is isostatically compensated, probably by emplacement of relatively less dense material in the upper mantle beneath a fairly normal oceanic crustal layer [Bowin, 1973]. Such a structure is also consistent with seismic refraction data [Francis and Raitt, 1967]. The Ninetyeast Ridge apparently has always been attached to the Indian plate and has subsided at the same rate as normal oceanic lithosphere [Sclater and Fisher, 1974; Detrick et al., 1977].

Schlich [1982] summarizes early theories on the origin of the Ninetyeast Ridge, which range from its being a microcontinent to being an uplifted horst-like feature resulting from compression between the Indian and Australian halves of the plate. There is now general

agreement that the bathymetric expression of the Ninetyeast Ridge results from the passage of the Indian plate over a mantle hotspot during its rapid northward motion since the late Cretaceous, but the number of hotspots involved is still a matter of controversy. Morgan [1972] proposed the Kerguelen hotspot as the source of the Ninetyeast Ridge and Curry et al. [1982] also favor this view, but Luyendyk and Rennick [1977] argue that a second hotspot (at Amsterdam Island) is also required by the data. The two-hotspot model accounts more easily for some details of the tectonic evolution at the southern end of the Ninetyeast Ridge. The existence of a separate Amsterdam hotspot and its relevance to the formation of the Ninetyeast Ridge is brought into question, however, by Sr isotope and trace-element studies which find that the Ninetyeast Ridge has a strong affinity with the Kerguelen Plateau, but not with Amsterdam Island or normal mid-ocean ridges [Whitford and Duncan, 1978]. Fortunately, this issue has little bearing on present-day intraplate tectonics in the northern Indian Ocean. Further support for a hotspot origin for the Ninetyeast Ridge comes from paleomagnetic data which indicate that the ridge was formed at high southern latitudes [Peirce, 1978] and paleontological evidence that it formed at or near sealevel [Luyendyk and Davies, 1974].

According to this model, the hotspot lay beneath the Indian continent until about 90 m.y.B.P. The rapid northward motion of the Indian plate after this time carried the en echelon pattern of former spreading ridge segments of the northern part of the Ninetyeast Ridge over the hotspot, building the bathymetric level up to near sea-level [Curry et al., 1982]. The change in morphology of the ridge near the prominent Osborn Knoll at about 15°S, where the ridge becomes wider and

more massive than it is to the north, corresponds to the location of the hotspot at the time of initial collision between India and Asia, when the northward motion of the Indian plate is likely to have slowed [Curray et al., 1982].

Although the model of the tectonic evolution of the Indian Ocean outlined above cannot explain every observation, it accounts for the major tectonic elements of this complex region in a consistent manner and provides an adequate tectonic context in which to interpret the source mechanisms of oceanic intraplate earthquakes presented below.

#### SOURCE MECHANISMS

In this section we present the source mechanisms of 11 oceanic intraplate earthquakes in the northern Indian Ocean, obtained from the inversion of P and SH waveforms using the procedure developed by Nabelek [1984], as described in Chapter 3. Epicentral data for these earthquakes are listed in Table 5.1. The focal mechanisms and the observed and synthetic seismograms are given in a series of figures, with P waves and SH waves shown on separate focal spheres (with the appropriate radiation pattern) for clarity. The synthetics shown were generated with the single best-fit solution, and have not been individually rescaled for improved fit. The station code and geographic location of all stations used in the inversions are listed in Appendix E. The best-fitting source parameters for all earthquakes, together with formal errors, are given in Table 5.2.

#### May 25, 1964

The May 25, 1964 earthquake ( $m_b = 5.7$ ,  $M_s = 6.0$ ) occurred on the northern Ninetyeast Ridge (Figure 5.2), somewhat south of the portion of the ridge which has been most seismically active in this century

[Stein and Okal, 1978]. This event was very well recorded: for both P and SH waves we obtained usable waveforms at stations in 3 quadrants (Figure 5.3). Consequently, the best-fitting double couple (180/85/1) is tightly constrained and quite similar to the mechanism found by Banghar and Sykes [1969]. The source study thus reduces to the determination of the moment, centroid depth, and time function, but this proved to be a rather difficult task. Although the earthquake is deep enough so that direct and surface-reflected phases are clearly separated at most stations, the delay between phases (and therefore the best-fitting depth) for the P waves varies significantly from station to station. This event may have a relatively complex rupture history.

In addition to the variability of the P waveforms, the delay between direct and reflected SH phases is consistent with a centroid depth of about 12 km below the seafloor, while the P waves are fit better at a depth of about 19 km. A likely cause for at least some of this discrepancy is the source velocity structure assumed for the inversion. As discussed in Chapter 3, the velocity structure was chosen to approximate typical oceanic crust and upper mantle and we resist the temptation to try to fine-tune the crustal structure for individual earthquakes. If we were to adjust the crustal structure simply to achieve a better fit we would still have to be concerned about the bias introduced in other source parameters and in most cases, there is seldom independent information on the velocity structure.

The solution shown in Figure 5.3 has a centroid depth of 14.8 km, but for the reasons discussed above there is more uncertainty in this depth than usual. Wiens and Stein [1983a] estimated a depth of 17 km by matching P waveforms, and our tests show that the P waves alone can

be well matched with depths of up to 20 km. The seismic moment estimated in the inversion is  $1.2 \times 10^{25}$  dyne-cm, virtually identical with the moment of  $1.1 \times 10^{25}$  dyne-cm found from surface waves by Stein and Okal [1978].

#### October 31, 1965

The earthquake on October 31, 1965 ( $m_b = 5.3$ ,  $M_s = 5.4$ ) occurred southwest of the Cocos-Keeling Seamount in the northeast Indian Ocean (Figure 5.2). This earthquake was well recorded on long period instruments and station coverage for both P and SH waves is very good, considering the remoteness of the epicenter. Normally, the quality of the fit at individual stations tends to deteriorate with increasingly complete coverage, but the observed P and SH waves are exceptionally well matched. The polarity of the horizontal component instruments at PRE was found to be reversed. The mechanism is characterized by strike-slip faulting, with a P axis oriented NW-SE (166/68/11, Figure 5.4). The seismic moment is  $5.3 \times 10^{24}$  dyne-cm and the centroid depth is 19.7 km below the seafloor. Our mechanism is quite similar to that reported by Wiens and Stein [1983a], from first motions and P wave modeling (167/77/3), but they estimated the depth to be 24 km.

#### September 14, 1968

Sykes and Sbar [1974] found a thrust-faulting mechanism for the September 14, 1968 earthquake ( $m_b = 5.4$ ), but they were unable to determine the strike of the nodal planes. The epicenter lies in an area where major fracture zone trends change direction from NE-SW to N-S, and thus the lithosphere may be expected to be relatively disturbed (Figure 5.2). This small event ( $M_0 = 1.1 \times 10^{24}$  dyne-cm) wrote clear short period records at many stations, but we were able to

obtain only 4 usable long-period P waves and an equal number of SH waves. Because of the poor station distribution, the uncertainty in the focal mechanism is greater than usual (Table 5.2), but the data are adequate to constrain the P axis to be oriented close to N-S (Figure 5.5). The nodal planes of the mechanism (307/28/117) do not appear to parallel either fracture zone trend in the epicentral region (Figure 5.2). The focal depth is only 1.7 km below the seafloor, making this one of the few oceanic intraplate events to have occurred in the crust.

#### October 10, 1970

Fitch [1972] studied the focal mechanism of the October 10, 1970 earthquake ( $m_b = 5.8$ ,  $M_s = 6.3$ ) with P wave first motions and SH wave polarizations, determining a nearly pure strike-slip mechanism (126/83/164). On the basis of magnetic anomaly identifications, Sclater and Fisher [1974] propose a large N-S trending fracture zone through the epicenter of this event (Figure 5.2). Curry et al. [1982] question Sclater and Fisher's interpretation, however, because the dominant trend in the bathymetry, at least to the south where it is not obscured by sediments, is NE-SW.

This earthquake presented major problems for the body-waveform inversion because of the strong trade-off between depth and source time function for strike-slip mechanisms. Nabelek [1984] discusses the problem in detail, but we can summarize the difficulty as follows: For a pure strike-slip mechanism, the direct and major reflected phases have the same polarity. This is the case for both SH and P waves. At shallow depths, the delay between direct and reflected phases becomes so small that all the phases merge into one pulse. Therefore, it is possible to match the waveforms of a deep, simple strike-slip

earthquake with a very shallow source depth and a complex time function.

After extensive testing of both deep and shallow models, we prefer a deeper centroid (about 26 km) with a relatively simple time function, although the residual error is not significantly lower than the best shallow solutions with complex time functions. There are two main reasons for this preference: (1) Shallow solutions consistently place the centroid at the crust-water interface; the inversion frequently attempted to move it into the water layer. The centroid of an event this size is unlikely to be so shallow, even if it ruptured through to the seafloor. We take this as evidence that the inversion is trying to reduce the delay between direct and reflected phases to the absolute minimum so that the waveforms may be fit solely with the time function. (2) The deeper solution, a single point source with a relatively simple time function, does a better job of matching the later parts of the P waveforms than any shallow solution, even when we used 3 point sources with multi-element time functions in the shallow model. The one advantage of the shallow model over the deep model is in reproducing the impulsive nature of the first half-cycle of the P waves. This is a frequently encountered problem in modeling P waveforms from strike-slip events at any depth and not a sufficient reason to prefer the shallow solution in our judgement.

The preferred source mechanism for the October 1970 earthquake (Figure 5.6) has a nearly pure strike-slip mechanism (25/86/7), quite similar to Fitch's, but rotated about  $10^\circ$  counterclockwise. The centroid depth is 25.8 km and the seismic moment is  $5.2 \times 10^{25}$  dyne-cm. Richardson and Solomon [1977] estimated the moment to be  $6.7 \times 10^{25}$

dyne-cm from a spectral study of the long-period SH waves; we performed an inversion using only the SH waves and obtained a moment of  $6.1 \times 10^{25}$  dyne-cm. Stein and Okal [1978] found a moment of  $2.9 \times 10^{25}$  dyne-cm from the surface waves at one station.

#### June 26, 1971

The large ( $m_b = 5.9$ ,  $M_s = 6.4$ ) earthquake on June 26, 1971 in the northeast Indian Ocean (Figure 5.2) was studied by Sykes and Sbar [1974], who found a predominantly thrust faulting mechanism with a significant component of left-lateral strike-slip motion on a plane striking NNE. By matching observed P waveforms with synthetics generated using this mechanism, Weins and Stein [1983] estimated a focal depth of 30 km, which is indistinguishable from the centroid depth of 29.9 km found in the inversion. The mechanism (13/62/22, Figure 5.7) is very similar to the result of the first motion study. The seismic moment is  $4.9 \times 10^{25}$  dyne-cm. The horizontal component instruments at SBA were found to have reversed polarity.

#### November 24, 1972

The November 24, 1972 earthquake ( $m_b = 5.2$ ,  $M_s = 5.2$ ) occurred beneath the east flank of the N-S trending  $85^\circ\text{E}$  Ridge [Liu et al., 1982] in the Bay of Bengal (Figure 5.2). For the inversion, the thick sedimentary layer in the epicentral region [Curry et al., 1982] was approximated by a 5 km thick layer with  $\alpha = 2.94$  km/s,  $\beta = 1.60$  km/s, and  $\rho = 2.30$  g/cm<sup>3</sup>. A study of the gravity anomaly over the  $85^\circ\text{E}$  Ridge indicates that it is probably a volcanic feature, formed on relatively young lithosphere (5-15 m.y.) and buried when the lithosphere was 40-80 m.y. old [Liu et al., 1982]. The focal mechanism (253/50/80, Figure 5.8) is characterized by thrust faulting with a P axis trending nearly



N-S. The seismic moment is  $3.0 \times 10^{24}$  dyne-cm. The centroid depth of 31.8 km below the sediment-water interface is reasonably well constrained, but there is a small discrepancy between the depths which best fit the P and SH waves. The P waves alone indicate a centroid depth several kilometers shallower than the solution shown in Figure 5.8. The source time function for this small event has a duration of only about 2 s, but unless elements significantly longer than this are used (thus degrading the fit), the amplitude of the second element always converges to a small negative value. We suspect that, rather than displaying back-slip on the fault, the time function is absorbing some of the error associated with unmodeled reflectors in the crustal velocity structure.

#### April 7, 1973

The large April 7, 1973 earthquake ( $m_b = 5.8$ ,  $M_s = 6.6$ ) occurred on the northern end of the Ninetyeast Ridge, near the point at which it intersects the western end of the Sunda Arc (Figure 5.2). The signal-to-noise ratio for the waveforms used in the inversion is quite high and we obtained good azimuthal coverage. The vertical component instrument at MAT was found to have reversed polarity. This earthquake can be characterized quite readily as a large ( $M_0 = 9.5 \times 10^{25}$  dyne-cm), left-lateral strike-slip event (203/83/348) on a plane which parallels the extinct NNE-trending spreading ridge segments thought to compose the northern part of the Ninetyeast Ridge [Curry et al., 1982]. The source time function is remarkably simple, with a duration of about 12 s. The centroid depth is 14.4 km. The observed and synthetic waveforms for this mechanism are shown in Figure 5.9. Even though the high-frequency parts of some of the P waveforms are poorly

matched (e.g., MUN and AAE), the overall fit is quite good and the robustness of the solution is reflected in the low formal errors for the source parameters (Table 5.2).

#### August 30, 1973

The August 30, 1973 earthquake ( $m_b = 5.8$ ,  $M_s = 5.2$ ) is located in the Bay of Bengal, directly east of Sri Lanka (Figure 5.2). Bergman and Solomon [1980] presented the results of a first motion study of this event, finding a predominantly thrust-faulting mechanism with P axis oriented NW-SE. As is usually the case for such mechanisms, the strike is poorly constrained and depends critically on the correct identification of emergent waveforms. Using this mechanism, Wiens and Stein [1983a] modeled the P waveforms from this earthquake to estimate a depth of 23 km below the seafloor. In the source velocity structure for the inversion, we approximated the sediments of the Bengal Deep-Sea Fan by a 4.0 km thick layer with  $\alpha = 3.3$  km/s,  $\beta = 1.9$  km/s, and  $\rho = 2.3$  g/cm<sup>3</sup> [Curry et al., 1983]. The focal mechanism found in the inversion (284/50/115, Figure 5.10) has dip and slip angles very similar to the mechanism reported by Bergman and Solomon [1980] but the strike is rotated clockwise about 40° relative to the first motion solution. Weissel et al. [1980] show only the direction of maximum principal stress for this event, but it appears they obtained a mechanism from P wave first motions quite similar to that of Bergman and Solomon [1980]. The small number of SH waveforms used in the inversion results in larger than usual formal errors for the focal mechanism (Table 5.2), but the essentially N-S trend of the P axis is well constrained. The centroid depth is 23.6 km, in excellent agreement with Wiens and Stein [1983a]. The seismic moment is  $4.7 \times 10^{24}$  dyne-cm.

June 25, 1974

The epicenter of the June 25, 1974 ( $m_b = 6.1$ ,  $M_s = 6.6$ ) earthquake is in lithosphere created while the spreading direction in the central Indian Ocean was changing from approximately N-S to NE-SW, a setting similar to that of the September 14, 1968 event discussed above (Figure 5.2). The source mechanism was first studied by Stein and Okal [1978], using first motion polarities to constrain one nodal plane to strike at  $242^\circ$  and dip to the NW at about  $74^\circ$ . Stein and Okal used the Love wave radiation pattern to constrain the slip angle to about  $97^\circ$ , and estimated a seismic moment of  $2.5 \times 10^{25}$  dyne-cm. Such a mechanism suggests that this earthquake represents near-vertical dip-slip faulting on a plane close in strike to the fracture zone to the SE, in which case differential subsidence on the fracture zone (see Chapter 4) would be a likely source for the stress relieved in this earthquake.

The mechanism proposed by Stein and Okal [1978], however, produces a very poor fit to the observed P and SH waves. In fact, no single point source mechanism was found which produces satisfactory fits for both the P and SH waves. A point source which fits all except one (GUA) of the SH waveforms quite well (281/82/167,  $M_0 = 1.1 \times 10^{26}$  dyne-cm, with a 10 second source time function and  $h = 20.3$  km, Figure 5.11) represents nearly pure left-lateral strike-slip faulting on a plane striking slightly east of north, parallel to the fracture zone north of the epicentral region. This mechanism produces synthetic P waveforms which are much smaller than the observed waveforms, however. Conversely, most of the P waveforms (and the SH waveform at GUA) are well fit by a thrust-faulting mechanism (250/58/115) similar to, but with a shallower dip angle than the mechanism proposed by Stein and

Okal [1978], at a depth of 14.7 km. As with the SH-wave solution shown in Figure 5.11, the inversion solution using only P waves has a significantly larger moment than was estimated by Stein and Okal ( $7.5 \times 10^{25}$  dyne-cm).

In order to achieve a reasonable fit to all the observed waveforms for this event we performed the inversion with a model consisting of two point sources, inverting for the usual source parameters for each subevent plus the time delay between them. We specify the relative epicentral location of the second subevent with respect to the first subevent, in this case a distance of 10 km at an azimuth of  $220^\circ$ . This choice is based on our tectonic interpretation of the event (discussed below), but this separation is too small to be resolved by long-period waveforms and has an insignificant effect on the solution.

The first subevent is similar to the strike-slip mechanism which produces a good fit to the SH waves (265/76/149,  $M_0 = 9.2 \times 10^{25}$  dyne-cm,  $h = 20.8$  km). The source time function for this subevent appears to consist of 3 distinct pulses, with a total duration of about 14 s, but since the inversion solution based solely on SH waves failed to show a similarly complex time function (Figure 5.11), it may be caused by trade-offs with source parameters of the second subevent. This is invariably a problem when multiple source models are used. The P waveforms are dominated by the second, thrust-faulting subevent (252/45/98,  $M_0 = 4.4 \times 10^{25}$  dyne-cm,  $h = 16.6$  km), which is delayed by 1.7 seconds and has a simple source time function about 6 s in duration. Because it is completely buried in the waveforms of the first subevent, the source parameters for the second subevent have larger uncertainties than usual (Table 5.2). The total moment for this

event is  $1.4 \times 10^{26}$  dyne-cm, over five times larger than that estimated by Stein and Okal [1978]. The observed P and SH waveforms and the synthetic waveforms generated with this multiple source model are shown in Figure 5.12.

This source mechanism is most readily interpreted as follows: The earthquake initiated with left-lateral strike-slip motion on a north-trending fault, probably related to the proposed fracture zone north of the epicentral region. As the rupture propagated south, the fault changed strike to approximately northeast and the style of faulting changed from strike-slip motion to thrust faulting on the northeast-striking branch of the fault. Although the two branches of the proposed fault are subparallel to the two major fracture zone trends in the area (Figure 5.2) it is unlikely that the two fracture zones themselves can be traced to a common junction. Instead they probably converge in a zone of deformed lithosphere, within which faults of many orientations may be found.

#### August 3, 1978

The August 3, 1978 earthquake ( $m_b = 5.5$ ,  $M_s = 5.5$ ) is located west of the Ninetyeast Ridge in an area which has been quite active seismically over the last two decades (Figure 5.2) and in which Weissel et al. [1980] and Geller et al. [1983] have observed other evidence of recent large-scale deformation. Weissel et al. [1980] indicate that this event is characterized by thrust faulting with a P axis oriented slightly west of north, but they do not report the focal mechanism. Using forward modeling of P waveforms, Bergman and Solomon [1982] found a similar mechanism and estimated the depth to be about 40 km below the seafloor, making it one of the deepest known oceanic intraplate earthquakes. From a similar analysis, Wiens and Stein [1983a] also

obtained a thrust-faulting mechanism (265/57/90) and a depth of 40 km. Station coverage is reasonably good for this event and the inversion converged very quickly to a pure thrust-faulting mechanism (261/52/90, Figure 5.13), with a centroid depth of 38.3 km. The seismic moment is  $5.8 \times 10^{24}$  dyne-cm.

#### December 2, 1981

The epicenter of the December 2, 1981 earthquake ( $m_b = 5.7$ ,  $M_S = 5.5$ ) is on the east flank of the Ninetyeast Ridge, at the latitude of the Osborn Knoll (Figure 5.2). The entry in the PDE monthly summary for this event includes a source mechanism found from a semi-automated inversion of GDSN data [e.g., Dziewonski et al., 1983]:  $M_0 = 5.0 \times 10^{24}$  dyne-cm, focal mechanism = 192/49/34, with the depth held constant at 10 km. Using WWSSN data in addition to several GDSN stations, we determined a centroid depth of 22.3 km and a mechanism characterized by a larger component of thrust faulting (221/45/74, Figure 5.14). The mediocre station coverage is reflected in relatively large formal errors for the source parameters (Table 5.2). The seismic moment estimated in the body-waveform inversion ( $5.6 \times 10^{24}$  dyne-cm) is in close agreement with the previous estimate.

#### INTERNAL DEFORMATION OF THE INDIAN PLATE

The portion of the Indian plate under consideration in this chapter is quite large, has a complex and incompletely understood tectonic history, and is currently undergoing internal deformation, probably in several distinct modes. The seismological data set available to investigate this deformation consists of the 11 source mechanisms discussed above, focal mechanisms of two older earthquakes (1939 and 1955) [Stein and Okal, 1978], and focal mechanisms of several

smaller events inferred from first motion data [Bergman and Solomon, 1982].

Interpretations of the pattern of seismicity in this region are known to be subject to bias from too brief a span of observations [e.g., Sykes, 1970a]. Similarly, the focal mechanisms of a small subset of these earthquakes may be unrepresentative of the long-term average seismogenic deformation of the lithosphere in the northern Indian Ocean. In fact, we as yet have little knowledge of what the appropriate time scale for such a long-term average model might be. The repeat time of major earthquakes, typically hundreds of years, provides an estimate of this characteristic time scale for plate boundary tectonics [e.g., Muller, 1983]. There is some evidence of repeated activity at specific sites of oceanic intraplate seismicity, including sites in the Indian Ocean (Chapter 2), but the overall pattern of seismicity suggests that seismogenic deformation of the Indian plate is distributed throughout a significant volume of the lithosphere (Figure 5.2). If this is the case, the repeat time of major earthquakes at any one site may not be a good measure of the characteristic time scale for the seismogenic deformation of an extended region. In either case, it is unlikely that the seismological observations currently available can be taken with confidence as completely representative of the long-term average deformation occurring in the northern Indian Ocean.

The nature of the internal deformation at several localities in the Indian plate has also been investigated with seismic reflection techniques [Eittreim and Ewing, 1972; Weissel et al., 1980] and heat flow measurements [Geller et al., 1983]. These data are quite limited

spatially, but are far more likely than the seismological data to accurately represent features of the long-term average internal deformation of the Indian plate. Finally, the bathymetry may offer clues to the tectonic processes active in this region [e.g., Stein and Okal, 1978], but it is quite difficult to distinguish between ancient features related to the tectonic evolution of the plates in the Indian Ocean and bathymetric features produced by currently active deformational processes.

Judging from the available source mechanisms, the intraplate seismicity of the northern Indian Ocean is dominated by thrust and strike-slip faulting. Stein and Okal [1978] reported a normal faulting mechanism for the large March 22, 1955 earthquake on the eastern side of the Ninetyeast Ridge, but the analysis was based on a very small set of surface waves and first motion polarities of questionable reliability. A good example of the potential for error in a source study of this type is the June 25, 1974 earthquake discussed above. The data available for the 1974 event were far superior to those used in the source study of the 1955 earthquake. With the exception of earthquakes representing the release of bending stresses seaward of trenches, normal faulting has been observed for no other oceanic intraplate earthquake in lithosphere older than about 35 m.y. (Chapter 9). Furthermore, there is no satisfactory explanation for the occurrence of normal faulting east of the Ninetyeast Ridge, while the observed faulting styles of the other earthquakes in the region can all be accommodated within the framework of a general model of the deformation of the Indian plate first suggested by Stein and Okal [1978]. The additional earthquake source mechanisms presented here are



consistent with the basic elements of this model. Unless and until an unambiguous example of normal faulting is found in this area, we presume that the mechanism of the 1955 earthquake is essentially unconstrained.

The basic element of the model for the deformation of the Indian plate suggested by Stein and Okal [1978] is the idea that the northern part of the Ninetyeast Ridge may be the site of a certain amount of decoupling between the Indian and Australian halves of the plate, prompted by the great change in plate boundary type which occurs at this longitude. East of the Ninetyeast Ridge, the plate encounters little resistance as it is subducted at the Sunda Arc. To the west, however, the northward movement of the Indian half of the plate is impeded by the continental collision with Asia.

The expected result of this system of forces on the northern plate boundary is left-lateral shear stress (on a N-S plane) in the vicinity of the Ninetyeast Ridge, as represented by the focal mechanism of the May 25, 1964 earthquake (Figure 5.2) and to a lesser extent, the mechanism proposed by Stein and Okal [1978] for the March 21, 1939 earthquake. First motion polarities for several smaller earthquakes located near the site of the 1939 event are also consistent with left-lateral strike-slip motion on a N-S plane [Bergman and Solomon, 1982]. The mechanism of the April 7, 1973 earthquake indicates that this left-lateral strike-slip motion on the Ninetyeast Ridge presently extends to the northern termination of the ridge at the western end of the Sunda Arc (Figure 5.2).

The southern extent of strike-slip faulting on the Ninetyeast Ridge is less clear. The December 2, 1981 earthquake at about 16°S is

the only large earthquake on the Ninetyeast Ridge south of the May 1964 event and it is characterized by thrust faulting with a P axis oriented NW-SE (Figure 5.2). At 26°S and a short distance west of the Ninetyeast Ridge, however, the major component of the complex June 25, 1974 earthquake is left-lateral strike-slip faulting on a N-S plane (Figure 5.2), presumably the fracture zone inferred at this site by Sclater and Fisher [1974]. If this event is responding to the same stress system which produces strike-slip faulting on the northern part of the Ninetyeast Ridge, we must expect that the southern half of the ridge occasionally experiences strike-slip faulting as well.

East of the Ninetyeast Ridge, the level of seismicity appears to decline, but the two earthquakes in this region with known focal mechanisms (June 26, 1971 and October 31, 1965) are both characterized by left-lateral strike-slip motion on nodal planes oriented within about 15° of N-S (Figure 5.2). The trend of the bathymetry in the epicentral region of the 1971 event parallels the nodal plane striking N13°E and this nodal plane probably corresponds to the fault plane, but there is little basis for selecting one of the nodal planes of the 1965 earthquake as the fault plane. There appears to be a tendency for the intraplate epicenters east of the Ninetyeast Ridge to be associated with bathymetric ridges. If this correlation indeed exists, it suggests that the ridges are relatively weak portions of the lithosphere. If the dominant type of faulting in this region is strike-slip, however, it is unlikely that intraplate deformation has produced the bathymetric relief.

The source mechanisms of earthquakes west of the Ninetyeast Ridge indicate that the stress field is dominated by N-S compression. Three

of the four earthquakes north of about  $5^{\circ}\text{S}$  are characterized by thrust faulting with the P axis oriented essentially N-S (Figure 5.2). First motion polarities indicate a similar thrust-faulting mechanism for a fourth event (April 12, 1981) located a short distance northeast of the August 30, 1973 earthquake [Bergman and Solomon, 1982].

The October 1970 earthquake has a pure left-lateral strike-slip mechanism on a plane striking  $\text{N}25^{\circ}\text{E}$ , fairly close to the trend of the fracture zone which passes through the epicentral area (Figure 5.2). For this reason and the obvious similarity to the style of deformation on the Ninetyeast Ridge, we take this nodal plane to correspond to the fault plane. The P axis of this event is oriented at  $\text{N}20^{\circ}\text{W}$ .

A better estimate of the true direction of maximum compressive stress, however, can be made when the fault plane is known. The direction of greatest compression is obtained by rotating the P axis about  $15^{\circ}$  toward the slip vector [Raleigh et al., 1972]. The deviation of the orientation of maximum principal stress from the P axis, which is at an angle of  $45^{\circ}$  to both nodal planes, is caused by the internal friction of rocks; the preferred orientation of the fault maximizes the resolved shear stress but minimizes the resolved normal stress on the fault plane, thus reducing frictional resistance to faulting. This argument assumes the existence of potential fault planes with the appropriate orientation; otherwise the true direction of maximum principal stress may vary considerably [McKenzie, 1969]. In the case of the October 1970 event, we estimate an orientation of  $\text{N}5^{\circ}\text{W}$  for the maximum compressive stress, essentially parallel to the direction inferred from the thrust-faulting mechanisms of the other events west of the Ninetyeast Ridge.

There is very little seismicity west of the Ninetyeast Ridge between the latitudes  $4^{\circ}\text{S}$  and  $24^{\circ}\text{S}$ , but both earthquakes (September 1968 and June 1975) in the southwestern part of the study area have at least a component of thrust faulting (Figure 5.2). The second, thrust-faulting subevent of the June 25, 1974 earthquake is more likely to have resulted from a change in direction of a fault experiencing predominantly strike-slip motion, as discussed above. The September 1968 earthquake is quite small and one of the few intraplate events known to have occurred in the crust (Chapter 9). Both events seem to be associated with areas of the lithosphere which have been disrupted by a major change in the spreading direction. These earthquakes are unlikely to represent a continuation of the distinctive pattern of seismicity and source mechanisms observed in the Bay of Bengal and adjacent to the northern Ninetyeast Ridge.

The obvious source of a large N-S compressive stress west of the Ninetyeast Ridge is the continental collision between India and Asia. Weissel et al. [1980] and Geller et al. [1983] have suggested a connection between the late Miocene onset of the Himalayan orogeny and the principal stress directions of intraplate earthquakes, unusually high heat flow, and deformational structures in the crust and sediments of the northern Indian Ocean (Figure 5.15).

Observations of deformational structures in the sediments of the Bengal Fan were reported by Curray and Moore [1971], Eittreim and Ewing [1972], and Moore et al. [1974]. Weissel et al. [1980] determined that clear evidence for such features is found only in the southern portions of the Bengal and Nicobar Fans. Furthermore, they found that the deformation of the acoustic basement (oceanic crust?) and overlying

sediment layers could be resolved into two dominant wavelengths, the more interesting of the two being an undulatory pattern in the acoustic basement with wavelengths of 100-300 km and relief of up to 3 km. Although this pattern appears analogous to the buckling of an elastic plate under horizontal compression, it is most unlikely that lithospheric buckling is the source of the long-wavelength deformational pattern in the northern Indian Ocean because such a model would require stress implausibly high stress levels (over 20 kbar) and an elastic plate thickness (12 km) less than half the value estimated from the age of the lithosphere [Weissel et al., 1980].

The earthquake source mechanisms presented here are relevant both to the extent and the nature of the deformation observed by Weissel et al. [1982]. The intraplate earthquakes in this region are unusually deep (see Chapter 9), suggesting that the deformation involves the entire elastic core of the lithosphere. The centroid depths of the three thrust-faulting events west of the Ninetyeast Ridge are 32 km (November 1972), 24 km (August 1973), and 38 km (August 1978) below the seafloor (Table 5.2). The October 1970 strike-slip event is 26 km deep. The focal mechanisms of these earthquakes indicate that the deformational mechanism involves compressional failure at all depths. This observation tends to rule out flexural or thermoelastic stresses as possible causes of the deformation, since both would be expected to produce extensional deformation over some depth interval in the lithosphere (see Chapters 4 and 8). Finally, the mechanism presented here for the November 24, 1972 earthquake increases the latitudinal extent of the deformation to over 1000 km (from just south of the equator to at least 11°N).

The high heat flow values reported by Weissel et al. [1980] in the region where a variety of deformational structures are observed in the crust and sediments have been confirmed with more recent measurements Geller et al. [1983]. Based on an extensive analysis of nonlinear temperature-depth profiles observed during these measurements, Geller et al. conclude that the excess heat flow results from heat released at depths of up to 35 km. The centroid depths of the earthquakes west of the Ninetyeast Ridge are in good agreement with this depth range, suggesting that frictional heating on faults may be the source of the high heat flow values observed in this area.

#### STATE OF STRESS IN THE INDIAN PLATE

The relatively high density of intraplate earthquakes with known focal mechanisms in the northern Indian Ocean provides an excellent opportunity to observe large-scale features in the intraplate stress field. It also allows us to consider the degree to which any single focal mechanism accurately reflects the regional stress pattern inferred from a number of earthquake mechanisms.

Supplementing the few oceanic intraplate earthquake mechanisms then available with data from India and Australia, Fitch [1972] and Fitch et al. [1973] proposed that the various indicators of stress delineated a single long-wavelength feature of the intraplate stress field: The orientation of the greatest horizontal compressive stress is oriented roughly N-S in India, swings to NW-SE in the northern Indian Ocean and is nearly E-W in Australia. With a few more observations, Bergman and Solomon [1980] also inferred a consistent NW-SE trend for the orientation of greatest horizontal compression in the northern Indian Ocean. They also noted that the Ninetyeast Ridge,

a major bathymetric feature and site of intraplate deformation, appears to have little effect on the inferred stress field, lending confidence to the use of focal mechanisms of intraplate earthquakes to infer the geometry of the stress field.

With the source studies reported in this chapter, we now have available a larger (and more accurate) set of focal mechanisms with which to investigate the regional stress field in the northern Indian Ocean. The principal stress axes of these events are plotted in Figure 5.15. For thrust-faulting events, the orientation of the horizontal projection of the P axis has been plotted. In the case of the five strike-slip faulting events for which fault planes can be specified with some confidence (May 25, 1964, October 10, 1970, June 26, 1971 April 7, 1973, and the first subevent of the June 25, 1974 earthquake), we have plotted the orientation of the the maximum horizontal compressive stress estimated in the manner suggested by Raleigh et al. [1972]: the direction of maximum principal stress is assumed to be oriented along the direction obtained by rotating the slip vector by an angle of  $30^\circ$  toward the P axis. The horizontal projection of the P axis of the October 31, 1965 earthquake has been plotted, since we found no basis for selecting one of the nodal planes as the fault plane for that event.

The stress field orientations shown in Figure 5.15 confirm and refine the results of the previous studies mentioned above. The data available to Bergman and Solomon [1980], for example, supported a general NW-SE trend to the stress field, but no curvature was observable. In the present study we have modified several of the previously reported mechanisms, obtained several new mechanisms, and

used an improved technique to infer the orientation of principal stresses from focal mechanisms. Figure 5.15 clearly indicates a curvature in the regional stress field, with the direction of maximum horizontal stress changing from about N10°W in the Bay of Bengal to approximately N45°W to the east of the Ninetyeast Ridge. The Ninetyeast Ridge appears to have little or no influence on the inferred direction of the stress field, although there is a gap in the data in the immediate vicinity of the northern part of the ridge. This image of the intraplate stress field is completely consistent with the original proposal by Fitch [1972] and also with numerical models of the intraplate stress field in the Indian plate based on assumed plate boundary forces [Richardson et al., 1979].

In the northern Indian Ocean, intraplate earthquakes appear to be quite reliable indicators of the intraplate stress field, even though the region is experiencing significant internal deformation in at least two distinct modes. This conclusion should not be taken to mean, however, that all oceanic intraplate events are equally accurate indicators of the long-wavelength intraplate stress field. Many such events may be influenced primarily by locally-produced stresses which have no relation to the plate-wide stress field. The reliability of the focal mechanisms in the northern Indian Ocean may be plausibly attributed to the presence of unusually large and homogeneous deviatoric stresses throughout a large volume of lithosphere, as the result of the peculiar boundary conditions of the Indian plate. Because the typical stress level in the long-wavelength part of the intraplate stress field in other oceanic regions is almost certainly lower, intraplate earthquakes elsewhere may be somewhat less reliable indicators of the plate-wide stress field.



Table 5.1. Epicentral data\* for earthquakes studied

Date	Origin time h m s	Lat. °N	Long. °E	$m_b$	$M_S$	Age** (m.y.)
May 25, 1964	19 44 5.9	-9.08	88.89	5.7	6.0	56
October 31, 1965	17 24 9.5	-14.22	95.27	5.3	5.4	64
September 14, 1968	1 25 18.9	-24.45	80.41	5.4		36
October 10, 1970	8 53 4.5	-3.56	86.19	5.8	6.3	64-80
June 26, 1971	19 27 11	-5.18	96.90	5.9	6.4	58
November 24, 1972	13 19 14.3	11.67	85.34	5.2	5.2	95
April 7, 1973	3 0 59.6	7.00	91.32	5.8	6.6	75
August 30, 1973	19 50 3.9	7.15	84.33	5.8	5.2	95
June 25, 1974	17 22 17.9	-26.02	84.30	6.1	6.6	36-50
August 3, 1978	1 10 26	-0.93	84.24	5.5	5.5	82
December 2, 1981	19 1 53.9	-15.76	88.39	5.7	5.5	60

\* Sources of data: ISC (1964-1978) and NEIS (1981), except for  $M_S$  magnitudes for May 25, 1964 [Stein and Okal, 1978] and October 31, 1965 [Wiens and Stein, 1983a].

\*\* Age of lithosphere estimated from magnetic anomaly identifications of Sclater and Fisher [1974], Sclater et al. [1976], and Liu et al. [1983], and magnetic chronology of LaBrecque et al. [1977], or from the isochrons determined by Sclater et al. [1980, 1981a].

Table 5.2 Source mechanisms obtained from body-wave inversion<sup>a</sup>

Date	Moment <sup>b</sup>	$t_s^c$	Depth <sup>d</sup>	Strike	Dip	Slip
May 25, 1964	12. $\pm$ 3.	6.6 $\pm$ 1.1	14.8 $\pm$ 0.1	179.6° $\pm$ 0.9	84.7° $\pm$ 0.6	0.7° $\pm$ 0.8
October 31, 1965	5.3 $\pm$ 0.9	4.0 $\pm$ 1.0	19.7 $\pm$ 0.1	165.7 $\pm$ 1.3	67.9 $\pm$ 0.9	10.7 $\pm$ 1.2
September 14, 1968	1.1 $\pm$ 0.2	2.3 $\pm$ 0.8	1.7 $\pm$ 0.1	287.6 $\pm$ 3.6	26.9 $\pm$ 2.1	110.3 $\pm$ 3.6
October 10, 1970	52. $\pm$ 6.	9.0 $\pm$ 1.5	25.8 $\pm$ 0.1	25.1 $\pm$ 1.1	86.4 $\pm$ 0.6	7.0 $\pm$ 0.6
June 26, 1971	49. $\pm$ 7.	4.8 $\pm$ 1.2	29.9 $\pm$ 0.1	13.3 $\pm$ 1.2	62.4 $\pm$ 0.9	22.0 $\pm$ 1.1
November 24, 1972	3.0 $\pm$ 0.5	2.0 $\pm$ 1.0	31.8 $\pm$ 0.1	252.5 $\pm$ 1.4	49.6 $\pm$ 0.5	80.3 $\pm$ 1.2
April 7, 1973	96. $\pm$ 3.	12.0 $\pm$ 2.0	14.4 $\pm$ 0.1	202.6 $\pm$ 0.6	82.7 $\pm$ 0.6	347.7 $\pm$ 0.6
August 30, 1973	4.7 $\pm$ 0.9	2.0 $\pm$ 1.0	23.6 $\pm$ 0.2	284.0 $\pm$ 3.0	50.4 $\pm$ 0.7	115.3 $\pm$ 1.8
June 25, 1974 <sup>e</sup>	92. $\pm$ 7. 44. $\pm$ 3.	14.0 $\pm$ 2.0 6.0 $\pm$ 2.0	20.8 $\pm$ 0.1 16.6 $\pm$ 0.4	265.1 $\pm$ 1.5 251.8 $\pm$ 3.9	76.3 $\pm$ 0.9 45.0 $\pm$ 0.8	149.2 $\pm$ 1.8 97.8 $\pm$ 2.0
August 3, 1978	5.8 $\pm$ 0.8	2.7 $\pm$ 0.9	38.3 $\pm$ 0.2	260.9 $\pm$ 0.8	52.4 $\pm$ 0.3	89.6 $\pm$ 0.8
December 2, 1981	5.6 $\pm$ 0.9	3.0 $\pm$ 1.0	22.3 $\pm$ 0.3	220.7 $\pm$ 3.2	44.6 $\pm$ 0.7	73.7 $\pm$ 1.8

Table 5.2 (continued)

- a) The range indicated for each parameter is one standard deviation (formal error). The range of  $t_s$  is one half the width of the source time function element used in the inversion.
- b)  $\times 10^{24}$  dyne-cm ( $10^{17}$  N-m).
- c) Total duration of the source time function, sec.
- d) Relative to the top of the crust (or sediment layer, if used), km.
- e) This event was modeled with two point sources, the second delayed by 1.7 s.

## FIGURE CAPTIONS

Figure 5.1. Major phases of the tectonic evolution of the plates in the Indian Ocean, reproduced from Figure 18 of Curry et al. [1982].

Figure 5.2. Seismicity and bathymetry of the study area in the northern Indian Ocean. Bathymetric contours (3000, 4000 and 5000 m) are from Laughton [1975] and Fisher et al. [1982]. Several fracture zones west of the Ninetyeast Ridge identified by Sclater and Fisher [1974] are indicated by dashed lines. Open circles indicate epicenters from Appendix A (1906-1963), with larger symbols for events with  $M$  or  $M_s \geq 6.0$ . Solid circles indicate ISC epicenters of earthquakes for the years 1964-1979 which were detected at 10 or more stations and have focal depths of 100 km or less. Epicenters are also shown of more recent oceanic intraplate earthquakes from Appendix B, with epicentral data from the ISC (January 1980 - August 1981) and the NEIS (September 1981 - December 1983). For oceanic intraplate events, larger symbols indicate  $m_b \geq 5.4$ . Focal mechanisms were determined by body-waveform inversion, as described in the text and summarized in Table 5.2. Waveforms from the June 25, 1974 event were modeled with a source model consisting of two point sources, as described in the text.

Figure 5.3. Comparison of observed (solid lines) long-period P and SH waves from the May 25, 1964 earthquake with synthetic waveforms (dashed lines) generated for the best-fitting point source mechanism found in the body-waveform inversion (Table 5.2). P and SH radiation patterns are shown on the lower focal hemisphere (equal area projection). All amplitudes are normalized to an instrument magnification of 3000; the amplitude scales correspond to the

waveforms that would be observed on an original seismogram from such an instrument. The two vertical lines delimit the portion of each time series used in the inversion. Symbols for both types of waves are: open circle - dilatation, closed circle - compression, cross - emergent arrival. For SH waves, compression corresponds to positive motion as defined by Aki and Richards [1980]. First motions read from long-period seismograms but not used in the inversion are also plotted.

Figure 5.4. Comparison of observed P and SH waves from the October 31, 1965 earthquake with synthetic waveforms generated for the best-fitting point source mechanism found in the body-waveform inversion (Table 5.2). See Figure 5.3 for further explanation.

Figure 5.5. Comparison of observed P and SH waves from the September 14, 1968 earthquake with synthetic waveforms generated for the best-fitting point source mechanism found in the body-waveform inversion (Table 5.2). See Figure 5.3 for further explanation.

Figure 5.6. Comparison of observed P and SH waves from the October 10, 1970 earthquake with synthetic waveforms generated for the best-fitting point source mechanism found in the body-waveform inversion (Table 5.2). See Figure 5.3 for further explanation.

Figure 5.7. Comparison of observed P and SH waves from the June 26, 1971 earthquake with synthetic waveforms generated for the best-fitting point source mechanism found in the body-waveform inversion (Table 5.2). See Figure 5.3 for further explanation.

Figure 5.8. Comparison of observed P and SH waves from the November 24, 1972 earthquake with synthetic waveforms generated for the best-fitting point source mechanism found in the body-waveform inversion (Table 5.2). See Figure 5.3 for further explanation.

- Figure 5.9. Comparison of observed P and SH waves from the April 7, 1973 earthquake with synthetic waveforms generated for the best-fitting point source mechanism found in the body-waveform inversion (Table 5.2). See Figure 5.3 for further explanation.
- Figure 5.10. Comparison of observed P and SH waves from the August 30, 1973 earthquake with synthetic waveforms generated for the best-fitting point source mechanism found in the body-waveform inversion (Table 5.2). See Figure 5.3 for further explanation.
- Figure 5.11. Comparison of observed P and SH waves from the June 25, 1974 earthquake with synthetic waveforms generated for the best-fitting point source mechanism found when SH waves only are used in the body-waveform inversion. See Figure 5.3 for further explanation.
- Figure 5.12. Comparison of observed P and SH waves from the June 25, 1974 earthquake with synthetic waveforms generated for a source model consisting of two point sources, the parameters of which were found in the body-waveform inversion (Table 5.2). The dotted nodal lines in the focal mechanisms and the source time function represent the second subevent. See text and Figure 5.3 for further explanation.
- Figure 5.13. Comparison of observed P and SH waves from the August 3, 1978 earthquake with synthetic waveforms generated for the best-fitting point source mechanism found in the body-waveform inversion (Table 5.2). See Figure 5.3 for further explanation.
- Figure 5.14. Comparison of observed P and SH waves from the December 2, 1981 earthquake with synthetic waveforms generated for the best-fitting point source mechanism found in the body-waveform inversion (Table 5.2). See Figure 5.3 for further explanation.

Figure 5.15. Map of the orientation of maximum horizontal compressive stress in the northern Indian Ocean, inferred from the focal mechanisms of earthquakes studied in this chapter. See the text for a description of the method.

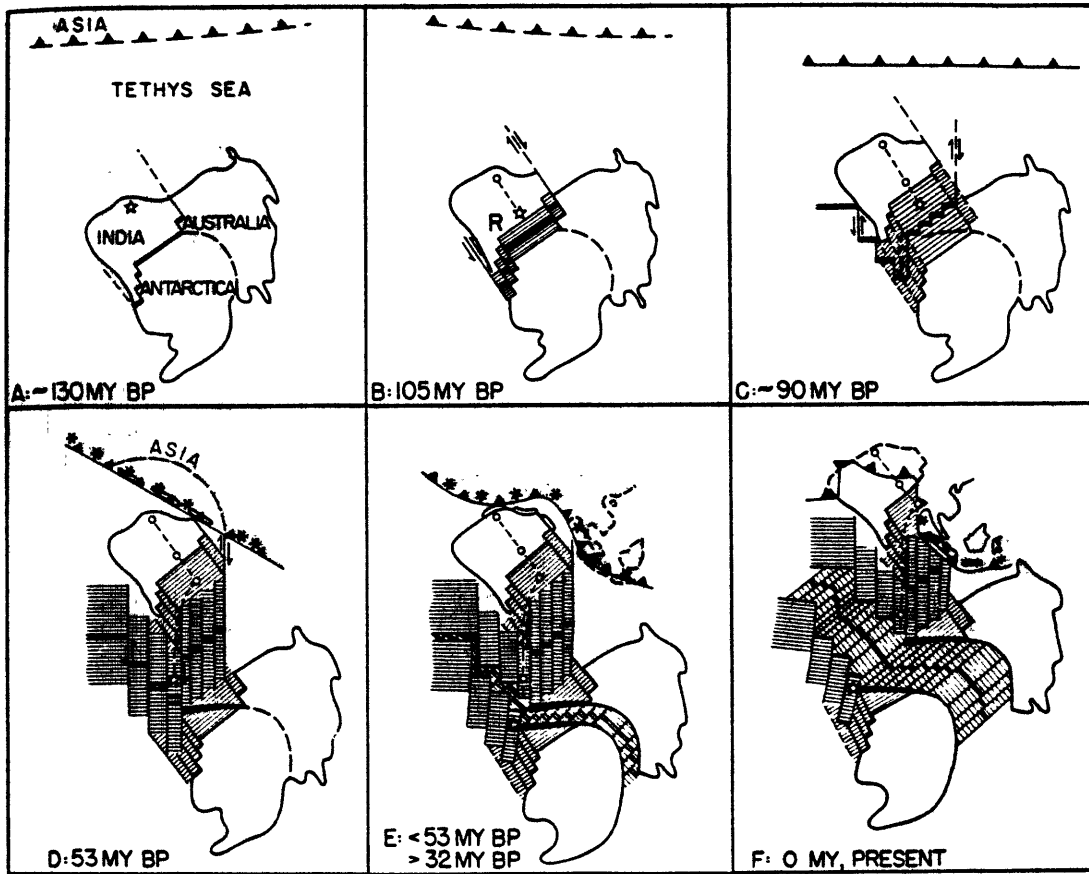


Figure 5.1



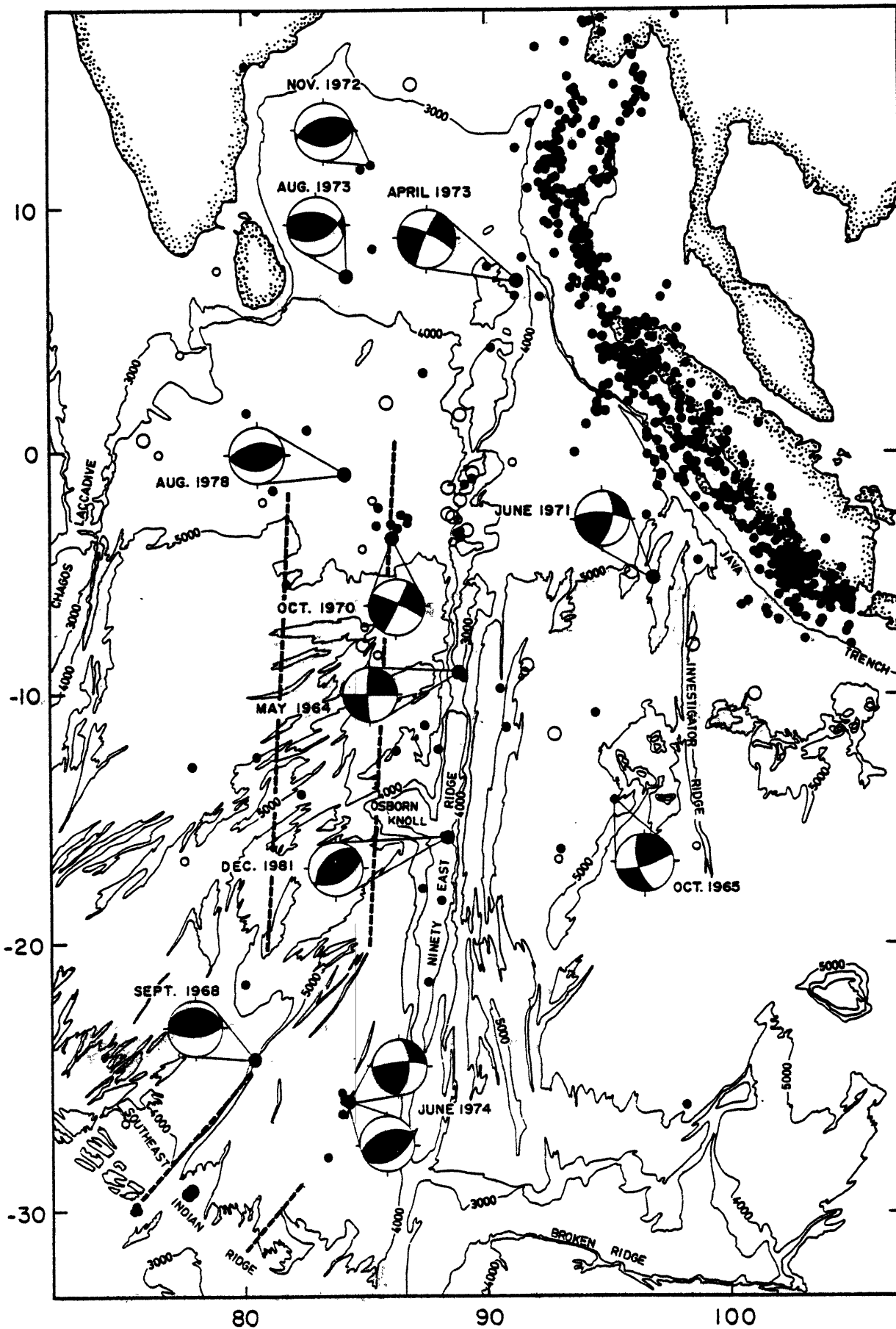


Figure 5.2

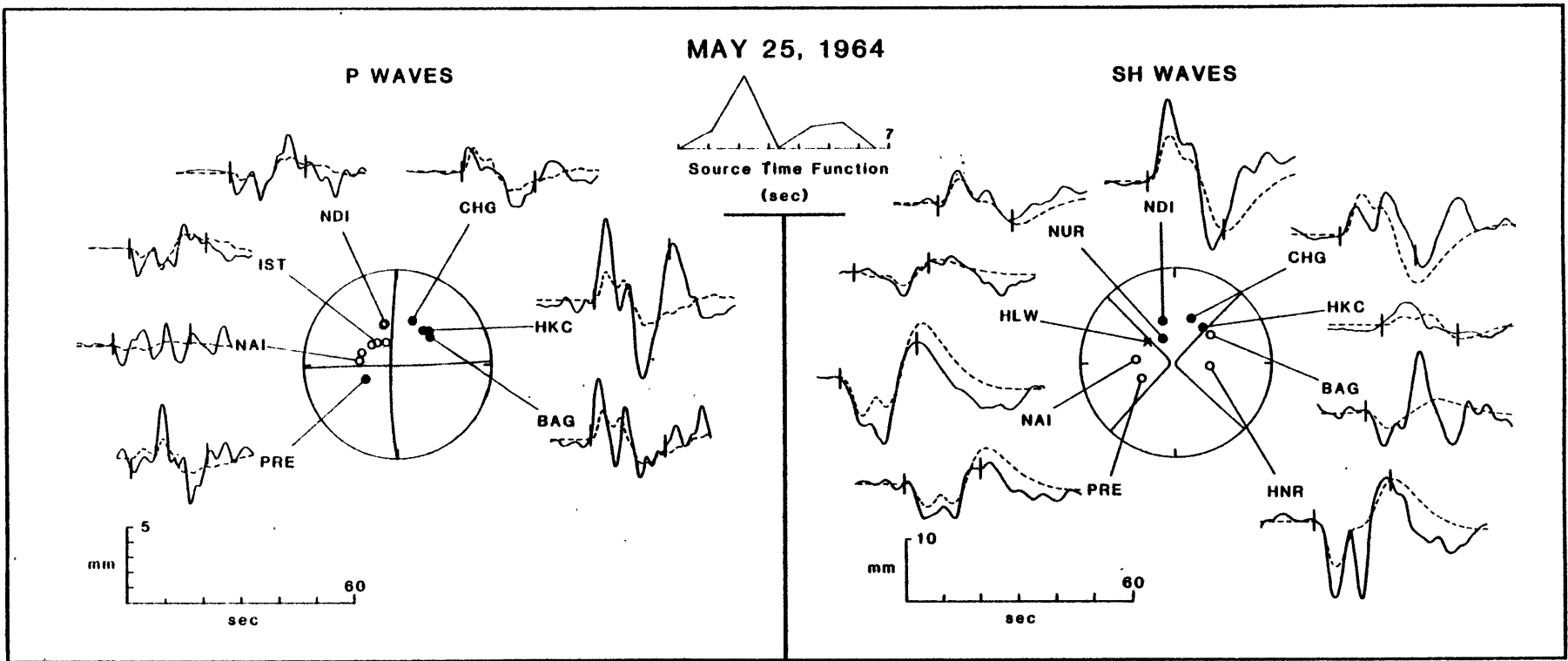


Figure 5.3

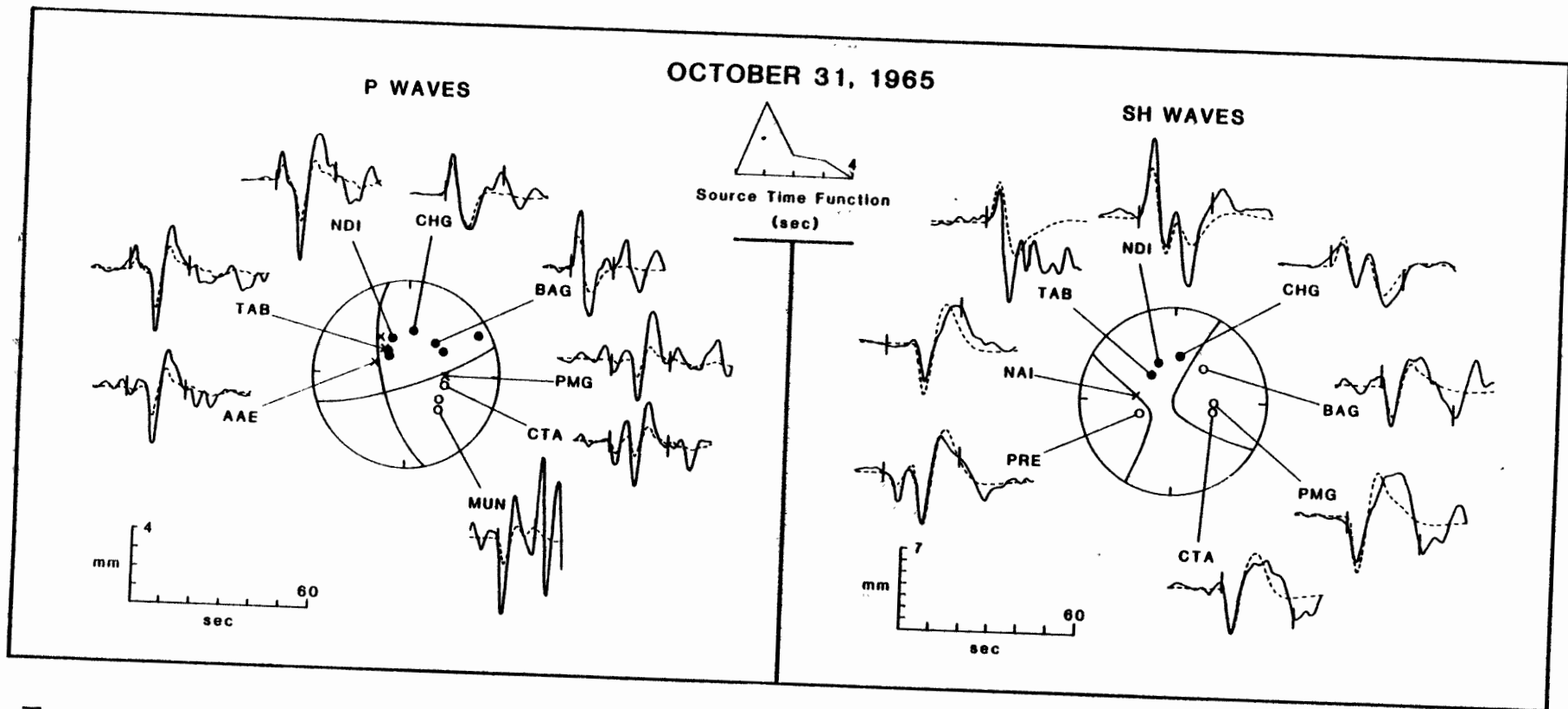


Figure 5.4

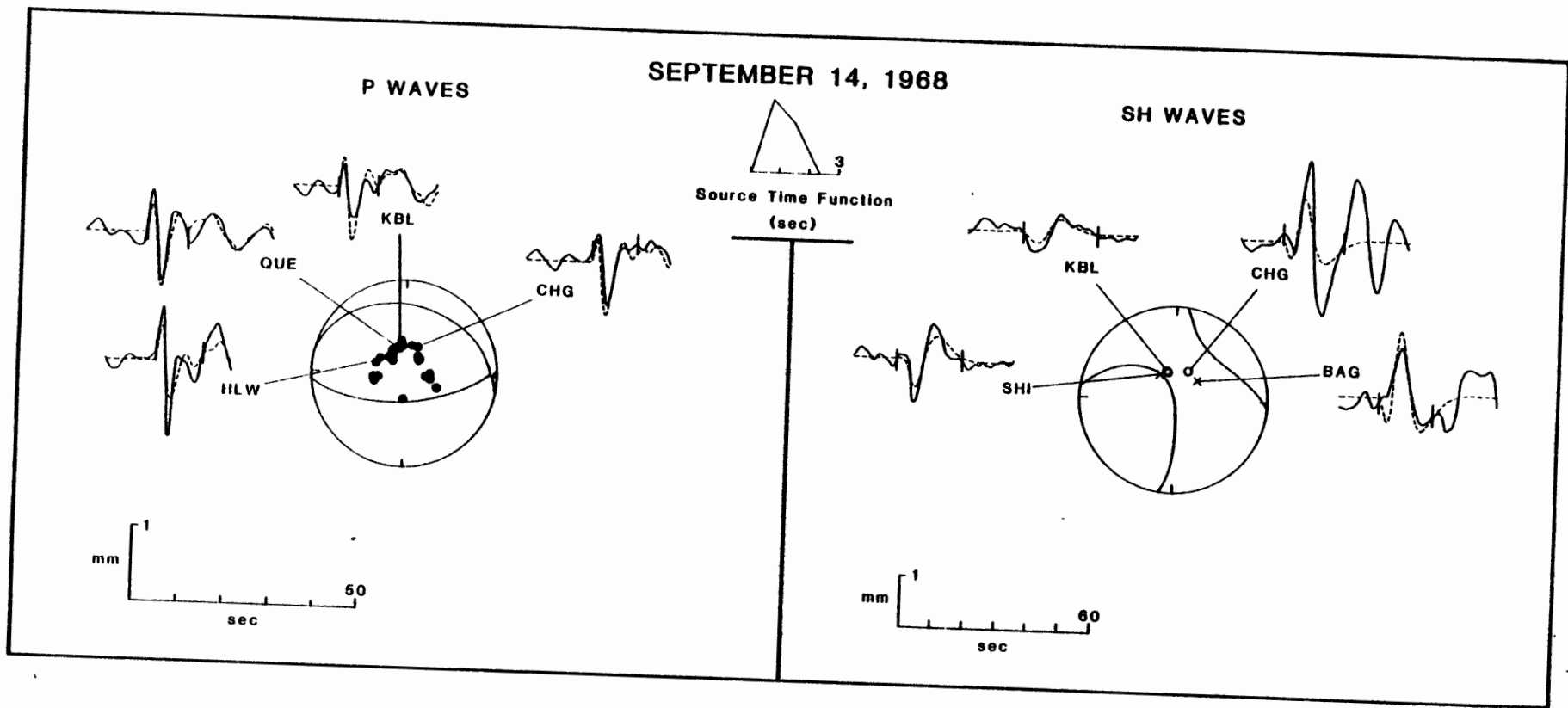


Figure 5.5

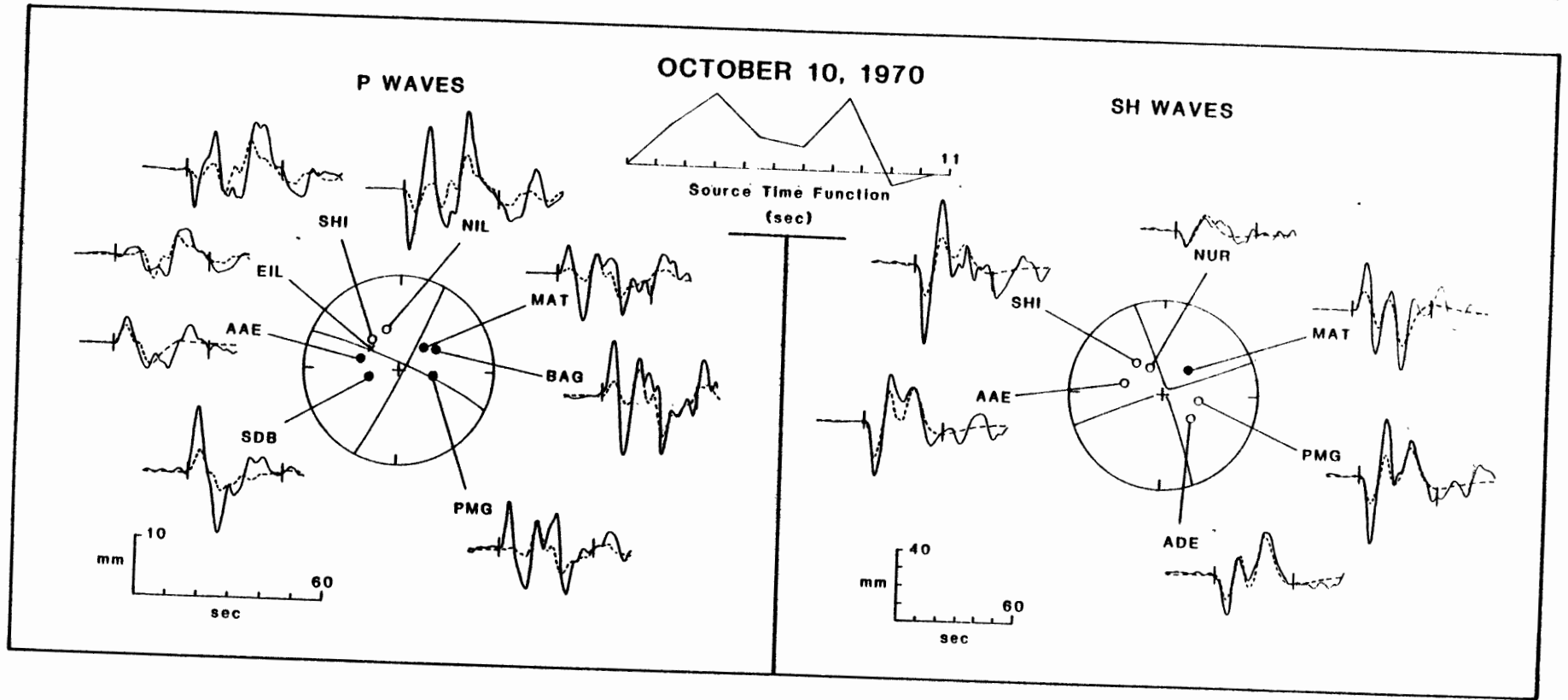


Figure 5.6

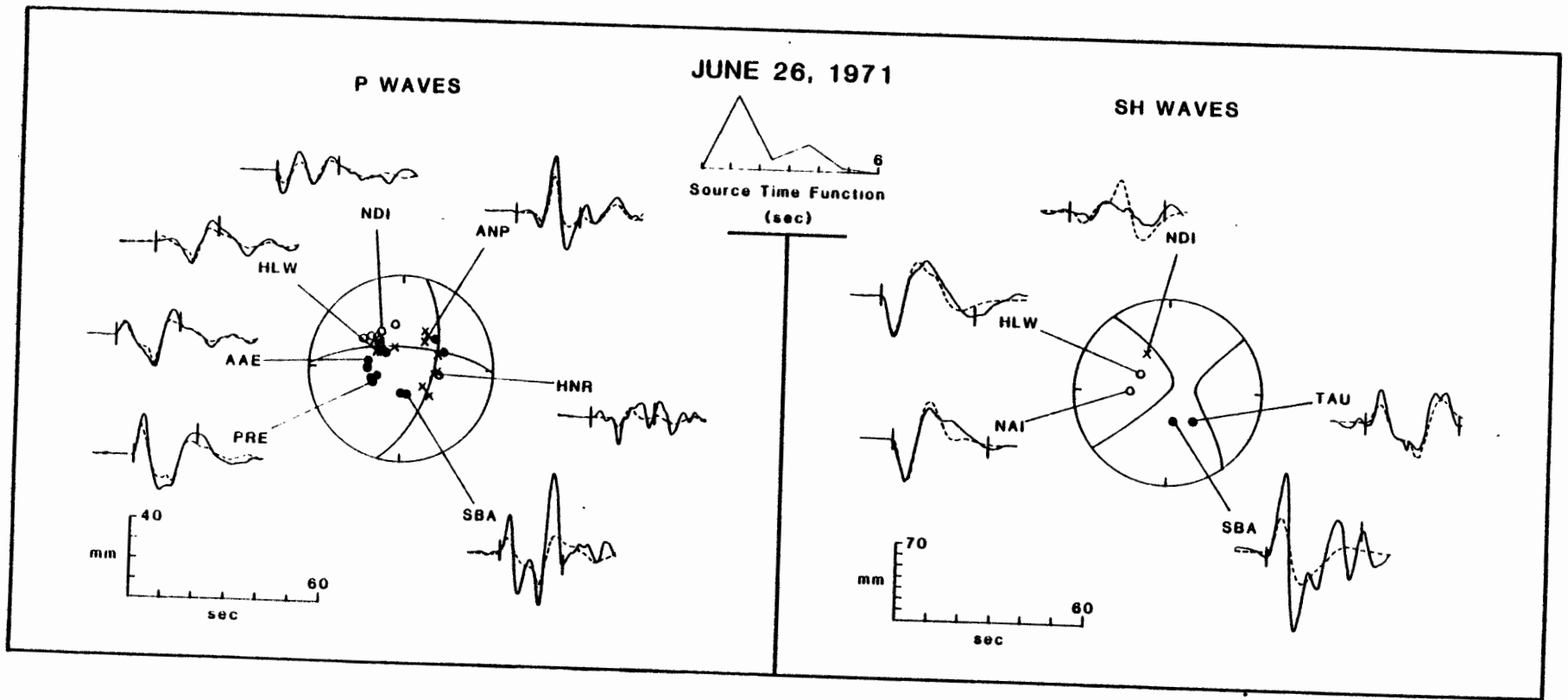


Figure 5.7

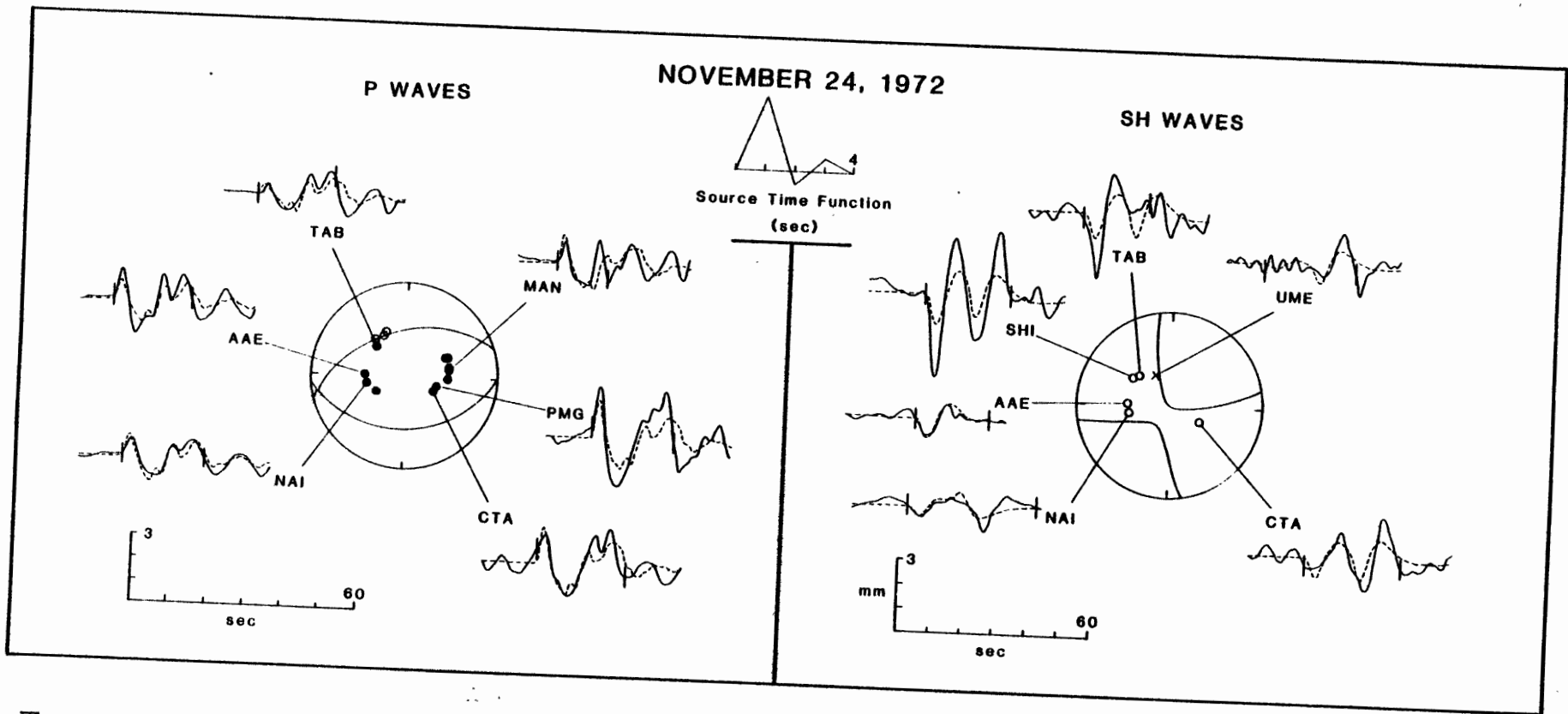


Figure 5.8

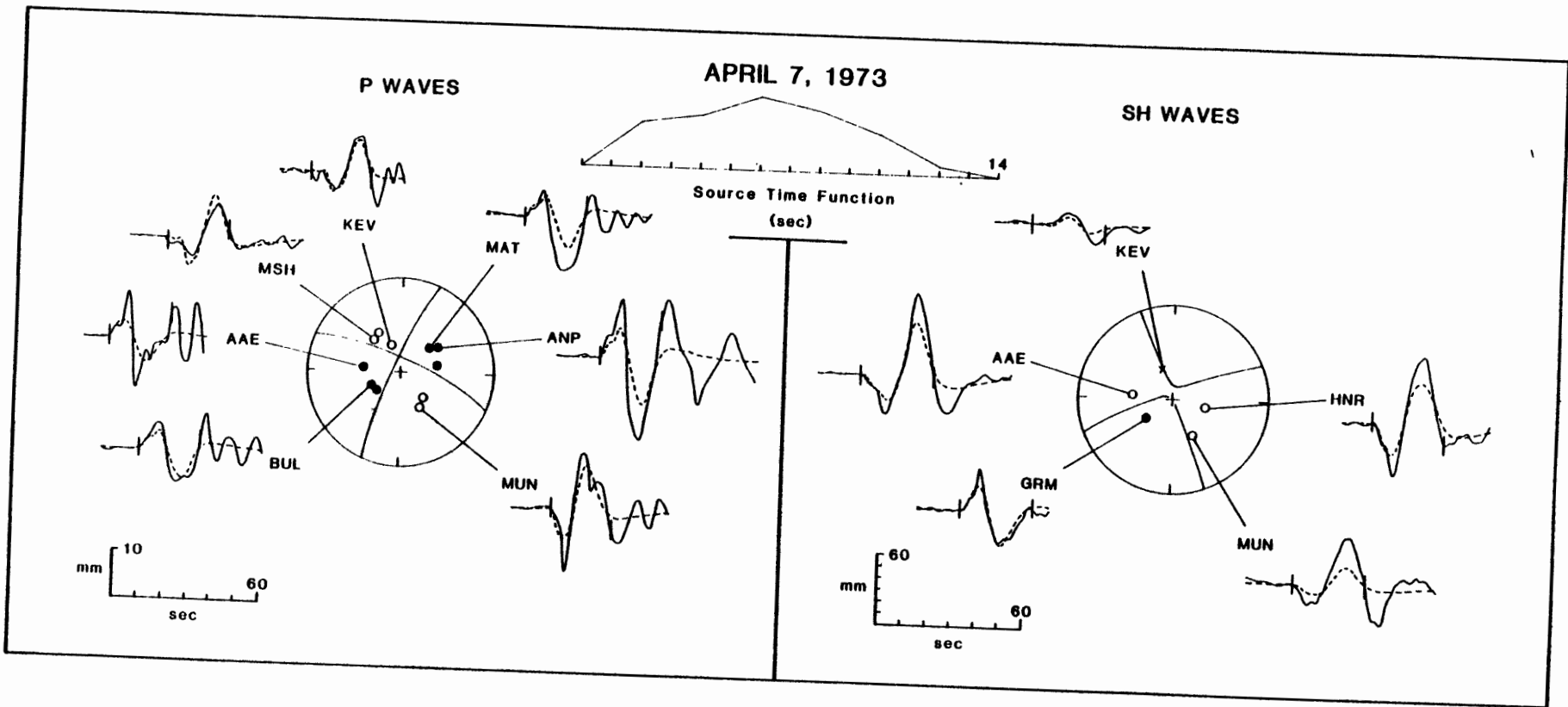


Figure 5.9



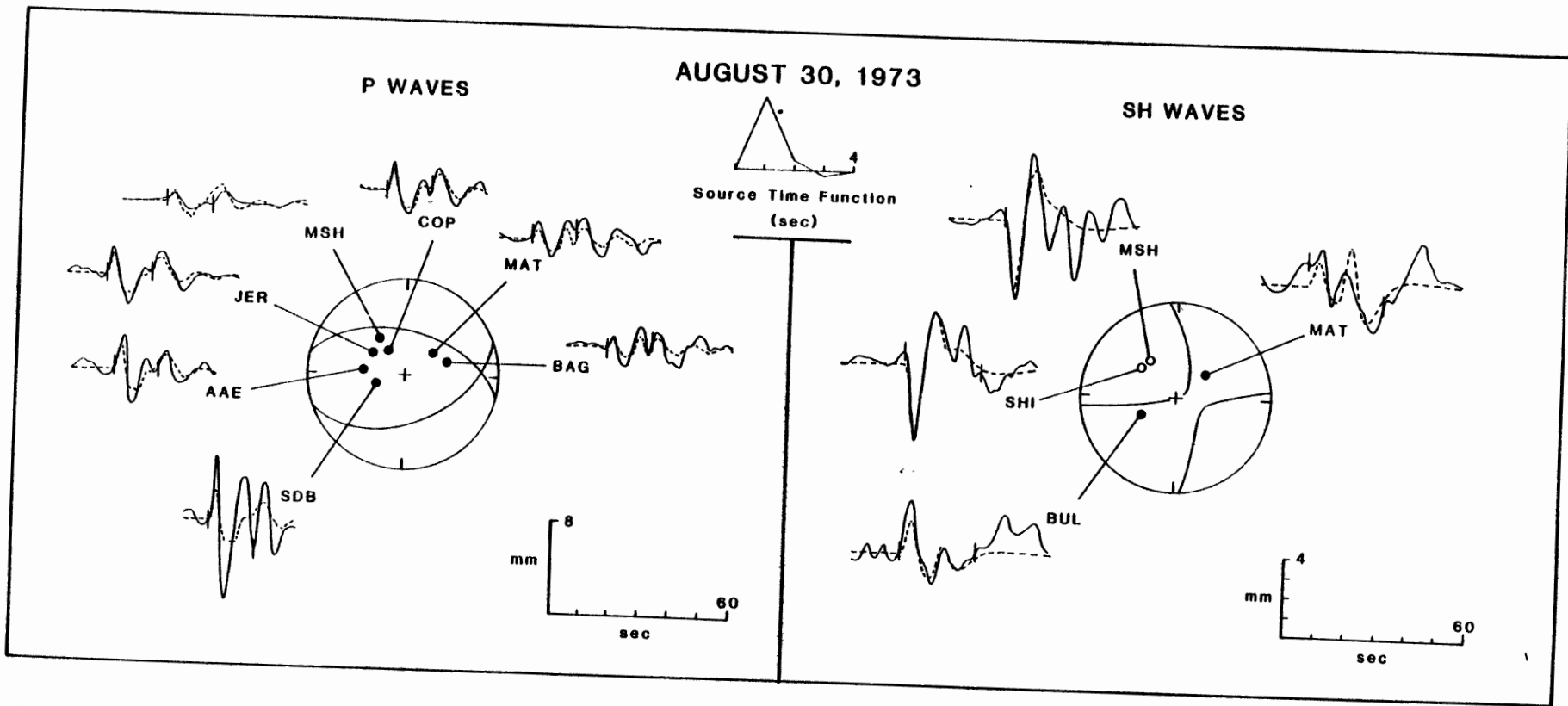


Figure 5.10

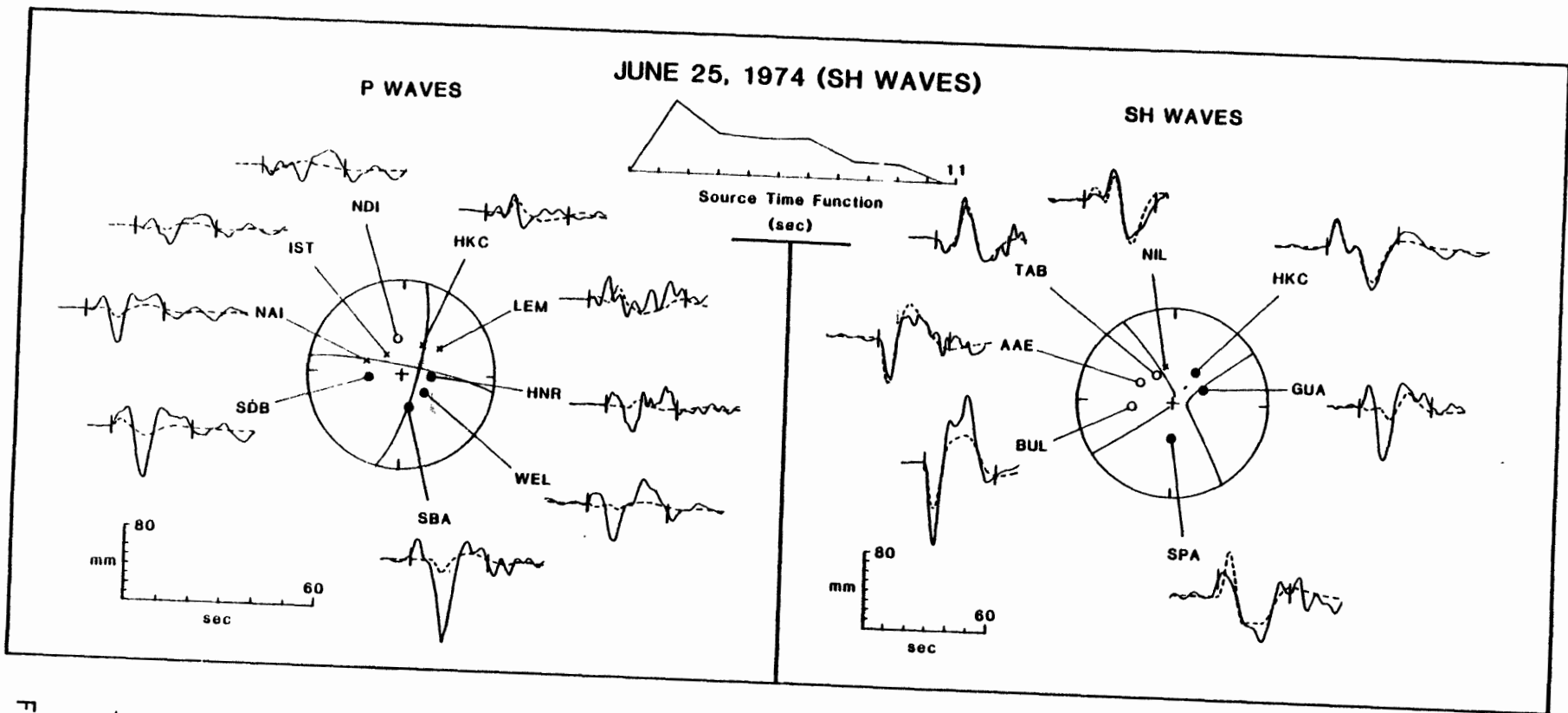


Figure 5.11

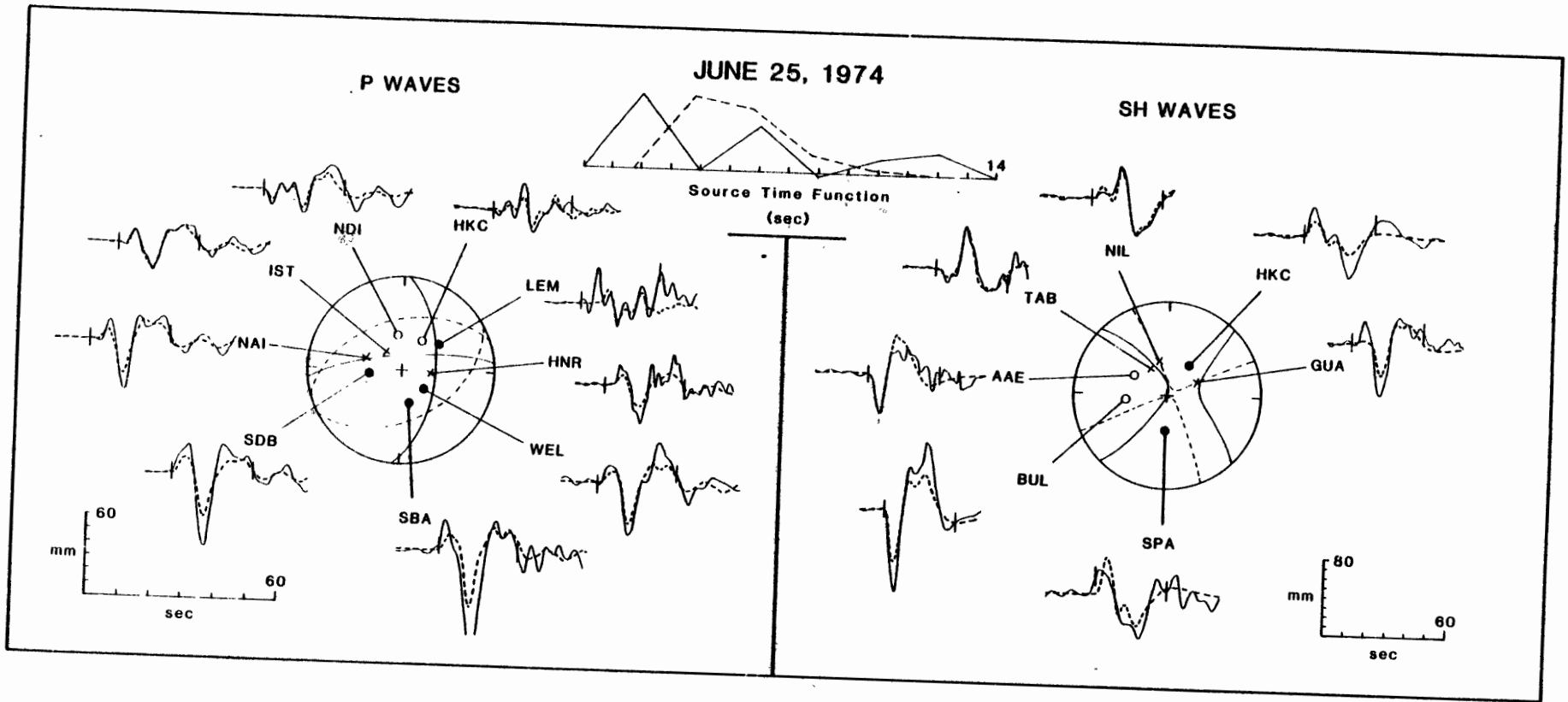


Figure 5.12

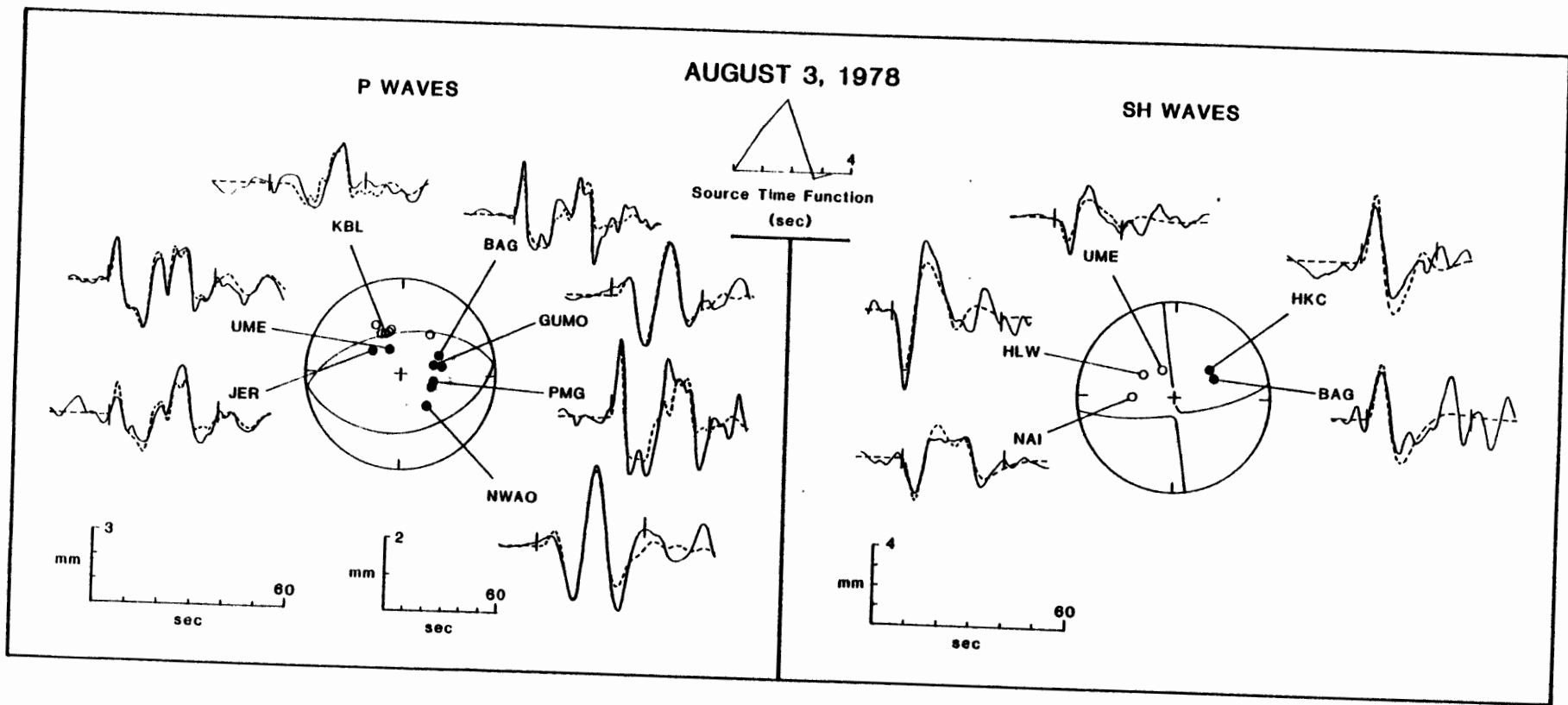


Figure 5.13

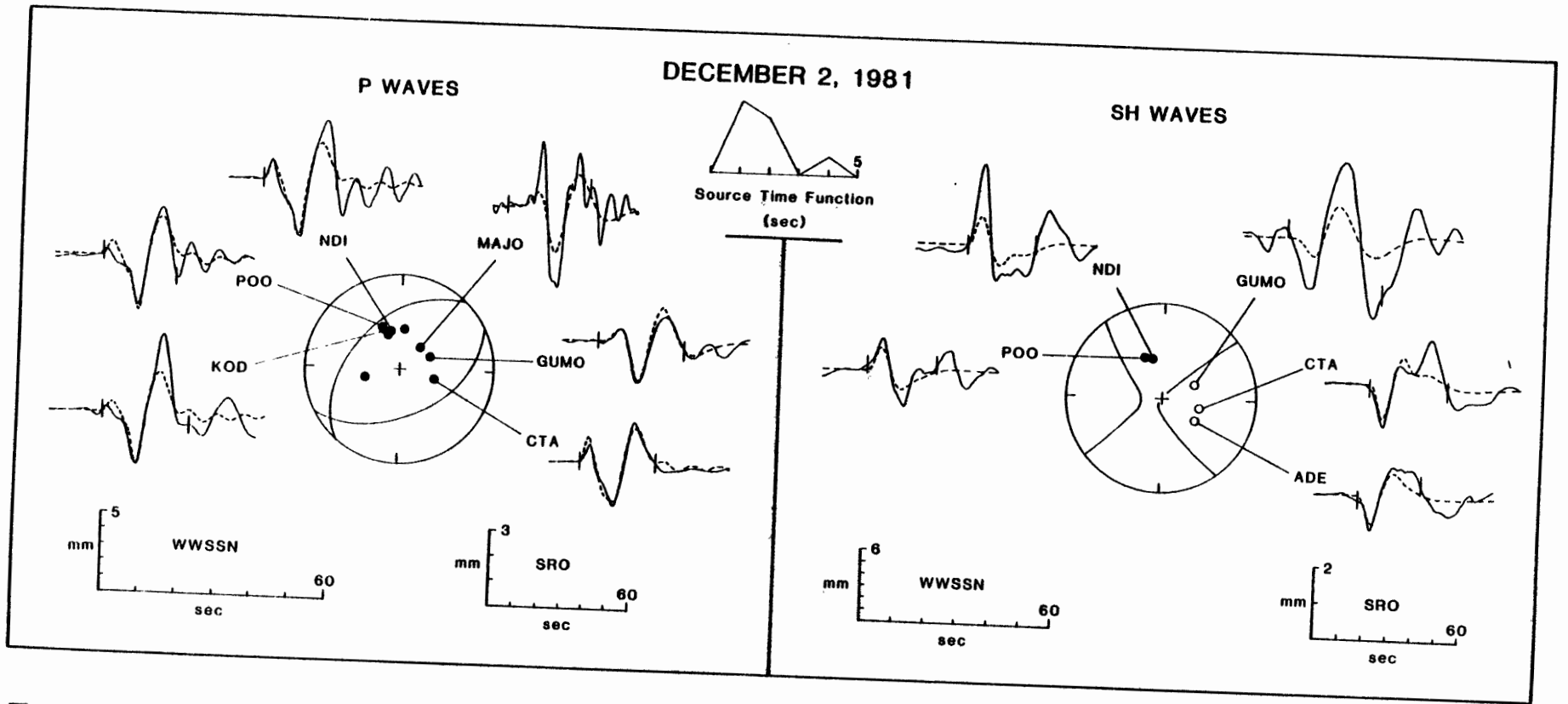


Figure 5.14

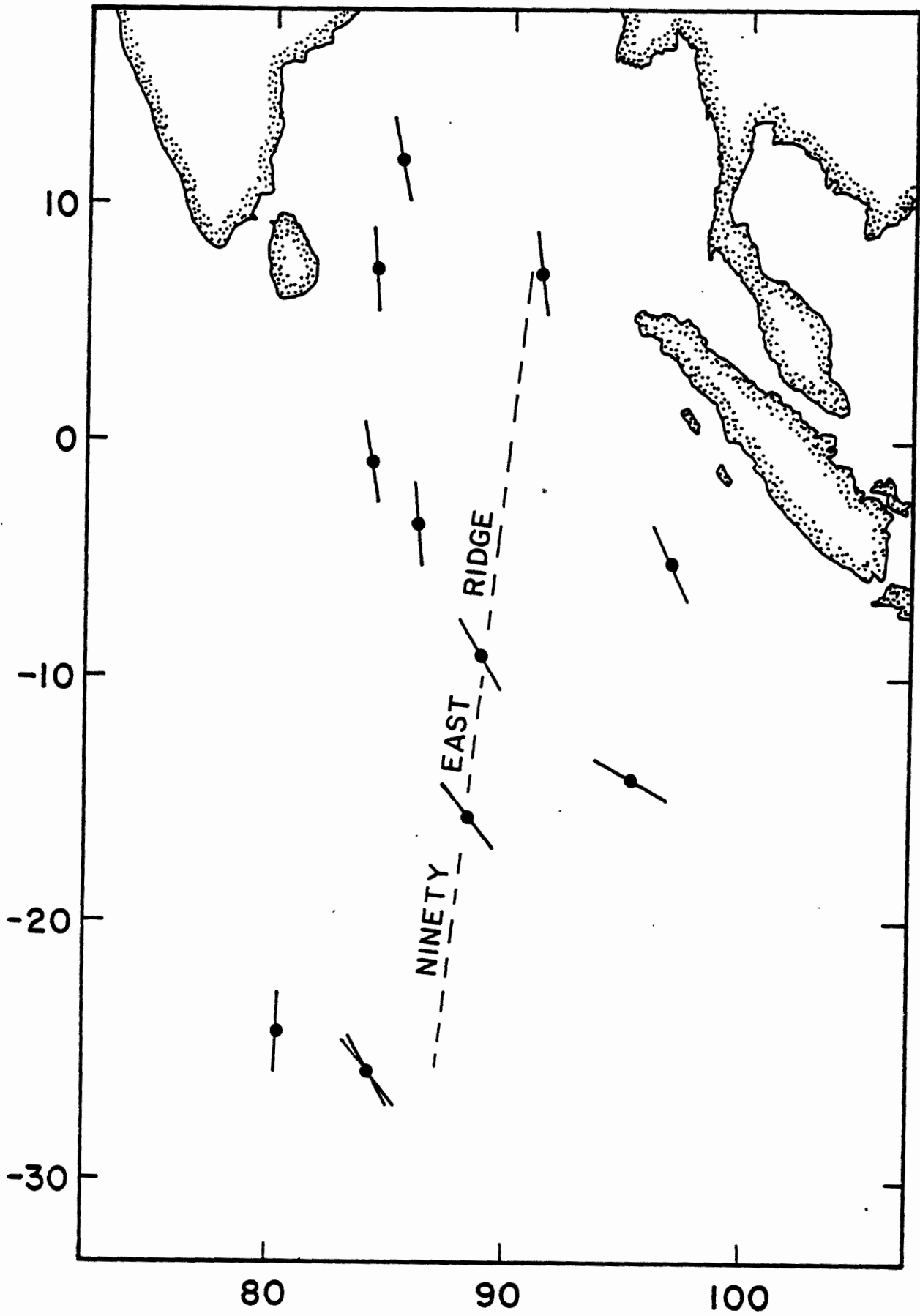


Figure 5.15

## CHAPTER 6. INTRAPLATE EARTHQUAKES IN THE ATLANTIC OCEAN

## INTRODUCTION

In this chapter, we present the results of source studies of earthquakes in older oceanic lithosphere in the North and South Atlantic Oceans. Source mechanisms of intraplate earthquakes near the Mid-Atlantic Ridge system (in lithosphere younger than about 30 m.y.) are presented in Chapter 8. Most of the events we have studied are in the North Atlantic, in both the North American and African plates. A large intraplate earthquake (January 24, 1983) recently occurred in the Eurasian plate a short distance west of Portugal, but seismograms are not yet available. Two of the earthquakes in this chapter are located in the far South Atlantic, near the South Sandwich Arc. One of them (August 26, 1977) occurred in lithosphere no more than about 17 m.y. old, but the unusual tectonic setting of this event persuaded us to isolate it from other events in young oceanic lithosphere (Chapter 8). There have been no significant intraplate earthquakes in older oceanic lithosphere of the main South Atlantic basin since the establishment of the WSSN, possibly a reflection of the extremely symmetric and simple tectonic history of this ocean basin.

## SOURCE MECHANISMS

In this section we present the source mechanisms of 8 oceanic intraplate earthquakes in the North and South Atlantic Oceans, obtained from the inversion of P and SH waveforms using the procedure developed by Nabelek [1984], as described in Chapter 3. Epicentral data for these earthquakes are listed in Table 6.1. The focal mechanisms and

the observed and synthetic seismograms are given in a series of figures, with P waves and SH waves shown on separate focal spheres (with the appropriate radiation pattern) for clarity. The synthetics shown were generated with the single best-fit solution, and have not been individually rescaled for improved fit. The station code and geographic location of all stations used in the inversions are listed in Appendix E. The best-fitting source parameters for all earthquakes, together with formal errors, are given in Table 6.2.

#### October 23, 1964

On October 23, 1964, a large ( $m_b = 6.2$ ,  $M_s = 6.3$ ) earthquake occurred northeast of the Lesser Antilles Arc, about 1000 km west of the Mid-Atlantic Ridge (Figure 6.1). Little is known of the structure of the epicentral region, but the regional trend of fracture zones is WNW. The lithosphere in the source region is about 65 m.y. old.

Molnar and Sykes [1969] examined the first motion data and determined a strike-slip mechanism (with a small component of thrusting): 284/52/137. The source mechanism of this earthquake was also studied by Fitch et al. [1980], who estimated the full moment tensor using a formal inversion of long-period P waveforms. They used a triangle 4 s in duration for the source time function. The results had to be modified somewhat after an error was discovered in the formulation of the forward problem [Fitch, 1981]. The focal mechanism was found to be similar to that of Molnar and Sykes, but closer to pure strike-slip. They report a centroid depth of 23 km and a seismic moment of  $8.1 \times 10^{25}$  dyne-cm. Liu and Kanamori [1980] modeled P waveforms from this earthquake, finding a focal mechanism of 296/66/158, a seismic moment of  $6.2 \times 10^{25}$  dyne-cm and a depth of 23



km. A trapezoid 2.5 s in duration was used for the source time function. Stein et al. [1982] also modeled the P waveforms of the October 23, 1964 earthquake, reaching conclusions similar to the other investigators: their preferred focal mechanism is 302/62/160, with a seismic moment of  $4.5 \times 10^{25}$  dyne-cm and a depth of 30 km.

The distribution and quality of P waveform data for the inversion is quite good, but we obtained only 4 usable SH waves. The best -fitting focal mechanism is similar to the others discussed above (278/57/154; Figure 6.2), except that it is rotated about  $24^\circ$  counterclockwise from that of Stein et al. [1982]. The seismic moment is  $4.9 \times 10^{25}$  dyne-cm, in acceptable agreement with the estimate of Liu and Kanamori and Stein et al. The discrepancy between our moment estimate and that of Fitch [1980] is difficult to understand, however, since both are based on a least-squares criterion. The centroid depth is found to be 28.0 km in our study; both Liu and Kanamori [1980] and Fitch et al. [1980] used halfspace source structures with crustal velocities and thus underestimated the depth of the earthquake. The depth determination is controlled primarily by the P waveforms at stations to the west and southwest (ARE, QUI, LPS, DAL, and COL). The other P waveforms are near-nodal and therefore contain little depth information. The delay between what appear to be direct and surface-reflected SH phases at VAL indicates a shallower depth, but the P wave data were given more weight in this case. The source time function found in the inversion is quite simple and about 4 s in length (Figure 6.2).

September 3, 1968

The September 3, 1968 earthquake ( $m_b = 5.6$ ,  $M_S = 5.9$ ) is located in the outer rise of the Puerto Rico trench, about 150 km north of the trench axis (Figure 6.1). Although the morphology of the trench system is quite similar to that of active subduction zones in the Pacific, the present relative motion of the North American plate with respect to the Caribbean plate along the trench is nearly parallel to the trench axis [e.g., Jordan, 1975]. The strain rate of the lithosphere in the upwarped outer rise is therefore very low at present, and the September 1968 earthquake should not necessarily be attributed to the release of plate bending stresses [e.g., Chapple and Forsyth, 1979].

Sykes and Sbar [1974] reported a thrust-faulting mechanism for this event (209/55/95), based on first motion polarities, but Wiens and Stein [1983a] found that the P waveforms required a strike-slip mechanism (176/76/0). The body-waveform inversion converged to a mechanism quite similar to that of Wiens and Stein: 168/77/4 (Figure 6.3). The station distribution is very good both for P and SH waves. Both nodal planes of the SH wave radiation pattern are well-constrained by stations with nodal direct phases (UME and ALQ). The centroid depth of this event is 24.2 km, slightly shallower than the 27 km depth reported by Wiens and Stein [1983a]. The seismic moment is  $5.9 \times 10^{24}$  dyne-cm.

September 30, 1971

The epicenter of the September 30, 1971 earthquake ( $m_b = 6.0$ ,  $M_S = 5.5$ ) is in the equatorial eastern Atlantic, in the Gulf of Guinea (Figure 6.4). There are numerous closely-spaced fracture zones (trending approximately N75°E) throughout the region, but none has been

identified in the immediate epicentral area [Sibuet and Mascle, 1978]. There are distinct linear trends in the bathymetry, however.

Sykes and Sbar [1974] reported a predominantly thrust-faulting mechanism (72/60/117) for this earthquake, based on P wave first motions and shear wave polarizations. Liu and Kanamori [1980] studied the source mechanism by modeling P and SH waveforms, preferring a mechanism with a larger (and in the opposite sense) component of strike-slip motion (72/60/60). Liu and Kanamori found a best-fitting depth of 13 km below the top of a halfspace with crustal velocities and a seismic moment of  $7 \times 10^{24}$  dyne-cm. The source time function they used is a symmetric trapezoid with a total length of 1.6 s.

The source velocity structure used for the inversion includes a sediment layer 1.5 km thick, with  $\alpha = 2.0$  km/s,  $\beta = 0.9$  km/s, and  $\rho = 2.3$  g/cm<sup>3</sup> [Sibuet and Mascle, 1978]. The station distribution is excellent and we obtained a very good fit to the observed waveforms with a mechanism similar to that of Liu and Kanamori, but with a larger component of thrust faulting (78/60/74, Figure 6.5). One nodal plane is essentially parallel with the local strike of fracture zones. The centroid depth is 11.6 km below the top of the sediment layer. The seismic moment is  $9.2 \times 10^{24}$  dyne-cm and the source time function (4 s) is over twice as long as that of Liu and Kanamori.

#### October 20, 1972

The October 20, 1972 earthquake ( $m_b = 5.7$ ,  $M_s = 5.8$ ) is located northwest of the Cape Verde Archipelago, in the eastern Atlantic (Figure 6.6). Although the epicentral region is poorly surveyed, the tectonic history of this region is reasonably simple and fracture zones are expected to trend WNW.

The source mechanism of this earthquake was first studied by Richardson and Solomon [1977], using P wave first motions and shear of wave polarizations. Neither nodal plane of the strike-slip mechanism (248/80/171) is close to the local trend of fracture zones. They also reported a seismic moment, estimated from long-period SH wave spectra,  $2.8 \times 10^{25}$  dyne-cm. From P-wave modeling, the depth of this event was estimated to be 20 km by Wiens and Stein [1983a].

Station coverage for this event is exceptionally good; we have data in all four quadrants of both the P and SH radiation patterns. The vertical component instrument at LOR was found to have reversed polarity. With a mechanism (248/80/171) very close to that of Richardson and Solomon, the fit to the observed waveforms is also quite good, especially considering the strong constraints on the focal mechanism (Figure 6.7). Note that both the direct and reflected SH phases at LPA are nodal. The seismic moment found in the inversion ( $2.5 \times 10^{25}$  dyne-cm) is also in excellent agreement with the estimate of Richardson and Solomon [1977]. The centroid depth is 15.4 km, somewhat shallower than that of Wiens and Stein [1983a]. The P waves alone might prefer a depth perhaps a kilometer or two deeper, but the SH waves require the shallower depth.

#### November 20, 1974

The epicenter of the November 20, 1974 earthquake ( $m_b = 5.8$ ,  $M_s = 5.6$ ) is about 150 km north of the South Sandwich arc, in a tectonically complex and poorly surveyed area (Figure 6.8). Wiens and Stein [1983a] proposed a strike-slip mechanism for this event (275/82/5), based on first motion polarities and P waveform modeling. They also report a depth of 8 km below the seafloor. We were able to obtain usable

waveform data at only a few stations, but they are fairly well distributed. The mechanism found in the inversion is quite similar to that of Wiens and Stein, except that it is rotated clockwise by almost  $25^\circ$  (298/87/5, Figure 6.9). The strike is well constrained by the SH waves, particularly at WIN and PRE, between which one nodal plane must pass. The nodal P waveforms at CAR and LPB also fix the strike of the mechanism. The best-fitting centroid depth is 4.5 km, placing this event in the oceanic crust. The seismic moment is estimated to be  $6.6 \times 10^{24}$  dyne-cm, but there is greater than usual uncertainty in this value (Table 6.2).

#### August 26, 1977

On August 26, 1977, one of the largest known oceanic intraplate earthquakes ( $m_b = 6.3$ ,  $M_s = 7.1$ ) occurred in the far southeast corner of the South American plate, a few hundred km east of the South Sandwich Arc (Figure 6.8). The epicenter appears to be located on a fracture zone trending E-W from the nearby spreading ridge segments of the American -Antarctic Ridge [Lawver and Dick, 1983]. The age of the lithosphere in the epicentral region is between about 10 and 17 m.y., depending on which side of the fracture zone one references. The aftershocks of this earthquake also define an E-W trend. This earthquake therefore occurred very near and about equally distant from a convergent, an accretionary, and a transform plate boundary. Frankel and McCann [1979] observed that the seismicity in the subduction zone appears to be strongly influenced by the variation in the age of subducted lithosphere along the arc (as a result of the offsets of the ridge segments to the east). It is also likely that the intraplate stress regime in this isolated corner of the South American plate is

strongly perturbed by the interactions of the nearby plate boundaries. For this reason, we have not included this event in our survey of earthquakes in young oceanic lithosphere (Chapter 8).

In a preliminary study of the August 1977 earthquake, Creavan et al. [1979] reported a mechanism based on first motion polarities and several records of long-period Rayleigh waves: the mechanism is characterized by nearly pure right-lateral strike-slip motion on an E-W striking plane. They also estimated the seismic moment to be about  $1 \times 10^{27}$  dyne-cm. We were unable to obtain any SH waveforms for this event, because every shear wave record we examined was either clipped or too faint to digitize, making this the only event in this thesis study for which the inversion was performed with P waves only. We used P waves at 6 well-distributed stations, but with such a small data set we can expect to achieve only a rather crude understanding of such a large and undoubtedly complex event. The point source approximation for the long-period body-wave modeling technique is certainly invalid for an earthquake this large. Nevertheless, we were able to achieve a reasonably good fit to the P waveforms with a simple source about 8 s in duration and a mechanism of the sort proposed by Creavan et al. (91/85/175; Figure 6.10). The centroid depth was found to be 8.8 km, but the uncertainty is greater than usual (Table 8.2). The seismic moment is  $5.4 \times 10^{26}$  dyne-cm, several times larger than any other event in this thesis study. It is quite likely that the true seismic moment of this event is larger, however, as suggested by Creavan et al.

#### December 13, 1977

The December 13, 1977 earthquake ( $m_b = 5.7$ ,  $M_s = 6.4$ ) is located a short distance northeast of the Barracuda Ridge, an aseismic ridge

between the Lesser Antilles and the Mid-Atlantic Ridge (Figure 6.1). The trend of fracture zones in the area is WNW. The mechanism of this event was first studied by Bergman and Solomon [1980], using first motion polarities and shear wave polarizations; they reported a strike-slip mechanism with a component of thrust faulting (238/72/38). Stein et al. [1982] modeled the P waveforms from this earthquake and found a similar mechanism, but with a larger component of thrust faulting (244/68/65). They found a depth of 25 km and a seismic moment (from surface waves) of  $5.4 \times 10^{25}$  dyne-cm. As expected for a large event in the central Atlantic, the station coverage is excellent. The fit to the observed waveforms is very good with a mechanism intermediate between the two previously published solutions: 238/60/51 (Figure 6.11). The centroid depth is 22.8 km and the seismic moment is  $2.8 \times 10^{25}$  dyne-cm. The body waveform data cannot possibly support a moment as high as  $5 \times 10^{25}$  dyne-cm. Given the relatively poor quality of the surface wave data shown by Stein et al., we suspect they have overestimated the moment.

#### March 24, 1978

The March 24, 1978 earthquake ( $m_b = 6.0$ ,  $M_s = 6.0$ ) is located 375 km southwest of Bermuda, in the western Atlantic (Figure 6.12a). The epicenter is at the edge of the uplifted Bermuda platform and in the M11-M4 spreading discontinuity (Figure 6.12b). The age of the lithosphere in the epicentral region is therefore about 118 m.y. The trend of fracture zones changes from about  $300^\circ$  (on the east) to about  $290^\circ$  in the epicentral region, but the epicenter itself is not associated with a fracture zone (Figure 6.12b).

Because of its size and location near the east coast of the U.S. (it was felt in Boston) and the rarity of large intraplate earthquakes in this region, this earthquake attracted an unusual amount of interest. Nishenko et al. [1978] and Stewart [1979] quickly determined that it is a shallow thrust-faulting event. Stewart and HelMBERGER [1981] modeled P and SH waveforms from this earthquake and reported the best-fitting mechanism to be 340/42/90, with a seismic moment of  $3.4 \times 10^{25}$  dyne-cm and a depth of about 6 km below the seafloor. A seismic moment of  $3.1 \times 10^{25}$  was estimated from long-period Rayleigh waves recorded by the IDA network. Nishenko and Kafka [1982] studied the source mechanism with first motion data and Rayleigh wave amplitude spectra, finding a mechanism (340/55/90) nearly identical to that of Stewart and HelMBERGER, a seismic moment of  $3.6 \times 10^{25}$  dyne-cm, and an identical depth of 6 km. The results of a microearthquake survey of the aftershocks of the March 24, 1978 earthquake are reported by Nishenko et al. [1982].

The source structure used in the body-waveform inversion incorporated a 1.2 km thick sediment layer [Ewing et al., 1954], with  $\alpha = 2.0$  km/s,  $\beta = 0.8$  km/s, and  $\rho = 2.3$  g/cm<sup>3</sup>. Station coverage for this event is quite good in the northern hemisphere, but we obtained only one P and one SH waveform to the south. The focal mechanism (333/46/99; Figure 6.13) is reasonably well constrained, particularly by the SH wave data. We have data in three quadrants of the SH radiation pattern and both the direct and reflected SH phases at COL are nodal, which limits the range of acceptable fault strike. The centroid depth found in the body-waveform inversion (6.0 km) agrees perfectly with previous estimates, but the seismic moment is somewhat smaller ( $2.0 \times 10^{25}$  dyne-cm).



The centroid depth is immediately below the crustal layer in our source structure, raising the possibility that the inversion settled into a local minimum in residual error controlled by the crust-mantle interface. We performed the inversion a second time, using a 5 km thick crust (as Stewart and HelMBERGER did), and verified that the best-fitting centroid was still at a depth of about 6 km. With both crustal models, we began the inversion both in the mantle and in the crust; in all cases, the inversion converged to essentially the same depth.

## DISCUSSION

The eight earthquakes studied in this chapter can be grouped, for the purposes of this discussion, into three categories: (1) Isolated events unrelated to major intraplate deformation. (2) Events belonging to a diffuse zone of intraplate seismicity which may be associated with a distributed plate boundary. (3) Intraplate earthquakes in the vicinity of a complex plate boundary which may strongly influence the local intraplate stress field. In the first category we place the September 30, 1971 (Guinea Basin), October 20, 1972 (Cape Verde), and March 24, 1978 (Bermuda) earthquakes. The second category includes the events on October 23, 1964, September 3, 1968, and December 13, 1977, between the Caribbean Arc and the Mid-Atlantic Ridge. The two earthquakes in the vicinity of the South Sandwich Arc, on November 20, 1974 and August 26, 1977 belong to the third category.

Large, isolated (seismically) intraplate earthquakes such as those in the first category above are important sources of information on the state of stress in oceanic lithosphere because, for many large oceanic areas, they are the only source of such information. The lack of other

seismicity near them is an advantage in one respect, since it suggests that no major intraplate deformation is occurring, but it also means that there can be no confirmation of the inferred stress orientation by comparison with the focal mechanisms of nearby events. With a single event, the possibility of bias in the inferred stress direction because the earthquake occurred in a fracture zone (or other feature representing disturbed lithosphere) is also greater.

Both the September 30, 1971 and March 24, 1978 events can be associated with disturbed lithosphere with some certainty. The 1971 earthquake almost certainly occurred on a fracture zone. The focal mechanism of this event indicates predominantly reverse motion on the fault, but there is a modest component of strike-slip motion which may represent the influence of the fracture zone as a pre-existing zone of weakness (Figure 6.4). Fracture zones in the epicentral region of the 1978 earthquake are extremely well-mapped and the epicenter clearly lies between fracture zones, but it is associated with the Mesozoic spreading discontinuity in the North Atlantic which certainly represents significant disturbance of the lithosphere (Figure 6.12). Fracture zones in the epicentral region of the third earthquake, on October 20, 1972, are not well mapped, but their general orientation (WNW) is reasonably certain and neither nodal plane of the focal mechanism is close to this trend.

Because of its location in a very well surveyed part of the western Atlantic and the fact that a microearthquake survey of the aftershocks was conducted [Nishenko et al., 1982], more is known about the circumstances of the 1978 Bermuda event than almost any other oceanic intraplate event, yet the source of the stress released in this

event has not been clearly identified. The P axis is oriented radially to the island of Bermuda, but the epicenter is too far away for the mechanism to be explained by simple topographic effects. Plate bending stresses in the lithosphere resulting from a large seamount load can be significant at greater distances, but the shallow depth and thrust-faulting mechanism are inconsistent with such a model. Nishenko and Kafka [1982] argue that the 1978 Bermuda earthquake may have released stresses related to crustal thickness inhomogeneities at the perimeter of the Bermuda rise. They also point out that the P axis of this earthquake is subparallel with the absolute motion vector of the North American plate [Minster and Jordan, 1978]. The P axis is not inconsistent with the predicted orientation of maximum horizontal compressive stress from a model of the intraplate stress field incorporating 'ridge push' and basal drag [Richardson et al., 1979].

In contrast, there is little to be said about the source of the stress released in the 1971 and 1972 earthquakes. The October 1972 earthquake occurred near the perimeter of the Cape Verde Rise, but the P axis of this event is parallel to any presumed gradient in crustal thickness. There is no significant topographic relief in the area. The September 1971 Guinea Basin earthquake has a thrust-faulting mechanism with the P axis roughly perpendicular to the continental margin of Africa to the north, but the margin is too far away (300-400 km) for it to be a likely source of the stress released in this earthquake. There is no obvious reason to reject these two events as indicators of the regional stress field in the African plate.

Several of the larger oceanic intraplate earthquakes in the western Atlantic have occurred between the Caribbean Arc and the

Mid-Atlantic Ridge (MAR), an area in which any relative motion between the North and South American plates should occur [e.g., Ball and Harrison, 1970]. Bergman and Solomon [1980] and Stein et al. [1982] found no clear relation between the mechanisms of several of these events and a postulated plate boundary, in part because the expected sense of motion is not well resolved (Figure 6.14).

Further constraint on this interesting problem can be gained by considering intraplate seismicity at magnitudes below that necessary for a source study. Figure 2.3 reveals a diffuse, but distinct band of earthquake activity extending SE from the northern end of the Lesser Antilles to the MAR. This seismicity pattern was also noticed by Lilwall [1982]. The absence of a similar pattern in Figure 2.1 can be attributed to the fact that it is largely defined by the smaller events which are not adequately represented in Appendix A. This region is shown in more detail in Figure 6.1. Only events recorded at 10 or more stations are shown; the proposed diffuse band of seismicity between the MAR and the northern end of the Caribbean Arc is much more prominent if events recorded at fewer than 10 stations are included.

The proposed band of intraplate seismicity intersects the MAR where it undergoes a major left-lateral offset, involving several transform faults. The general trend of the intraplate seismicity is also roughly parallel to fracture zones in the area. If the lithosphere in this region is disrupted by numerous closely-spaced fracture zones, it may explain the average width and trend of the pattern of intraplate seismicity.

The focal mechanisms of both the October 1964 and the December 1977 earthquake have a nodal plane which is subparallel to the trend of

fracture zones, approximately WNW. (A 1978 event very near the 1977 earthquake was found by Stein et al. [1982] to have a very similar mechanism. We were unable to study this event with the body waveform inversion because of interference from surface waves from an earlier earthquake.) If we take these nodal planes to represent the fault planes, all three events are characterized by a combination of thrust-faulting and right-lateral strike-slip faulting. The September 1968 event is also characterized by right-lateral strike-slip motion, but on a nodal plane striking about  $25^\circ$  from the general trend of fracture zones.

If these earthquakes represent a diffuse plate boundary between the North and South American plates, as we are inclined to believe, our interpretation is more consistent with the plate motions predicted by model RM2 [Minster and Jordan, 1978] than by RM1 [Minster et al., 1974] (Figure 6.14). A combination of compression and right-lateral shear in a boundary zone trending WNW is also in excellent agreement with the relative motion between North and South America predicted by Chase [1978].

The last two events whose source mechanisms were investigated for this chapter are located in the far South Atlantic, near the South Sandwich Arc (Figure 6.8). The August 26, 1977 earthquake is one of the largest known oceanic intraplate events. As we discussed above, this event represents the release of stresses accumulated in a very unusual tectonic setting. The fracture zone on which this event occurred is one of several (not the largest offset, however) which continue west to intersect the South Sandwich trench, thus causing significant variations in the age (and buoyancy) of lithosphere

subducted at various points along the trench. Frankel and McCann [1979] have attributed variations in the seismicity of the arc to this process.

It seems very likely that this process also perturbs the state of stress in the lithosphere east of the trench. The sense of motion on the E-W trending nodal plane can be explained in this model if the lithosphere south of the fracture zone had been 'locked' at the subduction zone for some time, resisting subduction because of its relative buoyancy compared to the older lithosphere being subducted immediately to the north. When a section of the younger lithosphere is finally consumed, the release of stress in the small area of oceanic lithosphere to the east could result in a large earthquake. There have been several earthquakes with  $M > 7$  in the southern part of the arc in this century, and a 1949 earthquake with  $M = 7.1$  occurred near the site of the 1977 event [Frankel and McCann, 1979]. The overall coupling between the subducting and overriding plates at the South Sandwich Arc is rather weak, judging by the relatively small number of large shallow events in this century [Frankel and McCann, 1979], but there may still be significant perturbations to the state of stress in the small corner of the South American plate to the east of the arc.

The November 20, 1974 earthquake is located in a region in which the South American plate is being deformed in a complex manner as the South Sandwich Arc propagates east at the full spreading rate of the Scotia Ridge (70-90 mm/yr), shearing off and subducting a strip of the South American plate [Barker, 1972; Forsyth 1975]. Given the lack of knowledge about the tectonics of this area, it is difficult to know how to interpret this single focal mechanism, other than to expect that it may be dominated by large locally-produced stresses.

In summary, the larger oceanic intraplate earthquakes of the Atlantic Ocean exhibit characteristics which we also observe in the earthquakes of other regions. Some can clearly be associated with fracture zones or other disturbed regions of the oceanic lithosphere, while others can almost certainly be acquitted of such associations. Some clusters of intraplate seismicity accompany the formation of new plate boundaries or perhaps represent plate boundaries that never quite coalesced. Some are quite likely to have resulted from stresses accumulated through local tectonic processes, while others seem to have no significant local source of stress and thus are likely the products of the regional lithospheric stress field.

Table 6.1. Epicentral data\* for earthquakes studied

Date	Origin time h m s	Lat. °N	Long. °E	$m_b$	$M_S$	Age** (m.y.)
October 23, 1964	1 56 5.1	19.80	-56.11	6.2	6.3	65
September 3, 1968	15 37 0.3	20.58	-62.30	5.6	5.9	80
September 30, 1971	21 24 10.8	-0.45	-4.89	6.0	5.5	46
October 20, 1972	4 33 49.9	20.60	-29.69	5.7	5.8	90
November 20, 1974	13 21 41.6	-53.59	-28.26	5.8	5.6	70
August 26, 1977	19 50 02.3	-59.54	-20.59	6.3	7.1	10-17
December 13, 1977	1 14 20.5	17.33	-54.91	5.7	6.4	68
March 24, 1978	0 42 36.7	29.68	-67.45	6.0	6.0	118

\* Epicentral data from the ISC, except  $M_S$  magnitudes for October 23, 1964 [Stein et al., 1982] and September 3, 1968 [Wiens and Stein, 1983a].

\*\* Age of lithosphere estimated from magnetic anomaly identifications and magnetic chronology of LaBrecque et al. [1977], or from the isochrons determined by Slater et al. [1980, 1981a].



Table 6.2 Source mechanisms obtained from body-wave inversion<sup>a</sup>

Date	Moment <sup>b</sup>	$t_s$ <sup>c</sup>	Depth <sup>d</sup>	Strike	Dip	Slip
October 23, 1964	49. $\pm$ 5.	3.9 $\pm$ 1.3	28.0 $\pm$ 0.1	278.2° $\pm$ 1.9	56.5° $\pm$ 1.4	153.6° $\pm$ 1.2
September 3, 1968	5.9 $\pm$ 0.6	4.5 $\pm$ 1.5	24.2 $\pm$ 0.1	168.1 $\pm$ 0.5	76.7 $\pm$ 0.8	3.8 $\pm$ 0.6
September 30, 1971	9.2 $\pm$ 1.5	4.0 $\pm$ 1.0	11.6 $\pm$ 0.1	78.2 $\pm$ 1.1	60.4 $\pm$ 0.6	73.9 $\pm$ 1.0
October 20, 1972	25. $\pm$ 3.	5.0 $\pm$ 1.0	15.4 $\pm$ 0.1	247.5 $\pm$ 0.4	79.5 $\pm$ 0.4	170.6 $\pm$ 0.5
November 20, 1974	6.6 $\pm$ 3.2	3.3 $\pm$ 1.1	4.5 $\pm$ 0.1	298.0 $\pm$ 0.9	87.3 $\pm$ 1.0	5.1 $\pm$ 0.8
August 26, 1977	540. $\pm$ 61.	8.0 $\pm$ 2.0	8.8 $\pm$ 0.7	91.3 $\pm$ 0.9	85.2 $\pm$ 1.0	175.3 $\pm$ 0.8
December 13, 1977	28. $\pm$ 1.	4.2 $\pm$ 1.4	22.8 $\pm$ 0.1	237.6 $\pm$ 1.4	59.9 $\pm$ 0.9	50.8 $\pm$ 1.1
March 24, 1978	20. $\pm$ 2.	3.0 $\pm$ 1.0	6.0 $\pm$ 0.1	333.2 $\pm$ 1.1	45.8 $\pm$ 0.3	98.8 $\pm$ 1.3

a) The range indicated for each parameter is one standard deviation (formal error). The range of  $t_s$  is one half the width of the source time function element used in the inversion.

b)  $\times 10^{24}$  dyne-cm ( $10^{17}$  N-m).

c) Total duration of the source time function, sec.

d) Relative to the top of the crust (or sediment layer, if used), km.

## FIGURE CAPTIONS

Figure 6.1. Map of the seismicity of a portion of the western Atlantic, with focal mechanisms for three earthquakes determined by inversion of body waveforms (October 23, 1964, September 3, 1968, and December 13, 1977; Table 6.2). Oceanic intraplate earthquakes from Appendix B are shown as solid circles, with larger symbols for events with  $m_b \geq 5.4$ . Small open circles indicate the seismicity of the Mid-Atlantic Ridge. Earthquakes in the Lesser Antilles Arc are not shown. The Puerto Rico Trench (outlined by the 6000 m isobath) and the Barracuda Ridge (5000 m isobath) are also shown.

Figure 6.2. Comparison of observed (solid line) long-period P and SH waves from the October 23, 1964 earthquake with synthetic waveforms (dashed lines) generated for the best-fitting point source mechanism found in the body-waveform inversion (Table 6.2). P and SH radiation patterns are shown on the lower focal hemisphere (equal area projection). All amplitudes are normalized to an instrument magnification of 3000; the amplitude scales correspond to the waveforms that would be observed on an original seismogram from such an instrument. The two vertical lines delimit the portion of each time series used in the inversion. Symbols for both types of waves are: open circle - dilatation, closed circle - compression, cross - emergent arrival. For SH waves, compression corresponds to positive motion as defined by Aki and Richards [1980]. First motions read from long-period seismograms but not used in the inversion are also plotted.

Figure 6.3. Comparison of observed P and SH waves from the September 3, 1968 earthquake with synthetic waveforms generated for the best-fitting point source mechanism found in the body-waveform inversion (Table 6.2). See Figure 6.2 for further explanation.

Figure 6.4. Major fracture zones (dashed where less certain) in the Gulf of Guinea and the location and mechanism of the September 30, 1971 earthquake (Table 6.2). Adapted from Figure 8 of Sibuet and Mascle [1978].

Figure 6.5. Comparison of observed P and SH waves from the September 30, 1971 earthquake with synthetic waveforms generated for the best-fitting point source mechanism found in the body-waveform inversion (Table 6.2). See Figure 6.2 for further explanation.

Figure 6.6. Bathymetry in the vicinity of the Cape Verde Rise in the eastern Atlantic and the epicenter and focal mechanism of the October 20, 1972 earthquake (Table 6.2). Bathymetry from Perry et al. [1981]; 1000 m contour interval.

Figure 6.7. Comparison of observed P and SH waves from the October 20, 1972 earthquake with synthetic waveforms generated for the best-fitting point source mechanism found in the body-waveform inversion (Table 6.2). See Figure 6.2 for further explanation.

Figure 6.8. Bathymetry and seismicity in the vicinity of the South Sandwich Arc and the focal mechanisms of the November 20, 1974 and August 26, 1977 earthquakes (Table 6.2). Adapted from Figure 2 of Lawver and Dick [1983]; 2 km contour interval.

Figure 6.9. Comparison of observed P and SH waves from the November 20, 1974 earthquake with synthetic waveforms generated for the best-fitting point source mechanism found in the body-waveform inversion (Table 6.2). See Figure 6.2 for further explanation.

Figure 6.10. Comparison of observed P waves from the August 26, 1977 earthquake with synthetic waveforms generated for the best-fitting point source mechanism found in the body-waveform inversion (Table 6.2). See Figure 6.2 for further explanation.

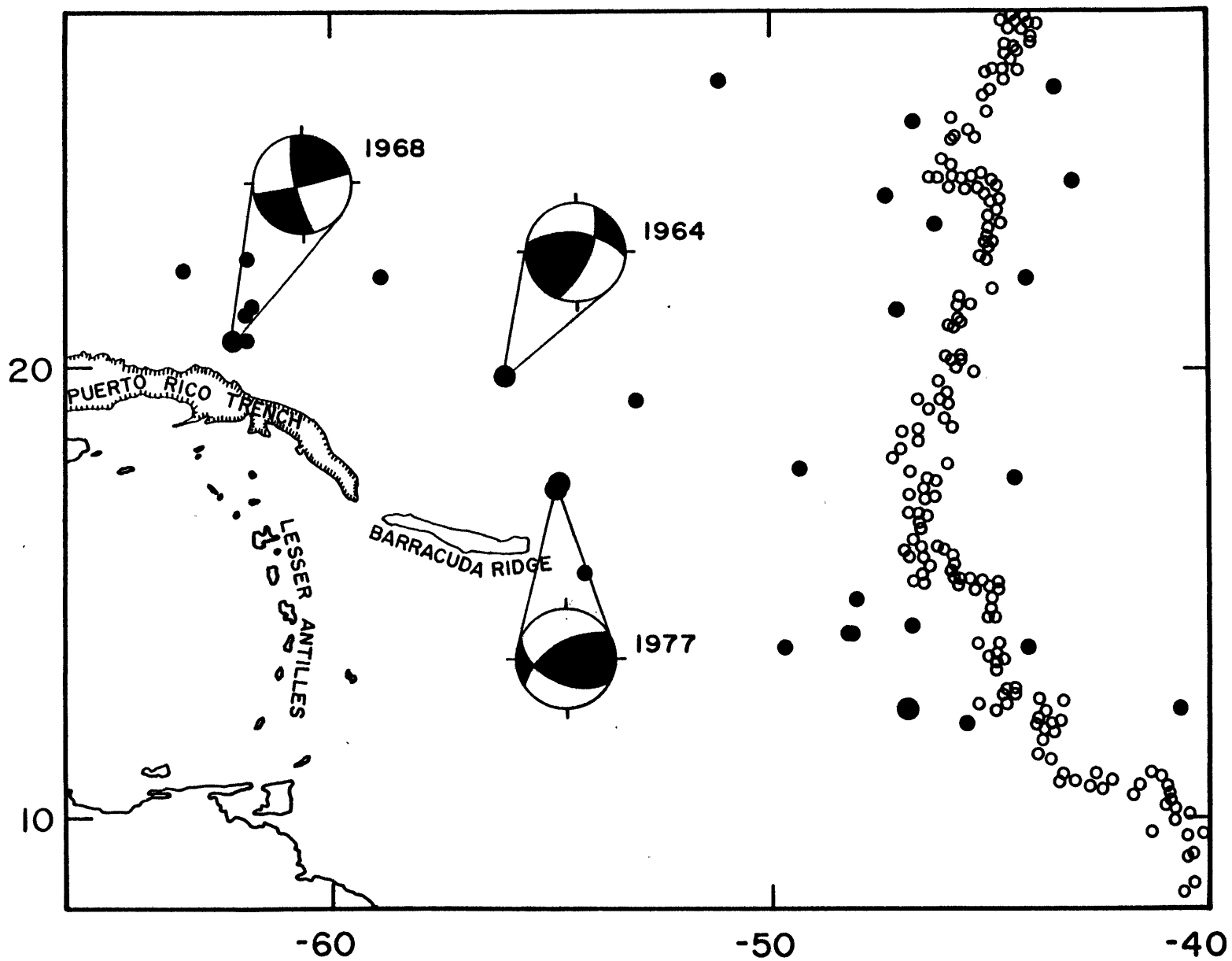
Figure 6.11. Comparison of observed P and SH waves from the December 13, 1977 earthquake with synthetic waveforms generated for the best-fitting point source mechanism found in the body-waveform inversion (Table 6.2). See Figure 6.2 for further explanation.

Figure 6.12. (a) Bathymetry in the vicinity of the Bermuda Rise, in the eastern Atlantic, and the location and focal mechanism of the March 24, 1978 earthquake (Table 6.2). Bathymetry from Perry et al. [1981]; 1000 m contour interval. (b) Locations of fracture zones and the M11-M4 spreading discontinuity (stippled region) in the epicentral region of the March 24, 1978 earthquake (solid circle). Adapted from Figure 9 of Nishenko and Kafka [1982].

Figure 6.13. Comparison of observed P and SH waves from the March 24, 1978 earthquake with synthetic waveforms generated for the best-fitting point source mechanism found in the body-waveform inversion (Table 6.2). See Figure 6.2 for further explanation.

Figure 6.14. Relative plate motions between North and South America predicted by relative plate motion models RM1 [Minster et al., 1974], and RM2 [Minster and Jordan, 1978]. Reproduced from Figure 2 of Stein et al. [1982].

Figure 6.1



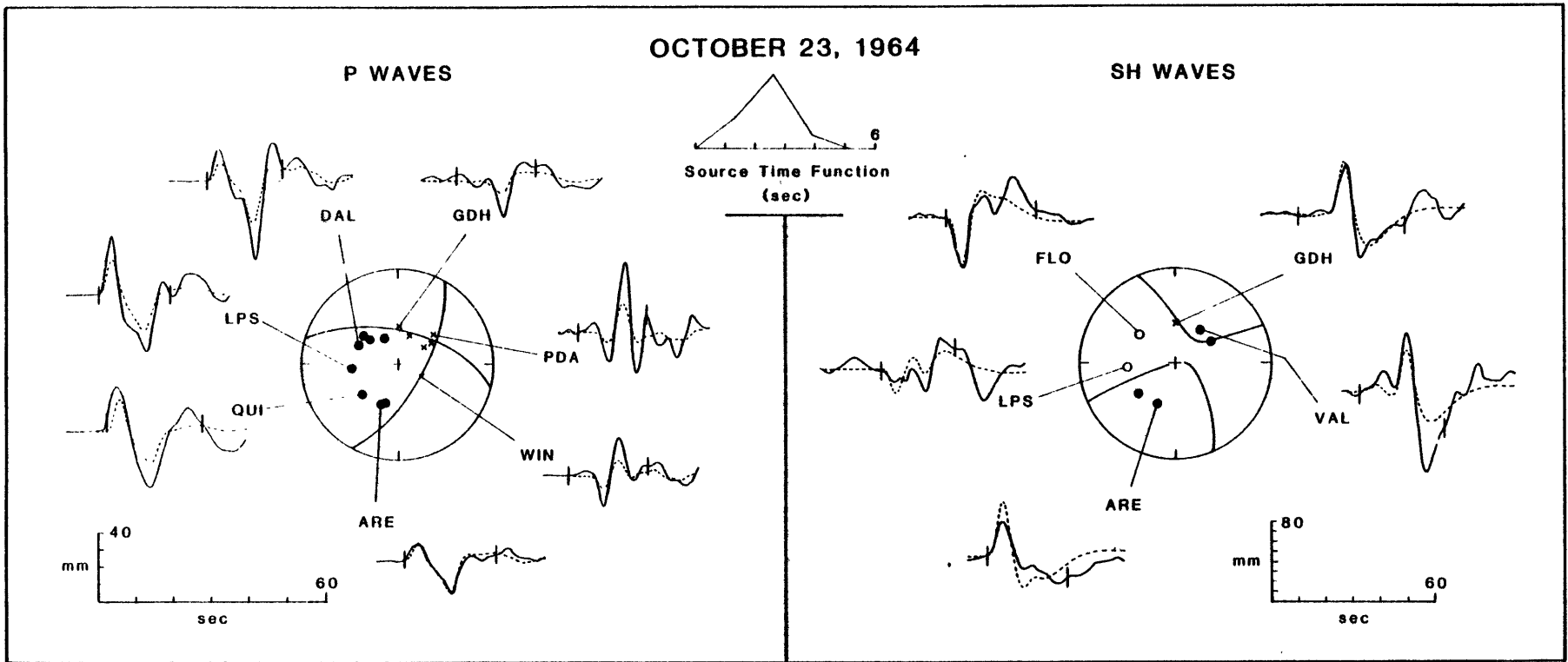


Figure 6.2

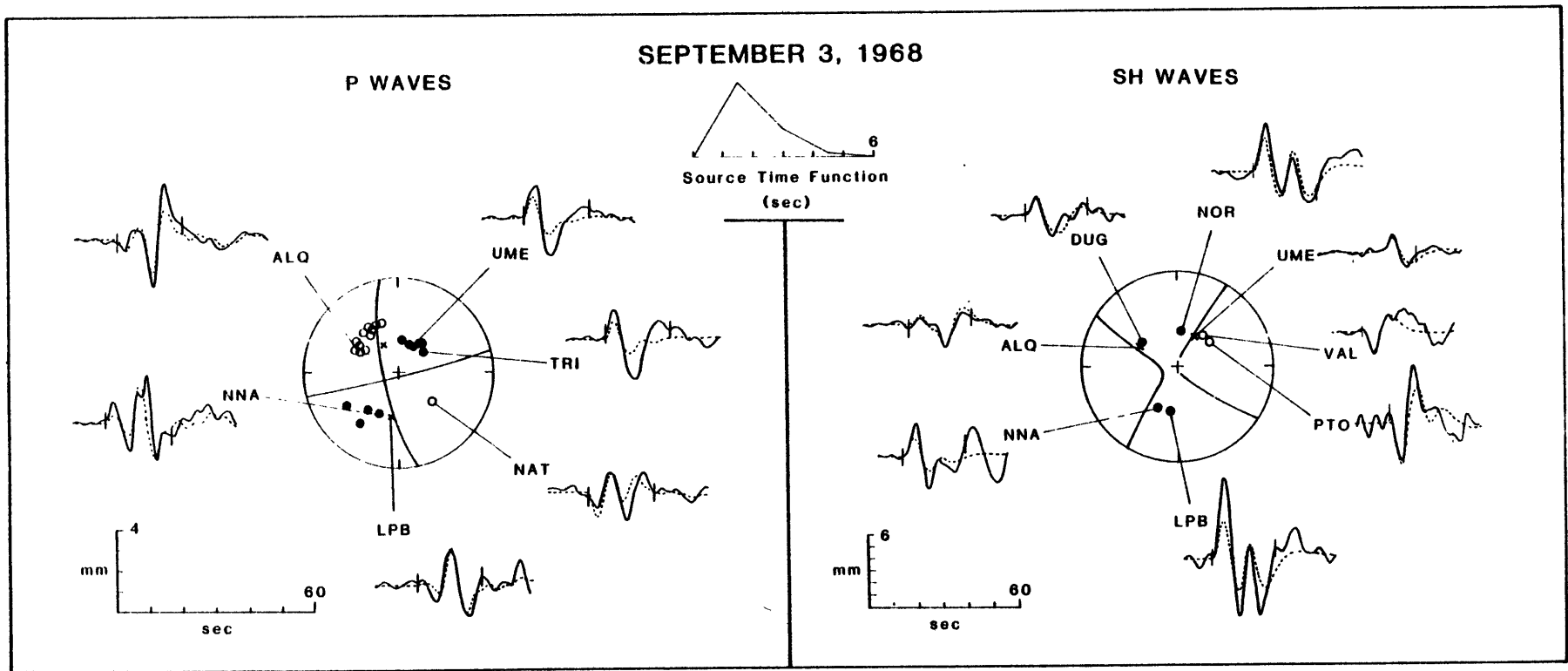


Figure 6.3

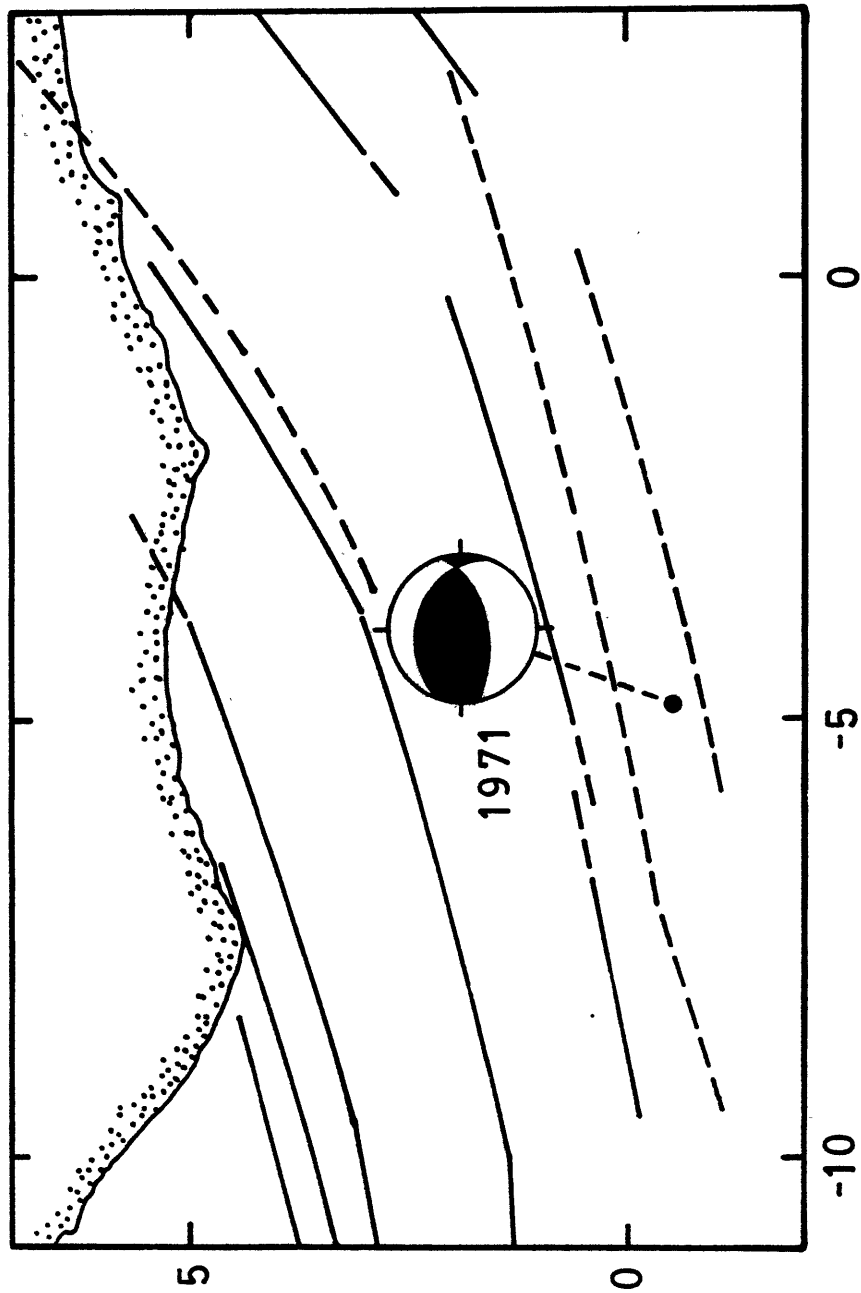


Figure 6.4



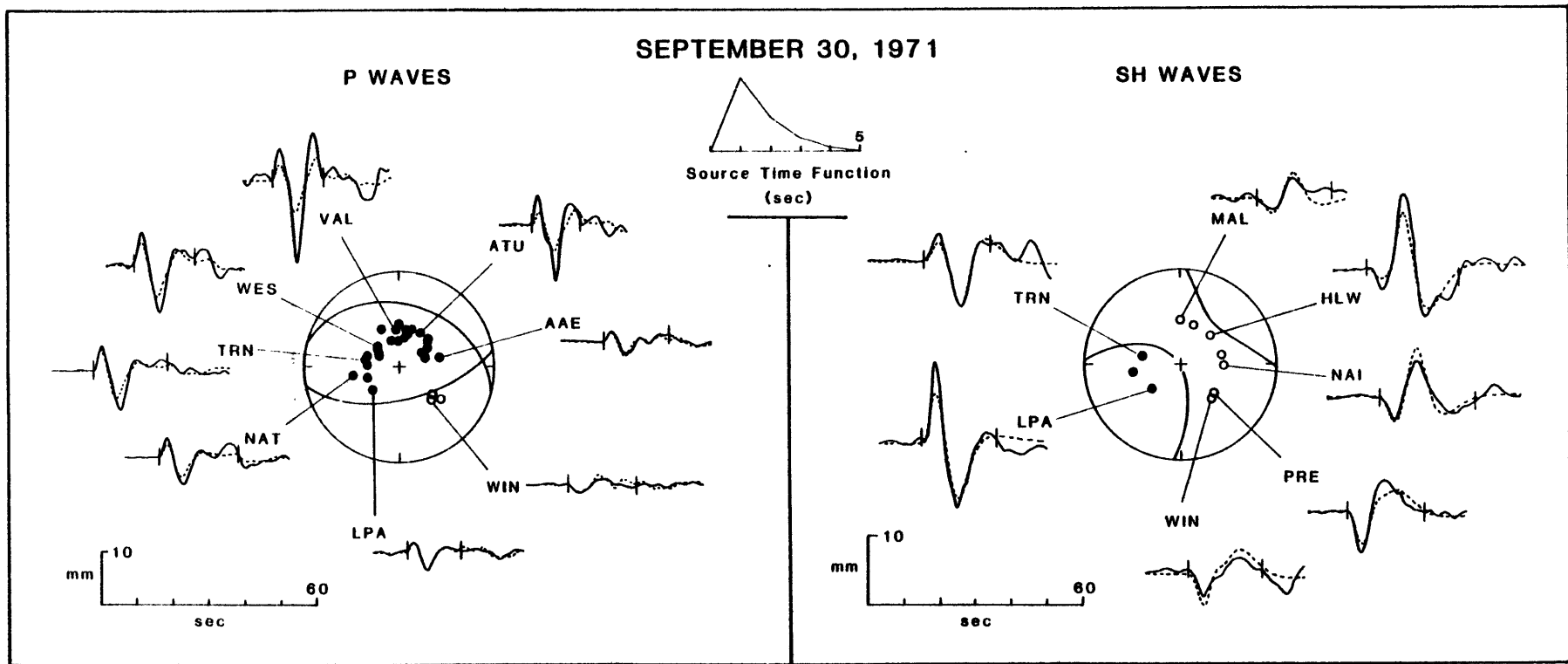
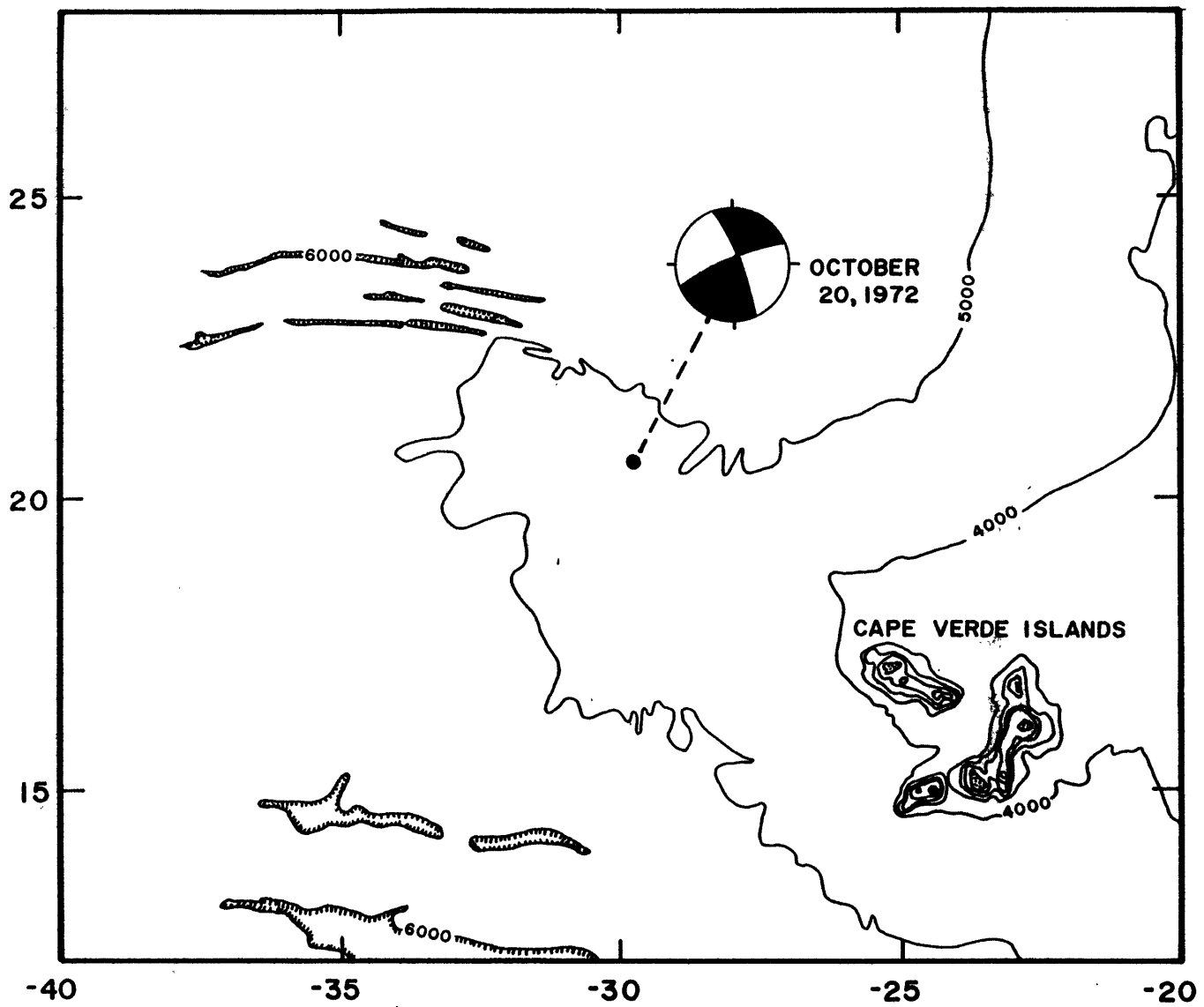


Figure 6.5

Figure 6.6



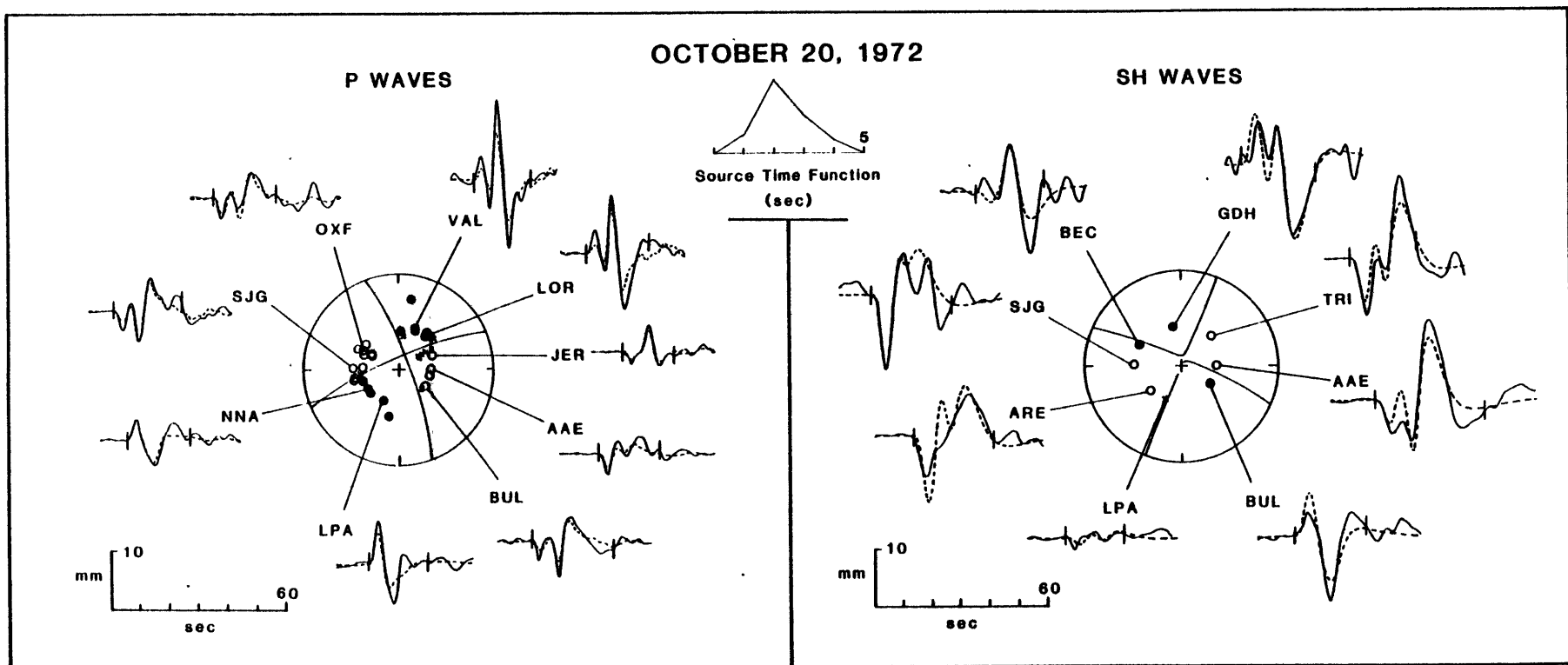


Figure 6.7

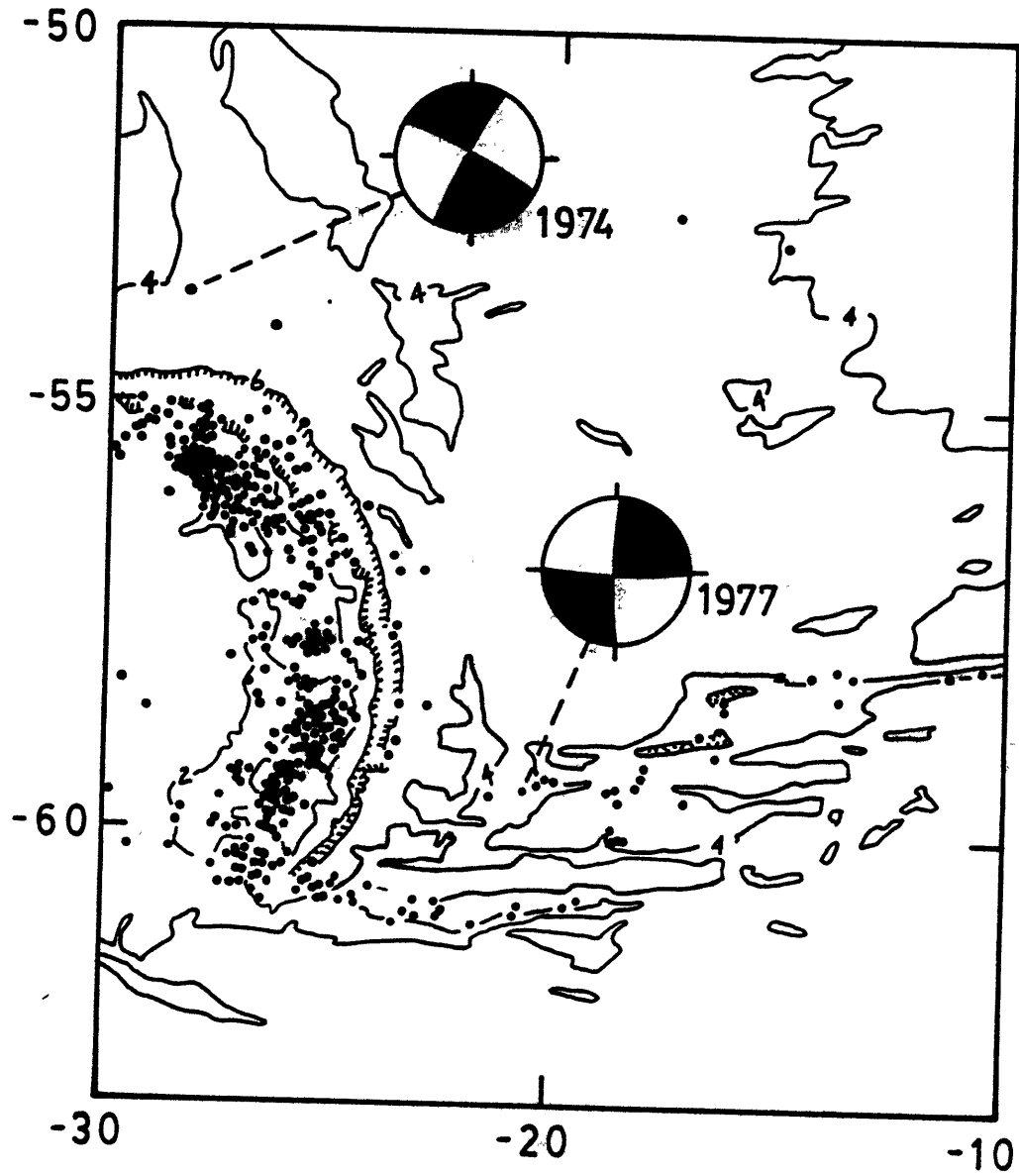


Figure 6.8

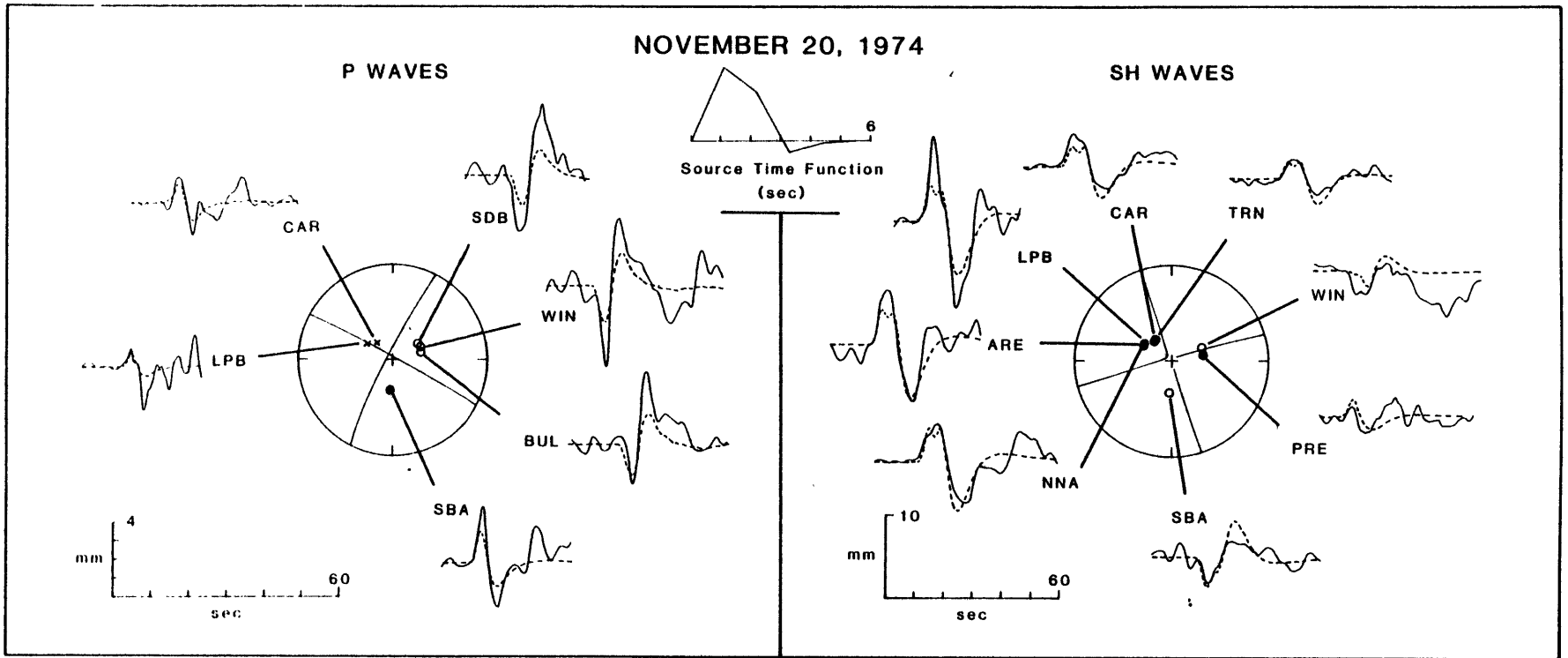
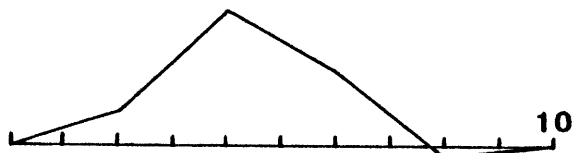


Figure 6.9

AUGUST 26, 1977



Source Time Function  
(sec)

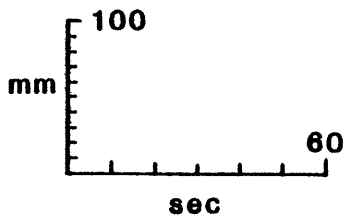
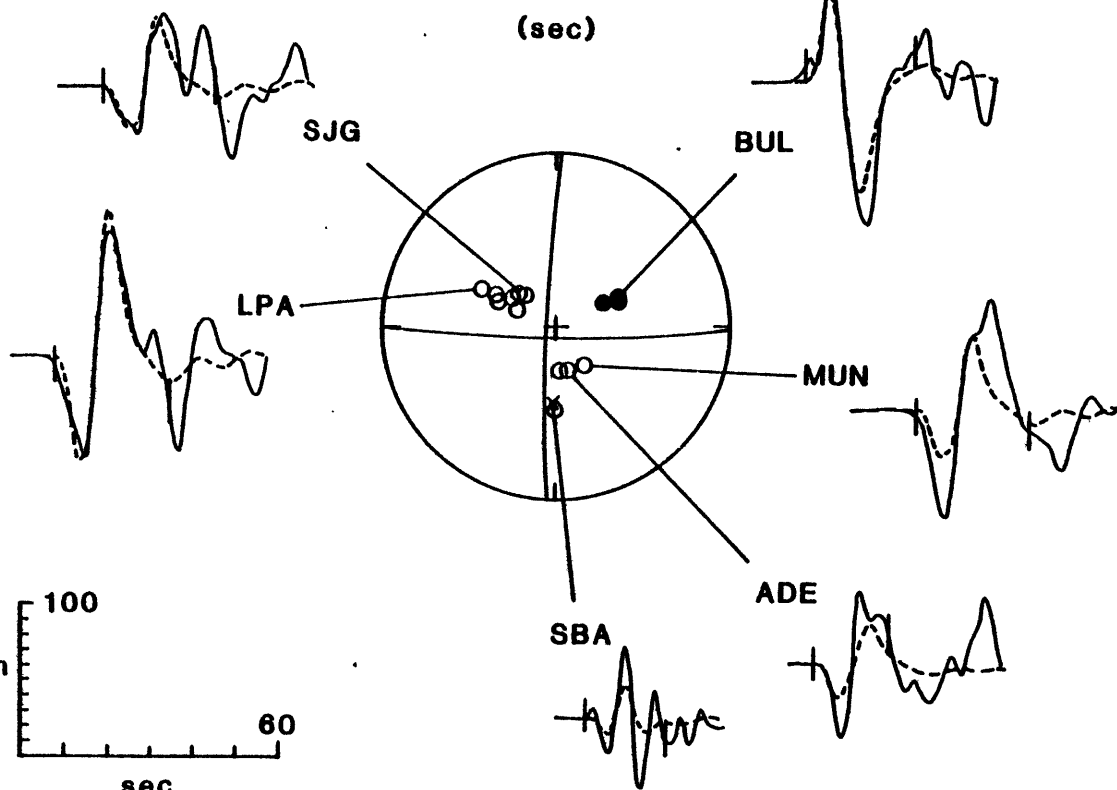


Figure 6.10

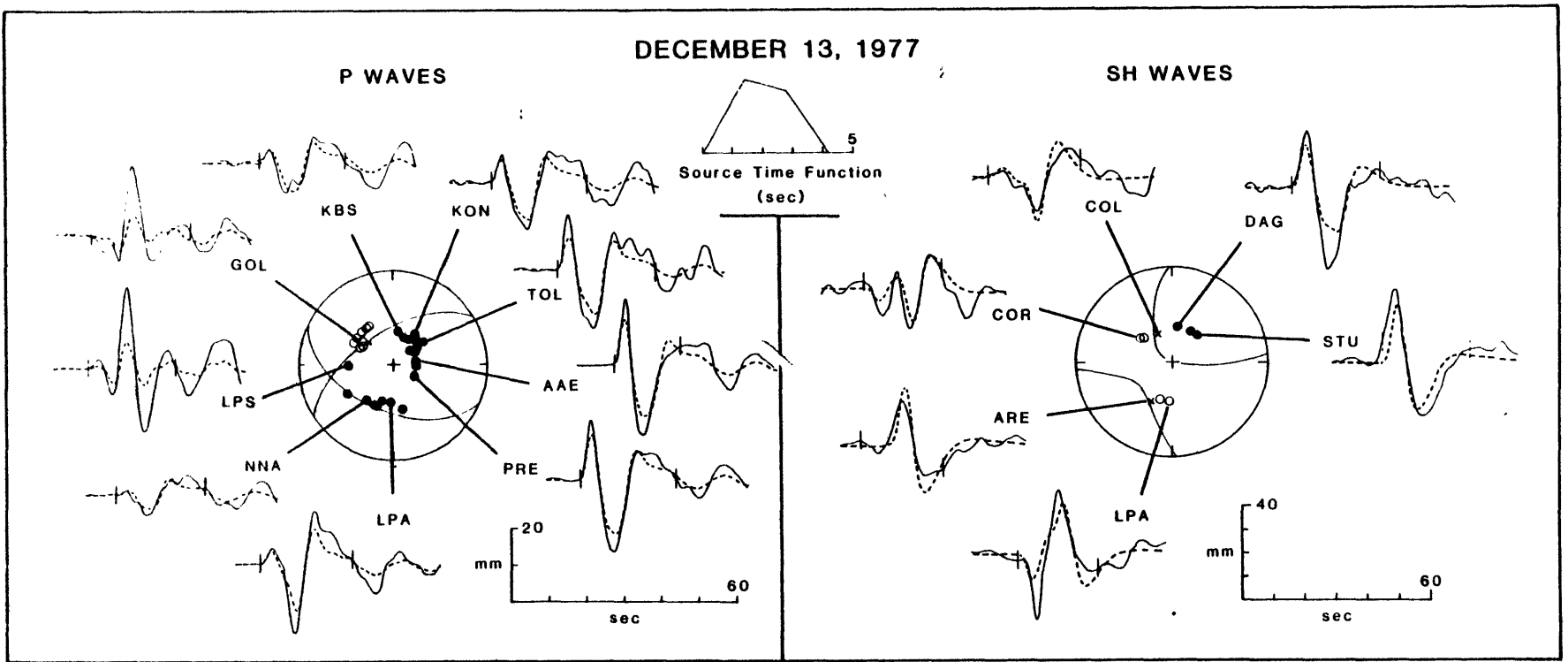


Figure 6.11

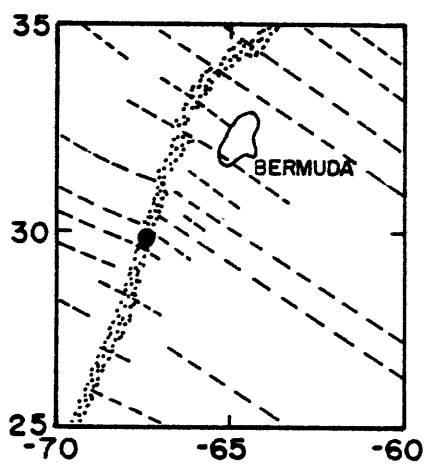
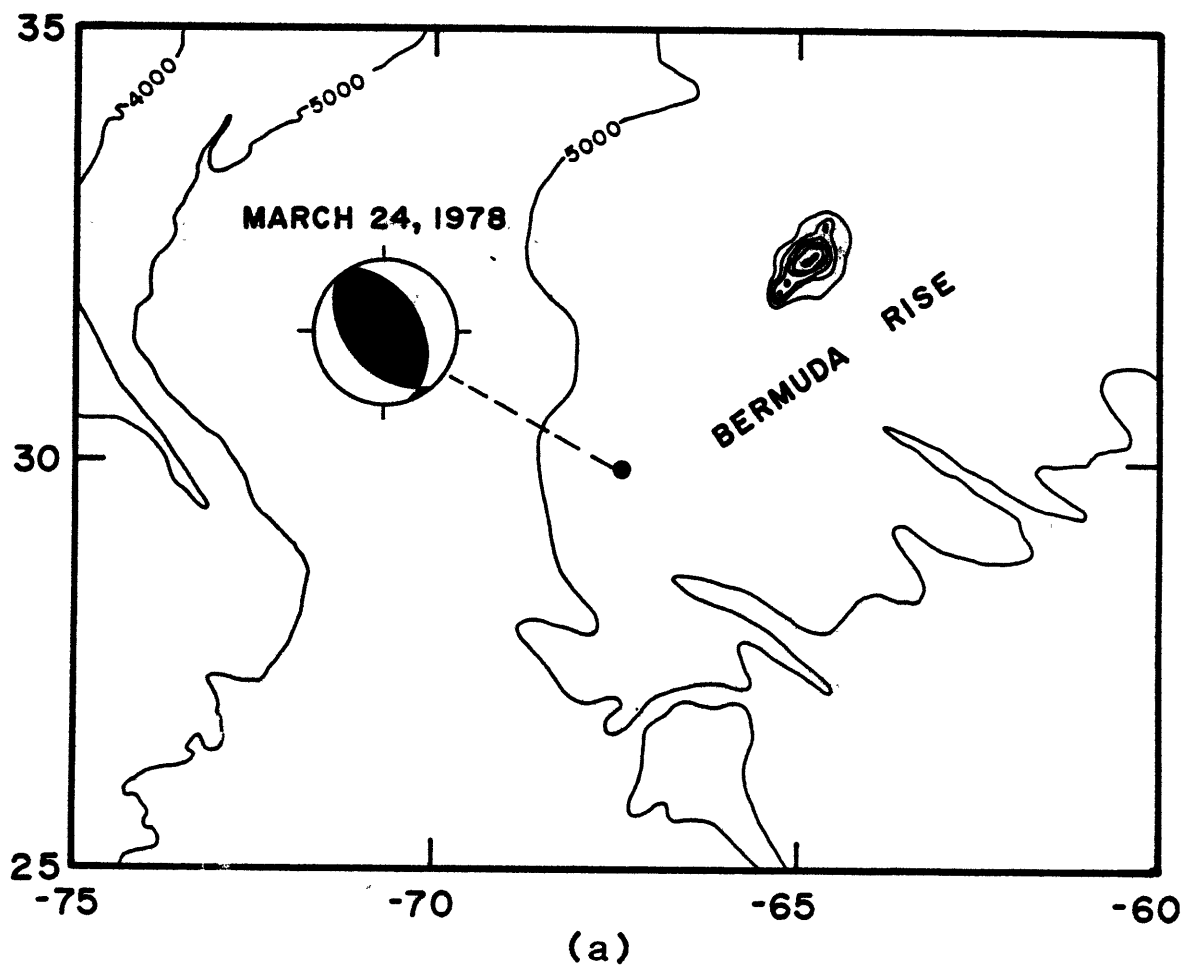


Figure 6.12



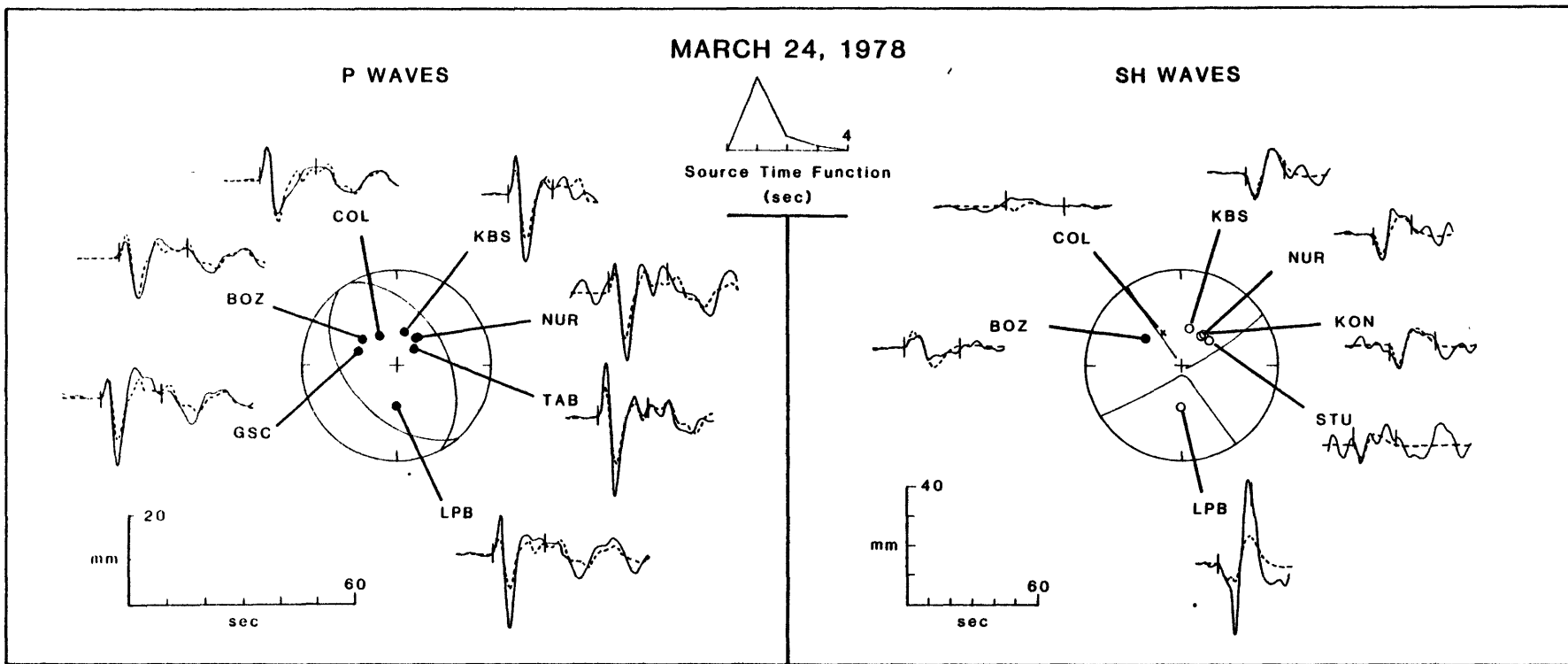


Figure 6.13

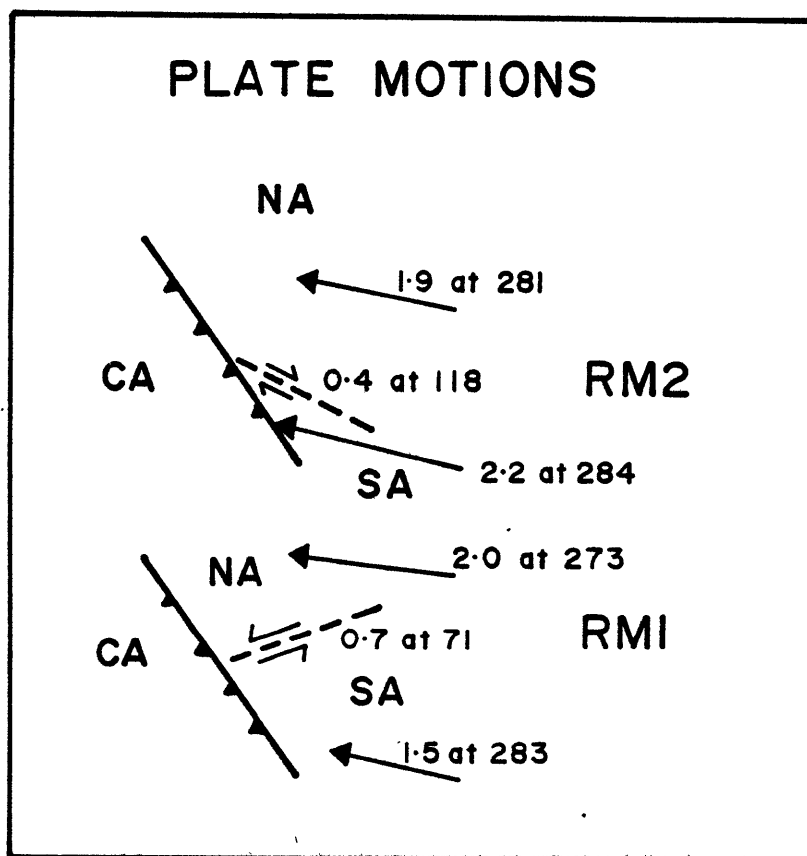


Figure 6.14

## CHAPTER 7. INTRAPLATE EARTHQUAKES IN THE PACIFIC OCEAN

## INTRODUCTION

In this chapter, we present source studies of oceanic intraplate earthquakes in older oceanic lithosphere of the Pacific Basin and in several back-arc or marginal basins. Source studies of events along the mid-ocean ridge system in the Pacific (in lithosphere less than about 30 m.y. old) are presented in Chapter 8. The observation in Chapter 2 that older oceanic lithosphere is much less seismically active than young lithosphere is largely based on the fact that the western Pacific (which contains most of the oldest oceanic lithosphere at present) is virtually aseismic. Implications of this observation for the physical state of oceanic lithosphere and the intraplate stress field are discussed in Chapter 9. Aside from Hawaii (represented by one event in this chapter), the region of the Gilbert Islands swarm of 1981-83 (Chapter 2) and a diffuse zone of seismicity in the eastern Caroline Islands are the major sites of intraplate seismicity in the western Pacific. The South China Sea, Philippine Sea, and South Fiji Basin have also been the locus of intraplate earthquakes large enough to study. One large event is known in older lithosphere of the Antarctic plate in the southeastern Pacific.

Stein [1978] conducted a source study of a small earthquake on the Emperor Trough using surface waves; this event was a little too small and poorly recorded for us to attempt a body-wave inversion study. Because data have only recently become available, we have not investigated the larger events of the Gilbert Islands swarm, but comprehensive source studies of four of them are presented by Lay and Oka [1983].

Unlike the earthquakes in Chapter 4 or 5, there is no single Pacific-wide tectonic context in which to interpret the source mechanisms of the intraplate earthquakes in this chapter. Our discussion of the tectonic significance of these events will focus on local rather than plate-wide processes, in particular the association of present-day seismicity with relict tectonic features.

#### SOURCE MECHANISMS

In this section we present the source mechanisms of 8 oceanic intraplate earthquakes in the Pacific Ocean and several of its marginal basins, obtained from the inversion of P and SH waveforms using the procedure developed by Nabelek [1984], as described in Chapter 3. Epicentral data for these earthquakes are listed in Table 7.1. The focal mechanisms and the observed and synthetic seismograms are given in a series of figures, with P waves and SH waves shown on separate focal spheres (with the appropriate radiation pattern) for clarity. The synthetics shown were generated with the single best-fit solution, and have not been individually rescaled for improved fit. The station code and geographic location of all stations used in the inversions are listed in Appendix E. The best-fitting source parameters for all earthquakes, together with formal errors, are given in Table 7.2.

#### October 7, 1965

The epicenter of the October 7, 1965 earthquake ( $m_b = 5.8$ ,  $M_S = 5.6$ ) is in the southwestern end of the South China Basin, the westernmost marginal basin in the Pacific. Karig [1971] classified it as an 'inactive' marginal basin. A few earthquakes have been located along the margin of the basin, but the interior of the basin has been fairly quiet [Wang et al., 1979]. The epicenter is a short distance

northwest of the Reed Bank, an apparently continental block rifted away from China [Taylor and Hayes, 1980] (Figure 7.1). Most of the oceanic lithosphere of the South China Basin formed between 32 and 17 m.y.B.P. at a spreading center trending E-W. The southwestern part of the basin, however, apparently was created at a NE-trending spreading center whose axis is located only about 60 km northwest of the epicenter [Taylor and Hayes, 1983]. Unfortunately, no magnetic anomalies have been identified in the area and thus there is no reliable information about the timing of this minor spreading episode. Heat flow measurements are consistent with an age similar to the rest of the South China Basin, however [Taylor and Hayes, 1983]. The sediments in the epicentral region are relatively undisturbed, indicating that major intraplate deformation has not occurred there [Wang et al., 1979].

Using surface wave radiation patterns, Wang et al. [1979] determined a thrust-faulting mechanism for this event (240/50/100) and a seismic moment of  $1 \times 10^{25}$  dyne-cm. They also modeled P waveforms to constrain the depth to be very shallow, about 5 km below the seafloor. A seismic moment of  $9 \times 10^{24}$  was estimated from the body waves. The inversion solution is similar, but rotated counterclockwise about  $20^\circ$  (220/46/79; Figure 7.2) from that of Wang et al. Taylor and Hayes [1983] observed that the nodal planes of this earthquake are subparallel to the nearby relict spreading center and suggested that it "occurred along a fault plane whose strike was largely determined by the pre-existing spreading fabric of the oceanic basement".

The centroid depth is 3.6 km and the moment is  $5.5 \times 10^{24}$  dyne-cm. The P waveforms are well-matched in shape and amplitude by this

solution; it is difficult to see how the P waves could support a moment as high as that suggested by Wang et al. The time function found in the inversion (4 s in duration) is quite similar to the 4.5 s trapezoid time function they used. The SH waves from this earthquake are relatively small and the signal-to-noise ratio is poor. The emergent character of the SH wave at QUE is fairly clear on the original horizontal components.

#### August 20, 1968

The August 20, 1968 ( $m_b = 5.6$ ,  $M_s = 5.0$ ) earthquake is located at the eastern end of the Sorol Trough in the western Pacific (Figure 7.3). It belongs to a diffuse cluster of earthquakes in the eastern Caroline Islands which may be related to a developing plate boundary between the Pacific plate and a separate Caroline plate [Weissel and Anderson, 1978]. The relation of the source mechanisms of this event and the August 30, 1976 earthquake to the tectonics of this area are discussed further in a later section of this chapter.

A thrust-faulting mechanism (160/43/60) was obtained for this event by Bergman and Solomon [1980], using first motion polarities. The slip angle is constrained only by the polarity of several near-nodal arrivals. Using this mechanism, Wiens and Stein [1983a] modeled P waveforms and estimated the depth to be 10 km below the seafloor. The body-waveform inversion indicates that this earthquake has a larger component of strike-slip motion than the mechanism of Bergman and Solomon: 126/68/30 (Figure 7.4). One nodal plane is subparallel with the trend of the Sorol Trough (Figure 7.3). The distribution of P-wave stations for this event is quite poor, but

the few SH waveforms are well-distributed and clearly recorded. The centroid depth is 8.0 km and the seismic moment is  $4.5 \times 10^{24}$  dyne-cm.

#### May 21, 1972

The small May 21, 1972 earthquake ( $m_b = 5.6$ ,  $M_s = 4.9$ ) is located in the South Fiji marginal basin. The only other seismicity in the region consists of a very large event in October 1977 and its aftershocks. The source mechanism for the main shock is discussed below. According to Watts et al. [1977] the oceanic lithosphere in this area was created at a system of three spreading ridges which were active between 35 and 28 m.y.B.P. Most of the oceanic lithosphere in the southwest of this area has apparently been consumed in a subduction zone which is preserved in the complex, rugged bathymetry between New Caledonia and Northland, New Zealand. The extinct RRR triple junction is located at  $26.7^\circ\text{S}$  and  $174.5^\circ\text{E}$ , a short distance northwest of the epicenter of the May 1972 earthquake (Figure 7.5). This event appears to be located precisely on the southeast-trending relict spreading center.

Bergman and Solomon [1980] presented first-motion polarities for this earthquake, but the distribution is inadequate to completely constrain the focal mechanism; compressional first arrivals are consistently observed to the northwest, however. Wiens and Stein [1983a] inferred a mechanism from this data (but did not specify it) and modeled P waveforms to estimate the depth of the May 1972 earthquake to be 10 km. The distribution of usable P waveforms for this event, like the first motion data, is poor. The SH waves, while few in number, are clearly recorded and better-distributed (Figure 7.6) so the mechanism is fairly well constrained. Note, however, that the

formal errors for the source parameters found in the inversion for this event are larger than usual (Table 7.2). The focal mechanism (330/71/164) is characterized by right-lateral strike-slip motion on a nodal plane which is very nearly parallel to the relict spreading center on which the event is located. The centroid depth is 10.8 km (in good agreement with Wiens and Stein) and the seismic moment is  $4.1 \times 10^{24}$  dyne-cm.

#### April 26, 1973

A large earthquake beneath the northeast coast of Hawaii on April 26, 1973 ( $m_b = 5.9$ ,  $M_s = 5.9$ ) caused extensive damage in Hilo and attracted more interest than most intraplate earthquakes. The focus was located beneath the flank of Mauna Kea, a volcano which has been dormant in historical times (Figure 7.7). Most investigators have concluded that the April 1973 earthquake is not directly related to the movement of magma, which accounts for much of the seismicity occurring beneath Kilauea and Mauna Loa, the two currently active volcanoes on Hawaii. Shallow magmatic activity beneath Mauna Loa has been clearly identified as the cause of the only Hawaiian earthquake since 1951 which is larger than the 1973 Hilo event: the November 29, 1975 Kalapana earthquake [Ando, 1979]. In a later section, we discuss further the tectonic significance of the 1973 Hilo earthquake, including its possible relation to bending stresses induced in the lithosphere by the load of the island.

Unger and Ward [1979] made an extensive study of the location of the mainshock and its many aftershocks, using data from the local seismic array on Hawaii. They found a depth of 48 km for the mainshock (35-55 km for the aftershocks), making this one of the deepest known



events in the interior of an oceanic plate. Supplementing the local seismic array data with first motion polarities at teleseismic stations, they proposed a predominantly strike-slip focal mechanism for this earthquake: 110/61/345.

An extensive body-wave modeling study of the 1973 Hilo earthquake was conducted by Butler [1982]. He used long-period teleseismic P, SH, and SV waveforms in a trial-and-error approach and refined the model with a formal inversion of P and SH waveforms. Butler emphasizes the complex nature of the faulting in this earthquake and refers to it as a double event. He was unable to find a mechanism for the first subevent which would satisfactorily fit both the P and SH waveforms, although his "1P" and "1S" mechanisms are not very different (0/94/141 and 351/81/152, respectively). The second subevent, located northeast of the first and delayed by several seconds, is 346/95/145. The depths of the two subevents are 42 and 32 km, respectively, and the total seismic moment is approximately  $4.5 \times 10^{25}$  dyne-cm.

Butler's mechanism is similar to, but rotated by  $33^\circ$  with respect to the mechanism proposed by Unger and Ward [1979]. He explains both this discrepancy and the difference in depth by reference to the complicated and largely unknown velocity structure of Hawaii, which can have a severe effect on the travel paths to the local stations. Another factor in the depth discrepancy is that Unger and Ward's depth would correspond to the point at which faulting initiated, while the depth given by Butler would correspond to the centroid depth, or the approximate center of the ultimate fault area.

For our inversion study, we adapted the layered source structure of Butler [1982]: the upper three layers are identical, but we

approximated the lower part as a halfspace with  $\alpha = 8.5$  km/s,  $\beta = 4.6$  km/s, and  $\rho = 3.5$  g/cm<sup>3</sup>. Station coverage for this earthquake is good and the signal-to-noise ratio at most stations was excellent. The 8 P and 8 SH waves selected for the inversion provide very good azimuthal coverage.

We began our study by using the double event solution of Butler [1982] as a starting point for the inversion, but it became immediately apparent that a double source provided at best a very weak minimum in the residual error. Our preferred solution for this event is a single source, with a mechanism of 87/64/346 (Figure 7.8), quite similar to Butler's 1P solution. The centroid depth is 41.1 km, and the seismic moment is  $3.7 \times 10^{25}$  dyne-cm. We found that a significant reduction in the residual (mostly from the SH waves) could be obtained by modeling this event as a horizontally-propagating point source with the direction of propagation toward the east (N87°E). For such a model, the source time function is merely expanded or compressed at different stations, depending on the orientation of the rupture vector and the departing ray from the source. Note that the source time function found in the inversion has two rather distinct pulses (Figure 7.8). A rupture velocity of 3.2 km/s was used, but it is not well-constrained by the waveforms.

While we do not dispute Butler's claim for a certain amount of complexity to this event, we disagree with his characterization of this earthquake as a double event. Although our inversion solution and Butler's multiple source model obviously provide a very similar picture of this earthquake, the multiple source mechanism results in no significant decrease in the residual error over a single source

geometry with simple horizontal rupture propagation and some complexity in the source time function. We are inclined to reserve terms such as "double event" for earthquakes in which there is a more significant change in the rupture geometry or a longer delay between subevents than appears to be the case for the 1973 Hilo earthquake. Among oceanic intraplate earthquakes, those on June 25, 1974 (Chapter 5) and May 9, 1971 (Chapter 8) are good examples of double (or triple, in the second case) events.

#### April 12, 1974

A small ( $m_b = 5.5$ ,  $M_s = 4.9$ ) earthquake occurred on April 12, 1974 at the intersection of the extinct Central Basin Spreading Center (CBSC) and the Palau-Kyushu Ridge, in the Philippine Sea (Figure 7.9). The tectonic history of the western Philippine Basin has been the subject of much dispute; our interpretation of the source mechanism of the April 1974 earthquake relies on the recent synthesis of Hilde and Lee [1984], but does not depend crucially on it. Creation of oceanic lithosphere at the CBSC occurred in two phases: 1) From 60-45 m.y.B.P., the direction of spreading was NE-SW. 2) At about 45 m.y.B.P., the CBSC was reorganized into small, slower spreading, E-W trending ridge segments offset in a right-lateral sense by N-S trending fracture zones. At the same time, the initiation of subduction on the Palau-Kyushu Ridge (possibly a long transform fault during the earlier spreading episode) trapped a large area of oceanic lithosphere into what is today the West Philippine Basin. Spreading on the CBSC ceased at about 35 m.y.B.P. Subsequent development of the Parece Vela marginal basin east of the Palau-Kyushu Ridge isolated the epicentral region from the active boundaries of the Philippine plate.

A focal mechanism for the April 12, 1974 earthquake, characterized by right-lateral strike-slip motion on a nodal plane striking E-W (274/76/180), was reported by Bergman and Solomon [1980], based on first motion polarities. Wiens and Stein [1983a] modeled P waves for this event, using Bergman and Solomon's mechanism, and estimated the depth to be 7 km below the seafloor. Because of the small size of this event and its location (there are virtually no seismograph stations to the east), the number of stations with usable waveform data is small and the distribution of stations is also poor. Even so, the available P and SH waveform data are incompatible with the strike-slip mechanism of Bergman and Solomon [1980]. The preferred mechanism is characterized by thrust faulting on nodal planes striking roughly E-W, subparallel with the strike of ridge axis segments on the CBSC (80/51/77; Figure 7.10). The seismic moment is quite small,  $1.6 \times 10^{24}$  dyne-cm, and the centroid depth is 11.6 km.

#### August 30, 1976

The large earthquake on August 30, 1976 ( $m_b = 5.8$ ,  $M_s = 5.9$ ), like the August 20, 1968 earthquake discussed above, belongs to a group of earthquakes which may be associated with the development of a true plate boundary between the Pacific plate and what may evolve into a separate Caroline plate (Figure 7.3). The source mechanisms of these two earthquakes are discussed in the context of this interesting tectonic situation in a later section of this chapter.

Both Hegarty et al. [1983] and Wiens and Stein [1983a] have reported source mechanisms for this earthquake, based on first motions and waveform modeling (both P and SH waves in the case of Hegarty et al.). The focal mechanisms are quite similar, but they disagree

somewhat as to the source depth: Hegarty et al. give a mechanism of 330/69/175, a depth of 20 km, and a seismic moment of  $1.5 \times 10^{25}$  dyne-cm, while Wiens and Stein's mechanism is 338/77/180, with a depth of 28 km.

This earthquake was very well recorded; we obtained clear P and SH waveform data over an azimuthal range of  $270^\circ$  (Figure 7.11). The focal mechanism found in the inversion (327/74/176) is closer to that of Hegarty et al., possibly because SH waves were used in both studies. The centroid depth is 21.3 km, in good agreement with Hegarty et al. The depth signature in the SH waves for this event is remarkably clear at several stations (e.g., RIV, ANP, and SHK) and we suspect that the discrepancy with the depth reported by Wiens and Stein is largely due to their using only P waveforms in their study. The seismic moment found in the inversion ( $1.8 \times 10^{25}$  dyne-cm) is also in close agreement with Hegarty et al.

#### February 5, 1977

On February 5, 1977 a large ( $m_b = 6.1$ ,  $M_s = 6.4$ ) earthquake occurred in a remote corner of the southeast Pacific, a region with a very complex tectonic history [e.g., Weissel et al., 1977; Cande et al., 1981]. The lithosphere of the epicentral region was formed at the former Antarctic-Aluk spreading ridge, which along with most of the Aluk plate, has been subducted beneath the Antarctic Peninsula [e.g., Barker, 1982]. The epicenter lies between two major fracture zones trending NW-SE (Figure 7.12).

Bergman and Solomon [1980] noted that all teleseismic first motions for this event are compressional, indicating a thrust faulting mechanism for the February 1977 event, but the first motion data

provide no constraint on the strike of the nodal planes. Using surface wave radiation patterns, Okal [1981] determined that the mechanism involved thrust faulting on planes striking nearly N-S (1/58/82). He also reported a seismic moment of  $4.4 \times 10^{25}$  dyne-cm and a depth of 35 km, based on the ratio of amplitudes of Love and Rayleigh waves. A forward-modeling study of the P waveforms for this event by the author indicated that it actually occurred about 15 km below the seafloor (unpublished data), a conclusion confirmed by Wiens and Stein [1983a].

The source structure for the inversion included a 1.4 km thick sediment layer [Hegarty et al., 1983]. with  $\alpha = 2.0$  km/s,  $\beta = 0.8$  km/s, and  $\rho = 2.0$  g/cm<sup>3</sup>. The distribution of stations at which clear P and SH waveforms were recorded is quite good and the inversion quickly converged to a solution very similar to the previous solutions (Figure 7.13). The best-fitting focal mechanism is 4/43/74, with a seismic moment of  $3.6 \times 10^{25}$  dyne-cm, and a centroid depth of 14.7 km. The source time function has a small initial pulse, followed by the main rupture (Figure 7.13).

#### October 17, 1977

The epicenter of the large October 17, 1977 event ( $m_b = 6.2$ ,  $M_s = 6.7$ ) is located a short distance southwest of the May 21, 1972 earthquake discussed above, at the northern end of the Three Kings Rise in the South Fiji marginal basin (Figure 7.5). According to the tectonic history proposed for this region by Watts et al. [1977], the October 1977 event is close to the boundary between oceanic lithosphere created at a system of three spreading ridges and a relict subduction zone trending roughly NW-SE between New Caledonia and Northland, New Zealand. The origin of the Three Kings Rise is unclear, but Watts et al. do not associate it with the extinct spreading ridge system.

Because of the magnitude of this earthquake (causing most of the shear waves to be clipped or too faint to digitize), only 3 usable SH waveforms were obtained, but they straddle one nodal plane of the SH radiation pattern. In the epicentral distance range used in the inversion, most of the P waveform data for this event are in the west and north, but we obtained several waveforms to the east and south as well. Not surprisingly, many of the P waveforms show strong finiteness effects. For the point source inversion, we selected a small but well-distributed set of the simplest P waveforms. The focal mechanism of this event is very well constrained, even by the small set of data used here, to be a predominantly strike-slip mechanism (263/77/11; Figure 7.14) with right-lateral motion on the N-S trending nodal plane which parallels the eastern scarp of the Three Kings Rise (Figure 7.5). Because of its similarity to the inferred fault plane for the nearby May 1972 event, the nodal plane striking approximately N5°W is perhaps more likely to correspond to the fault plane of this event. An argument could also be made that the fault plane trends E-W, however, if the morphology of the northern end of the Three Kings Rise were attributed to its truncation by an E-W trending fracture zone. The seismic moment is  $1.7 \times 10^{26}$  dyne-cm, making this one of the largest known oceanic intraplate earthquakes, and the centroid depth is 13.2 km.

The P waveforms which show the most complexity are those located nearest to the nodal planes; they are probably influenced more by directivity in the rupture propagation than by any intrinsic complexity (e.g., multiple rupture or changes in mechanism) in the rupture history of this earthquake. The source time function is 7.5 s in duration and

remarkably simple. Because of the paucity of SH wave data, we did not attempt to infer the fault plane for this event by using a horizontally -propagating point source model.

## DISCUSSION

Relationships between the local tectonic setting and the earthquakes studied in this chapter have been discussed briefly in the presentation of the individual source mechanisms. In this section we extend the discussion of the tectonic significance of the earthquake source mechanisms for two cases (Caroline Islands and South Fiji Basin) in which two earthquakes are involved. We also consider further the significance of the 1973 Hawaiian earthquake.

### Caroline Islands

A variety of geophysical evidence indicates that lithosphere in the East and West Caroline Basins at one time constituted a separate plate but subsequently became attached to the Pacific plate [e.g., Bracey, 1975; Mammerickx, 1978; Weissel and Anderson, 1978; Fornari et al., 1979; Hegarty et al., 1983]. Although there is evidence that deformation has occurred recently around the northern and eastern margins of the former Caroline plate, it is not yet clear that a true plate boundary between the Caroline and Pacific plates has developed. Hegarty et al., [1983] suggest that the northern and eastern boundaries of the plate, with which we are concerned here, have been active only since about 1 m.y.B.P. The seismicity of the area, while high by intraplate standards, is diffuse and for the most part not clearly associated with the proposed plate boundaries.

The August 20, 1968 event studied here is one of the few events which does seem to be directly associated with one of the zones of



deformation identified as an incipient plate boundary (Figure 7.3). The epicenter is in a transitional part of the proposed Pacific-Caroline plate boundary: to the south, the deformation is expected to be mainly compressional across the Mussau Trough, while along the Sorol Trough to the west, horizontal shear is expected to dominate [Weissel and Anderson, 1978; Fornari et al., 1979]. Hegarty et al. [1983] noted that the thrust-faulting mechanism (P axis oriented approximately E-W) published by Bergman and Solomon [1980] for the August 20, 1968 event is roughly consistent with this model. Our preferred mechanism for this event, however, involves a larger component of strike-slip motion than the previous mechanism. The nodal plane striking NNW, parallel to the Sorol Trough and the structural grain in the epicentral area (Figure 7.3) is the preferred fault plane for this event. The inferred orientation of maximum horizontal compression at this part of the proposed plate boundary is then nearly E-W (not significantly different than the orientation inferred from the thrust-faulting mechanism). The sense of motion on this plane is left-lateral. A large strike-slip component to the deformation along the eastern end of the Sorol Trough is consistent with the magnetic data [Hegarty et al., 1983], and is in better agreement than the earlier thrust-faulting mechanism with the expected style of deformation in this part of the Caroline-Pacific boundary zone.

The other large earthquake in the eastern Caroline Islands for which we have a source mechanism, on August 30, 1976, appears to be unrelated to any of the zones of deformation outlining the proposed Caroline plate and thus should probably be considered a true intraplate event [Hegarty et al., 1983]. If the nodal plane striking ENE

corresponds to the fault plane, the direction of maximum horizontal compressive stress is approximately NE-SW, in reasonable agreement with the relative motion between the Pacific-Caroline plate and the Indo-Australian plate at the New Guinea Trench to the southwest [Nishiwaki, 1981]. There is no independent evidence for selecting this nodal plane as the fault plane, however. Finally, it is worth noting that a large ( $m_b = 5.9$ ,  $M_s = 6.0$ ) earthquake occurred on December 8, 1983 at  $3.78^\circ\text{N}$  and  $149.00^\circ\text{E}$ , on a portion of the proposed Caroline-Pacific plate boundary which has been relatively aseismic until now. Its mechanism will provide additional constraint on the present nature of deformation in this area.

#### South Fiji Basin

The focal mechanisms of the May 1972 and October 1977 earthquakes in the South Fiji Basin are quite similar, indicating right-lateral strike-slip motion on a plane striking slightly west of north. We take these to be the fault planes of these two events, for the reasons described in the individual source studies. Both events are clearly associated with relict features in the oceanic lithosphere, although the origin of Three Kings Rise is unclear. Presumably, these features represent zones of weakness, but there are certainly many other such features with a variety of orientations in a region with such a complex tectonic history [Watts et al., 1977].

Assuming that these two earthquakes occurred on faults which are optimally oriented with respect to the existing stress field, we infer that the state of stress in the South Fiji Basin is characterized by a maximum horizontal compressive stress oriented approximately NNE. The minimum principal stress is subhorizontal and oriented ESE. Such a

stress field cannot be readily related to the complex system of plate boundaries around the South Fiji Basin, but the consistency of the two earthquake mechanisms suggests that they provide a significant constraint on future such efforts.

### Hawaii

The source of the stress relieved in the April 26, 1973 Hilo earthquake is of particular interest, because this event, at a depth of 41 km, is the deepest large oceanic intraplate earthquake known (Chapter 9). Smaller earthquakes have been located at depths of up to 60 km beneath the summits of the two presently active volcanoes on Hawaii, Mauna Loa and Kilauea, but the deepest such events are thought to be related to the migration of magma [Eaton, 1962; Koyanagi and Endo, 1971; Koyanagi et al., 1972]. Mantle-depth earthquakes also occur rather uniformly beneath the entire island; it has been suggested that such events result from bending stresses in the lithosphere beneath the island load [Rogers and Endo, 1977]. but too few focal mechanisms are reliably known to evaluate this possibility.

The orientation of principal stresses inferred from this earthquake can be compared to the predictions of several models of the stress field in the central Pacific and the origin of the Hawaiian Island chain. The P axis of the focal mechanism of this earthquake is subhorizontal and oriented at N45°E, roughly radially to the island. As discussed above, the observed body waveforms (particularly SH waves) are better fit by synthetic waveforms generated with a source model incorporating a horizontally propagating point source from west to east. Assuming the nodal plane striking E-W corresponds to the fault

plane, therefore, we can make an improved estimate of the orientation of maximum horizontal compressive stress of  $N60^{\circ}E$ . Unger and Ward [1979] and Butler [1982] evaluated possible sources of stress released by the Hilo earthquake using the P axes of their focal mechanisms ( $N73^{\circ}E$  and  $N45^{\circ}E$ , respectively), since they found no justification for specifying one of the nodal planes of their mechanisms as the fault plane.

The orientation of the least horizontal compressive stress (approximately  $N30^{\circ}W$ ) inferred from the Hilo earthquake is not consistent with the formation of the Hawaiian Island Chain as a propagating tensional fracture in the lithosphere [Green, 1971] or with model of Jackson and Shaw [1975], in which the loci of volcanoes in the chain delineate the direction perpendicular to the least principal horizontal stress. A horizontal least principal stress striking  $N30^{\circ}W$  is also incompatible (but less so) with the suggestion of Turcotte and Oxburgh [1973] that the Hawaiian Island Chain represents deformation of the Pacific plate caused by the latitudinal component of its motion over a non-spherical earth (see Chapter 4).

Although the inferred orientation of the maximum horizontal compressive stress is not particularly close to the direction radial to the island of Hawaii, we carried out a preliminary investigation of the possibility that lithospheric bending stresses, induced by the island load, could be the dominant cause of the 1973 Hilo earthquake. The method is identical to that used to evaluate possible bending stresses in the lithosphere near the Kerguelen Plateau (Chapter 4), utilizing an analytical solution to the response of an elastic plate over a fluid to a cylindrical vertical load [Brotchie, 1971]. Below the neutral plane

near the edge of the load, the relative location of the 1973 earthquake, the radial deviatoric stress is extensional, not compressive, with a magnitude of several kilobars. Introduction of a weak zone beneath the island reduces the level of extensional stress, but never brings the part of the plate below the neutral plane into compression. We have not attempted a detailed quantitative model of bending stresses beneath Hawaii because there is still controversy concerning some of the fundamental parameters of the problem [e.g., Suyenaga, 1979]. It is unlikely, however, that refinements to the model used here will lead to a reversal in the sign of the bending stresses.

Finally, we consider the possible relationship between the Hilo earthquake and the East Rift Zone of the volcano Mauna Kea, dormant, but not extinct [Jackson et al., 1972]. The Hilo earthquake is approximately 45 km east of the central core of Mauna Kea. Figure 7.7 shows that the epicenter is about 5 km north of the surface expression of the rift zone, to which the inferred fault plane is parallel. The depth extent of the rift zone is unknown, but seismic activity associated with other volcanic rift zones on Hawaii is usually shallow, at depths of 15 km or less [Fiske and Jackson, 1972].

It is possible that this earthquake reflects the regional stress field in this portion of the Pacific and the hypocenter was simply localized on a conveniently oriented fault system. Until further data on the stress field are obtained to confirm this possibility, however, the principal stress directions inferred from the Hilo earthquake should probably not be given great weight in delineating the regional stress field in the central Pacific plate.

Table 7.1. Epicentral data\* for earthquakes studied

Date	Origin time h m s	Lat. °N	Long. °E	$m_b$	$M_S$	Age** (m.y.)
October 7, 1965	3 36 1.4	12.46	114.45	5.8	5.6	17-32
August 20, 1968	11 16 58.5	5.43	147.11	5.6	5.0	32
May 21, 1972	6 1 54.3	-27.10	174.97	5.6	4.9	28
April 26, 1973	20 26 27	20.05	-155.16	5.9	5.9	90
April 12, 1974	17 45 18.7	14.27	134.37	5.5	4.9	35
August 30, 1976	8 37 54.4	1.03	147.56	5.8	5.9	34
February 5, 1977	3 29 19	-66.49	-82.45	6.1	6.2	53
October 17, 1977	17 26 40.4	-27.93	173.13	6.2	6.7	28-35

\* Epicentral data from the ISC, except for  $M_S$  magnitude for October 7, 1965 [Wang et al., 1979].

\*\* Age of lithosphere estimated from magnetic anomaly identifications and magnetic chronology of LaBrecque et al. [1977], or from the isochrons determined by Sclater et al. [1980, 1981a].

Table 7.2 Source mechanisms obtained from body-wave inversion<sup>a</sup>

Date	Moment <sup>b</sup>	$t_s$ <sup>c</sup>	Depth <sup>d</sup>	Strike	Dip	Slip
October 7, 1965	5.5 ± 0.4	4.0 ± 1.0	3.6 ± 0.1	220.3° ± 1.8	45.9° ± 0.5	78.6° ± 1.6
August 20, 1968	4.5 ± 0.2	4.5 ± 1.5	8.0 ± 0.2	126.2 ± 1.2	67.9 ± 1.2	29.8 ± 1.8
May 21, 1972	4.1 ± 2.3	4.0 ± 1.0	10.8 ± 0.3	330.1 ± 4.2	70.5 ± 3.7	164.1 ± 4.4
April 26, 1973	37. ± 4.	7.5 ± 1.5	41.1 ± 0.1	86.6 ± 0.6	63.8 ± 0.9	346.2 ± 1.0
April 12, 1974	1.6 ± 0.2	1.5 ± 0.8	11.6 ± 0.1	80.0 ± 2.6	51.4 ± 0.8	77.2 ± 2.1
August 30, 1976	18. ± 2.	7.5 ± 1.5	21.3 ± 0.1	327.2 ± 1.2	73.9 ± 0.8	176.4 ± 1.1
February 5, 1977	36. ± 3.	5.0 ± 1.0	14.7 ± 0.1	3.5 ± 0.7	42.6 ± 0.2	74.2 ± 0.7
October 17, 1977	170. ± 10.	7.5 ± 1.5	13.2 ± 0.2	262.8 ± 0.9	76.6 ± 0.9	11.5 ± 1.1

a) The range indicated for each parameter is one standard deviation (formal error). The range of  $t_s$  is one half the width of the source time function element used in the inversion.

b)  $\times 10^{24}$  dyne-cm ( $10^{17}$  N-m).

c) Total duration of the source time function, sec.

d) Relative to the top of the crust (or sediment layer, if used), km.

## FIGURE CAPTIONS

Figure 7.1. Summary map of inferred tectonic elements in the South China Sea, together with the location and focal mechanism of the October 7, 1965 earthquake. Map reproduced from Figure 17 of Taylor and Hayes [1983]. Isobaths are 200 m (dotted), 2 km, and 4 km. Dashed parallel lines in the southwest part of the South China Sea denote the position of a relict spreading center. Dots outline area of normal oceanic crust. Magnetic anomalies are numbered.

Figure 7.2. Comparison of observed (solid line) long-period P and SH waves from the October 7, 1965 earthquake with synthetic waveforms (dashed lines) generated for the best-fitting point source mechanism found in the body-waveform inversion (Table 7.2). P and SH radiation patterns are shown on the lower focal hemisphere (equal area projection). All amplitudes are normalized to an instrument magnification of 3000; the amplitude scales correspond to the waveforms that would be observed on an original seismogram from such an instrument. The two vertical lines delimit the portion of each time series used in the inversion. Symbols for both types of waves are: open circle - dilatation, closed circle - compression, cross - emergent arrival. For SH waves, compression corresponds to positive motion as defined by Aki and Richards [1980]. First motions read from long-period seismograms but not used in the inversion are also plotted.

Figure 7.3. Locations and focal mechanisms of the August 20, 1968 and August 30, 1976 earthquakes in the eastern Caroline Islands. Tectonic elements and bathymetry (2000 and 4000 m contours) from Nishiwaki [1981]. Heavy line with teeth indicates proposed site of



compressional plate boundary between the Caroline and Pacific plates [Nishiwaki, 1981]. Other epicenters in the region are indicated by solid circles.

Figure 7.4. Comparison of observed P and SH waves from the August 20, 1968 earthquake with synthetic waveforms generated for the best-fitting point source mechanism found in the body-waveform inversion (Table 7.2). See Figure 7.2 for further explanation.

Figure 7.5. Locations and focal mechanisms of the May 21, 1972 and October 17, 1977 earthquakes in the South Fiji Basin. Bathymetric map reproduced from Figure 6 of Watts et al. [1977]. Isobaths at 100 m intervals. Stippling identifies ridges which may be associated with three formerly active spreading ridges in the area. Magnetic anomalies are numbered.

Figure 7.6. Comparison of observed P and SH waves from the May 21, 1972 earthquake with synthetic waveforms generated for the best-fitting point source mechanism found in the body-waveform inversion (Table 7.2). See Figure 7.2 for further explanation.

Figure 7.7. Location and focal mechanism of the April 26, 1973 earthquake beneath the northeast coast of Hawaii. (a) Regional bathymetry, from Drummond [1981]; 500 m contours. The trend of the Molokai Fracture Zone is shown by the dashed line. (b) Detail map showing the surface projection of aftershock zone and the location of the East Rift Zone of the volcano Mauna Kea, adapted from Figure 1 of Butler [1982].

Figure 7.8. Comparison of observed P and SH waves from the April 26, 1973 earthquake with synthetic waveforms generated for the source mechanism found in the body-waveform inversion (Table 7.2). The

source model for this event incorporates a horizontally-propagating point source (in the direction of strike,  $N87^{\circ}E$ , at a velocity of 3.2 km/s). The source time function shown is that which would be observed at an azimuth perpendicular to the rupture vector. The source time function is composed of trapezoidal elements with a rise time of 0.7 s and a flat portion 0.8 s in duration. Consecutive elements overlap by 0.7 s. See Figure 7.2 for further explanation.

Figure 7.9. Location and focal mechanism of the April 12, 1974 earthquake in the Philippine Sea. Bathymetry (500 m contour interval) from Nishiwaki [1981].

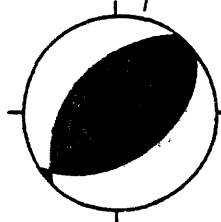
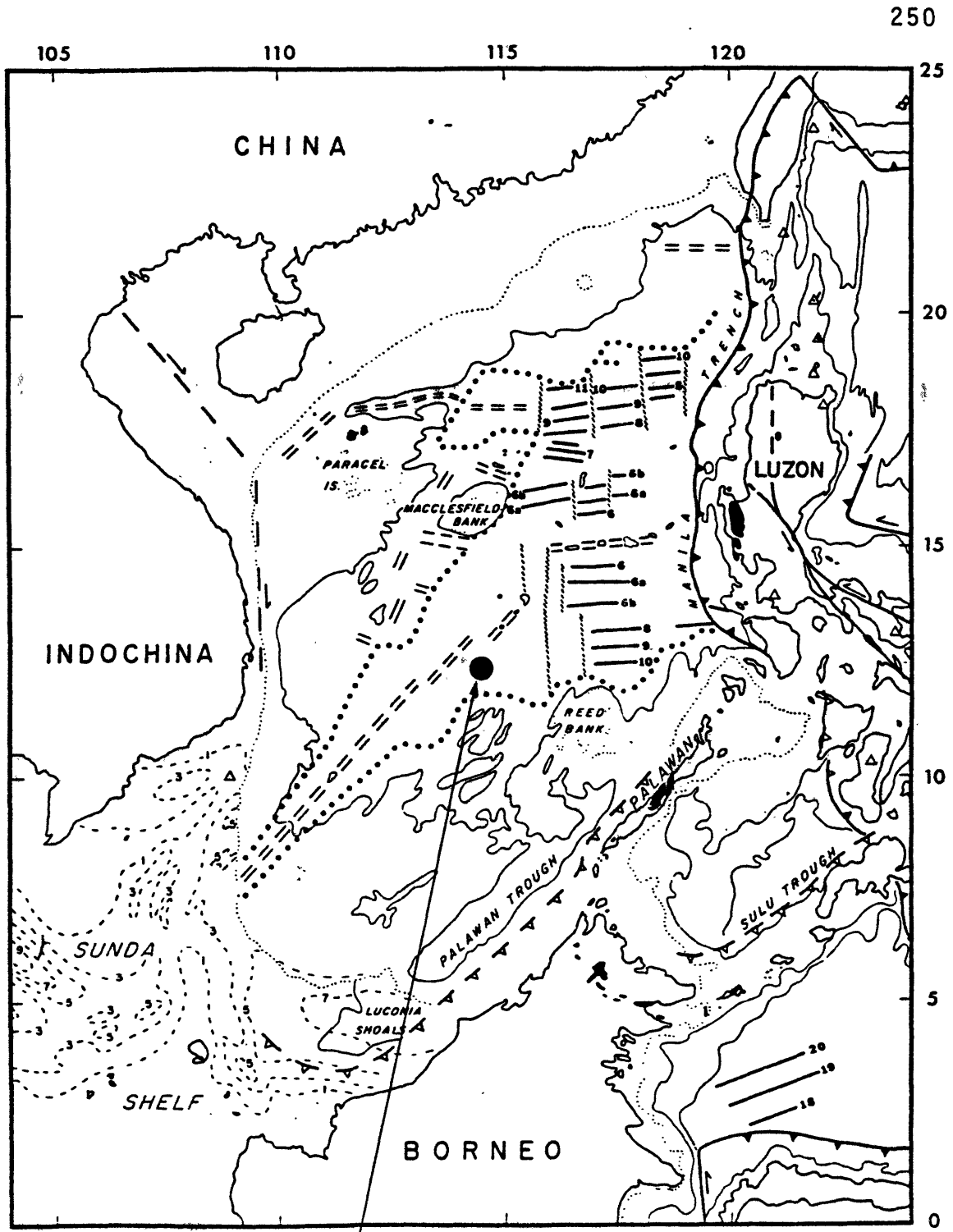
Figure 7.10. Comparison of observed P and SH waves from the April 12, 1974 earthquake with synthetic waveforms generated for the best-fitting point source mechanism found in the body-waveform inversion (Table 7.2). See Figure 7.2 for further explanation.

Figure 7.11. Comparison of observed P and SH waves from the August 30, 1976 earthquake with synthetic waveforms generated for the best-fitting point source mechanism found in the body-waveform inversion (Table 7.2). See Figure 7.2 for further explanation.

Figure 7.12. Location and focal mechanism of the February 5, 1977 earthquake in the southeast Pacific. Bathymetry (1000 m contour interval) and tectonic elements from Craddock [1981]. Dashed lines indicate location of fracture zones inferred from magnetic anomaly offsets. Heavy toothed line indicates location of a relict subduction zone.

Figure 7.13. Comparison of observed P and SH waves from the February 5, 1977 earthquake with synthetic waveforms generated for the best-fitting point source mechanism found in the body-waveform inversion (Table 7.2). See Figure 7.2 for further explanation.

Figure 7.14. Comparison of observed P and SH waves from the October 17, 1977 earthquake with synthetic waveforms generated for the best-fitting point source mechanism found in the body-waveform inversion (Table 7.2). See Figure 7.2 for further explanation.



October 7, 1965

Figure 7.1

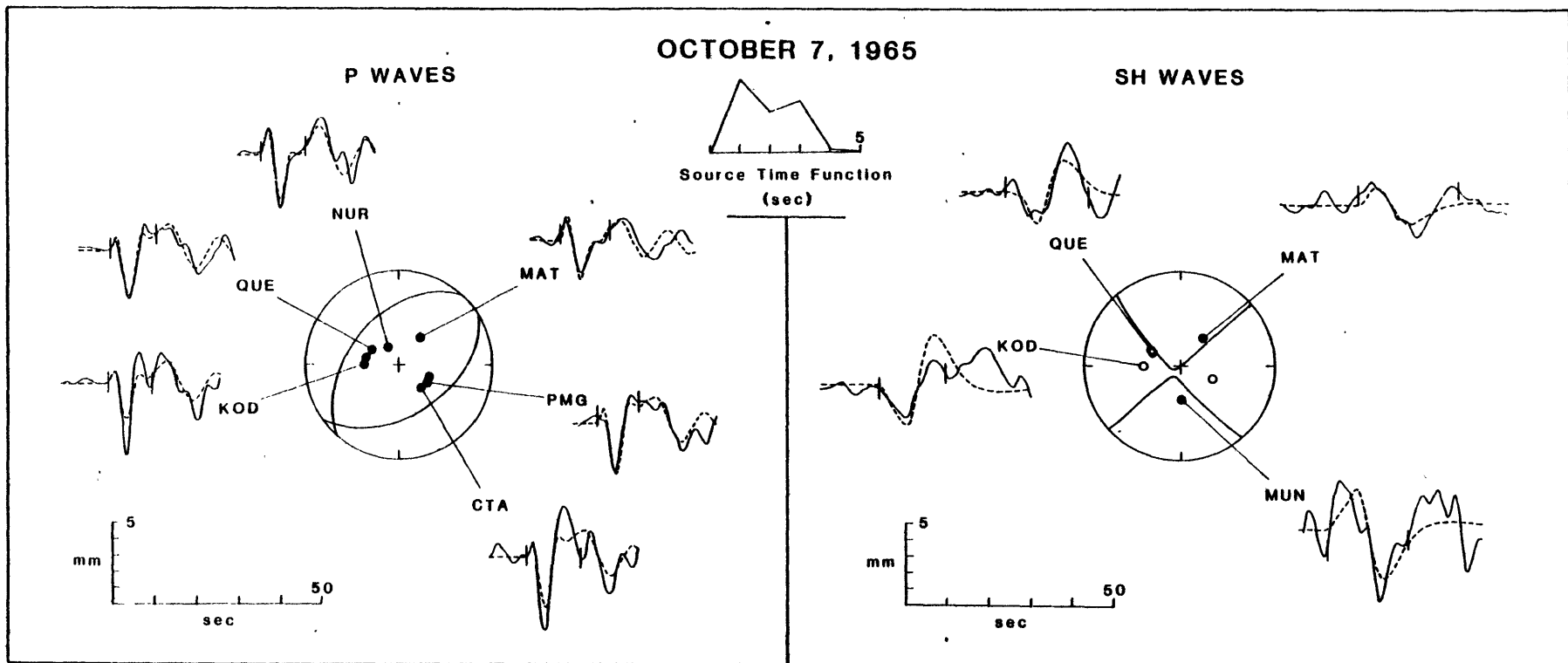
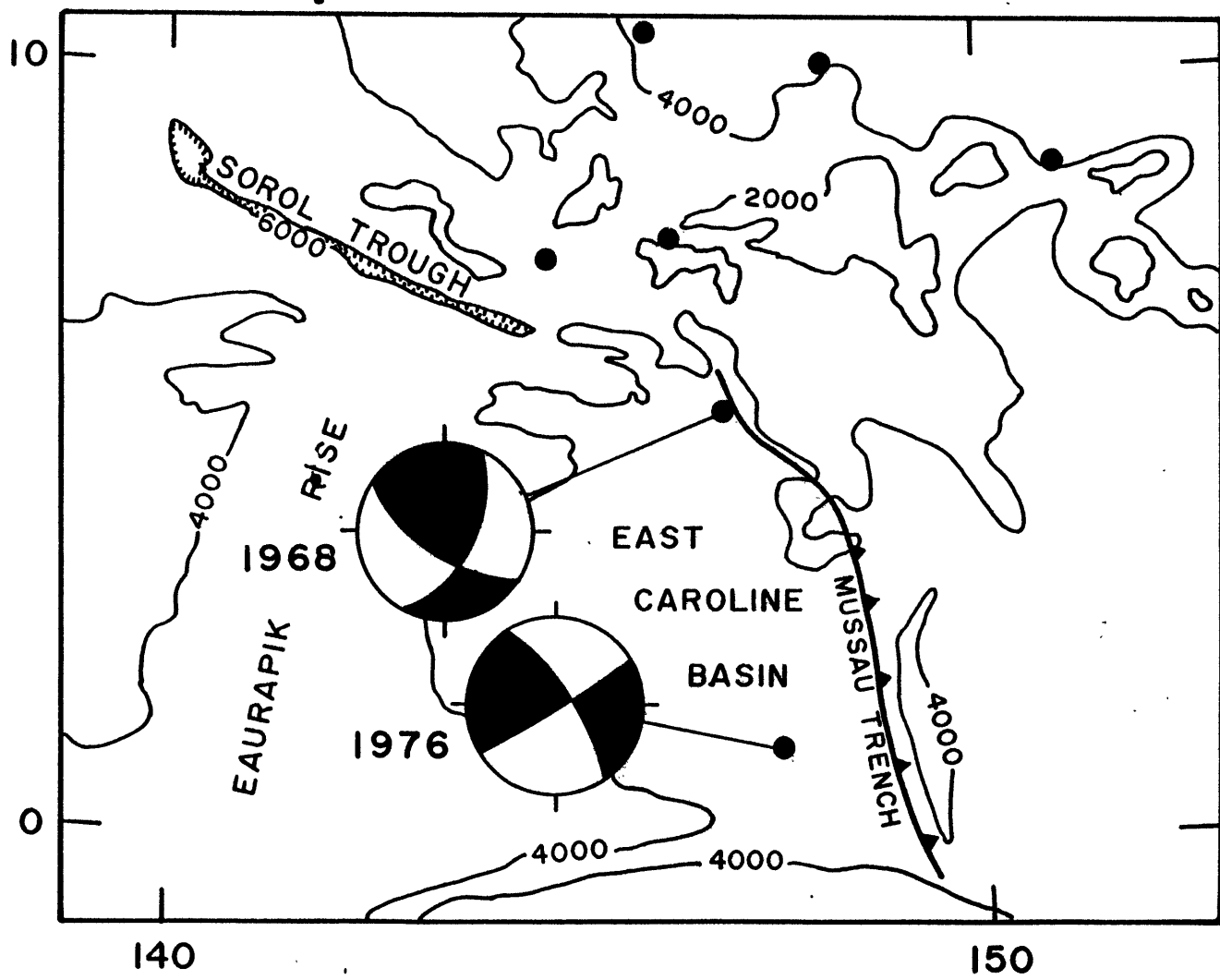


Figure 7.2

Figure 7.3



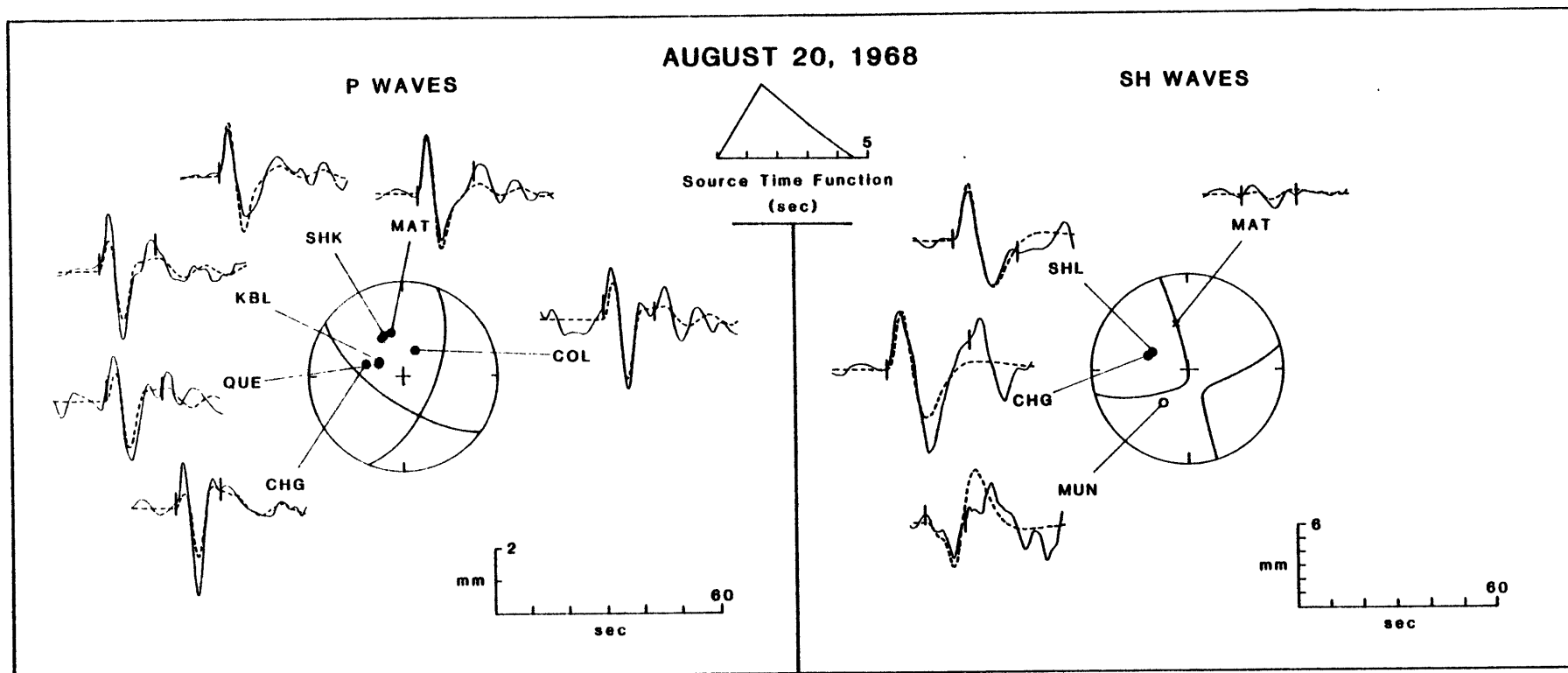
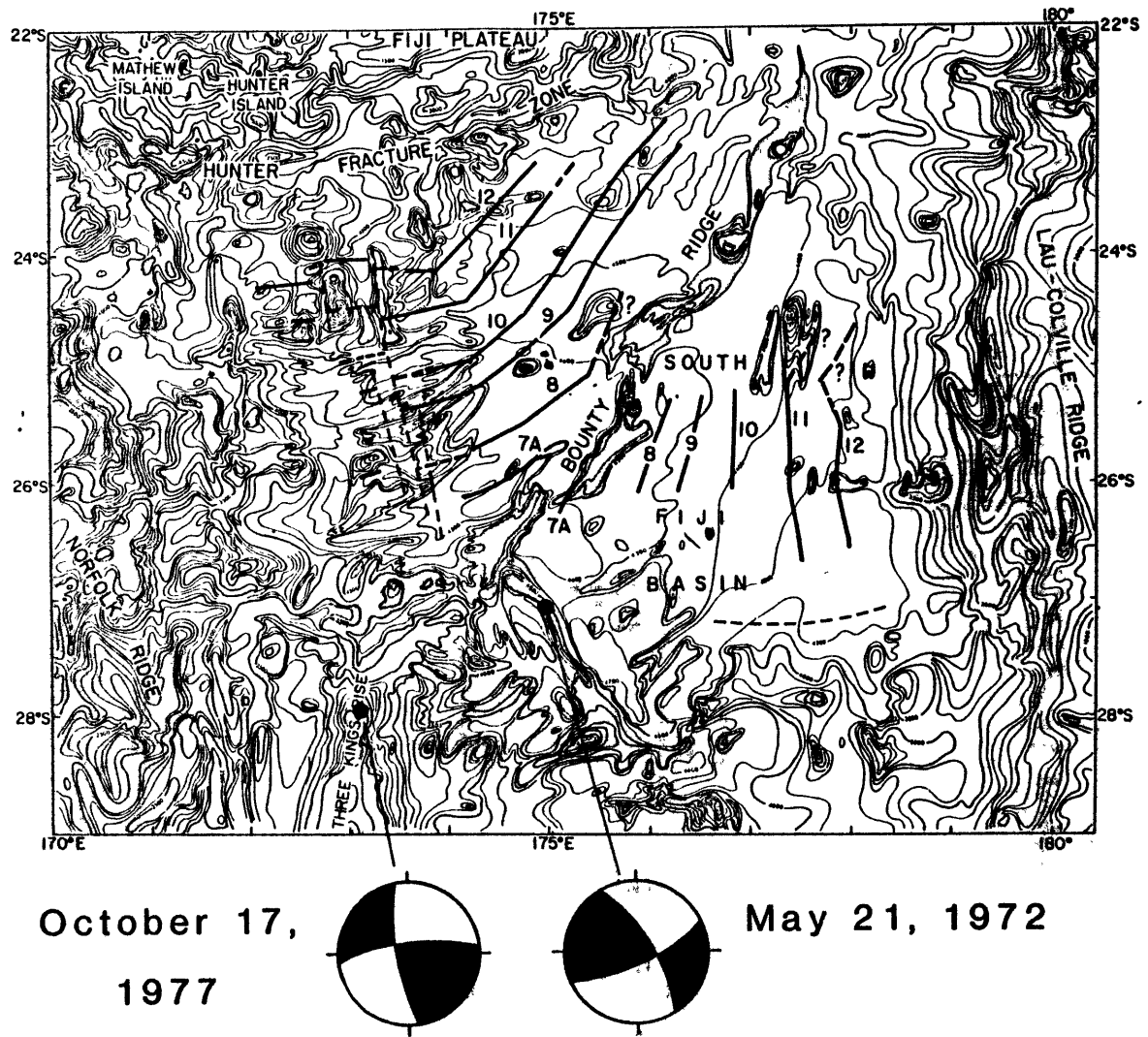


Figure 7.4

Figure 7.5





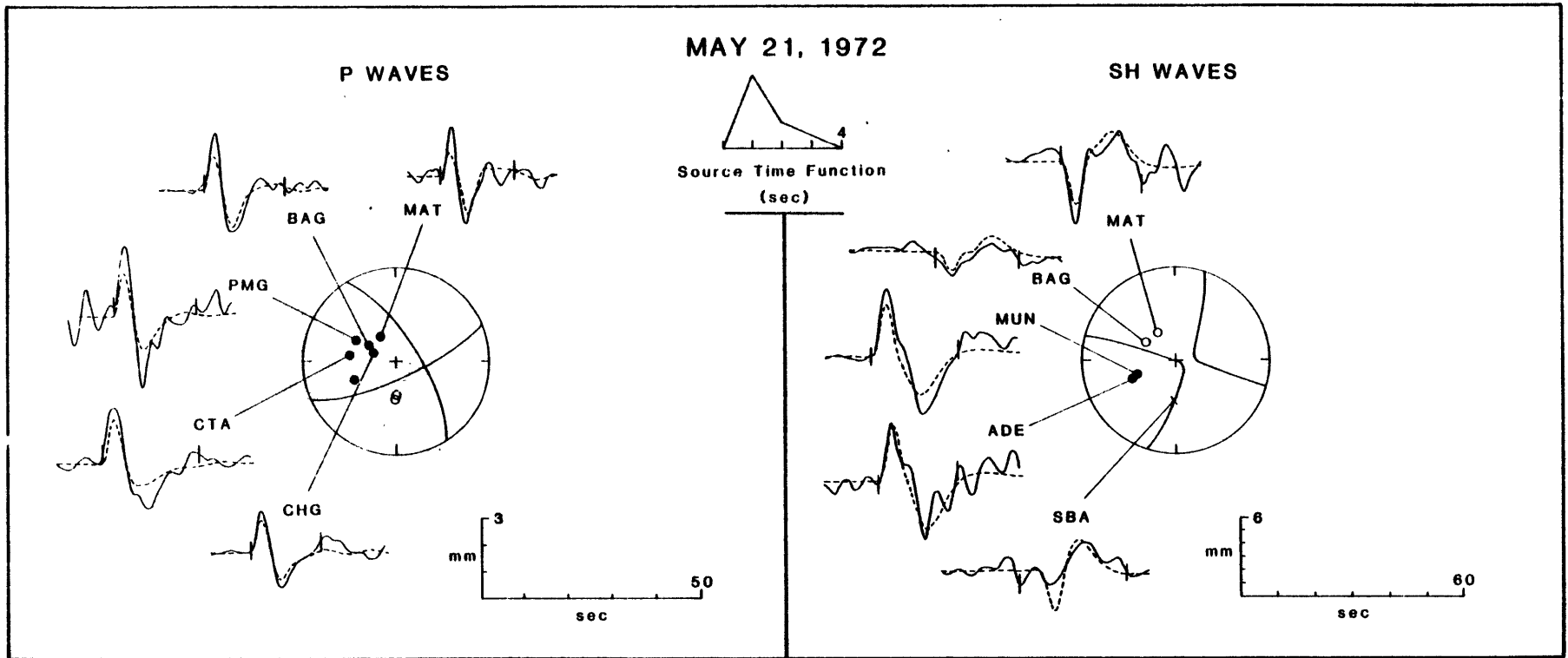
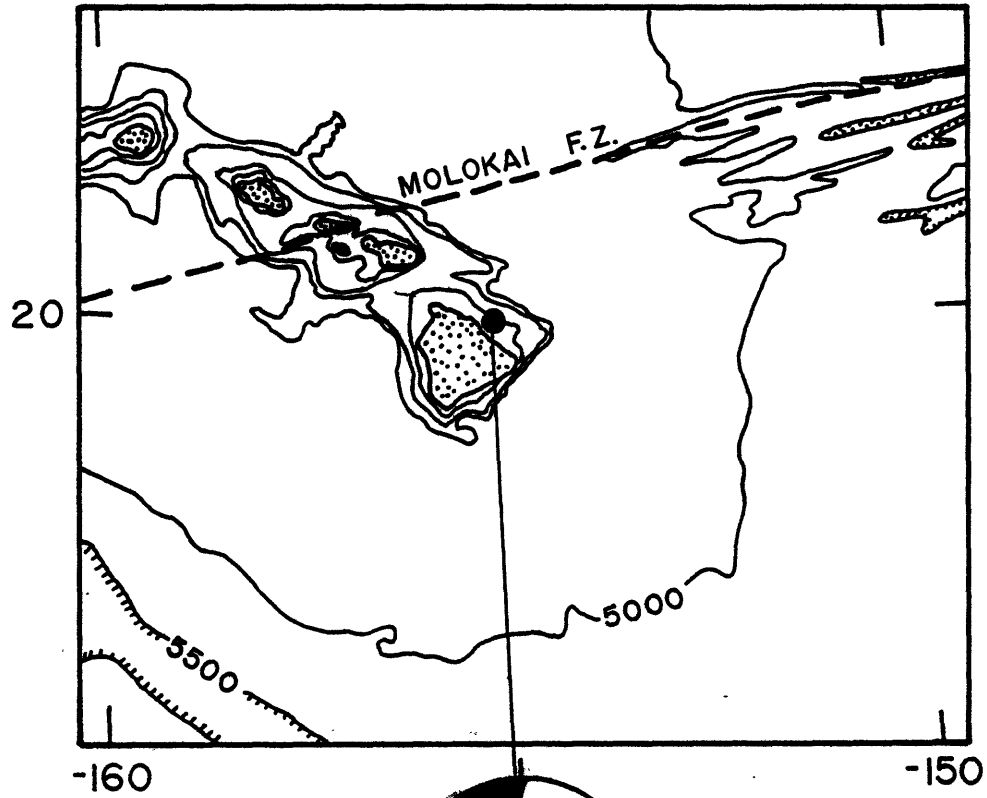


Figure 7.6



APRIL 26  
1973

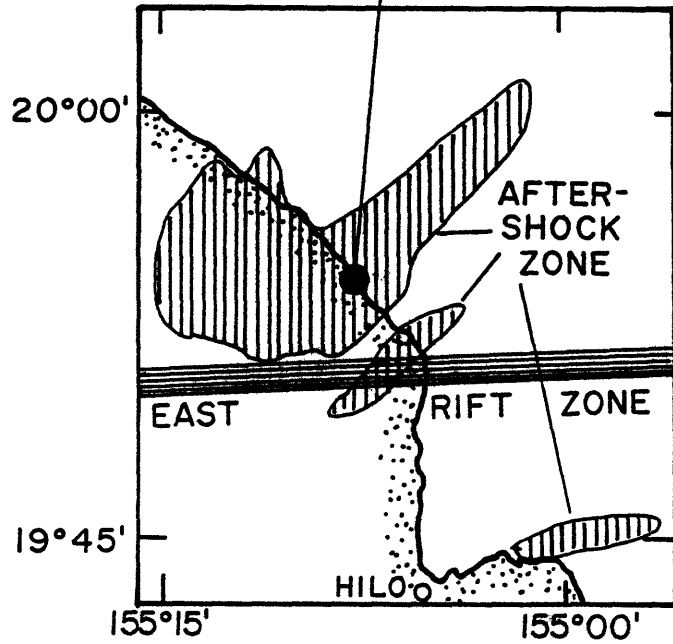
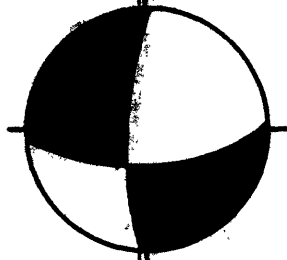


Figure 7.7

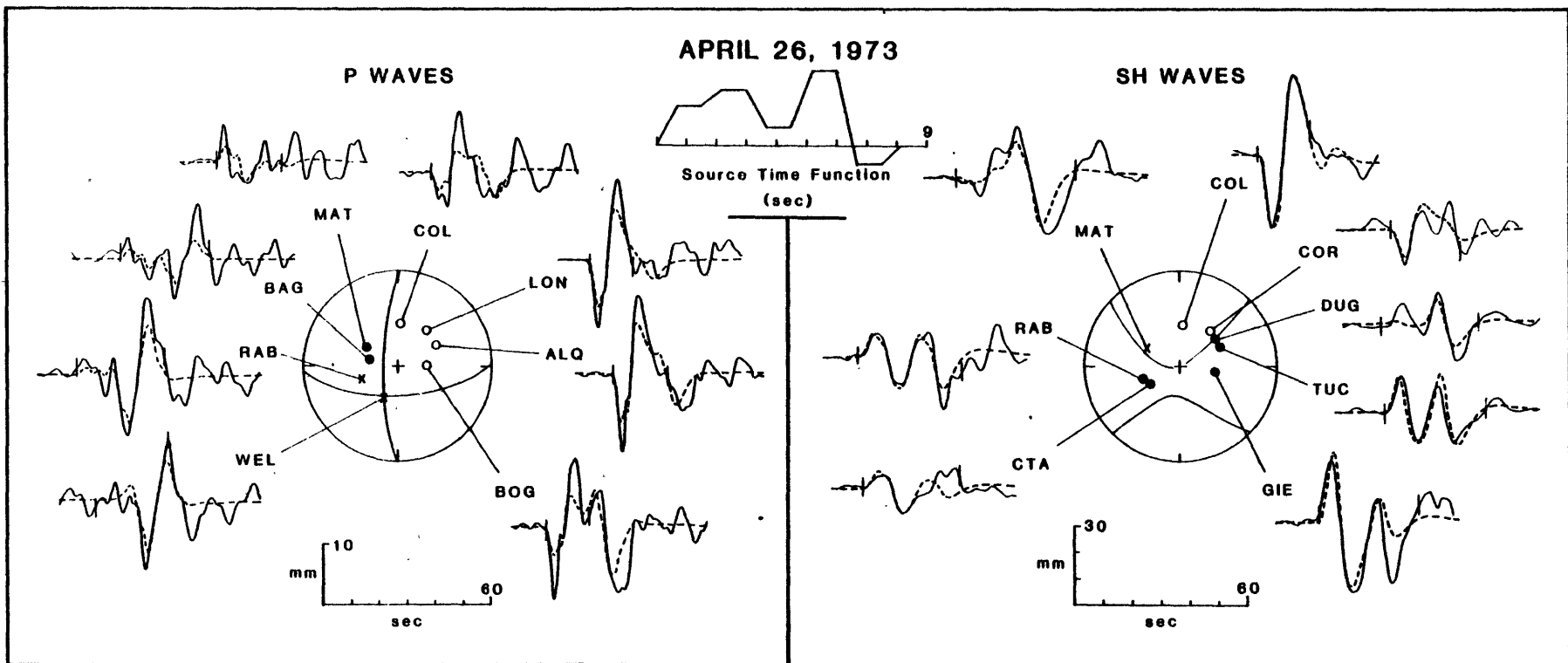
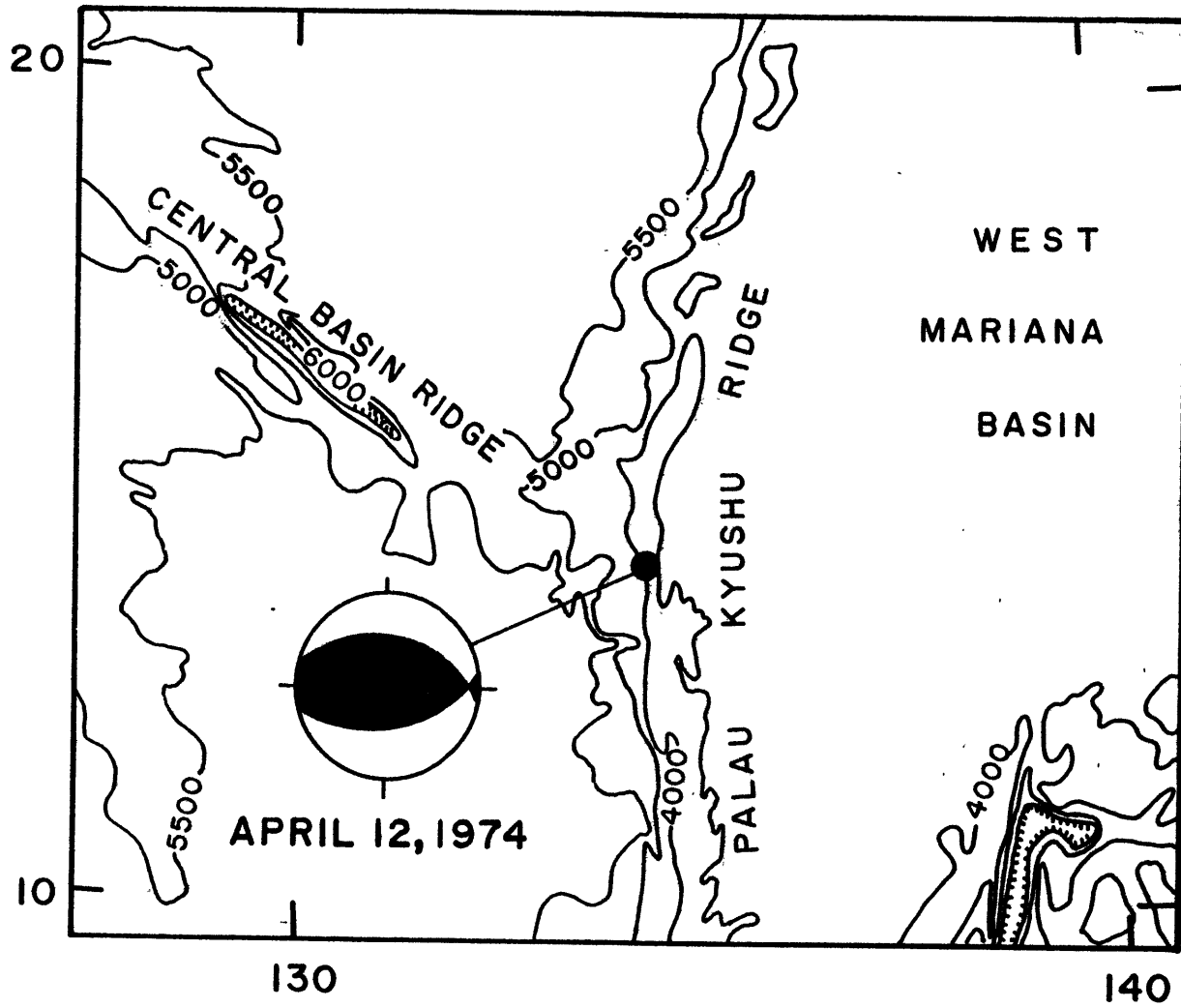


Figure 7.8

Figure 7.9



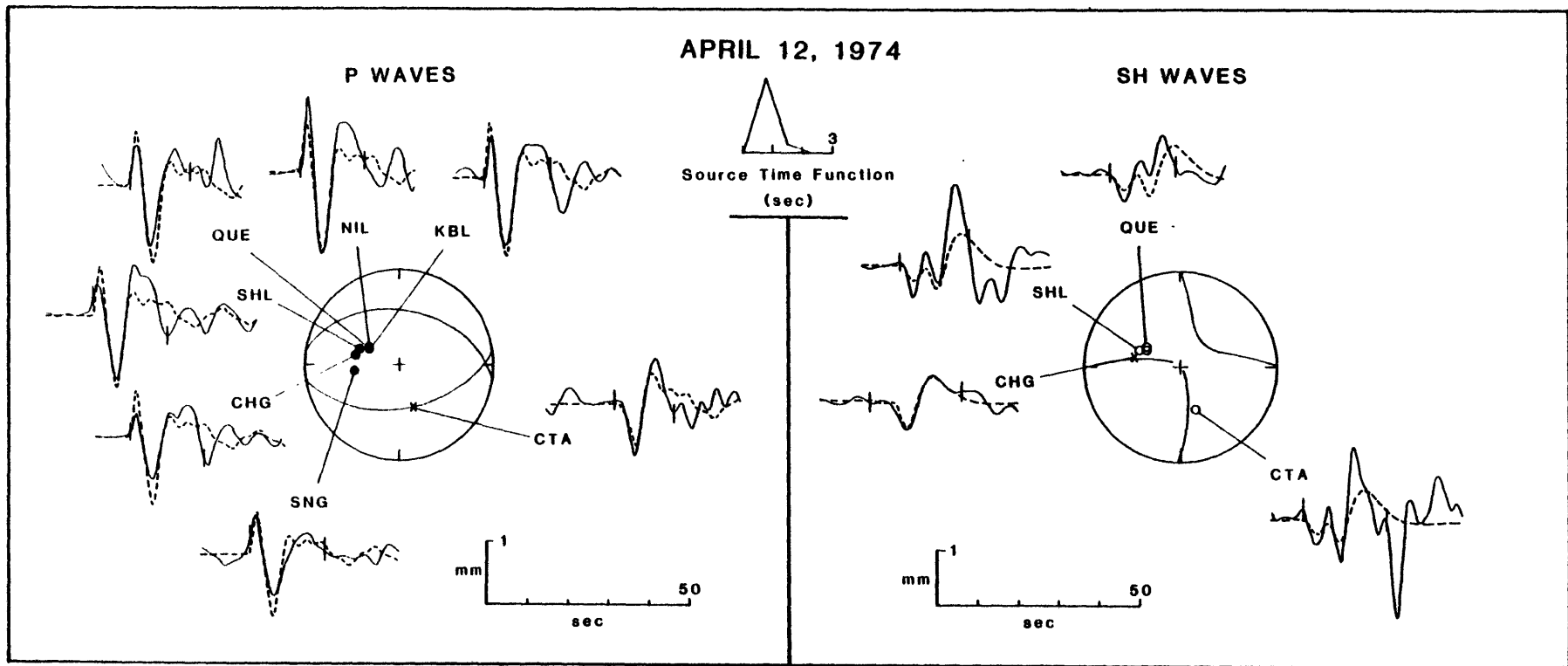


Figure 7.10

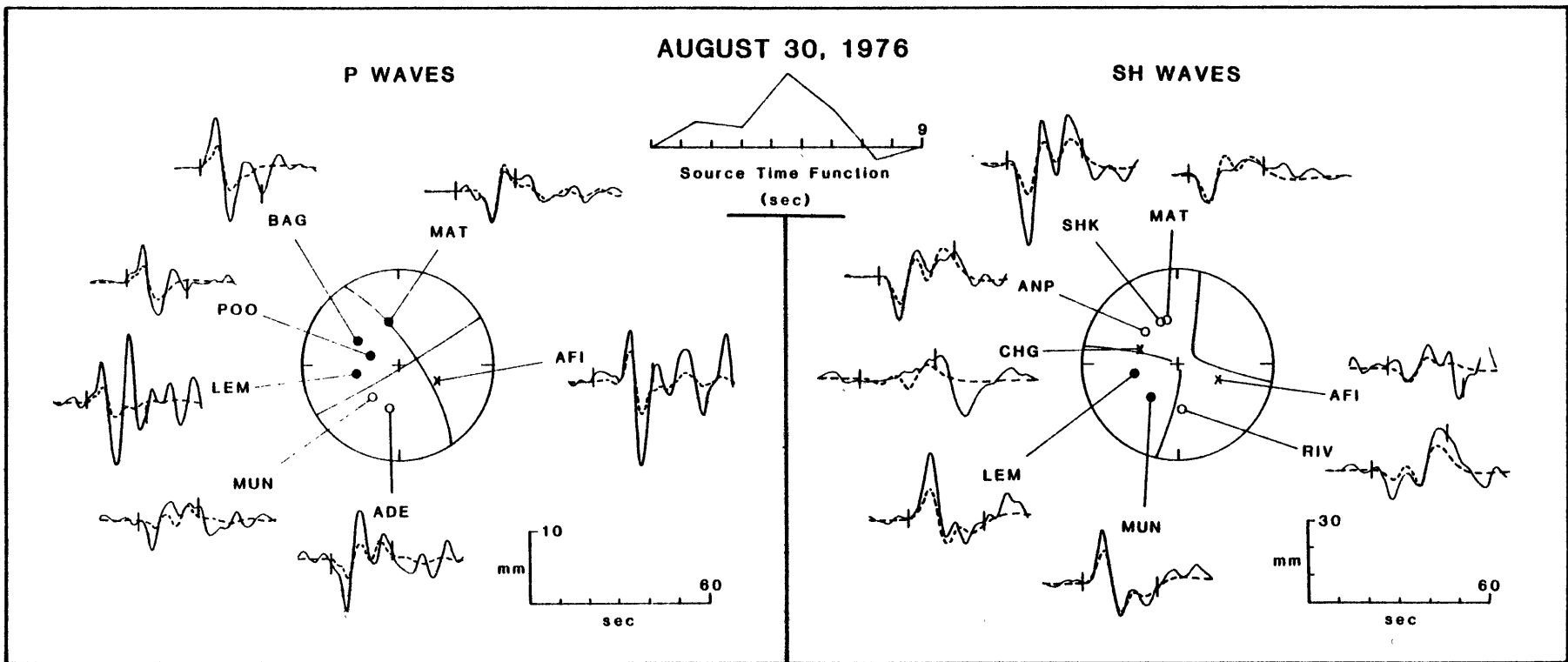
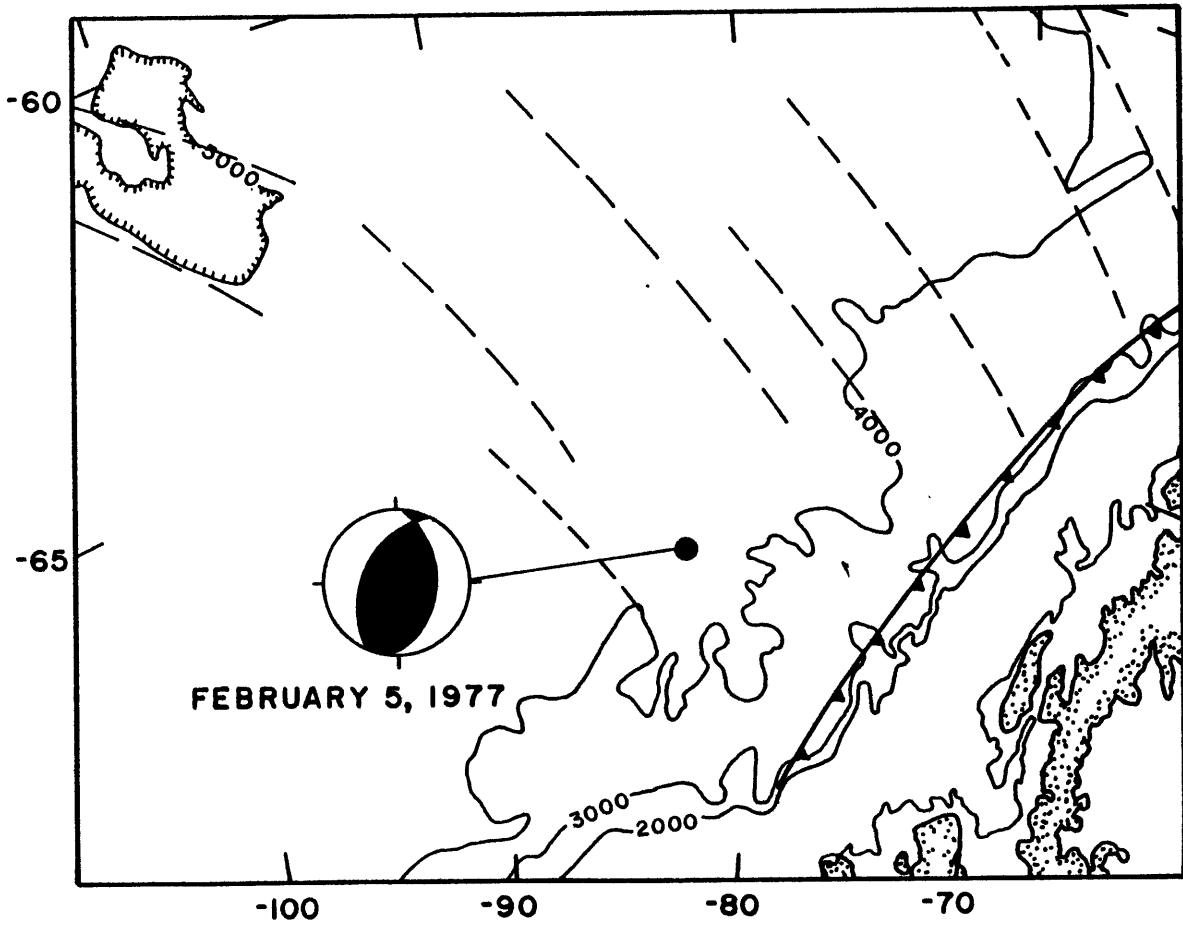


Figure 7.11

Figure 7.12



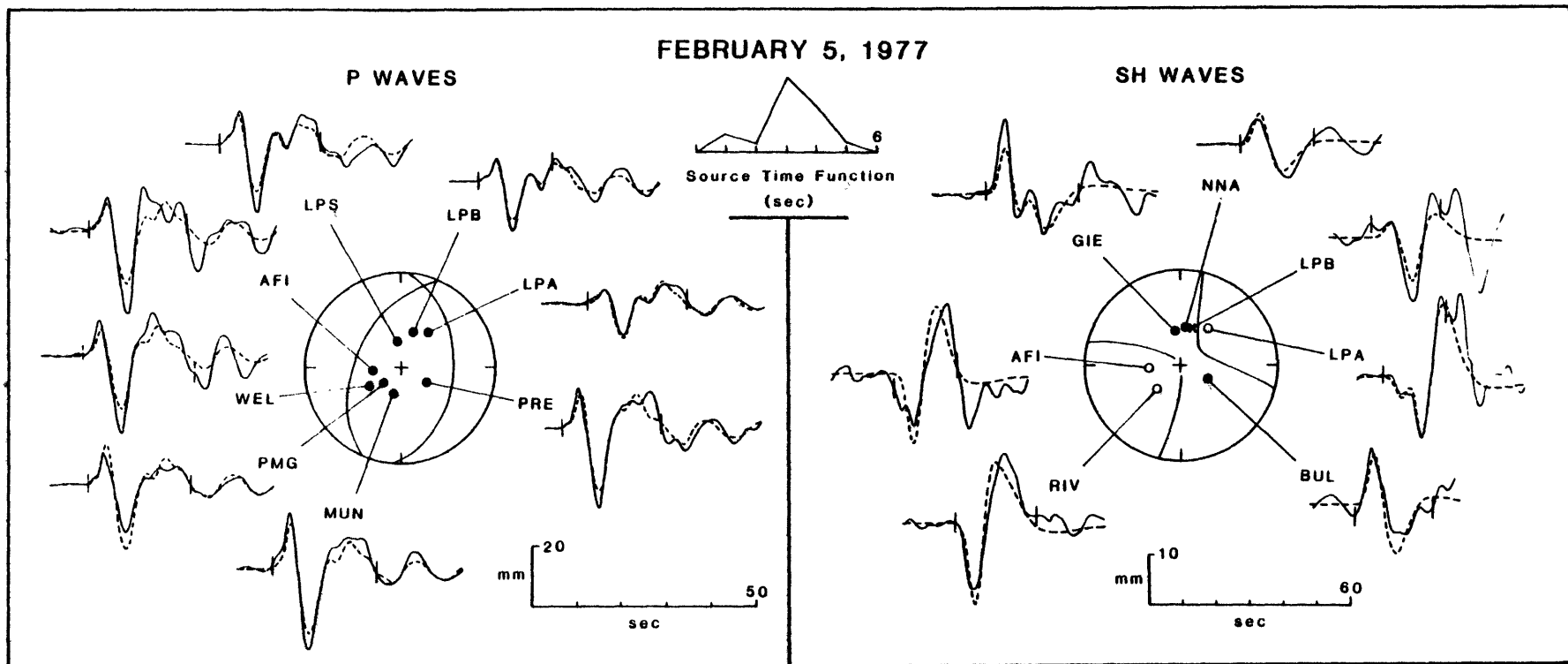


Figure 7.13



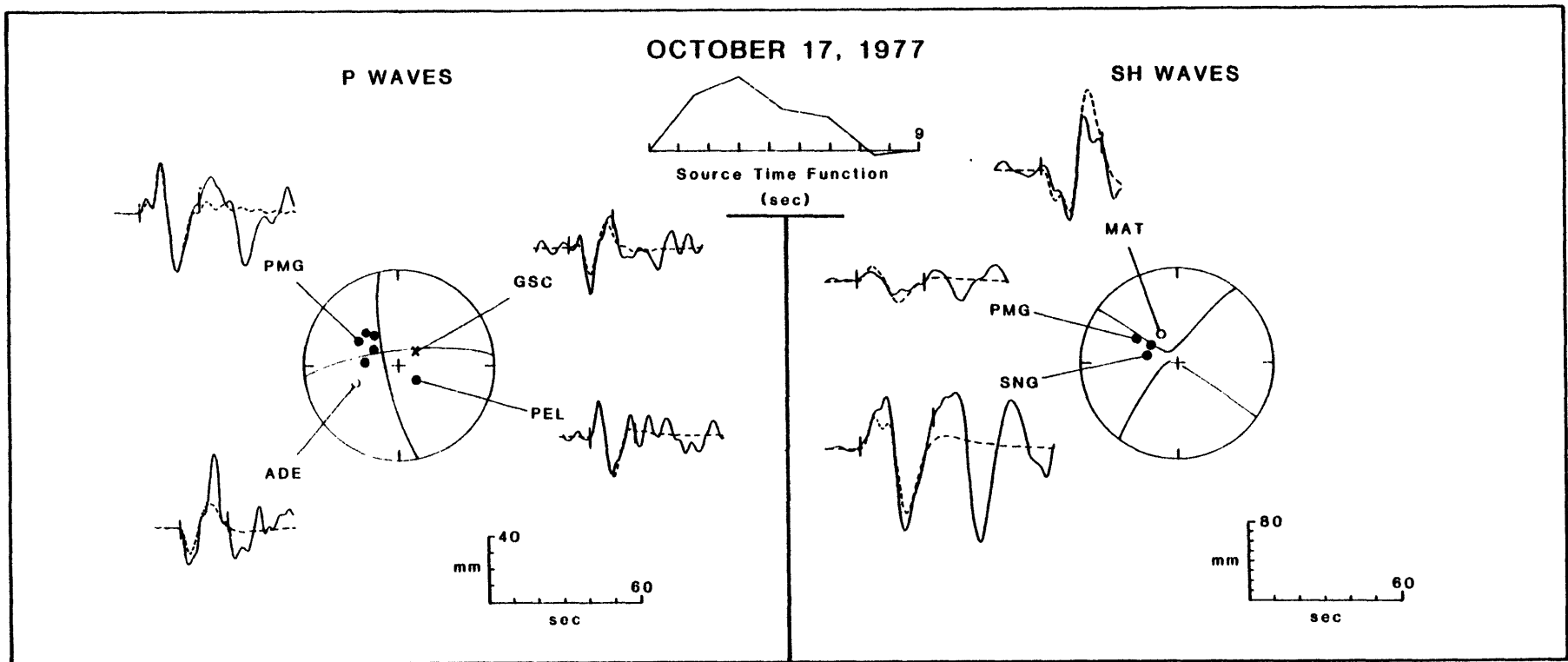


Figure 7.14

## CHAPTER 8. NEAR-RIDGE EARTHQUAKES AND THE TECTONIC EVOLUTION OF YOUNG OCEANIC LITHOSPHERE

### INTRODUCTION

Earthquakes occurring in very young oceanic lithosphere, but off the ridge axis, resist easy classification as intraplate or plate-boundary events in the usual sense (e.g., Chapters 5-7) and until recently have received little attention [Wiens and Stein, 1983b; Wiens et al., 1983; Bergman and Solomon, 1983, 1984; Bergman et al., 1984]. In Chapter 4 we presented source studies of nine large, normal-faulting earthquakes in young (4-27 m.y.) oceanic lithosphere on both sides of the Southeast Indian Ridge and considered several tectonic processes which might account for the distinctive features of this group of earthquakes. This chapter presents a more general evaluation of the tectonics of the near-ridge environment based on a global survey of the source mechanisms of earthquakes in young oceanic lithosphere.

The near-ridge tectonic environment is potentially influenced by a variety of processes. The most rapid evolution of the thermal and mechanical state of oceanic lithosphere generally occurs during the first few tens of millions of years [e.g., Parsons and Sclater, 1977; Watts et al., 1980]. Complications to the simple conductive cooling of the lithosphere may arise both from hydrothermal convection in the oceanic crust [e.g., Lister, 1977; Fehn and Cathles, 1979] and from secondary convection in the asthenosphere [Parsons and McKenzie, 1978; Buck, 1984]. The consequent spatial and temporal variations in temperature are likely to be large enough to produce tectonically significant thermoelastic stresses, at least locally [Turcotte and Oxburgh, 1973; Turcotte, 1974]. During the first few tens of millions

of years the large topographic relief of the median valley and flanking mountains along slow-spreading ridges is reduced, by presumably tectonic processes [e.g., Macdonald and Atwater, 1978; Tapponnier and Francheteau, 1978], and the area-integrated "ridge push" begins to have an appreciable effect on the state of stress [e.g., Lister, 1975; Dahlen, 1981]. Nonuniformity in the spreading process may produce localized stress concentrations. Stresses transmitted through the lithosphere from other plate boundaries may also be significant in some areas. Focal mechanisms and depths of earthquakes near ridges may be expected to reflect many of these processes and provide one of the more direct methods for studying their relative importance.

A thorough synthesis of the source mechanisms of near-ridge earthquakes provides a means as well for determining the nature and location of the transition between the ridge-axis tectonic regime, characterized by horizontal extension perpendicular to the ridge axis [Sykes, 1967], and the stress regime in stable plate interiors, generally characterized by horizontal compression [Sykes and Sbar, 1974; Richardson et al., 1979]. A better understanding of this transition facilitates the interpretation of other features of the intraplate stress field and provides a constraint on models of the interaction between the lithosphere and the upper mantle convective system [e.g., Stein and Wiens, 1983]. Sykes and Sbar [1974] concluded on the basis of the limited data then available that this transition occurs at a lithospheric age of 10 to 20 m.y., and others [e.g., Fleitout and Froidevaux, 1983] have used this result as a major constraint in modeling the state of stress in oceanic lithosphere.

In order to address these issues, we have determined the source mechanism and focal depth of 22 near-ridge earthquakes (in addition to the Southeast Indian Ridge events studied in Chapter 4), using the body-waveform inversion technique described in Chapter 3. The source parameters of these earthquakes, together with other source mechanism data from the literature, allow a much more detailed examination than was previously possible of the deformation and causative processes accompanying the thermal and mechanical evolution of young oceanic lithosphere.

#### A CATALOG OF NEAR-RIDGE EARTHQUAKES

We began our study by assembling a complete list of near-ridge earthquakes which occurred since the establishment of the World-Wide Standard Seismograph Network (WWSSN) and which are large enough to study with body-wave synthesis techniques. The search for such near-ridge earthquakes was based primarily on the catalog of the International Seismological Centre (ISC) for the years 1964 - 1979 and was an integral part of the assembly of the master catalog of oceanic intraplate seismicity presented in Chapter 2. All epicenters along and near the major mid-ocean ridge systems were plotted at a scale and projection which could be directly overlaid on maps of seafloor bathymetry. The locations of all earthquakes with a body-wave magnitude ( $m_b$ ) of at least 5.4 were separately noted and judged as to whether they were resolvably off the ridge axis. For the purposes of this study, the near-ridge environment was taken to include oceanic lithosphere less than about 35 m.y. old. We have excluded earthquakes in back-arc or marginal basins, however, since such regions may not be representative of young oceanic lithosphere. The epicentral data of

the near-ridge earthquakes satisfying these criteria are listed in Table 8.1.

The approach taken here may introduce a bias in the representation of seismicity in the very youngest lithosphere, since the typical epicentral uncertainty (10-20 km) is such that we might have difficulty distinguishing between ridge-axis earthquakes and earthquakes in very young (2 to 5 m.y. old) lithosphere along slow-spreading ridges. Source studies of ridge-axis earthquakes along slow-spreading ridges, performed with the same body-wave inversion technique as is used here, enable the identification of several consistent features of such earthquakes which give added confidence that our catalog of near-ridge events is both relatively complete and uncontaminated by ridge-axis events near slow-spreading ridges. Ridge axis events are found to be extremely shallow (< 2 km below the seafloor), located within the median valley (strongly constrained by the water depth inferred from the prominent reverberations in the water column observed on vertical component seismograms), and characterized by nearly pure normal faulting with nodal planes dipping at about 45° and striking parallel to the overall trend of the ridge axis [Solomon et al., 1983]. We will see that none of these features is shared by the near-ridge earthquakes with known focal mechanism and depth. We are thus reasonably confident that our catalog provides an unbiased global view of the last two decades of near-ridge seismicity within oceanic lithosphere between the ages of a few and 35 m.y.

Table 8.1 includes several events which occurred before 1964 and which have published mechanisms from P-wave first motions [Sykes, 1967; Tobin and Sykes, 1968] and several events since 1980, primarily

earthquakes from the catalogs of Dziewonski and Woodhouse [1983] and Dziewonski et al. [1983]. In addition, Table 8.1 includes several events with  $m_b < 5.4$  where there is some information about the source, either a published focal mechanism or a successful body-wave inversion. The age listed for each event in Table 8.1 is determined either from published identifications of magnetic anomalies and the chronology of LaBrecque et al. [1977] or from the compilation of isochrons of Sclater et al. [1980]. Where an epicenter lies near a fracture zone with significant offset or there is considerable uncertainty in the age, a range of possible ages is given.

The global distribution of the 69 near-ridge earthquakes in Table 8.1 is shown in Figure 8.1. Except for the central Indian Ocean and a small area in the eastern Pacific, which are notably more active, near-ridge earthquakes are distributed rather evenly along the major mid-ocean spreading centers. This is in striking contrast to ridge-axis earthquakes: no such events have been observed at teleseismic distances from the fast-spreading East Pacific Rise, yet several dozen earthquakes with  $m_b \geq 5.4$  have been observed on the slow-spreading Mid-Atlantic Ridge. These variations cannot be attributed to different detection limits, since the ISC has nearly complete global detection capability for earthquakes with  $m_b > 5.2$  [Chinnery, 1978]. Thus, there appears to be no correlation between the levels of near-ridge and ridge-axis seismicity.

#### SOURCE MECHANISMS FROM BODY-WAVEFORM INVERSION

For 31 of the earthquakes listed in Table 8.1, seismograms from stations of the WWSSN or GDSN were available in sufficient numbers to permit source studies by inversion of the long-period P and SH

waveforms, as described in Chapter 3. The source mechanisms of 9 events along the Southeast Indian Ridge have been presented in Chapter 4 and are summarized in Table 4.2. The source mechanisms of the remaining 22 earthquakes are discussed below. The source parameters of these events, together with the formal errors, are given in Table 8.2. The focal mechanisms and the observed and synthetic seismograms are given in a series of figures, with P waves and SH waves shown on separate focal spheres (with the appropriate radiation pattern) for clarity. The synthetics shown were generated with the single best-fit solution, and have not been individually rescaled for improved fit. The station code and geographic location of all stations used in the inversions are listed in Appendix E.

#### August 6, 1962

The epicenter of the August 6, 1962 earthquake is west of the Mid-Atlantic Ridge, in lithosphere approximately 8 m.y. old (Figure 8.2). Sykes [1967] reported a poorly-constrained normal-faulting mechanism for this earthquake and treated it as a ridge-axis event, although he later noted that the epicenter definitely lies outside the rift valley, along a section of the ridge with no significant offsets [Sykes, 1970a]. The inversion solution (287/44/316, Figure 8.3) is essentially identical with Sykes's mechanism, having a significant component of strike-slip motion and a T-axis striking at an angle of 63° from the direction of spreading. The observed P and SH waves are well fit by this mechanism with a centroid depth of 9.3 km and a seismic moment of  $1.3 \times 10^{25}$  dyne-cm. The emergent character of the SH wave at NUR is clearly revealed in the unrotated horizontal component records.

### September 9, 1965

The epicenter of the September 9, 1965 earthquake ( $m_b = 5.8$ ) is on the southeast flank of the northeast-trending Cocos Ridge, which was formed near the Cocos-Nazca spreading center by unusually active volcanism associated with the Galapagos hotspot [Hey, 1977]. The earthquake occurred near the intersection of the ridge with a north-trending fracture zone (Figure 8.4), where the estimated age of the lithosphere is 10 to 15 m.y. [Hey et al., 1977]. Molnar and Sykes [1969] found a strike-slip focal mechanism with a significant component of thrust faulting (173/84/150) for this event. The inversion solution is similar, but closer to pure strike-slip (357/88/200, Figure 8.5), at a depth of 6.5 km and with a seismic moment of  $2.4 \times 10^{25}$  dyne-cm. Wiens and Stein [1983a] estimated a depth of 7 km for this event, using Molnar and Sykes's mechanism. The nodal plane striking at  $357^\circ$ , subparallel to the fracture zone, is probably the fault plane.

### September 12, 1965

The September 12, 1965 ( $m_b = 6.1$ ,  $M_s = 6.0$ ) earthquake occurred between the Central Indian Ridge and the Chagos-Laccadive Ridge, in the northeastern Indian Ocean (Figure 8.6). Two years later a swarm of similar earthquakes occurred to the east, on the flank of the Chagos Bank [Stein, 1978]. Banghar and Sykes [1969] proposed a normal-faulting mechanism with a large component of strike-slip motion for this event (270/54/230). Stein [1978] found that the surface wave radiation patterns are better fit by a nearly pure normal-faulting mechanism (270/60/260), and he matched synthetic waveforms to the P waves to constrain the depth to about 15 km below the seafloor. Stein noted a significant discrepancy between the seismic moments inferred



from the P waves ( $3.5 \times 10^{25}$  dyne-cm) and the surface waves ( $6.8 \times 10^{25}$  dyne-cm).

The body-wave inversion solution supports the conclusions of Stein [1978] concerning the depth (15.9 km) and seismic moment ( $3.7 \times 10^{25}$  dyne-cm). The P and SH waves from this earthquake differ somewhat in the double-couple mechanism which they best fit. The focal mechanism which best fits both the P and SH waves (266/43/250, Figure 8.7) is intermediate between previously proposed mechanisms. In order to model the low amplitudes of the P waves in Africa (BUL and AAE) relative to stations such as SBA and MUN, the mechanism must have a larger component of strike-slip motion (slip angle of approximately  $240^\circ$ ) than the focal mechanism suggested by Stein [1978], but the mechanism of Banghar and Sykes [1969] results in significant misfit to the observed SH waves at three stations to the northwest (AAE, SHI, and NUR). The prominent positive motion of the direct S wave at these stations requires a slip angle of approximately  $260^\circ$ , as do the surface waves.

#### January 7, 1967

The epicenter of the January 7, 1967 earthquake ( $m_b = 5.5$ ) is near a small-offset fracture zone of the Southeast Indian Ridge, south of Australia (Figure 8.8). The age of the lithosphere is about 2.5 m.y. [Weissel and Hayes, 1972]. One nodal plane of the focal mechanism (19/42/238, Figure 8.9) is subparallel to the fracture zone trend of  $N15^\circ E$ . The mechanism has a significant component of strike-slip motion in the same sense as the ridge offset. A pure normal-faulting mechanism would not account for the differences between the P waves at WIN and PMG. The emergent nature of the SH wave at PMG is well determined: both observed horizontal components break clearly, but

when they are rotated to the transverse component, the direct S wave is cancelled. The emergent SH wave at RIV is a similar case. At SNG, both observed components break clearly upward, as the SH wave does, but the inversion solution shows a small dilatation for the direct phase. The correct starting point for the SH wave at WIN is not clear on the observed records; the small positive motion prior to the main pulse may simply be noise. Using an earlier starting point for WIN (i.e., assuming the direct phase is nodal) results in a poor fit at all stations. The seismic moment of this earthquake is  $1.2 \times 10^{25}$  dyne-cm, and the depth is 6.9 km.

#### November 10, 1967

The November 10, 1967 earthquake ( $m_b = 5.2$ ) occurred on the west flank of the Chagos Bank (Figure 8.6), one day before an unusual swarm of normal-faulting earthquakes [Stein, 1978]. The focal mechanism of this event, however, is characterized by nearly pure strike-slip faulting (229/80/188, Figure 8.10), in a right-lateral sense on the northeast-striking nodal plane, parallel to the strike of local fracture zones. The P-wave polarities could be fit with a normal-faulting mechanism (e.g., 270/60/270), but the fit of the synthetics to the observed waveforms with such a mechanism is very poor. The basic shapes of both the P and SH waves are well fit with the strike-slip solution at a depth of 15.6 km and with a seismic moment of  $2.8 \times 10^{24}$  dyne-cm. Many details of the waveforms are not reproducible, however.

#### November 11, 1967

This earthquake ( $m_b = 5.3$ ,  $M_s = 5.2$ ) is the first event in an unusual swarm of normal-faulting earthquakes on November 11, 1967

located on the west scarp of the Chagos Bank (Figure 8.6). Stein [1978] fixed one nodal plane, based on P-wave first motions, and constrained the slip angle with surface waves, obtaining a pure normal-faulting mechanism (280/65/270) with a seismic moment of  $4.5 \times 10^{24}$  dyne-cm. The inversion solution is also characterized by normal faulting, but with a different strike (264/50/265, Figure 8.11). The strike is not very well constrained by the first motions of the emergent P waves to the north; the strike of the inversion solution is controlled mostly by the SH waves. A strike of  $280^\circ$  would produce a nodal arrival for the SH wave at NDI instead of the observed strong dilatation. The overall fit of the SH waves is mediocre at best. The inversion yields a depth of 16.3 km and a seismic moment of  $3.5 \times 10^{24}$  dyne-cm.

#### March 2, 1968

The earthquake on March 2, 1968 ( $m_b = 5.5$ ,  $M_s = 5.4$ ) was the last moderate-size event on the west scarp of the Chagos Bank (Figure 8.6). Using the same approach as for the November 11, 1967 event discussed above, Stein [1978] found a normal-faulting solution for this event (280/60/270) with a seismic moment of  $8.8 \times 10^{24}$  dyne-cm. The inversion solution (281/53/281,  $M_0 = 8.4 \times 10^{24}$  dyne-cm, Figure 8.12) is in very close agreement with Stein's results. The source time function is rather long for an earthquake of this size, suggesting a relatively low stress drop. The later portions of several of the SH waves (i.e., NDI, CHG, LEM) are disturbed, possibly by contamination from the large SV waves generated by a dip-slip event, but the early portions of the waveforms are fit reasonably well. The emergent nature of the SH wave at SDB (which is naturally rotated onto the N-S

component) is confirmed by the clear arrival of SV energy at that time on the E-W component. The centroid depth is 13.1 km.

#### August 8, 1969

The epicenter of the August 8, 1969 earthquake ( $m_b = 5.7$ ) is on a fracture zone west of a major offset of the ridge axis in the South Atlantic (Figure 8.13). The age of the lithosphere is either 6 or 16 m.y., depending on which side of the fracture zone the epicenter is located. Forsyth [1975] found a strike-slip mechanism (8/74/200) from P-wave first motions. The inversion solution (10/64/221, Figure 8.14) is similar, except that it has a larger component of normal faulting. The sense of slip on the nodal plane parallel to the fracture zone is the same as the offset of the ridge. The centroid depth is 6.1 km, and the seismic moment is  $1.8 \times 10^{25}$  dyne-cm.

#### January 21, 1970

The epicenter of the large January 21, 1970 earthquake ( $m_b = 6.1$ ,  $M_s = 6.8$ ) is west of the East Pacific Rise in lithosphere 3 m.y. old (Figure 8.15). Anderson et al. [1974] reported a normal-faulting mechanism for this event. Bergman and Solomon [1980] found that a thrust-fault solution provides a good fit to the first motions, but the position of the second nodal plane was unconstrained. The inversion solution is characterized by thrust faulting (332/43/108, Figure 8.16) with a centroid depth of 6.5 km and a seismic moment of  $1.4 \times 10^{26}$  dyne-cm, the largest of any event in this chapter. We found only three usable SH waves for this event because the huge SV waves caused the horizontal components to be clipped at many stations. The later part of the SH wave at PEL is quite disturbed, but the inversion converges to the same solution even if this station is given no weight. The P

waves are well fit by the point source synthetics, despite the size of this event.

#### March 31, 1970

The epicenter of the March 31, 1970 earthquake ( $m_b = 5.5$ ,  $M_s = 5.5$ ) is slightly north of the Chagos Bank swarm [Stein, 1978], in lithosphere about 11 m.y. old (Figure 8.6). Sykes and Sbar [1974] reported a large number of first motion polarities which apparently constrain the mechanism of this event to a combination of strike-slip and normal faulting (260/57/220), but this mechanism results in a poor fit to the observed P and SH waveforms. A good fit to the SH waves and most of the P waves is obtained in the inversion solution (44/86/185, Figure 8.17), which is characterized by right-lateral strike-slip motion on the northeast-striking nodal plane which parallels the strike of local fracture zones. The observed distribution of first motion polarities is best fit by a mechanism of approximately 216/85/185, but such a mechanism provides a very poor fit to the SH waveforms at NIL and MSH. The P waveform at SNG (and several other stations to the east) is incompatible with the point source solution which best fits the remaining P waves and SH waves. The source of the discrepancy is not readily apparent, but complexities in the rupture process presumably contribute. The depth is 11.7 km, and the seismic moment is  $7.6 \times 10^{24}$  dyne-cm.

#### April 25, 1970

The earthquake on April 25, 1970 ( $m_b = 5.1$ ,  $M_s = 5.1$ ) is located south of the March 31, 1970 event, between the Chagos Bank swarm and the Central Indian Ridge, in lithosphere about 14 m.y. old (Figure 8.6). An exceptionally good fit to both P and SH waves was obtained

with a strike-slip focal mechanism (251/81/196, Figure 8.18) which is nearly identical with that of the March 31 event. The seismic moment is  $1.7 \times 10^{24}$  dyne-cm, and the centroid depth is 8.7 km.

#### May 9, 1971

The epicenter of the May 9, 1971 earthquake ( $m_b = 6.0$ ,  $M_s = 6.0$ ) is on the Antarctic plate, southeast of the Antarctic-Pacific-Nazca triple junction (Figure 8.19). The age of the lithosphere is about 10 m.y. The event was first studied by Forsyth [1973], who used P-wave first motion polarities and the radiation pattern of Rayleigh waves to infer a thrust-faulting mechanism (196/60/90) with the P axis roughly perpendicular to the ridge axis. Forsyth proposed a shallow depth (< 10 km), and Wiens and Stein [1983a] obtained a depth of 8 km by matching synthetics to the observed P waves, using Forsyth's mechanism. The inversion solution is consistent with the multiple source model used by Wiens and Stein [1983a] to match the observed P waves. We performed the inversion twice, once with three separate point sources (also inverting for the relative timing of the subevents) and once with a single source, but with a time function long enough to include all the subevents. The multiple source model offers no improvement over the single source model. The source process of this earthquake is well described by a single rupture geometry with three distinct episodes of faulting (24/45/102, Figure 8.20). The mechanism is very similar to Forsyth's, at a depth of 8.2 km and with a total moment of  $5.5 \times 10^{25}$  dyne-cm. Earthquakes characterized by multiple ruptures are generally very difficult to model, but the synthetic seismograms for this event provide an exceptionally good fit to the observed body waves.

May 2, 1972

The earthquake of May 2, 1972 ( $m_b = 5.9$ ,  $M_S = 5.5$ ) occurred east of the East Pacific Rise in 3 m.y. old lithosphere of the Cocos plate (Figure 8.15). Anderson et al. [1974] reported a normal-faulting mechanism which is very similar to the inversion solution (332/49/282, Figure 8.21). The SH waves are not very well recorded, but the synthetic waveforms match the overall character of the observed records at most stations. The depth is 10.6 km, and the seismic moment is  $1.8 \times 10^{25}$  dyne-cm.

June 29, 1973

The epicenter of the June 29, 1973 earthquake ( $m_b = 5.4$ ,  $M_S = 4.9$ ) is near the southern flank of the Cocos Ridge, in lithosphere 5 to 10 m.y. old (Figure 8.4). Station coverage for this small event is poor, but the observed waveforms are very well fit by a combination thrust-strike-slip mechanism (352/58/169, Figure 8.22) at a depth of 4.6 km, near the base of the oceanic crust. The seismic moment is  $2.8 \times 10^{24}$  dyne-cm. The nodal plane striking at  $352^\circ$  is subparallel to the fracture zone in the epicentral region. A much larger earthquake occurred near this one on March 29, 1976, but the two focal mechanisms are only vaguely similar (Figure 8.4).

November 17, 1973

The epicenter of the November 17, 1973 earthquake ( $m_b = 5.4$ ,  $M_S = 5.5$ ) is a short distance north of the March 31, 1970 earthquake discussed above (Figure 8.6), in 13 m.y. old lithosphere of the Indian plate. A very good fit to observed P and SH waveforms is obtained with a mechanism characterized by a combination of normal and strike-slip faulting (45/52/224, Figure 8.23). The depth is 16.4 km, and the seismic moment is  $4.8 \times 10^{24}$  dyne-cm.

July 1, 1974

The July 1, 1974 earthquake ( $m_b = 5.5$ ,  $M_s = 5.5$ ) is the largest event of a cluster of earthquakes which have occurred in a small region of the African plate in the South Atlantic (Figure 8.24). The epicenter is apparently on a zero-offset fracture zone [Schouten and White, 1980], in lithosphere about 9 m.y. old. The small size and remoteness of this event make it difficult to obtain good station coverage for the inversion, but the available records are of high quality. The inversion solution is characterized by nearly pure thrust-faulting (71/37/95, Figure 8.25) at a very shallow depth (2.4 km). The P axis of this event is nearly perpendicular to the direction of spreading. The seismic moment is  $3.2 \times 10^{24}$  dyne-cm.

September 11, 1975

The epicenter of the September 11, 1975 earthquake ( $m_b = 6.3$ ,  $M_s = 5.8$ ) is indistinguishable from that of the large January 21, 1970 event discussed above. Both are located west of the East Pacific Rise in 3 m.y. old lithosphere (Figure 8.15). As with other events in the eastern Pacific, station distribution is poor. The inversion converges to a thrust-faulting mechanism (309/45/94, Figure 8.26) which is very similar to that of the 1970 event. Both original horizontal component waveforms at NNA are large and clearly recorded; the absence of either direct or reflected SH energy at this station provides a strong constraint on the mechanism. The SH waves at GSC and GOL are almost naturally rotated onto the E-W component and are clearly recorded, but the SH waves at several other stations, although large, appear to have been contaminated by SV energy and were not used in the inversion. The depth is 5.7 km, and the seismic moment is  $1.2 \times 10^{25}$  dyne-cm.



March 29, 1976

The epicenter of the March 29, 1976 earthquake ( $m_b = 5.8$ ,  $M_s = 6.5$ ) is on the southern flank of the Cocos Ridge, along with several other near-ridge events (Figure 8.4). The age of the lithosphere is about 10 m.y. A good match to the observed waveforms is obtained with a focal mechanism (201/81/181, Figure 8.27) characterized by nearly pure strike-slip motion. The mechanism is similar to that of the nearby September 9, 1965 earthquake, but the nodal planes differ in strike by about  $25^\circ$  (Figure 8.4). The depth is 8.1 km, and the seismic moment is  $9.0 \times 10^{25}$  dyne-cm.

December 14, 1977

The December 14, 1977 earthquake ( $m_b = 5.5$ ,  $M_s = 5.1$ ) is located on the Antarctic plate, near the Southwest Indian Ridge (Figure 8.28). The tectonics of this area are complex and poorly known. The age of the lithosphere in the epicentral region is estimated to be about 27 m.y. [Sciater et al., 1981]. The station distribution for this event is poor, but the P waveforms clearly require a normal-faulting mechanism and the SH waveforms constrain the strike (25/51/290, Figure 8.29). The centroid depth which provides the best fit to both P and SH waves is 5.6 km, but the source time function is unusually long (6 s) for the seismic moment ( $3.0 \times 10^{24}$  dyne-cm), implying a very low stress drop for this event. An equally good fit to the P waveforms, with a 3 s source time function, is obtainable at a centroid depth of about 17 km, but none of the SH waves could be satisfactorily matched at this depth. The nodal planes are subparallel to the trend of the many fracture zones in the epicentral region. Dziewonski et al. [1983] report mechanisms for two other small events (April 10, 1982 and

September 8, 1982) very near this one, both with larger components of strike-slip motion than we found for the December 1977 event (Table 8.3, Figure 8.28).

#### December 13, 1979

The epicenter of the December 13, 1979 earthquake ( $m_b = 5.4$ ,  $M_s = 5.5$ ) is in the Panama Basin, east of the highly active Panama Fracture Zone (Figure 8.4). The age of the lithosphere is about 21 m.y. [Hey et al., 1977]. The station distribution for this event is very poor, and very few P waves are suitable for waveform modeling. The SH waves are relatively large and well recorded, however, because the mechanism is characterized by nearly pure strike-slip motion (350/82/186, Figure 8.30). The first-motion polarities which appear to be violated by the inversion mechanism may have been read from one of the surface-reflected phases, rather than the direct P phase, which is very small at some stations (e.g., WES). The depth is 6.0 km, and the seismic moment is  $7.2 \times 10^{24}$  dyne-cm. North-striking fracture zones are found in the region, and the nodal plane striking slightly west of north is probably the fault plane for this event.

#### September 13, 1981

The epicenter of September 13, 1981 earthquake ( $m_b = 5.8$ ,  $M_s = 5.5$ ) is in young (approximately 4 m.y. [Rona and Gray, 1980]) lithosphere of the North American plate, along the Mid-Atlantic Ridge (Figure 8.31). There is obviously enough potential error in the location for it to be a typical ridge axis event, and we probably would not have considered it for the present study, except that Dziewonski and Woodhouse [1983] reported a focal mechanism (74/29/290) characterized by normal faulting on nodal planes striking at a high

angle to the trend of the ridge axis. Such a mechanism would be persuasive evidence that it actually is a near-ridge event, considering the strong similarity to the mechanisms of all the other near-ridge normal-faulting earthquakes in this study.

This earthquake was very well recorded and the station distribution for both P and SH waves is excellent. The best-fitting mechanism (15/33/260; Figure 8.32) is very similar to that of Dziewonski and Woodhouse [1983] except that the strike is rotated nearly  $60^\circ$ , bringing it parallel with the trend of the ridge axis. The inversion converged to this solution even when the Dziewonski and Woodhouse mechanism was used as a starting model. The nodal SH wave at TUC is the major factor controlling the strike; the Dziewonski and Woodhouse mechanism produces a severe misfit at this station. The steeply-dipping nodal plane is required to fit the P waveforms at LPS and SCP (a number of other nearby stations have similar waveforms), at which no dilatational motion is seen. The seismic moment is  $8.4 \times 10^{24}$  dyne-cm, in good agreement with the moment found by Dziewonski and Woodhouse:  $8.95 \times 10^{24}$  dyne-cm.

Our mechanism might appear to confirm the initial suspicion that this is merely a mislocated ridge axis earthquake, except that the centroid of this earthquake is found to be 13.2 km below the seafloor. Source studies of several tens of ridge axis earthquakes with the same technique used here have never yielded a centroid depth of more than about 3.0 km [unpublished data and P.Y. Huang, personal communication, 1984]. Ridge axis earthquakes are also found to have mechanisms with both nodal planes dipping close to  $45^\circ$ . Finally, all 'typical' normal-faulting ridge axis earthquakes are found to occur in the rift valley,

constrained by the period of the very prominent water column reverberations observed immediately after the P phases. We conclude that the September 13, 1981 earthquake is indeed a 'near-ridge' event, the only known example of a normal-faulting event in young oceanic lithosphere which indicates extension in the direction of spreading.

#### December 12, 1981

The December 12, 1981 earthquake ( $m_b = 5.5$ ,  $M_s = 5.1$ ) is located in lithosphere about 35 m.y. old near the Maldivé Islands, in the northern Indian Ocean (Figure 8.33). There are numerous NW-SE trending fracture zones from the Carlsberg Ridge in the area; the epicenter appears to be located on one. Because of the small size and recent vintage of this event, few waveforms usable for the inversion were obtained. Our P waveform data cover an azimuthal arc of only about  $60^\circ$ . We found three usable SH waves which cover one hemisphere. These data, while sparse, yielded a reasonably good solution (56/49/303; Figure 8.34) characterized by normal faulting on planes parallel to the local fracture zone trend. The formal errors of the source parameters are only slightly larger than usual (Table 8.2). The centroid depth is 16.3 km and the seismic moment is only  $2.2 \times 10^{24}$  dyne-cm.

#### OTHER SOURCE MECHANISM DATA FOR NEAR-RIDGE EARTHQUAKES

Because the mechanical properties of the oceanic lithosphere depend strongly on depth as well as age, source depth is an extremely important source parameter. Aside from the 31 events for which source parameters were determined with the body-waveform inversion technique, the only other well-resolved source depth published for a near-ridge earthquake is for an event in the Nazca plate [Mendigüren, 1971] that was too small and too remote to permit an inversion of the long-period body waveforms.

Tobin and Sykes [1968] and Sykes and Sbar [1974] reported first motion solutions for several of the near-ridge earthquakes listed in Table 8.1. Wiens and Stein [1983b] studied several of the events in Table 8.1 for which the body-waveform inversion is inapplicable with a combination of first motion, body waveform, and surface wave techniques. The seismic moments and focal mechanisms of several of the more recent near-ridge earthquakes have been determined by Dziwowski and Woodhouse [1983] and Dziwowski et al. [1983], using a semi-automated inversion of waveform data from the Global Digital Seismic Network (GDSN). The long-period passband of the data used in this technique precludes good resolution of the centroid depth for shallow events, however. This additional information on the global character of near-ridge seismicity is summarized in Table 8.3.

#### SOURCE PARAMETER - AGE RELATIONS.

The deformation represented by near-ridge earthquakes is strongly influenced by the mechanical properties of young oceanic lithosphere and is thus likely to be a strong function of both depth and lithosphere age [Chen and Molnar, 1983; Wiens and Stein, 1983a]. The well-determined centroidal depths of the 31 near-ridge earthquakes studied in this chapter, distinguished on the basis of the ocean in which they occurred, are shown as a function of lithosphere age in Figure 8.35. As noted above (Figure 8.1), an unusually large number of near-ridge earthquakes have occurred in the Indian Ocean. Figure 8.35 also demonstrates that the Indian Ocean accounts for virtually all the near-ridge seismicity at focal depths in excess of 10 km. The deeper earthquakes in the Indian Ocean and one event each near the East Pacific Rise and the Mid-Atlantic Ridge occur at depths where the

standard plate-cooling model [Parsons and Sclater, 1977] predicts a temperature of approximately 800°C. In contrast, few earthquakes in older oceanic lithosphere are found to occur at depths corresponding to such a high temperature [Chen and Molnar, 1983; Wiens and Stein, 1983a].

The depth range of near-ridge earthquakes in areas other than the central Indian Ocean is restricted to depths between 5 and 10 km. In normal oceanic lithosphere, the Moho is found at a depth of about 6 km [e.g., Ewing and Houtz, 1979]. The data of Figure 8.35 suggest that, with the exception of the Indian Ocean, the deformation represented by earthquakes in young oceanic lithosphere occurs mostly in the uppermost mantle, immediately below the Moho. The larger earthquakes, however, almost certainly rupture through the lower crust.

Another feature of near-ridge seismicity evident from Figure 8.35 is that the number of earthquakes is greater in the age range 0-15 m.y. than in the range 15-30 m.y. The decline in seismic activity is even more pronounced if the seismic moments ( $M_0$ ) of the earthquakes are considered. In Figure 8.36, the 31 earthquakes with well-determined centroid depths are divided into three categories: those with  $10^{24} \leq M_0 < 10^{25}$ , those with  $10^{25} \leq M_0 < 10^{26}$ , and those with  $M_0 \geq 10^{26}$ , where  $M_0$  is given in dyne-cm ( $10^{-7}$  N-m). The only earthquake with  $M_0 > 10^{26}$  dyne-cm (January 21, 1970) occurred in lithosphere only about 3 m.y. old, and nearly all the earthquakes with  $M_0 > 10^{25}$  dyne-cm occurred in lithosphere 15 m.y. old or younger. (The apparent scarcity of smaller events in lithosphere less than 10 m.y. old is probably not a real effect, since Table 8.1 includes several such earthquakes for which we were unable to obtain source parameters through long-period

body-wave inversion.) We interpret these data as indicating that deformation accompanying the thermal and mechanical evolution of young oceanic lithosphere is largely accomplished in the first 10 to 15 m.y.

Several interesting features of near-ridge tectonics emerge when the near-ridge earthquakes with known centroidal depths are distinguished on the basis of focal mechanism type (Figure 8.37). We emphasize that the normal-faulting focal mechanisms of near-ridge earthquakes are distinct (with the partial exception of the September 13, 1981 earthquake) from the mechanisms of earthquakes at the ridge axis. Focal mechanisms of normal-faulting near-ridge earthquakes frequently have large strike-slip components and generally have T-axes which are oblique or perpendicular to the local spreading direction. In contrast, ridge axis earthquakes seem to be remarkably consistent in their mechanisms; body-waveform inversions indicate nearly pure normal faulting on nodal planes striking parallel to the ridge axis and dipping at about  $45^\circ$  [Trehu et al., 1981; Solomon et al., 1983].

Similarly, the near-ridge earthquakes characterized by strike-slip faulting are distinct from transform fault earthquakes. In every case one nodal plane is subparallel with the local trend of fracture zones, and many of the near-ridge events are clearly located on fracture zones, but the sense of motion is nearly always the same as the offset of the local ridge axis segments, opposite that expected for a transform fault earthquake.

A distinct stratification of fault type is evident in Figure 8.37: thrust faulting is confined to shallow depths ( $< 10$  km), while the deepest events at all ages are characterized by normal faulting. Strike-slip faulting occurs at intermediate depths. There also seems

to be a strong regional bias to fault type. Reference to Figure 8.35 reveals that 16 of the 19 events in the Indian Ocean represent normal faulting, and only three normal-faulting earthquakes are found outside the Indian Ocean. Tables 8.2 and 8.3 list two additional events outside the Indian Ocean with reported normal-faulting mechanisms (one in the north Atlantic, one in the east Pacific), but we were unable to conduct body-wave inversions for these earthquakes. Four of the five thrust-faulting events occur in the Pacific Ocean, and none occur in the Indian Ocean. Strike-slip faulting occurs in all three oceans. The implications of these characteristics for the tectonic evolution of young oceanic lithosphere are discussed in the following sections.

#### NEAR-RIDGE SEISMICITY OF THE INDIAN OCEAN

A clear conclusion from our brief survey of near-ridge seismicity is that the Indian Ocean is distinctive in at least several respects: it accounts for a disproportionate share of global near-ridge seismicity; the near-ridge earthquakes in the Indian Ocean are found to be deeper than most events in the Pacific or Atlantic Oceans at comparable age; and the Indian Ocean near-ridge earthquakes have dominantly normal-faulting mechanisms. There are several ways to interpret these observations. One view is that the Indian Ocean events are fully representative of near-ridge tectonics, and that only the limited span of observations has prevented the detection of comparable behavior near other ridge systems. An opposite interpretation is that the tectonic processes responsible for the Indian Ocean events are unique to the region, and thus the mechanisms of these earthquakes are not relevant to the general question of the evolution of young oceanic lithosphere.



We favor an intermediate interpretation: the near-ridge earthquakes of the Indian Ocean are at least partly the product of processes common to all young oceanic lithosphere, but the stress field near some portions of the Indian Ocean ridge system has been enhanced or modified by processes peculiar to the region. One piece of evidence in support of this view is that relatively deep normal-faulting earthquakes are found in young oceanic lithosphere in the Pacific (May 2, 1972) and the Atlantic (September 13, 1981). Comparatively deep normal-faulting events in young oceanic lithosphere occur, therefore, in regions other than the Indian Ocean.

For nine of the Indian Ocean events (Figure 4.11), located along the Southeast Indian Ridge (SEIR) and studied in detail in Chapter 4, the perturbing physical process may be tentatively identified. Three of the earthquakes, clustered in a small region of the Antarctic plate between the Kerguelen Plateau and the SEIR, are attributed to thermal and bending stresses associated with a residual depth anomaly in the vicinity of a proposed horizontal 'pipeline' for flow of asthenospheric material from the Kerguelen hotspot to the Amsterdam and St. Paul Islands region of the SEIR [Morgan, 1978]. The remaining six earthquakes, located at four sites spaced along a considerable length of the SEIR on the Indian plate, are speculatively attributed to the response of the Indian plate (and its associated upper mantle convective pattern) to the ongoing collision between the Indian and Asian plates.

Stein [1978] found focal mechanisms of the same type (normal faulting with T-axis oblique to the local spreading direction) for several earthquakes comprising a swarm on the Chagos Bank, in young

oceanic lithosphere of the Indian plate, near the Central Indian Ridge (CIR). We performed body-waveform inversions for three of the Chagos Bank events studied by Stein [1978], confirming the basic source parameters. We also inverted the waveforms from four other near-ridge events in the same area, including one member of the Chagos Bank swarm not studied by Stein (November 10, 1967). The source mechanisms of these latter events reveal an aspect of the deformation of the lithosphere in this area not previously noted: three of the earthquakes, including the November 10, 1967 event, have right-lateral strike-slip mechanisms on planes striking northeast, parallel to the many fracture zones offsetting the CIR. The focal mechanism of the fourth earthquake (November 17, 1973) is a combination of the strike-slip and normal-faulting mechanisms observed in the area. The focal mechanisms of all the events near the CIR are shown in Figure 8.6.

Clearly, the deformation represented by the near-ridge seismicity near the CIR is not an exact analog of the SEIR situation, since no strike-slip faulting has been observed in the latter region. The observation of a component of right-lateral shear along with the extensional deformation near the CIR, however, still permits the hypothesis that the near-ridge seismicity in both areas to some degree reflects plate-wide consequences of the continental collision. The geometry of the mid-ocean ridge system varies considerably between the SEIR and CIR, and horizontally-transmitted stresses in the lithosphere may be expected to vary as well. All the strike-slip mechanisms on the Indian plate near the CIR have a right-lateral sense of slip, the same sense of offset as the many short spreading segments of the CIR (Figure

8.6), raising the possibility that the spreading geometry is still evolving. Such a process is a plausible consequence of a large perturbation to the boundary conditions of a plate, such as has undoubtedly occurred in the case of the Indian plate.

The remaining near-ridge seismicity in the Indian Ocean consists of three events in a tight cluster on the Antarctic side of the Southwest Indian Ridge (SWIR) and several events along a short section of the SEIR south of Australia (Figure 8.1). All these earthquakes are quite small; we were able to perform waveform inversions for only one event in each location. Both events are characterized by normal faulting, with a significant component of strike-slip motion, and both are shallower than any of the near-ridge normal-faulting events along the CIR or western portion of the SEIR. Dziewonski et al. [1983] obtained focal mechanisms for the other two events near the SWIR; the mechanisms are rather different from each other and from that of the third event. There is no evidence to suggest that these last two groups of near-ridge earthquakes in the Indian Ocean are in any way atypical.

#### DEEP NORMAL FAULTING IN YOUNG OCEANIC LITHOSPHERE

Normal-faulting earthquakes occur in young lithosphere in all oceans, and constitute most of the deeper events at any lithosphere age between 3 and 35 m.y. (Figure 8.37). Whether the Indian Ocean is truly anomalous with respect to the processes producing the large number of normal-faulting earthquakes observed there, the depth distribution of such events has important implications for the mechanical and thermal structure of young oceanic lithosphere and for the sources of lithospheric stress near mid-ocean ridges. We consider some of these implications in this section.

Of particular interest are those normal-faulting earthquakes which occur at depths within the oceanic lithosphere at which the temperature is thought to be high enough to reduce through ductile flow the expected ability of the lithosphere to sustain significant differential stresses at an appropriate strain rate. Studies of the focal depths of earthquakes in older oceanic lithosphere have produced estimates of limiting isotherms in the range of 600° to 800°C, with very few events approaching the depth of the latter isotherm [Chen and Molnar, 1983; Wiens and Stein, 1983a]. We have seen that there are at least three sites in the Indian Ocean and one each in the Pacific and Atlantic which experience normal-faulting earthquakes at depths at which standard plate-cooling models [Parsons and Sclater, 1977] predict temperatures in the neighborhood of 800°C. To infer the nature and cause of the deformation represented by these deep normal-faulting earthquakes, estimates of the strength of the lithosphere as a function of temperature (i.e., depth) are necessary.

Strength envelopes for the lithosphere, giving the maximum sustainable differential stress as a function of depth, are now commonly encountered in the geophysical literature [e.g., Goetze and Evans, 1979; Brace and Kohlstedt, 1980; Meissner and Strehlau, 1982]. They all feature a near-surface strength which increases linearly with confining pressure according to a brittle failure law, typically that of Byerlee [1978]. The slope of this part of the strength envelope is a strong function of the assumed pore pressure; zero strength is predicted if pore pressure equals lithostatic pressure. The maximum strength occurs at the brittle-ductile transition, below which thermally-activated ductile flow rapidly reduces the differential

stress which may be sustained. For a given geotherm, the ductile flow law is primarily controlled by the assumed strain rate, with a higher strain rate allowing greater differential stress to be maintained at greater depths. The depth of the brittle-ductile transition is increased and the maximum sustainable differential stress is lowered with an increase in the pore pressure. A higher strain rate increases both the depth of the brittle-ductile transition and the maximum sustainable stress difference. Figure 8.38 illustrates these relationships for 15 m.y. old lithosphere.

Our arguments in this section obviously depend on the accuracy of the geotherm calculated from the plate-cooling model, since the ductile flow laws are highly temperature-dependent. Hydrothermal circulation in the crust is thought to remove some fraction of the heat in young oceanic lithosphere [Lister, 1977; Fehn and Cathles, 1979], but little is known about the extent to which this circulation perturbs the geotherm in young oceanic lithosphere. The agreement between the observed seafloor depth-age relation and the subsidence curve calculated from the conductive cooling model [Parsons and Sclater, 1977] suggests that the theoretical geotherm is a good approximation to the average thermal state of at least the mantle portion of the oceanic lithosphere. Local departures are certainly a possibility, however.

If earthquakes occur only at depths at which the strength envelope is controlled by the brittle failure law, extremely high pore pressures (approaching the lithostat) and very low limits to the differential stress must exist at the depth of the deepest normal-faulting earthquakes. This can be seen by comparing the 22 km depth of an earthquake in 13 m.y. old lithosphere (Figure 8.37) with the strength

envelope for normal faulting in Figure 8.38. Kirby [1980] has argued that pore pressure in the oceanic upper mantle is near-zero, but we consider the question open, given the near-absence of evidence. Near-lithostatic pore pressure is not required, however, if earthquakes can occur below the brittle-ductile transition, at depths for which the ductile flow law still allows significant differential stress to be maintained. This position implies either that brittle failure may occur at lower differential stress than predicted by Byerlee's law or that some earthquakes may represent rapid ductile failure.

If we assume that the deepest normal-faulting events define the depth at which lithospheric strength is reduced by ductile flow to a level insufficient for seismic failure, a joint constraint may be placed on the differential stress at which failure occurred and the corresponding strain rate of the deformation leading to seismic failure. If a minimum differential stress level is specified, a lower bound on the strain rate is implied. In Figure 8.39, curves defining the depth at which a representative range of stress levels are reached with the ductile flow law for dry olivine [Goetze and Evans, 1979] are shown for strain rates of  $10^{-13}$  sec $^{-1}$  and  $10^{-15}$  sec $^{-1}$ . In order for a strain rate as low as  $10^{-15}$  sec $^{-1}$  to be accommodated, the stress level associated with the deepest events can be no greater than a few hundred bars. A stress level in the kilobar range requires a strain rate of about  $10^{-13}$  sec $^{-1}$ .

Wiens and Stein [1983a] estimated a strain rate of  $10^{-15}$  sec $^{-1}$  for the highly active Ninetyeast Ridge area of the Indian Ocean. If this strain rate were applicable to near-ridge deformation, a relatively low level of stress in young oceanic lithosphere would be implied. An

average strain rate estimated from the seismic moments of a small number of earthquakes distributed over a broad region will always tend to be a lower bound, however, given the possibility that oceanic intraplate deformation is concentrated near zones of significant strength variation, as is commonly observed in continental tectonics [Sykes, 1978]. Strain rates as high as  $10^{-13}$  sec<sup>-1</sup> have been inferred from naturally deformed rocks [e.g., Pfiffner and Ramsay, 1982].

In Chapter 4, we calculated stress drops for nine of the deep normal-faulting events in this study, obtaining values in the range of 1 to 30 bars (10 bars = 1 MPa). The static stress drop, of course, represents only a lower bound on estimates for the shear stress across the fault plane prior to the earthquake. There is great controversy concerning the average level of stress in the lithosphere, with estimates ranging from a few hundred bars to several kilobars [e.g., Hanks and Raleigh, 1980]. In a later section, we will argue that a minimum differential stress of several hundred bars is indicated by the lack of a clear influence of "ridge push" stress on the focal mechanisms of near-ridge earthquakes. All these lines of evidence suggest that the characteristic strain rate of the deformation represented by near-ridge earthquakes is at least  $10^{-15}$  sec<sup>-1</sup>.

#### THERMOELASTIC STRESS AND NEAR-RIDGE EARTHQUAKES

An important question concerns the source of the stress which gives rise to normal-faulting earthquakes in young oceanic lithosphere. We note that normal faulting characterizes virtually all near-ridge earthquakes (with known depths and mechanisms) at depths below 10 km (Figure 8.37). Thermoelastic stresses resulting from the cooling of the lithosphere can account both for the observation of normal faulting

at depth and the fact that the T-axes of the focal mechanisms tend to be subparallel to the ridge axis [Turcotte and Oxburgh, 1973; Turcotte, 1974]. Bergman et al. [1984] discounted this mechanism as the primary cause of the earthquakes along the SEIR on the grounds that so little similar seismicity has been reported in other near-ridge areas. While the activity in the Indian Ocean is clearly occurring more intensely (at least over the last 20 years) than most other areas, the results of this study show that normal-faulting near-ridge events are not confined to the central Indian Ocean. We consider here the implications of the assumption that thermoelastic cooling stresses are typical of all near-ridge environments, but have been enhanced or modified in some manner at certain sites of anomalous near-ridge seismicity in the Indian Ocean.

The largest rate of release of thermoelastic stress in the cooling lithosphere is likely to be found near the region experiencing the highest differential cooling rate. The cooling rate as a function of age and depth in the plate-cooling model of Parsons and Sclater [1977] may be found analytically [e.g., Carslaw and Jaeger, 1959]. In Figure 8.40 are plotted contours of equal cooling rate as well as the curve defining the depth of the maximum cooling rate as a function of lithosphere age. At shallow depths near the ridge, very high cooling rates ( $> 100^\circ/\text{m.y.}$ ) are predicted, but hydrothermal circulation in the crust probably modifies significantly the shallow geotherm in this region, and much of the thermoelastic stress is likely to be relieved by shallow cracking within instantaneous volumes too small to result in a significant earthquake [e.g., Lister, 1977]. By 30 m.y., the upper 30 km of the oceanic lithosphere cools at a rate of  $10^\circ/\text{m.y.}$  or less.



To an age of about 15 m.y., the deepest normal-faulting earthquakes parallel at a somewhat shallower depth the contour of maximum cooling rate. The concentration near-ridge seismicity in lithosphere less than about 15 m.y. old supports the hypothesis of an important role for thermoelastic stresses, particularly since the vertical gradient of cooling rate is relatively high in this age range. Significant thermoelastic stresses can be expected in regions where the cooling rate varies rapidly with distance. A natural explanation for the cessation of seismicity short of the depth of maximum cooling rate is that the strength of the lithosphere at that depth is too low for significant strain to accumulate.

Thermoelastic stresses related to plate cooling may also account for some instances of shallow thrust faulting in young oceanic lithosphere. The thermal stress in an elastic body is proportional to the product  $\alpha E$  of the coefficient of thermal expansion and Young's modulus. Turcotte [1974] noted that, for the oceanic crust,  $\alpha E$  may well be different from that of the upper mantle, so that the oceanic lithosphere reacts to temperature changes like a bimetallic strip. Using available (but not well-constrained) material constants, Turcotte found that  $\alpha E_{\text{crust}} < \alpha E_{\text{mantle}}$ , in which case plate cooling produces higher thermal stresses in the upper mantle than the crust, which is consistent with the observation that near-ridge seismicity is concentrated below the Moho (Figure 8.36). The bimetallic strip analog, however, predicts thrust faulting only in the crust. The July 1, 1974 earthquake is entirely consistent with this model: it clearly occurred in the crust ( $h = 2.4$  km) and the thrust faulting mechanism has a P axis nearly perpendicular to the spreading direction. The June

29, 1973 event is also quite shallow ( $h = 4.6$  km) and has a large component of thrust motion. The other examples of thrust faulting for which we have accurate depths are at or below the Moho, although none is more than 10 km below the seafloor (Figure 8.37).

Thermoelastic stresses related to cooling of the lithosphere are thus consistent with the depth and age extent of near-ridge earthquakes and can account for the observation of deep normal faulting and at least some shallow thrust faulting. The higher level of near-ridge seismicity in general and deep normal faulting in particular in certain portions of the central Indian Ocean, however, still requires that additional local processes act to accentuate the typical rate of stress release.

#### SECONDARY CONVECTION BENEATH YOUNG OCEANIC LITHOSPHERE ?

One process which could play an important role in modifying the near-ridge stress regime in some areas is secondary convection immediately below the lithosphere. Secondary convection will obviously perturb the geotherm relative to simple plate cooling, thus inducing thermoelastic stresses. In addition, it may alter the state of stress directly through viscous drag on the base of the lithosphere. We will argue in Chapter 9 that the coupling between lithosphere and asthenosphere is likely to be too weak for significant stress to accumulate in older lithosphere from this source. We suspect thermoelastic stresses will be far more important than basal shear stress in young lithosphere. The evidence supporting the existence of small-scale convection beneath young oceanic lithosphere is summarized in Chapter 4. This is currently an area of active research; development of the ability to identify more reliably the sites and

platforms of small-scale convective patterns and to compare this information with the epicenters and mechanisms of near-ridge earthquakes is a particularly exciting prospect.

#### TECTONIC EVOLUTION OF YOUNG OCEANIC LITHOSPHERE

In this section, we draw together a number of observations concerning near-ridge earthquakes and consider some of the broader tectonic implications. These interpretations apply to young oceanic lithosphere in general rather than to a particular region.

##### Influence of Other Plate Boundaries

We have assumed that near-ridge earthquakes are generally related to tectonic processes associated with the early evolution of the oceanic lithosphere created at the nearby spreading center, but in some cases, stresses associated with other plate boundaries may also be significant. The most likely such case in our set of earthquakes occurs in the eastern Pacific, in the vicinity of the Panama Fracture Zone (Figure 8.4). All four events in this area with known mechanisms are characterized by right-lateral strike-slip motion on planes striking roughly north-south. The relatively frequent occurrence of near-ridge earthquakes in this region and the uniformity of the focal mechanisms may reflect the significance of stresses related to the nearby Central and South American convergent zones. Another region of concentrated near-ridge seismicity is near the intersection of the East Pacific Rise and the Cocos-Nazca spreading boundary (Figure 8.15), but the seismicity appears to be associated only with one arm of the triple junction. We have suggested that the notable concentration of near-ridge seismicity at several sites in the central Indian Ocean may reflect the influence of stresses related to the continental

convergence between India and Asia (Chapter 4), but the distance involved is quite large and the relationship must clearly be considered speculative.

#### Aseismicity of the Oceanic Crust

One of the more striking features of the earthquakes for which we have reliable depths is the low level of seismicity in the oceanic crust. The only event which is clearly located in the crust (July 1, 1974, at a depth of 2.4 km) is also very small, and therefore may have only ruptured a portion of the upper oceanic crust. Some of the larger events at greater depth may have ruptured into the crust, but it is difficult to avoid the conclusion that either the source of the seismogenic stress lies within the upper mantle or the crust is much weaker than the uppermost mantle (or both).

Studies of continental seismicity have indicated a tendency for hypocenters to cluster at two depths, in the upper crust and just below the Moho [Meissner and Strehlau, 1982; Chen and Molnar, 1983]. This observation has been interpreted in terms of a strength envelope for which the crustal and mantle materials have very different ductile flow laws. With reasonable assumptions as to the thermal structure and strain rate, the relative strength of the lower continental crust may be substantially reduced by ductile flow, producing a strength envelope with two peaks, one in the upper crust and another just below the Moho. Diabase is often chosen as an analog for the oceanic crust, but diabase remains entirely in the brittle field under the pressure and temperature conditions in the off-ridge oceanic crust [Caristan, 1982]. A single -peaked strength envelope (such as in Figure 8.38) is thus predicted, and it is difficult to explain the concentration of

near-ridge seismicity just below the Moho. One possibility is that a material considerably weaker than diabase, perhaps because of hydrothermal alteration, is a more appropriate choice to represent the strength of the oceanic crust in near-ridge environments [e.g., Epp and Suyenaga, 1978].

The bimetallic strip analog for the oceanic lithosphere [Turcotte, 1974] provides an alternative explanation, as discussed above, in that it predicts a concentration of thermoelastic stress in the upper mantle, just below the Moho. Furthermore, if thermoelastic stresses resulting from plate cooling are considered as a significant source of stress in young oceanic lithosphere, the aseismicity of the oceanic crust may be attributed to the prior relief of those stresses near the ridge axis by cooling and cracking associated with hydrothermal circulation [Lister, 1977], provided that this circulation extended at least to the base of the crust.

#### Transition from Ridge-Axis to Intraplate Stress Regime

There is no evidence in the data assembled here for the proposed transition from horizontal extension to compression at around 20 m.y. [Sykes and Sbar, 1974]. Large thrust-faulting events are observed in lithosphere as young as 3 m.y., while normal faulting is observed at ages approaching 35 m.y. (Figure 8.37). It is true that normal faulting is not observed in oceanic lithosphere older than 35 m.y., except in the presence of large bending stresses seaward of subduction zones [e.g., Chapple and Forsyth, 1979], but none of the near-ridge normal-faulting events resembles a ridge-axis earthquake in terms of focal depth or (with one exception) T-axis orientation. The transition from teleseismically-identifiable extensional faulting in the direction

of plate motion apparently occurs very soon after plate creation. The use of a general transition in the stress field at 20 m.y. age, from extension parallel to the spreading direction to compression in the same direction [Fleitout and Froidevaux, 1983], is not justified by the source mechanism data of this study.

#### Near-Ridge Earthquakes and 'Ridge Push'

We see little evidence to suggest that a "ridge push" compressive stress associated with subsidence of the cooling lithosphere [Lister, 1975; Dahlen, 1981] is a dominant component of the deviatoric stress released by near-ridge earthquakes. The only support for this hypothesis comes from two earthquakes (November 25, 1965 and May 9, 1971) which are characterized by thrust faulting with the P-axis oriented nearly perpendicular to the nearby ridge axis.

A P-axis oriented along the spreading direction is not, however, a general feature of near-ridge thrust events. Figure 8.15 shows a short length of the East Pacific Rise near which several earthquakes have occurred. On the Pacific plate side, two large thrust events occurred about five years apart in the same location. The focal mechanisms of these events are very well constrained by the body-wave inversion and are essentially identical. The P-axes for these events make an angle of approximately  $30^\circ$  with the spreading direction. On the Cocos plate side of the ridge occurred a normal-faulting earthquake with a T-axis parallel to the P-axes of the two thrust events. Another event on the Pacific plate side, which we were unable to study because of contamination of the body waves by an earlier event, is also characterized by normal faulting (D.A. Wiens, personal communication, 1983). We see no possibility of accounting for these events with either horizontal principal stress oriented perpendicular to the ridge.

The only other thrust-faulting earthquake for which we obtained a focal mechanism by body-wave inversion (July 1, 1974) has a P axis nearly perpendicular to the spreading direction. Further, none of the remaining events in Table 8.3 with proposed thrust-faulting mechanisms provides convincing evidence of the importance of ridge-perpendicular compressive stress. All the strike-slip events have one nodal plane parallel to the local trend of fracture zones; thus their inferred P-axes are also oblique to the spreading direction.

The lack of a clear influence of 'ridge push' on the state of stress near mid-ocean ridge systems permits a lower bound to be placed on the typical level of stress differences in young oceanic lithosphere, if the assumption is made that the stress differences are nearly zero at the ridge axis [e.g., Artyushkov, 1973; Dahlen, 1981]. Under this assumption, the stress difference in oceanic lithosphere increases linearly with age to about 100 bars (10 MPa) at 30 m.y. age. The typical stress differences in young oceanic lithosphere must significantly exceed this value; i.e., stress differences of a few hundred bars or greater must be present in the regions of near-ridge earthquake hypocenters. From our earlier discussion, this bound on the level of stress and the depth extent of normal-faulting earthquakes suggest associated strain rates of at least  $10^{-15}$  sec<sup>-1</sup> in areas of near-ridge seismicity.

Table 8.1. Epicentral data<sup>1</sup> for near-ridge earthquakes<sup>2</sup>

Date	Origin time			Lat. °N	Long. °E	$m_b$	$M_s$	Age <sup>3</sup> (m.y.)
	h	m	s					
a August 6, 1962	1	35	27.7	32.26	-41.03			8
August 22, 1963	9	27	5.8	42.08	-126.19			3
June 12, 1964	16	44	35.6	2.19	-83.13	5.4		3
September 17, 1964	15	2	1.5	44.58	-31.34	5.5		20
a September 9, 1965	10	2	25.7	6.51	-84.44	5.8	6.2	12/18
a September 12, 1965	22	2	37.7	-6.46	70.76	6.1	6.0	18/35
November 25, 1965	10	50	50.8	-17.07	-100.24	5.3	4.9	20
b December 19, 1965	22	6	33.0	-32.24	78.87	5.5		4
b February 17, 1966	11	47	57.3	-32.20	79.93	6.0		4
February 17, 1966	12	43	2.0	-32.15	79.04	5.6		4
March 28, 1966	4	44	12.2	-32.12	78.84	5.5		4
a January 7, 1967	0	27	23.0	-48.80	112.76	5.5		2.5
a November 10, 1967	18	38	34	-6.03	71.34	5.2		20/35
a November 11, 1967	11	55	56	-6.01	71.36	5.3	5.2	20/35
November 11, 1967	12	14	55.0	-6.03	71.34	5.6	5.8	20/35
November 11, 1967	17	59	57.0	-6.10	71.32	5.4		20/35
November 21, 1967	17	2	25.8	72.66	8.14	5.4		10
February 20, 1968	2	19	49.5	12.40	-46.94	5.5		17
a March 2, 1968	22	2	24.2	-6.09	71.41	5.5	5.4	20/35
b October 8, 1968	7	43	22.8	-39.85	87.74	5.8	5.8	5
July 25, 1969	21	30	33.3	12.44	-40.75	4.8		20/35
a August 8, 1969	11	8	13.2	-47.76	-15.66	5.7		8/19
a January 21, 1970	17	51	37.4	7.03	-104.24	6.1	6.8	3
a March 31, 1970	18	18	28.0	-3.78	69.70	5.5	5.5	11



Table 8.1. (continued)

Date	Origin time			Lat. °N	Long. °E	m <sub>b</sub>	M <sub>s</sub>	Age <sup>3</sup> (m.y.)
	h	m	s					
a April 25, 1970	3	43	31	-6.29	69.84	5.1	5.1	14
a May 9, 1971	8	25	1.1	-39.78	-104.87	6.0	6.0	9
May 9, 1971	18	1	0.3	-39.77	-105.10	5.4		9
a May 2, 1972	6	56	23.2	5.22	-100.32	5.9	5.5	3
b May 3, 1973	23	11	4	-46.14	73.22	5.5	5.5	27
a June 29, 1973	7	55	12.7	3.93	-85.03	5.4	4.9	7/11
a November 17, 1973	10	51	19.6	-1.59	69.85	5.4	5.5	13
January 18, 1974	21	14	51.2	-34.08	-20.15	5.4		22/25
a July 1, 1974	23	11	14.5	-22.57	-10.68	5.5	5.5	9
a September 11, 1975	22	0	1.3	7.05	-104.18	6.3	5.8	3
b September 19, 1975	3	37	11	-34.74	81.88	5.9	6.1	13
October 29, 1975	5	1	49	4.07	-103.51	5.4		2.5
a March 29, 1976	5	39	36.3	3.96	-85.88	5.8	6.5	11
August 4, 1976	14	0	1.6	-35.62	-14.02	5.7	5.4	5/17
October 21, 1976	3	56	28.1	-57.37	-161.07	5.4		21
b November 2, 1976	7	13	17	-29.36	77.65	5.8	6.5	10
b November 2, 1976	11	19	15	-29.24	77.79	5.6		10
February 17, 1977	20	25	21.5	-45.39	-19.06	5.4	5.2	14/18
April 11, 1977	2	15	18.4	-52.24	114.66	5.4	5.4	5
a December 14, 1977	3	0	14.0	-33.84	57.98	5.5	4.7	27
January 5, 1978	3	23	26.2	-20.79	-126.95	5.5		23
April 3, 1978	6	9	36.6	-52.21	114.61	5.4		5
July 25, 1978	7	54	08.9	-20.75	-126.95	5.1	3.8	23
b May 22, 1979	1	55	55.8	-43.81	79.00	5.5	5.1	9

Table 8.1. (continued)

Date	Origin time h m s	Lat. °N	Long. °E	$m_b$	$M_s$	Age <sup>3</sup> (m.y.)
a December 13, 1979	2 43 36.9	5.55	-80.48	5.4	5.5	21
March 6, 1981	19 43 0.3	3.93	-85.88	5.9	6.5	11
a September 13, 1981	9 19 30.9	24.87	-46.30	5.8	5.5	4
b September 24, 1981	21 9 42.6	-45.65	79.86	5.4	5.5	14
September 30, 1981	23 3 54.4	-5.09	-111.98	5.9	5.2	6/15
a December 12, 1981	23 31 10.9	4.89	70.15	5.5	5.1	35
April 10, 1982	6 47 54.3	-34.33	58.33	5.6	5.4	32/38
April 18, 1982	11 31 4.3	-29.07	-113.84	5.9	5.8	3
June 18, 1982	3 4 5.5	-34.03	58.39	5.5		32/38
June 20, 1982	23 51 30.4	-28.50	50.79	5.5		
September 8, 1982	21 12 31.5	-34.50	58.29	5.4	5.2	32/38
July 31, 1983	10 26 0.3	-20.13	-126.93	6.0	5.3	23
July 31, 1983	11 57 50.0	-20.12	-127.01	5.4		23
November 30, 1983	17 46 0.4	-6.89	72.12	6.6	7.5	35
November 30, 1983	19 16 33.8	-6.84	72.26	5.4		35
November 30, 1983	21 42 08.0	-6.71	71.35	5.5		35
December 1, 1983	5 45 34.2	-6.66	71.43	5.9	5.6	35
December 1, 1983	12 22 22.3	-6.76	71.85	5.4		35
December 1, 1983	22 29 29.6	-6.68	71.81	5.4	5.3	35
December 3, 1983	17 43 14.4	-6.54	71.41	6.3	6.3	35
December 8, 1983	17 23 13.3	-6.61	71.46	5.9	6.0	35

Table 8.1. (continued)

- 1) Sources of data: Same as Appendix B.
- 2) Source mechanism determined by body-waveform inversion, presented in this chapter (a) or Chapter 4 (b)
- 3) Lithosphere age estimated from magnetic anomaly identifications and the magnetic chronology of LaBrecque et al. [1977] or from the isochrons determined by Sclater et al. [1980, 1981a].

Table 8.2 Source mechanisms obtained from body-wave inversion<sup>a</sup>

Date	Moment <sup>b</sup>	$t_s^c$	Depth <sup>d</sup>	Strike	Dip	Slip
August 6, 1962	13. $\pm$ 1.	3.0 $\pm$ 1.0	9.3 $\pm$ 0.1	287.4° $\pm$ 1.1	43.8° $\pm$ 0.6	315.9° $\pm$ 1.0
September 9, 1965	24. $\pm$ 2.	4.0 $\pm$ 1.0	6.5 $\pm$ 0.1	177.0 $\pm$ 0.1	91.5 $\pm$ 0.5	160.4 $\pm$ 0.5
September 12, 1965	37. $\pm$ 6.	4.0 $\pm$ 1.0	15.9 $\pm$ 0.1	266.3 $\pm$ 2.3	43.2 $\pm$ 0.4	249.6 $\pm$ 1.1
January 7, 1967	12. $\pm$ 2.	4.0 $\pm$ 1.0	6.9 $\pm$ 0.1	18.5 $\pm$ 2.3	41.6 $\pm$ 0.7	237.8 $\pm$ 1.8
November 10, 1967	2.8 $\pm$ 0.2	3.0 $\pm$ 1.0	15.6 $\pm$ 0.1	229.3 $\pm$ 1.0	79.7 $\pm$ 1.1	188.3 $\pm$ 1.1
November 11, 1967	3.5 $\pm$ 0.3	3.0 $\pm$ 1.0	16.3 $\pm$ 0.2	264.1 $\pm$ 1.7	49.7 $\pm$ 0.6	265.0 $\pm$ 1.3
March 2, 1968	8.4 $\pm$ 1.0	4.8 $\pm$ 1.2	13.1 $\pm$ 0.1	281.3 $\pm$ 0.9	53.3 $\pm$ 0.3	281.2 $\pm$ 1.0
August 8, 1969	18. $\pm$ 3.	4.0 $\pm$ 1.0	6.1 $\pm$ 0.2	10.1 $\pm$ 1.3	64.0 $\pm$ 1.2	220.9 $\pm$ 1.5
January 21, 1970	140. $\pm$ 5.	10.5 $\pm$ 1.5	6.5 $\pm$ 0.2	331.6 $\pm$ 1.4	43.3 $\pm$ 0.4	108.2 $\pm$ 1.7
March 31, 1970	7.5 $\pm$ 1.6	4.0 $\pm$ 1.0	11.7 $\pm$ 0.1	44.0 $\pm$ 1.7	86.1 $\pm$ 1.1	185.3 $\pm$ 1.0
April 25, 1970	1.7 $\pm$ 0.2	2.0 $\pm$ 1.0	8.7 $\pm$ 0.1	251.3 $\pm$ 1.3	81.3 $\pm$ 1.2	196.0 $\pm$ 1.6
May 9, 1971	55. $\pm$ 9.	10.0 $\pm$ 1.0	8.2 $\pm$ 0.1	24.2 $\pm$ 0.9	45.0 $\pm$ 0.3	102.3 $\pm$ 1.2
May 2, 1972	18. $\pm$ 2.	4.5 $\pm$ 1.5	10.6 $\pm$ 0.2	331.9 $\pm$ 1.4	49.3 $\pm$ 0.5	281.5 $\pm$ 1.8
June 29, 1973	2.8 $\pm$ 0.6	4.0 $\pm$ 1.0	4.6 $\pm$ 0.2	351.9 $\pm$ 2.2	58.4 $\pm$ 3.3	169.2 $\pm$ 4.1
November 17, 1973	4.8 $\pm$ 0.4	3.0 $\pm$ 1.5	16.4 $\pm$ 0.1	45.3 $\pm$ 2.0	52.0 $\pm$ 1.2	224.2 $\pm$ 1.4

Table 8.2 (continued)

Date	Moment <sup>b</sup>	$t_s$ <sup>c</sup>	Depth <sup>d</sup>	Strike	Dip	Slip
July 1, 1974	3.2 $\pm$ 0.3	2.0 $\pm$ 1.0	2.4 $\pm$ 0.1	71.2 $\pm$ 1.4	36.8 $\pm$ 0.5	95.1 $\pm$ 1.3
September 11, 1975	12. $\pm$ 1.	4.0 $\pm$ 1.0	5.7 $\pm$ 0.2	308.5 $\pm$ 3.1	44.9 $\pm$ 0.9	94.0 $\pm$ 2.6
March 29, 1976	90. $\pm$ 6.	6.0 $\pm$ 1.5	8.1 $\pm$ 0.1	200.5 $\pm$ 0.6	80.6 $\pm$ 0.6	180.5 $\pm$ 1.2
December 14, 1977	3.0 $\pm$ 0.5	6.0 $\pm$ 1.0	5.6 $\pm$ 0.1	24.9 $\pm$ 1.6	51.2 $\pm$ 0.6	290.0 $\pm$ 1.6
December 13, 1979	7.2 $\pm$ 1.4	4.5 $\pm$ 1.5	6.0 $\pm$ 0.1	350.2 $\pm$ 1.1	81.9 $\pm$ 1.5	185.9 $\pm$ 1.4
September 13, 1981	8.4 $\pm$ 0.8	3.9 $\pm$ 1.3	13.2 $\pm$ 0.1	14.6 $\pm$ 2.5	32.7 $\pm$ 0.5	259.8 $\pm$ 1.6
December 12, 1981	2.2 $\pm$ 0.4	2.0 $\pm$ 1.0	16.3 $\pm$ 0.3	56.2 $\pm$ 2.0	49.0 $\pm$ 1.2	303.2 $\pm$ 2.2

a) The range indicated for each parameter is one standard deviation (formal error). The range of  $t_s$  is one half the width of the source time function element used in the inversion.

b)  $\times 10^{24}$  dyne-cm ( $10^{17}$  N-m).

c) Total duration of the source time function, sec.

d) Relative to the top of the crust (or sediment layer, if used), km.

Table 8.3. Other source mechanism data<sup>1</sup> for near-ridge earthquakes

<u>Date</u>	<u>M<sub>0</sub></u>	<u>Depth</u>	<u>Mechanism</u>	<u>Ref.<sup>2</sup></u>
August 22, 1963			043/90/180	a
September 17, 1964			222/68/130	b
November 25, 1965	1.8	9.0	022/46/110	c
February 20, 1968			normal	b
July 25, 1969			thrust	b
October 29, 1975			normal	f
September 30, 1981	2.2		270/47/054	d
April 10, 1982	2.5		133/36/319	e
April 18, 1982	14.		140/43/085	e
September 8, 1982	2.6		335/42/341	e

1) Same data conventions as Table 8.2.

2) Source mechanism references:

a - Tobin and Sykes [1968]

b - Sykes and Sbar [1974]

c - Mendiguren [1971]

d - Dziewonski and Woodhouse [1983]

e - Dziewonski et al. [1983]

f - D.A. Wiens, personal communication, 1983

## FIGURE CAPTIONS

Figure 8.1. Epicentral locations of the 67 near-ridge earthquakes listed in Table 8.1. Coastlines and oceanic spreading centers are also shown. Mollweide projection.

Figure 8.2. Bathymetry, seismicity, and isochrons in the epicentral region of the August 6, 1962 earthquake, near the Mid-Atlantic Ridge. The 3000 m bathymetric contour is from Searle et al. [1982]. Also shown is the focal mechanism of a ridge-axis earthquake (November 16, 1965) determined with the body-waveform inversion technique used in this paper [Solomon et al., 1983]. Solid dots indicate epicenters from the ISC (1964-1979), located from reported arrival times at 10 or more stations. Large dots indicate events with  $m_b \geq 5.4$ . The heavy dashed line indicates the position of the ridge axis. Isochrons (4, 9, 20, and 35 m.y.) are from the compilation of Sclater et al. [1980].

Figure 8.3. Comparison of observed (solid line) and synthetic (dashed line) long-period P and SH waves for the August 6, 1962 earthquake; the focal mechanism solution obtained from the inversion is plotted on the lower focal hemisphere (equal-area projection). All amplitudes are normalized to an instrument magnification of 3000; the amplitude scales correspond to the waveforms that would be observed on an original seismogram from such an instrument. The two vertical lines delimit the portion of each time series, digitized at 0.5 sec intervals, used in the inversion. Symbols for both types of waves are open circle - dilatation, closed circle - compression, cross - emergent arrival. For SH waves, compression corresponds to

positive motion as defined by Aki and Richards [1980]. The source time function obtained from the inversion is also shown.

Figure 8.4. Bathymetry, seismicity, and identified magnetic lineations in the epicentral region of the September 9, 1965, June 29, 1973, March 29, 1976, and December 13, 1979 earthquakes, in the eastern Pacific. The epicenter of the June 12, 1964 earthquake is also indicated. The 3000 m bathymetric contour is from Mammerickx and Smith [1982]. Identified magnetic lineations are from Drummond [1981]. See Figure 8.2 for further explanation.

Figure 8.5. Comparison of the observed and synthetic P and SH waves for the September 9, 1965 event. See Figure 8.3 for further explanation.

Figure 8.6. Bathymetry, seismicity, and isochrons between the Central Indian Ridge and the Chagos Bank. The bathymetry of the region is represented by the 4000 m contour, from Laughton [1975] and Fisher et al. [1982]. The Chagos Bank is outlined by the 200 m contour. Focal mechanisms of near-ridge earthquakes determined in this study are shown. See Figure 8.2 for further explanation.

Figure 8.7. Comparison of the observed and synthetic P and SH waves for the September 12, 1965 event. See Figure 8.3 for further explanation.

Figure 8.8. Bathymetry, seismicity, and isochrons in the epicentral region of the January 7, 1967 earthquake, south of Australia. Bathymetric contours (3000 and 4000 m) are from Hayes and Vogel [1981], Falconer and Tharp [1981], and Fisher et al. [1982]. See Figure 8.2 for further explanation.



Figure 8.9. Comparison of the observed and synthetic P and SH waves for the January 7, 1967 event. See Figure 8.3 for further explanation.

Figure 8.10. Comparison of the observed and synthetic P and SH waves for the November 10, 1967 event. See Figure 8.3 for further explanation.

Figure 8.11. Comparison of the observed and synthetic P and SH waves for the November 11, 1967 event. See Figure 8.3 for further explanation.

Figure 8.12. Comparison of the observed and synthetic P and SH waves for the March 2, 1968 event. See Figure 8.3 for further explanation.

Figure 8.13. Bathymetry, seismicity, and isochrons in the epicentral region of the August 8, 1969 earthquake, near the South Atlantic Ridge. Bathymetric contours (3000 and 4000 m) are from La Brecque and Rabinowitz [1981]. The epicenter of another near-ridge event from Table 8.1 (February 17, 1977) is also shown. See Figure 8.2 for further explanation.

Figure 8.14. Comparison of the observed and synthetic P and SH waves for the August 8, 1969 event. See Figure 8.3 for further explanation.

Figure 8.15. Bathymetry, seismicity, and isochrons in the epicentral region of the January 21, 1970, May 2, 1972, and September 11, 1975 earthquakes, near the East Pacific Rise. The 3000 m bathymetric contour is from Mammerickx and Smith [1982]. See Figure 8.2 for further explanation.

Figure 8.16. Comparison of the observed and synthetic P and SH waves for the January 21, 1970 event. See Figure 8.3 for further explanation.

Figure 8.17. Comparison of the observed and synthetic P and SH waves for the March 31, 1970 event. See Figure 8.3 for further explanation.

Figure 8.18. Comparison of the observed and synthetic P and SH waves for the April 25, 1970 event. See Figure 8.3 for further explanation.

Figure 8.19. Bathymetry, seismicity, and isochrons in the epicentral region of the May 9, 1971 earthquake, near the Pacific-Antarctic Ridge. Bathymetric contours (3000 and 4000 m) are from Mammerickx and Smith [1980]. See Figure 8.2 for further explanation.

Figure 8.20. Comparison of the observed and synthetic P and SH waves for the May 9, 1971 event. See Figure 8.3 for further explanation.

Figure 8.21. Comparison of the observed and synthetic P and SH waves for the May 2, 1972 event. See Figure 8.3 for further explanation.

Figure 8.22. Comparison of the observed and synthetic P and SH waves for the June 29, 1973 event. See Figure 8.3 for further explanation.

Figure 8.23. Comparison of the observed and synthetic P and SH waves for the November 17, 1973 event. See Figure 8.3 for further explanation.

Figure 8.24. Bathymetry, seismicity and isochrons in the epicentral region of July 1, 1974 earthquake, near the South Atlantic Ridge. Bathymetric contours (3000 and 4000 m) are from Heezen and Tharp [1978]. See Figure 8.2 for further explanation.

Figure 8.25. Comparison of the observed and synthetic P and SH waves for the July 1, 1974 event. See Figure 8.3 for further explanation.

Figure 8.26. Comparison of the observed and synthetic P and SH waves for the September 11, 1975 event. See Figure 8.3 for further explanation.

Figure 8.27. Comparison of the observed and synthetic P and SH waves for the March 29, 1976 event. See Figure 8.3 for further explanation.

Figure 8.28. Bathymetry, seismicity, and isochrons in the epicentral region of the December 14, 1977 earthquake, near the Southwest Indian Ridge. Bathymetric contours (3000 and 5000 m) are from Fisher et al. [1982]. The focal mechanisms for two other earthquakes near the December 1977 event, determined by Dziewonski et al. [1983], are also shown. See Figure 8.2 for further explanation.

Figure 8.29. Comparison of the observed and synthetic P and SH waves for the December 14, 1977 event. See Figure 8.3 for further explanation.

Figure 8.30. Comparison of the observed and synthetic P and SH waves for the December 13, 1979 event. See Figure 8.3 for further explanation.

Figure 8.31. Bathymetry and tectonic elements in the epicentral region of the September 13, 1981 earthquake, adapted from Figure 3 of Rona and Gray [1980]. Rift mountains are outlined by the 3000 m isobath. The position of ridge axis segments and the Kane Fracture Zone are indicated by heavy lines.

Figure 8.32. Comparison of the observed and synthetic P and SH waves for the September 13, 1981 earthquake. See Figure 8.3 for further explanation.

Figure 8.33. Bathymetry and seismicity in the epicentral region of the December 12, 1981 earthquake. Bathymetry from Laughton [1975]; 1000 m contour interval.

Figure 8.34. Comparison of the observed and synthetic P and SH waves for the December 12, 1981 event. See Figure 8.3 for further explanation.

Figure 8.35. Centroidal depth versus lithosphere age for near-ridge earthquakes occurring in the Atlantic, Pacific, and Indian Oceans. All depths are relative to the seafloor. The horizontal dashed line indicates the depth of the Moho (6 km) in the velocity model used for the body-waveform inversions. The error bars with respect to age for some events correspond to the range in age given in Table 8.1. The 600° and 800°C isotherms, calculated from the plate-cooling model of Parsons and Sclater [1977], are also shown.

Figure 8.36. Centroidal depth versus lithosphere age for near-ridge earthquakes distinguished on the basis of seismic moment. See Figure 8.35 for further explanation.

Figure 8.37. Centroidal depth versus lithosphere age for near-ridge earthquakes distinguished on the basis of whether the focal mechanism is characterized by thrust, strike-slip, or normal faulting. Where a focal mechanism is a combination of two of the basic faulting types, both symbols are superposed. See Figure 8.35 for further explanation.

Figure 8.38. Strength envelope for 15 m.y. old lithosphere. - Geotherm calculated from the model of Parsons and Sclater [1977]. The brittle failure law is from Byerlee [1978], shown for several different values of the ratio  $\lambda$  of pore pressure to lithostatic pressure. The ductile flow law is for dry olivine [Goetze and Evans, 1979], shown at two values of strain rate  $\dot{\epsilon}$ . The hatchured regions indicate the depth range through which the brittle-ductile transition may be moved by making different assumptions concerning the strain rate and pore pressure.

Figure 8.39. Depth at which the ductile flow law exceeds a range of differential stresses (0.2, 0.5, 1.0, 2.0, and 3.0 kbar) for strain rates of (a)  $10^{-15}$  and (b)  $10^{-13}$  sec $^{-1}$ . Near-ridge earthquakes are plotted as in Figure 8.37.

Figure 8.40. Contours of equal cooling rate, calculated from the model of Parsons and Sclater [1977]. The dashed line traces the depth at which the cooling rate is a maximum as a function of age. Near-ridge earthquakes are plotted as in Figure 8.37.

# NEAR-RIDGE EARTHQUAKES

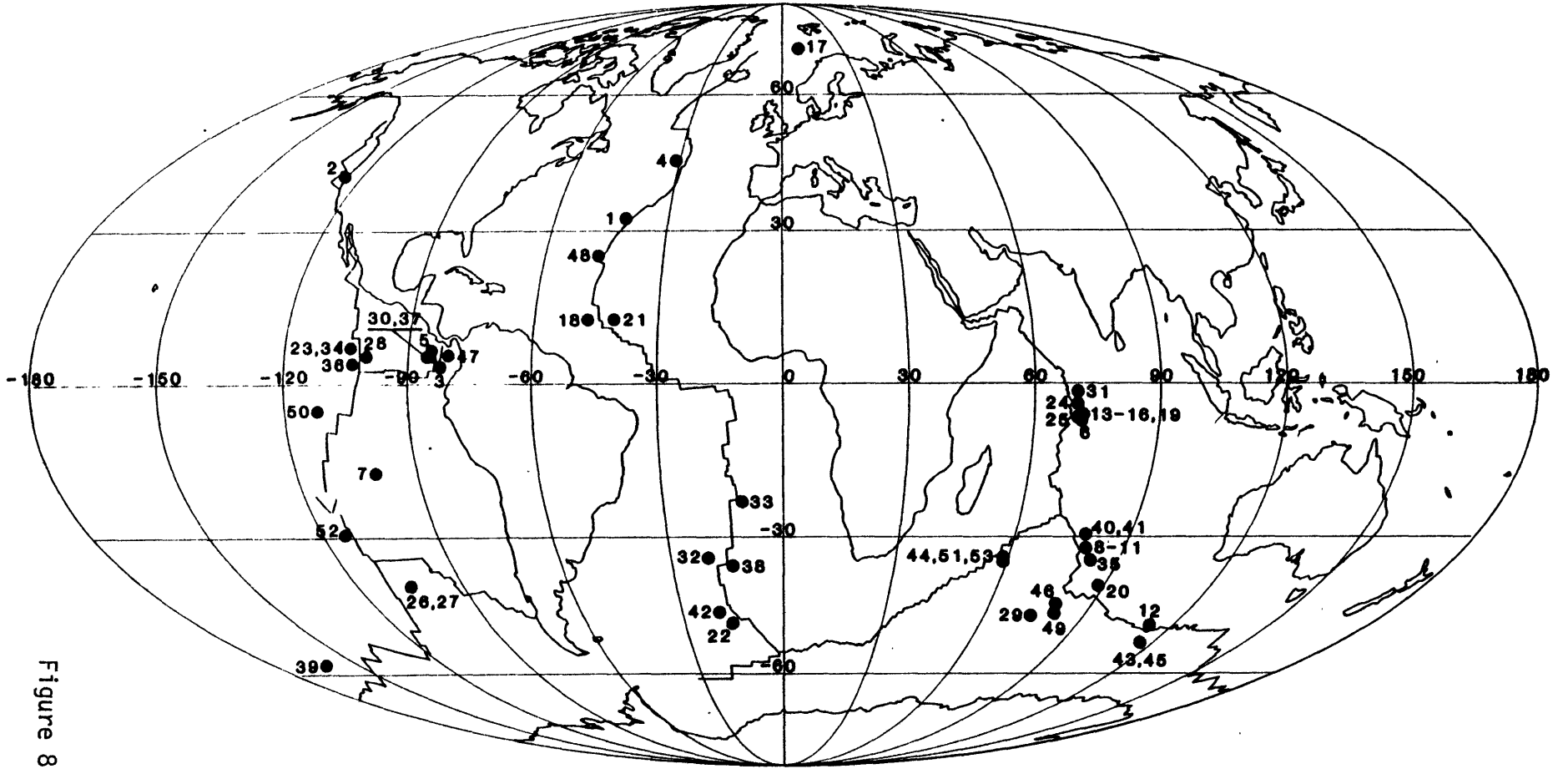


Figure 8.1

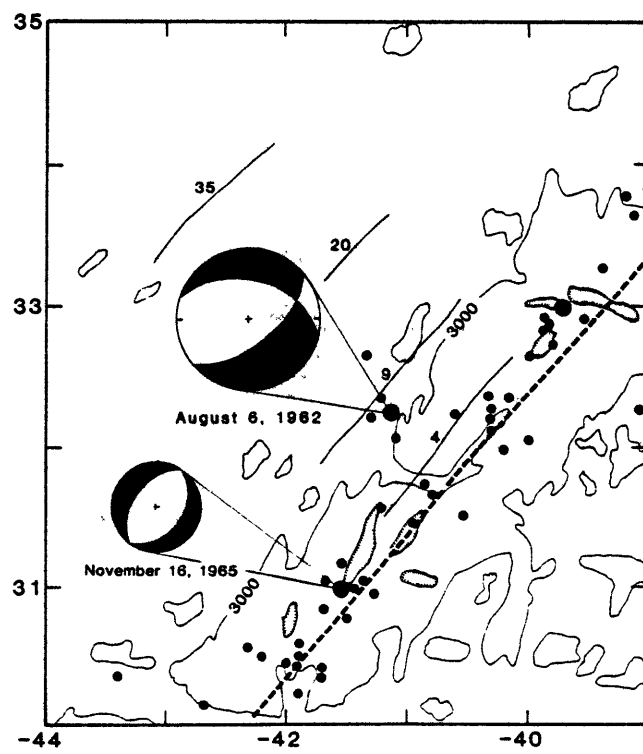


Figure 8.2

Figure 8.3

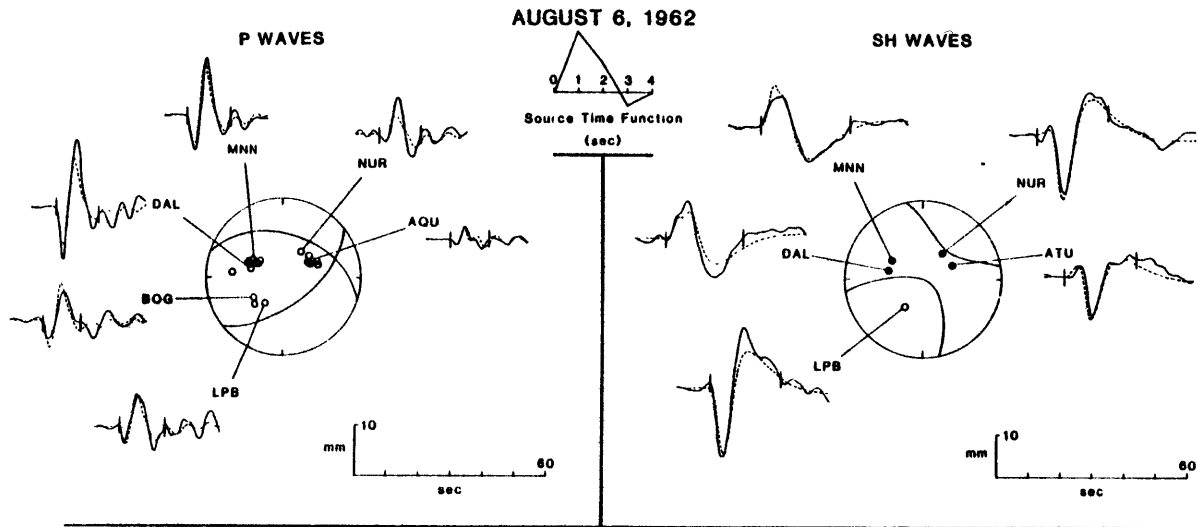




Figure 8.4

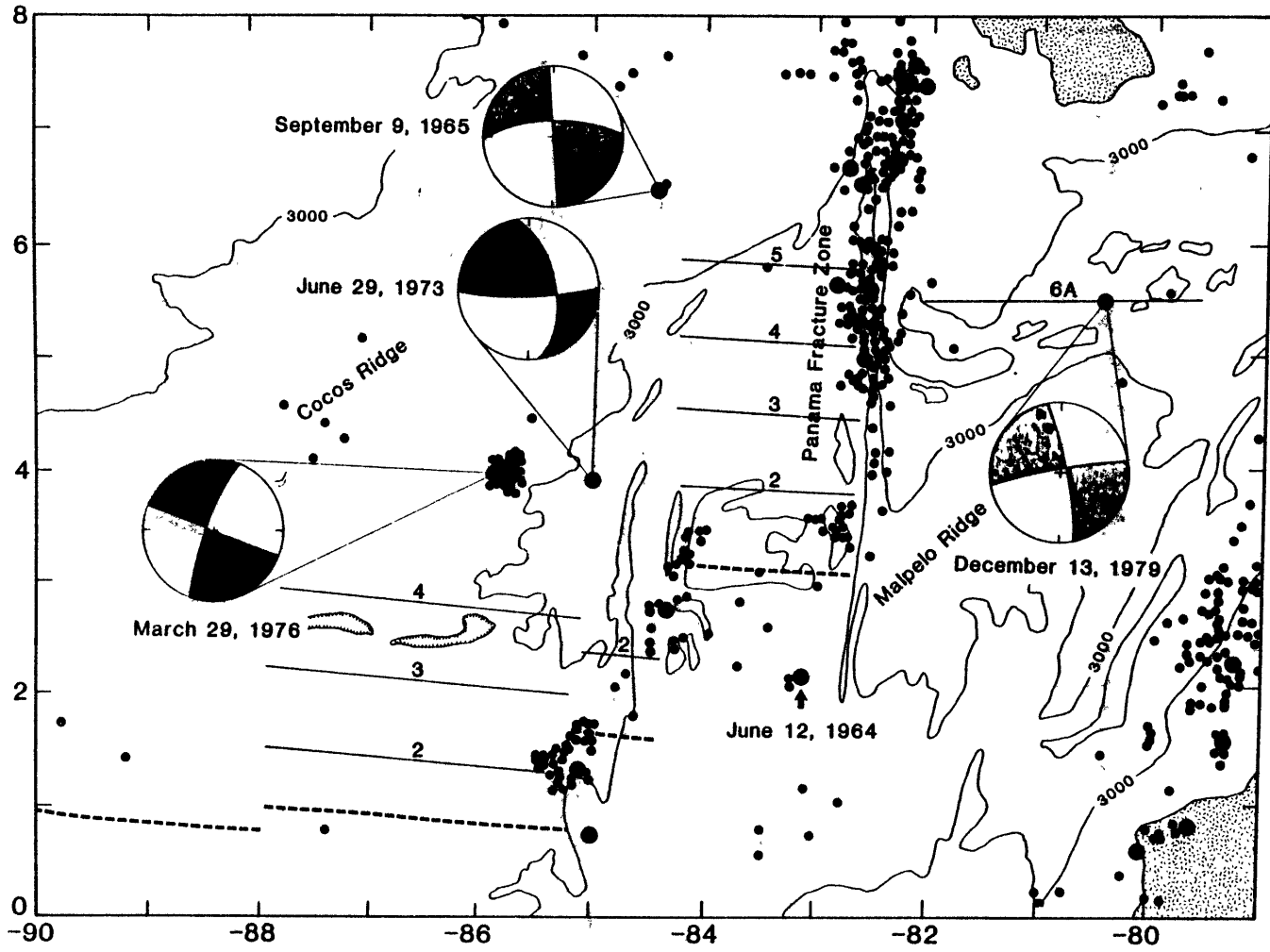
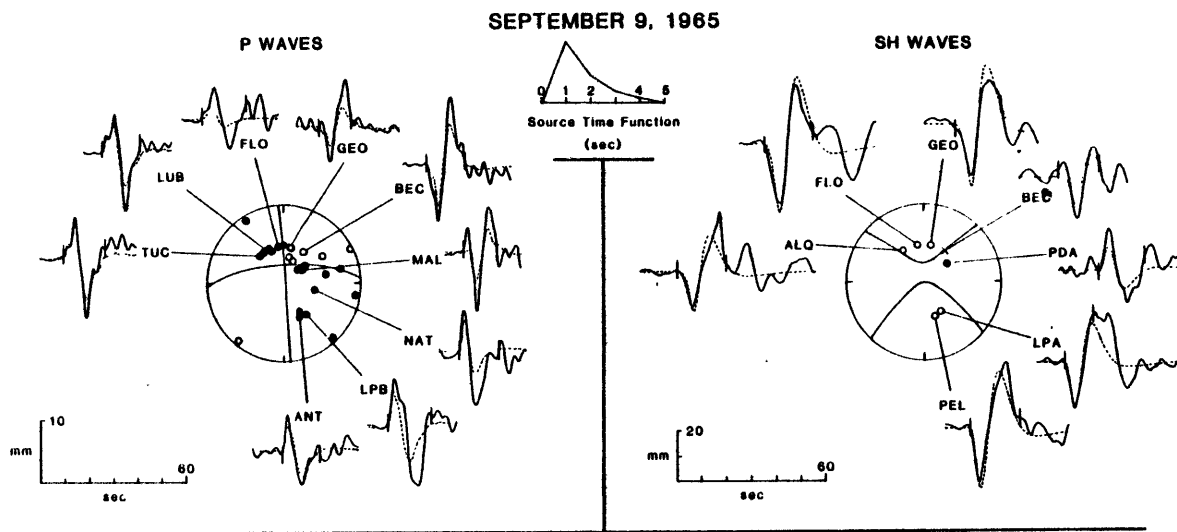


Figure 8.5



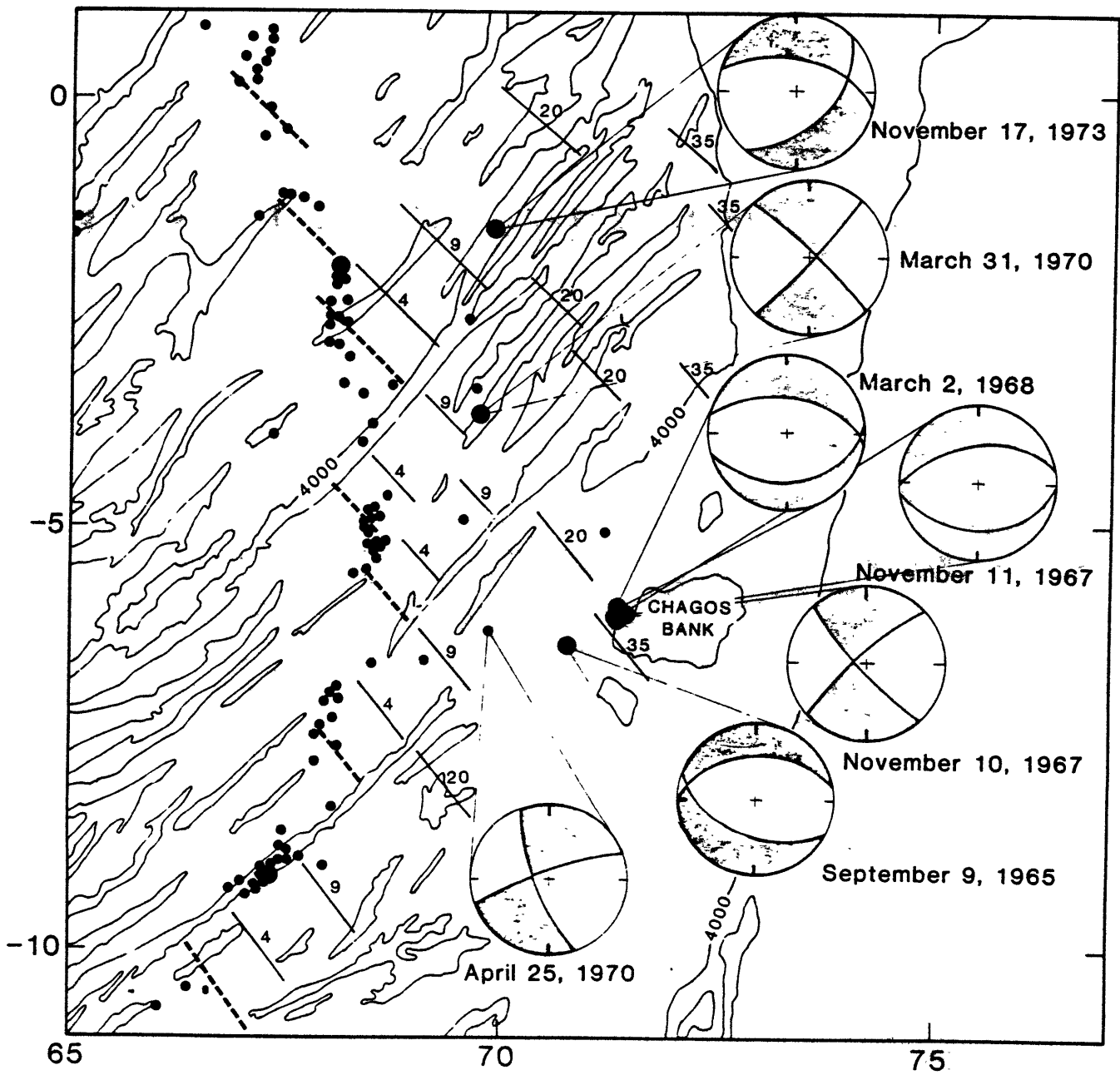


Figure 8.6

Figure 8.7.

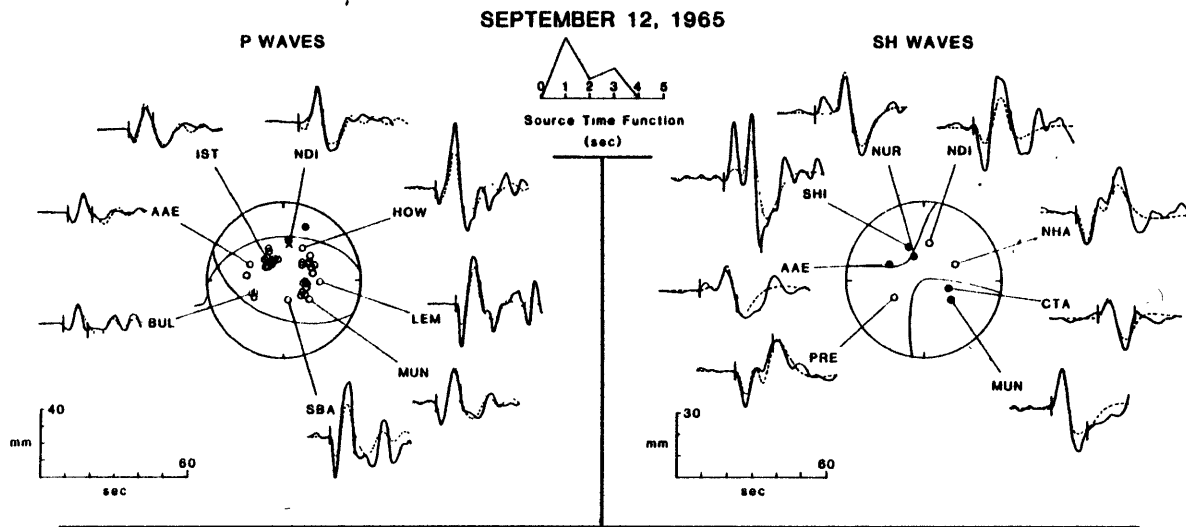


Figure 8.8

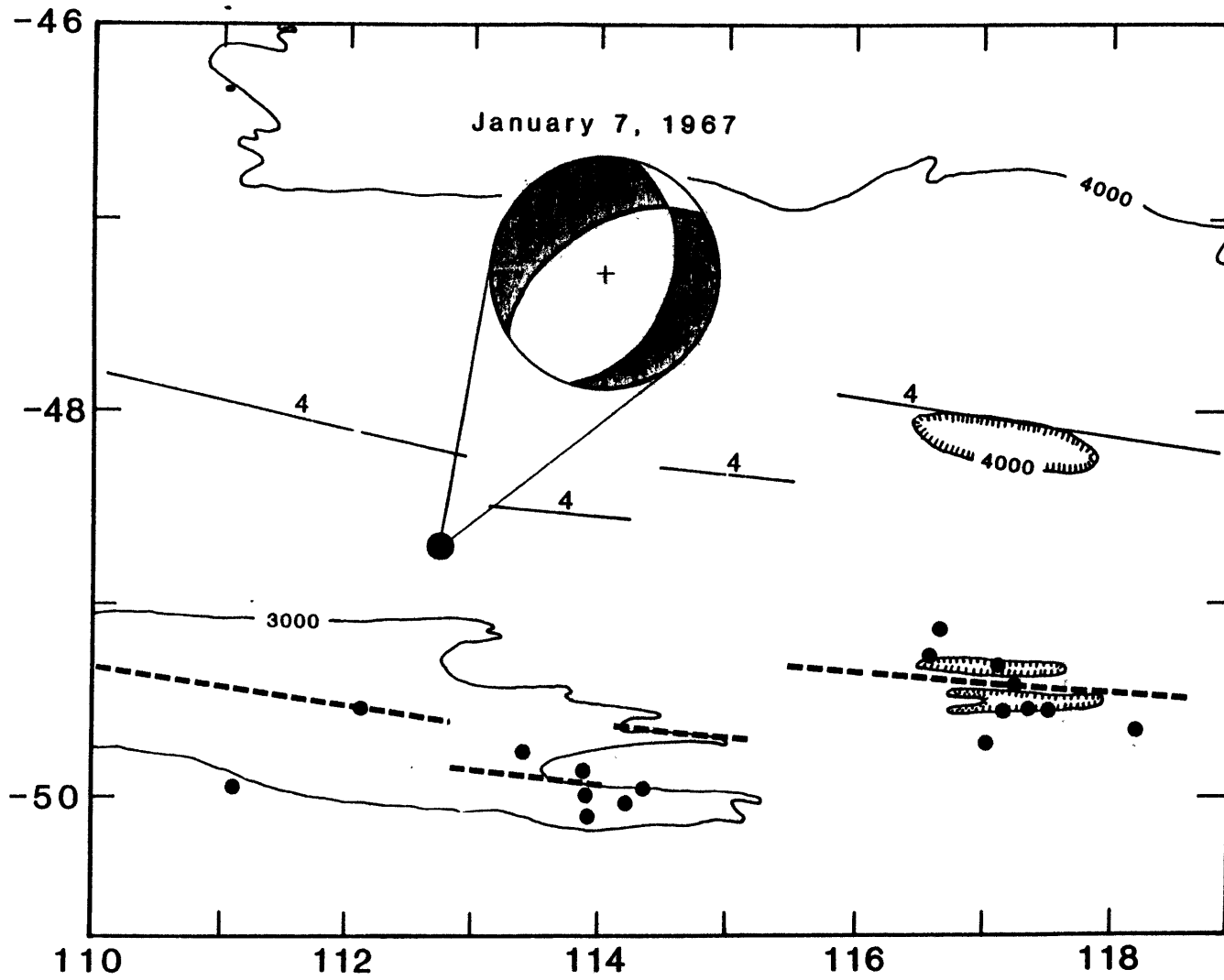


Figure 8.9

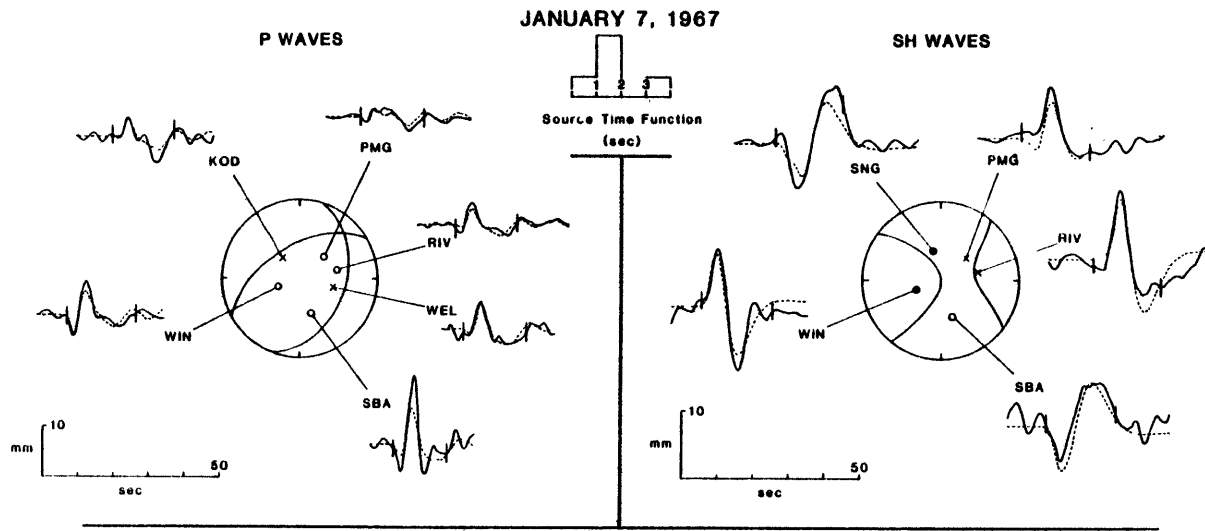


Figure 8.10

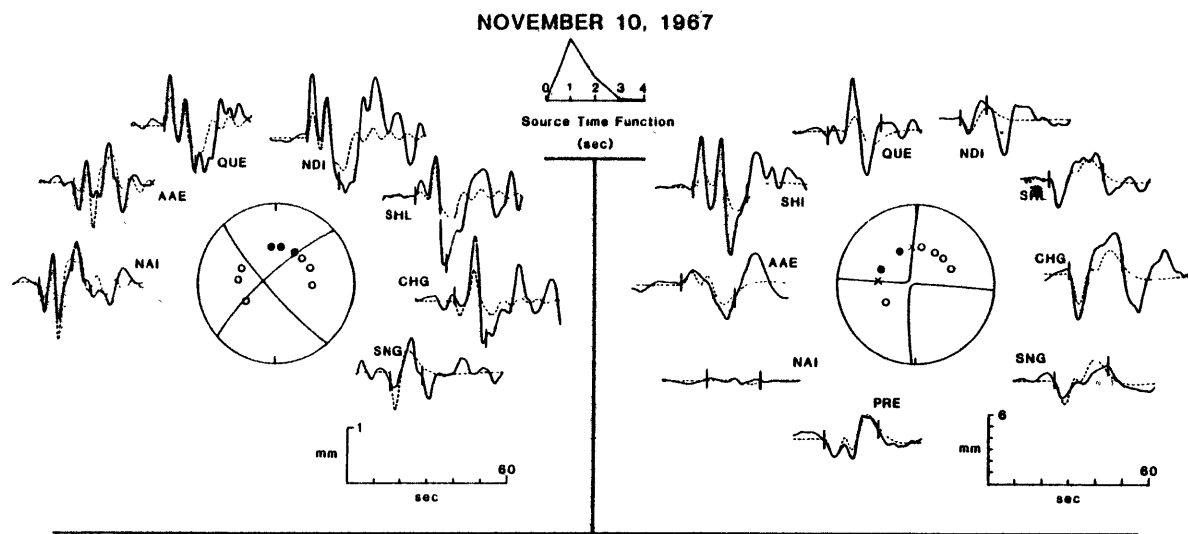


Figure 8.11

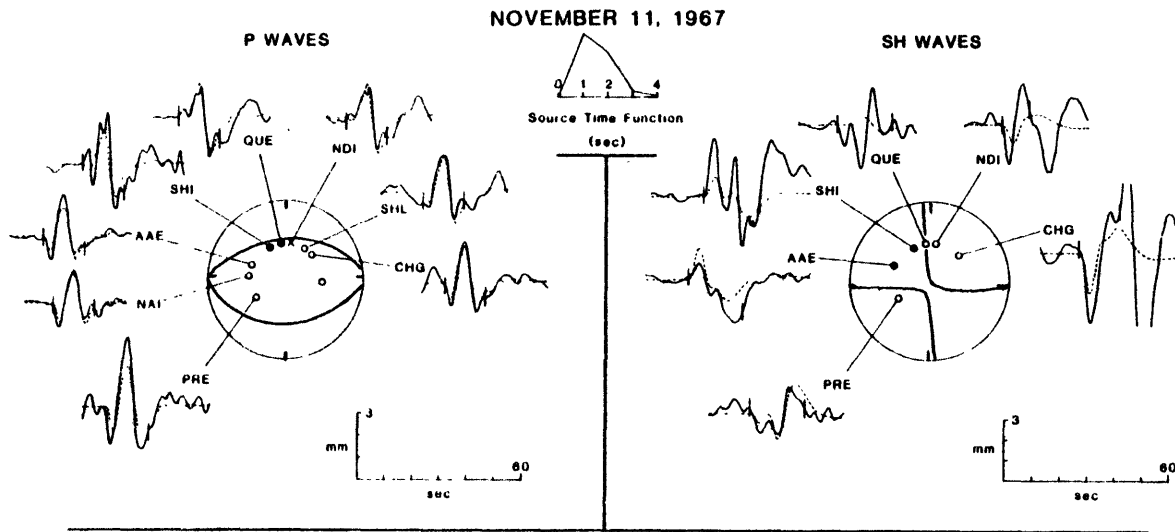




Figure 8.12

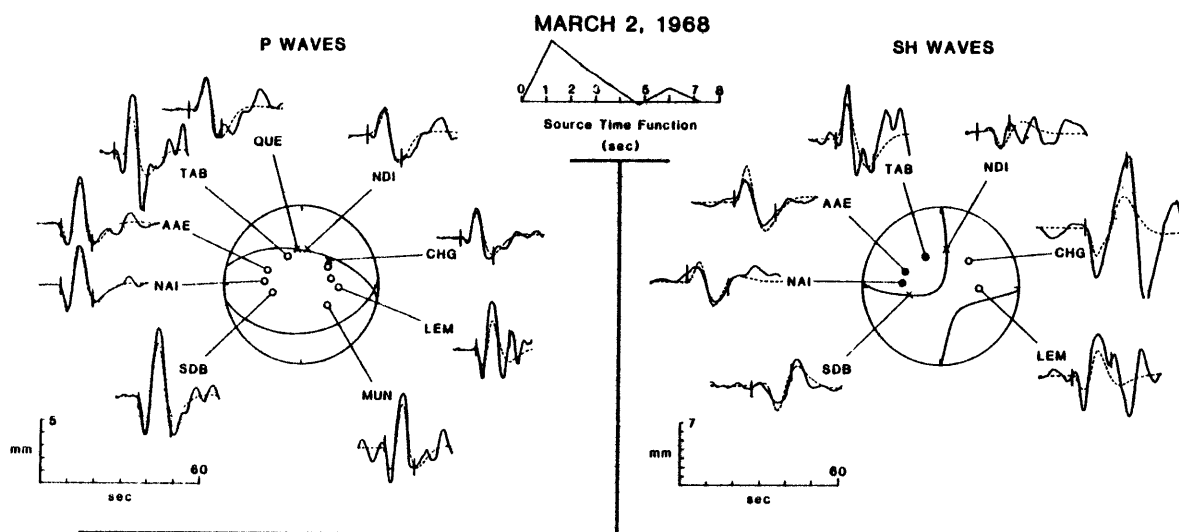


Figure 8.13

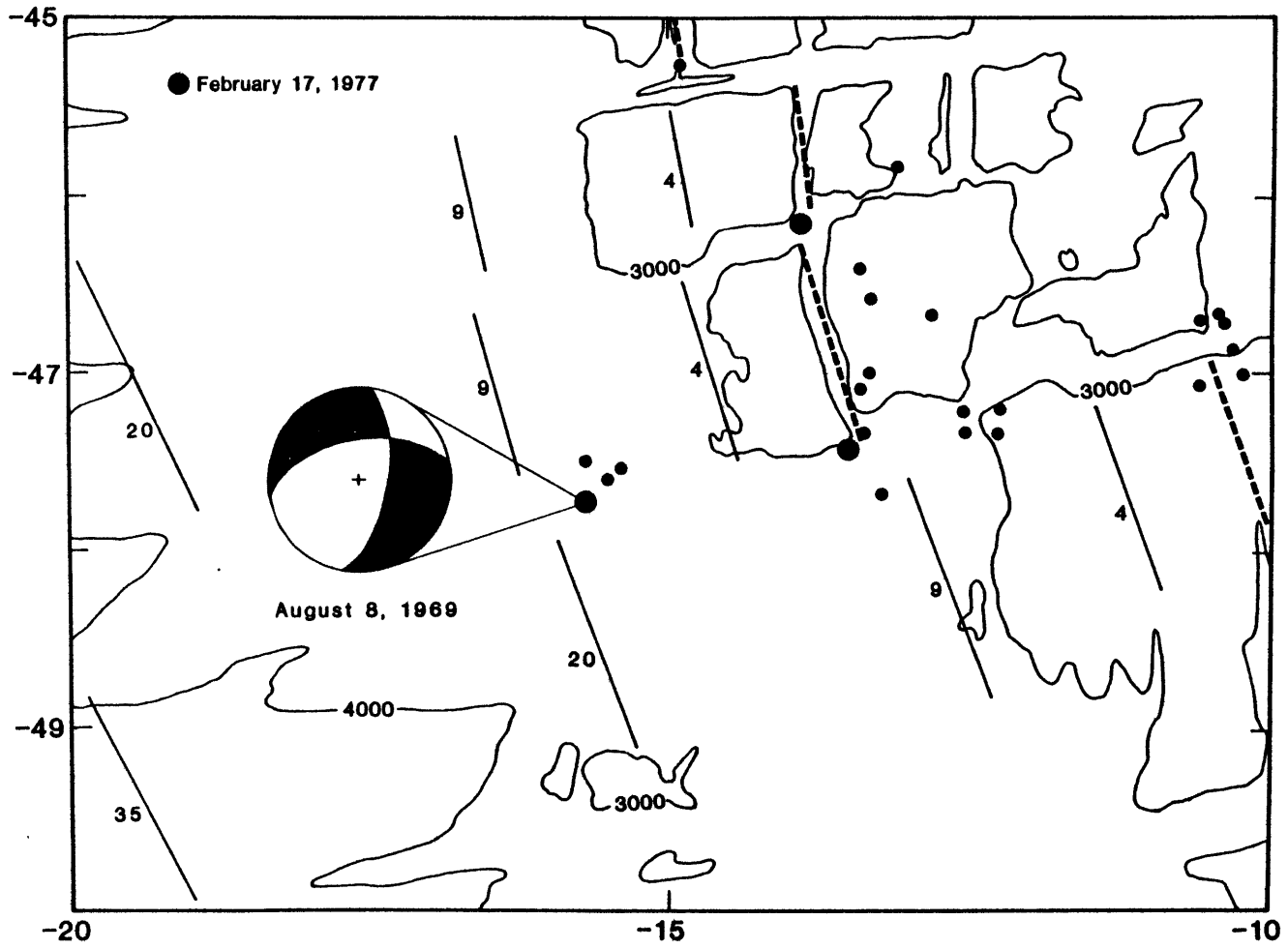


Figure 8.14

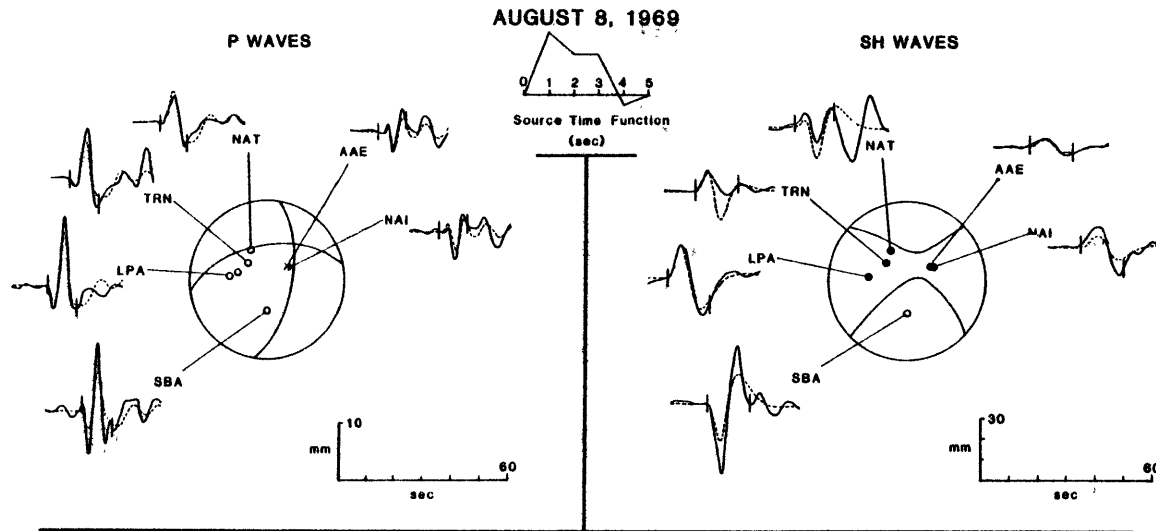


Figure 8.15

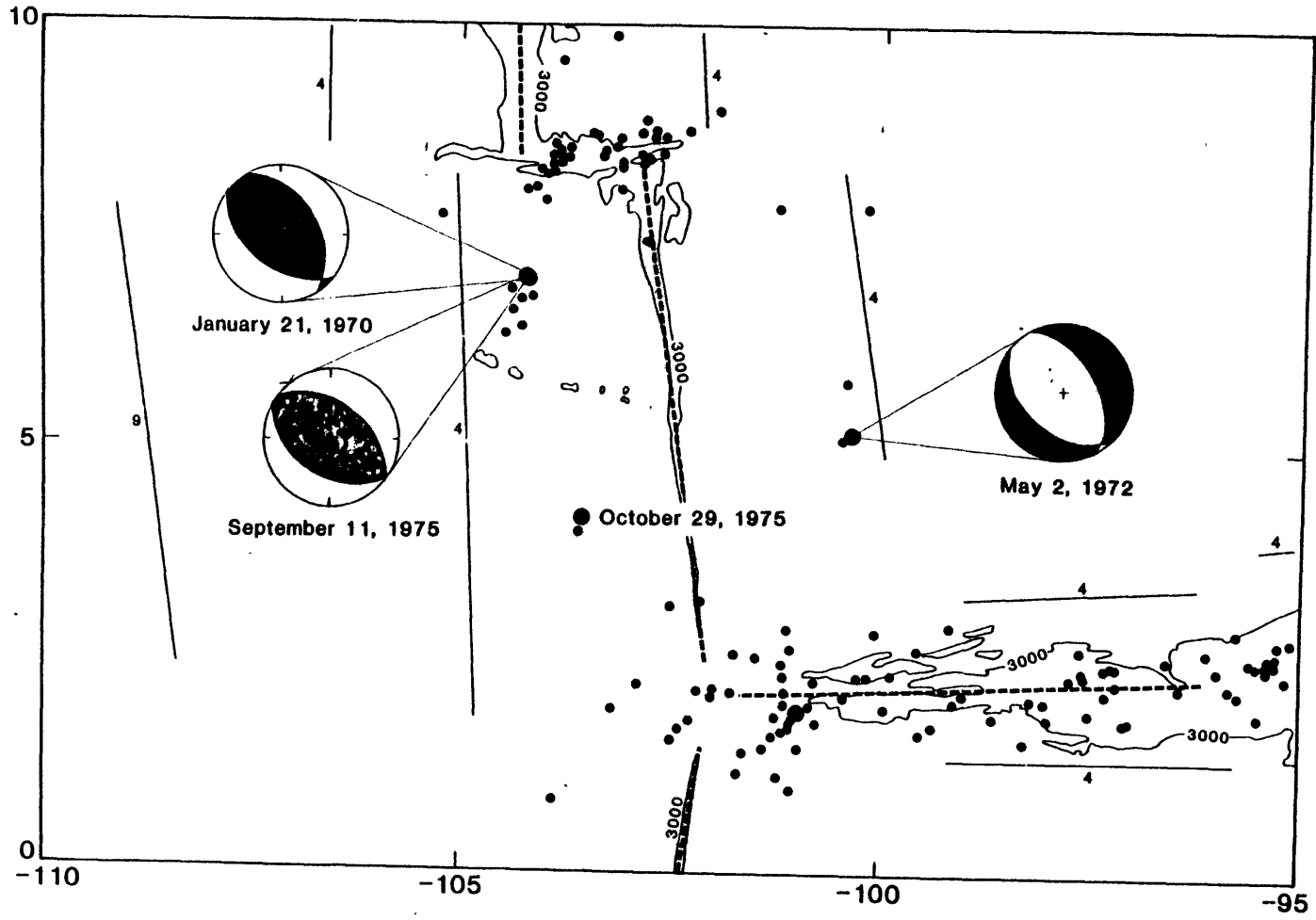


Figure 8.16

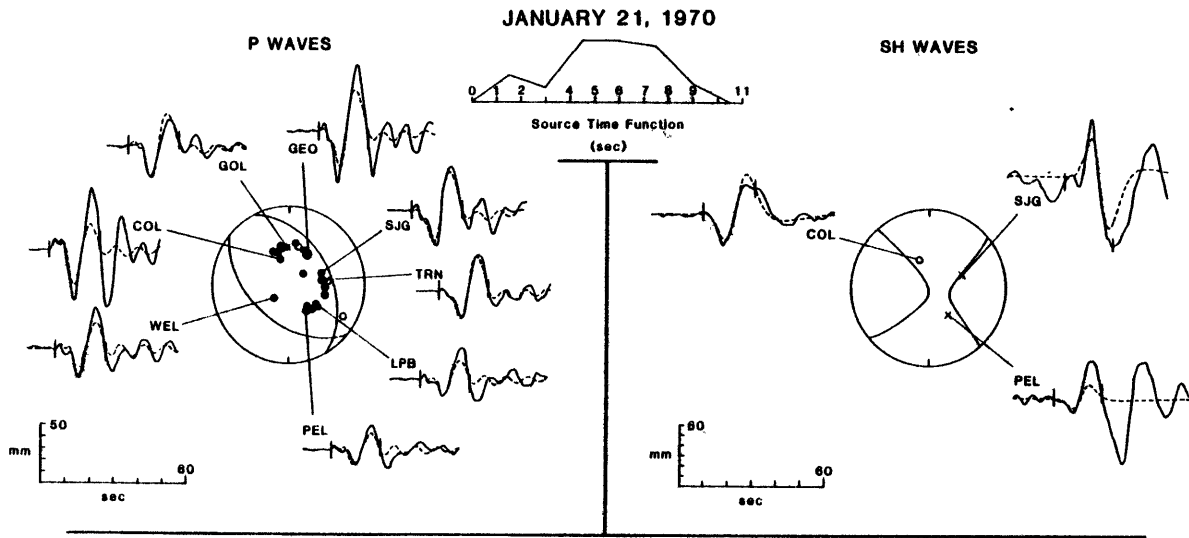


Figure 8.17

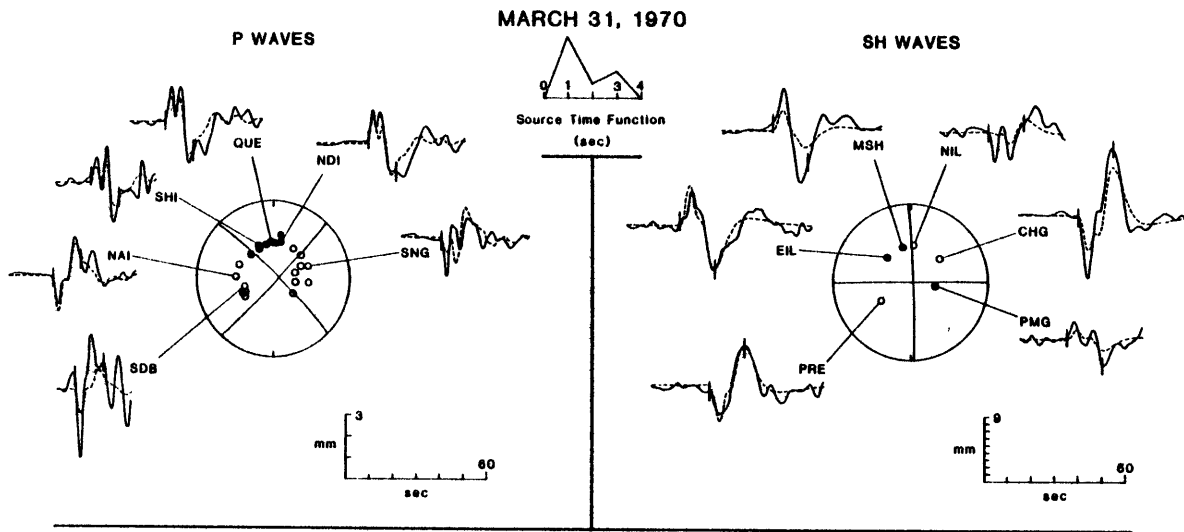
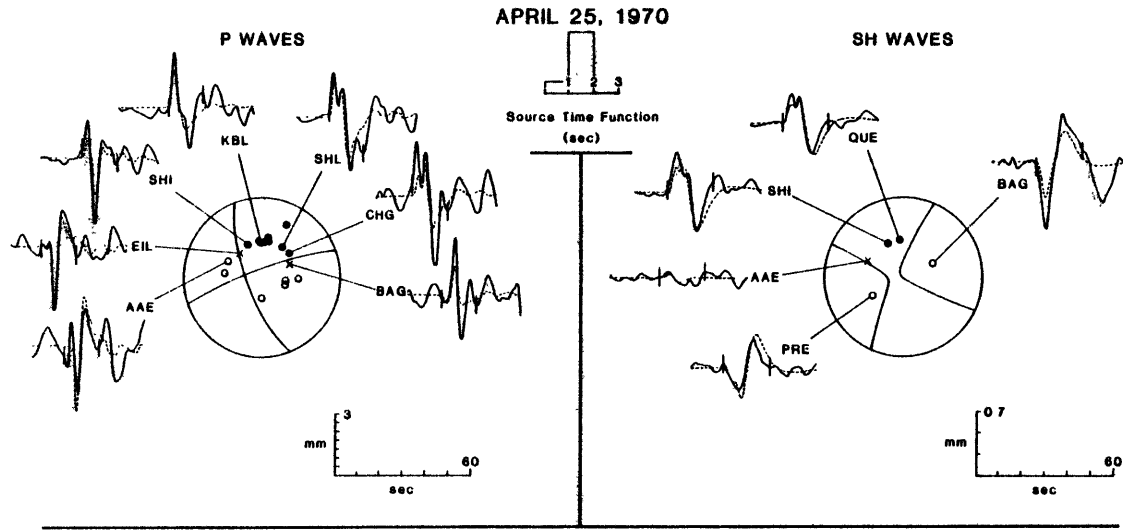


Figure 8.18



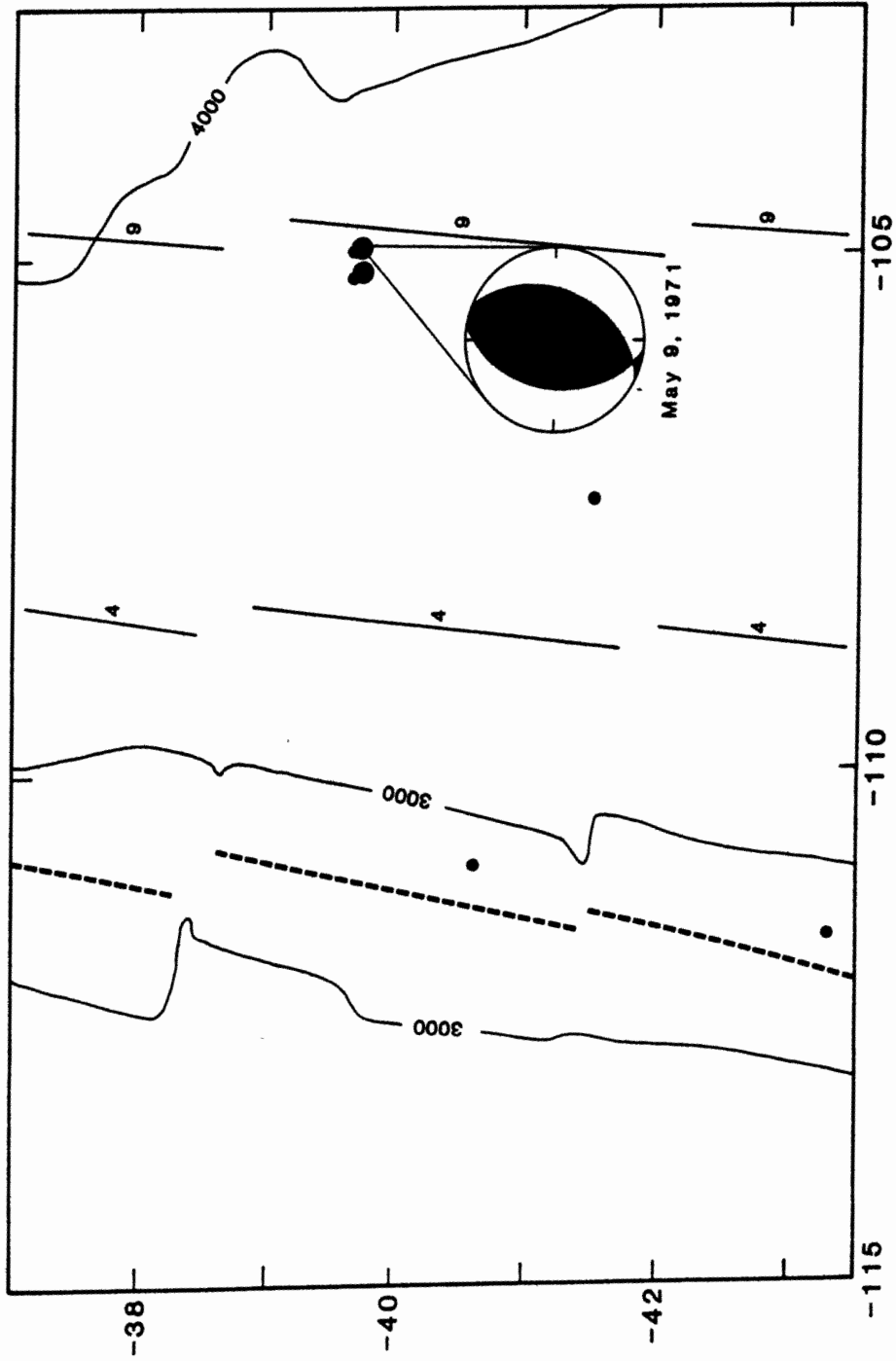


Figure 8.19



Figure 8.20

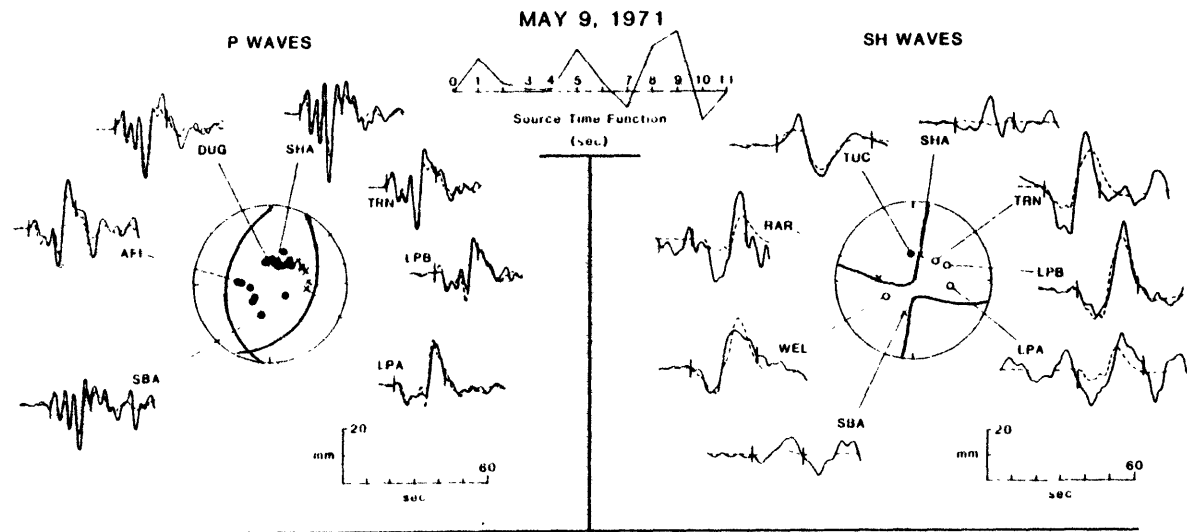


Figure 8.21

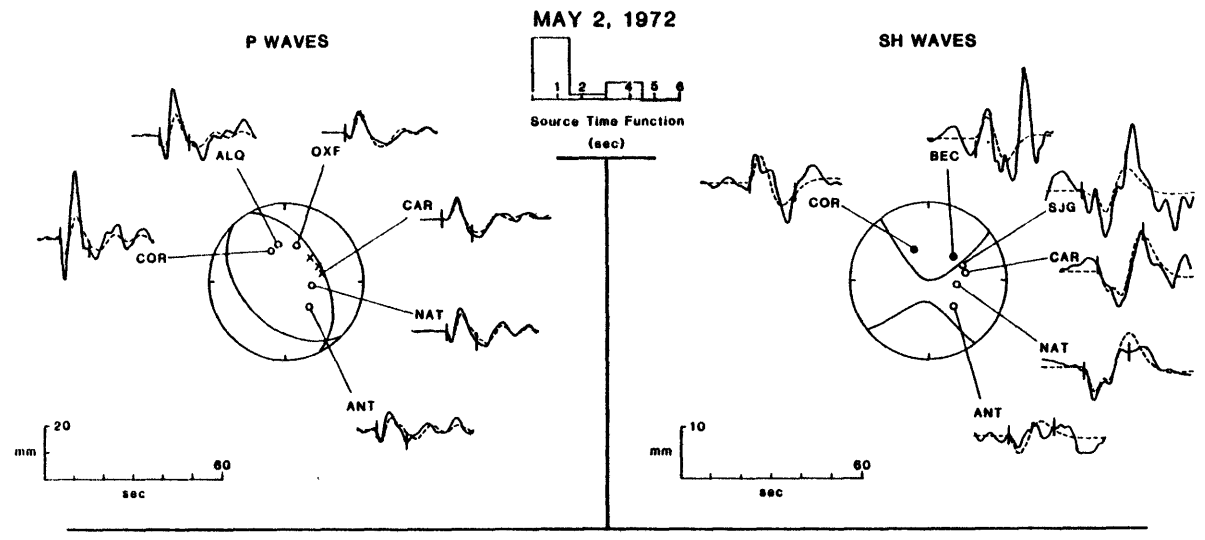


Figure 8.22

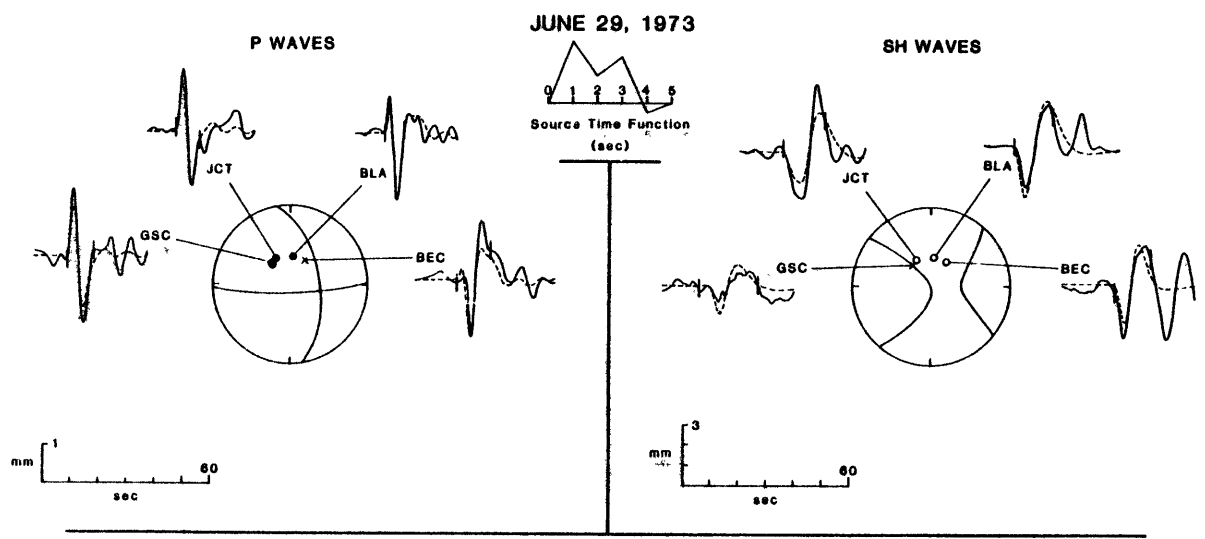


Figure 8.23

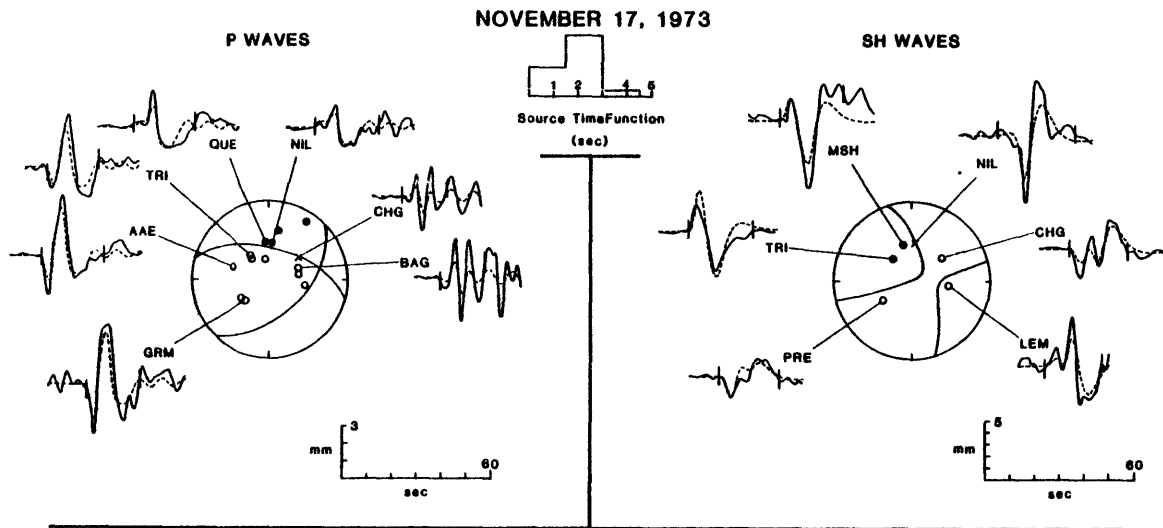


Figure 8.24

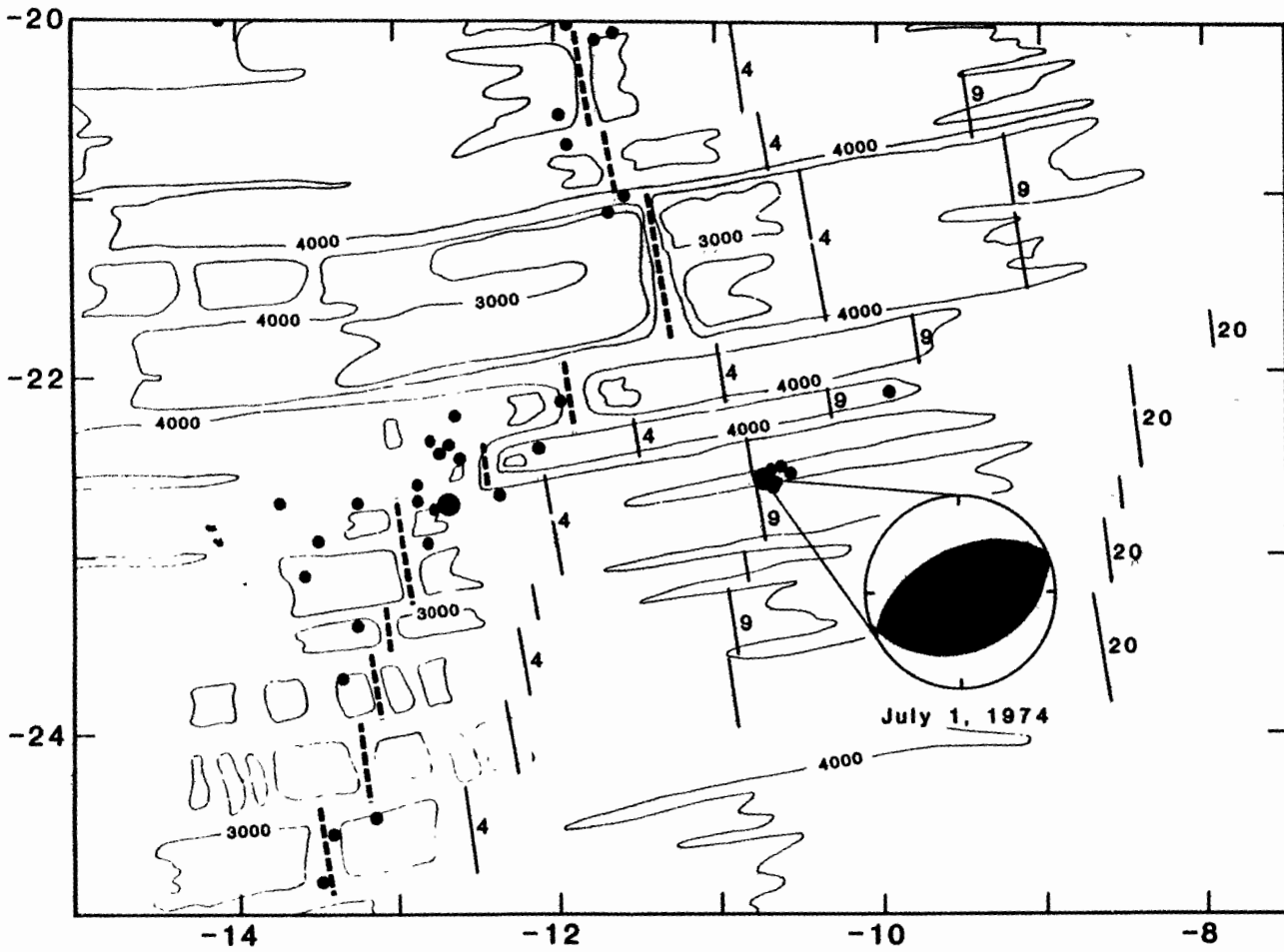


Figure 8.25

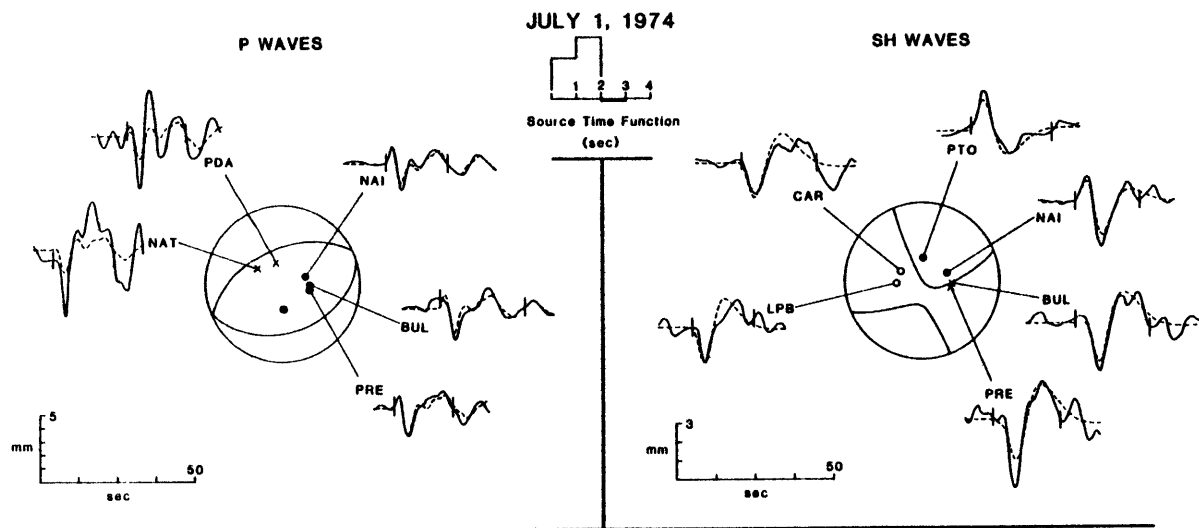


Figure 8.26

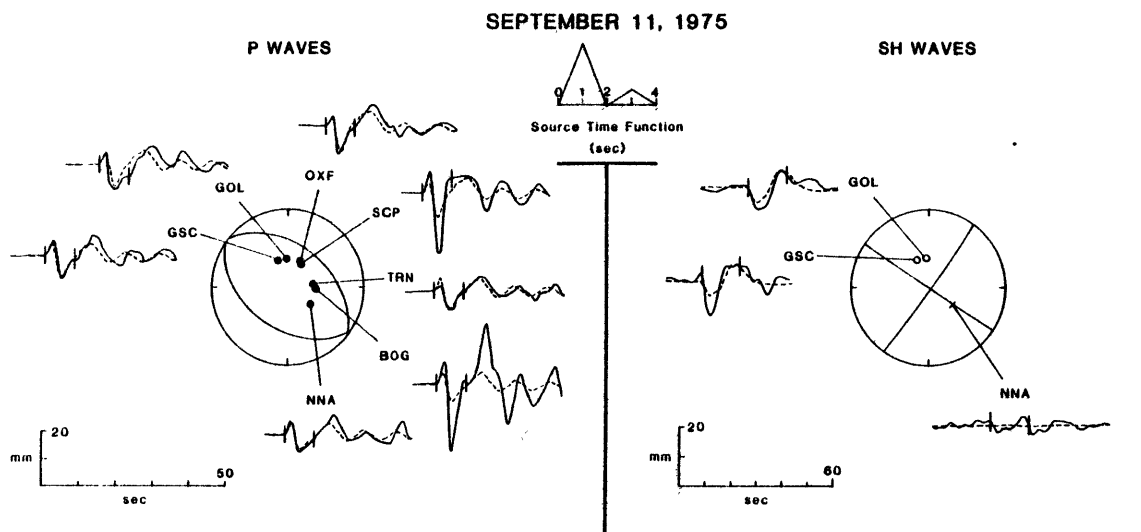
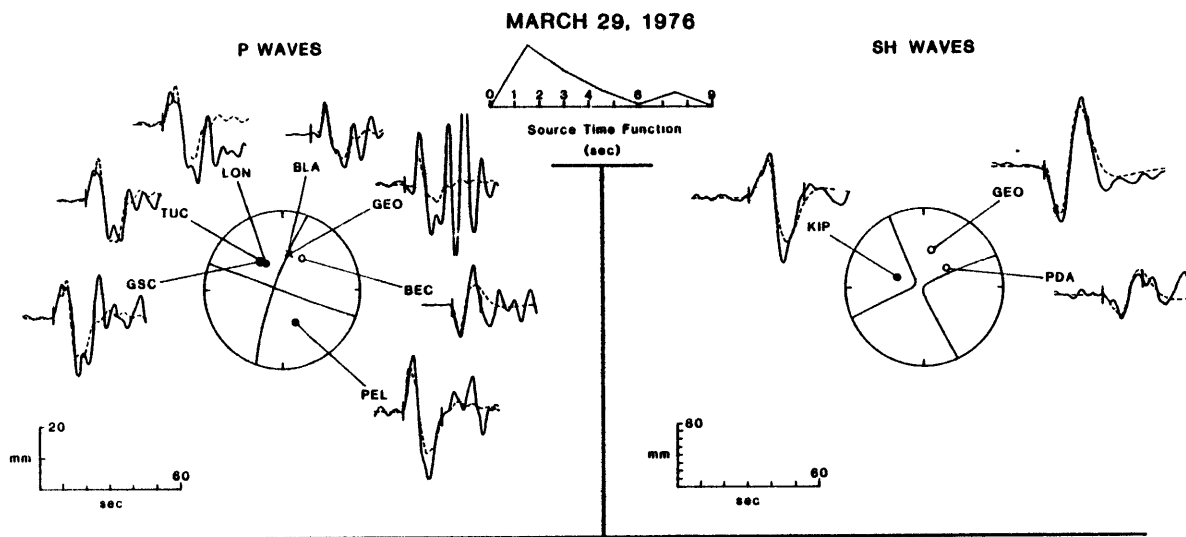


Figure 8.27





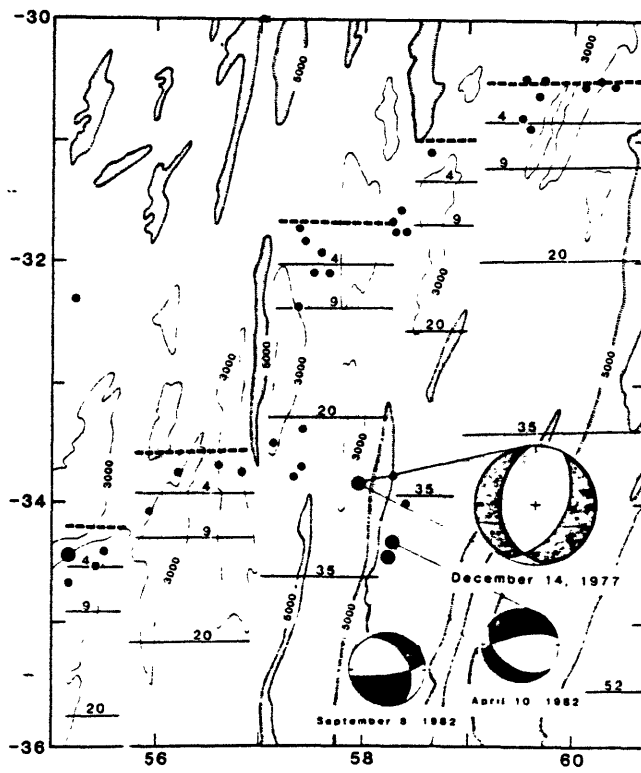


Figure 8.28

Figure 8.29

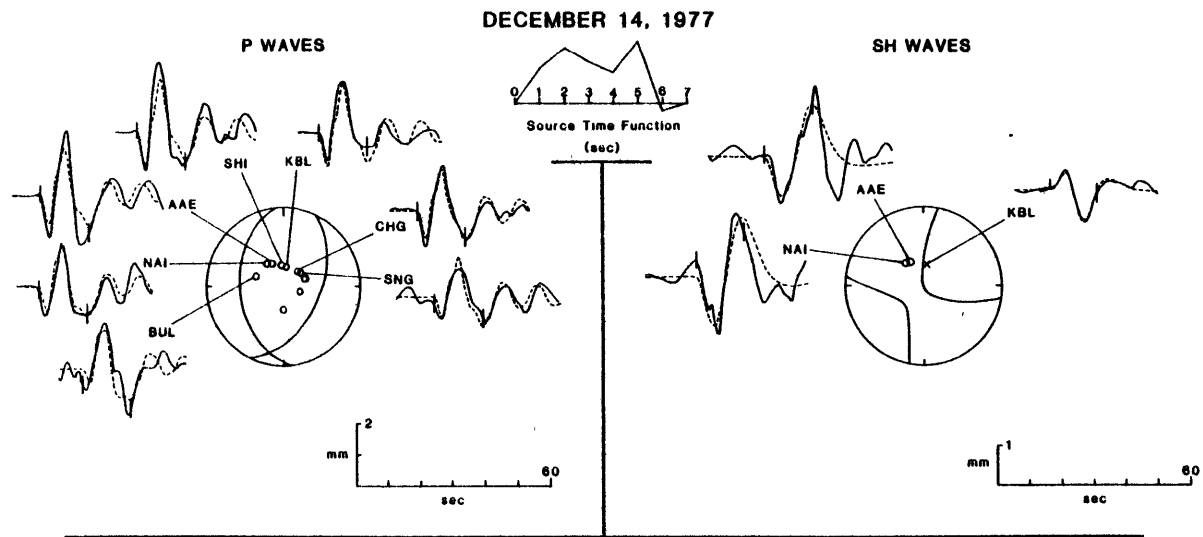
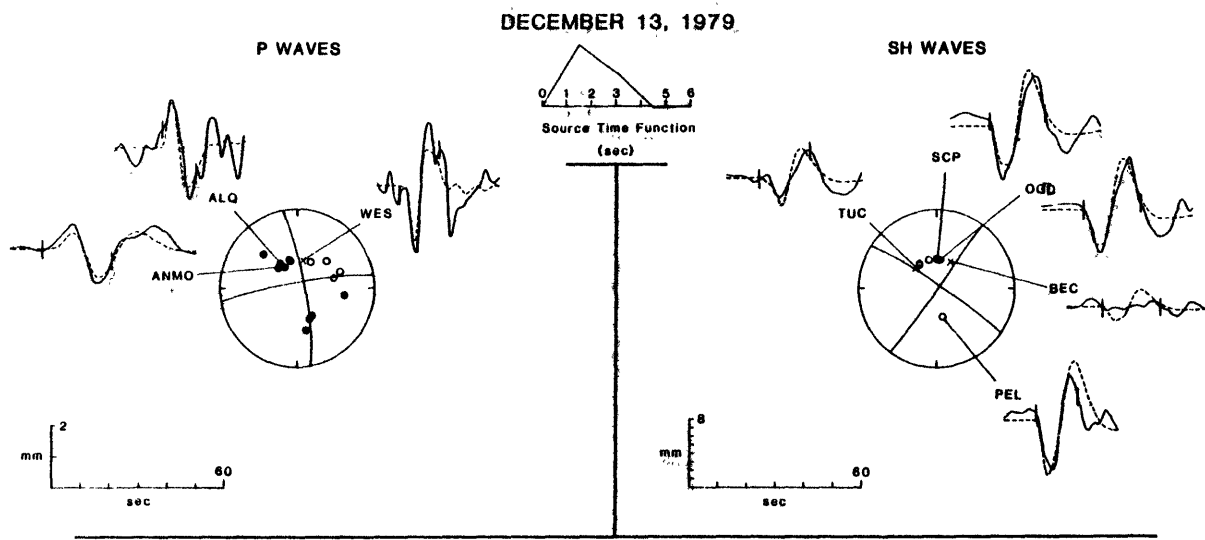


Figure 8.30



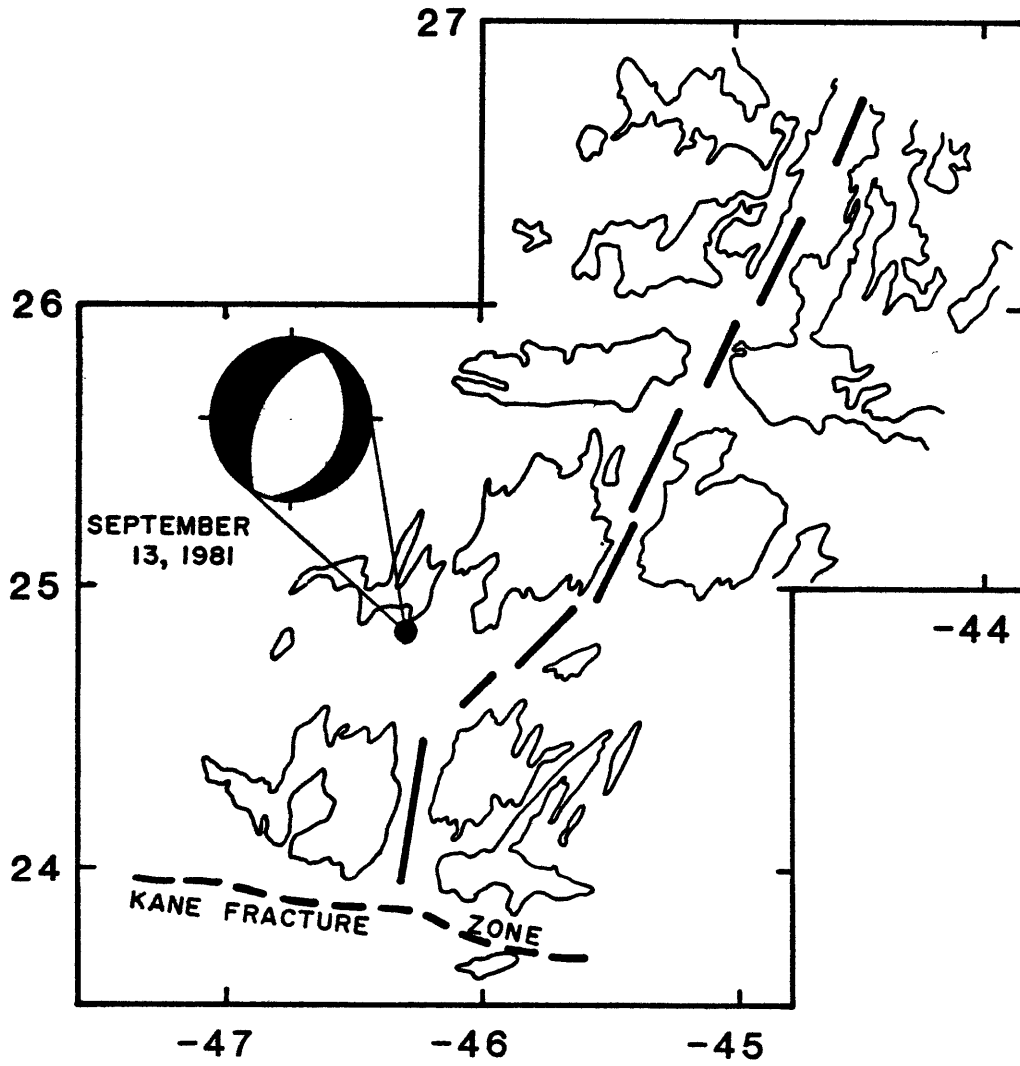


Figure 8.31

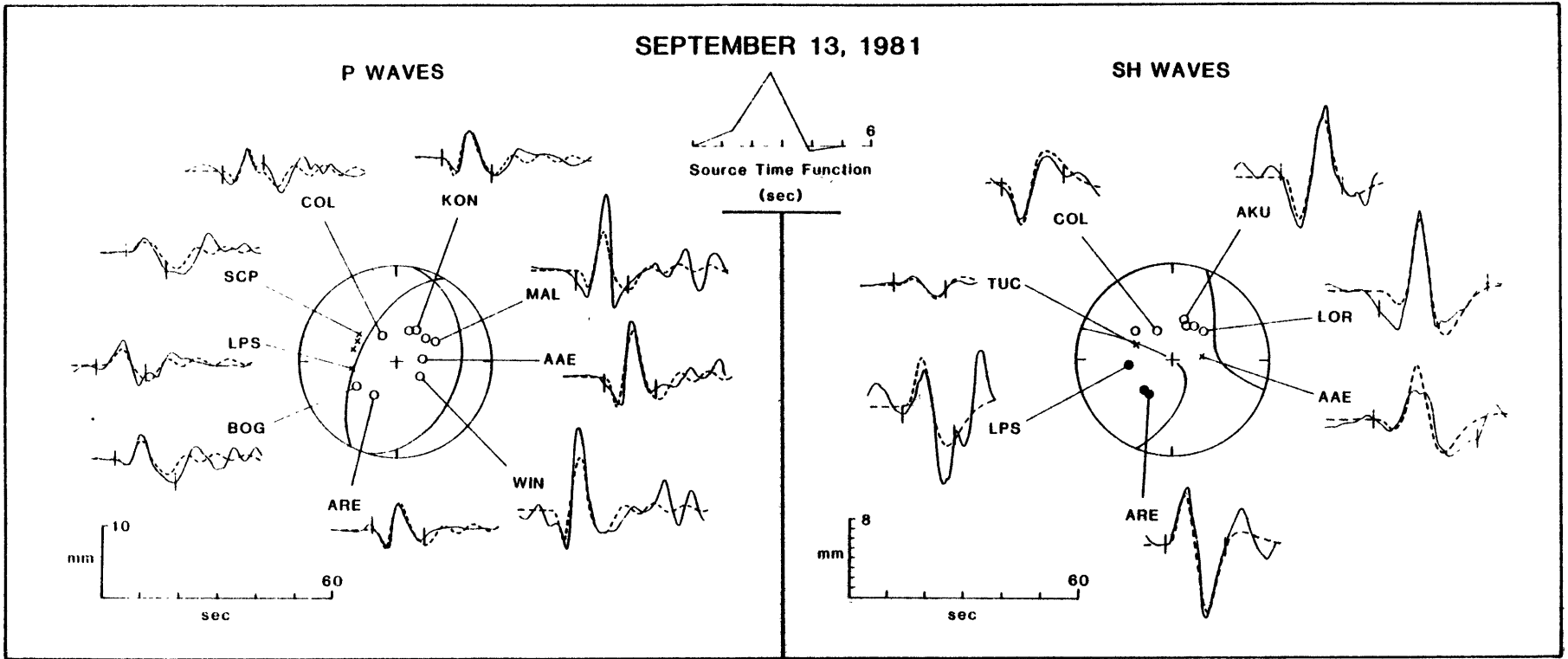


Figure 8.32

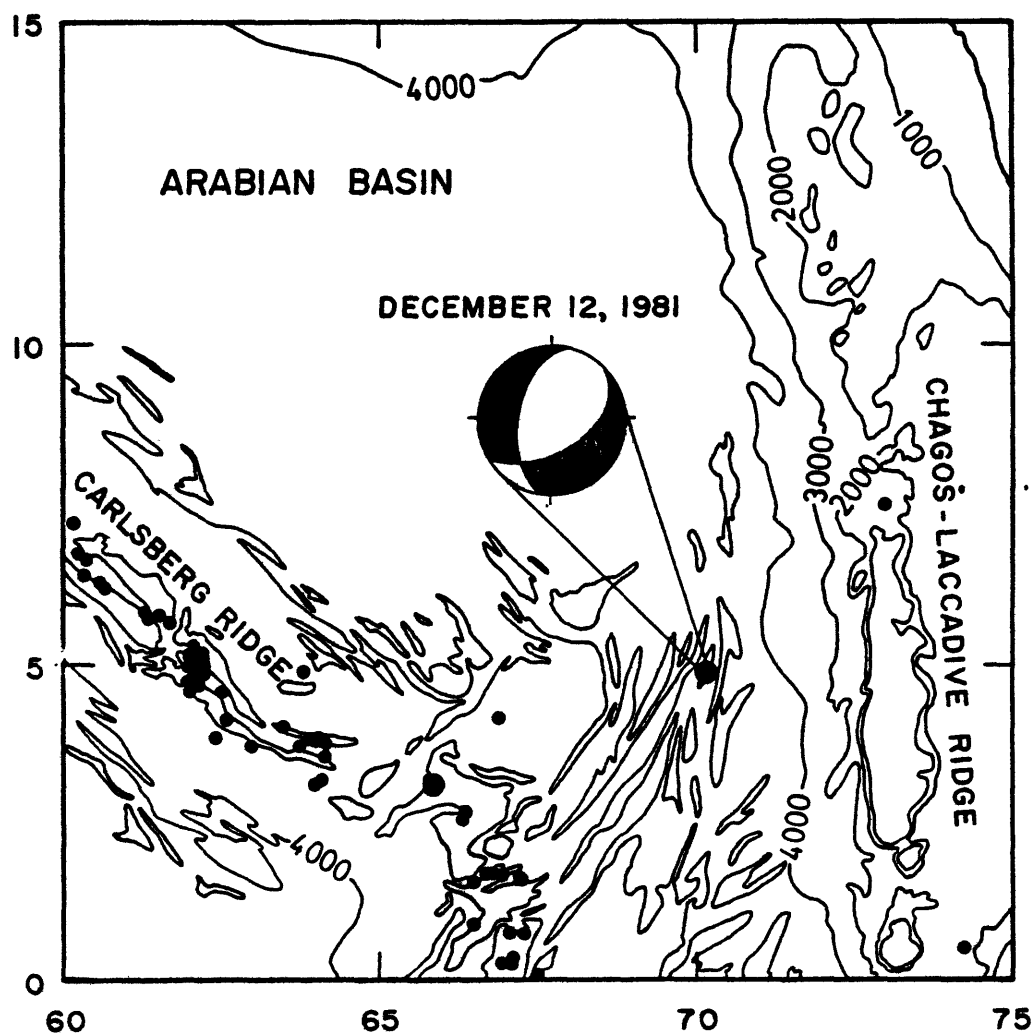


Figure 8.33

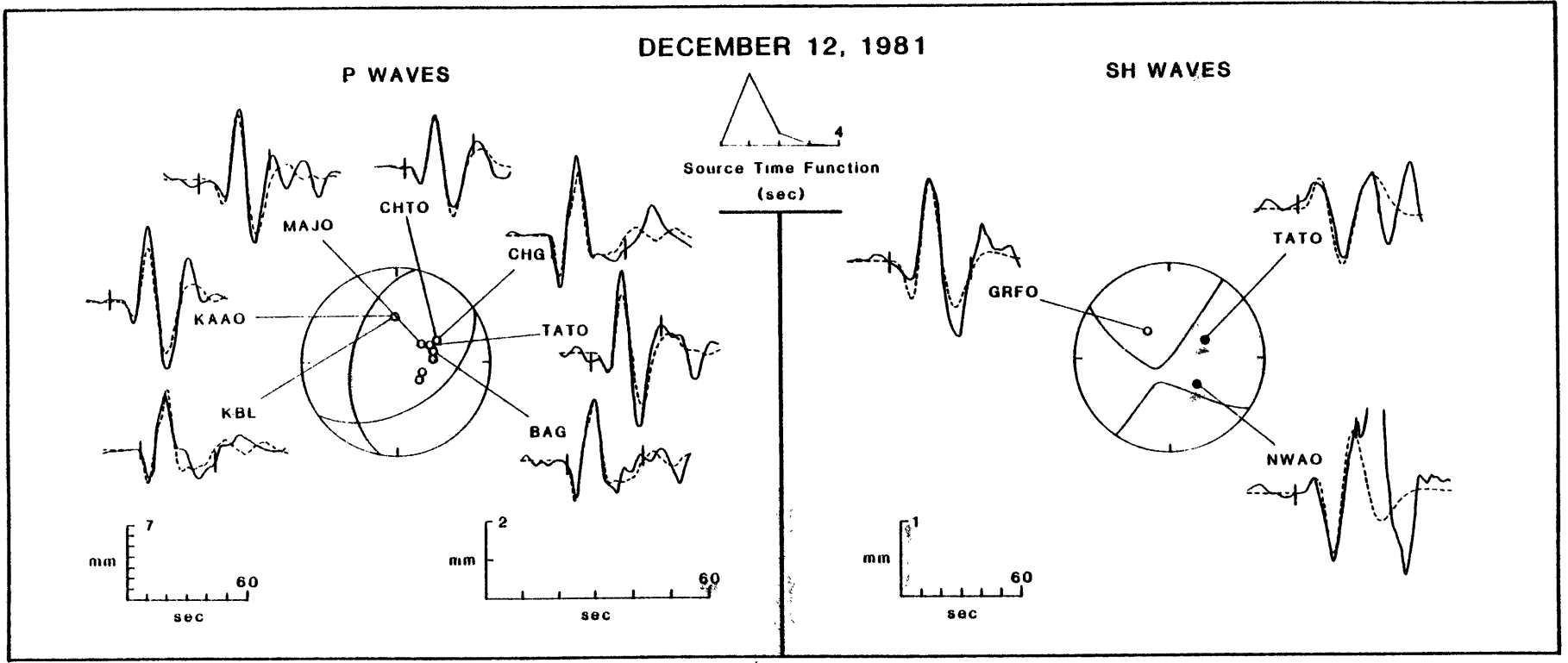
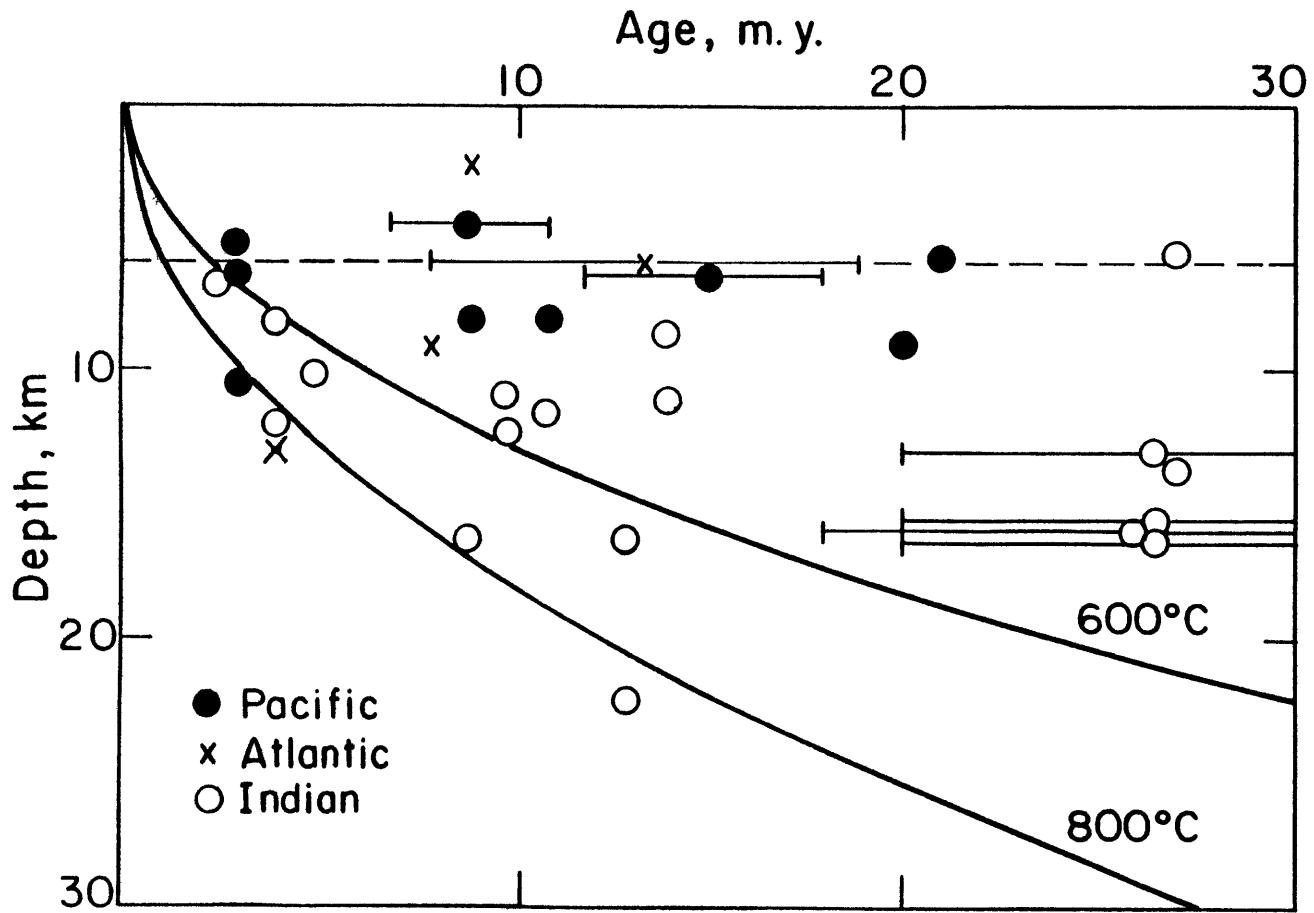


Figure 8.34

Figure 8.35





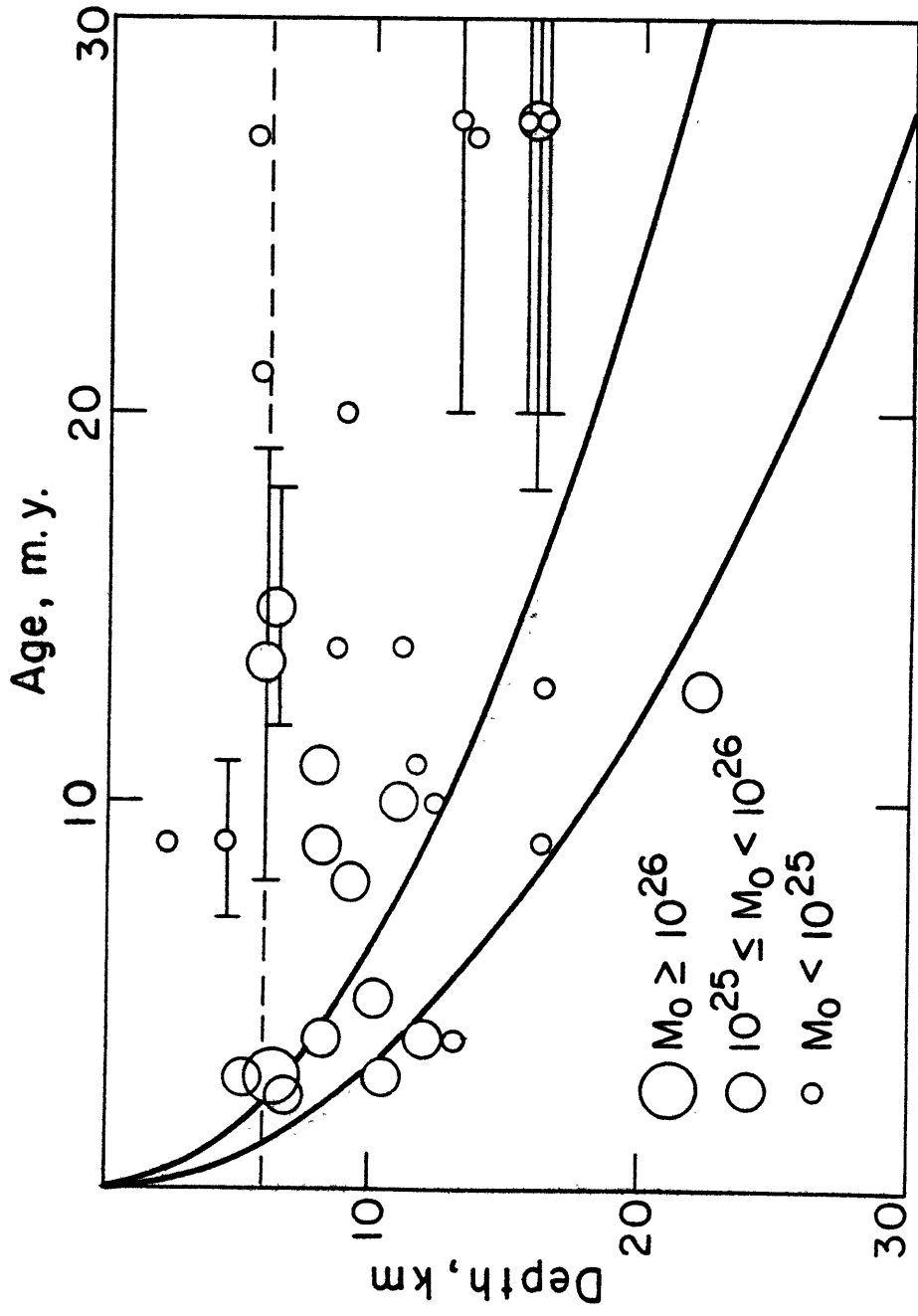


Figure 8.36

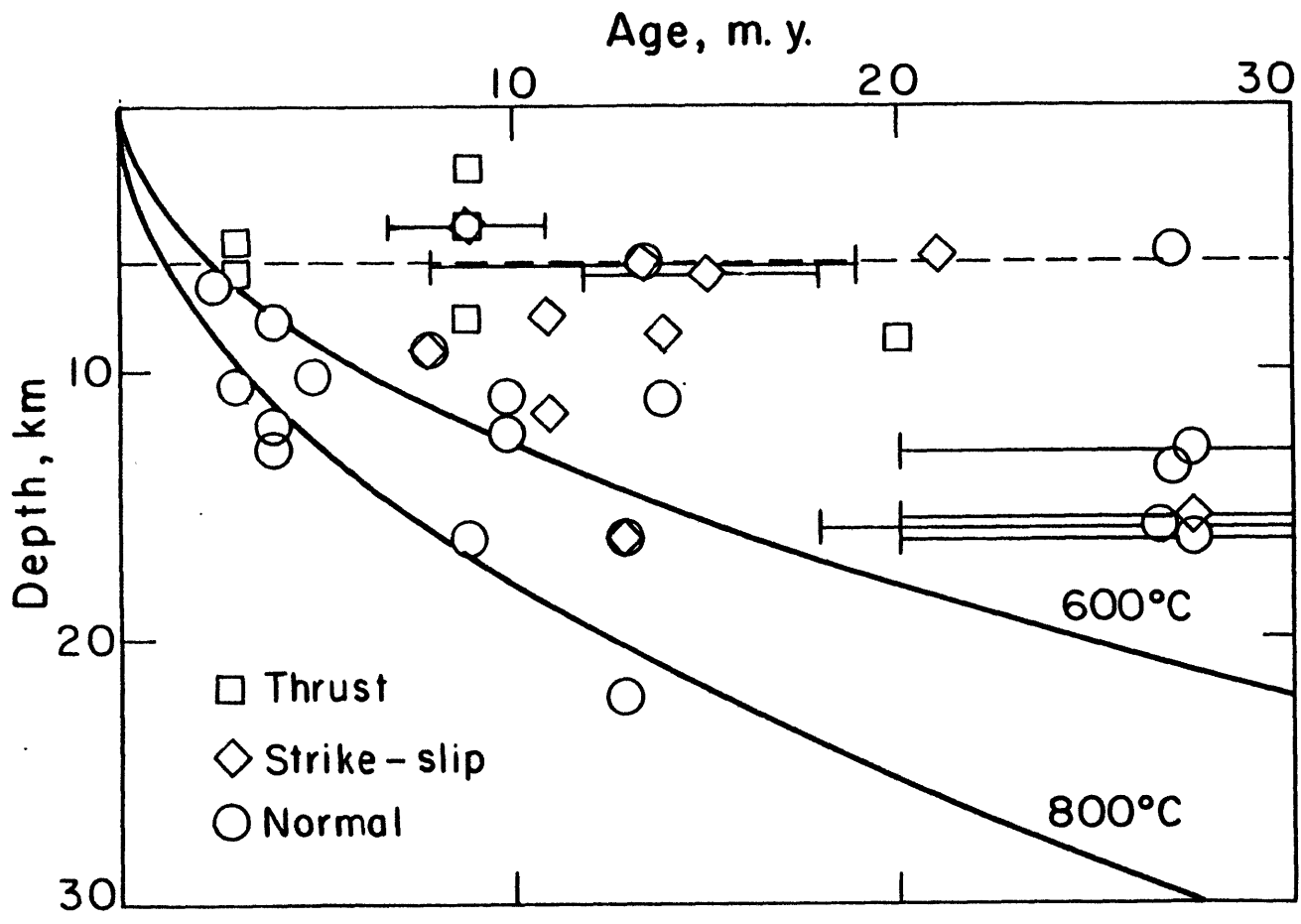


Figure 8.37

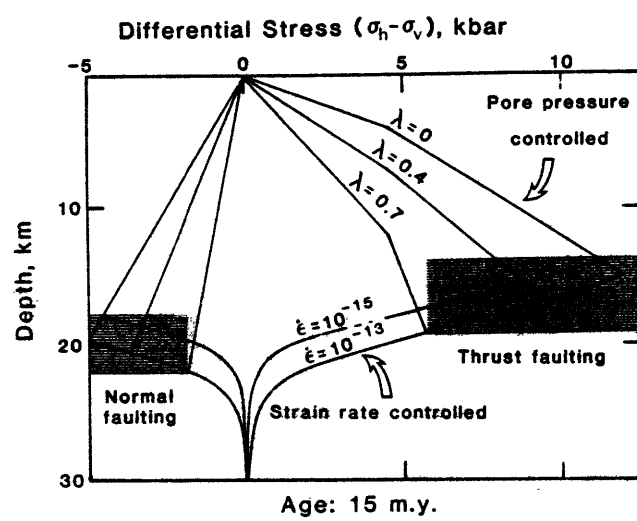


Figure 8.38

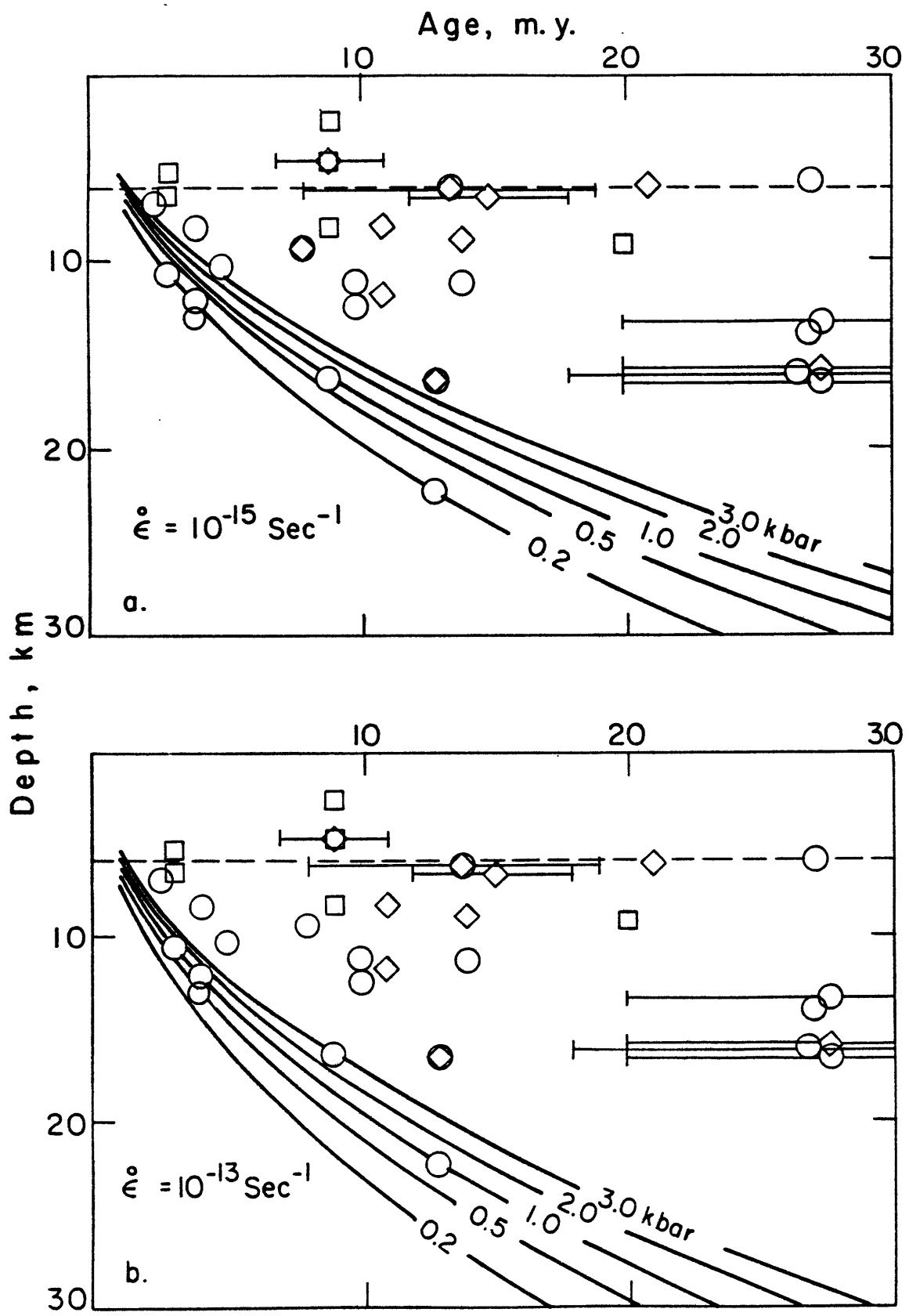
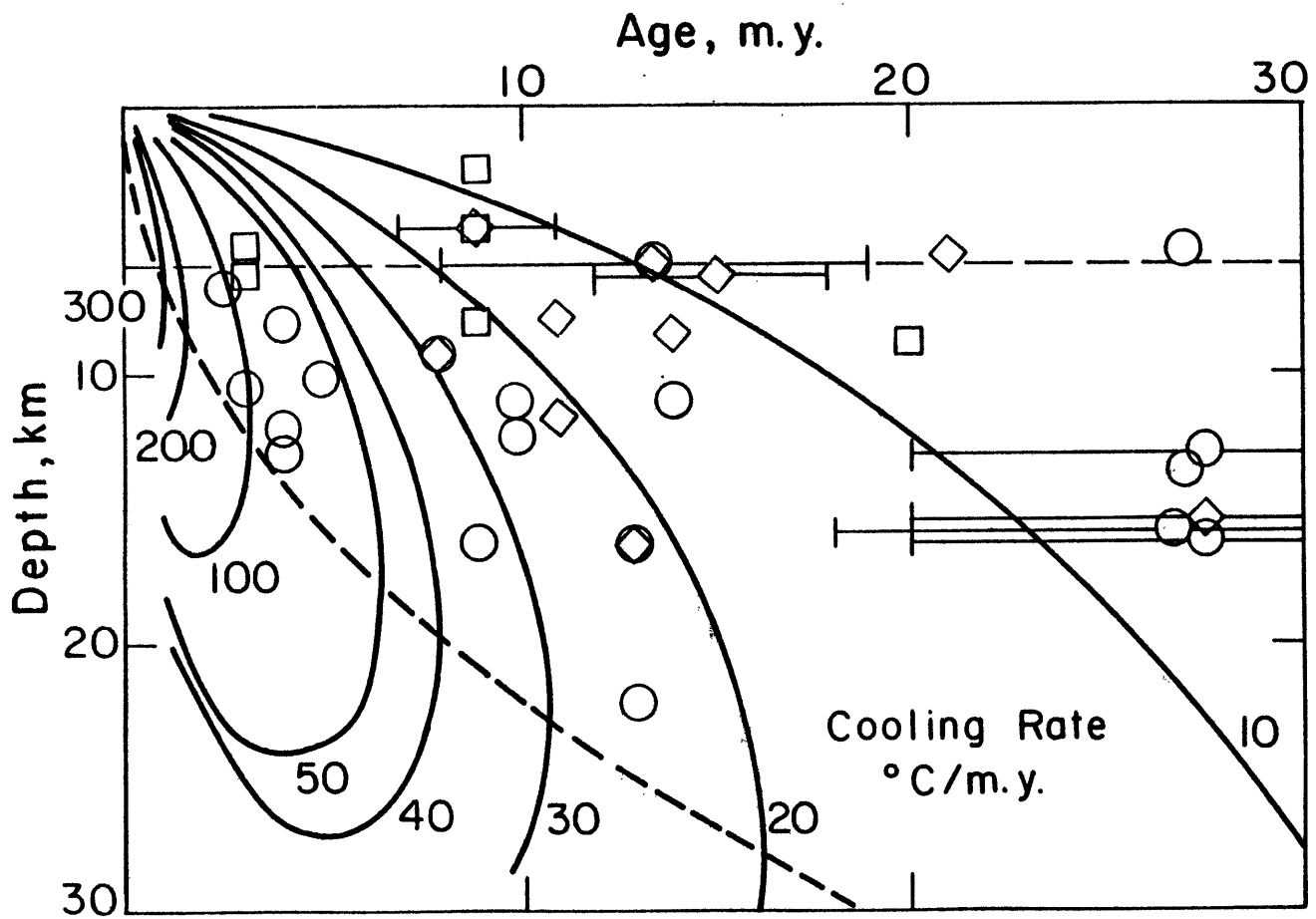


Figure 8.39

Figure 8.40



## CHAPTER 9. INTRAPLATE EARTHQUAKES AND THE STATE OF STRESS IN OCEANIC LITHOSPHERE: SUMMARY OF RESULTS

### INTRODUCTION

In previous chapters, we presented source mechanisms of 58 of the largest oceanic intraplate earthquakes to have occurred in the last 20 years. Except for Chapter 8, in which events in young oceanic lithosphere were considered as a distinct subset of oceanic intraplate seismicity, the primary emphasis in these chapters was to determine the degree to which the distribution and source mechanisms of these earthquakes can be related to local tectonic problems. Our source studies of oceanic intraplate earthquakes have been presented in this manner for two reasons: (1) Well-constrained earthquake source mechanisms are an excellent supplement to other geophysical data for investigating the nature of active deformation in many regions. (2) An appreciation for the extent of the involvement of individual events with local tectonism is an essential prerequisite for an understanding of the relation of oceanic intraplate earthquakes to the regional lithospheric stress field, particularly that component related to the system of forces which drive plate motions. Toward an achievement of such an understanding, we present in this chapter a synthesis of the data and results of Chapters 4-8.

The first subject considered below is the reliability of oceanic intraplate earthquakes as indicators of the state of stress, regardless of the source of stress. Next we consider what the distribution of oceanic intraplate seismicity, both geographically and in lithospheric cross-section, implies about the important sources of stress. For this discussion, we assemble all the centroid depths reported in earlier

chapters and consider relations between the depth of seismicity and lithospheric age.

Finally, the major conclusions of this thesis are summarized and suggestions for future research offered.

#### INTRAPLATE EARTHQUAKES AS INDICATORS OF THE STATE OF STRESS

Uncertainty concerning the use of focal mechanisms to infer the state of stress in the lithosphere arises from two sources, uncertainty in the focal mechanism itself and theoretical problems with the relationship between the principal axes of the focal mechanism and the pre-earthquake state of stress in the volume of lithosphere encompassing the earthquake source.

As we have seen in several cases, focal mechanisms derived from first motion studies (particularly for dip-slip events) are subject to large errors. Beyond the obvious problem of picking first motions correctly, there is an additional difficulty: the first motions may represent a component of the rupture history which is unrepresentative of the overall character of the stress drop in the earthquake. The best-fitting double-couple point source found in the body-waveform inversion technique used for the source studies in this thesis provides a much more reliable model of the earthquake source mechanism for the purpose of inferring the state of stress in the lithosphere. A further advantage of the waveform inversion technique occasionally accrues when we are able to resolve the fault plane of the focal mechanism from horizontal directivity in the rupture, allowing a better estimate of the principal stress directions to be made [Raleigh et al., 1972]. With the body-waveform inversion method, uncertainty in the focal

mechanism contributes in only a minor way to errors in the inferred orientations of principal stresses.

In a paper frequently cited in the literature on intraplate seismicity, McKenzie [1969] demonstrated that only constraints so loose as to be nearly useless could be placed on the principal axes of an arbitrary stress field from the focal mechanism of an earthquake occurring on a pre-existing fault, assuming no knowledge of which nodal plane corresponds to the fault plane. Abundant evidence, however, demonstrates that focal mechanisms are a much more reliable indicator of stress than McKenzie's theoretical analysis might suggest. The Rangely, Colorado experiment in induced seismicity [Raleigh et al., 1972] is perhaps the classic demonstration of the reliability of stress directions inferred from intraplate focal mechanisms. The agreement between stress orientations derived from a variety of indicators, including focal mechanisms, young geological features, and direct stress measurements, throughout most of the United States reported by Zoback and Zoback [1980] is an even more encouraging demonstration of the utility of focal mechanisms for inferring the state of stress in the lithosphere.

From the realm of oceanic intraplate studies, the consistency of stress orientations inferred from focal mechanisms (often with different faulting styles) in the northern Indian Ocean (Chapter 5), between the lesser Antilles and the Mid-Atlantic Ridge (Chapter 6), in the South Fiji Basin (Chapter 7), and from the Gilbert Islands earthquake series [Lay and Okal, 1983] and earthquakes in the south-central Pacific [Okal et al., 1980] support the contention that focal mechanisms are generally reliable indicators of the average



stress field in the lithosphere. Finally, a direct measurement (hydrofracture) of the state of stress in the upper oceanic crust at DSDP hole 504B in the northeastern Nazca plate [Newmark et al., 1984] is in good agreement with the directions of principal stresses inferred from focal mechanisms of several intraplate earthquakes in the region, even some on the opposite side of the Cocos-Nazca spreading center (Figure 9.1).

The reasons behind the apparent failure of McKenzie's theory to describe the actual relationship between intraplate earthquakes and the state of stress in the lithosphere are not entirely clear, but one likely factor deserves mention. In a given volume of lithosphere, an intraplate earthquake is not required to occur along any particular line of pre-existing weakness in the lithosphere. Given a 'choice', such an earthquake likely occurs on the most favorably oriented fault plane, i.e., one oriented with respect to the existing stress field so that the resolved shear stress is maximized while the normal stress across the fault and thus the frictional resistance to faulting [Byerlee, 1978] is minimized. The scale of heterogeneity relevant to earthquake faulting is perhaps several tens of kilometers at most, and at the dominant wavelength of the intraplate stress field (hundreds to thousands of kilometers), oceanic lithosphere in most regions contains such heterogeneities in virtually every orientation. Thus, intraplate earthquakes tend to occur on faults oriented favorably with respect to the ambient stress field, and their focal mechanisms are therefore relatively reliable indicators of the orientations of the principal stress axes (particularly if the fault plane can be identified).

## CENTROID DEPTH - AGE RELATIONS

The relationship between the depth of oceanic intraplate seismicity and lithospheric age is an important source of information on the evolution of the thermal and physical state of oceanic lithosphere. It also provides constraints on the relative importance of various sources of stress in the lithosphere, particularly when the source mechanisms of intraplate earthquakes are considered, as well as their depths. Chen and Molnar [1983] and Wiens and Stein [1983a] have previously studied age-depth relations for oceanic intraplate earthquakes, but the data set used here is more extensive, particularly for younger lithosphere. In Chapter 8, we examined the depth-age relations of earthquakes in young oceanic lithosphere at some length; in this section we extend the analysis to include earthquakes in older lithosphere.

For each of the 58 earthquakes studied with body-waveform inversion, we estimated the age of the lithosphere in the epicentral region; these ages are listed in Tables 4.1, 5.1, 6.1, 7.1, and 8.1. In Figure 9.2, the centroid depth of each event, relative to the seafloor, is plotted against the lithospheric age. Where a range of lithosphere ages is given for an event, that range is indicated. The centroid depths are listed in Tables 4.2, 5.2, 6.2, 7.2, and 8.2. The basic faulting type of each event is also shown in Figure 9.2. The 600° and 800°C isotherms calculated with the cooling plate model of Parsons and Sclater [1977] are also plotted.

On the basis of previous studies of the variation of the maximum depth of oceanic intraplate seismic activity with lithospheric age, the maximum depth at any given age appears to be limited by the depth to an

isotherm in the range of 600° to 800°C [Chen and Molnar, 1983; Wiens and Stein, 1983a]. The data in Figure 9.2 are consistent with this conclusion, but with the addition of many more data for young oceanic lithosphere, an apparent discontinuity in the limiting isotherm at a lithospheric age of about 15 m.y. is revealed. In younger lithosphere, the maximum depth of seismicity corresponds to temperatures nominally in excess of 800°C, while the limiting isotherm in older oceanic lithosphere appears to be closer to 600°C.

Assuming this feature in the age-depth data is genuine, it suggests that at least the deepest events in young lithosphere may represent the release of stresses originating in a different physical process than that which results in seismic activity in older lithosphere. This hypothesis is supported by the observation that all the events in young lithosphere whose centroid depths approach or exceed the depth of the 800°C isotherm are characterized by normal faulting, whereas the deepest events in older lithosphere are all characterized by strike-slip or thrust faulting. In Chapter 8, we suggested thermoelastic stresses arising during the phase of rapid early plate cooling (and possibly intensified by thermal perturbations associated with small-scale convection near the lithosphere-asthenosphere boundary) as the most likely cause of deep, normal-faulting earthquakes in young oceanic lithosphere.

The deepest earthquakes at all ages occur below the brittle-ductile transition, thus raising questions concerning the nature of the physical process of the seismic source (see Chapple and Forsyth [1979] for an excellent discussion of this issue). Lacking knowledge of the dependence of the physical processes limiting the

depth of intraplate seismicity on depth, temperature, and faulting type, it is impossible to interpret quantitatively the observation that the limiting isotherm for intraplate seismicity in lithosphere between about 15 and 100 m.y. old is as much as  $200^{\circ}$  lower than that for younger lithosphere. One qualitative explanation, of course, is that the average strain rate associated with deformation in older lithosphere is lower than that accompanying the early evolution of oceanic lithosphere.

In Chapter 8, we noted that thrust-faulting earthquakes in young oceanic lithosphere seemed to be confined to depths shallower than about 10 km below the seafloor. Figure 9.2 shows that thrust-faulting occurs throughout the seismically-active depth interval in lithosphere older than about 30 m.y., but most of these events are found in the northern Indian Ocean, where the entire elastic core of the lithosphere may be subject to an unusually large horizontal compressive stress (Chapter 5). The only other earthquake with a significant component of thrust-faulting deeper than 20 km in old oceanic lithosphere is the December 13, 1977 earthquake in the western Atlantic, which we have suggested is related to a diffuse plate boundary zone. If we exclude these possibly anomalous earthquakes, it appears that thrust-faulting in the oceanic lithosphere is normally observed only at relatively shallow depths (and very seldom in lithosphere older than about 50 m.y.).

In young oceanic lithosphere a further stratification of focal mechanisms appears to exist at any given lithospheric age, with normal-faulting earthquakes found at the greatest depth and strike-slip faulting characterizing seismic failure at intermediate depths (Chapter

8). The only location in which thrust and normal-faulting events are found near one another in young oceanic lithosphere is in the eastern Pacific (Figure 8.15). The thrust-faulting earthquakes are both shallower than the normal-faulting event, although the fact that they lie on opposite sides of the East Pacific Rise complicates the comparison. No clear stratification is evident among the normal-faulting and strike-slip events in the vicinity of the Chagos Bank (Chapter 8). Normal faulting is not observed in lithosphere older than 35 m.y.; all intraplate seismicity in older oceanic lithosphere is characterized by thrust and strike-slip faulting.

Several cases may be noted in which thrust faulting is found to occur at shallower depths than strike-slip faulting at approximately the same site in old oceanic lithosphere. One is the June 25, 1974 earthquake (36-50 m.y. old lithosphere) which we modeled as a double event (Chapter 5). The thrust-faulting subevent of our solution is 4 km shallower than the subevent characterized by strike-slip faulting. Because of interference between the two subevents, however, the depth resolution of the inversion procedure is somewhat poorer than usual. A second example among oceanic intraplate events occurs in the Gilbert Islands earthquake swarm of 1981-83 (lithosphere approximately 115 m.y. old). Well-resolved focal mechanisms and centroid depths for four of the largest earthquakes in this swarm were obtained by Lay and Okal [1983]. The three events characterized by thrust faulting are all at a depth of about 15 km, whereas the single strike-slip event is 21 km deep. The observation that the P axes of all four events have a similar trend led Lay and Okal to conclude that the focal mechanisms accurately reflect the regional stress field, but the details of the

focal mechanism are controlled by local complexities in the stress field. We suggest that the variation in mechanism with depth is perhaps a more general phenomenon, related to an increase in overburden stress with depth, which in a stress field dominated by horizontal compression favors strike-slip faulting over thrust faulting at increasing depths.

Because we suspect that deep normal-faulting in young oceanic lithosphere may be related to thermoelastic stresses in the lower part of the lithosphere, the depth-dependence of normal-faulting earthquake mechanisms may be unrelated to that postulated for thrust and strike-slip earthquakes. The tendency for strike-slip faulting to occur at greater depths than thrust faulting in the same stress environment, however, appears to be a consistent feature of oceanic intraplate seismicity at all lithospheric ages. A similar phenomenon, in which strike-slip faulting is observed at shallower depths than normal-faulting, has been observed in the crust of the western U.S. [Vetter and Ryall, 1983]. Using independent information (from in situ stress measurements) on the increase in shear stress with depth and assuming that an increasing overburden pressure accounts for the change in mechanism, Vetter and Ryall were able to constrain the magnitudes of the principal stresses of the regional stress field.

We have resisted the temptation to perform a similar calculation with the oceanic intraplate earthquake data because we believe the evidence for depth-dependence of focal mechanism type, while suggestive, is far from conclusive. Furthermore, some of the other constraints exploited by Vetter and Ryall are not yet available for the oceanic case. As more data become available, however, an analysis of

this type holds the promise of providing an estimate of the average level of stress in oceanic lithosphere. This is an extremely important problem which has to date been rather intractable [e.g., Hanks and Raleigh, 1980], and thus warrants considerable attention. In particular, an effort should be made to study sites of repeated seismicity with the goal of determining if any variation of focal mechanism type with depth can be resolved. Body-waveform inversion using short period records may enable us to exploit smaller earthquakes for this purpose.

Finally, we note that in lithosphere older than about 30 m.y., virtually all the larger oceanic intraplate earthquakes have centroid depths in excess of about 12 km (Figure 9.2). We interpret this to indicate that most of the seismicity represents release of stresses transmitted through the strong elastic core of the lithosphere. Seismicity in the oceanic crust is more likely to represent stresses produced locally in the shallow portion of the lithosphere. The March 24, 1978 earthquake, at a depth of 6 km in lithosphere 118 m.y. old, is a good example of this. Nishenko and Kafka [1982] make a good case that the stresses released in this event were related to crustal thickness inhomogeneities at the edge of the Bermuda Rise. The brittle strength of the oceanic crust and uppermost oceanic mantle is probably too low for significant stresses to be transmitted very far from their source. Therefore, very shallow events are more likely a response to local rather than regional stresses. The majority of deeper oceanic intraplate earthquakes in older lithosphere, by this argument, are likely to be reliable indicators of the long-wavelength tectonic stress field.

## GEOGRAPHIC DISTRIBUTION OF SEISMICITY AND LITHOSPHERIC STRESS

The distribution of oceanic intraplate seismicity is another source of information on the most important sources of stress in the lithosphere. The first aspect of this topic to be addressed in this section is the virtual aseismicity of the old oceanic lithosphere of the western Pacific. The second concerns a possible relationship between long-wavelength gravity anomalies and the distribution of intraplate seismicity, which, if confirmed, would have significant consequences for the use of stress field orientations obtained from intraplate focal mechanisms to infer the relative importance of various proposed plate driving forces.

### Aseismicity of Older Lithosphere in the Western Pacific

Of the eight earthquakes in the Pacific Basin discussed in Chapter 7, six are associated either with back-arc or marginal basins or an incipient plate boundary, all in relatively young (< 35 m.y.) lithosphere. Another is almost certainly dominated by, if not the product of, local tectonics of the island of Hawaii. Only the February 5, 1977 earthquake in the far southeastern Pacific appears to be a true intraplate event in normal old lithosphere. In contrast, younger lithosphere in the Pacific Ocean, as in most other regions, is quite active seismically (Chapter 8). Compared to the Atlantic Ocean (Chapter 6), the Cretaceous lithosphere of the western Pacific is notably lacking in larger intraplate earthquakes. The scarcity of smaller events can presumably be attributed to detection thresholds.

The rarity of larger earthquakes in the western Pacific is a significant observation which should be accounted for in any general theory of the relationship between intraplate seismicity and the state



of stress in oceanic lithosphere. Oka1 [1984] proposed that the aseismicity of older oceanic lithosphere in the Pacific is the result of an unfortunate orientation of the major fracture zones relative to the regional stress field. As we discussed above, however, the heterogeneities in lithospheric strength which are relevant to intraplate seismicity have length scales significantly shorter than that of major fracture zones, and over areas with dimensions equivalent to the dominant wavelengths of the lithospheric stress field, such heterogeneities occur in virtually every orientation.

The increase in strength of oceanic lithosphere as it cools and thickens is a possible explanation for the decline in seismicity in the oldest oceanic lithosphere. Thermoelastic stresses which may be an important source of stress in younger lithosphere may have been largely relieved by fracture and flow. The dominant source of stress in a large expanse of old oceanic lithosphere such as the western Pacific is likely to be the area-integrated 'ridge push', but the incremental change in this stress with lithospheric age is very small in lithosphere older than 80 m.y. [e.g., Dahlen, 1981].

Larger earthquakes in old lithosphere of the Indian and Atlantic Oceans are nearly all associated either with a local source of stress in the shallow part of the plate (March 24, 1978 Bermuda event), with a diffuse plate boundary zone (between Lesser Antilles and the MAR), or unusually high stresses and/or strain rates (northern Indian Ocean). Therefore the aseismicity of the western Pacific is best explained by the interaction of a very large expanse of old, strong lithosphere and a stress field, arising primarily from 'ridge push', which is of too small a magnitude and too homogeneous to produce large earthquakes.

This is an unfortunate result, because it implies that we will have great difficulty using focal mechanisms of intraplate earthquakes to infer the geometry of the intraplate stress field in a region from which such information would be highly desirable.

#### Intraplate Seismicity and Long-Wavelength Gravity Anomalies

In Chapters 4 and 8 we discussed the possible role of secondary convection beneath young oceanic lithosphere in perturbing the lithospheric stress field enough to account for the observation of deep normal-faulting earthquakes. In this section we consider whether convective patterns under older oceanic lithosphere, as evidenced by long-wavelength gravity anomalies, might influence the distribution of seismicity. Long-wavelength (1200-3500 km) free-air gravity anomalies are thought to reflect to a certain extent the flow field in the asthenosphere [e.g., Kaula, 1972], but the detailed relationship between the pattern of flow and gravity anomalies has been difficult to confirm [e.g., McKenzie et al., 1980]. If vigorous horizontal flow in the asthenosphere is indeed associated with long-wavelength gravity anomalies, one might also expect that shear stresses transmitted to the lithosphere would intensify intraplate seismicity in these areas and possibly be evident in focal mechanisms. In order to test this hypothesis, Vogt [1981] examined the topography, gravity field and seismicity of two areas, one centered on Iceland in the North Atlantic and another southeast of India, in the vicinity of a large and well-known gravity low. With the data then available, he found a weak correlation, i.e., some evidence of enhanced intraplate seismicity in regions of strong gradient of the gravity field.

We are now in a much better position to investigate this proposed relationship with regard to oceanic intraplate seismicity. We make no attempt to update the other evidence (in particular, the intraplate seismicity in other than oceanic areas) cited by Vogt, however. In the case of the North Atlantic, the level of seismicity in the oceanic region around Iceland is moderate at best (Figure 2.3). All the oceanic intraplate events in this area are relatively small; none is large enough to be suitable for study with the body-waveform inversion technique. It should be noted that much of the 'enhanced' seismicity cited by Vogt [1978] appears to be associated with continental margins on both sides of the ocean basin. Continental margins are known to be the site of somewhat higher levels of seismicity, presumably because of major lateral variations in density and, at high latitudes, because of stresses related to the most recent episode of deglaciation [e.g., Stein et al., 1979].

The Indian Ocean example is perhaps more interesting, because there is no doubt that the prominent gravity and geoid low south of India coincides with a region of unusually intense intraplate seismicity. Vogt notes one significant discrepancy between the model and observations in this case, however: there is no topographic low accompanying the gravity anomaly, as one would expect if the gravity low is indeed related to a strong downward flow pattern in the asthenosphere. Also, the focal mechanisms of oceanic intraplate earthquakes in this region do not obviously reflect the importance of viscous shear stress from a radially-inward flow pattern centered on the gravity low. The high level of intraplate seismicity and the character of the source mechanisms is reasonably well explained without reference to such additional sources of stress (Chapter 5).

Using the absence of normal-faulting earthquakes in older oceanic lithosphere as a constraint, Wiens and Stein [1984] estimate that the coupling between lithosphere and asthenosphere is relatively weak; the viscous drag on a fast-moving plate should be no more than a few bars. From other considerations, Richter and McKenzie [1978] reached a similar conclusion. Stresses of this magnitude are unlikely to have an appreciable effect on intraplate seismicity in any but the very youngest oceanic lithosphere.

#### SUMMARY

In this section we summarize the major results of this thesis. The backbone of the summary is an appraisal of the relationship between intraplate earthquakes and the state of stress in oceanic lithosphere, based on our study of the global distribution of such earthquakes and, in particular, the detailed source studies conducted for 58 of the largest events of the last two decades.

Oceanic intraplate earthquakes are frequently associated with disturbed regions of the oceanic lithosphere, such as fracture zones, relict spreading centers, and lithosphere created during episodes of reorientation of spreading centers. Because the heterogeneities which may act to localize seismic failure are found in many orientations throughout most ocean basins, oceanic intraplate earthquakes are nonetheless generally reliable indicators of the stress field in the source region.

A large proportion of oceanic intraplate seismicity occurs in lithosphere younger than about 35 m.y. old. Much of this seismicity is dominated by stresses related to the early thermal evolution of the lithosphere. In particular, extensional stress roughly parallel to the

nearby ridge axis is frequently indicated. A broad region astride the Southeast Indian Ridge is notable for an unusually high and consistent level of such seismicity. Near-ridge normal faulting earthquakes in this area and several other sites are found to occur at depths at which temperatures in the neighborhood of 800°C are predicted by simple plate cooling models. Thermoelastic stresses related to plate cooling, possibly enhanced by the effects of small-scale convection, are a likely cause of such earthquakes, and may account for other features of near-ridge seismicity, including the rapid decline in activity at a lithospheric age of about 15 m.y. and some cases of thrust faulting near the crust-mantle boundary.

The only example of normal faulting in young oceanic lithosphere in which the axis of greatest extension appears to be in the direction of spreading occurred in very young (2 m.y. old) lithosphere. Active extension parallel to the spreading direction thus appears to cease very soon after creation of the lithosphere. Normal faulting indicating extension perpendicular to the spreading direction is observed in lithosphere as old as 35 m.y. All earthquakes in lithosphere older than 35 m.y. are characterized by thrust or strike-slip faulting, indicating an intraplate stress field dominated by horizontal compression.

The P axes of thrust-faulting events in young oceanic lithosphere are often oblique or perpendicular to the direction of spreading, suggesting significant contributions from sources of stress other than 'ridge push'. Thrust-faulting earthquakes are not observed at depths greater than about 10 km below the seafloor in young oceanic lithosphere, but very little activity of any type occurs in the oceanic crust.

Until we achieve the understanding necessary to allow us to segregate earthquakes related principally to the early tectonic evolution of the lithosphere, earthquakes in young oceanic lithosphere should probably not be considered reliable indicators of the portion of long-wavelength intraplate stress field potentially related to plate driving forces.

In lithosphere older than perhaps 60 m.y., the lithosphere has cooled, thickened, and stabilized to the extent that the ambient compressive stress field from 'ridge push' is only rarely large enough to induce seismic failure. This explains the near-aseismicity of the western Pacific plate. Most of the examples of large earthquakes in old oceanic lithosphere are associated with zones of major intraplate deformation or diffuse plate boundaries, where strain rates or stresses (or both) are significantly higher than normal. The regional state of stress in these regions is accurately reflected in the focal mechanisms of intraplate events, but the number of such regions is limited.

In the northern Indian Ocean, focal mechanisms of a number of large intraplate events reveal a striking pattern of deformation. The northern part of the Ninetyeast Ridge appears to be the site of partial decoupling between the Indian and Australian halves of the plate. Earthquakes on the ridge itself are characterized by left-lateral strike-slip faulting, while earthquakes to the west are characterized by thrust faulting on planes striking E-W. These earthquakes occur to depths of up to 40 km below the seafloor and indicate that the entire elastic portion of the lithosphere is involved in the N-S compressional tectonics inferred for the upper portion of the plate from deformational structures in the sediments and acoustic basement of

this region. The intraplate deformation in this area is best explained as a consequence of the major change in plate boundary tectonics occurring along the northern boundary of the combined Indo-Australian plate. The Ninetyeast Ridge separates the portion of the plate subducting smoothly at the Sunda Arc from that actively involved in the Himalayan orogeny.

Several large oceanic intraplate events in the western Atlantic belong to a diffuse pattern of seismicity trending NW-SE between the Lesser Antilles and the Mid-Atlantic Ridge. This seismicity appears to comprise a diffuse plate boundary zone between the North and South American plates; the focal mechanisms of the larger earthquakes are consistent with recent global relative plate motion studies which predict right-lateral shear and compression across a boundary with the observed orientation.

A middle range of lithospheric ages may exist in which the stress field is no longer dominated by the early thermal evolution of the oceanic lithosphere but the lithosphere is still weak enough to fail seismically with some frequency under the influence of ambient stress fields on the order of several hundred bars, the probable level of the long-wavelength tectonic stress field in most regions. Our ability to resolve the regional intraplate stress field reflecting plate driving forces with focal mechanisms of intraplate earthquakes may be limited to this portion of the oceanic lithosphere and those few regions in older lithosphere undergoing active intraplate deformation.

The data accumulated for this thesis suggest that, over a broad range of lithospheric ages, thrust-faulting is restricted to shallower depths than strike-slip faulting. In young oceanic lithosphere, normal

faulting characterizes the deepest events at any age, but this type of faulting may be related to thermoelastic stresses induced in the deeper portions of the plate. To the extent that nearby thrust and strike-slip earthquakes, which both reflect a horizontal maximum compressive stress, follow this pattern, the variation of mechanism type with depth may be used to estimate the magnitude of principal stresses characterizing the long-wavelength lithospheric stress field. An effort to verify this relationship and acquire sufficient data for a meaningful analysis should have high priority in future research on oceanic intraplate seismicity.



## FIGURE CAPTIONS

Figure 9.1. Orientation of maximum horizontal compression inferred from an in-situ stress measurement at DSDP hole 504B compared with the orientations inferred from focal mechanisms of several oceanic intraplate earthquakes in the eastern Pacific (see Figure 8.4).

Adapted from Figure 5 of Newmark et al. [1984].

Figure 9.2. Centroid depth versus lithosphere age for all 58 earthquakes studied in this thesis with the body-waveform inversion technique. Data are listed in tables in Chapters 4-8. The earthquakes are distinguished on the basis of focal mechanism type. Symbols are: open circle - normal, solid circle - thrust, diamond - strike-slip. Two symbols are superposed for events with mechanisms intermediate between the basic types. Depths are relative to the seafloor. The horizontal dashed line indicates the depth of the Moho (6 km) in the velocity model used for the inversion, but the velocity model used for some events in older lithosphere also has a sediment layer (see individual source studies). Error bars are given for some events (usually those located on fracture zones with significant offset) for which significant uncertainty exists in the appropriate lithospheric age. The 600° and 800°C isotherms, calculated from the plate-cooling model of Parsons and Sclater [1977] are also shown.

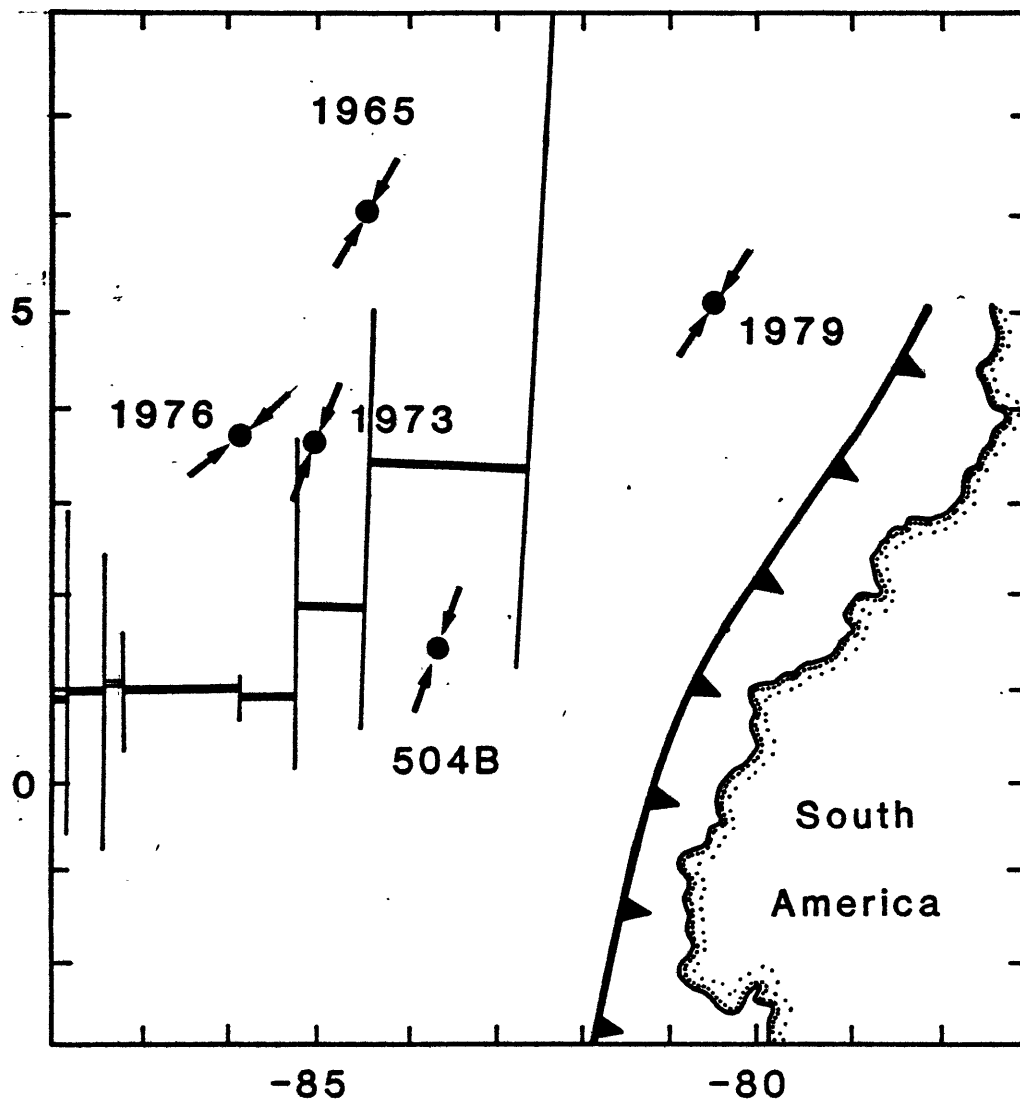


Figure 9.1

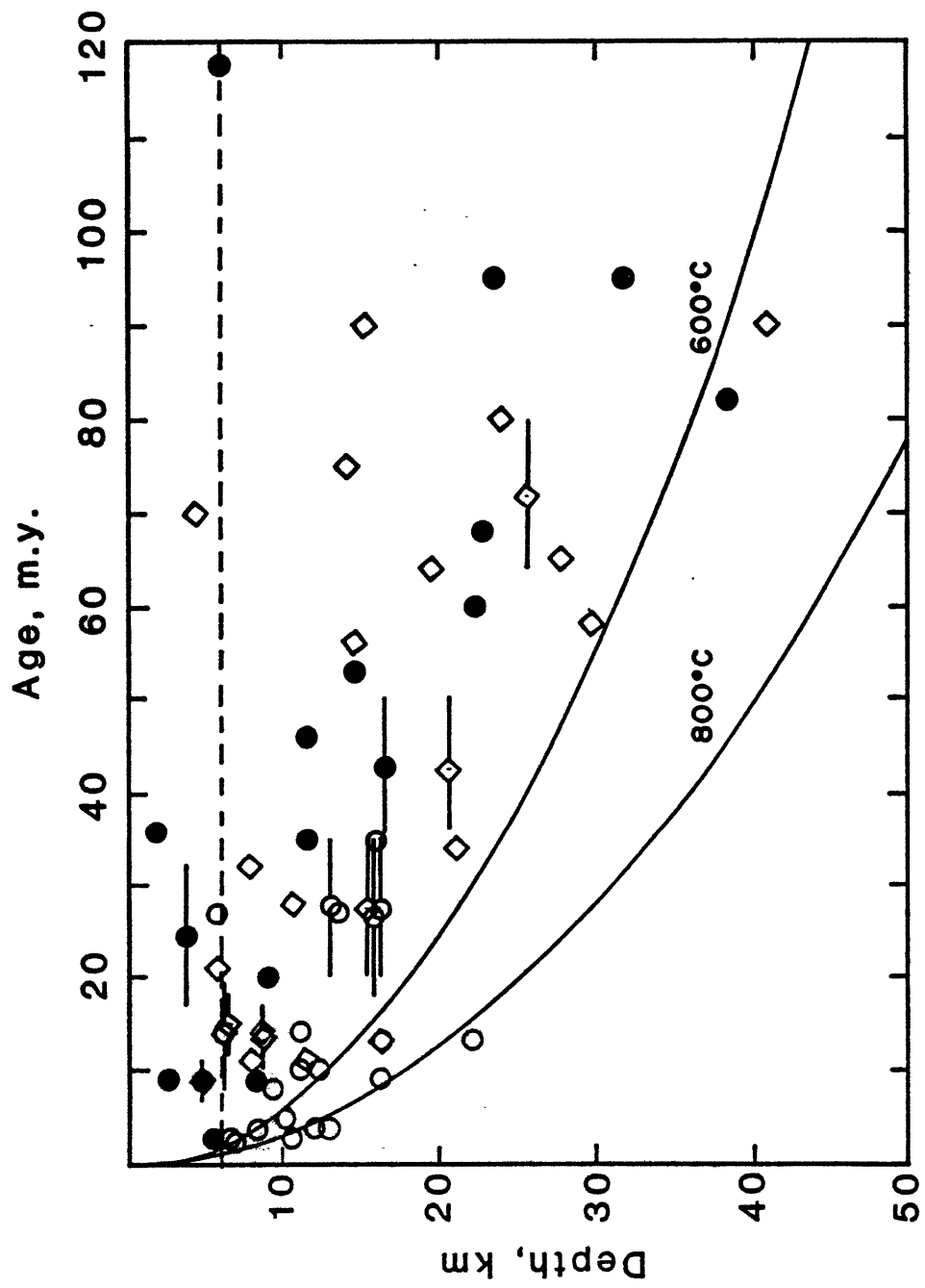


Figure 9.2

## REFERENCES

- Aki, K., Maximum likelihood estimate of  $b$  in the formula  $\log N = a - bM$  and its confidence limits, Bull. Earthquake Res. Inst., Tokyo Univ., 43, 237-239, 1965.
- Aki, K., and H. Patton, Determination of seismic moment tensor using surface waves, Tectonophysics, 49, 213-222, 1978.
- Aki, K., and P.G. Richards, Quantitative Seismology: Theory and Methods, Vol. 1, p. 114, W.H. Freeman, San Francisco, Calif., 1980.
- Anderson, R.N., D.W. Forsyth, P. Molnar, and J. Mammerrickx, Fault plane solutions of earthquakes on the Nazca plate boundaries and the Easter plate, Earth Planet. Sci. Lett., 24, 188-202, 1974.
- Ando, M., The Hawaii earthquake of November 29, 1975: Low dip angle faulting due to forceful injection of magma, J. Geophys. Res., 84, 1979.
- Artyushkov, E.V., Stresses in the lithosphere caused by crustal thickness inhomogeneities, J. Geophys. Res., 78, 7675-7708, 1973.
- Atwater, T., Implications of plate tectonics for the Cenozoic tectonic evolution of western North America, Bull. Geol. Soc. Amer., 81, 3513-3536, 1970.
- Ball, M.M., and C.G. Harrison, Crustal plates in the central Atlantic, Science, 167, 1128-1129, 1970.
- Banghar, A.R., and L.R. Sykes, Focal mechanisms of earthquakes in the Indian Ocean and adjacent regions, J. Geophys. Res., 74, 632-649, 1969.
- Barazangi, M., and J. Dorman, World seismicity maps from ESSA, Coast and Geodetic Survey, epicenter data, 1961-1967, Bull. Seismol. Soc. Amer., 59, 369-380, 1969.

- Barker, J.S., and C.A. Langston, Inversion of teleseismic body waves for the moment tensor of the 1978 Thessaloniki, Greece, earthquake, Bull. Seismol. Soc. Amer., 71, 1423-1444, 1981.
- Barker, P.F., A spreading centre in the east Scotia Sea, Earth Planet. Sci. Lett., 15, 123-132, 1972.
- Barker, P.F., The Cenozoic subduction history of the Pacific margin of the Antarctic Peninsula: Ridge crest - trench interactions, J. Geol. Soc. Lond., 139, 787-801, 1982.
- Batiza, R., Abundances, distribution and sizes of volcanoes in the Pacific Ocean and implications for the origin of non-hotspot volcanoes, Earth Planet. Sci. Lett., 60, 195-206, 1982.
- Bergman, E.A., and S.C. Solomon, Oceanic intraplate earthquakes: Implications for local and regional intraplate stress, J. Geophys. Res., 85, 5389-5410, 1980.
- Bergman, E.A., and S.C. Solomon, Recent studies in Indian Ocean intraplate seismicity (abstract), EOS Trans. AGU, 63, 1092, 1982.
- Bergman, E.A., and S.C. Solomon, Source studies of near-ridge earthquakes: Implications for the early evolution of oceanic lithosphere (abstract), EOS Trans. AGU, 64, 759, 1983.
- Bergman, E.A., and S.C. Solomon, Source mechanisms of earthquakes near mid-ocean ridges from body waveform inversion: Implications for the early evolution of oceanic lithosphere, J. Geophys. Res., in press, 1984.
- Bergman, E.A., J.L. Nabelek, and S.C. Solomon, An extensive region of off-ridge normal-faulting earthquakes in the southern Indian Ocean, J. Geophys. Res., 89, 2425-2443, 1984.

- Bouchon, M., Teleseismic body wave radiation from a source in a layered medium, Geophys. J. Roy. Astron. Soc., 47, 515-530, 1976.
- Bowin, C., Origin of the Ninetyeast Ridge from studies near the equator, J. Geophys. Res., 78, 6029-6043, 1973.
- Brace, W.F., and D.L. Kohlstedt, Limits on lithospheric stress imposed by laboratory experiments, J. Geophys. Res., 85, 6248-6252, 1980.
- Bracey, D.R., Reconnaissance geophysical survey of the Caroline Basin, Geol. Soc. Amer. Bull., 86, 775-784, 1975.
- Brotchie, J.F., Flexure of a liquid-filled spherical shell in a radial gravity field, Modern Geol., 3, 15-23, 1971.
- Brumbaugh, D.S., Classical focal mechanism techniques for body waves, Geophys. Surveys, 3, 297-329, 1979.
- Buck, W.R., When does small-scale convection begin beneath oceanic lithosphere?, Nature, submitted, 1984.
- Bungum, H., and J. Capon, Coda pattern and multipath propagation of Rayleigh waves at NORSAR, Phys. Earth Planet. Int., 9, 111-127, 1974.
- Burdick, L.J., and G.R. Mellman, Inversion of the body waves of the Borrego Mountain earthquake to the source mechanism, Bull. Seismol. Soc. Amer., 66, 1485-1499, 1976.
- Butler, R., The 1973 Hawaii earthquake: A double earthquake beneath the volcano Mauna Kea, Geophys. J. Roy. Astron. Soc., 69, 173-186, 1982.
- Byerlee, J.D., Friction of rocks, Pure Appl. Geophys., 116, 615-626, 1978.
- Cande, S.C., E.M. Herron, and B.R. Hall, The early Cenozoic tectonic history of the southeast Pacific, Earth Planet. Sci. Lett., 57, 63-74, 1982.

- Caristan, Y., The transition from high-temperature creep to fracture in Maryland diabase, J. Geophys. Res., 87, 6781-6790, 1982.
- Carpenter, E.W., Teleseismic signals calculated for underground, underwater, and atmospheric explosions, Geophysics, 32, 17-32, 1967.
- Carslaw, H.S., and J.C. Jaeger, Conduction of Heat in Solids, 2<sup>nd</sup> ed., 510 pp., Oxford University Press, Oxford, England, 1959.
- Cazenave, A., B. Lago, K. Dominh, and K. Lambeck, On the response of the ocean lithosphere to seamount loads from Geos 3 satellite radar altimeter observations, Geophys. J. Roy. Astron. Soc., 63, 233-252, 1980.
- Chapple, W.M., and D.W. Forsyth, Earthquakes and bending of plates at trenches, J. Geophys. Res., 84, 6729-6749, 1979.
- Chase, C.G., Plate kinematics: The Americas, East Africa, and the rest of the world, Earth Planet. Sci. Lett., 37, 355-368, 1978.
- Chen, W.-P., and P. Molnar, Focal depths of intracontinental and intraplate earthquakes and their implications for the thermal and mechanical properties of the lithosphere, J. Geophys. Res., 88, 4183-4215, 1983.
- Chinnery, M.A., Measurement of  $m_b$  with a global network, Tectonophysics, 49, 139-144, 1978.
- Cipar, J., Teleseismic observations of the 1976 Friuli, Italy earthquake sequence, Bull. Seismol. Soc. Amer., 70, 963-983, 1980.
- Cipar, J., Broadband time domain modeling of the earthquakes from Friuli, Italy, Bull. Seismol. Soc. Amer., 71, 1215-1232, 1981.
- Creavan, C.T., H. Kanamori, and K. Fujita, A large intraplate event near the Scotia Arc (abstract), EOS Trans. AGU, 60, 894, 1979.

- Curry, J.R., and D.G. Moore, Growth of the Bengal Deep-Sea Fan and denudation in the Himalayas, Geol. Soc. Amer. Bull., 82, 563-572, 1971.
- Curry, J.R., F.J. Emmel, D.G. Moore, and R.W. Raitt, Structure, tectonics, and geological history of the northeastern Indian Ocean, in The Ocean Basins and Margins, Vol. 6: The Indian Ocean, edited by A.E.M. Nairn and F.G. Stehli, pp. 399-450, Plenum Press, New York, 1982.
- Dahlen, F.A., Isostasy and the ambient state of stress in the oceanic lithosphere, J. Geophys. Res., 86, 7801-7807, 1981.
- DeLong, S.E., J. Dewey, and P.J. Fox, Displacement history of oceanic fracture zones, Geology, 5, 199-202, 1977.
- Detrick, R.S., J.G. Sclater, and J. Thiede, The subsidence of aseismic ridges, Earth Planet. Sci. Lett., 34, 185-196, 1977.
- Dewey, J.F., and J.M. Bird, Mountain belts and the new global tectonics, J. Geophys. Res., 75, 2625-2647, 1970.
- Drummond, K.J., Plate Tectonic Map of the Circum-Pacific Region, Northeast Quadrant, Amer. Assoc. Petr. Geol., Tulsa, OK, 1981.
- Duda, S.J., Secular seismic energy release in the circum-Pacific belt, Tectonophysics, 2, 409-452, 1965.
- Duschenes, J.D., and S.C. Solomon, Shear wave travel time residuals from oceanic earthquakes and the evolution of oceanic lithosphere, J. Geophys. Res., 82, 1985-2000, 1977.
- Dziewonski, A.M., and J.H. Woodhouse, An experiment in systematic study of global seismicity: Centroid-moment tensor solutions for 201 moderate and large earthquakes of 1981, J. Geophys. Res., 88, 3247-3272, 1983.



- Dziwonski, A.M., T.A. Chou, and J.H. Woodhouse, Determination of earthquake source parameters from wave-form data for studies of global and regional seismicity, J. Geophys. Res., 86, 2825-2852, 1981.
- Dziwonski, A.M., A. Friedman, D. Giardini, and J.H. Woodhouse, Global seismicity of 1982: Centroid-moment tensor solutions for 308 earthquakes, Phys. Earth Planet. Int., 33, 76-90, 1983.
- Eaton, J.P., Crustal structure and volcanism in Hawaii, in The Crust of the Pacific Basin, Geophys. Monogr. Ser., Vol. 6, edited by G.A. Macdonald and H. Kuno, pp. 13-29, AGU, Washington, D.C., 1962.
- Ebel, J.E., L.J. Burdick, and G.S. Stewart, The source mechanism of the August 7, 1966 El Golfo earthquake, Bull. Seismol. Soc. Amer., 68, 1281-1292, 1978.
- Eittreim, S.L., and J.I. Ewing, Midplate tectonics in the Indian Ocean, J. Geophys. Res., 77, 6413-6421, 1972.
- Epp, D., and W. Suyenaga, Thermal contraction and alteration of the oceanic crust, Geology, 6, 726-728, 1978.
- Ewing, J.I., and R. Houtz, Acoustic stratigraphy and structure of the oceanic crust, in Deep Drilling Results in the Atlantic Ocean: Ocean Crust, Maurice Ewing Ser., vol. 2, edited by M. Talwani, C.G. Harrison, and D.E. Hayes, pp. 1-14, AGU, Washington, D.C., 1979.
- Ewing, M., G.H. Sutton, and C.B. Officer, Seismic refraction measurements in the Atlantic Ocean, VI, Typical deep stations, North American basin, Bull. Seismol. Soc. Amer., 44, 21-38, 1954.
- Ewing, M., S.L. Eittreim, M. Trauchan, and J.I. Ewing, Sediment distribution in the Indian Ocean, Deep-Sea Res., 16, 231-248, 1969.
- Falconer, R.H.K, and M. Tharp, General Bathymetric Chart of the Oceans (GEBCO), Sheet 5.14, Canadian Hydrographic Service, Ottawa, Canada, 5<sup>th</sup> ed., 1981.

- Fehn, U., and L.M. Cathles, Hydrothermal convection at slow-spreading mid-ocean ridges, Tectonophysics, 55, 239-260, 1979.
- Fischer, O., Method of least squares, in Survey of Applicable Mathematics, edited by K. Rektorys, pp. 1285-1299, Iliffe Books, London, 1969.
- Fisher, R.L., M.Z. Jantsch, and R.L. Comer, General Bathymetric Chart of the Oceans (GEBCO), Sheet 5.09, Canadian Hydrographic Service, Ottawa, Canada, 5<sup>th</sup> ed., 1982.
- Fiske, R.S., and E.D. Jackson, Orientation and growth of Hawaiian rifts: The effect of regional structure and gravitational stresses, Proc. Roy. Soc. Lond., 329, 299-326, 1972.
- Fitch, T.J., Plate convergence, transcurrent faults, and the internal deformation adjacent to Southeast Asia and the western Pacific, J. Geophys. Res., 77, 4432-4460, 1972.
- Fitch, T.J., Correction and addition to 'Estimation of the seismic moment tensor from teleseismic body wave data with applications to intraplate and mantle earthquakes' by T.J. Fitch, D.W. McCowan, and M.W. Shields, J. Geophys. Res., 86, 9375-9376, 1981.
- Fitch, T.J., M.H. Worthington, and I.B. Everingham, Mechanisms of Australian earthquakes and contemporary stresses in the Indian Ocean plate, Earth Planet. Sci. Lett., 18, 345-356, 1973.
- Fitch, T.J., D.W. McCowan, and M.W. Shields, Estimation of the seismic moment tensor from teleseismic body wave data with applications to intraplate and mantle earthquakes, J. Geophys. Res., 85, 3817-3828, 1980.
- Fleitout, L., and C. Froidevaux, Tectonic stresses in the lithosphere, Tectonics, 2, 315-324, 1983.

- Flinn, E.A., and E.R. Engdahl, A proposed basis for geographical and seismic regionalization, Rev. Geophys., 3, 123-149, 1965.
- Flinn, E.A., E.R. Engdahl, and A.R. Hill, Seismic and geographical regionalization, Bull. Seismol. Soc. Amer., 64, 771-793, 1974.
- Fornari, D.J., J.K. Weissel, M.R. Perfit, and R.N. Anderson, Petrochemistry of the Sorol and Ayu troughs: Implications for crustal accretion at the northern and western boundaries of the Caroline plate, Earth Planet. Sci. Lett., 45, 1-15, 1979.
- Forsyth, D.W., Compressive stress between two mid-ocean ridges, Nature, 243, 78-79, 1973.
- Forsyth, D.W., Fault plane solutions and tectonics of the South Atlantic and Scotia Sea, J. Geophys. Res., 80, 1429-1443, 1975.
- Forsyth, D.W., Lithospheric flexure, Rev. Geophys. Space Phys., 17, 1109-1114, 1979.
- Forsyth, D.W., Determinations of focal depths of earthquakes associated with the bending of oceanic plates at trenches, Phys. Earth Planet. Int., 28, 141-160, 1982.
- Francis, T.J.G., The detailed seismicity of mid-oceanic ridges, Earth Planet. Sci. Lett., 4, 39-46, 1968.
- Francis, T.J.G., A new interpretation of the 1968 Fernandina caldera collapse and its implications for the mid-ocean ridges, Geophys. J. Roy. Astron. Soc., 39, 310-318, 1974.
- Francis, T.J.G., and R.W. Raitt, Seismic refraction measurements in the Southern Indian Ocean, J. Geophys. Res., 72, 3015-3042, 1967.
- Frankel, A., and W. McCann, Moderate and large earthquakes in the South Sandwich Arc: Indicators of tectonic variation along a subduction zone, J. Geophys. Res., 84, 5571-5577, 1979.

- Fujita, K., and N.H. Sleep, Membrane stresses near mid-ocean ridge-transform intersections, Tectonophysics, 50, 207-221, 1978.
- Furumoto, A.S., N.N. Nielson, and W.R. Phillips, A study of past earthquakes, isoseismic zones of intensity, and recommended zones for structural design for Hawaii, Report HIG-73-4, Hawaii Inst. Geophys., 100 pp., 1973.
- Futterman, W.I., Dispersive body waves, J. Geophys. Res., 67, 5279-5291, 1962.
- Geller, C.A., J.K. Weissel, and R.N. Anderson, Heat transfer and intraplate deformation in the central Indian Ocean, J. Geophys. Res., 88, 1018-1032, 1983.
- Goetze, C., and B. Evans, Stress and temperature in the bending lithosphere as constrained by experimental rock mechanics, Geophys. J. Roy. Astron. Soc., 59, 463-478, 1979.
- Green, D.H., Composition of basaltic magmas as indicators on conditions of origin: Application to oceanic volcanism, Phil. Trans. Roy. Soc. Lond., Ser. A, 268, 707-725, 1971.
- Gutenberg, B., and C.F. Richter, Seismicity of the Earth, 2<sup>nd</sup> ed., 310 pp., Princeton Univ. Press, Princeton, N.J., 1954.
- Hanks, T.C., and C.B. Raleigh, The conference on magnitude of deviatoric stresses in the Earth's crust and uppermost mantle, J. Geophys. Res., 85, 6083-6085, 1980.
- Hart, R.S., and R. Butler, Shear wave travel times and amplitudes for two well constrained earthquakes, Bull. Seismol. Soc. Amer., 68, 973-985, 1978.
- Haxby, W.F., and J.K. Weissel, Evidence for small-scale mantle convection from SEASAT altimeter data (abstract), EOS Trans. AGU, 64, 838, 1983.

- Hayes, D.E., and M. Vogel, General Bathymetric Chart of the Oceans (GEBCO), Sheet 5.13, Canadian Hydrographic Service, Ottawa, Canada, 5th ed., 1981.
- Heezen, B.C., and M. Tharp, General Bathymetric Chart of the Oceans (GEBCO), Sheet 5.12, Canadian Hydrographic Service, Ottawa, Canada, 5th ed., 1978.
- Heezen, B.C., R.P. Lynde, Jr., and D.J. Fornari, Geological Map of the Indian Ocean, Supplemental map to accompany Indian Ocean Geology and Biostratigraphy, edited by J.R. Heirtzler, H.M. Bolli, T.A. Davies, J.B. Saunders, and J.G. Sclater, AGU, Washington, D.C., 1977.
- Hegarty, K.A., J.K. Weissel, and D.E. Hayes, Convergence at the Caroline-Pacific plate boundary: Collision and subduction, in The Tectonic and Geologic Evolution of Southeast Asian Seas and Islands, Part 2, Geophys. Monogr. Ser., Vol. 27, edited by D.E. Hayes, pp. 326-348, AGU, Washington, D.C., 1983.
- Helmlberger, D.V., and L.J. Burdick, Synthetic seismograms, Ann. Rev. Earth Planet. Sci., 7, 417-442, 1979.
- Hey, R., Tectonic evolution of the Cocos-Nazca spreading center, Geol. Soc. Amer. Bull., 88, 1404-1420, 1977.
- Hey, R., G.L. Johnson, and A. Lowrie, Recent tectonic evolution of the Galapagos area and plate motions in the east Pacific, Geol. Soc. Amer. Bull., 88, 1385-1403, 1977.
- Hilde, T.W.C., and C.-S. Lee, Origin and evolution of the West Philippine Basin: A new interpretation, Tectonophysics, 102, 85-104, 1984.
- Houtz, R.E., D.E. Hayes, and R.G. Markl, Kerguelen Plateau bathymetry, sediment distribution and crustal structure, Mar. Geol., 25, 85-130, 1977.

- Isacks, B., J. Oliver, and L.R. Sykes, Seismology and the new global tectonics, J. Geophys. Res., 73, 5855-5899, 1968.
- Jackson, D.D., Interpretation of inaccurate, insufficient and inconsistent data, Geophys. J. Roy. Astron. Soc., 28, 97-109, 1972.
- Jackson, D.D., The use of a priori data to resolve nonuniqueness in linear inversion, Geophys. J. Roy. Astron. Soc., 57, 137-157, 1979.
- Jackson, E.D., and H.R. Shaw, Stress fields in central portions of the Pacific plate: Delineated in time by linear volcanic chains, J. Geophys. Res., 80, 1861-1874, 1975.
- Jackson, E.D., E.A. Silver, and G.B. Dalrymple, Hawaiian-Emperor chain and its relation to Cenozoic circum-Pacific tectonics, Geol. Soc. Amer. Bull., 83, 601-617, 1972.
- Johnson, B.D., C.M. Powell, and J.J. Veevers, Spreading history of the eastern Indian Ocean and greater India's northward flight from Antarctica and Australia, Geol. Soc. Amer. Bull., 87, 1560-1566, 1976.
- Jordan, T.H., and K.A. Sverdrup, Teleseismic location techniques and their application to earthquake clusters in the southcentral Pacific, Bull. Seismol. Soc. Amer., 71, 1105-1130, 1981.
- Kafka, A.L., and D.J. Weidner, The focal mechanisms and depths of small earthquakes as determined from Rayleigh-wave radiation patterns, Bull. Seismol. Soc. Amer., 69, 1379-1390, 1979.
- Kanamori, H., and D.L. Anderson, Theoretical basis of some empirical relations in seismology, Bull. Seismol. Soc. Amer., 65, 1073-1095, 1975.
- Karig, D.E., Origin and development of marginal basins in the western Pacific, J. Geophys. Res., 76, 2542-2561, 1971.

- Kaula, W.M., Global gravity and mantle convection, in The Upper Mantle, edited by A.R. Ritsema, pp. 341-359, Elsevier, Amsterdam, 1972.
- Kirby, S.H., Tectonic stresses in the lithosphere, constraints provided by the experimental deformation of rocks, J. Geophys. Res., 85, 6353-6363, 1980.
- Koyanagi, R.Y., and E.T. Endo, Hawaiian seismic events during 1969, U.S. Geol. Surv., Profess. Paper 750-C, C158-C164, 1971.
- Koyanagi, R.Y., D.A. Swanson, and E.T. Endo, Distribution of earthquakes related to mobility of the south flank of Kilauea Volcano, Hawaii, U.S. Geol. Surv., Profess. Paper 800-D, D89-D97, 1972.
- Koyanagi, R.Y., E.T. Endo, and P.L. Ward, Seismic activity on the island of Hawaii, 1970 to 1973, in The Geophysics of the Pacific Ocean Basin and its Margin, Geophys. Monogr. Ser., Vol. 19, edited by G.H. Sutton, M.H. Manghnani, and R. Moberly, pp. 169-172, AGU, Washington, D.C., 1976.
- La Brecque, J.L., and P.D. Rabinowitz, General Bathymetric Chart of the Oceans (GEBCO), Sheet 5.16, Canadian Hydrographic Service, Ottawa, Canada, 5<sup>th</sup> ed., 1981.
- La Brecque, J.L., D.V. Kent, and S.C. Cande, Revised magnetic polarity time scale for Late Cretaceous and Cenozoic time, Geology, 5, 330-335, 1977.
- Lambeck, K., and S.M. Nakiboglu, Seamount loading and stress in the ocean lithosphere, 2, viscoelastic and elastic-viscoelastic models, J. Geophys. Res., 86, 6961-6984, 1981.
- Langston, C.A., Source inversion of seismic waveforms: The Koyna, India, earthquake of 14 September, 1967, Bull. Seismol. Soc. Amer., 71, 1-24, 1981.

- Laughton, A.S., General Bathymetric Chart of the Oceans (GEBCO), Sheet 5.05, Canadian Hydrographic Service, Ottawa, Canada, 5<sup>th</sup> ed., 1975.
- Lawver, L.A., and H.J.B. Dick, The American-Antarctic Ridge, J. Geophys. Res., 88, 8193-8202, 1983.
- Lay, T., and E.A. Okal, The Gilbert Islands (Republic of Kiribati) earthquake swarm of 1981-83, Phys. Earth Planet. Inter., 33, 284-303, 1983.
- Le Pichon, X., Sea-floor spreading and continental drift, J. Geophys. Res., 73, 3661-3697, 1968.
- Le Pichon, X., and J.R. Heirtzler, Magnetic anomalies in the Indian Ocean and seafloor spreading, J. Geophys. Res., 73, 2101-2117, 1968.
- Lilwall, R.C., Intraplate seismicity and seismic risk in the Atlantic Ocean based on teleseismically observed earthquakes, Institute of Oceanographic Sciences, Report, No. 136, 43 pp., 1982.
- Lister, C.R.B., Gravitational drive on oceanic plates caused by thermal contraction, Nature, 257, 663-665, 1975.
- Lister, C.R.B., Qualitative models of spreading-center processes, including hydrothermal penetration, Tectonophysics, 37, 203-218, 1977.
- Liu, C.-S., D.T. Sandwell, and J.R. Curray, The negative gravity field over the 85°E Ridge, J. Geophys. Res., 87, 7673-7686, 1982.
- Liu, C.-S., J.R. Curray, and J.M. McDonald, New constraints on the tectonic evolution of the eastern Indian Ocean, Earth Planet. Sci. Lett., 65, 331-342, 1983.
- Liu, H.-L., and H. Kanamori, Determination of source parameters of midplate earthquakes from the wave forms of body waves, Bull. Seismol. Soc. Amer., 70, 1989-2004, 1980.



- Lort, J.M., The tectonics of the eastern Mediterranean: A geophysical review, Rev. Geophys. Space Phys., 9, 189-216, 1971.
- Luyendyk, B.P., and T.A. Davies, Results of DSDP Leg 26 and the geologic history of the Southern Indian Ocean, in Initial Reports of the Deep Sea Drilling Project, 26, 909-943, 1974.
- Luyendyk, B.P., and W. Rennick, Tectonic history of aseismic ridges in the eastern Indian Ocean, Geol. Soc. Amer. Bull., 88, 1347-1356, 1977.
- Macdonald, K.C., and T.M. Atwater, Evolution of rifted ocean ridges, Earth Planet. Sci. Lett., 39, 319-327, 1978.
- Mammerickx, J., Re-evaluation of some geophysical observations in the Caroline basins, Geol. Soc. Amer. Bull., 89, 192-196, 1978.
- Mammerickx, J., and S.M. Smith, General Bathymetric Chart of the Oceans (GEBCO), Sheet 5.11, Canadian Hydrographic Service, Ottawa, Canada, 5<sup>th</sup> ed., 1980.
- Mammerickx, J., and S.M. Smith, General Bathymetric Chart of the Oceans (GEBCO), Sheet 5.07, Canadian Hydrographic Service, Ottawa, Canada, 5<sup>th</sup> ed., 1982.
- Mareschal, J.C., Uplift by thermal expansion of the lithosphere, Geophys. J. Roy. Astron. Soc., 66, 535-552, 1981.
- Maxwell, A.E., R.P. Von Herzen, K.J. Hsu, J.E. Andrews, T. Saito, S.F. Percival, Jr., E.D. Milow, and R.E. Boyce, Deep sea drilling in the South Atlantic, Science, 168, 1047-1059, 1970.
- McGarr, A., Amplitude variations of Rayleigh waves - horizontal refractions, Bull. Seismol. Soc. Amer., 59, 1307-1334, 1969.
- McKenzie, D.P., The relation between fault plane solutions for earthquakes and the directions of the principal stresses, Bull. Seismol. Soc. Amer., 59, 591-601, 1969.

- McKenzie, D.P., Active tectonics of the Mediterranean Region, Geophys. J. Roy. Astron. Soc., 30, 109-185, 1972.
- McKenzie, D.P., and R.L. Parker, The north Pacific: An example of tectonics on a sphere, Nature, 216, 1276-1280, 1967.
- McKenzie, D.P., A.B. Watts, B. Parsons, and M. Roufosse, Planform of mantle convection beneath the Pacific Ocean, Nature, 288, 442, 1980.
- Meissner, R., and J. Strehlau, Limits of stresses in continental crusts and their relation to the depth-frequency distribution of shallow earthquakes, Tectonics, 1, 73-90, 1982.
- Mendiguren, J.A., Focal mechanism of a shock in the middle of the Nazca plate, J. Geophys. Res., 76, 3861-3879, 1971.
- Mendiguren, J.A., and F.M. Richter, On the origin of compressional intraplate stresses in South America, Phys. Earth Planet. Int., 16, 318-326, 1978.
- Minster, J.B., and T.H. Jordan, Present-day plate motions, J. Geophys. Res., 83, 5331-5354, 1978.
- Minster, J.B., T.H. Jordan, P. Molnar, and E. Haines, Numerical modelling of instantaneous plate tectonics, Geophys. J. Roy. Astron. Soc., 36, 541-576, 1974.
- Molnar, P., and L.R. Sykes, Tectonics of the Caribbean and Middle America regions from focal mechanisms and seismicity, Geol. Soc. Amer. Bull., 80, 1639-1684, 1969.
- Monahan, D., R.H.K. Falconer, and M. Tharp, General Bathymetric Chart of the Oceans (GEBCO), Sheet 5.10, Canadian Hydrographic Service, Ottawa, Canada, 5<sup>th</sup> ed., 1982.
- Moore, D.G., J.R. Curray, R.W. Raitt, and F.J. Emmel, Stratigraphic - seismic section correlations and implications to Bengal Fan history, Init. Rep. Deep Sea Drilling Proj., 22, 403-412, 1974.

- Morgan, W.J., Rises, trenches, great faults and crustal blocks, J. Geophys. Res., 73, 1959-1982, 1968.
- Morgan, W.J., Deep mantle convection plumes and plate motions, Amer. Assoc. Pet. Geol. Bull., 56, 203-213, 1972.
- Morgan, W.J., Rodriguez, Darwin, Amsterdam,..., A second type of hotspot island, J. Geophys. Res., 83, 5355-5360, 1978.
- Muller, J.L., Earthquake source parameters, seismicity, and tectonics of North Atlantic transform faults, Ph.D. thesis, Mass. Inst. of Technol., Cambridge, Mass., 243 pp., 1983.
- Mutter, J.C., and S.C. Cande, The early opening between Broken Ridge and Kerguelen Plateau, Earth Planet. Sci. Lett., 65, 369-376, 1983.
- Nabelek, J.L., Determination of earthquake source parameters from inversion of body waves, Ph.D. thesis, Mass. Inst. of Technol., Cambridge, Mass., 361 pp., 1984.
- Newmark, R.L., M.D. Zoback, and R.N. Anderson, Orientation of in-situ stresses near the Costa Rica rift and the Peru-Chile trench: DSDP hole 504B, Nature, in press, 1984.
- Nishenko, S.P., and A.F. Kafka, Earthquake focal mechanisms and the intraplate setting of the Bermuda Rise, J. Geophys. Res., 87, 3929-3941, 1982.
- Nishenko, S.P., G.M. Purdy, and J.I. Ewing, Microaftershock survey of the 1978 Bermuda Rise earthquake, J. Geophys. Res., 87, 10624-10636, 1982.
- Nougier, J., Geochronology of the volcanic activity in Iles Kerguelen, in Antarctic Geology and Geophysics, edited by R.J. Adie, pp. 809-815, Universitetsforlaget, Oslo, 1972.
- Okal, E.A., The Bellingshausen Sea earthquake of February 5, 1977: Evidence for ridge-generated compression in the Antarctic plate, Earth Planet. Sci. Lett., 46, 306-310, 1980.

- Okal, E.A., Intraplate seismicity of Antarctica and tectonic implications, Earth Planet. Sci. Lett., 52, 397-409, 1981.
- Okal, E.A., Oceanic intraplate seismicity, Ann. Rev. Earth Planet. Sci., 11, 195-214, 1983.
- Okal, E.A., Intraplate seismicity of the southern part of the Pacific plate, J. Geophys. Res., submitted, 1984.
- Okal, E.A., J. Talandier, K.A. Sverdrup, and T.H. Jordan, Seismicity and tectonic stress in the South-Central Pacific, J. Geophys. Res., 85, 6479-6495, 1980.
- Parsons, B., and D. McKenzie, Mantle convection and the thermal structure of the plates, J. Geophys. Res., 83, 4485-4496, 1978.
- Parsons, B., and J.G. Sclater, An analysis of the variation of ocean floor bathymetry and heat flow with age, J. Geophys. Res., 82, 803-827, 1977.
- Patton, H., and K. Aki, Bias in the estimate of seismic moment tensor by the linear inversion method, Geophys. J. Roy. Astron. Soc., 59, 479-495, 1979.
- Peirce, J.W., The northward motion of India since the late Cretaceous, Geophys. J. Roy. Astron. Soc., 52, 277-311, 1978.
- Perry, R.K., H.S. Fleming, P.R. Vogt, et al., North Atlantic Ocean: Bathymetry and Plate Tectonic Evolution, Acoustics Division, Acoustic Media Characterization Branch, Naval Research Laboratory, 1981.
- Pfiffner, O.A., and J.G. Ramsay, Constraints on geological strain rates: Arguments from finite strain states of naturally deformed rocks, J. Geophys. Res., 87, 311-321, 1982.
- Plafker, G., Tectonic deformation associated with the 1964 Alaska earthquake, Science, 148, 1675-1687, 1965.

- Pollack, H.N., I.G. Gass, R.S. Thorpe and D.S. Chapman, On the vulnerability of lithospheric plates to mid-plate volcanism: Reply to comments by P.R. Vogt, J. Geophys. Res., 86, 961-966, 1981.
- Raleigh, C.B., J.H. Healy, and J.D. Bredehoeft, Faulting and crustal stress at Rangely, Colorado, in Flow and Fracture of Rocks, Geophys. Monogr. Ser., Vol. 16, edited by H.C. Heard, I.Y. Borg, N.L. Carter, and C.B. Raleigh, pp. 275-284, AGU, Washington, D.C., 1972.
- Richardson, R.M., Inversion for the driving forces of plate tectonics, in: Proceedings, IEEE International Geoscience and Remote Sensing Symposium, II, p. FA2.3.1-FA2.3.6, 1983.
- Richardson, R.M., and S.C. Solomon, Apparent stress and stress drop for intraplate earthquakes and tectonic stress in the plates, Pure Appl. Geophys., 115, 317-331, 1977.
- Richardson, R.M., S.C. Solomon, and N.H. Sleep, Tectonic stress in the plates, Rev. Geophys. Space Phys., 17, 981-1019, 1979.
- Richter, F.M., Convection and large-scale circulation of the mantle, J. Geophys. Res., 78, 8735-8745, 1973.
- Richter, F.M., and D.P. McKenzie, Simple plate models of mantle convection, J. Geophys., 44, 441-471, 1978.
- Richter, F.M., and B. Parsons, On the interaction of two scales of convection in the mantle, J. Geophys. Res., 80, 2529-2541, 1975.
- Rogers, D.B., and E.T. Endo, Focal mechanisms for upper mantle earthquakes and flexure of the lithosphere near Hawaii (abstract), EOS Trans. AGU, 58, 1231, 1977.
- Romanowicz, B., Depth resolution of earthquakes in central Asia by moment tensor inversion of long-period Rayleigh waves: Effects of phase velocity variations across Eurasia and their calibration, J. Geophys. Res., 86, 5963-5984, 1981.

- Romanowicz, B., Moment tensor inversion of long period Rayleigh waves: A new approach, J. Geophys. Res., 87, 5395-5407, 1982.
- Rothe, J.P., The Seismicity of the Earth, 1953-1965, 336 pp., UNESCO, Paris, 1969.
- Sandwell, D., and G. Schubert, Lithospheric flexure at fracture zones, J. Geophys. Res., 87, 4657-4667, 1982.
- Schlich, R., The Indian Ocean: Aseismic ridges, spreading centers, and ocean basins, in The Ocean Basins and Margins, Vol. 6: The Indian Ocean, edited by A.E.M. Nairn and F.G. Stehli, pp. 51-148, Plenum Press, New York, 1982.
- Schlich, R., and P. Patriat, Profils magnetiques sur le dorsale mediooceanique "Indo-Pacifique", Ann. de Geophys., 23, 629-633, 1967.
- Schlich, R., and P. Patriat, Anomalies magnetiques de la branche est de la dorsale medio-indienne entre les iles Amsterdam et Kerguelen, C.R. Acad. Sci., Paris, 272B, 773-776, 1971.
- Schouten, H., and R.S. White, Zero offset fracture zones, Geology, 8, 175-179, 1980.
- Schubert, G., D.A. Yuen, C. Froidevaux, L. Fleitout, and M. Souriau, Mantle circulation with partial shallow return flow: Effects on stresses in oceanic plates and topography of the sea floor, J. Geophys. Res., 83, 745-758, 1978.
- Sclater, J.G., and R.L. Fisher, The evolution of the east central Indian Ocean, with emphasis on the tectonic setting of the Ninetyeast Ridge, Geol. Soc. Amer. Bull., 85, 683-702, 1974.
- Sclater, J.G., B.P. Luyendyk, and L. Meinke, Magnetic lineations in the southern part of the Central Indian Basin, Geol. Soc. Amer. Bull., 87, 371-378, 1976.

- Sclater, J.G., C. Jaupart, and D. Galson, The heat flow through oceanic and continental crust and the heat loss of the Earth, Rev. Geophys. Space Phys., 18, 269-311, 1980.
- Sclater, J.G., B. Parsons, and C. Jaupart, Oceans and continents: Similarities and differences in the mechanisms of heat loss, J. Geophys. Res., 86, 11535-11552, 1981a.
- Sclater, J.G., R.L. Fisher, P. Patriat, C. Tapscott, and B. Parsons, Eocene to recent development of the Southwest Indian Ridge, a consequence of the evolution of the Indian Ocean triple junction, Geophys. J. Roy. Astron. Soc., 64, 587-604, 1981b.
- Searle, R.C., D. Monahan, and G.L. Johnson, General Bathymetric Chart of the Oceans (GEBCO), Sheet 5.08, Canadian Hydrographic Service, Ottawa, Canada, 5<sup>th</sup> ed., 1982.
- Shi, Y., and B. Bolt, The standard error of the magnitude - frequency b value, Bull. Seismol. Soc. Amer., 72, 1677-1688, 1982.
- Smith, W.D., The b-value as an earthquake precursor, Nature, 289, 136-139, 1981.
- Solomon, S.C., E.A. Bergman, and P.Y. Huang, Earthquakes and tectonics at mid-ocean ridge axes (abstract), EOS Trans. AGU, 64, 759, 1983.
- Stark, M., and D.W. Forsyth, The geoid, small-scale convection, and differential travel time anomalies of shear waves in the central Indian Ocean, J. Geophys. Res., 88, 2273-2288, 1983.
- Stein, S., An earthquake swarm on the Chagos-Laccadive Ridge and its tectonic implications, Geophys. J. Roy. Astron. Soc., 55, 577-588, 1978.
- Stein, S., Intraplate seismicity on bathymetric features: The 1968 Emperor Trough earthquake, J. Geophys. Res., 84, 4763-4768, 1979.

- Stein, S., and E.A. Okal, Seismicity and tectonics of the Ninetyeast Ridge area: Evidence for internal deformation of the Indian plate, J. Geophys. Res., 83, 2233-2246, 1978.
- Stein, S., and D.A. Wiens, Implications of oceanic intraplate seismicity for intraplate stresses, plate driving forces and mantle viscosity (abstract), EOS Trans. AGU, 64, 759, 1983.
- Stein, S., H.J. Melosh, and J.B. Minster, Ridge migration and asymmetric sea-floor spreading, Earth Planet. Sci. Lett., 36, 51-62, 1977.
- Stein, S., N.H. Sleep, R.J. Geller, S.-C. Wang, and G.C. Kroeger, Earthquakes along the passive margin of eastern Canada, Geophys. Res. Lett., 6, 537-540, 1979.
- Stein, S., J. Engeln, D. Wiens, K. Fujita, and R. Speed, Subduction seismicity and tectonics in the Lesser Antilles arc, J. Geophys. Res., 87, 8642-8664, 1982.
- Stewart, G.S., and D.V. Helmberger, The Bermuda earthquake of March 24, 1978: A significant oceanic intraplate event, J. Geophys. Res., 86, 7027-7036, 1981.
- Strelitz, R.A., Moment tensor inversions and source models, Geophys. J. Roy. Astron. Soc., 52, 359-364, 1978.
- Stover, C.W., Seismicity of the Indian Ocean, J. Geophys. Res., 71, 2575-2581, 1966.
- Suyenaga, W., Isostasy and flexure of the lithosphere under the Hawaiian Islands, J. Geophys. Res., 84, 5599-5604, 1979.
- Sykes, L.R., Mechanism of earthquakes and the nature of faulting on the mid-ocean ridges, J. Geophys. Res., 72, 2131-2153, 1967.
- Sykes, L.R., Seismicity of the Indian Ocean and a possible nascent island arc between Ceylon and Australia, J. Geophys. Res., 75, 5041-5055, 1970a.



- Sykes, L.R., Earthquake swarms and sea-floor spreading, J. Geophys. Res., 75, 6598-6611, 1970b.
- Sykes, L.R., Intraplate seismicity, reactivation of preexisting zones of weakness, alkaline magmatism, and other tectonism postdating continental fragmentation, Rev. Geophys. Space Phys., 16, 621-688, 1978.
- Sykes, L.R., and M.L. Sbar, Intraplate earthquakes, lithospheric stresses and the driving mechanism of plate tectonics, Nature, 245, 298-302, 1973.
- Sykes, L.R., and M.L. Sbar, Focal mechanism solutions of intraplate earthquakes and stresses in the lithosphere, in Geodynamics of Iceland and the North Atlantic Area, edited by L. Kristjansson, pp. 207-224, D. Reidel, Hingham, Mass., 1974.
- Talandier, J., and G.T. Kuster, Seismicity and submarine volcanic activity in French Polynesia, J. Geophys. Res., 81, 936-948, 1976.
- Tapponnier, P., and J. Francheteau, Necking of the lithosphere and the mechanics of slowly accreting plate boundaries, J. Geophys. Res., 83, 3955-3970, 1978.
- Tarantola, A., and B. Valette, Generalized nonlinear inverse problems solved using the least squares criterion, Rev. Geophys. Space Phys., 20, 219-232, 1982.
- Taylor, B., and D.E. Hayes, The tectonic evolution of the South China Basin, in The Tectonic and Geologic Evolution of Southeast Asian Seas and Islands, Geophys. Monogr. Ser., Vol. 23, edited by D.E. Hayes, pp. 89-104, AGU, Washington, D.C., 1980.

- Taylor, B., and D.E. Hayes, Origin and history of the South China Basin, in The Tectonic and Geologic Evolution of Southeast Asian Seas and Islands, Part 2, Geophys. Monogr. Ser., Vol. 27, edited by D.E. Hayes, pp. 23-56, AGU, Washington, D.C., 1983.
- Tobin, D.G., and L.R. Sykes, Seismicity and tectonics of the northeast Pacific Ocean, J. Geophys. Res., 73, 3821-3845, 1968.
- Trehu, A.M., J.L. Nabelek, and S.C. Solomon, Source characterization of two Reykjanes Ridge earthquakes: Surface waves and moment tensors; P waveforms and nonorthogonal nodal planes, J. Geophys. Res., 86, 1701-1734, 1981.
- Tsai, Y.-B., Determination of focal depths of earthquakes in the mid-oceanic ridges from amplitude spectra of surface waves, Ph.D. thesis, Mass. Inst. of Technol., Cambridge, MA, 144 pp., 1969.
- Turcotte, D.L., Are transform faults thermal contraction cracks?, J. Geophys. Res., 79, 2573-2577, 1974a.
- Turcotte, D.L., Membrane tectonics, Geophys. J. Roy. Astron. Soc., 36, 33-42, 1974b.
- Turcotte, D.L., and E.R. Oxburgh, Mid-plate tectonics, Nature, 244, 337-339, 1973.
- Unger, J.D., and P.L. Ward, A large deep Hawaiian earthquake - The Honomu, Hawaii event of April 26, 1973, Bull. Seismol. Soc. Amer., 69, 1771-1781, 1979.
- Upton, B.G.J., Oceanic islands, in The Ocean Basins and Margins Vol. 6: The Indian Ocean, edited by A.E.M. Nairn and F.G. Stehli, pp. 585-648, Plenum Press, New York, 1982.

- Veevers, J.J., Models of the evolution of the eastern Indian Ocean, in Indian Ocean Geology and Biostratigraphy, edited by J.R. Heirtzler, H.M. Bolli, T.A. Davies, J.B. Saunders, and J.G. Sclater, pp. 151-163, AGU, Washington, D.C., 1977.
- Vetter, U.R., and A.S. Ryall, Systematic change of focal mechanism with depth in the western Great Basin, J. Geophys. Res., 88, 8237-8250, 1983.
- Vine, F.J. and D.H. Matthews, Magnetic anomalies over ocean ridges, Nature, 199, 947-949, 1963.
- Wang, S.-C., R.J. Geller, S. Stein, and B. Taylor, An intraplate thrust faulting earthquake in the South China Sea, J. Geophys. Res., 84, 5627-5631, 1979.
- Ward, S.N., A technique for the recovery of the seismic moment tensor applied to the Oaxaca, Mexico earthquake of November 1978, Bull. Seismol. Soc. Amer., 70, 717-734, 1980.
- Ward, S.N., Body wave inversion: Moment tensors and depths of oceanic intraplate bending earthquakes, J. Geophys. Res., 88, 9315-9330, 1983.
- Watts, A.B., J.K. Weissel, and F.J. Davey, Tectonic evolution of the South Fiji marginal basin, in Island Arcs, Deep Sea Trenches, and Back-Arc Basins, Maurice Ewing Ser., Vol. 1, edited by M. Talwani and W.C. Pittman III, pp. 419-428, AGU, Washington, D.C., 1977.
- Watts, A.B., J.H. Bodine, and M.S. Steckler, Observations of flexure and the state of stress in the oceanic lithosphere, J. Geophys. Res., 85, 6369-6376, 1980.
- Weidner, D.J., The effects of oceanic sediments on surface-wave propagation, Bull. Seismol. Soc. Amer., 65, 1531-1551, 1975.

- Weidner, D.J., and K. Aki, Focal depth and mechanism of mid-ocean earthquakes, J. Geophys. Res., 78, 1818-1831, 1973.
- Weissel, J.K., and R.N. Anderson, Is there a Caroline plate?, Earth Planet. Sci. Lett., 41, 143-158, 1978.
- Weissel, J.K., and D.E. Hayes, Magnetic anomalies in the southeast Indian Ocean, in Antarctic Research Series, 19, Antarctic Oceanology II: The Australia - New Zealand Sector, edited by D.E. Hayes, pp. 165-196, AGU, Washington, D.C., 1972.
- Weissel, J.K., D.E. Hayes, and E.M. Herron, Plate tectonic synthesis: The displacements between Australia, New Zealand, and Antarctic since the late Cretaceous, Mar. Geol., 25, 231-277, 1977.
- Weissel, J.K., R.N. Anderson, and C.A. Geller, Deformation of the Indo-Australian plate, Nature, 287, 284-291, 1980.
- Whitford, D.J., and R.A. Duncan, Origin of the Ninetyeast Ridge - Sr isotope and trace-element evidence, in USGS Open File Report, pp. 451-453, 1978.
- Wiens, D.A., and S. Stein, Age dependence of oceanic intraplate seismicity and implications for lithospheric evolution, J. Geophys. Res., 88, 6455-6468, 1983a.
- Wiens, D.A., and S. Stein, Near ridge intraplate stress heterogeneities inferred from earthquake mechanisms (abstract), EOS Trans. AGU, 64, 269, 1983b.
- Wiens, D.A., and S. Stein, Intraplate seismicity and stresses in young oceanic lithosphere, J. Geophys. Res., submitted, 1984.
- Wiens, D.A., C.M. Helm, and S. Stein, Intraplate seismicity and stresses in young oceanic lithosphere (abstract), EOS Trans. AGU, 64, 759, 1983.

- Wiggins, R., The general linear inverse problem: Implications of surface waves and free oscillations on earth structure, Rev. Geophys. Space Phys., 10, 251-285, 1972.
- Wilson, J.T., A new class of faults and their bearing on continental drift, Nature, 207, 343-347, 1965.
- Withjack, M., A convective heat transfer model for lithospheric thinning and crustal uplift, J. Geophys. Res., 84, 3008-3022, 1979.
- York, D., Least-squares fitting of a straight line, Can. J. Phys., 44, 1079-1086, 1966.

## Appendix A. Oceanic intraplate seismicity 1906-1963

Ref.	Date	Time	/s.d.	Lat. /s.d.	Long. /s.d.	mb	Ms	No.	Region
GR	Nov. 19, 1906	0718:18		-22	109		7.75		Indian Ocean
GR	May 11, 1912	1726:24		-9	72.		6.8		Indian Ocean
GR	Jan. 19, 1913	1705:36		2.	86.		7.0		Indian Ocean
GR	April 7, 1916	0926:12		-30.	55.		7.4		Indian Ocean
GR	May 9, 1916	1433:42		1.5	89.		6.3		Indian Ocean
GR	April 13, 1918	0051:15		-8.	85.		6.5		Indian Ocean
GR	May 25, 1918	1929:20		-30.5	-92.5		7.0		Pacific Ocean
L	Aug. 15, 1919	0417:03.1		-34.90	-40.12				Atlantic Ocean
L	April 20, 1921	1846:16.1		31.37	-47.36				Atlantic Ocean
L	April 22, 1921	1604:01.7		43.33	-15.69		5.5		Atlantic Ocean
L	Aug. 21, 1921	0109:15.6		30.23	-56.15				Atlantic Ocean
L	Feb. 19, 1922	2152:37.7		30.74	-29.76				Atlantic Ocean
GR	May 28, 1923	0125:53		-1.5	88.5		6.5		Indian Ocean
L	Oct. 11, 1923	1228:58.9		42.71	-39.15				Atlantic Ocean
L	Oct. 25, 1924	1909:37.7		25.02	-23.37				Atlantic Ocean
L	June 13, 1925	2022:55.7		-33.41	-20.71		6.0		Atlantic Ocean
L	Dec. 15, 1925	1031:41.3		-22.35	-5.29		5.5		Atlantic Ocean
GR	Jan. 18, 1926	2107:23		-2.	89.		6.75		Indian Ocean
L	Sept. 30, 1926	0416:50.2		19.84	-39.26				Atlantic Ocean
GR	Dec. 27, 1926	0842:55		-57.	-110.		6.0		Pacific Ocean
GR	Dec. 27, 1926	0920:30		-57.	-110.		6.25		Pacific Ocean
GR	March 12, 1927	1844:32		-41.	-106.		6.5		Pacific Ocean
GR	July 29, 1927	0003:11		15.	87.		6.5		Indian Ocean
L	Dec. 30, 1927	1231:13.2		17.11	-56.62				Atlantic Ocean
GR	Jan. 26, 1928	2151:34		-5.	96.		6.25		Indian Ocean
SO	Feb. 7, 1928	0001:43		-2.6	88.5		6.75		Indian Ocean
SO	March 9, 1928	1805:20		-2.7	88.7		7.7		Indian Ocean
	March 10, 1928	0317:53		-3.7	88.7				Indian Ocean
	March 10, 1928	0553:26		-2.8	88.9				Indian Ocean
L	Nov. 28, 1928	0736:47.1		27.03	-53.20				Atlantic Ocean
L	March 15, 1929	1757:23.7		32.08	-46.06				Atlantic Ocean
GR	Sept. 26, 1929	0450:56		19.75	-156.				Pacific Ocean
GR	Oct. 6, 1929	0751:31		19.75	-156.		6.5		Pacific Ocean
L	March 7, 1930	0641:03.5		32.85	-11.73		5.5		Atlantic Ocean
GR	March 9, 1930	0852:26		-3.	71.				Indian Ocean
L	Aug. 16, 1931	0806:23.7		28.70	-64.86		5.5		Atlantic Ocean
GR	March 28, 1932	0035:34		-8.	98.5		6.0		Indian Ocean
GR	Jan. 4, 1933	2110:46		28.	-126.5		5.5		Pacific Ocean
L	Jan. 6, 1933	1910:17.1		-23.11	0.09		6.0		Atlantic Ocean
L	Sept. 12, 1933	1253:14.7		7.15	-44.92				Atlantic Ocean
L	June 15, 1934	0634:26.3		61.13	-58.66		5.5		Atlantic Ocean
GR	July 12, 1934	1424:18		-15.	112.5		6.0		Indian Ocean
GR	April 24, 1935	1552:18		0.5	74.25		6.0		Indian Ocean
GR	June 28, 1935	1930:05		19.5	-155.25				Pacific Ocean
GR	Jan. 13, 1936	1810:16		-4.	85.				Indian Ocean

## Appendix A. (continued)

Ref.	Date	Time	/s.d.	Lat. /s.d.	Long. /s.d.	mb	Ms	No.	Region
O	April 24, 1937	0458:30		-10.14	-176.00	6.2			Pacific Ocean
L	Sept. 25, 1937	0429:45.0		44.29	-24.86				Atlantic Ocean
O	Oct. 4, 1937	0740:34.8		-22.01	-166.99		6.2		Pacific Ocean
O	Jan. 13, 1938	0315:22.5		-36.67	-160.39	5.6			Pacific Ocean
GR	Jan. 23, 1938	0832:43		21.	-156.		6.75		Pacific Ocean
L	Feb. 15, 1938	0327:43.1		19.32	-26.17		6.2		Atlantic Ocean
L	Feb. 15, 1938	0657:11.1		19.33	-26.21				Atlantic Ocean
L	May 23, 1938	0812:23.0		-2.55	-28.88				Atlantic Ocean
O	Sept. 5, 1938	1442:31.0		-54.74	-148.35		6.0		Pacific Ocean
GR	Sept. 10, 1938	2223:57		7.5	79.				Indian Ocean
	Sept. 23, 1938	0103:05		-2.0	85.4				Indian Ocean
L	Nov. 25, 1938	0007:03.0		46.18	-34.04				Atlantic Ocean
GR	Feb. 20, 1939	1648:55		-12.	70.				Indian Ocean
L	March 5, 1939	1511:51.8		23.09	-69.38		5.5		Atlantic Ocean
SO	March 21, 1939	0111:12		-0.9	89.5		7.2		Indian Ocean
L	June 12, 1939	0405:08.5		20.51	-65.83		6.2		Atlantic Ocean
GR	Aug. 7, 1939	2359:42		4.	77.5				Indian Ocean
O	Jan. 4, 1940	0110:21.4		-33.84	-162.47		5.9		Pacific Ocean
ISS	April 25, 1940	1018:42		-8.5	-176.5				Pacific Ocean
GR	June 17, 1940	1026:47		20.5	-155.25				Pacific Ocean
GR	July 16, 1940	0317:33		20.5	-155.				Pacific Ocean
GR	Sept. 2, 1940	0844:42		21.	-155.25				Pacific Ocean
GR	March 16, 1941	2054:53		7.5	73.				Indian Ocean
L	Aug. 15, 1941	0609:23.1		19.29	-26.36		6.7		Atlantic Ocean
GR	Sept. 25, 1941	1748:38		19.5	-155.5		6.0		Pacific Ocean
GR	Feb. 29, 1944	1628:07		0.5	76.		7.2		Indian Ocean
GR	Aug. 5, 1944	0057:17		-13.5	-92.5		6.0		Pacific Ocean
GR	Aug. 5, 1944	0124:08		-13.5	-92.5		6.25		Pacific Ocean
GR	Dec. 27, 1944	1411:40		19.5	-155.5				Pacific Ocean
GR	June 30, 1945	0531:18		17.	-115.		6.75		Pacific Ocean
	March 2, 1944	1116:20		-0.1	76.6				Indian Ocean
GR	Dec. 10, 1944	0511:28		-24.5	65.5		6.75		Indian Ocean
O	Dec. 15, 1947	1920:26.3		-58.76	-159.20		6.9		Pacific Ocean
GR	Dec. 24, 1947	0522:00		-54.	114.		7.0		Indian Ocean
SO	Jan. 23, 1949	0631:04		-11.6	92.8		6.75		Indian Ocean
L	July 9, 1949	1844:43.4		32.47	-70.58		5.7		Atlantic Ocean
GR	July 20, 1949	2220:07		-10.	101.		6.25		Indian Ocean
O	Sept. 17, 1949	2246:34		-58.8	-157.7		6.2		Pacific Ocean
GR	Dec. 10, 1949	1915:42		4.	-129.		5.75		Pacific Ocean
O	April 10, 1950	0606:43.7		-58.70	-159.11		6.4		Pacific Ocean
GR	May 30, 1950	0116:15		19.5	-156.		6.25		Pacific Ocean
S70	Sept. 1, 1950	0246:58.5		-3.24	89.27		6.0		Indian Ocean
L	Dec. 1, 1950	1451:00.3		13.86	-47.26		7.2		Atlantic Ocean
S70	Jan. 25, 1951	1635:32.2		-2.06	80.90				Indian Ocean
S70	May 1, 1951	0502:38.8		-50.60	148.98		7.0		Indian Ocean

## Appendix A. (continued)

Ref.	Date	Time	/s.d.	Lat. /s.d.	Long. /s.d.	mb	Ms	No.	Region
O	July 14, 1951	0621:19.7		-52.94	-126.57		5.5		Pacific Ocean
U	Aug. 3, 1951	1920:15		-28.	-121.	5.6			Pacific Ocean
GR	Aug. 21, 1951	1057:00		19.75	-156.		6.9		Pacific Ocean
O	Sept. 29, 1951	1815:00		-26.55	-121.95	5.9			Pacific Ocean
L	April 5, 1952	0026:33.9		-28.18	-5.86				Atlantic Ocean
L	April 9, 1952	0808:08.7		42.36	-34.34				Atlantic Ocean
L	Oct. 20, 1952	0104:53.9		56.96	-57.20				Atlantic Ocean
R	Jan. 15, 1953	1204:35		19.3	-155.4				Pacific Ocean
S70	June 21, 1953	2358:31.2		-0.44	91.13				Indian Ocean
O	Aug. 1, 1953	1336:28		-44.8	-175.8	5.3			Pacific Ocean
L	Sept. 27, 1953	0605:24.8		13.60	-57.84		6.0		Atlantic Ocean
S70	Nov. 28, 1953	2311:13.5		-16.66	92.97				Indian Ocean
R	March 30, 1954	1640:02		19.5	-155.1		6.0		Pacific Ocean
R	March 30, 1954	1841:54		19.5	-155.1		6.5		Pacific Ocean
S70	Jan. 7, 1955	0944:28		-16.70	77.56				Indian Ocean
R	Jan. 18, 1955	0842:03		5.	-87.5				Pacific Ocean
L	Feb. 27, 1955	1637:00.0		7.62	-42.56		6.0		Atlantic Ocean
L	March 1, 1955	0146:13.1		-19.81	-36.75		6.0		Atlantic Ocean
S0	March 22, 1955	1405:07		-8.8	91.7		7.1		Indian Ocean
S70	March 23, 1955	0454:31.4		-9.08	91.63				Indian Ocean
S70	April 6, 1955	1948:45.1		-33.80	86.91		6.0		Indian Ocean
R	May 14, 1955	2000:00		28.9	-126.2		6.0		Pacific Ocean
R	Sept. 8, 1955	0203:19		-58.7	-19.6		6.5		Atlantic Ocean
L	Oct. 6, 1955	1055:40.2		33.53	-48.05		5.5		Atlantic Ocean
S70	Oct. 16, 1955	0441:48.8		-5.41	51.38				Indian Ocean
O	Nov. 22, 1955	0324:05		-24.27	-122.77	6.8	6.2		Pacific Ocean
R	Jan. 13, 1956	0616:15		-29.7	167.9		6.0		Pacific Ocean
R	Feb. 17, 1956	0953:54		-48.7	-15.7		6.1		Atlantic Ocean
S70	April 29, 1956	2152:29.2		-6.84	52.10				Indian Ocean
S70	June 24, 1956	1254:58.9		-39.59	36.93				Indian Ocean
ISS	June 26, 1956	1123:09		-10.	-173.5				Pacific Ocean
S70	July 29, 1956	0713:44.6		-8.36	85.60				Indian Ocean
R	Dec. 4, 1956	1007:54		-45.5	-106.9		6.6		Pacific Ocean
S70	Dec. 18, 1956	1920:06.0		-36.10	76.77				Indian Ocean
R	June 18, 1957	1756:06		-25.7	169.9		6.7		Pacific Ocean
S70	June 26, 1957	0247:36.9		-7.22	85.07				Indian Ocean
S70	Aug. 4, 1957	0924:27.6		-40.58	53.56				Indian Ocean
R	Aug. 18, 1957	1041:54		20.0	-155.7				Pacific Ocean
S70	Oct. 2, 1957	2058:40.1		-6.28	69.57		6.0		Indian Ocean
ISS	Oct. 3, 1957	1344:30		-10.	-179.				Pacific Ocean
S70	Nov. 30, 1957	0159:39.7		-6.78	52.05				Indian Ocean
S70	Jan. 3, 1958	1747:12.3		-22.11	64.72				Indian Ocean
R	April 9, 1958	0615:11.6		56.14	-139.23				Pacific Ocean
S70	May 11, 1958	0837:36.9		-26.76	75.09				Indian Ocean
R	July 26, 1958	0835:03.5		-59.6	-166.1				Pacific Ocean



Appendix A. (continued)

Ref.	Date	Time	/s.d.	Lat. /s.d.	Long. /s.d.	mb	Ms No.	Region
L	July 29, 1958	2137:22.1		3.67	-26.64		6.2	Atlantic Ocean
ISS	July 30, 1958	1510:12		-48	-120.			Pacific Ocean
R	Aug. 9, 1958	1247:52		-49.4	-13.2			Atlantic Ocean
S70	Oct. 30, 1958	0226:12.0		-0.75	48.28			Indian Ocean
R	Dec. 13, 1958	0907:34		-55.5	-22.0			Atlantic Ocean
R	Jan. 28, 1959	1004:09		-30.7	-78.9		6.2	Pacific Ocean
R	March 25, 1959	1457:03		-54.0	163.0			Pacific Ocean
L	April 1, 1959	0034:18.3		27.56	-20.83		6.2	Atlantic Ocean
S70	April 4, 1959	1507:19.1		-6.30	51.75			Indian Ocean
S70	April 9, 1959	0618:34.1		-36.29	76.78			Indian Ocean
R	Aug. 20, 1959	0718:34		-6.9	-85.2			Pacific Ocean
ISS	Oct. 17, 1959	0123:00		-54.	-165.			Pacific Ocean
O	Oct. 17, 1959	0835:02.5		-57.36	-161.00		5.5	Pacific Ocean
S70	Dec. 26, 1959	1211:10.4		-51.62	102.00			Indian Ocean
R	Feb. 1, 1960	0208:29.8		42.1	-133.4			Pacific Ocean
R	Feb. 13, 1960	0755:34		27.7	-21.			Atlantic Ocean
R	May 20, 1960	1112:31		-28.0	167.5		6.5	Pacific Ocean
S70	June 7, 1960	0525:13.7		-16.15	98.61			Indian Ocean
R	July 10, 1960	2022:51		-53.5	134.0			Indian Ocean
S70	July 18, 1960	1850:35.3		-6.74	51.71			Indian Ocean
R	Sept. 23, 1960	0020:32.2		20.4	-56.7			Atlantic Ocean
S70	Nov. 2, 1960	1809:47.8		-44.97	80.45			Indian Ocean
R	Jan. 11, 1961	1631:51		-54.7	162.9			Pacific Ocean
R	July 23, 1961	1437:56.9		6.8	-123.5		5.9	Pacific Ocean
R	Sept. 25, 1961	0528:57.8		19.8	-155.2		5.9	Pacific Ocean
U	Jan. 25, 1962	1003:06.8		-4.6	-152.6			Pacific Ocean
U	Jan. 25, 1962	1003:06.8		-4.6	-152.6		4.6	Pacific Ocean
R	Jan. 26, 1962	1434:45.7		-36.9	-88.9			Pacific Ocean
L	May 20, 1962	1501:15.0		20.53	-65.88			Atlantic Ocean
R	June 28, 1962	0427:16.1		19.8	-155.5		5.7	Pacific Ocean
S67	Aug. 6, 1962	0135:27.7		32.26	-41.03			Atlantic Ocean
R	April 10, 1963	1139:03		3.7	148.3			Pacific Ocean
MS	Aug. 21, 1963	0339:17.8		14.4	-72.4		5.5	Atlantic Ocean
TS	Aug. 22, 1963	0927:05.8		42.08	-126.19			Pacific Ocean
O	Sept. 14, 1963	1616:48.0		-33.46	-126.56		4.9	Pacific Ocean

Appendix A. (continued)

Ref.	Date	Time /s.d.	Lat. /s.d.	Long. /s.d.	mb	Ms	No.	Region
R	Oct. 6, 1963	0848:12.4	21.9	-127.4				Pacific Ocean
R	Oct. 23, 1963	2024:05.5	19.4	-155.5				Pacific Ocean
R	Oct. 27, 1963	0130:32	-29.5	-101.2				Pacific Ocean
R	Nov. 11, 1963	1621:14.4	-32.8	-95.5				Pacific Ocean

## Reference codes for epicentral data:

- GR Epicenter and M from Gutenberg and Richter [1954].
- ISS International Seismological Summary.
- L Epicenter relocated by Lilwall [1982]. M from Gutenberg and Richter [1954] (1906-1952) and Rothe [1969] (1953-1963).
- MS Epicenter relocated by Molnar and Sykes [1969].
- O Epicenter relocated by Oka1 [1984].
- R Rothe [1969]. Epicentral coordinates from ISS (1953-1959) and USCGS (1960-1963).  $M < 7$  from Rothe [1969].  $M \geq 7$  from Duda [1965].
- S67 Epicenter relocated by Sykes [1967].
- S70 Epicenter relocated by Sykes [1970]. M from Gutenberg and Richter [1954] (1906-1952) and Rothe [1969] (1953-1963).
- S0 Epicenter relocated by Stein and Oka1 [1978]. M from Gutenberg and Richter [1954].
- TS Epicenter relocated by Tobin and Sykes [1968].
- U U.S. Coast and Geodetic Survey (USCGS).

Appendix B. Oceanic intraplate seismicity 1964-1983

Age	Date	Time	/s.d.	Lat. /s.d.	Long. /s.d.	mb	Ms	No.	Region
6	Jan. 11, 1964	1023:10.5/0.30		-11.32/.083	90.84/.075			35	South Indian Ocean
2	April 8, 1964	0808:12.4/0.19		-6.62/.056	69.10/.068	5.1		100	Chagos Archipelago Region
3	April 17, 1964	0444:37.2/0.16		-22.53/.064	-10.66/.055	5.1		33	South Atlantic Ridge
6	May 25, 1964	1944:05.9/0.11		-9.08/.029	88.89/.033	5.7	6.0	156	South Indian Ocean
6	June 11, 1964	1751:50.8/0.56		-9.3 /.14	89.1 /.14			47	South Indian Ocean
3	June 21, 1964	0742:55.7/0.38		-30.1 /.10	-91.5 /.11	4.5		11	Southeast Central Pacific Ocean
3	June 21, 1964	2116:29.6/0.31		14.3 /.11	-46.82/.090	4.5		12	North Atlantic Ridge
4	Aug. 18, 1964	1526:24.0/0.15		5.75/.035	57.88/.038	5.3		64	Carlsberg Ridge
2	Sept. 6, 1964	1551:24.2/0.51		-10.6 /.14	-107.3 /.47	4.4		13	Northern Easter Island Cordillera
4	Sept. 17, 1964	1502:01.5/0.08		44.58/.026	-31.34/.017	5.5		173	North Atlantic Ridge
4	Oct. 18, 1964	2155:59.7/0.24		7.15/.039	144.58/.065	4.7		25	Caroline Islands Region
7	Oct. 23, 1964	0156:05.1/0.12		19.80/.030	-56.11/.029	6.2	6.3	236	North Atlantic Ocean
4	Nov. 10, 1964	1926:41.2/0.47		47.4 /.14	-23.6 /.10	4.3		26	North Atlantic Ocean
4	Dec. 8, 1964	0914:31.6/0.21		-21.30/.038	-82.0 /.15	5.0		30	Southeast Central Pacific Ocean
4	March 6, 1965	1110:52.8/0.10		-18.42/.036	-132.82/.038	5.4		103	South Pacific Ocean
11	March 29, 1965	1310:18.2/0.44		34.2 /.19	-64.3 /.18	4.1		18	North Atlantic Ocean
6	April 2, 1965	1552:48.3/0.68		65.8 /.10	0.1 /.24	4.2		15	Norwegian Sea
4	July 9, 1965	0041:48.0/0.50		7.38/.088	147.4 /.12	4.7		21	Caroline Islands Region
4	July 18, 1965	0532:43.5/0.50		7.78/.067	142.20/.092	4.4		30	Caroline Islands Region
3	Sept. 6, 1965	2113:33.1/0.18		6.55/.039	-84.39/.041	5.2		76	Off Coast of Central America
3	Sept. 9, 1965	1002:25.7/0.15		6.51/.037	-84.44/.040	5.8	6.2	198	Off Coast of Central America
4	Sept. 12, 1965	2202:37.7/0.09		-6.46/.023	70.76/.022	6.1	6.0	253	Chagos Archipelago Region
3	Sept. 25, 1965	1627:26 /0.67		-30.5 /.22	-90.6 /.19	4.6		20	Southeast Central Pacific Ocean
4	Oct. 7, 1965	0336:01.4/0.08		12.46/.025	114.45/.020	5.8	5.6	196	South China Sea
6	Oct. 31, 1965	1724:09.5/0.15		-14.22/.031	95.27/.045	5.3	5.4	121	South Indian Ocean
3	Nov. 4, 1965	1402:52.1/0.45		-47.1 /.10	-10.6 /.13	5.1		42	South Atlantic Ridge
3	Nov. 25, 1965	1050:50.8/0.13		-17.07/.035	-100.24/.049	5.3	4.9	93	Southeast Central Pacific Ocean
3	Dec. 7, 1965	2125:46.0/0.62		-43.1 /.16	37.8 /.42	4.7		20	Prince Edward Islands Region
2	Dec. 19, 1965	2206:33.0/0.17		-32.24/.04	78.87/.05	5.5		142	Mid-Indian Rise
2	Dec. 22, 1965	1409:07.6/0.20		-32.17/.04	79.00/.06	5.3		29	Mid-Indian Rise
9	Jan. 8, 1966	1538:15 /1.2		11.6 /.13	84.93/.08	5.2		11	Bay of Bengal
1	Jan. 26, 1966	0549:05.8/0.16		-48.87/.029	-111.17/.062	4.7		13	Easter Island Cordillera
3	Feb. 4, 1966	2044:55.7/0.30		-45.82/.050	123.03/.063	5.0		46	South of Australia
4	Feb. 4, 1966	2053:31 /2.4		12.39/.045	114.32/.036	4.9		34	South China Sea
2	Feb. 17, 1966	1147:57.3/0.12		-32.20/.03	78.93/.03	6.0		226	Mid-Indian Rise
2	Feb. 17, 1966	1243:02 /2.8		-32.15/.04	79.04/.04	5.6		110	Amsterdam-Naturaliste Ridge
4	March 14, 1966	2328:53 /2.1		6.02/.022	146.32/.046	4.8		19	Caroline Islands Region
7	March 20, 1966	1828:35.8/0.70		21.96/.035	-58.9 /.12	5.0		16	North Atlantic Ocean
4	March 22, 1966	0752:51 /1.0		10.13/.027	147.9 /.10	4.7		24	Caroline Islands Region
2	March 28, 1966	0444:12.2/0.20		-32.12/.04	78.84/.05	5.5		49	Mid-Indian Rise
6	June 12, 1966	2020:59 /2.7		-2.93/.060	-28.29/.039	4.8		41	South Atlantic Ocean
2	June 24, 1966	1702:04.8/0.29		-32.04/.06	78.82/.05	4.7		13	Mid-Indian Rise
2	Aug. 4, 1966	0326:00.9/0.54		-1.58/.07	-105.96/.09	4.6		24	Northern Easter Island Cordillera
2	Aug. 6, 1966	0510:12.2/0.47		72.6 /.16	-1.6 /.31	4.2		14	Jan Mayen Island Region
3	Sept. 8, 1966	1207:49.7/0.18		-22.56/.034	-10.72/.038	5.2		47	South Atlantic Ridge

## Appendix B. (continued)

Age	Date	Time	/s.d.	Lat. /s.d.	Long. /s.d.	mb	Ms	No.	Region
4	Sept. 18, 1966	0640:41	/1.9	-18.38/.032	-132.87/.054	5.0		46	South Pacific Ocean
5	Sept. 24, 1966	0857:17	/4.3	12.06/.063	-130.82/.047	4.9		46	North Pacific Ocean
3	Nov. 18, 1966	2117:33	/1.9	23.1/.38	-46.3/.33	4.5		15	North Atlantic Ridge
6	Nov. 29, 1966	0921:22.4	/0.16	-9.76/.031	90.58/.034	5.0		62	South Indian Ocean
6	Dec. 15, 1966	1908:26.3	/0.38	-40.50/.057	155.79/.050			24	Southeast of Australia
1	Jan. 7, 1967	0027:23	/3.6	-48.80/.048	112.76/.065	5.5		171	Southeast Indian Ridge
5	Feb. 25, 1967	2135:55	/2.0	0.0/.30	93.70/.05			13	Off W. Coast of Northern Sumatra
4	March 4, 1967	2241:17.6	/0.37	7.70/.067	146.00/.093	5.0		73	Caroline Islands Region
2	April 13, 1967	1135:37	/2.5	7.9/.35	-100.2/.47	4.1		10	Off Coast of Mexico
8	April 13, 1967	1426:51.0	/0.38	-6.76/.061	-151.06/.076	5.1		51	South Pacific Ocean
3	April 20, 1967	0417:42.1	/0.25	-41.14/.056	-23.33/.055	4.9		25	South Atlantic Ridge
8	April 23, 1967	1501:06.2	/0.21	1.60/.039	80.22/.040	4.9		87	North Indian Ocean
7	April 26, 1967	1311:44.2	/0.45	-1.10/.096	89.47/.095	4.9		123	South Indian Ocean
2	June 25, 1967	0059:14.3	/0.97	60.8/.11	-25.7/.21	4.5		11	North Atlantic Ocean
6	June 30, 1967	0304:41.5	/0.83	38.90/.079	-36.7/.15	4.5		23	North Atlantic Ocean
1	July 4, 1967	1929:38	/1.3	-36.6/.25	-109.2/.12	4.3		11	Easter Island Cordillera
5	July 10, 1967	1943:58.6	/0.78	19.30/.087	-53.1/.13	4.8		20	North Atlantic Ocean
6	July 16, 1967	0920:56.5	/0.48	-1.5/.11	-28.07/.084	4.5		18	South Atlantic Ocean
6	Aug. 23, 1967	0419:30.5	/0.31	-54.13/.071	-23.23/.081	4.6		14	South Sandwich Islands Region
2	Sept. 5, 1967	1024:09	/1.4	3.6/.26	-30.4/.25	4.2		10	Central Mid-Atlantic Ridge
3	Sept. 12, 1967	0023:25.7	/0.34	-22.56/.063	-10.62/.073	4.9		92	South Atlantic Ridge
2	Sept. 15, 1967	0002:03.4	/0.32	-31.97/.06	78.79/.05	4.7		15	Mid-Indian Rise
2	Oct. 8, 1967	2343:43.1	/0.34	-17.25/.05	-106.0/.24	4.4		14	Southeast Central Pacific Ocean
3	Oct. 27, 1967	1258:51.8	/0.39	-46.90/.071	-10.3/.12	4.6		12	South Atlantic Ridge
4	Nov. 10, 1967	1838:34	/4.2	-6.03/.031	71.34/.030	5.2		173	Chagos Archipelago Region
4	Nov. 11, 1967	1155:56	/1.5	-6.01/.024	71.36/.023	5.3	5.2	181	Chagos Archipelago Region
4	Nov. 11, 1967	1214:55	/3.4	-6.03/.030	71.34/.028	5.6		204	Chagos Archipelago Region
4	Nov. 11, 1967	1505:09	/3.2	-6.12/.033	71.27/.035	5.0		97	Chagos Archipelago Region
4	Nov. 11, 1967	1742:17	/4.1	-6.16/.051	71.45/.044	4.9		35	Chagos Archipelago Region
4	Nov. 11, 1967	1759:57	/4.3	-6.10/.029	71.32/.030	5.4		141	Chagos Archipelago Region
4	Nov. 11, 1967	1907:32.6	/0.45	-6.26/.074	71.29/.079	4.4		35	Chagos Archipelago Region
4	Nov. 11, 1967	2018:15	/1.6	-5.99/.029	71.34/.028	5.1		102	Chagos Archipelago Region
3	Nov. 21, 1967	1702:25.8	/0.15	72.66/.02	8.14/.09	5.4		192	Norwegian Sea
3	Nov. 21, 1967	1943:55	/1.8	72.43/.07	8.8/.30	4.2		12	Norwegian Sea
2	Nov. 27, 1967	1046:49	/1.0	-12.7/.24	67.0/.14	4.6		18	Mid-Indian Rise
4	Nov. 28, 1967	0221:57	/2.3	-6.20/.059	71.31/.045	4.6		32	Chagos Archipelago Region
4	Dec. 28, 1967	0730:26	/2.9	44.8/.35	-135.6/.36	4.2		17	North Pacific Ocean
9	Jan. 6, 1968	1513:28.1	/0.19	16.40/.03	92.08/.03	4.9		83	Bay of Bengal
2	Jan. 20, 1968	1122:57	/3.9	41.7/.18	-28.8/.20	3.9		15	Azores Region
6	Feb. 9, 1968	2046:45.1	/0.62	-14.0/.12	82.4/.12	4.7		30	South Indian Ocean
4	Feb. 20, 1968	0219:49.5	/0.13	12.40/.024	-46.94/.017	5.5		172	North Atlantic Ridge
7	Feb. 20, 1968	0808:31.2	/0.52	16.72/.028	-57.76/.055	4.3		17	North Atlantic Ocean
4	March 2, 1968	2202:24.2	/0.16	-6.09/.030	71.41/.029	5.5	5.4	210	Chagos Archipelago Region
4	March 15, 1968	1751:56.9	/0.36	-6.16/.073	71.36/.060	4.7		29	Chagos Archipelago Region
4	March 20, 1968	2200:04	/3.0	-6.06/.073	71.22/.047	4.8		29	Chagos Archipelago Region

## Appendix B. (continued)

Age	Date	Time	/s.d.	Lat. /s.d.	Long. /s.d.	mb	Ms	No.	Region
5	March 25, 1968	1128:20.1	0.25	70.81/.04	7.4 /.10	4.2		17	Norwegian Sea
3	March 31, 1968	0416:04	/1.7	5.2 /.11	-87.1 /.16	4.1		19	Off Coast of Central America
2	April 16, 1968	0517:30	/1.1	-4.0 /.17	67.3 /.20	4.3		20	Carlsberg Ridge
8	April 28, 1968	0418:15.5	0.13	44.76/.028	174.58/.035	5.5	5.2	157	North Pacific Ocean
8	April 28, 1968	0623:02.0	0.59	44.86/.093	174.67/.072	4.4		32	North Pacific Ocean
2	May 18, 1968	1137:24	/1.1	-6.9 /.17	-111.8 /.25	4.5		19	Northern Easter Island Cordillera
2	June 16, 1968	0456:02.9	0.77	-36.1 /.17	-15.9 /.18	5.1	6.1	70	Tristan da Cunha Region
7	July 29, 1968	0245:46.1	0.24	-7.52/.038	-148.32/.077	4.9		43	Line Islands Region
4	Aug. 20, 1968	1116:58.5	0.12	5.43/.021	147.11/.033	5.6	5.0	170	Caroline Islands Region
7	Sept. 3, 1968	0112:28.2	0.42	-37.84/.074	38.0 /.17	5.0		41	South Indian Ocean
8	Sept. 3, 1968	1537:00.3	0.13	20.58/.020	-62.30/.024	5.6	5.9	191	North Atlantic Ocean
4	Sept. 14, 1968	0125:18.9	0.12	-24.45/.027	80.41/.027	5.4		138	South Indian Ocean
5	Sept. 14, 1968	0137:06	/1.4	56.8 /.31	-39.8 /.33	5.2		37	North Atlantic Ocean
3	Sept. 16, 1968	0052:36.0	0.24	-33.75/.041	-102.02/.086	4.7		25	West Chile Rise
2	Oct. 8, 1968	0743:22.8	0.15	-39.85/.034	87.74/.038	5.8	5.8	234	South-East Indian Ridge
7	Oct. 8, 1968	2250:06.1	0.22	-7.63/.030	-148.09/.074	4.3		12	Line Islands Region
7	Oct. 10, 1968	0104:33.0	0.19	-7.65/.027	-148.09/.076	4.3		15	Line Islands Region
3	Oct. 18, 1968	1550:20.5	0.23	-47.03/.039	-10.23/.068	4.3		31	South Atlantic Ridge
3	Oct. 31, 1968	2318:07.8	0.25	-36.34/.044	-92.66/.085	4.5		18	West Chile Rise
2	Nov. 10, 1968	0829:46	/1.2	-29.7 /.20	-117.0 /.31	4.2		17	Easter Island Cordillera
7	Nov. 23, 1968	0013:35.3	0.22	-7.62/.034	-148.13/.082	4.6		25	Line Islands Region
3	Nov. 24, 1968	0657:16.6	0.34	-46.73/.074	-10.57/.071	4.8		19	South Atlantic Ridge
7	Nov. 26, 1968	0608:55	/4.5	-3.15/.057	86.41/.051	4.7		20	South Indian Ocean
1	Dec. 2, 1968	1324:51	/1.6	6.91/.061	-104.32/.065	4.8		37	East Central Pacific Ocean
1	Dec. 2, 1968	1347:14.2	0.90	7.0 /.12	-104.2 /.15	4.5		20	East Central Pacific Ocean
4	Dec. 3, 1968	1040:29.9	0.77	-6.1 /.13	71.3 /.13	4.6		21	Chagos Archipelago Region
7	Dec. 14, 1968	1143:13.6	0.22	-3.03/.038	85.53/.048	4.9		41	South Indian Ocean
7	Dec. 28, 1968	2023:04.7	0.16	-7.55/.021	-148.58/.062	4.6		14	Line Islands Region
6	Jan. 3, 1969	0356:59.4	0.20	-18.30/.035	88.15/.050			19	South Indian Ocean
4	Jan. 27, 1969	1440:02.3	0.85	12.43/.029	114.37/.028	5.0		66	South China Sea
6	Feb. 14, 1969	0614:53.4	0.20	-17.84/.046	87.37/.039	4.7		31	South Indian Ocean
2	April 11, 1969	0409:19	/2.5	4.9 /.47	63.8 /.45	4.6		10	Carlsberg Ridge
3	April 19, 1969	0816:16	/1.9	25.22/.040	-46.79/.032	4.9		84	North Atlantic Ridge
11	May 3, 1969	0822:20	/2.5	8.34/.038	-175.59/.038	5.0		62	North Pacific Ocean
5	May 5, 1969	1415:17.0	0.40	-44.29/.054	141.45/.056	5.2		33	South of Australia
8	May 14, 1969	0852:24	/1.7	-41.90/.04	33.6 /.16	4.1		19	Prince Edward Island Region
7	June 1, 1969	0335:30.0	0.28	-7.64/.041	-148.2 /.10	4.5		17	Line Islands Region
7	June 6, 1969	1753:45	/2.6	-8.0 /.16	-147.8 /.18	4.5		18	Line Islands Region
4	June 30, 1969	2012:36.7	0.41	-33.9 /.10	57.81/.09	4.2		12	Atlantic-Indian Ridge
1	July 10, 1969	0811:00	/3.5	6.5 /.44	-104.2 /.18	4.2		10	East Central Pacific Ocean
4	July 12, 1969	0557:11	/1.5	-6.03/.027	71.35/.028	5.2	5.0	116	Chagos Archipelago Region
5	July 23, 1969	0834:37.7	0.69	56.0 /.20	-47.0 /.13	4.1		12	North Atlantic Ocean
4	July 25, 1969	2130:33.3	0.15	12.44/.031	-40.75/.027	4.8		60	North Atlantic Ocean
7	July 26, 1969	1224:30.4	0.37	43.70/.046	-14.56/.058	4.6		75	North Atlantic Ocean
7	Aug. 6, 1969	1715:40.1	0.17	-7.61/.027	-148.14/.063	5.0		41	Line Islands Region

## Appendix B. (continued)

Age	Date	Time	/s.d.	Lat. /s.d.	Long. /s.d.	mb	Ms	No.	Region
3	Aug. 8, 1969	1108:13.2	/0.21	-47.76/.048	-15.66/.060	5.7	6.0	125	South Atlantic Ridge
3	Aug. 8, 1969	1246:46.8	/0.31	-47.54/.064	-15.69/.081	4.8		27	South Atlantic Ridge
3	Aug. 8, 1969	1253:07.5	/0.36	-47.59/.078	-15.37/.082	4.8		21	South Atlantic Ridge
3	Aug. 12, 1969	0410:01.6	/0.46	-47.63/.097	-15.5 / .11	4.7		22	South Atlantic Ridge
11	Aug. 27, 1969	0326:36	/2.6	40.6 / .38	148.2 / .30			11	North Pacific Ocean
2	Oct. 14, 1969	0425:00.8	/0.17	-25.03/.04	67.82/.04	4.8		41	South Indian Ocean
3	Nov. 3, 1969	0330:19.3	/0.23	-45.82/.039	123.13/.055	5.1		67	South of Australia
3	Nov. 3, 1969	0733:43.2	/0.34	-45.68/.070	123.05/.069	4.5		25	South of Australia
4	Nov. 21, 1969	0726:36.3	/0.30	8.04/.038	147.42/.079	4.9		44	Caroline Islands Region
4	Jan. 11, 1970	0314:24.0	/0.50	-6.20/.080	71.33/.092	4.9		71	Chagos Archipelago Region
1	Jan. 21, 1970	1751:37.4	/0.11	7.03/.020	-104.24/.021	6.1	6.6	286	Off Coast of Mexico
1	Jan. 22, 1970	0611:52	/1.8	7.29/.078	-104.27/.091	4.7		42	Off Coast of Mexico
1	Feb. 22, 1970	0414:53	/1.6	6.8 / .21	-104.2 / .11	4.4		17	East Central Pacific Ocean
7	March 5, 1970	0456:24.9	/0.41	53.89/.06	-19.70/.07	4.6		77	North Atlantic Ocean
3	March 31, 1970	1818:28	/1.9	-3.78/.031	69.70/.027	5.5	5.7	170	Chagos Archipelago Region
7	April 19, 1970	1232:28.2	/0.19	-7.63/.028	-148.04/.076	4.6		11	Line Islands Region
3	April 25, 1970	0343:31	/2.3	-6.29/.040	69.84/.039	5.1	5.1	143	Chagos Archipelago Region
2	May 20, 1970	1645:44.6	/0.26	-32.13/.04	78.87/.06	4.9		39	Mid-Indian Rise
4	May 23, 1970	0139:21.0	/0.53	8.18/.065	147.4 / .13	4.4		12	Caroline Islands Region
6	June 6, 1970	0614:13.3	/0.35	-62.76/.074	-93.5 / .20	4.8		39	Southern Pacific Ocean
4	July 10, 1970	0700:04.1	/0.34	-55.87/.062	-48.4 / .14	4.9		27	Scotia Sea
10	Sept. 17, 1970	1129:24.8	/0.35	26.65/.063	-22.86/.051	4.5		49	North Atlantic Ocean
1	Sept. 19, 1970	0402:20.9	/0.28	13.81/.050	-44.21/.042	4.6		29	North Atlantic Ridge
7	Oct. 10, 1970	0853:04.5	/0.12	-3.56/.025	86.19/.022	5.8	6.3	296	South Indian Ocean
5	Oct. 22, 1970	0236:24	/2.3	13.81/.044	-49.73/.032	4.8		58	North Atlantic Ocean
2	Dec. 23, 1970	0826:37	/1.1	42.84/.035	-129.5 / .14	4.5		27	Off Coast of Oregon
3	Jan. 23, 1971	2316:03.1	/0.38	-46.70/.085	-10.44/.072	4.7		20	South Atlantic Ridge
3	Feb. 23, 1971	0909:25.0	/0.51	72.51/.08	-5.4 / .23			31	Jan Mayen Island Region
4	April 4, 1971	1343:53.4	/0.40	-32.38/.09	54.97/.05	4.4		25	Atlantic-Indian Ridge
1	April 11, 1971	0753:06	/4.0	-12.58/.035	67.05/.036	4.9		82	Mid-Indian Rise
5	April 21, 1971	0050:11.0	/0.35	-55.59/.067	-15.2 / .12			11	South-Western Atlantic Ocean
6	May 1, 1971	0406:37.6	/0.47	18.30/.091	-36.93/.060	4.8		38	North Atlantic Ocean
2	May 9, 1971	0825:01.1	/0.12	-39.78/.027	-104.87/.031	6.0	6.0	338	Southern Pacific Ocean
2	May 9, 1971	0853:26.0	/0.35	-39.71/.065	-105.1 / .11	5.1		28	Easter Island Cordillera
2	May 9, 1971	1801:00.3	/0.15	-39.77/.030	-105.10/.053	5.4		106	Easter Island Cordillera
2	May 9, 1971	1835:17	/3.8	-39.72/.039	-104.90/.082	5.3	5.4	141	Southern Pacific Ocean
2	May 18, 1971	0301:17.9	/0.27	-32.30/.05	78.88/.06	4.9		26	Mid-Indian Rise
5	May 27, 1971	2049:59	/2.2	-53.85/.042	150.03/.080	5.3	5.7	72	West of Macquarie Island
6	June 4, 1971	2047:33	/2.1	33.9 / .21	-46.7 / .37	4.7		14	North Atlantic Ocean
5	June 12, 1971	1914:57.3	/0.51	-23.8 / .11	-137.2 / .10			14	Tuamotu Archipelago Region
6	June 26, 1971	1927:11	/2.9	-5.18/.025	96.90/.024	5.9	6.4	264	Southwest of Sumatera
7	June 26, 1971	2202:18.2	/0.63	-51.35/.066	167.6 / .10			48	Auckland Islands Region
4	Aug. 3, 1971	0534:27.1	/0.14	28.44/.027	-39.21/.021	4.9		87	North Atlantic Ridge
4	Aug. 3, 1971	2059:30.3	/0.50	28.38/.092	-39.40/.082	4.7		36	North Atlantic Ridge
2	Sept. 9, 1971	0325:47.6	/0.21	-33.30/.042	-115.20/.051	4.7		22	Easter Island Cordillera

## Appendix B. (continued)

Age	Date	Time	/s.d.	Lat. /s.d.	Long. /s.d.	mb	Ms	No.	Region
2	Sept. 25, 1971	1026:42	/2.6	-43.49/.050	-84.9 /.13	5.1		45	West Chile Rise
5	Sept. 30, 1971	2124:10.8	/0.10	-0.45/.017	-4.89/.017	6.0	5.5	261	South Atlantic Ocean
4	Feb. 27, 1972	1108:22	/4.1	-1.44/.077	65.05/.066	4.8		44	South Indian Ocean
5	April 12, 1972	2142:46	/1.2	6.2 /.17	-130.33/.066	4.4		14	North Pacific Ocean
11	April 17, 1972	1516:55	/2.7	-26.2 /.13	35.6 /.26			10	South Indian Ocean
4	April 22, 1972	0222:50.8	/0.18	-52.86/.039	-14.96/.049	5.0		33	Southwestern Atlantic Ocean
2	May 2, 1972	0656:23.2	/0.10	5.22/.02	-100.32/.02	5.9	5.5	229	East Central Pacific Ocean
4	May 21, 1972	0601:54.3	/0.26	-27.10/.032	174.97/.049	5.6	4.9	117	West of Tonga
3	May 28, 1972	0838:51.8	/0.32	-32.78/.056	-92.20/.052	4.9		38	Southeast Central Pacific Ocean
4	July 14, 1972	0253:30	/3.8	-55.75/.051	-48.01/.093	4.8		44	Scotia Sea
3	July 22, 1972	1111:10	/1.6	-2.4 /.22	-116.3 /.14	4.8		15	East Central Pacific Ocean
2	July 26, 1972	0820:59	/1.3	-5.0 /.25	69.5 /.29			19	Chagos Archipelago Region
6	Aug. 14, 1972	1045:57.0	/0.40	14.20/.062	-68.46/.062	4.7	4.5	93	Caribbean Sea
3	Sept. 15, 1972	2313:43.6	/0.24	-38.01/.06	76.29/.05	4.5		21	Mid-Indian Rise
3	Sept. 28, 1972	0657:35.6	/0.19	-47.71/.041	-119.88/.099	5.1		34	South Pacific Ocean
4	Oct. 19, 1972	2031:54.3	/0.34	-22.51/.05	-82.94/.06	4.3		29	Southeast Central Pacific Ocean
8	Oct. 20, 1972	0433:49.9	/0.11	20.60/.021	-29.69/.017	5.7	5.8	312	North Atlantic Ocean
8	Oct. 30, 1972	0150:35.7	/0.22	22.35/.030	-61.97/.043	4.9	4.2	72	North Atlantic Ocean
6	Nov. 7, 1972	1205:14.3	/0.14	49.06/.033	-39.42/.022	5.1		142	North Atlantic Ocean
2	Nov. 24, 1972	0116:00	/1.5	3.6 /.37	-33.0 /.21	4.7		10	Central Mid-Atlantic Ridge
9	Nov. 24, 1972	1319:14.3	/0.12	11.67/.03	85.34/.02	5.2	5.2	192	Bay of Bengal
3	Nov. 30, 1972	1346:47	/1.5	-39.9 /.32	-84.8 /.17	5.1		15	Southwest Central Pacific Ocean
6	Dec. 3, 1972	1758:59	/1.9	-11.24/.031	87.49/.030	5.2		76	South Indian Ocean
2	Dec. 12, 1972	1743:41	/1.5	26.0 /.26	-43.6 /.18	4.9		22	North Atlantic Ridge
7	Dec. 14, 1972	2049:35.4	/0.23	-1.34/.053	89.17/.048	5.3	5.2	171	South Indian Ocean
3	Dec. 17, 1972	1600:34	/1.6	-11.03/.05	-90.25/.06	4.7		39	Southeast of Galapagos Islands
2	Dec. 22, 1972	0006:06	/1.3	-41.5 /.28	-107.3 /.24	4.9		13	Easter Island Cordillera
7	Dec. 27, 1972	0440:39.0	/0.61	-33.57/.045	167.95/.069			15	North-west of New Zealand
5	Jan. 4, 1973	0408:01.9	/0.43	-49.79/.056	154.98/.068			56	North of Macquarie Island
7	Jan. 16, 1973	0727:27.5	/0.32	-49.57/.078	-31.89/.071	4.6		12	South Atlantic Ocean
7	Jan. 19, 1973	0736:33.7	/0.17	-7.59/.022	-148.18/.058	4.9	4.6	43	Line Islands Region
7	Jan. 19, 1973	1419:11.8	/0.17	-7.54/.014	-148.39/.059			12	Line Islands Region
7	Jan. 19, 1973	1526:26.4	/0.19	-7.63/.024	-148.08/.082	4.8		37	Line Islands Region
7	Jan. 19, 1973	1556:24.4	/0.35	-7.63/.029	-148.3 /.11			12	Line Islands Region
2	Feb. 3, 1973	1436:16.9	/0.54	-7.46/.082	68.85/.089	4.6		16	Chagos Archipelago Region
5	Feb. 25, 1973	0637:13.7	/0.62	-50.60/.072	158.52/.072			21	North of Macquarie Island
5	March 20, 1973	1813:24.7	/0.21	-57.82/.054	83.59/.063	5.2		62	Kerguelen-Gaussberg Ridge
6	April 7, 1973	0300:59.6	/0.08	7.00/.02	91.32/.02	5.8	6.6	356	Nicobar Islands Region
6	April 7, 1973	0314:47.2	/0.18	6.90/.04	91.39/.04	4.8		67	Nicobar Islands Region
1	April 14, 1973	0937:27	/1.9	6.3 /.24	-104.0 /.10	4.7		17	East Central Pacific Ocean
2	April 21, 1973	1926:53.8	/0.76	-31.3 /.13	-108.5 /.16	4.8		22	Easter Islands Region
4	May 3, 1973	2311:04	/2.9	-46.14/.031	73.22/.033	5.5	5.5	198	Kerguelen Islands Region
6	May 7, 1973	1053:28	/2.0	7.13/.05	91.22/.05	4.9	4.6	79	Nicobar Islands Region
3	May 7, 1973	1627:13.1	/0.43	16.65/.052	-116.12/.057	4.7		77	East Central Pacific Ocean
4	May 27, 1973	2117:18.2	/0.40	-2.38/.065	64.96/.057	4.8		40	South Indian Ocean



## Appendix B. (continued)

Age	Date	Time	/s.d.	Lat. /s.d.	Long. /s.d.	mb	Ms	No.	Region
3	June 29, 1973	0755:12.7	/0.66	3.93/.032	-85.03/.030	5.4	4.9	120	Off Coast of Central America
6	June 29, 1973	2344:17.6	/0.72	51.8 /.16	-39.7 /.10			21	North Atlantic Ocean
6	Aug. 4, 1973	0728:00	/2.7	7.00/.05	91.36/.05	4.7		36	Nicobar Islands Region
9	Aug. 30, 1973	1950:03.9	/0.12	7.15/.024	84.33/.020	5.8	5.2	264	Bay of Bengal
4	Sept. 15, 1973	1505:25.3	/0.22	7.54/.029	144.60/.052	5.0		56	Caroline Islands Region
4	Oct. 29, 1973	0707:36.5	/0.20	-28.02/.057	83.43/.035	4.9		16	South Indian Ocean
9	Oct. 29, 1973	1221:01.8	/0.32	17.29/.054	-26.60/.044	4.5		18	North Atlantic Ocean
3	Nov. 17, 1973	1051:19.6	/0.18	-1.59/.033	69.85/.032	5.4	5.5	240	Carlsberg Ridge
2	Nov. 18, 1973	0801:41.2	/0.53	-10.52/.08	-108.0 /.12	4.9	4.3	18	Northern Easter Island Cordillera
1	Dec. 13, 1973	0434:07	/1.6	-29.4 /.28	-115.0 /.25	4.8		22	Easter Island Region
2	Jan. 7, 1974	1308:15.5	/0.78	0.6 /.11	-105.5 /.21	4.5		19	East Central Pacific Ocean
4	Jan. 18, 1974	2114:51.2	/0.20	-34.08/.036	-20.15/.050	5.4		63	South Atlantic Ridge
6	Feb. 11, 1974	1410:12.7	/0.16	6.86/.03	91.31/.03	4.8	5.0	87	Nicobar Islands Region
2	Feb. 14, 1974	1201:05.9	/0.15	21.95/.029	-44.25/.018	5.3		138	North Atlantic Ridge
13	March 12, 1974	1511:03	/2.0	8.79/.022	151.02/.026	5.4	4.8	136	Caroline Islands Region
13	March 14, 1974	2322:12.8	/0.19	8.72/.032	151.06/.027	4.8		10	Caroline Islands Region
9	March 31, 1974	2113:00	/2.5	17.04/.028	-26.42/.035	4.9		86	North Atlantic Ocean
5	April 12, 1974	1745:18.7	/0.10	14.27/.018	134.37/.021	5.5	4.9	172	Philippine Sea
6	April 21, 1974	0654:28.3	/0.67	-55.28/.081	164.3 /.19	5.1		36	South of New Zealand
1	May 6, 1974	1736:05.5	/0.52	-30.83/.088	-108.9 /.16	4.9		12	Easter Island Region
2	May 15, 1974	0604:23.3	/0.34	-32.20/.06	78.68/.06	4.8		16	Mid-Indian Rise
4	May 15, 1974	1650:35	/2.0	24.0 /.37	-43.2 /.14	4.3		11	North Atlantic Ridge
6	June 1, 1974	1111:01	/1.3	-12.9 /.29	77.9 /.29			11	South Indian Ocean
3	June 6, 1974	1837:07	/1.5	4.16/.041	66.88/.041	5.2	5.5	115	Carlsberg Ridge
6	June 6, 1974	2126:05	/3.5	7.0 /.22	91.2 /.19	4.4		31	Nicobar Islands Region
3	June 20, 1974	0903:20.4	/0.71	-44.0 /.12	-88.8 /.15	4.8		15	Southern Pacific Ocean
5	June 25, 1974	1722:17.9	/0.13	-26.02/.030	84.30/.029	6.1	6.6	346	South Indian Ocean
5	June 25, 1974	1831:36.9	/0.32	-25.9 /.10	84.10/.053	5.1		18	South Indian Ocean
5	June 26, 1974	0559:26.4	/0.54	-26.0 /.12	84.1 /.10	4.8		11	South Indian Ocean
5	June 26, 1974	0907:25.7	/0.38	-25.95/.095	84.11/.066	4.7		11	South Indian Ocean
5	June 28, 1974	0845:43.7	/0.34	-25.69/.062	84.01/.068	5.2		59	South Indian Ocean
3	July 1, 1974	2311:14.5	/0.11	-22.57/.023	-10.68/.023	5.5	5.6	231	South Atlantic Ridge
3	July 6, 1974	2126:18.5	/0.22	-22.53/.048	-10.57/.035	4.7		34	South Atlantic Ridge
2	July 17, 1974	0908:23.8	/0.21	-49.39/.037	-11.13/.057	4.7		20	South-Western Atlantic Ocean
2	Aug. 6, 1974	1003:19.8	/0.78	-62.54/.065	151.8 /.38			20	Balleny Islands Region
4	Aug. 17, 1974	1843:45.5	/0.44	-54.77/.047	156.3 /.10			19	Macquarie Island Region
7	Aug. 18, 1974	1524:42.2	/0.49	-2.60/.071	86.55/.081	5.1		24	South Indian Ocean
7	Sept. 21, 1974	0146:14.4	/0.56	-46.15/.059	53.6 /.24			10	Crozet Islands Region
5	Sept. 21, 1974	0919:28.1	/0.26	37.61/.044	-35.78/.053	4.7		33	North Atlantic Ridge
3	Sept. 22, 1974	1102:15.9	/0.23	-46.75/.048	-10.39/.053	4.8		27	South Atlantic Ridge
4	Oct. 12, 1974	0755:19	/1.2	2.97/.048	146.61/.044	4.8		27	Caroline Islands Region
2	Oct. 15, 1974	2136:30	/2.1	32.3 /.43	-39.1 /.25	4.3		14	North Atlantic Ridge
3	Oct. 28, 1974	1036:52	/2.3	-2.3 /.47	-16.2 /.32			11	North of Ascension Island
6	Nov. 9, 1974	0714:23.9	/0.61	69.64/.04	9.7 /.16			13	Norwegian Sea
7	Nov. 20, 1974	1321:41.6	/0.18	-53.59/.043	-28.26/.060	5.8	5.6	114	South-Western Atlantic Ocean

## Appendix B. (continued)

Age	Date	Time	/s.d.	Lat. /s.d.	Long. /s.d.	mb	Ms	No.	Region
6	Nov. 20, 1974	1627:41.9/0.72		-2.5 / .15	-28.0 / .10	4.9		24	South Atlantic Ocean
4	Dec. 20, 1974	1449:37.6/0.49		-12.98/.091	63.85/.099			14	South Indian Ocean
4	Jan. 13, 1975	0438:31.7/0.21		23.70/.040	-47.41/.038	4.5		22	North Atlantic Ridge
2	Feb. 12, 1975	0238:16.8/0.33		-43.57/.07	-107.5 / .15	5.1		12	Easter Island Cordillera
5	Feb. 21, 1975	0038:13.5/0.63		-52.5 / .15	-17.4 / .17	4.8		46	South-Western Atlantic Ocean
8	March 8, 1975	0840:29.4/0.26		38.62/.030	-14.80/.036	4.7	4.3	134	North Atlantic Ocean
4	March 23, 1975	1503:10.8/0.38		-34.04/.085	58.12/.074	4.9		26	South Indian Ocean
6	March 29, 1975	1502:29.6/0.19		-37.77/.048	-138.90/.055	5.0		56	South Pacific Ocean
10	April 7, 1975	1438:07 /3.7		-37.62/.068	30.98/.096	5.0		59	Off coast of South Africa
6	April 19, 1975	1735:50 /1.5		6.5 / .20	52.9 / .31	4.8		16	North Indian Ocean
1	April 26, 1975	2005:12 /1.9		5.9 / .24	-104.2 / .14	4.8		16	East Central Pacific Ocean
8	May 2, 1975	0715:44.0/0.80		8.07/.059	-156.1 / .10	4.5		25	Line Islands Region
5	May 14, 1975	1149:41.9/0.26		-17.62/.045	-136.32/.034	5.0		45	Tuamotu Archipelago Region
4	May 25, 1975	1416:30.8/0.17		-18.39/.030	-132.99/.026	4.9	3.7	67	South Pacific Ocean
1	May 26, 1975	1645:42.7/0.20		-28.50/.035	-114.09/.064	5.1		52	Easter Island Region
2	June 16, 1975	0505:24.6/0.38		-20.32/.06	-109.16/.07	4.8		20	Easter Island Cordillera
6	Aug. 22, 1975	1940:47.7/0.44		-12.26/.072	86.30/.085	4.9		12	South Indian Ocean
5	Aug. 28, 1975	1825:45.0/0.39		-25.98/.078	84.10/.079	5.1	5.0	95	South Indian Ocean
1	Sept. 11, 1975	1605:27.4/0.42		7.05/.053	-104.0 / .15	4.4		11	Off Coast of Mexico
1	Sept. 11, 1975	2200:01.3/0.63		7.05/.016	-104.18/.018	6.3	5.8	315	Off Coast of Mexico
3	Sept. 19, 1975	0337:11 /2.6		-34.74/.036	81.88/.032	5.9	6.1	260	Amsterdam-Naturaliste Ridge
4	Sept. 26, 1975	0442:54 /3.2		-53.27/.069	156.5 / .11			23	Macquarie Island Region
5	Oct. 23, 1975	0536:36.0/0.32		-47.65/.052	4.48/.098	4.7		22	South Atlantic Ocean
1	Oct. 29, 1975	0501:49 /1.4		4.07/.03	-103.51/.03	5.4		128	East Central Pacific Ocean
1	Nov. 1, 1975	2215:04 /1.8		4.22/.05	-103.47/.05	4.7		52	East Central Pacific Ocean
5	Dec. 13, 1975	0924:22.7/0.93		58.0 / .13	-52.1 / .15	4.4		22	East of Labrador
1	Dec. 18, 1975	0958:40 /1.6		-37.2 / .27	-93.3 / .13	4.1		10	West Chile Rise
2	Jan. 9, 1976	1722:36 /1.3		-41.8 / .24	-15.3 / .18	5.0		22	Tristan da Cunha Region
4	Jan. 11, 1976	2322:41.2/0.29		-46.40/.064	-101.1 / .11	5.3	5.0	56	Southern Pacific Ocean
12	Feb. 20, 1976	1926:39 /1.5		23.7 / .20	154.2 / .45	4.8		11	North Pacific Ocean
3	March 11, 1976	0045:19.9/0.95		4.7 / .13	-112.1 / .17	4.9		25	East Central Pacific Ocean
3	March 11, 1976	0920:17 /1.3		4.07/.050	-85.64/.067	4.7		31	Off Coast of Central America
3	March 12, 1976	0131:44 /2.5		4.14/.040	-85.88/.055	4.8	3.8	28	Off Coast of Central America
3	March 12, 1976	0650:02.3/0.52		4.05/.026	-85.77/.033	5.0	4.0	75	Off Coast of Central America
3	March 13, 1976	0307:41 /1.9		4.11/.040	-85.75/.043	5.0	4.3	59	Off Coast of Central America
3	March 13, 1976	1031:47.9/0.86		4.02/.041	-85.76/.042	5.0	4.7	67	Off Coast of Central America
3	March 14, 1976	1247:19.8/0.57		3.99/.093	-85.76/.070	5.0		39	Off Coast of Central America
3	March 18, 1976	0109:13.8/0.29		4.14/.056	-85.67/.095	4.6		17	Off Coast of Central America
3	March 20, 1976	1053:22 /2.5		4.13/.066	-85.9 / .10	4.7		27	Off Coast of Central America
3	March 22, 1976	0238:56 /1.6		4.18/.052	-85.75/.070	4.6		13	Off Coast of Central America
3	March 24, 1976	1643:37 /1.5		3.97/.053	-85.70/.076	4.5	4.1	23	Off Coast of Central America
3	March 24, 1976	2043:21 /2.0		4.07/.039	-85.89/.055	4.7		29	Off Coast of Central America
3	March 26, 1976	1515:25 /1.7		4.02/.048	-85.70/.089	4.6		22	Off Coast of Central America
3	March 27, 1976	2314:18.1/0.68		3.95/.027	-85.83/.031	5.1		88	Off Coast of Central America
3	March 28, 1976	0019:19.9/0.80		3.91/.039	-85.76/.038	4.9	4.3	73	Off Coast of Central America

## Appendix B. (continued)

Age	Date	Time	/s.d.	Lat. /s.d.	Long. /s.d.	mb	Ms	No.	Region
3	March 28, 1976	0702:05.0	/0.72	3.89/.090	-86.04/.086	4.8		22	Off Coast of Central America
3	March 28, 1976	1452:20	/1.3	3.93/.047	-85.72/.055	4.8		56	Off Coast of Central America
3	March 28, 1976	1458:21	/2.5	3.97/.052	-85.79/.058	5.0	4.2	55	Off Coast of Central America
2	March 28, 1976	1802:28	/2.0	5.18/.07	-100.41/.07	4.8		51	East Central Pacific Ocean
3	March 29, 1976	0539:36.3	/0.67	3.96/.026	-85.88/.029	5.8	6.5	295	Off Coast of Central America
3	April 3, 1976	2057:43	/2.2	3.95/.094	-85.8 /.11	4.3		23	Off Coast of Central America
7	April 20, 1976	1828:05.4	/0.71	15.47/.089	-54.27/.097	4.5		12	North Atlantic Ocean
3	April 22, 1976	1107:01	/2.5	3.90/.080	-85.9 /.11	4.7		28	Off Coast of Central America
3	May 1, 1976	1000:31.0	/0.37	4.10/.034	-85.73/.070	4.2		16	Off Coast of Central America
3	May 8, 1976	2206:22	/1.1	3.82/.049	-85.92/.064	4.8		44	Off Coast of Central America
10	May 8, 1976	2311:35.4	/0.44	13.5 /.39	-176.2 /.14			13	North Pacific Ocean
3	May 15, 1976	2109:54	/2.3	3.9 /.12	-85.7 /.21	4.4		22	Off Coast of Central America
2	May 29, 1976	0109:27.4	/0.74	5.9 /.11	-100.4 /.17	4.7	4.4	11	East Central Pacific Ocean
10	July 14, 1976	1558:22.8	/0.44	21.72/.051	-67.52/.071			18	North Atlantic Ocean
6	July 14, 1976	1923:57.6	/0.22	-36.29/.042	43.30/.037	5.2		71	South Indian Ocean
1	July 23, 1976	1744:29	/1.0	-29.7 /.18	-114.2 /.27	5.0	5.6	39	Easter Island Region
4	July 31, 1976	0511:21	/1.8	-38.7 /.36	-123.0 /.29	4.3		17	South Pacific Ocean
3	Aug. 4, 1976	1400:01.6	/0.11	-35.62/.026	-14.02/.025	5.7	5.4	152	Tristan da Cunha Region
4	Aug. 17, 1976	1637:18.3	/0.24	-42.45/.037	120.15/.054			14	South of Australia
3	Aug. 30, 1976	0837:54.4	/0.14	1.03/.023	147.56/.031	5.8	5.9	239	Caroline Islands Region
4	Sept. 6, 1976	2316:44.4	/0.58	-1.65/.092	64.76/.099	4.7		11	South Indian Ocean
1	Sept. 12, 1976	0706:27	/2.7	-28.4 /.45	-114.3 /.34	4.6	4.3	18	Easter Island Region
4	Oct. 21, 1976	0356:28	/3.5	-57.37/.067	-161.1 /.12	5.4		42	South Pacific Ocean
2	Nov. 2, 1976	0713:17	/1.1	-29.36/.020	77.65/.019	5.8	6.5	373	Mid-Indian Rise
2	Nov. 2, 1976	1119:15	/1.7	-29.24/.027	77.79/.024	5.6		246	Mid-Indian Rise
10	Nov. 24, 1976	2150:54.5	/0.19	33.01/.03	-61.66/.03	5.1		135	North Atlantic Ocean
6	Dec. 14, 1976	1144:38.5	/0.40	7.57/.069	90.07/.058	4.7		48	Nicobar Islands Region
8	Dec. 28, 1976	0257:38.5	/0.25	22.10/.023	-63.45/.044	5.0	4.4	98	North Atlantic Ocean
2	Jan. 3, 1977	1005:15.6	/0.27	-29.25/.065	77.82/.049	4.9		20	Mid-Indian Rise
2	Jan. 7, 1977	0709:35.4	/0.31	-52.25/.044	114.65/.078	5.3		58	South of Australia
2	Jan. 7, 1977	0752:44	/2.9	-52.28/.044	114.70/.076	5.1		34	South of Australia
4	Jan. 9, 1977	0831:16.1	/0.33	6.00/.045	146.77/.097	4.9		55	Caroline Islands Region
2	Feb. 2, 1977	0142:55.0	/0.63	-21.57/.096	-110.6 /.13			11	Easter Island Cordillera
5	Feb. 5, 1977	0329:19	/2.6	-66.49/.027	-82.45/.087	6.1	6.2	319	Southern Pacific Ocean
4	Feb. 6, 1977	0030:50.7	/0.24	17.78/.050	-49.38/.028	5.2		171	North Atlantic Ocean
8	Feb. 16, 1977	0049:31.7	/0.11	25.96/.022	-26.21/.014	5.4		277	North Atlantic Ocean
3	Feb. 17, 1977	2025:21.5	/0.33	-45.39/.091	-19.06/.053	5.4	5.2	69	South Atlantic Ridge
4	Feb. 19, 1977	1413:47	/1.2	3.9 /.22	148.5 /.41	4.9		10	Caroline Islands Region
8	April 5, 1977	2029:16.8	/0.96	39.34/.024	-12.2 /.12			20	North Atlantic Ocean
3	April 8, 1977	1106:52	/1.2	2.5 /.15	-115.8 /.10	4.6		30	East Central Pacific Ocean
2	April 11, 1977	0215:18.3	/0.18	-52.24/.034	114.66/.047	5.4	5.4	165	South of Australia
3	May 15, 1977	1648:14	/1.7	-35.6 /.29	-85.3 /.12	4.6		11	Southeast Central Pacific Ocean
7	May 26, 1977	0537:13	/1.9	-31.86/.033	167.56/.054	4.6		22	North-west of New Zealand
7	July 4, 1977	0218:29.6	/0.11	-19.12/.008	-148.93/.016			10	Society Islands Region
11	July 25, 1977	2007:44	/1.9	-26.3 /.12	38.4 /.19			16	South Indian Ocean

## Appendix B. (continued)

Age	Date	Time	/s.d.	Lat. /s.d.	Long. /s.d.	mb	Ms	No.	Region
3	July 31, 1977	0108:40.0/0.19		21.26/.032	-47.15/.035	4.8		30	North Atlantic Ridge
3	Aug. 26, 1977	1950:02.3/0.21		-59.54/.051	-20.59/.087	6.3	7.1	334	South-Western Atlantic Ocean
3	Aug. 26, 1977	2238:59.6/0.21		-59.49/.045	-20.24/.068	4.8		35	South-Western Atlantic Ocean
3	Aug. 27, 1977	0016:01.9/0.57		-59.4 / .11	-20.2 / .16	4.4		15	South-Western Atlantic Ocean
3	Aug. 29, 1977	1232:39.6/0.26		-59.61/.057	-21.32/.092	5.2	5.4	86	South-Western Atlantic Ocean
3	Sept. 5, 1977	0923:10.9/0.40		-59.42/.073	-19.9 / .14	5.1		23	South-Western Atlantic Ocean
7	Sept. 13, 1977	0311:50.8/0.09		-21.10/.005	-149.75/.025			10	Tubuai Islands Region
3	Sept. 29, 1977	0528:36.1/0.76		4.2 / .13	-95.0 / .12			12	East Central Pacific Ocean
4	Oct. 3, 1977	0438:35 /1.5		14.12/.038	-48.27/.028	5.0	4.7	118	North Atlantic Ocean
3	Oct. 5, 1977	0221:38.6/0.93		3.9 / .13	-85.6 / .11	4.6		25	Off Coast of Central America
4	Oct. 12, 1977	0053:31 /1.7		14.12/.040	-48.19/.040	5.1	4.6	61	North Atlantic Ocean
4	Oct. 17, 1977	1726:40.4/0.10		-27.93/.020	173.13/.021	6.2	6.7	427	North of New Zealand
4	Oct. 17, 1977	1912:20.3/0.30		-27.95/.034	173.65/.050	4.9		62	North of New Zealand
4	Oct. 18, 1977	0157:55.7/0.32		-27.89/.043	173.22/.055	5.0		44	North of New Zealand
4	Oct. 18, 1977	0546:35.3/0.85		-27.65/.082	173.7 / .13			20	North of New Zealand
4	Oct. 21, 1977	2214:00.5/0.76		-27.71/.032	173.75/.048	5.2		47	North of New Zealand
4	Oct. 22, 1977	0536:03.6/0.98		-27.90/.048	173.83/.073	4.7		19	North of New Zealand
4	Oct. 22, 1977	1748:43.1/0.72		-27.76/.032	173.24/.044	4.9		26	North of New Zealand
4	Oct. 26, 1977	1601:44.8/0.13		-20.77/.022	-126.86/.027	4.9		36	South Pacific Ocean
4	Oct. 29, 1977	1852:53.8/0.33		-20.89/.053	-126.3 / .11	4.7		19	South Pacific Ocean
4	Oct. 31, 1977	0819:15.0/0.21		-20.71/.038	-126.76/.031	5.0	4.2	61	South Pacific Ocean
4	Nov. 5, 1977	0351:24.1/0.16		-20.79/.027	-126.72/.038	4.8		33	South Pacific Ocean
8	Nov. 20, 1977	1939:02 /5.4		20.6 / .41	-62.0 / .21	4.8		10	North Atlantic Ocean
7	Dec. 13, 1977	0114:20.5/0.09		17.33/.018	-54.91/.015	5.7	6.4	395	North Atlantic Ocean
4	Dec. 14, 1977	0300:14 /1.5		-33.84/.03	57.98/.03	5.5	4.7	234	Atlantic-Indian Ridge
7	Dec. 15, 1977	1551:35.7/0.30		-2.30/.041	85.61/.054	4.9		28	South Indian Ocean
2	Dec. 22, 1977	0257:50.4/0.59		10.82/.093	-107.5 / .12	4.9		20	Off Coast of Mexico
4	Jan. 5, 1978	0323:26.2/0.89		-20.79/.023	-126.95/.023	5.5		148	South Pacific Ocean
4	Jan. 30, 1978	1834:22.0/0.24		-16.06/.041	-126.39/.035	5.0		59	South Pacific Ocean
4	Feb. 19, 1978	2358:00.9/0.24		-20.78/.044	-126.6 / .12	4.7		22	South Pacific Ocean
4	March 11, 1978	0332:11.2/0.25		-20.88/.043	-126.86/.052	4.8		43	South Pacific Ocean
7	March 12, 1978	0142:01.5/0.47		-2.91/.085	86.81/.046	4.8		30	South Indian Ocean
4	March 17, 1978	1034:02 /1.7		0.2 / .27	-12.3 / .26	4.9		15	North of Ascension Island
11	March 24, 1978	0042:36.7/0.10		29.68/.016	-67.45/.020	6.0	6.0	448	North Atlantic Ocean
11	March 24, 1978	0532:31.6/0.63		29.64/.051	-67.39/.071			16	North Atlantic Ocean
11	March 24, 1978	1338:04.9/0.64		29.56/.051	-67.61/.092			15	North Atlantic Ocean
10	March 24, 1978	2149:26.7/0.88		41.5 / .15	151.5 / .24	5.4		57	North Pacific Ocean
10	March 26, 1978	0539:14 /1.7		43.1 / .27	153.1 / .41	4.5		14	North Pacific Ocean
2	April 3, 1978	0609:36.6/0.21		-52.21/.037	114.61/.053	5.4		83	South of Australia
3	April 3, 1978	0742:54 /1.0		-28.7 / .22	-10.7 / .13	4.6		19	South Atlantic Ridge
11	April 12, 1978	0029:53 /6.1		30.0 / .38	-67.3 / .37			11	North Atlantic Ocean
4	April 12, 1978	1915:26.5/0.62		-21.2 / .12	-126.2 / .18	4.6		20	South Pacific Ocean
4	April 13, 1978	0600:36.7/0.99		57.08/.02	-36.64/.02	5.2		233	North Atlantic Ocean
3	April 13, 1978	1524:39.7/0.49		-59.59/.080	-19.9 / .17	4.8		15	South-Western Atlantic Ocean
11	April 13, 1978	2115:18 /2.4		29.7 / .18	-67.2 / .11			27	North Atlantic Ocean

## Appendix B. (continued)

Age	Date	Time	/s.d.	Lat. /s.d.	Long. /s.d.	mb	Ms	No.	Region
11	April 15, 1978	1626:10.7	/0.78	29.68/.070	-67.42/.070	4.7		23	North Atlantic Ocean
11	April 19, 1978	1132:17	/1.3	29.83/.099	-67.50/.088	4.2		46	North Atlantic Ocean
11	April 24, 1978	0544:55	/1.1	29.92/.084	-67.6 / .12	4.4		32	North Atlantic Ocean
3	May 3, 1978	1148:38	/1.7	50.45/.07	-31.97/.07	4.4		40	North Atlantic Ridge
11	May 4, 1978	0544:47.3	/0.59	29.93/.044	-67.56/.060	4.4		49	North Atlantic Ocean
3	May 20, 1978	0715:26	/1.5	-3.45/.03	69.70/.03	5.2	4.9	165	Chagos Archipelago Region
6	May 21, 1978	1813:13.4	/0.18	-21.52/.036	87.58/.031	5.0	4.5	82	South Indian Ocean
6	May 29, 1978	0612:54.4	/0.37	66.53/.05	-0.96/.08	4.1		16	Norwegian Sea
7	June 3, 1978	1807:26	/1.2	-16.24/.024	93.03/.028	5.2		172	South Indian Ocean
7	July 1, 1978	0416:36.3	/0.99	-35.0 / .12	166.8 / .11	3.8		15	North-west of New Zealand
3	July 3, 1978	1001:24.1	/0.52	-46.7 / .13	-10.57/.092	4.8		22	South Atlantic Ridge
4	July 13, 1978	1804:19.5	/0.24	-20.73/.042	-127.05/.054	5.0		52	South Pacific Ocean
4	July 25, 1978	0754:08.9	/0.16	-20.75/.029	-126.95/.043	5.1	3.8	63	South Pacific Ocean
4	July 27, 1978	0349:30.4	/0.71	-21.0 / .14	-126.6 / .20	4.5		23	South Pacific Ocean
8	Aug. 3, 1978	0110:26	/1.4	-0.93/.023	84.24/.021	5.5	5.5	316	South Indian Ocean
11	Aug. 11, 1978	0806:23	/1.4	29.6 / .11	-67.82/.087			33	North Atlantic Ocean
6	Sept. 5, 1978	0339:41.3	/0.39	4.30/.09	90.26/.06	4.7		66	Off W. Coast of Northern Sumatra
7	Sept. 25, 1978	1844:01.9	/0.73	-1.57/.092	81.3 / .14	4.7		21	South Indian Ocean
11	Sept. 26, 1978	0651:09.8	/0.49	30.02/.041	-67.57/.056	4.4		28	North Atlantic Ocean
4	Oct. 17, 1978	0814:03.5	/0.61	14.89/.089	-48.10/.085	4.7	3.9	22	North Atlantic Ocean
4	Oct. 18, 1978	0203:57.7	/0.20	-20.93/.030	-126.69/.058	5.0		39	South Pacific Ocean
6	Nov. 3, 1978	1207:14.4	/0.38	-15.70/.070	88.26/.056	4.9		31	South Indian Ocean
4	Nov. 4, 1978	1822:57.0	/0.80	53.98/.072	-139.8 / .10	4.4		17	West of Vancouver Island
7	Dec. 6, 1978	1328:35.8	/0.09	17.44/.017	-54.83/.015	5.4	5.7	236	North Atlantic Ocean
2	Dec. 29, 1978	2237:08	/3.1	-47.9 / .36	127.3 / .24	4.6		14	South of Australia
6	Jan. 20, 1979	0826:18	/1.4	-40.40/.079	155.6 / .15			10	Southeast of Australia
5	Jan. 21, 1979	0546:14	/2.7	32.9 / .17	-131.8 / .22	3.5		19	North Pacific Ocean
5	Feb. 4, 1979	2125:41.9	/0.43	42.40/.062	-149.19/.049	5.1	4.1	90	North Pacific Ocean
4	Feb. 5, 1979	1735:49.2	/0.28	-20.66/.052	-126.90/.041	5.1		75	South Pacific Ocean
3	Feb. 16, 1979	0432:32.4	/0.66	-17.3 / .24	68.5 / .15	5.0		22	Mid-Indian Rise
4	Feb. 26, 1979	0631:53.5	/0.40	-20.99/.072	-126.99/.057	5.0		47	South Pacific Ocean
3	April 7, 1979	0606:51.5	/0.33	32.65/.061	-41.31/.062	4.8		29	North Atlantic Ridge
10	April 19, 1979	1014:39.0	/0.56	42.57/.095	151.3 / .13	4.5		10	North Pacific Ocean
3	May 5, 1979	0759:20.7	/0.84	4.06/.047	-85.76/.059	4.6		45	Off Coast of Central America
8	May 9, 1979	1835:37.1	/0.30	21.15/.037	-61.99/.086	4.7		40	North Atlantic Ocean
4	May 21, 1979	1534:01.4	/0.35	-20.82/.059	-126.64/.079	5.1		34	South Pacific Ocean
2	May 22, 1979	0155:55.8	/0.14	-43.81/.030	79.00/.037	5.5	5.1	109	Mid-Indian Rise
2	May 22, 1979	0204:47	/1.2	-43.9 / .30	79.4 / .26	4.7		17	Mid-Indian Rise
5	May 29, 1979	2100:30.9	/0.64	-51.56/.072	151.6 / .10	4.9		25	North of Macquarie Island
8	June 4, 1979	0128:05	/3.5	21.3 / .26	-61.9 / .12			15	North Atlantic Ocean
2	June 6, 1979	2208:48.8	/0.55	-54.8 / .11	-4.0 / .16	4.5		11	South Atlantic Ridge
4	July 8, 1979	1329:55.8	/0.18	9.21/.038	144.1 / .15	4.7		10	Caroline Islands Region
2	July 30, 1979	1320:56	/1.9	28.2 / .25	-42.9 / .20	4.6		21	North Atlantic Ridge
4	Aug. 18, 1979	1817:04.0	/0.30	-57.00/.048	-58.5 / .14	5.0		51	Scotia Sea
3	Sept. 12, 1979	1326:28.2	/0.69	1.4 / .11	148.6 / .11	5.4	4.2	15	Caroline Islands Region

## Appendix B. (continued)

Age	Date	Time	/s.d.	Lat. /s.d.	Long. /s.d.	mb	Ms	No.	Region
3	Sept. 13, 1979	2000:55.5	0.36	-59.43/.069	-20.1/.12	4.6		23	South-Western Atlantic Ocean
5	Sept. 15, 1979	2326:17	/1.5	21.25/.026	135.23/.043	4.9		47	Philippine Sea
6	Oct. 16, 1979	2251:23.4	0.12	6.37/.02	91.21/.02	5.2		163	Nicobar Islands Region
5	Oct. 23, 1979	1101:40	/1.2	59.7/.22	-53.9/.31	4.6		13	East of Labrador
3	Oct. 28, 1979	2229:07.7	0.25	-34.40/.048	75.29/.046	5.0		27	Mid-Indian Rise
4	Nov. 7, 1979	1131:49.5	0.30	-62.58/.042	-72.9/.16	4.9		37	Southern Pacific Ocean
4	Nov. 20, 1979	0545:00	/2.9	-1.59/.039	65.02/.033	4.9		33	South Indian Ocean
5	Nov. 20, 1979	0645:05.4	0.28	-26.42/.053	-139.08/.054	5.0	6.7	120	South Pacific Ocean
8	Dec. 4, 1979	1959:14	/1.2	39.29/.029	-12.9/.14			20	North Atlantic Ocean
4	Dec. 13, 1979	0243:36.9	0.14	5.55/.023	-80.48/.022	5.4	5.5	211	South of Panama
3	Dec. 30, 1979	1738:17.5	0.48	-36.3/.12	-15.41/.072	4.4		10	Tristan da Cunha Region
4	Jan. 19, 1980	1605:48.3	0.49	5.61/.070	-80.49/.066	4.6		23	South of Panama
6	Jan. 28, 1980	1445:40.4	0.63	-3.27/.099	88.98/.060	4.9	5.3	42	South Indian Ocean
6	Jan. 28, 1980	1446:39.1	0.11	-3.37/.022	88.89/.018	5.3	5.2	207	South Indian Ocean
6	Jan. 28, 1980	1913:11.9	0.77	-3.5/.12	89.02/.061	4.7		24	South Indian Ocean
3	Jan. 30, 1980	0031:14.0	0.46	-5.33/.060	-115.98/.071	5.3	4.2	57	East Central Pacific Ocean
7	Jan. 31, 1980	0132:12.6	0.47	-5.45/.077	81.84/.069	4.8		18	South Indian Ocean
6	Feb. 29, 1980	0910:25.4	0.45	-3.33/.071	88.84/.052	4.8		65	South Indian Ocean
6	March 11, 1980	0624:07.6	0.13	-3.36/.024	88.85/.022	5.2	5.3	151	South Indian Ocean
5	April 24, 1980	2344:39.5	0.20	-48.78/.039	69.24/.058	4.6		29	Kerguelen Islands Region
5	April 25, 1980	1550:04.9	0.68	-48.6/.15	69.5/.21	4.9		19	Kerguelen Islands Region
7	Aug. 18, 1980	2336:10.5	0.24	-2.76/.042	86.83/.036	4.7		39	South Indian Ocean
8	Sept. 8, 1980	2043:45.4	0.17	-26.13/.032	98.18/.029	5.1		104	South Indian Ocean
4	Oct. 17, 1980	1649:25.6	0.44	-7.20/.089	69.52/.080	4.5		22	Chagos Archipelago Region
6	Nov. 22, 1980	1624:26.3	0.71	-12.20/.099	88.05/.087	3.9		22	South Indian Ocean
4	Dec. 25, 1980	2313:07.3	0.98	6.8/.10	147.7/.24	4.4		26	Caroline Islands Region
6	Jan. 9, 1981	1954:56.9	0.45	-12.5/.10	80.56/.067	4.7		20	South Indian Ocean
3	March 6, 1981	1943:00.3	0.14	3.93/.023	-85.88/.025	5.9	6.5	382	Off Coast of Central America
3	March 6, 1981	2349:12	/2.5	3.86/.058	-86.18/.066	5.0	4.7	39	Off Coast of Central America
6	April 6, 1981	2153:21.6	0.25	-57.99/.052	82.50/.079	4.7		14	Kerguelen-Gaussberg Ridge
9	April 12, 1981	1018:29.4	0.16	8.28/.029	85.40/.021	5.2	5.2	219	Bay of Bengal
12	April 18, 1981	0300:26.9	0.34	6.88/.046	159.68/.061	4.8		37	Caroline Islands Region
9	June 3, 1981	2215:14.1	0.22	-5.34/.048	-175.20/.047	5.3	3.9	82	Phoenix Islands Region
4	June 4, 1981	0739:41.5	0.29	-34.16/.049	-78.74/.045	5.1	4.8	90	Juan Fernandez Islands Region
3	Sept. 24, 1981	2109:42.6		-45.65	79.86	5.4	5.5	89	Mid-Indian Rise
3	Sept. 30, 1981	2303:47.5		-4.80	-112.01	5.9	5.2	132	East Central Pacific Ocean
5	Nov. 5, 1981	2111:22.8		-21.61	80.02	5.1		35	South Indian Ocean
6	Dec. 2, 1981	1901:53.9		-15.76	88.39	5.7	5.5		South Indian Ocean
5	Dec. 12, 1981	2331:10.9		4.89	70.15	5.5	5.1		Maldiv Islands Region
4	Feb. 4, 1982	1337:58.1		-6.44	70.79	4.9		22	Chagos Archipelago Region
3	Feb. 8, 1982	1503:07.6		-17.86	-90.06	4.7		12	Southeast Central Pacific Ocean
12	March 22, 1982	0604:10.7		6.65	175.06	5.6	5.4	165	Marshall Islands Region
4	April 10, 1982	0647:51.9		-33.91	58.03	5.6	5.4	128	Atlantic-Indian Ridge
5	April 16, 1982	0252:52.1		-15.64	-137.94	4.8		21	Tuamotu Archipelago Region
1	April 18, 1982	1130:55.3		-28.19	-114.07	5.9	5.8	206	East Pacific Rise

Appendix B. (continued)

Age	Date	Time	/s.d.	Lat. /s.d.	Long. /s.d.	mb	Ms	No.	Region
6	May 9, 1982	1000:56.6		-10.73	94.51	5.5		17	South Indian Ocean
4	June 18, 1982	0304:05.5		-34.03	58.39	5.5		69	South Indian Ocean
7	June 20, 1982	2351:30.4		-28.50	50.79	5.5		46	South Indian Ocean
4	July 24, 1982	1143:38.2		5.62	-79.91	4.9	4.1	60	South of Panama
7	July 31, 1982	2152:06.2		0.90	82.72	5.1		10	South Indian Ocean
4	Sept. 8, 1982	2112:26.2		-34.29	58.08	5.4	5.2	140	Atlantic-Indian Ridge
4	Oct. 15, 1982	1058:39.0		32.87	-125.76	5.1	4.4	86	North Pacific Ocean
4	Oct. 27, 1982	1333:44.0		32.68	-126.02			16	North Pacific Ocean
5	Dec. 17, 1982	2215:16.5		-26.46	84.04	4.7	5.0	16	South Indian Ocean
4	Jan. 6, 1983	1721:25.2		8.07	147.19	5.1		30	Caroline Islands Region
3	Jan. 23, 1983	0600:52.2		-17.94	-96.77	4.4		17	Southeast Central Pacific Ocean
8	Jan. 24, 1983	1634:09.1		39.79	-14.39	5.8	5.5	146	North Atlantic Ocean
7	March 28, 1983	0146:01.4		-2.98	86.14	4.5		19	South Indian Ocean
1	April 29, 1983	0347:29.2		6.98	-104.17	4.9		26	East Central Pacific Ocean
4	July 31, 1983	1026:00.3		-20.13	-126.93	6.0	5.3	212	South Pacific Ocean
4	July 31, 1983	1157:50.0		-20.12	-127.01	5.4		47	South Pacific Ocean
	Aug. 3, 1983	2228:44.6		-22.29	7.46	5.1		64	South Atlantic Ocean
	Aug. 21, 1983	1206:48.1		3.25	87.49	5.3	5.5	101	North Indian Ocean
	Nov. 5, 1983	0052:27.4		31.51	-57.38	5.0		69	North Atlantic Ocean
	Nov. 25, 1983	1956:08.5		-40.44	155.58	6.0	5.8	107	Southeast of Australia
	Nov. 30, 1983	1746:00.4		-6.89	72.12	6.6	7.5	232	Chagos Archipelago Region
	Nov. 30, 1983	1916:33.8		-6.84	72.26	5.4		77	Chagos Archipelago Region
	Nov. 30, 1983	2012:00.7		-6.50	71.43	4.9		10	Chagos Archipelago Region
	Nov. 30, 1983	2109:16.0		-6.59	71.98	4.8		19	Chagos Archipelago Region
	Nov. 30, 1983	2142:08.0		-6.71	71.35	5.5		87	Chagos Archipelago Region
	Nov. 30, 1983	2202:01.0		-6.83	72.31	5.1		50	Chagos Archipelago Region
	Nov. 30, 1983	2205:21.5		-6.87	72.28	5.2		58	Chagos Archipelago Region
	Dec. 1, 1983	0545:34.2		-6.66	71.43	5.9	5.6	140	Chagos Archipelago Region
	Dec. 1, 1983	0657:47.5		-6.48	72.09	5.0		13	Chagos Archipelago Region
	Dec. 1, 1983	0720:06.7		-6.76	71.38	5.1		41	Chagos Archipelago Region
	Dec. 1, 1983	0751:16.7		-6.65	71.30	5.2	4.1	48	Chagos Archipelago Region
	Dec. 1, 1983	0915:30.4		-49.64	-15.62	5.1		10	Southwestern Atlantic Ocean
	Dec. 1, 1983	1222:22.3		-6.76	71.85	5.4		83	Chagos Archipelago Region
	Dec. 1, 1983	1509:07.6		-6.67	71.74	5.1		30	Chagos Archipelago Region
	Dec. 1, 1983	1823:41.4		-6.43	71.34	5.3	4.8	71	Chagos Archipelago Region
	Dec. 1, 1983	2229:29.6		-6.68	71.81	5.4	5.3	101	Chagos Archipelago Region
	Dec. 2, 1983	2038:15.9		-6.53	71.15	5.2	5.0	71	Chagos Archipelago Region
	Dec. 2, 1983	2059:07.1		-6.77	72.20	5.0		28	Chagos Archipelago Region
	Dec. 3, 1983	1155:43.2		-6.65	72.34	5.0		23	Chagos Archipelago Region
	Dec. 3, 1983	1743:14.4		-6.54	71.41	6.3	6.3	196	Chagos Archipelago Region
	Dec. 4, 1983	1306:30.2		-6.81	72.30	5.0		35	Chagos Archipelago Region
	Dec. 5, 1983	0001:35.8		-6.74	71.49	4.8		25	Chagos Archipelago Region
	Dec. 6, 1983	0930:20.4		-6.96	72.35	5.2		36	Chagos Archipelago Region
	Dec. 7, 1983	0132:47.5		-6.75	71.45	4.8		19	Chagos Archipelago Region
	Dec. 7, 1983	0744:09.7		-6.86	71.63	5.0		27	Chagos Archipelago Region

Appendix B. (continued)

Age	Date	Time	/s.d.	Lat.	/s.d.	Long.	/s.d.	mb	Ms	No.	Region
	Dec. 8, 1983	1317:59.5		3.78		149.00		5.9	6.0	78	Caroline Islands Region
	Dec. 12, 1983	1723:13.3		-6.61		71.46		5.3	5.2	89	Chagos Archipelago Region
	Dec. 13, 1983	1647:44.2		-6.40		71.26		5.2		12	Chagos Archipelago Region
	Dec. 20, 1983	1222:34.2		-6.72		72.30		5.1	4.9	26	Chagos Archipelago Region
	Dec. 23, 1983	1809:54.6		-6.60		71.40		5.0	5.1	21	Chagos Archipelago Region
	Dec. 27, 1983	0311:57.7		-6.64		71.19		5.1		59	Chagos Archipelago Region
	Dec. 29, 1983	0551:43.1		-6.61		71.19		5.1	5.4	50	Chagos Archipelago Region



## Code for Lithospheric Ages:

1	0 - 4 m.y.
2	4 - 9 m.y.
3	9 - 20 m.y.
4	20 - 35 m.y.
5	35 - 52 m.y.
6	52 - 65 m.y.
7	65 - 80 m.y.
8	80 - 95 m.y.
9	95 - 110 m.y.
10	110 - 125 m.y.
11	125 - 140 m.y.
12	140 - 160 m.y.
13	> 160 m.y.

Appendix C. Hawaiian seismicity 1964-1979

Age	Date	Time	/s.d.	Lat. /s.d.	Long. /s.d.	mb	Ms	No.	Region
8	Sept. 18, 1964	1025:28.2	0.23	19.38/.06	-155.29/.03	4.7		42	Hawaiian Islands
8	Oct. 11, 1964	1006:43.0	0.18	19.06/.05	-156.63/.04	5.2		97	Hawaiian Islands
8	Dec. 3, 1964	0828:37.6	0.23	19.38/.08	-155.52/.05	4.4		27	Hawaiian Islands
8	Dec. 10, 1964	1153:44.6	0.24	19.40/.05	-155.37/.05	4.7		31	Hawaiian Islands
8	Feb. 13, 1965	2306:28.0	0.20	18.82/.06	-155.44/.07			10	Hawaiian Islands
8	Sept. 5, 1965	1633:21	/1.2	19.1/.15	-155.7/.12	4.5		33	Hawaiian Islands
8	Feb. 2, 1967	0930:44	/1.8	19.5/.14	-155.4/.10	4.5		42	Hawaiian Islands
8	May 4, 1967	0500:31.4	0.74	19.45/.09	-155.53/.07	4.4		37	Hawaiian Islands
8	July 1, 1967	1503:49.1	0.32	19.48/.04	-155.32/.04	4.2		17	Hawaiian Islands
8	Sept. 8, 1967	1222:29.9	0.37	19.39/.04	-155.43/.04	4.1		26	Hawaiian Islands
8	March 31, 1968	1056:12.2	0.23	21.55/.03	-156.97/.02	4.0		22	Hawaiian Islands
8	April 28, 1968	1408:53	/2.9	19.1/.11	-155.56/.03	4.7		47	Hawaiian Islands
8	Aug. 1, 1968	1034:36.0	0.38	19.37/.05	-155.24/.03	4.0		20	Hawaiian Islands
8	Aug. 3, 1968	0436:52.3	0.10	19.87/.02	-155.99/.02			16	Hawaiian Islands
8	Aug. 9, 1968	1104:49	/2.2	19.44/.03	-155.45/.03	4.0		18	Hawaiian Islands
8	Dec. 17, 1968	0233:02.3	0.37	19.35/.05	-155.41/.04	4.5		41	Hawaiian Islands
8	Feb. 22, 1969	2224:17.9	0.53	19.42/.06	-156.50/.04			14	Hawaiian Islands
8	April 9, 1969	1730:53.9	0.21	20.85/.02	-155.93/.02			20	Hawaiian Islands
8	May 7, 1969	1436:01.3	0.41	20.27/.09	-156.06/.08			21	Hawaiian Islands
8	May 10, 1969	0133:27.3	0.38	19.38/.05	-155.34/.03	4.9		58	Hawaiian Islands
8	June 6, 1969	2155:32.1	0.40	19.42/.05	-155.49/.04			12	Hawaiian Islands
8	Sept. 3, 1969	1940:08.3	0.37	19.38/.05	-155.61/.03	4.5		25	Hawaiian Islands
8	Nov. 10, 1969	0512:08.9	0.67	19.22/.07	-155.65/.04			15	Hawaiian Islands
8	Nov. 24, 1969	1912:17.3	0.25	19.76/.05	-156.22/.04			14	Hawaiian Islands
8	Dec. 28, 1969	0259:42.0	0.90	18.9/.11	-156.0/.13	4.3		11	Hawaiian Islands
8	March 18, 1970	1623:26.0	0.75	19.25/.05	-154.99/.04			11	Hawaiian Islands
8	Oct. 25, 1970	1955:23.8	0.20	21.19/.03	-156.65/.03	4.5		21	Hawaiian Islands
8	March 31, 1971	1108:51.9	0.12	20.33/.04	-156.22/.03			14	Hawaiian Islands
8	April 26, 1971	0956:11.5	0.36	19.40/.05	-155.41/.03			28	Hawaiian Islands
8	May 14, 1971	0629:01.8	0.18	19.94/.03	-156.29/.03			24	Hawaiian Islands
8	Aug. 1, 1971	1852:32.9	0.68	18.02/.08	-154.87/.05	4.7		46	Hawaiian Islands
8	Aug. 4, 1971	1136:41.2	0.12	20.03/.02	-155.98/.02			13	Hawaiian Islands
8	Aug. 16, 1971	0135:07	/1.1	19.43/.03	-155.45/.03	4.5		27	Hawaiian Islands
8	March 27, 1972	1600:56.2	0.34	21.14/.04	-156.31/.04			16	Hawaiian Islands
8	Sept. 5, 1972	1131:32.1	0.31	19.34/.04	-155.40/.04	4.4		33	Hawaiian Islands
8	Sept. 6, 1972	0941:03.8	0.45	19.35/.05	-155.23/.04			20	Hawaiian Islands
8	Dec. 23, 1972	1904:45.7	0.90	19.55/.02	-156.10/.02	4.8		62	Hawaiian Islands
8	April 23, 1973	0707:50.4	0.19	20.09/.02	-154.76/.02	4.1		19	Hawaiian Islands
8	April 26, 1973	2026:27	/1.5	20.05/.02	-155.16/.02	5.9	6.1	302	Hawaiian Islands
8	Sept. 16, 1973	0949:10.2	0.25	19.44/.03	-155.36/.03			20	Hawaiian Islands
8	Oct. 1, 1973	1643:04.3	0.13	20.12/.02	-155.90/.02			20	Hawaiian Islands
8	Oct. 9, 1973	1153:41	/1.1	19.40/.02	-155.41/.02	4.8		48	Hawaiian Islands
8	Oct. 9, 1973	1201:00	/1.9	19.35/.04	-155.35/.04			23	Hawaiian Islands
8	Oct. 13, 1973	1611:06.5	0.15	20.56/.02	-156.02/.02			23	Hawaiian Islands
8	Nov. 11, 1973	0938:53.8	0.70	20.56/.05	-155.29/.06			13	Hawaiian Islands

Appendix C. (continued)

Age	Date	Time	/s.d.	Lat. /s.d.	Long. /s.d.	mb	Ms	No.	Region
8	Dec. 13, 1973	1425:54.2	/0.87	19.43/.02	-155.41/.02	4.4		28	Hawaiian Islands
8	Jan. 12, 1974	1604:31.4	/0.34	19.33/.04	-155.22/.03	4.8		41	Hawaiian Islands
8	Feb. 5, 1974	0416:51.3	/0.18	19.54/.02	-155.97/.02			25	Hawaiian Islands
8	Feb. 6, 1974	1439:19.6	/0.21	19.54/.02	-156.46/.02			22	Hawaiian Islands
8	May 5, 1974	1137:21.4	/0.24	19.34/.03	-155.30/.02	4.4		30	Hawaiian Islands
8	June 19, 1974	1505:40.8	/0.39	19.34/.05	-155.50/.04	5.1		61	Hawaiian Islands
8	June 21, 1974	0650:22.2	/0.20	19.35/.02	-155.23/.02			20	Hawaiian Islands
8	Aug. 8, 1974	1112:57	/1.5	19.43/.02	-155.40/.02			25	Hawaiian Islands
8	Aug. 28, 1974	0749:37.2	/0.26	19.33/.03	-155.24/.02			34	Hawaiian Islands
8	Nov. 22, 1974	0749:13.4	/0.20	19.45/.03	-155.38/.02			26	Hawaiian Islands
8	Dec. 15, 1974	2053:44.9	/0.52	19.39/.06	-155.66/.05	4.2		32	Hawaiian Islands
8	Dec. 16, 1974	0917:28.1	/0.36	19.38/.05	-155.50/.05	5.0		64	Hawaiian Islands
8	Dec. 25, 1974	1747:46	/1.2	19.45/.02	-155.39/.02	4.5		39	Hawaiian Islands
8	Dec. 31, 1974	2240:47.8	/0.26	19.33/.04	-155.47/.04	5.4		90	Hawaiian Islands
8	Jan. 1, 1975	0128:58.9	/0.31	19.27/.04	-155.35/.03			15	Hawaiian Islands
8	Jan. 1, 1975	0741:47.6	/0.69	19.08/.06	-155.40/.04			14	Hawaiian Islands
8	Jan. 1, 1975	0745:38	/1.9	20.4 / .31	-155.65/.04	4.0		10	Hawaiian Islands
8	Jan. 1, 1975	1318:58.9	/0.73	18.95/.09	-155.97/.05	4.5		30	Hawaiian Islands
8	Jan. 1, 1975	1320:55.5	/0.37	19.57/.06	-155.60/.04	5.0		57	Hawaiian Islands
8	Jan. 1, 1975	1344:35	/4.7	18.9 / .26	-156.0 / .14	4.6		22	Hawaiian Islands
8	Jan. 2, 1975	0927:52.7	/0.16	19.24/.02	-155.40/.01			11	Hawaiian Islands
8	Jan. 2, 1975	1327:41.4	/0.40	19.19/.05	-155.72/.04	4.5		37	Hawaiian Islands
8	Jan. 5, 1975	0132:07.2	/0.37	19.52/.06	-155.67/.04	5.0		57	Hawaiian Islands
8	May 22, 1975	0832:54	/1.5	20.37/.03	-155.69/.04	4.3		22	Hawaiian Islands
8	May 28, 1975	1201:54	/1.2	18.0 / .16	-153.76/.05	4.4		19	Hawaiian Islands
8	July 5, 1975	0340:53.8	/0.26	19.43/.03	-155.43/.02			20	Hawaiian Islands
8	July 7, 1975	1539:45.1	/0.13	19.50/.01	-155.44/.01			10	Hawaiian Islands
8	July 8, 1975	0047:40.1	/0.62	19.38/.07	-155.40/.06			17	Hawaiian Islands
8	July 8, 1975	0439:49.0	/0.11	19.51/.01	-155.45/.01			19	Hawaiian Islands
8	July 9, 1975	0606:59.1	/0.11	19.50/.01	-155.44/.01			12	Hawaiian Islands
8	July 9, 1975	1349:24.4	/0.25	19.51/.03	-155.44/.02			11	Hawaiian Islands
8	July 9, 1975	1547:39.3	/0.11	19.50/.01	-155.44/.01			12	Hawaiian Islands
8	July 9, 1975	1839:59.6	/0.12	19.52/.01	-155.47/.01			10	Hawaiian Islands
8	Nov. 6, 1975	1205:26.9	/0.21	19.41/.02	-155.39/.02	4.3		27	Hawaiian Islands
8	Nov. 6, 1975	1321:17.2	/0.26	19.40/.03	-155.38/.03			15	Hawaiian Islands
8	Nov. 6, 1975	1402:55.0	/0.28	19.39/.03	-155.39/.03			14	Hawaiian Islands
8	Nov. 10, 1975	1126:29.4	/0.40	19.49/.03	-155.21/.03			13	Hawaiian Islands
8	Nov. 29, 1975	1335:41.0	/0.13	19.48/.02	-155.17/.02	5.7	5.1	215	Hawaiian Islands
8	Nov. 29, 1975	1447:41.1	/0.42	19.46/.03	-155.14/.03	5.9	7.1	342	Hawaiian Islands
8	Nov. 29, 1975	1843:57.8	/0.66	19.23/.08	-155.38/.05	4.8		20	Hawaiian Islands
8	Dec. 3, 1975	0643:49.9	/0.35	19.25/.03	-155.31/.02			12	Hawaiian Islands
8	Dec. 27, 1975	0855:22.6	/0.15	19.94/.02	-155.92/.02			12	Hawaiian Islands
8	Jan. 11, 1976	2226:06.3	/0.33	19.99/.03	-155.71/.04			10	Hawaiian Islands
8	Jan. 12, 1976	0005:39.2	/0.27	19.50/.03	-155.36/.03	4.3		28	Hawaiian Islands
8	Jan. 15, 1976	2259:26.0	/0.28	19.42/.04	-155.46/.03	4.8		55	Hawaiian Islands

## Appendix C. (continued)

Age	Date	Time	/s.d.	Lat. /s.d.	Long. /s.d.	mb	Ms	No.	Region
8	Jan. 17, 1976	0529:09.4	/0.24	19.36/.02	-155.09/.02			14	Hawaiian Islands
8	Jan. 29, 1976	2019:54.2	/0.35	19.40/.05	-155.15/.03	4.5		29	Hawaiian Islands
8	Feb. 21, 1976	0551:13.7	/0.29	20.16/.03	-156.31/.04	5.0		57	Hawaiian Islands
8	April 2, 1976	1814:02.9	/0.49	19.36/.06	-155.17/.03	4.4		24	Hawaiian Islands
8	Dec. 18, 1976	1400:58.8	/0.38	19.31/.05	-155.36/.03	4.9		54	Hawaiian Islands
8	Jan. 12, 1977	1305:56.7	/0.12	19.40/.01	-155.30/.01			10	Hawaiian Islands
8	Jan. 14, 1977	2326:40.0	/0.43	19.33/.05	-155.24/.04	4.5		25	Hawaiian Islands
8	Jan. 23, 1977	2048:58.0	/0.27	19.35/.03	-155.23/.02			14	Hawaiian Islands
8	Feb. 4, 1977	0120:46.9	/0.28	19.36/.04	-155.20/.03	4.5		30	Hawaiian Islands
8	Feb. 4, 1977	1425:07.9	/0.20	20.17/.02	-155.47/.02			12	Hawaiian Islands
8	March 9, 1977	1029:15.8	/0.22	19.42/.03	-155.57/.02			19	Hawaiian Islands
8	April 21, 1977	0449:19.1	/0.18	20.03/.01	-155.33/.02			21	Hawaiian Islands
8	June 6, 1977	0942:17.9	/0.20	19.50/.02	-155.26/.03	4.8		55	Hawaiian Islands
8	July 5, 1977	1759:42.1	/0.10	19.44/.01	-155.47/.01			12	Hawaiian Islands
8	Aug. 8, 1977	0754:20.1	/0.36	19.40/.04	-155.28/.03			18	Hawaiian Islands
8	Aug. 11, 1977	0519:17.1	/0.21	19.35/.02	-155.21/.01			13	Hawaiian Islands
8	Aug. 19, 1977	1819:13.6	/0.07	19.35/.01	-155.12/.01			15	Hawaiian Islands
8	Aug. 30, 1977	1246:21.1	/0.07	19.37/.01	-155.46/.01			12	Hawaiian Islands
8	Sept. 7, 1977	2351:04.8	/0.32	19.39/.03	-155.36/.03			26	Hawaiian Islands
8	Sept. 16, 1977	0450:05.6	/0.14	19.36/.01	-155.09/.01			13	Hawaiian Islands
8	Sept. 19, 1977	1901:45.6	/0.08	19.37/.01	-155.14/.01			13	Hawaiian Islands
8	Sept. 23, 1977	1208:43.7	/0.34	19.33/.02	-155.05/.01			11	Hawaiian Islands
8	Oct. 10, 1977	0038:50.9	/0.45	19.44/.05	-155.36/.04			10	Hawaiian Islands
8	April 8, 1978	0243:43.2	/0.51	19.85/.04	-155.17/.04			10	Hawaiian Islands
8	May 23, 1978	0709:26.3	/0.12	19.31/.01	-155.22/.01			12	Hawaiian Islands
8	June 3, 1978	0102:01.2	/0.36	19.64/.01	-155.16/.01			17	Hawaiian Islands
8	June 13, 1978	1654:01.3	/0.38	19.35/.01	-155.06/.01			11	Hawaiian Islands
8	June 21, 1978	1020:43.9	/0.13	19.32/.01	-155.22/.01			12	Hawaiian Islands
8	June 23, 1978	1147:57.9	/0.30	19.35/.04	-155.34/.03	4.8		30	Hawaiian Islands
8	Aug. 31, 1978	2307:20.2	/0.54	19.05/.05	-155.53/.03			12	Hawaiian Islands
8	Sept. 5, 1978	2026:46.2	/0.20	19.34/.02	-155.23/.02			12	Hawaiian Islands
8	Sept. 12, 1978	0616:05.6	/0.52	19.33/.04	-155.16/.03			10	Hawaiian Islands
8	Nov. 23, 1978	1316:15.1	/0.25	19.23/.02	-155.53/.02			11	Hawaiian Islands
8	Dec. 14, 1978	1412:43.9	/0.51	19.32/.02	-155.23/.02			11	Hawaiian Islands
8	Dec. 27, 1978	1040:55.5	/0.31	19.39/.03	-155.28/.02	4.6		43	Hawaiian Islands
8	Feb. 14, 1979	0252:52.5	/0.32	19.35/.02	-155.07/.02			14	Hawaiian Islands
8	March 6, 1979	1507:57.7	/0.19	19.53/.03	-155.37/.02	5.0		93	Hawaiian Islands
8	March 10, 1979	1355:14.9	/0.64	19.46/.07	-155.28/.05	4.0		13	Hawaiian Islands
8	March 22, 1979	0646:56.9	/0.38	20.13/.04	-155.96/.06	4.5		11	Hawaiian Islands
8	March 28, 1977	0730:08.2	/0.36	20.08/.03	-156.01/.03	4.3		17	Hawaiian Islands
8	March 30, 1979	0906:39.6	/0.35	20.61/.04	-158.86/.04	4.6		52	Hawaiian Islands
8	July 26, 1979	1950:38.6	/0.70	19.75/.02	-156.04/.04			10	Hawaiian Islands
8	July 31, 1979	1330:50.2	/0.26	19.47/.02	-155.45/.02	4.4		12	Hawaiian Islands
8	Aug. 14, 1979	1251:41.3	/0.33	20.62/.02	-156.29/.05	4.0		15	Hawaiian Islands
8	Aug. 16, 1979	2304:18.6	/0.18	19.38/.01	-155.46/.01			11	Hawaiian Islands

Appendix C. (continued)

Age	Date	Time /s.d.	Lat. /s.d.	Long. /s.d.	mb	Ms	No.	Region
8	Sept. 22, 1979	0759:37.6/0.22	19.44/.02	-155.14/.02	5.6	5.0	148	Hawaiian Islands
8	Sept. 27, 1979	1535:45.3/0.32	19.33/.04	-155.14/.02	4.6		23	Hawaiian Islands
8	Oct. 31, 1979	0535:15 /1.2	19.76/.04	-156.09/.08	4.0		12	Hawaiian Islands

Appendix D. Gilbert Islands seismicity 1981-1983

Age	Date	Time	/s.d.	Lat. /s.d.	Long. /s.d.	mb	Ms	No.	Region
10	Dec. 13, 1981	1604:53.4		-3.45	177.55	5.1			Gilbert Islands Region
10	Dec. 13, 1981	1617:05.9		-3.27	177.58	4.5			Gilbert Islands Region
10	Jan. 7, 1982	0842:50.8		-3.39	177.57	5.8	5.4	164	Gilbert Islands Region
10	Jan. 15, 1982	2216:52.1		-3.02	177.64	4.4		11	Gilbert Islands Region
10	Jan. 20, 1982	0158:42.3		-3.36	177.38	5.2	4.9	50	Gilbert Islands Region
10	Jan. 21, 1982	1750:26.3		-3.39	177.43	4.8		10	Gilbert Islands Region
10	Jan. 22, 1982	1321:16.7		-3.42	177.31	4.5		11	Gilbert Islands Region
10	Jan. 24, 1982	1617:35.2		-3.48	177.49	4.9		20	Gilbert Islands Region
10	Jan. 26, 1982	0014:53.0		-3.24	177.31	4.7		11	Gilbert Islands Region
10	Jan. 26, 1982	1616:02.4		-3.37	177.47	5.3		64	Gilbert Islands Region
10	Jan. 27, 1982	1446:01.3		-3.30	177.30	4.9		21	Gilbert Islands Region
10	Jan. 30, 1982	1130:34.1		-3.34	177.72	4.9		26	Gilbert Islands Region
10	Feb. 2, 1982	1958:11.1		-3.35	177.59	4.8		21	Gilbert Islands Region
10	Feb. 3, 1982	0336:45.2		-3.37	177.59	4.9		40	Gilbert Islands Region
10	Feb. 15, 1982	0550:12.2		-3.51	177.48	5.7	5.6	142	Gilbert Islands Region
10	Feb. 18, 1982	0617:39.3		-3.99	177.32	4.7		11	Gilbert Islands Region
10	Feb. 23, 1982	0634:48.3		-3.37	177.42	4.9		38	Gilbert Islands Region
10	Feb. 23, 1982	0908:41.2		-3.14	177.39	5.0		28	Gilbert Islands Region
10	Feb. 23, 1982	0911:04.8		-3.39	177.37	5.4	4.9	105	Gilbert Islands Region
10	March 7, 1982	2157:52.3		-3.04	177.64	5.0		13	Gilbert Islands Region
10	March 10, 1982	2200:05.0		-3.28	177.63	4.9		37	Gilbert Islands Region
10	March 10, 1982	2253:08.6		-3.36	177.52	5.2		71	Gilbert Islands Region
10	March 12, 1982	1720:31.5		-2.98	177.21	4.7		10	Gilbert Islands Region
10	March 13, 1982	0658:55.6		-3.17	177.45	5.0		45	Gilbert Islands Region
10	March 13, 1982	2017:28.6		-3.45	177.53	5.2	4.0	68	Gilbert Islands Region
10	March 14, 1982	0956:39.3		-3.42	177.40	4.9		20	Gilbert Islands Region
10	March 16, 1982	0020:44.0		-3.33	177.53	5.6	5.6	144	Gilbert Islands Region
10	March 17, 1982	0147:23.1		-3.28	177.47	5.0		29	Gilbert Islands Region
10	March 17, 1982	1945:47.9		-3.37	177.57	5.1		42	Gilbert Islands Region
10	March 19, 1982	1549:07.5		-3.28	177.73	5.1		25	Gilbert Islands Region
10	March 21, 1982	0541:33.3		-3.07	177.42	4.9		17	Gilbert Islands Region
10	March 22, 1982	0457:39.3		-3.24	177.34	4.5		10	Gilbert Islands Region
10	March 22, 1982	0539:27.8		-3.55	177.64	4.8		26	Gilbert Islands Region
10	March 22, 1982	0602:51.9		-3.19	177.45	5.0	5.0	33	Gilbert Islands Region
10	March 22, 1982	0722:18.8		-3.21	177.35	4.6		10	Gilbert Islands Region
10	March 22, 1982	0845:58.1		-3.35	177.53	5.4		67	Gilbert Islands Region
10	March 25, 1982	0944:54.9		-3.29	177.82	4.6		10	Gilbert Islands Region
10	March 26, 1982	1130:06.6		-3.23	177.40	5.1		58	Gilbert Islands Region
10	March 27, 1982	0644:18.3		-3.43	177.60	5.2		70	Gilbert Islands Region
10	April 5, 1982	1221:34.0		-3.30	177.35	4.7		18	Gilbert Islands Region
10	April 10, 1982	0143:39.3		-3.29	177.48	5.1		53	Gilbert Islands Region
10	April 13, 1982	2224:25.9		-3.23	177.40	4.5		14	Gilbert Islands Region
10	April 14, 1982	0930:49.6		-3.40	177.52	5.3	4.4	87	Gilbert Islands Region

## Appendix D. (continued)

Age	Date	Time	/s.d.	Lat. /s.d.	Long. /s.d.	mb	Ms	No.	Region
10	April 14, 1982	1538:33.8		-3.55	177.59	4.6		14	Gilbert Islands Region
10	April 15, 1982	0604:37.2		-3.52	177.52	4.8		20	Gilbert Islands Region
10	April 17, 1982	1256:27.7		-3.40	177.45	5.0		37	Gilbert Islands Region
10	April 18, 1982	0923:25.3		-3.39	177.47	5.5	5.5	141	Gilbert Islands Region
10	April 19, 1982	0504:02.5		-3.48	177.57	5.2		60	Gilbert Islands Region
10	April 20, 1982	0808:40.1		-3.45	177.45	4.8		20	Gilbert Islands Region
10	April 21, 1982	0629:37.6		-3.32	177.35	4.8		13	Gilbert Islands Region
10	April 21, 1982	0634:16.3		-3.18	177.22	4.7		10	Gilbert Islands Region
10	April 21, 1982	2336:42.5		-3.45	177.46	4.8		20	Gilbert Islands Region
10	April 22, 1982	0815:02.4		-3.38	177.45	4.8		27	Gilbert Islands Region
10	April 22, 1982	0843:22.4		-3.19	177.19	4.7		19	Gilbert Islands Region
10	April 22, 1982	0956:12.1		-3.46	177.61	5.4	4.8	68	Gilbert Islands Region
10	April 22, 1982	1608:07.9		-3.41	177.56	5.2		46	Gilbert Islands Region
10	April 24, 1982	0610:57.2		-3.31	177.51	5.1		53	Gilbert Islands Region
10	April 25, 1982	1434:59.8		-3.35	177.48	5.3	4.7	58	Gilbert Islands Region
10	April 25, 1982	2102:45.9		-3.23	177.44	4.8		22	Gilbert Islands Region
10	April 26, 1982	0005:09.3		-3.42	177.51	4.8		17	Gilbert Islands Region
10	April 26, 1982	0335:50.6		-3.18	177.24	4.6		11	Gilbert Islands Region
10	April 28, 1982	0430:00.7		-3.42	177.57	5.4	5.1	125	Gilbert Islands Region
10	April 28, 1982	1649:37.2		-3.34	177.47	4.9		28	Gilbert Islands Region
10	May 3, 1982	1443:55.8		-3.20	177.18	4.9		12	Gilbert Islands Region
10	May 8, 1982	1120:14.8		-3.36	177.37	4.7		16	Gilbert Islands Region
10	May 10, 1982	1140:46.5		-3.31	177.39	4.8		34	Gilbert Islands Region
10	May 11, 1982	1300:08.5		-3.52	177.40	4.6		14	Gilbert Islands Region
10	May 12, 1982	0325:22.5		-3.32	177.40	5.0		47	Gilbert Islands Region
10	May 12, 1982	1026:47.0		-3.33	177.33	4.6		18	Gilbert Islands Region
10	May 14, 1982	0722:37.8		-3.28	177.25	4.3		14	Gilbert Islands Region
10	May 17, 1982	0712:48.8		-3.46	177.54	5.5	5.0	136	Gilbert Islands Region
10	May 17, 1982	1300:10.7		-3.35	177.43	5.2	4.4	45	Gilbert Islands Region
10	May 19, 1982	0032:59.4		-3.52	177.44	4.8		11	Gilbert Islands Region
10	May 19, 1982	1315:32.6		-3.49	177.48	4.9		25	Gilbert Islands Region
10	May 23, 1982	2132:35.1		-3.39	177.40	5.9	5.7	176	Gilbert Islands Region
10	May 24, 1982	0125:10.4		-3.40	177.30	4.7		11	Gilbert Islands Region
10	May 24, 1982	1229:15.2		-3.22	177.63	5.0		25	Gilbert Islands Region
10	June 12, 1982	0616:12.5		-3.20	177.55	5.0		30	Gilbert Islands Region
10	July 1, 1982	1833:03.5		-3.22	177.45	5.0		33	Gilbert Islands Region
10	July 2, 1982	0836:36.7		-3.17	177.21	4.8		18	Gilbert Islands Region
10	July 7, 1982	0142:56.8		-3.25	177.47	5.3	5.4	93	Gilbert Islands Region
10	July 11, 1982	0553:50.1		-3.30	177.28	4.6		18	Gilbert Islands Region
10	July 11, 1982	1744:12.9		-3.21	177.55	5.2		80	Gilbert Islands Region
10	July 13, 1982	0603:41.7		-2.55	177.97	4.5		13	Gilbert Islands Region
10	July 13, 1982	1142:17.8		-3.20	177.51	5.3	4.4	61	Gilbert Islands Region
10	July 13, 1982	1349:48.3		-3.31	177.59	5.5	4.3	103	Gilbert Islands Region
10	July 13, 1982	2325:44.1		-3.49	177.63	4.7		13	Gilbert Islands Region
10	July 15, 1982	0213:49.3		-3.34	177.58	5.6	5.0	148	Gilbert Islands Region

## Appendix D. (continued)

Age	Date	Time	/s.d.	Lat. /s.d.	Long. /s.d.	mb	Ms	No.	Region
10	July 15, 1982	2256:13.3		-3.39	177.54	5.2	4.6	67	Gilbert Islands Region
10	July 17, 1982	1832:09.7		-3.25	177.62	5.4	4.4	92	Gilbert Islands Region
10	July 21, 1982	1118:54.7		-3.22	177.41	4.9		22	Gilbert Islands Region
10	July 22, 1982	0509:14.4		-3.29	177.51	5.0		31	Gilbert Islands Region
10	July 22, 1982	0518:12.1		-3.40	177.62	4.9		23	Gilbert Islands Region
10	July 22, 1982	1156:00.5		-3.40	177.52	5.0		51	Gilbert Islands Region
10	July 24, 1982	1135:27.2		-2.87	177.21	4.8		15	Gilbert Islands Region
10	July 25, 1982	1653:32.0		-3.32	177.52	4.9		17	Gilbert Islands Region
10	July 26, 1982	1443:25.8		-3.20	177.65	5.2		53	Gilbert Islands Region
10	July 30, 1982	0928:01.0		-3.25	177.50	4.7		21	Gilbert Islands Region
10	Aug. 2, 1982	0954:25.5		-3.61	177.77	4.6		12	Gilbert Islands Region
10	Aug. 2, 1982	2200:45.0		-3.29	177.60	4.9	4.5	28	Gilbert Islands Region
10	Aug. 2, 1982	2243:27.3		-3.26	177.42	4.7		10	Gilbert Islands Region
10	Aug. 4, 1982	0039:31.1		-3.33	177.71	4.8		34	Gilbert Islands Region
10	Aug. 4, 1982	0137:47.3		-3.35	177.66	4.8		32	Gilbert Islands Region
10	Aug. 5, 1982	1524:23.1		-3.38	177.66	5.2		80	Gilbert Islands Region
10	Aug. 6, 1982	1854:47.3		-3.23	177.55	4.8		14	Gilbert Islands Region
10	Aug. 8, 1982	1316:36.4		-3.27	177.54	4.4		10	Gilbert Islands Region
10	Aug. 9, 1982	0100:35.1		-3.42	177.64	4.8		43	Gilbert Islands Region
10	Aug. 12, 1982	1003:15.5		-3.39	177.57	5.5	5.4	125	Gilbert Islands Region
10	Aug. 12, 1982	1837:34.5		-3.25	177.47	4.7		15	Gilbert Islands Region
10	Aug. 13, 1982	0605:45.1		-3.30	177.60	5.3	4.4	78	Gilbert Islands Region
10	Aug. 13, 1982	2218:12.3		-3.84	177.84	4.7		14	Gilbert Islands Region
10	Aug. 15, 1982	0248:30.7		-3.56	177.66	4.9		30	Gilbert Islands Region
10	Aug. 16, 1982	0803:57.4		-3.46	177.61	4.8		35	Gilbert Islands Region
10	Aug. 16, 1982	2329:49.9		-3.35	177.60	4.7		22	Gilbert Islands Region
10	Aug. 17, 1982	0453:17.9		-3.46	177.62	4.8		21	Gilbert Islands Region
10	Aug. 17, 1982	1518:54.2		-2.83	177.68	4.8		15	Gilbert Islands Region
10	Aug. 18, 1982	1821:00.7		-3.37	177.67	5.2	4.4	70	Gilbert Islands Region
10	Aug. 19, 1982	1633:25.6		-3.42	177.67	5.1		51	Gilbert Islands Region
10	Aug. 21, 1982	1538:03.3		-3.68	177.84	5.0		33	Gilbert Islands Region
10	Aug. 21, 1982	1607:41.0		-3.39	177.71	5.2		94	Gilbert Islands Region
10	Aug. 21, 1982	2045:26.2		-3.51	177.71	4.8		30	Gilbert Islands Region
10	Aug. 24, 1982	2143:39.9		-3.37	177.40	5.3		50	Gilbert Islands Region
10	Aug. 30, 1982	0027:04.4		-3.53	177.72	4.7		22	Gilbert Islands Region
10	Sept. 8, 1982	0713:30.3		-3.28	177.51	5.1		48	Gilbert Islands Region
10	Sept. 9, 1982	0543:52.3		-3.27	177.57	5.4	4.9	124	Gilbert Islands Region
10	Sept. 10, 1982	0143:15.3		-3.43	177.65	5.1		66	Gilbert Islands Region
10	Sept. 12, 1982	0136:06.9		-3.64	177.66	4.3		10	Gilbert Islands Region
10	Sept. 13, 1982	1908:51.7		-3.51	177.58	5.2	5.1	109	Gilbert Islands Region
10	Sept. 14, 1982	0353:42.5		-3.47	177.70	5.4	5.3	133	Gilbert Islands Region
10	Sept. 15, 1982	0047:39.5		-3.55	177.74	4.8		20	Gilbert Islands Region
10	Sept. 16, 1982	0307:58.7		-3.49	177.62	4.8		15	Gilbert Islands Region
10	Sept. 16, 1982	1141:01.0		-3.33	177.60	5.3	4.7	94	Gilbert Islands Region
10	Sept. 16, 1982	1646:02.2		-3.42	177.60	4.9	4.4	49	Gilbert Islands Region



Appendix D. (continued)

Age	Date	Time	/s.d.	Lat. /s.d.	Long. /s.d.	mb	Ms	No.	Region
10	Sept. 17, 1982	0940:41.2		-3.39	177.58	4.8		18	Gilbert Islands Region
10	Sept. 18, 1982	1425:04.1		-3.49	177.73	5.1		50	Gilbert Islands Region
10	Sept. 22, 1982	0412:31.6		-3.68	177.76	4.7		18	Gilbert Islands Region
10	Sept. 24, 1982	2111:28.0		-3.35	177.59	5.1		61	Gilbert Islands Region
10	Sept. 25, 1982	0707:37.5		-3.35	177.43	4.8		27	Gilbert Islands Region
10	Sept. 26, 1982	0946:44.1		-3.43	177.56	4.6		11	Gilbert Islands Region
10	Sept. 26, 1982	1400:49.7		-3.44	177.66	5.4	4.5	115	Gilbert Islands Region
10	Sept. 27, 1982	0517:54.8		-3.68	177.69	4.6		11	Gilbert Islands Region
10	Sept. 28, 1982	0507:14.4		-3.34	177.60	4.9		24	Gilbert Islands Region
10	Oct. 1, 1982	1537:50.7		-3.75	177.76	4.7		10	Gilbert Islands Region
10	Oct. 1, 1982	1552:19.7		-3.60	177.69	4.8		19	Gilbert Islands Region
10	Oct. 3, 1982	0841:29.3		-3.48	177.66	5.1	4.8	89	Gilbert Islands Region
10	Oct. 5, 1982	0409:16.7		-3.49	177.69	5.3	4.8	101	Gilbert Islands Region
10	Oct. 6, 1982	1843:34.7		-3.83	177.85	4.9		17	Gilbert Islands Region
10	Oct. 7, 1982	0259:15.8		-3.65	177.76	4.8		30	Gilbert Islands Region
10	Oct. 7, 1982	0926:02.3		-3.50	177.52	4.7		12	Gilbert Islands Region
10	Oct. 7, 1982	1340:19.2		-3.57	177.73	4.9	4.4	39	Gilbert Islands Region
10	Oct. 9, 1982	1853:02.3		-3.44	177.76	5.3	4.7	102	Gilbert Islands Region
10	Oct. 9, 1982	1940:23.0		-3.47	177.70	5.3		142	Gilbert Islands Region
10	Oct. 15, 1982	0707:58.8		-3.60	177.66	4.8		25	Gilbert Islands Region
10	Oct. 15, 1982	1411:33.6		-3.83	177.77	4.7		10	Gilbert Islands Region
10	Oct. 19, 1982	1350:30.4		-2.75	177.89	4.7		21	Gilbert Islands Region
10	Oct. 22, 1982	0850:31.0		-3.44	177.72	4.9		34	Gilbert Islands Region
10	Oct. 24, 1982	0545:54.7		-3.27	177.50	4.6		13	Gilbert Islands Region
10	Oct. 27, 1982	0146:46.6		-3.41	177.62	4.7		21	Gilbert Islands Region
10	Oct. 28, 1982	0901:43.2		-3.26	177.62	4.7		10	Gilbert Islands Region
10	Nov. 5, 1982	0350:32.2		-3.55	177.71	4.9		20	Gilbert Islands Region
10	Nov. 8, 1982	1648:26.2		-3.68	177.83	5.0		18	Gilbert Islands Region
10	Nov. 9, 1982	0925:20.6		-3.46	177.76	5.2		76	Gilbert Islands Region
10	Nov. 25, 1982	0731:13.4		-3.65	177.81	5.1	4.5	58	Gilbert Islands Region
10	Dec. 8, 1982	1054:12.9		-3.37	177.57	5.2		61	Gilbert Islands Region
10	Dec. 9, 1982	0528:40.1		-3.51	177.68	5.6	5.3	144	Gilbert Islands Region
10	Dec. 17, 1982	1152:57.9		-3.49	177.73	5.1		28	Gilbert Islands Region
10	Dec. 19, 1982	2141:58.5		-2.99	177.78	5.1		32	Gilbert Islands Region
10	Dec. 24, 1982	0157:06.5		-3.86	177.88	4.7		10	Gilbert Islands Region
10	Dec. 26, 1982	0242:08.4		-3.61	177.68	5.0		31	Gilbert Islands Region
10	Dec. 26, 1982	0553:00.0		-3.42	177.61	4.9		13	Gilbert Islands Region
10	Dec. 26, 1982	2359:56.3		-3.39	177.82	4.8		27	Gilbert Islands Region
10	Dec. 28, 1982	2119:05.1		-3.52	177.70	5.0		64	Gilbert Islands Region
10	Dec. 31, 1982	0937:39.4		-3.37	177.57	4.9		11	Gilbert Islands Region
10	Dec. 31, 1982	1341:48.7		-3.56	177.73	5.3	4.4	113	Gilbert Islands Region
10	Jan. 8, 1983	0635:11.3		-3.60	177.71	5.0		31	Gilbert Islands Region
10	Jan. 8, 1983	0723:47.4		-3.54	177.65	5.0		19	Gilbert Islands Region
10	Jan. 11, 1983	0612:43.4		-3.41	177.59	5.0		33	Gilbert Islands Region
10	Jan. 12, 1983	0102:28.7		-3.49	177.62	4.8		26	Gilbert Islands Region

Appendix D. (continued)

Age	Date	Time	/s.d.	Lat.	/s.d.	Long.	/s.d.	mb	Ms	No.	Region
10	Jan. 13, 1983	1344:27.0		-3.26		177.40		4.3		10	Gilbert Islands Region
10	Jan. 21, 1983	1801:06.9		-3.53		177.67		5.2	4.8	71	Gilbert Islands Region
10	Jan. 28, 1983	2101:37.2		-3.03		177.84		4.9		29	Gilbert Islands Region
10	Jan. 31, 1983	2117:31.5		-3.48		177.71		5.8	5.3	141	Gilbert Islands Region
10	Feb. 5, 1983	1707:53.0		-3.50		177.70		5.2		70	Gilbert Islands Region
10	Feb. 5, 1983	2351:45.8		-3.51		177.77		5.8	5.6	160	Gilbert Islands Region
10	Feb. 6, 1983	1615:28.6		-3.58		177.81		5.0		37	Gilbert Islands Region
10	Feb. 13, 1983	1010:52.9		-3.63		177.82		4.6		11	Gilbert Islands Region
10	March 8, 1983	1321:46.9		-3.47		177.63		5.8	5.0	170	Gilbert Islands Region
10	March 8, 1983	1838:07.4		-3.57		177.72		5.1		76	Gilbert Islands Region

Appendix E. Seismograph Station Codes, Locations,  
and Network Affiliation<sup>1</sup>

433

AAE	Addis Ababa, Ethiopia
AAM	Ann Arbor, Michigan, USA
ADE	Adelaide, Australia
AFI	Afiamalau, Western Samoa (also DWSSN)
AKU	Akureyri, Iceland
ALQ	Albuquerque, New Mexico, USA (also HGLP, DWSSN)
ANMO	Albuquerque, New Mexico, USA (SRO)
ANP	Anpu, Taiwan
ANT	Antofagasta, Chile
ANTO	Antofagasta, Chile (SRO)
AQU	Aquila, Italy
ARE	Arequipa, Peru
ATL	Atlanta, Georgia, USA
ATU	Athens University, Greece
BAG	Baguio City, Philippines
BCAO	Rangui, Central African Republic (SRO)
BDF	Brasilia, Brazil (also DWSSN)
BEC	Bermuda (Columbia), Bermuda
BER	Bergen, Norway (DWSSN)
BHP	Balboa Heights, Panama
BKS	Berkeley (Byerly), California, USA
BLA	Blacksburg, Virginia, USA
BOCO	Bogota, Colombia (SRO)
BOG	Bogota, Colombia
BOZ	Bozeman, Montana, USA

BUL Bulawayo, Zimbabwe  
CAI Caico, Brazil  
CAR Caracas, Venezuela  
CCG Camp Century, Greenland  
CHG Chiang Mai, Thailand (also HGLP)  
CHTO Chiang Mai, Thailand (SRO)  
CMC Copper Mine, NWT, Canada  
COL College, Alaska, USA (also DWSSN)  
COP Copenhagen, Denmark  
COR Corvallis, Oregon, USA  
CTA Charters Towers, Australia (also HGLP)  
CTAO Charters Towers, Australia (ASRO)  
DAG Danmarkshavn, Greenland  
DAL Dallas, Texas, USA  
DAV Davao, Philippine Islands  
DUG Dugway, Utah, USA  
EIL Eilat, Israel (also HGLP)  
EPT El Paso, Texas, USA  
ESK Eskdalemuir, Scotland  
FBK Fairbanks, Alaska, USA (HGLP)  
FLO Florissant, Missouri, USA  
FVM French Village, Missouri, USA  
GDH Godhavn, Greenland (also DWSSN)  
GEO Georgetown, Dist. of Columbia, USA  
GIE Galapagos Islands  
GOL Golden (Bergen Pk.), Colorado, USA  
GRFO Graefenberg, German Federal Republic (SRO)

GRM Grahamstown, South Africa  
GSC Goldstone, California, USA  
GUA Guam (Santa Rosa), Mariana Islands  
GUMO Guam, Mariana Islands (SR0)  
HKC Hong Kong, British Crown Colony  
HLW Helwan, Egypt  
HNR Honiara, Solomon Islands  
HON Honolulu, Hawaii, USA (also DWSSN)  
HOW Howrah, India  
IST Istanbul, Turkey  
JAS Jamestown, California, USA (DWSSN)  
JCT Junction City, Texas, USA  
JER Jerusalem, Israel  
KAAO Kabul, Afghanistan (ASRO)  
KBL Kabul, Afghanistan  
KBS Kingsbay, Finland  
KEV Kevo, Finland (also DWSSN)  
KIP Kipapa, Hawaii, USA (also HGLP)  
KOD Kodaikanal, India  
KON Kongsberg, Norway (also HGLP)  
KONO Kongsberg, Norway (ASRO)  
KRK Kirkenes, Norway  
KTG Kap Tobin, Greenland  
LEM Lembang, Indonesia (also DWSSN)  
LON Longmire, Washington, USA (also DWSSN)  
LOR Lormes (Somee), France  
LPA La Plata, Argentina

LPB La Paz, Bolivia  
LPS La Palma, El Salvador  
LUB Lubbock, Texas, USA  
MAIO Mashad, Iran (SRO)  
MAJO Matsushiro, Japan (ASRO)  
MAL Malaga, Spain  
MAN Manila (Diliman), Philippine Islands  
MAT Matsushiro, Japan (also HGLP)  
MDS Madison, Wisconsin, USA  
MHI Mashad, Iran  
MNN Minneapolis, Minnesota, USA  
MSH Mashad, Iran  
MSO Missoula, Montana, USA  
MUN Mundaring, Australia  
NAI Nairobi, Kenya  
NAT Natal, Brazil  
NDI New Delhi (Delhi), India  
NHA Nhatrang, South Vietnam  
NIL Nilore, Pakistan  
NNA Nana, Peru  
NOR Nord, Greenland  
NUR Nurmijarvi, Finland  
NWA0 Mundaring (Narrogin), Australia (SRO)  
OGD Ogdensburg, New Jersey, USA (also HGLP)  
OXF Oxford, New Jersey, USA  
PDA Ponta Delgada, Azores  
PEL Peldehue, Chile

PLM Palomar, California, USA  
PMG Port Moresby, Papua-New Guinea  
POO Poona, India  
PRE Pretoria, South Africa  
PTO Porto (Serro do Pilar), Portugal  
QUE Quetta, Pakistan  
QUI Quito, Ecuador  
RAB Rabaul, New Britain  
RAR Rarotonga, Cook Islands  
RCD Rapid City, South Dakota, USA  
RIV Riverview, Australia  
SBA Scott Base, Antarctica  
SCP State College, Pennsylvania, USA (also DWSSN)  
SDB Sa Da Bandiera, Angola  
SEO Seoul (Keizyo), South Korea  
SHA Spring Hill, Alabama, USA  
SHI Shiraz, Iran  
SHIO Shillong, India (SRO)  
SHK Shiraki, Japan  
SHL Shillong, India  
SJG San Juan, Puerto Rico  
SLR Silverton, Republic of South Africa (also DWSSN)  
SNA Sanae, Antarctica  
SNG Songkhla, Thailand  
SNZO Wellington, New Zealand (SRO)  
SOM Sombrero, Chile  
SPA South Pole, Antarctica

STU Stuttgart, German Federal Republic 438  
 TAB Tabriz, Iran  
 TATO Taipei, Taiwan (SRO)  
 TAU Tasmania University, Australia (also DWSSN)  
 TLO Toledo, Spain (HGLP)  
 TOL Toledo, Spain (also DWSSN)  
 TRI Trieste (Groota Gigante), Italy  
 TRN Trinidad (St. Augustine), Trinidad  
 TUC Tucson, Arizona, USA  
 UME Umea, Sweden  
 UNM Universidad National, Mexico  
 VAL Valentia, Ireland  
 WEL Wellington, New Zealand  
 WES Weston, Massachusetts, USA  
 WIN Windhoek, Namibia  
 ZLP Zongo (La Paz), Bolivia (HGLP)  
 ZOBO Zongo (La Paz), Bolivia (ASRO)

1. Unless otherwise noted, stations are members of the World-Wide Standard Seismograph Network (WSSN). Other codes: ...

DWSSN Digital World-Wide Standard Seismograph Network  
 HGLP High-Gain Long-Period Network  
 SRO Seismic Research Observatory  
 ASRO Abbreviated Seismic Research Observatory